THE UNIVERSITY of MANCHESTER

UMIST

2nd EF Conference in

TURBULENT HEAT TRANSFER

Manchester, UK 1998

DISTRIBUTION STATEMENT A
Approved for public release;
Distribution Unlimited

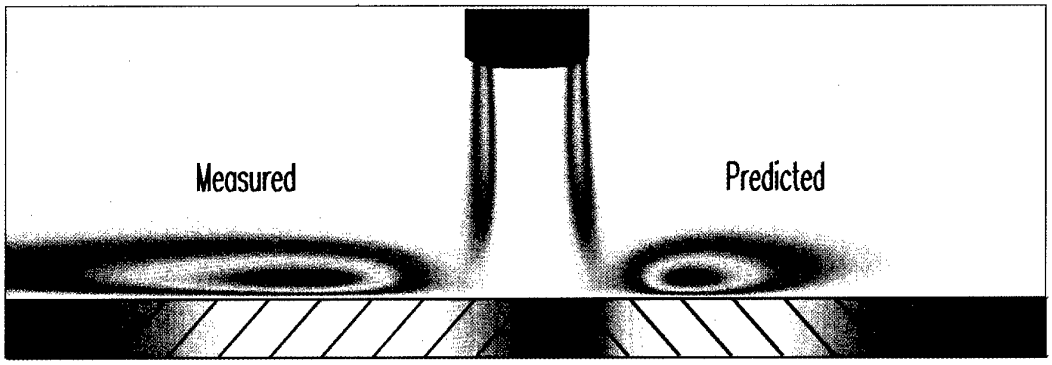

Volume I

ENGINEERING FOUNDATION

2nd International Conference

on

TURBULENT HEAT TRANSFER

Manchester

May 31 - June 4, 1998

Organized by UMIST and the University of Manchester

In collaboration with

ASME Heat Transfer Division

The Engineering Foundation

DISTRIBUTION STATEMENT A
Approved for public release;
Distribution Unlimited

Volume I

19980617 083

Sponsorship of THT-2

The Organizing Committee expresses its sincere appreciation to the following organizations for their support of this conference:

UK Health & Safety Executive
US Air Force
US Army
ABB
Electricité de France
Magnox Electric
Nuclear Electric
Shell Research, Amsterdam

Organizing Committee

Brian Launder, Chairman
Derek Jackson, Co-Chairman
Pepe Humphrey, Nobu Kasagi
Al Ortega, Frank Schmidt

Local Arrangements Committee

Pei An, Brian Axcell, John Byrne
Tim Craft, Shui-Sheng He,
Hector Iacovides, David Jackson
Derek Jackson, Catherine King,
Brian Launder

Scientific Committee

G Bergeles, K Bremhorst, J Coupland
J K Eaton, M Fiebig, K Hanjalic, J Hannis
B V Johnson, T V Jones, D Laurence,
Y Nagano, J M Owen, S Sarkar, A M Savill,
R M C So, K Suzuki, R Viskanta

DTIC QUALITY INSPECTED 1

CONTENTS
VOLUME I

Session 1: Heat Transfer Under Simple Shearing
(Chairmen: B. E. Launder and T. J. Hanratty)

Y. Na, D. V. Papavassiliou and T. J. Hanratty
Use of Direct Numerical Simulation to Study the Effect of Prandtl Number on Temperature Fields 1 - 3

H. Kawamura and H. Abe
DNS of Turbulent Heat Transfer in Channel Flow with Respect to Reynolds-Number Effect 1 -15

K. Matsubara, M. Kobayashi, H. Maekawa and K. Suzuki
DNS of Spanwise Turbulent Heat Transfer in a Channel 1 - 23

D. M. McEligot, A. Mohsen Shehata and T. Kunugi
Prediction of Strongly-Heated Internal Gas Flows 1 - 33

Y. Hagiwara, T. Okuda, M. Tanaka and S. Murai
The Modification of Quasi-Streamwise Vortices in Liquid Turbulent Flow in a Duct by the Injection of Polymer Solution 1 - 48

C. B. Lee
New Observations in Transitional Flat Plate Boundary Layers: Measurement and Visualisation 1 - 54

Session 2: Vertical Mixed and Natural Convection
(Chairman: A. Ortega)

P. Poškas, B. Jazbutis
Experimental Investigation of Turbulent Mixed Convection Heat Transfer in a Vertical Annulus for Aiding Flows 2 - 3

Y. S. Chumakov and S. B. Nikolskaja
Features of Dynamic and Heat Structure of Free Convection Boundary Layer near Vertical Heated Surface. 2 - 9

M. A. Cotton, J. O. Ismael and P.J. Kirwin
Variable Property Mixed Convection: Low-Reynolds-Number and Strain Parameter Eddy Viscosity Model Results 2 - 20

J. Li and J. D. Jackson
Buoyancy-Influenced Turbulent Heat Transfer to Air Flowing in a Uniformly Heated Vertical Tube 2 - 31

Session 3: Flows with Interfaces
(Chairman: N. Kasagi)

V. De Angelis and S. Banerjee
Turbulent Transport Processes Across Fluid-Fluid Interfaces 3 - 3

Session 4: Separating, Impinging and Recovering Flows (Chairmen: G. Hammond and K. Bremhorst)

K. Inaoka, J. Yamamoto and K. Suzuki
Dissimilarity Between Heat Transfer and Momentum Transfer in a Disturbed Turbulent Boundary Layer with Insertion of a Rod 4 - 3

T. J. Craft
Prediction of Heat Transfer in Turbulent Stagnation Flow with a New Second-Moment Closure 4 - 15

K. Bremhorst and N. D. Agnew
Surface Heat Transfer and Flow Structures of Steady and Fully Pulsed Radial Reattaching Jets 4 - 26

W. B. Tsai, W. W. Lin, C. C. Chieng
Computation of Enhanced Turbulent Heat Transfer in a Channel With Periodic Ribs 4 - 39

E. Ya. Epik, L. E. Yushyna and T. T. Suprun
Heat Transfer in Relaxation Zone after a Local Closed Separation of Various Types 4 - 49

S. He, Z. Xu and J. D. Jackson
Buoyancy-Opposed Turbulent Wall Jet Flow down a Vertical Plane Surface 4 - 59

Session 5: Horizontal, Stratified Flows (Chairmen: M. A. Leschziner and K. Hanjalic)

X. Chavanne, F. Chillà, B. Castaing, B Chabaud, B. Hébral and P. Roche
A Cryogenic Experiment for the Rayleigh-Bénard Convection Study 5 - 3

S. Kenjereš and K. Hanjalić
Transient Analysis of Rayleigh-Bénard Convection over Flat and Wavy Walls with a RANS Model 5 - 9

S-H. Peng and L. Davidson
Comparison of Subgrid-Scale Models in LES for Turbulent Convection Flow with Heat Transfer. 5 - 24

C. A. Armitage, B. E. Launder and M. A. Leschziner
Second-Moment Modelling of Combined Turbulent Heat and Species Transfer in Multiply Stratified Fluid Bodies 5 - 36

B. B. Ilyushin
Modelling the Non-Local Turbulent Transport of Momentum, Heat and Substance in the Convective PBL 5 - 48

S. Tsujimura, O. Iida and Y. Nagano
Effects of Rotation on Unstably Stratified Turbulence 5 - 58

Session 6: Engineering Turbulence Models (Chairmen:Y. Nagano and K. Suzuki)

D. E. Musielak
Numerical Simulation of Transverse Hydrogen Injection into Mach 6.3. Airflow and its Effect on Surface Cooling 6 - 3

C. B. Hwang and C. A. Lin
Low-Reynolds Number Modelling of Transpired Flows 6 - 9

T. V. Jones
Theory for the Use of Foreign Gas in Simulating Film Cooling 6 - 22

D. Giebert, R. Koch, A. Schulz and S. Wittig
Evaluation of Advanced Low-Reynolds Number k-ε Turbulence Models for Predicting Convective Heat Transfer 6 - 30

P. M. Wikström and A. V. Johansson
DNS and Scalar-Flux Transport Modelling in a Turbulent Channel Flow 6 - 46

S. Fu and C. Wang
A Proposal for Anisotropic Eddy-Diffusivity Model for Scalar Fluxes 6 - 52

VOLUME II

Session 7: Measurement and Modelling of 3D Separated Flows (Chairmen: D. Laurence and T. V. Jones)

X. Cheng, H. J. Neitzel
Heat Transfer of Naturally Induced Turbulent Convection in Advanced Reactor Containment 7 - 3

H. Iacovides, D. C. Jackson, G. Kelemenis, B. E. Launder and Y-M. Yuan
Recent Progress in the Experimental Investigation of Flow and Local Wall Heat Transfer in Internal Cooling Passages of Gas-Turbine Blades 7 - 14

B. Bonhoff, S. Parneix, J. Leusch, B. V. Johnson, J. Schabacker, A. Bölcs
Experimental and Numerical Study of Developed Flow and Heat Transfer in Coolant Channels with 45 and 90 Degree Ribs 7 - 29

H. Iacovides and M. Raisee
Recent Progress in the Computation of Flow and Heat Transfer in Internal Cooling Passages of Turbine Blades 7 - 42

E. R. Meinders and K. Hanjalić
Vortex Structure and Heat Transfer in Turbulent Flow over a Wall-Mounted Matrix of Cubes 7 - 58

B. P. Axcell, C. Thianpong and J.E. Byrne
Convective Heat Transfer to a Rotating Disk with Roughened Surfaces 7 - 72

Session 8: Large-Eddy Simulation for Industrial Flows (Chairman: J. D. Jackson)

P. R. Voke
Large-Eddy Simulation of Aeronautical Flows 8 - 3

K. Abe and K. Suga
Large-Eddy Simulation of Passive Scalar Fields under Several Strain Conditions 8 - 15

G. Grötzbach, M. Wörner
Direct Numerical and Large Eddy Simulations in Nuclear Applications 8 - 31

Poster Papers

D. J. Bergstrom and X. Huang
Large Eddy Simulation of Natural Convection in a Vertical Slot P - 3

L. Bogusławski
Influence of the Round Jet Flow Structure on the Distribution of Local Heat Transfer and its Fluctuations on Impinged Surface P - 15

P. W. Li, H. Daisaka, Y. Kawaguchi, A. Yabe, K. Hishida, M. Maeda
Experimental Investigation of Heat Transfer Enhancement for Turbulence Drag-Reducing Flow in a Two-Dimensional Channel P - 21

T. G. Karayiannis and Y. S. Tian
An Experimental Estimation of Turbulence Kinetic Energy in Low Turbulence Buoyant Flow P - 30

J-P. Moro, M. Saez and E. Hopfinger
An Experimental Study of Mixed Convection P - 39

A. F. Kurbatskii and S. V. Poroseva
Modelling Turbulent Diffusion in a Rotating Cylindrical Pipe Flow P - 46

S. A. M. Said, A. Al-Farayedhi, M. Habib, S. A. Gbadebo, A. Asghar, S. Al-Dini
Experimental Investigation of Heat Transfer in Pulsating Turbulent Pipe Flow P - 54

A. V. Gorin and D. Ph. Sikovsky
On the Ability of Turbulence Models to Predict the Complex Turbulent Flows: the Application of Scaling Analysis P - 63

V. G. Sviridov, N. G. Razuvanov, A. V. Ustinov
The Effect of Natural Convection of Local Heat Transfer for a Liquid Metal Flow in a Heated Horizontal Tube under a Longitudinal Magnetic Field P - 73

N. F. Yurchenko
Optimization of Heat Transfer Control Based on a Receptivity Approach P - 77

R. W. Hill and K. S. Ball
Direct Numerical Simulations of Turbulent Forced Convection Between Counter-Rotating Disks P - 83

P. Diamessis, D. Bouris and G. Bergeles
Prediction of Grid Turbulence Evolution with a Simple Multifractal Cascade Model P - 99

T. J. Craft
Second-Moment Computations of the Three-Dimensional Thermal Wall Jet P - 115

R. Bridon, G. P. Hammond and G. D Lock
Application of Thermal Imaging to Determine the Heat Transfer Characteristics of Three-Dimensional, Turbulent Wall Jets P - 123

A. V. Starchenko, A. M. Bubenchikov, E. S. Burlutsky
Mathematical Modelling of Heat Exchange by Turbulent Flow of Suspension in a Pipe P - 131

V. V. Ram, S. Lau and M. Kaniewski
A Visualisation Study of the Flow Patterns of Longitudinal Vortices Generated by Winglets in a Channel P - 141

P. Ya. Cherepanov and V. A. Babenko
Dissipative Properties of a Dynamic and Thermal Flat Wake with Negative Net Excessive Momentum in Stratified Flow P - 152

Author Index

Session 1

Heat Transfer under Simple Shearing

USE OF DIRECT NUMERICAL SIMULATION TO STUDY THE EFFECT OF PRANDTL NUMBER ON TEMPERATURE FIELDS

Yang Na, Dimitrios V. Papavassiliou*and Thomas J. Hanratty

University of Illinois at Urbana-Champaign, Urbana, U.S.A.

ABSTRACT

Fully developed turbulent heat transfer is being studied in a channel by using direct numerical solutions of the Eulerian balance equations for Pr=0.05-10 and by using Lagrangian studies, in a DNS, of the dispersion of heat markers from wall sources characterized by Pr=0.1-2400. The principal emphasis of this work is to study the effect of Pr on statistical properties characterizing the scalar field. Turbulent diffusivities are presented for Pr=0.1-2400. A time scale, τ, can be defined from the kinetic energy, k, and the dissipation of turbulence, ϵ, where $\tau = \frac{k}{\epsilon}$. The observed influence of Pr (0.05-10) on a time scale, τ_θ, defined from the dissipation of temperature fluctuations, ϵ_θ, suggests fundamental problems in developing relations for the turbulent diffusivity by a $k_\theta \tau \tau_\theta$ approach or by using τ_θ in developing a relation for $\overline{u_i\theta}$ from a consideration of the momentum and heat balance equations. The observed influence of Pr on the Reynolds transport coefficient, $\overline{u_i\theta}/(\overline{u_i^2})^{\frac{1}{2}}(\overline{\theta^2})^{\frac{1}{2}}$ presents difficulties in estimating $\overline{u_i\theta}$ from $\overline{\theta^2}$. Results for the DNS at Pr=10 are emphasized. Issues that need to be resolved in developing an understanding of turbulent transport are identified. The physics emerges in a more natural way by using a Lagrangian approach. Of particular importance is the recognition that the spectral function for the scalar field extends over a wider range of wavenumbers than does the spectral function for the velocity field and that temperature fluctuations close to the wall result from fluctuations in the heat transfer to the wall, rather than from mixing.

1 INTRODUCTION

The principal theoretical problem in turbulent transport is to relate local rates and temperature fluctuations to the properties of the fluctuating velocity. The classical approach has been to use the analogy which assumes the eddy diffusivity of heat, D^t, is proportional to the eddy kinematic viscosity, ν^t. The implementation of this approach requires the prediction of the turbulent Prandtl number, $Pr^t = \nu^t/D^t$. The modelling of Pr^t has often involved the utilization of the dissipation of the variance of the temperature fluctuations, $\overline{\theta^2}/2 = k_\theta$, in a framework similar to the use of k in k/ϵ equation for the momentum transport [Launder (1), Nagano & Kim (2), Youssef, Nagano & Tagawa (3)]. Another approach has been to develop an equation for the scalar transport term, $\overline{\theta u_i}$ [Launder & Samaraweera (4), Nagano & Tagawa (5,6)]. A critical test for models of scalar-transport is their ability to predict the influence of Prandtl number on statistical parameters that appear in the equations describing the system.

This laboratory has been addressing this question by studying fully developed heat transfer in a channel in which the bottom wall is heated and the top wall is cooled at the same rate so that both walls are kept at constant temperature (T_w and -T_w). Since the velocity and temperature fields are fully developed, the heat fluxes at different distances from the bottom wall are the same. Direct numerical simulations of the Eulerian balance equations for Pr=0.05-10 are being performed. Lagrangian studies involve the study of the dispersion of heat markers from wall sources characterized by Pr=0.1-2400. Preliminary results of these Eulerian and Lagrangian studies were presented at the International Conference on Heat Transfer, held in San Diego in 1996. This paper gives a more complete account. Particularly noteworthy are the DNS results for Pr=10 and the demonstration that Lagrangian methods can be used at arbitrarily large Pr.

Results are presented for the turbulent diffusivity, for the terms in the balance equation for k_θ, for the correlation coefficients, $\overline{\theta u_i}/(\overline{\theta^2})^{1/2}(\overline{u_i^2})^{1/2}$, and for the timescale defined from the thermal dissipation, $\tau_\theta = (\overline{\theta^2}/2)/\epsilon_\theta$. An important conclusion is that the use of τ_θ in developing models for the temperature field is flawed.

2 METHODOLOGY

2.1 Eulerian approach

Numerical solutions are obtained for the three-dimensional, time-dependent Navier-Stokes equation in a skew-symmetric form and the advection-diffusion equation.

$$\frac{\partial \mathbf{u}}{\partial t} = (\mathbf{u} \times \omega) - \nabla \Pi - P_x \mathbf{e}_x + \nabla^2 \mathbf{u}\,, \qquad (1)$$

$$\frac{\partial T}{\partial t} = \mathbf{u} \cdot \nabla T + \frac{1}{Pr} \nabla^2 T\,, \qquad (2)$$

*Mobil Technology, Upstream, SRC, Dallas, TX75244, U.S.A.

where

$$\omega = \nabla \times \mathbf{u} \tag{3}$$

$$\Pi = P - P_x x + (\mathbf{u} \cdot \mathbf{u})/2 \tag{4}$$

and $\mathbf{u}$ and P denote the velocity vector and the static pressure. All variables are made dimensionless by using wall variables. Solutions of equations (1) and (2) are obtained, which are periodic in the streamwise and spanwise directions, by using the algorithm described by Lyons *et al.* (7). The Reynolds number based on the friction velocity and the half-channel height, H, is 150. In presenting the results, x, y, z and u, v, w represent coordinates and velocity components in the streamwise, the wall-normal and the spanwise directions.

The results presented for Pr=10 are for an x, y, z grid of 128 × 193 × 128. The resolution in the y-direction varied from $\Delta y = 0.02$ at the wall to $\Delta y = 2.45$ at the center of the channel. The resolution in the x and z directions were Δx=15, Δz=7.5. Preliminary computations were conducted on a coarse grid and the flow field was interpolated onto the 128 × 193 × 128 grid. A time of about 800 ν/u_τ^2 was required to reach a stationary state and the averaging time was 715 ν/u_τ^2. Averaging was also carried out in the x and z directions so the statistics vary with only y. A memory of 2 gigabytes was required on a HP/Convex-X. Computer runs were also carried out with grids of 128 × 257 × 128 and 128 × 193 × 256 to ensure adequacy of the resolution. These computations were performed for long enough time to get reasonable mean statistics up to second order. The results show the following: (a) A wall-normal resolution of 193 grids is required; higher resolution in this direction improves the mean temperature and root-mean square temperature fluctuation only slightly (peak rms temperature fluctuations differ by 1.6%). (b) The use of a higher resolution in the spanwise direction (256 grid points) does not produce significant changes to the first-order statistics. The turbulent Prandtl number near the wall decreased by about 2.7%.

The results presented in this paper for Pr=0.3, 1 and 3 were obtained for a 128 × 129 × 128 grid for which Δy varied from 0.045 to 3.68. A time of about 1000 was needed to reach a stationary state; averaging was done over a time period of 775, 750, 370 ν/u_τ^2 for Pr=0.3, 1.0 and 3.0, respectively. A memory of 0.7 gigabytes was needed on an HP/Exemplar-S.

A principal focus of this paper are results for calculations with Pr=1, 3 and 10. For Pr=0.3, the ratio of the molecular diffusivity to the turbulent diffusivity is about 1/3. As a consequence, the turbulent diffusivity for Pr=0.3 is qualitatively different from what is found for Pr=1-10, in that molecular diffusion is causing the turbulent diffusivity to decrease because of "leakage" of the thermal tags from eddies [Kontomaris & Hanratty (8)].

2.2 Lagrangian calculations

The trajectories of heat markers released at time t_0 from a infinitesimal source on the wall were calculated in a DNS of channel flow. The Reynolds number based on the half-height of the channel and the friction velocity was 150. The calculations were done with an x, y, z grid of 128 × 65 × 128. The particle tracking method developed by Kontomaris *et al.* (9) was used. Each marker moves due to convective and to molecular effects. The convective part of the motion is calculated from the fluid velocity at the marker position. The effect of molecular diffusion is simulated by imposing a three-dimensional random walk on the particle motion; it is added to the convective part of the motion after each time step, Δt, and takes values from a Gaussian distribution with zero mean and standard deviation $\sigma = \sqrt{2\Delta t/Pr}$, in wall units [Papavassiliou & Hanratty (10); Kontomaris & Hanratty (8)]. A total of 16,128 markers were released on a 127 × 127 grid that covered the bottom wall. The behavior of the markers was followed over a time period of 2,750 wall units. A time step of $\Delta t = 0.25$ was used.

The experiments with instantaneous point sources provide the probability function, $P_1(x - x_0,\ y,\ t - t_0)dx_0dt_0$. A physical interpretation of P_1 is that it represents the evolution in time of the ensemble average of markers released instantaneously from a line source at the wall. Since the flow field is homogeneous in the x and z directions, there is no statistical dependence on the initial location of the point sources.

Probability P_1 can be used to obtain information about the behavior of a continuous line source at x_0 by integrating over time.

$$P_2(x - x_0, y) = \int_0^\infty P_1(x - x_0, y, t - t_0)d(t - t_0) \tag{5}$$

The distribution of mean temperature over a plane source is

$$\overline{T}(x, y) = \int_0^x P_2(x - x_0,\ y)d(x - x_0) \tag{6}$$

The temperature field from a heated bottom wall and a cooled top wall is then given as

$$\overline{T}(x, y) = \int_0^x [P_2(x - x_0, y) - P_2(x - x_0, -y)]d(x - x_0) \tag{7}$$

where y is the distance from the center of the channel. A fully developed temperature profile is obtained by letting $x \to \infty$.

The Eulerian simulations used T_w=constant as the boundary conditions for the mean temperature at the wall. In order to compare Lagrangian results with the Eulerian results, a weight function, $w(t)$,

needs to be introduced so that the number of markers at the wall remains constant throughout the time integration. Equation (6) thus becomes

$$\overline{T}(x,y) = \int_0^{\infty} \int_0^{x} w(t-t_0) P_1(x-x_0, y, t-t_0) \, d(x-x_0) d(t-t_0) \quad (8)$$

with

$$w(t-t_0) = \frac{T_w - T(y=-h, t-t_0)}{T_w} \quad (9)$$

3 RESULTS FROM LAGRANGIAN METHOD

Results from the Lagrangian analysis have been presented by Papavassiliou & Hanratty (10, 11). This section gives a brief review of the findings, in order to enhance the discussion of the effects of Pr on statistical properties of the temperature field. Figure 1 shows a typical path for a thermal marker with Pr=100, that started at the wall, $y = -\frac{H}{2}$, $t = t_0$. The ordinate is the dimensionless time, t, and y_w is the dimensionless distance from the wall. At small times the markers move away from the wall by molecular diffusion. Eventually they become entrained in the turbulence and turbulent motions dominate their dispersion from the wall. The distance from the wall at which the marker becomes entrained in the turbulence increases with decreasing Prandtl number. Three zones are observed: a region where molecular diffusion dominates, a region where there is an interaction between molecular and turbulent diffusion, a region where turbulent diffusion dominates. For very small Prandtl numbers only the first two regions are present. Figure 2 shows the average locations at two different times of a large number of Pr=1 markers that originate at the wall at t=0. This clearly shows that a specific region of space will be primarily affected by markers released over a specific time interval.

Results such as these can be used to calculate the average temperature field at a given distance downstream, x, from the entrance to a section where heat is added to the fluid from the bottom wall at a constant rate and removed from the top wall at the same rate. For large enough x the average temperature field, calculated in this way, was found to equal that given by the DNS described in the previous section [Papavassiliou & Hanratty (11)]. The analysis was used to calculate the mass transfer coefficients, made dimensionless with the friction velocity, that are presented in Figure 3. Results from three separate laboratory studies at Sc = 2400 are also presented, as are results from the DNS. The Lagrangian calculation agrees closely with these measurements. The straight line represents the relation developed by Shaw and Hanratty (12) from their measurements

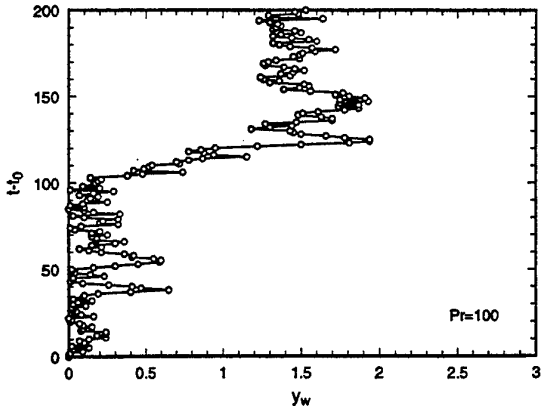

Figure 1: Typical trajectory for a thermal marker with Pr=100.

of mass transfer over a range of Schmidt numbers of 693 to 39,300. These calculations of mass transfer rates and eddy transport coefficients support the controversial suggestion of Shaw and Hanratty that $K \sim Sc^{-0.704}$ at large Sc, rather than as $Sc^{-2/3}$ or $Sc^{-3/4}$. They are represented by $D^t \sim y^{3.38}$ for a large Pr, rather than y^3. Interpretations of this result have been presented [Campbell & Hanratty (13); Hanratty & Vassiliadou (14)], but these have not been confirmed. Calculated mean temperature profiles for Pr=100, 500, 2400 are shown as symbols in Figure 4. The solid lines were calculated using $D^t = by_w^{3.38}$ with $b = 0.000495$. The dotted curves were calculated using $D^t = \nu^t = 0.000792y_w^3$. Here, D^t is made dimensionless with the kinematic viscosity and y_w is the distance from the wall made dimensionless with the friction velocity and the kinematic viscosity.

An interesting comparison between the Lagrangian and Eulerian computations can be made. Both use the turbulent velocity field obtained from a DNS. For the present, the Eulerian calculation is

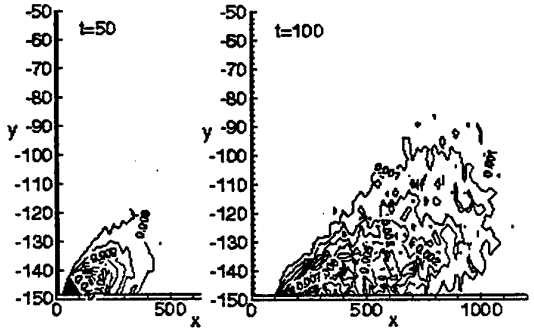

Figure 2: Spatial distributions of Pr=1, heat markers released at the wall at t=0.

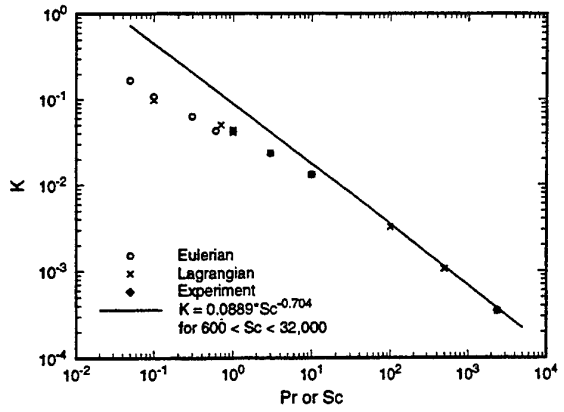

Figure 3: Comparison of values of K obtained by Eulerian and Lagrangian methods. The line indicates measurements for large Sc.

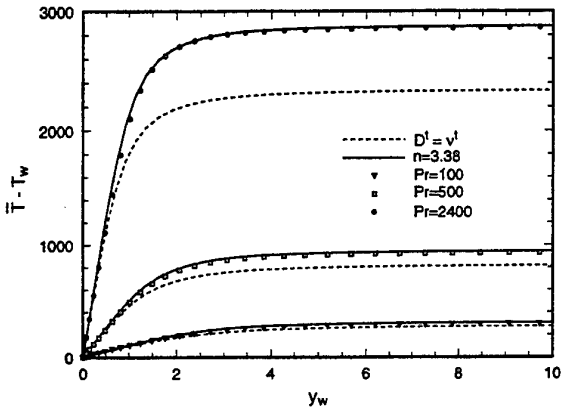

Figure 4: Mean temperature profiles for the high Pr cases close to the wall.

limited to $Pr \leq 10$. However the Lagrangian calculation can be done for arbitrarily large Pr. Another result [Papavassiliou & Hanratty (11)] coming from Lagrangian calculations is that the spatial variation of the turbulent diffusion coefficient observed in the Eulerian analysis is not entirely due to spatial variations of the turbulence - but is strongly affected by the time-dependency of turbulent diffusion. Many aspects of the physics of turbulent transport are understood more clearly with the Lagrangian analysis for the simple case of turbulent flow in channel. To complete this theoretical approach one needs to develop a model for diffusion from a wall source.

4 RESULTS FROM EULERIAN CALCULATIONS

4.1 Mean temperatures

Mean temperatures, obtained from the Eulerian calculations, are shown in Figure 5 for Pr=1, 3 and 10. The abscissa is the distance from the center of the channel made dimensionless with the half height. The ordinate is the mean temperature relative to the centerline temperature divided by the absolute value of the difference of the wall temperature and the centerline temperature. It is seen that as the Prandtl number decreases the temperature profile approaches the straight line relation that would be realized for a laminar flow. Lagrangian results for Pr=1,10 are also presented for comparison. The good agreement provides support for the accuracy of the Eulerian calculations. Figure 6 is a semi-logarithm plot in which the abscissa is the distance from the bottom wall made dimensionless with the friction velocity and the kinematic viscosity. The ordinate is the difference between the local mean temperature and the wall temperature made dimensionless with the friction temperature, $T^* = q_w/\rho c_p u^*$. Even though an extensive well-defined logarithm layer is not expected due to the low Reynolds number considered in the present work, the straight lines represent the equation

$$\frac{\overline{T} - T_w}{T^*} = \frac{1}{\kappa_\theta} \ln y_w + B_\theta \qquad (10)$$

where κ_θ=0.22,0.21,0.23 and B_θ= -1.0,14.7,49.5 for Pr=1, 3, 10. It is noted that the slope $1/\kappa_\theta$ is approximately constant for the Pr considered. These κ_θ are lower than the values of 0.48 obtained by Subramanian & Antonia (15) and 0.45 for measurements in an electrically heated pipe obtained by Johnk & Hanratty (16). This difference in κ_θ is thought to be due to the thermal boundary condition at the wall and much lower Reynolds number considered in the present work. A conductive sublayer exists close to the wall where turbulence is making a negligible contribution to the transfer of heat. Its thickness for Pr=1, 3, 10 is respectively, y_w=6.0, 3.6, 1.9. Thus, the thickness of conductive layer, $\Delta_\theta \sim Pr^{-1/2}$.

4.2 Balance equation for temperature variance

Measures of the magnitude of the temperature and velocity fluctuations are $\overline{\theta^2}$ and $q^2 = \overline{u^2} + \overline{v^2} + \overline{w^2}$. A balance equation for $k_\theta = \overline{\theta^2}/2$, analogous to the balance for $k = q^2/2$, can be written as follows for fully developed flow in a channel:

$$0 = -\overline{\theta v}\frac{dT}{dy} - \frac{1}{2}\frac{d(\overline{\theta^2 v})}{dy} + \frac{1}{Pr}\frac{d^2 k_\theta}{dy^2} - \frac{1}{Pr}\left[\overline{\left(\frac{\partial\theta}{\partial x}\right)^2} + \overline{\left(\frac{\partial\theta}{\partial y}\right)^2} + \overline{\left(\frac{\partial\theta}{\partial z}\right)^2}\right] \qquad (11)$$

where T and θ are the mean and fluctuating temperatures. All variables in this equation (and in subsequent discussions) are made dimensionless with the

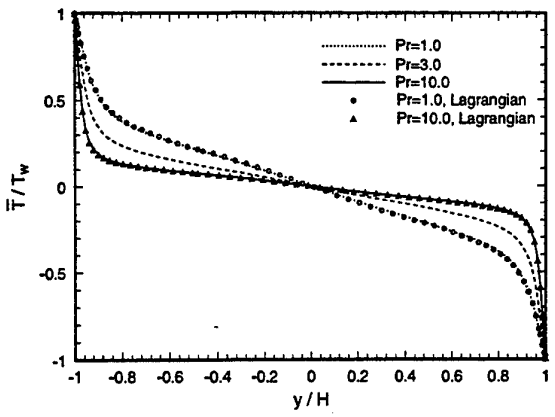

Figure 5: Comparison of mean temperature profiles.

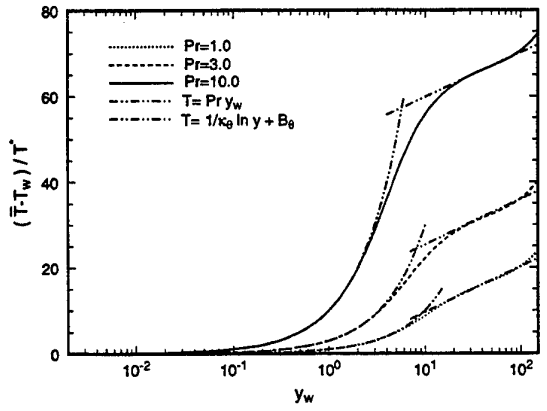

Figure 6: Mean temperature profiles in semi-log coordinate.

friction velocity, u^*, and the friction temperature, T^*. The terms in equation (11) are the production of k_θ, the turbulent transport of k_θ, the molecular transport of k_θ and the dissipation of k_θ, which has been designated as ϵ_θ. A sensitive test that a stationary state has been reached is when the sum of these terms equals zero. For Pr=10, the maximum imbalance, which occurs in the middle of the channel, is about 1.2% of the maximum production. As more samples are added, this imbalance decreases very slowly but the overall shapes of the curve representing terms in the budget hardly change.

Figures 7 and 8 present values of $\overline{\theta v}$ and the production of temperature fluctuations, P_θ, for different Pr. As the Pr increases, the heat flux by the turbulent transport, $\overline{\theta v}$, becomes increasingly important near the wall. In the middle of the channel, the effect of molecular conductivity is relatively small and heat is mainly transported by the turbulence. Due to the finite temperature gradient (Figure 5), the production does not go to zero in the middle of the channel. Sharp maxima in the production are noted close to the wall and a smaller broad maximum is obtained in the center of the channel. Figure 9 presents calculations of the root mean-square of θ. Maxima correspond roughly with the maxima in the production of k_θ. Due to the increase in production with increasing y_w in the middle of channel, temperature fluctuations increase with y_w in this region for all Pr. Plots of the correlation coefficient $R_{\theta u} = \overline{\theta u}/(\overline{\theta^2})^{1/2}(\overline{u^2})^{1/2}$ and $R_{\theta v} = \overline{\theta v}/(\overline{\theta^2})^{1/2}(\overline{v^2})^{1/2}$ are presented in Figures 10-11. The strong decrease of these correlations with increasing Pr is particularly noteworthy. As shown in Figure 7, $\overline{\theta v}$ is higher for higher Pr throughout the channel. Thus, in order to understand the decrease in $R_{\theta v}$, it is useful to look at the behavior of $\overline{\theta v}$ and $\overline{\theta^2}$ in the wavenumber space. Figures 12- 13 are the cumulative spectral density functions of $\overline{\theta v}$ and $\overline{\theta^2}$ versus wavenumber in the streamwise direction, k_x at $y_w = 25$. Plots of $\int_0^{k_x} W_{\theta\theta} dk_x$ show that the contribution from high wavenumber to $\overline{\theta^2}$ increases importance as Pr increases. However, its influence to the cumulative cospectral density function for $\overline{\theta v}$ is relatively small. This is because high wavenumbers do not contribute significantly to $\overline{v^2}$ as they do for $\overline{\theta v}$ at large Pr. Thus, the ratio of $\overline{\theta v}/(\overline{\theta^2})^{1/2}(\overline{v^2})^{1/2}$ decreases as Pr increases. It should be noted that the calculations for Pr=10 in Figure 13 used 256 grid points in the x-direction. This accounts for the larger range of k studied for this condition.

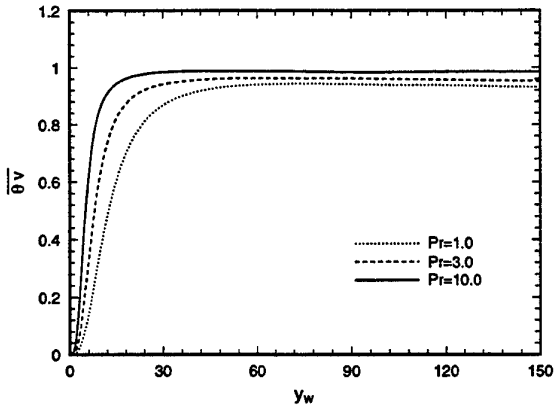

Figure 7: Comparison of $\overline{\theta v}$.

Calculations of ϵ_θ are presented in Figure 14. The very high values close to the wall are in a region where the instantaneous temperature profiles are linear but oscillating in time. Usual practice is to define a term $\tilde{\epsilon}_\theta = \epsilon_\theta - \frac{1}{Pr}\left(\frac{\partial\sqrt{\overline{\theta^2}}}{\partial y}\right)^2$ which does not include the dissipation associated with these oscillations. Thus, the modified dissipation can be repre-

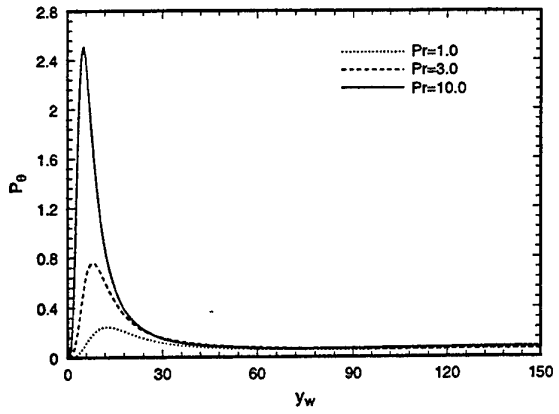

Figure 8: Production of k_θ, P_θ.

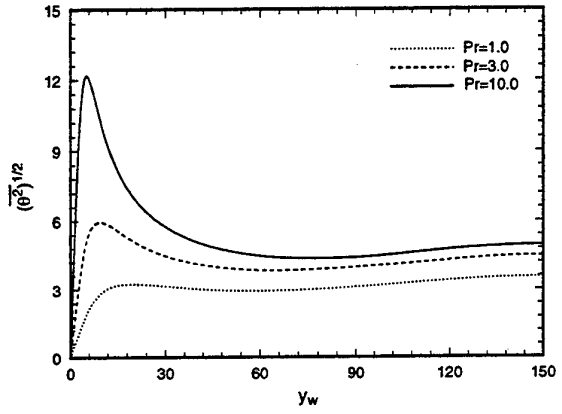

Figure 9: Temperature fluctuations.

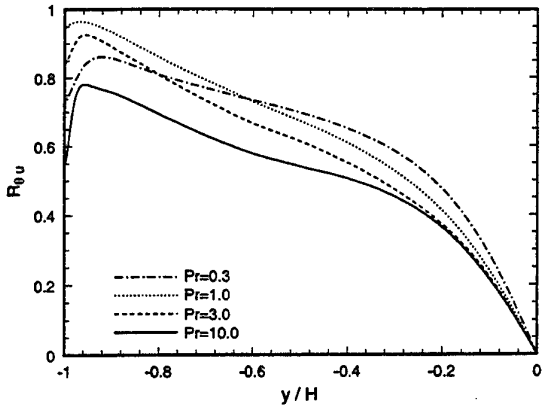

Figure 10: Correlation coefficient $R_{\theta u}$.

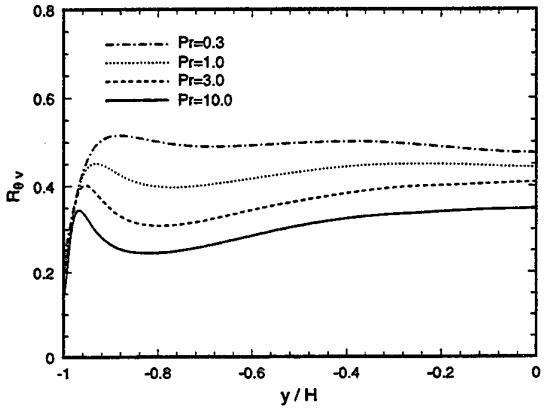

Figure 11: Correlation coefficient $R_{\theta v}$.

sented as follows:

$$\tilde{\epsilon}_\theta = \frac{1}{Pr}\left[\overline{\left(\frac{\partial\theta}{\partial x}\right)^2} + \overline{\left(\frac{\partial\theta}{\partial z}\right)^2}\right] + \frac{1}{Pr}\left[\overline{\left(\frac{\partial\theta}{\partial y}\right)^2} - \left(\frac{\partial\sqrt{\overline{\theta^2}}}{\partial y}\right)^2\right] \quad (12)$$

Values of $\tilde{\epsilon}_\theta$ are presented in Figure 15. One can use equation (12) to define a microscale, analogous to that defined by Talyor for the dissipation of turbulent energy.

$$\tilde{\epsilon}_\theta = \frac{1}{Pr}\frac{\overline{\theta^2}}{2}\left(\frac{1}{\lambda_\theta^2}\right) \quad (13)$$

where

$$\frac{1}{\lambda_\theta^2} = \frac{1}{\lambda_x^2} + \frac{1}{\lambda_y^2} + \frac{1}{\lambda_z^2} \quad (14)$$

The scale, λ_θ is found to decrease with increasing Pr. The plot $\lambda_\theta Pr^{1/3}$ for Pr=0.3, 1.0, 3.0, 10.0 in Figure 16 shows for a fixed Reynolds number that $\lambda_\theta \sim Pr^{-1/3}$. This result is consistent with Figure 13 which shows that the contributions of high wavenumbers to $\overline{\theta^2}$ becomes more important with increasing Pr.

5 RESULTS ON TURBULENT DIFFUSIVITY

A turbulent diffusivity of heat is defined as

$$\overline{\theta v} = D^t \frac{d\overline{T}}{dy} \quad (15)$$

This can be obtained from calculations of $\overline{\theta v}$ and $\frac{d\overline{T}}{dy}$. It can also be calculated from a knowledge of $\overline{T}(y)$ and the heat flux, q_w, at the wall. Since a fully developed condition is considered,

$$q(y) = q_w = -(D + D^t)\frac{(\rho c_p \overline{T})}{dy} \quad (16)$$

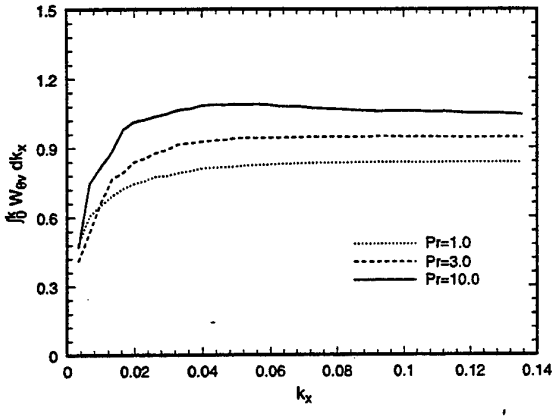

Figure 12: Cumulative co-spectral density function of $\overline{\theta v}$ at y=25.

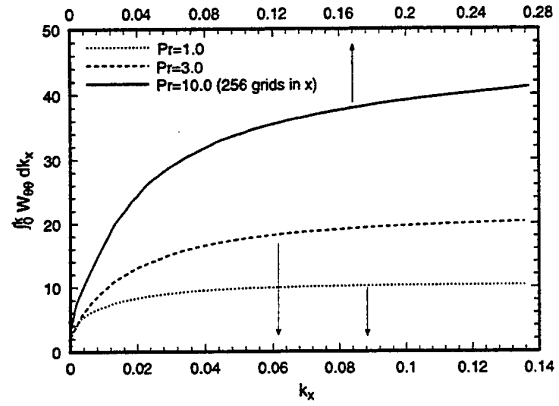

Figure 13: Cumulative spectral density function of $\overline{\theta^2}$ at y=25.

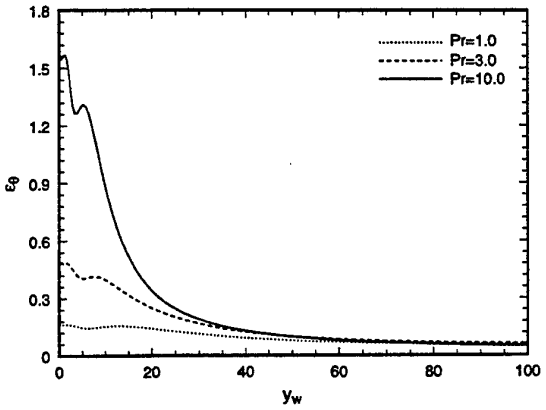

Figure 14: Total dissipation of temperature field.

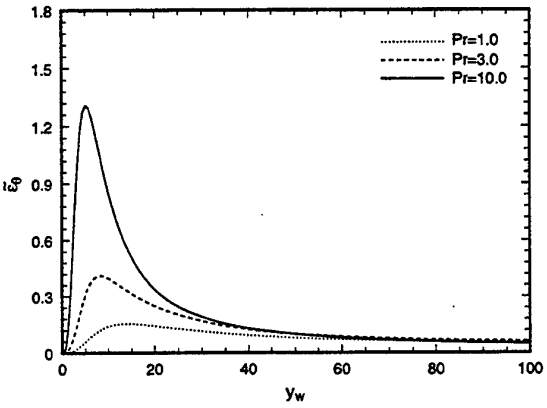

Figure 15: Plot of $\tilde{\epsilon}_\theta = \epsilon_\theta - \frac{1}{Pr}\left(\frac{\partial\sqrt{\overline{\theta^2}}}{\partial y}\right)^2$.

If this is written in a dimensionless form,

$$1 = -\left(\frac{1}{Pr} + D^t\right)\frac{d\overline{T}}{dy} \tag{17}$$

where D^t is made dimensionless with the molecular kinematic viscosity, $\overline{T}$, by the friction temperature and y, by the ratio of the kinematic viscosity to friction velocity. In the Eulerian calculations the same value of D^t was obtained by equations (15) and (17) after a stationary state was reached. In the Lagrangian calculation D^t was obtained from equation (17).

Values of D^t obtained from Eulerian calculations for Pr=1, 3, 10 are presented in Figure 17, along with the values of the turbulent kinematic viscosity, ν^t, obtained for H=150. The turbulent viscosity shown in in this figure was calculated with a 128 × 193 × 128 grid. It is noted in this plot that Pr is not having a strong effect on D^t for $Pr \geq 1$. In the central regions of the channel slight differences are noted. These could be real, but they also could reflect computational issues. As can be seen in Figure 5, the temperature gradient at the center decreases with increasing Pr so that the accuracy of the calculation becomes more important. Furthermore, the computations show that the central regions of the channel come to a stationary state slowly because the convection of temperature is influenced by large scale, small frequency velocity fluctuations. Thus, differences between Pr=1 and Pr=3 calculations could have arisen because insufficient time was allowed to reach a stationary state for Pr=3. This does not seem to be the case for Pr=10, so the difference could be real. However, the velocity field in the Pr=10 calculations was slightly different from that which existed for Pr=1 because a grid with a higher resolution was used. The results in this figure show that the turbulent diffusivities for Pr=1, 3, 10 are approximately equal to the turbulent viscosity for $y_w < 0.15H$ or $y_w < 22$ wall units. A comparison of the maximum ν^t with the maximum

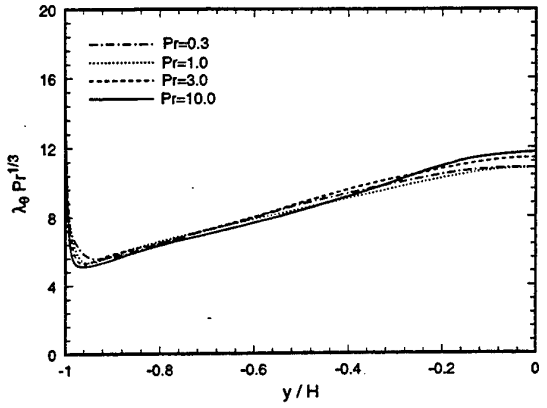

Figure 16: Comparison of $\lambda_\theta Pr^{\frac{1}{3}}$ at different Pr.

D^t for Pr=1 gives a turbulent Prandtl number approximately equal to 0.87 in the center regions of the channel. This is somewhat larger than what has been obtained in calculations for heat transfer from two walls at the same temperature [Antonia & Kim (17)]. This suggests that Pr^t could depend slightly on the boundary conditions for the heat transfer.

The balance of turbulent kinetic energy, k, has a term, ϵ, which represents the rate of energy dissipation. A bulwark of the $k-\epsilon$ model and the Reynolds stress closure model is the definition of a characteristic time scale, τ, by using $\epsilon = k\tau^{-1}$ as a model for ϵ. In the $k-\epsilon$ model the turbulent viscosity is taken as $\nu^t \sim k\tau \sim k^2/\epsilon$. In attempts to use the temperature balance equation to model D^t, an additional time scale, τ_θ has been introduced, which is defined as $\tilde{\epsilon}_\theta = k_\theta \tau_\theta^{-1}$. Assumptions that $D^t \sim k\tau_\theta$ or $D^t \sim k(\tau_\theta \tau)^{1/2}$ have been made [Nagano & Kim (2)]. Calculated values of τ_θ are plotted in Figure 18 for Pr=0.3, 1, 3, 10. Values of τ, calculated from the velocity field with a 128 × 193 × 128 grid, are also presented. Values of τ_θ are seen to be strongly affected by Pr and to have a different shape from τ. Since λ_θ varies as $Pr^{-1/3}$ from the Figure 16, it can be shown that $\tau_\theta \sim Pr^{1/3}$. This suggests that this model for ϵ_θ is flawed unless the effect of Pr on τ_θ can be explained more easily than the effect of Pr on ϵ_θ. Furthermore, relations for D^t of the type given above are inconsistent with the results in Figure 17 which shows a small effect (if any) of Pr on D^t.

The gradient transport model has also been used to calculate the turbulent convection of k_θ, by assuming

$$\overline{u_i\theta^2} = D^t \frac{\partial \overline{\theta^2}}{\partial x_i} \tag{18}$$

Values of $\overline{\theta^2 v}$ are plotted in Figures 19 and 20 for Pr=1 and 10. The curves are plots of $D^t(d\overline{\theta^2}/dy)$. It is seen that the model is fundamentally incorrect (as would be expected). Locations at which $\overline{v\theta^2}$=0 do not correspond to a location where $\frac{\partial \overline{\theta^2}}{\partial x_i}$. However, there is a rough agreement in the locations of maxima in $\overline{v\theta^2}$ and $D^t \frac{\partial \overline{\theta^2}}{\partial y}$.

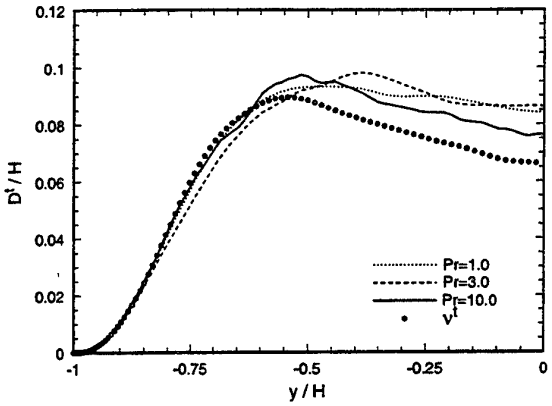

Figure 17: Turbulent diffusivity.

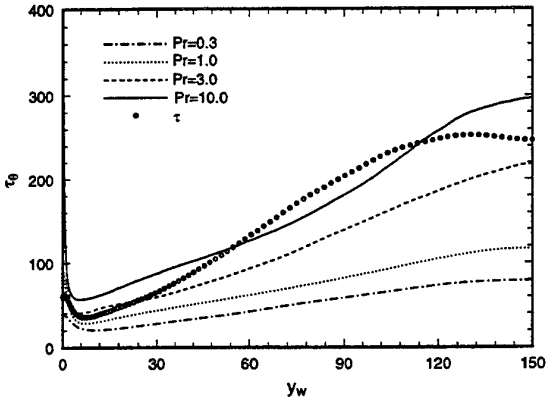

Figure 18: Time scale of temperature field in wall unit.

6 RESULTS CLOSE TO THE WALL

An examination of the temperature profile for Pr=10 in Figures 5 - 6 shows that about 85% of the drop occurs for $y_w < 20$, so the modeling of the region close to the wall is critical. This even becomes more important at large Pr where the heat flux is quite small and the temperature gradient in the central regions (where D^t is large) become negligibly small. Thus, Figure 4 shows that almost all of the temperature change occurs within $y_w < 5$ for $Pr > 100$. Therefore, it is of interest to give special consideration to the calculated temperature field close to the wall. If the fluctuating temperature and velocity fields are expanded in a Taylor series the following equations

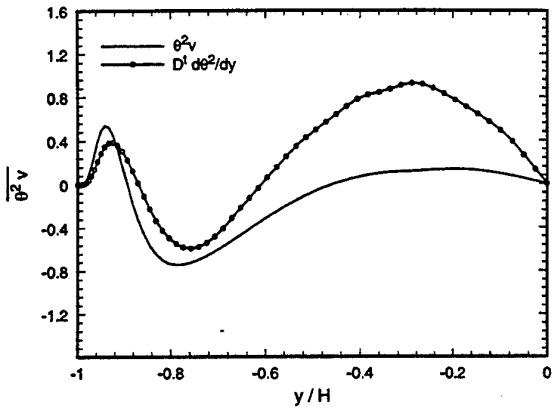

Figure 19: Test of gradient diffusion model for turbulent transport term at $Pr = 1$.

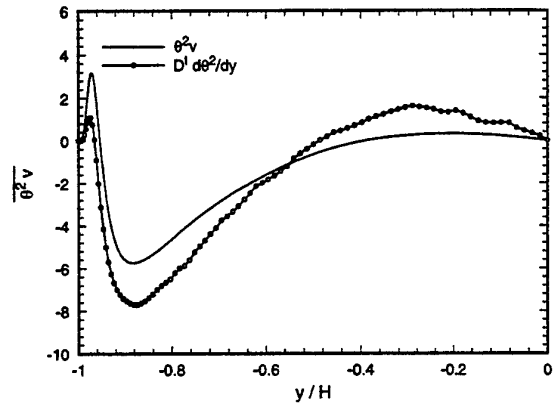

Figure 20: Test of gradient diffusion model for turbulent transport term at $Pr = 10$.

are obtained for a given Pr:

$$\theta = h_1 y_w + h_2 y_w^2 + h_3 y_w^3 + \cdots \quad (19)$$

$$u = b_1 y_w + c_1 y_w^2 + d_1 y_w^3 + \cdots \quad (20)$$

$$v = c_2 y_w^2 + d_2 y_w^3 + \cdots \quad (21)$$

where the coefficients are functions of t and of Pr. Then,

$$\overline{\theta u} = \overline{h_1 b_1} y_w^2 + \overline{(h_1 c_1 + h_2 b_1)} y_w^3 + \cdots \quad (22)$$

$$\overline{\theta v} = \overline{h_1 c_2} y_w^3 + \overline{(h_1 d_2 + c_2 h_2)} y_w^4 + \cdots \quad (23)$$

From equations (15), (17) and (23), the following limiting expression is obtained for the mean temperature profile:

$$\overline{T} - T_w = Pr y_w + \frac{Pr}{4}\overline{h_1 c_2} y_w^4 + \frac{Pr}{5}\overline{(h_1 d_2 + c_2 h_2)} y_w^5 + \cdots \quad (24)$$

Table 1: Limiting values

Pr	1.0	3.0	10.0
$\sqrt{\overline{h_1^2}}$	0.403	1.22	3.93
$\sqrt{\overline{h_1^2}}/Pr$	0.403	0.405	0.393
$\overline{h_1 c_2} \times 10^{-3}$	0.730	2.09	5.03
$\overline{h_1 c_2}/Pr \times 10^{-4}$	7.30	6.98	5.03
$\overline{h_1 b_1}$	0.137	0.372	0.782
$\overline{h_1 b_1}/Pr$	0.137	0.124	0.0782

Values of $\sqrt{\overline{h_1^2}}$, $\sqrt{\overline{h_1^2}}/Pr$, $\overline{h_1 c_2}$, $\overline{h_1 b_1}$ obtained from the Eulerian computations are listed in Table 1. It is noted that $\overline{T} - \overline{T}_w = Pr y_w$ and $(\overline{\theta^2})^{1/2} \approx 0.40 Pr y_w$ for Pr=1, 3, 10 for $y_w \to 0$. However, Table 1 indicates that $\sqrt{\overline{h_1^2}}/Pr$ is not completely independent of Pr so it is likely that $\overline{\theta^2}/\overline{T}^2$ in the limit of $y_w \to 0$ could decrease with Pr. In their study of turbulent mass transfer, Shaw & Hanratty (12) showed that $\frac{\sqrt{\overline{k^2}}}{K} \sim Sc^{-0.09}$ when Sc is large. The result for Pr=10 is in good agreement with this relation. From Table 1 it is seen that $\overline{h_1 c_2}/Pr$ decreases with Pr and is not constant, as suggested by Antonia & Kim (17).

The limiting behavior of D^t is given as

$$D^t = \frac{\overline{h_1 c_2}}{Pr} y_w^3 + \frac{\overline{(h_1 d_2 + c_2 h_2)}}{Pr} y_w^4 - \frac{(\overline{h_1 c_2})^2}{Pr} y_w^6 + \cdots \quad (25)$$

It is seen that the coefficient in the first term in equation (25) decreases with Pr. Therefore, the leading term in the expansion for Pr^t increases with Pr and is not just a function of y_w. Values of D^t are plotted versus y_w, in Figure 21 using log-log coordinates, so as to emphasize the behavior for small y_w. For $Pr = 10$, and for $Pr = 1$, D^t is seen to vary as y_w^3 for $y_w \to 0$; the results for $Pr = 10$ are below those for $Pr = 1$. The thickness of the conductive sublayers for Pr=1, 3, 10 are respectively y_w=6.0, 3.6, 1.9, as mentioned in §4.1.

An examination of Figure 21 shows that the limiting regions for D^t lie within the conductive sublayer so the behavior here is not important in calculating mean temperature profiles. Thus, the often used assumption that mean temperatures in the limit of very large Pr can be calculated by assuming $D^t = c y_w^3$ could be incorrect on two counts: The coefficient is probably a function of Pr and the region where this limiting behavior is valid probably resides in the conductive sublayer, where molecular transport is dominant. It is noted from Figure 21 that, in the region where turbulent transport is important, D^t has the same values for Pr=1, 3, 10. Figure 21 also presents values of D^t obtained from

the Lagragian analysis for Pr=100, 500, 2400. It is to be noted that, in these calculations, D^t is calculated with equation (17); it is not possible to obtain values of D^t in the conductive sublayer, *i.e.*, inside the region where $D^t \sim y_w^3$.

It is noted that the D^t relation for Pr=1 for $y_w < 4$ agrees with the relation for ν^t:

$$D^t = \nu^t = 0.00079 y_w^3 \qquad (26)$$

The values of D^t for Pr=10, 100, 500, 2400 lie below equation (26) for $y_w < 4$. For $Pr \geq 10$ a D^t relation could be developed for small y_w which involves an interpolation between $D^t = (\overline{h_1 c_2}/Pr) y_w^3$ for $y_w \to 0$ and equation (26) for larger y_w. In this relation $(\overline{h_1 c_2}/Pr)$ would decrease weakly with Pr. The results presented in Figure 21 and in Figure 4 for Pr=100, 500, 2400 indicate that the influence of turbulent transport is controlled by the intermediate region between the limiting behaviors and that D^t is fitted reasonably well with the relation $D^t = 0.000463 y_w^{3.38}$. From the viewpoint of doing practical calculations at large Pr, the above relation could be used up to $y_w = 5.0$ and D^t can be taken as equal to ν^t for $y > 5.0$. As already pointed out by Campbell & Hanratty (13) and by Hanratty & Vassiliadou (14), the influence of Pr on the limiting behavior of D^t can be related to its influence on $\overline{\theta^2}/\overline{T}^2$ for $y_w \to 0$. Velocity fluctuations in the immediate vicinity of the wall cause fluctuations in rate of heat transfer, which control the fluctuating temperature and $\overline{\theta v}$ in this region. Since the heat transfer rate cannot respond to velocity fluctuations with very high frequencies, the conductive sublayer acts as a low pass filter. This ineffectiveness of high frequency velocity fluctuations increases with increasing Pr. A consequence of this is that the limiting behavior of $\overline{\theta^2}/\overline{T}^2$ and of D^t are affected by Pr. The outcome is just the opposite of what is found in the central regions of the channel where the spectrum for $\overline{\theta^2}$ shows an increase in the contributions of large wavenumber temperature fluctuations with increasing Pr. This behavior is illustrated in Figures 22 - 23 which show the spectra of $\overline{\theta^2}$ and $\overline{\theta v}$ at y_w=0.2. In the vicinity of the wall, high wavenumbers do not contribute significantly to $\overline{\theta^2}$ as they do away from the wall (Figure 13).

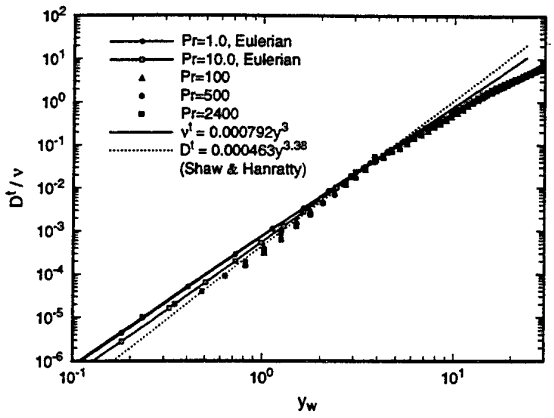

Figure 21: Turbulent conductivity close to the wall of the channel for high Pr or Sc numbers.

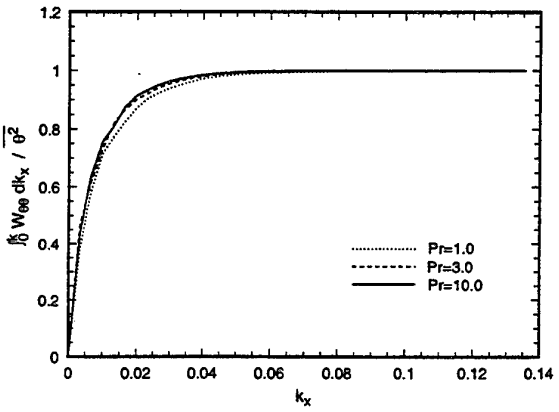

Figure 22: Cumulative spectral density function of $\overline{\theta^2}$ at $y_w = 0.2$.

7 CONCLUSION

For $Pr \geq 1$ and for $y_w > 5$, the influence of Prandtl number on D^t is quite small. However, large effects of Pr on $\overline{u_i \theta}/(\overline{u_i^2})^{\frac{1}{2}}(\overline{\theta^2})^{\frac{1}{2}}$, $\overline{\theta^2}$, τ_θ and λ_θ are observed. This can be understood by recognizing that the range of wavenumbers associated with the fluctuating temperature field increases with Pr. At large Pr the spectral function for $\overline{\theta^2}$ can extend to wavenumbers for which the spectral functions for the velocity field are close to zero [Batchelor (18), Tennekes & Lumley (19)]. However, the correlation between the velocity and temperature fluctuations is determined by a range of wavenumbers which is approximately independent of Pr. These results suggest that τ, rather than τ_θ is a more significant time scale characterizing turbulent transport of heat [This seems to be what was suggested by Horiuti (20)]. A corollary of this observation is that the use of a turbulent Prandtl number to relate scalar transport to the velocity field could be a sensible approach. In fact, the assumption that $D^t = \nu^t$ is a good approximation for the viscous wall region (beyond $y_w = 5$) and the log layer. In the outer flow, $D^t > \nu^t$ and the turbulent Prandtl number depends on the boundary conditions. The Lagrangian methods developed by Papavassiliou & Hanratty (10, 11) could provide an opportunity to explore these effects.

For Pr=1 the turbulent Prandtl number is unity for $y_w < 5$. At small y_w the turbulent diffusivity increases as y_w^3 for all Pr. However, D^t/y_w^3

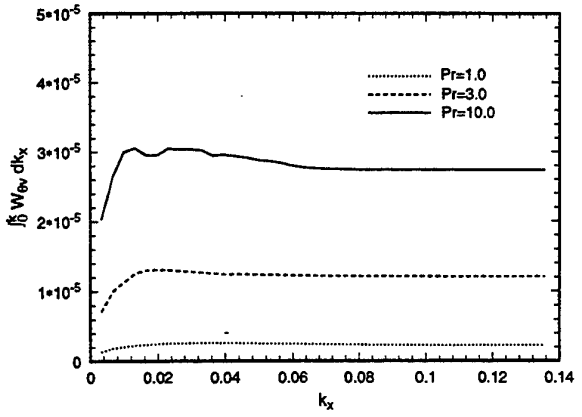

Figure 23: Cumulative co-spectral density function for $\overline{\theta v}$ at $y_w = 0.2$.

decreases weakly with increasing Pr as $y_w \to 0$. This can be understood if it is recognized that temperature fluctuations in this region are mainly governed by fluctuations in the rate of heat transfer at the wall, rather than hydrodynamic mixing of hot and cold fluid.

The thickness of the region where $D^t \sim y_w^3$ decreases with increasing Pr. However, it always lies in the conductive sublayer where turbulent transport is negligible compared to molecular transport; that is, turbulent effects in this region are not directly influencing the mean temperature profile. For very large Pr almost all of the temperature change occurs in the viscous sublayer where $\nu^t \sim y_w^3$. Because of this, the agreement is commonly made that temperature or concentration profiles can be calculated by assuming $D^t \sim y_w^3$. The results outlined above suggests that this approach is incorrect.

If D^t is known, the dependency of $\overline{\theta^2}$ on y and on Pr can be calculated from the balance equation for k_θ, but expressions for the dissipation and transport terms are needed. The dissipation can be represented by equation (13). For the range of Pr covered by the Eulerian calculations, λ_θ varies roughly with $Pr^{-1/3}$. The explanation of this dependency resides in understanding the effect of Pr on the spectral function for $\overline{\theta^2}$. The use of the gradient transport model, equation (18), gives only a crude representation of the turbulent transport of k_θ. The examination of the transport terms fro $Pr = 1$ and 10 suggests that the introduction of a proportionality constant in equation (18) will not provide a quick fix. However, the transport terms are not large, so even a rough approximation might be satisfactory.

Acknowledgements- This work is being supported by the National Science Foundation through grant CTS-95-03000. Computer resources have been provided by the National Center for Supercomputer Applications (NCSA), Urbana and the Computing Center at University of Kentucky, Lexington.

Nomenclature

c_p specific heat at constant pressure

D^t turbulent diffusivity

H half channel height

K mass transfer coefficient

k turbulent kinetic energy or fluctuating mass transfer coefficient

k_x streamwise wavenumber

k_θ twice the mean-square temperature fluctuations

n exponent that describes the variation of D^t with the distance from the wall

P pressure

P_x streamwise pressure gradient

P_θ production of $\overline{\theta^2}$

Pr Prandtl number

Pr^t turbulent Prandtl number

q heat flux

q^2 $u^2 + v^2 + w^2$

q_w heat flux at the channel wall

$R_{\theta u}$ correlation coefficient of θ and u

$R_{\theta v}$ correlation coefficient of θ and v

Sc Schmidt number

T temperature

$\overline{T}$ mean temperature

T_w temperature at the wall

T^* friction temperature

t time

u, v, w fluctuating velocity components in the x, y, z directions

$W_{\theta\theta}$ spectral density function for $\overline{\theta\theta}$

$W_{\theta v}$ co-spectral density function for $\overline{\theta v}$

x, y, z streamwise, normal and spanwise coordinates

y_w distance from the lower wall made dimensionless by wall variables

w weight function

Greek symbols:

Δ_θ thickness of conductive layer

ϵ dissipation of turbulent kinetic energy

ϵ_θ dissipation of temperature fluctuations

$\tilde{\epsilon}_\theta$ $\epsilon_\theta - \frac{1}{Pr}\left(\frac{\partial\sqrt{\overline{\theta^2}}}{\partial y}\right)^2$

κ_θ von Karman constant for temperature

λ_x Taylor microscale in the x direction

λ_y Taylor microscale in the y direction

λ_z Taylor microscale in the z direction

λ_θ Taylor microscale defined by $\frac{1}{\lambda_\theta^2} = \frac{1}{\lambda_x^2} + \frac{1}{\lambda_y^2} + \frac{1}{\lambda_z^2}$

ν kinematic viscosity

ν^t turbulent viscosity

ω vorticity vector

Π pseudo pressure

ρ fluid density

τ time scale of velocity field

τ_θ time scale of temperature field

θ fluctuating temperature

u^* friction velocity

References

(1) Launder, B. E., *Heat and Mass Transport* in *Turbulence*, edited by Bradshaw, P., 1978, Springer-Verlag, Berlin, pp. 231-287.

(2) Nagano, Y. and Kim, C., A two-equation model for heat transport in wall turbulent shear flow, *Journal of Heat Transfer*, 1988, vol. 100, pp. 583-589.

(3) Youssef, M. S., Nagano, Y. and Tagawa, M., A two-equation heat transfer model for predicting turbulent thermal fields under arbitrary wall thermal conditions, *Int. J. Heat Mass Transfer*, vol. 35, no. 11, pp. 3095-3104.

(4) Launder, B. E. and Samaraweera, Application of a second-moment turbulence closure to heat and mass transport in thin shear layer flows-I. Two-dimensional transport, *Int. J. Heat Mass Transfer*, 1979, 22, pp. 1631-1643.

(5) Nagano, Y. and Tagawa, M., Statistical characteristics of wall turbulence with a passive scalar, *J. Fluid Mech.*, 1988, 196, pp. 157-185

(6) Nagano, Y. and Tagawa, M., A structural turbulence model for triple products of velocity and scalar, *J. Fluid Mech.*, 1990, 215, pp. 639-657.

(7) Lyons, S. L., Hanratty, T. J. and McLaughlin, J. B., Large-scale computer simulation of fully developed turbulent channel flow with heat transfer, *Numerical Methods with Fluids*, 1991, 13, pp. 999-1028.

(8) Kontomaris, K. and Hanratty, T. J., Effect of molecular diffusivity on point source diffusion in the center of a numerically simulated turbulent channel flow, *Int. J. Heat Mass Transfer*, 1994, 37, pp. 1817-1828.

(9) Kontomaris, K., Hanratty, T. J. and McLaughlin, J. B.,, An algorithm for tracking fluid particles in a spectral simulation of turbulent channel flow. *Journal of Computational Physics*, 1992, 103, pp. 231-242.

(10) Papavassiliou, D. and Hanratty, T. J., The use of Lagrangian methods to describe turbulent transport of heat from a wall, *Industrial Engineering Chemical Research*, 1995, vol. 34, pp. 3359-3367.

(11) Papavassiliou, D. and Hanratty, T. J., Transport of a passive scalar in a turbulent channel flow, *Int. J. Heat Mass Transfer*, 1997, vol. 40, no. 6, pp. 1303-1311.

(12) Shaw, D. A. and Hanratty, T. J., Turbulent mass transfer to a wall for large Schmidt numbers. *A.I.Ch.E Journal*, 1977, 2, pp. 28-37.

(13) Campbell, J. A. and Hanratty, T. J., Mechanism of turbulent mass transfer at a solid boundary, *A.I.Ch.E. Journal*, 1983, 29, pp. 221.

(14) Hanratty, T.J. and Vassiliadou, E., Turbulent transfer to a wall at large Schmidt numbers, In *Transport phenomena in turbulent shear flows. Theory, Experiment and Numerical Simulation*, edited by Hirata and N. Kasagi. Hemisphere, New York, 1988, pp. 255-274.

(15) Subramanian, C. S. and Antonia, R. A., Effect of Reynolds number on a slightly heated turbulent boundary layer, 1981, *Int. J. Heat Mass Transfer*, vol. 24, no. 11, pp. 1833-1846.

(16) Johnk, R. E. and Hanratty, T. J., Temperature profiles for turbulent flow of air in a pipe-I. The fully developed heat transfer region, 1962, *Chemical Engineering Science*, vol. 17, pp. 867-879.

(17) Antonia, R. A. and Kim, J., Turbulent Prandtl number in the near-wall region of a turbulent channel flow, *Int. J. Heat Mass Transfer*, 1991, vol. 34, no. 7, pp. 1905-1908.

(18) Batchelor, G. K., Small-scale variation of convective quantities like temperature in a turbulent fluid, part1, *J. Fluid Mech.*, 1967, 5, pp. 113.

(19) Tennekes, H. and Lumley, J. L., A first course in turbulence, 1972, The MIT press, Cambridge.

(20) Horiuti, K., Assessment of two-equation models of turbulent passive-scalar diffusion in channel flow, *J. Fluid Mech.*, 1992, 238, pp. 405-433.

DNS OF TURBULENT HEAT TRANSFER IN CHANNEL FLOW WITH RESPECT TO REYNOLDS-NUMBER EFFECT

H. Kawamura and H. Abe

Department of Mechanical Engineering, Science University of Tokyo
Noda-shi, Chiba, 278, Japan

Y. Matsuo and K. Yamamoto

National Aerospace Laboratory
Choufu-shi, Tokyo, 182, Japan

ABSTRACT

The direct numerical simulation (DNS) of turbulent heat transfer in a channel flow has been carried out for $Pr = 0.025$, 0.2 and 0.71 with $Re_\tau = 180$ and 395 to investigate Reynolds number effect on the turbulent heat transport. The statistical quantities such as temperature variance, turbulent heat fluxes, turbulent Prandtl number and time scale ratio are obtained and the effect of the Reynolds number is examined. Budget terms of temperature variance and turbulent heat fluxes are also calculated. The instantaneous flow and thermal fields are visualized in order to investigate the structures of streaks and vortices.

1 INTRODUCTION

The direct numerical simulation (DNS) of turbulent heat transfer is now widely performed for various configurations. Among them, the DNS of the fully developed turbulent channel flow has often been performed because of its simple geometry and fundamental nature to understand the convective heat transfer between fluid and a solid wall. The first attempt on this subject was made by Kim-Moin [1] for $Pr = 0.1$, 0.71 and 2.0 with $Re_\tau = 180$, where Pr is the Prandtl number and Re_τ is the Reynolds number based on the wall friction velocity and the channel half width δ. Later, Kasagi et al. [2] and Kasagi-Ohtsubo [3] made the DNS for $Pr = 0.71$ and 0.025 with a slightly lower Reynolds number of $Re_\tau = 150$. They obtained the budget of the transport equations for the temperature variance, turbulent heat flux and their dissipations. More recently, Kawamura et al. [4,5] performed the DNS for a wider range of Prandtl numbers from $Pr = 0.025$ up to 5.0 with $Re_\tau = 180$.

As seen above, the DNS's of the turbulent heat transfer in the channel flow have been performed for Reynolds numbers not more than $Re_\tau = 180$, which corresponds to $Re_m = 5600$ based on the mean velocity and the channel width. Since this Reynolds number is rather low, the logarithmic and the wake regions can hardly be distinguished.

On the other hand, the Reynolds number of the DNS for turbulent channel flow itself has not been raised also for long time. Shortly after the well-known DNS with $Re_\tau = 180$ by Kim et al. [6] , the same group performed the one with a higher Re_τ of 395 (Kim et al. [7] , Antonia-Kim [8]).

To the author's knowledge, however, no higher Reynolds number was calculated. Recently, the present author's group (Kawamura [9]) performed a DNS with higher Reynolds numbers of $Re_\tau = 395$ and 640. In the present work, their DNS of $Re_\tau = 395$ is extended to the scalar tranport with Prandtl number of 0.025, 0.20 and 0.71. The results are compared with those of $Re_\tau = 180$ (Kawamura [4,5]) and the effect of the Reynolds number is discussed.

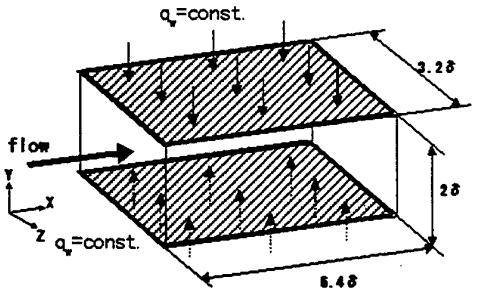

Figure 1: Calculation domain

2 FUNDAMENTAL EQUATIONS AND COMPUTATIONAL METHOD

The flow is assumed to be fully developed and heated by a uniform heat flux q_w from both walls. Calculation domain is shown in Fig. 1. The velocity and temperature are normalized by the half channel width δ, the friction velocity u_τ, the kinematic viscosity ν and the friction temperature $T_\tau (= q_w/\rho c_p u_\tau)$.

The fundamental equations are the continuity

Table 1: Computational and visualized conditions

Grid		Staggered Grid
Coupling Algorithm		Fractional Step Method
Time Advancement	Viscous Terms	2nd-order Crank-Nicolson Method (y-direction)
	Others	2nd-order Adams-Bashforth Method
Discretization Scheme	Nonlinear Terms	2nd-order Central Scheme (Consistent)
	Viscous Terms	2nd-order Central Scheme
Boundary Condition		Periodic(x, z direction), Non-slip (y-direction)
Grid Number		$128 \times 66 \times 128$, $256 \times 128 \times 256$
Computational Volume		$6.4\delta \times 2\delta \times 3.2\delta$
Visualized Volume		$3.2\delta \times \delta \times 1.6\delta$
Reynolds Number		$Re_\tau = 180, 395$
Prandtl Number		$Pr = 0.025, 0.2, 0.71$

equation:

$$\frac{\partial u_i^+}{\partial x_i^*} = 0, \tag{1}$$

and the Navier-Stokes equation:

$$\frac{\partial u_i^+}{\partial t^+} + u_j^+ \frac{\partial u_i^+}{\partial x_i^*} = \frac{\partial p^+}{\partial x_i^*} + \frac{1}{Re_\tau} \frac{\partial^2 u_i^+}{\partial x_j^{*2}}. \tag{2}$$

In this case, the statistically averaged temperature increases linearly with respect to x^*. Then the instantaneous temperature $T^+(x^*, y^*, z^*)$ can be divided into two parts

$$T^+(x^*, y^*, z^*) = \frac{d\left\langle \overline{T}_m^+ \right\rangle}{dx^*} x^* - \theta^+(x^*, y^*, z^*), \tag{3}$$

where $\left\langle \overline{T}_m^+ \right\rangle$ is the so-called mixed mean temperature defined as

$$\left\langle \overline{T}_m^+ \right\rangle = \int_0^1 \overline{u}_1^+ \overline{T}^+ dy^* / \int_0^1 \overline{u}_1^+ dy^*, \tag{4}$$

In the present configuration, its streamwise gradient becomes

$$\frac{d\left\langle \overline{T}_m^+ \right\rangle}{dx^*} = 1/\left\langle \overline{u}^+ \right\rangle, \tag{5}$$

where $\left\langle \overline{u}^+ \right\rangle$ is the average velocity over the channel section. With the above transform, the energy equation becomes

$$\frac{\partial \theta^+}{\partial t^+} + u_j^+ \frac{\partial \theta^+}{\partial x_j^*} = \frac{1}{Re_\tau \cdot Pr} \frac{\partial^2 \theta^+}{\partial x_j^{*2}} + \frac{u_1^+}{\left\langle \overline{u}^+ \right\rangle}. \tag{6}$$

The boundary conditions are

$$u_i^+ = 0, \quad \theta^+ = 0 \quad \text{at } y = 0 \text{ and } 2\,\delta. \tag{7}$$

The simulation is made with use of the finite difference method in which a special attention is paid to the consistency between the analytical and numerical differential operations (Kawamura [10]). The method was confirmed to give good agreements with the spectral method (Kawamura-Kondo [11]). The present numerical scheme consistent with the analytical operation ensures the balance of the transport equations for the statistical correlations such as the turbulent heat flux and the temperature variance. To perform a DNS with a higher Reynolds number, a larger grid size of $256 \times 128 \times 256$ is adopted. The calculation is carried out with use of a parallel computer called as Numerical Wind Tunnel (NWT) located at National Aerospace Laboratory.

The computational and visualized conditions are given in Table 1.

3 RESULTS

3.1 Velocity field

To examine the obtained velocity field, the mean velocity profile and the rms of the Reynolds normal stress are shown to be compared with those by Kim et al. [7] in Figs. 2 and 3. Although a small discrepancy is observed, the agreement is good enough.

3.2 Mean temperature profile

The mean temperature is given for two Reynolds numbers of 180 and 395 and for Prandtl numbers of 0.025, 0.20 and 0.71 in Fig. 4. Those by Kasagi's group ($Pr = 0.025$ and 0.71 for $Re_\tau = 150$) are also plotted for comparison. The logarithmic region can be better distinguished from the wake region with increase of the Reynolds and Prandtl numbers.

The Karman constant of the mean temperature profile (κ_θ) is obtained and shown in Fig. 5. In case of $Re_\tau = 180$, no plateau is observed for $Pr = 0.2$; while for $Pr = 0.71$, κ_θ exhibits a plateau. In case of $Re_\tau = 395$, the plateau can be seen for both $Pr = 0.2$ and 0.71. Moreover, κ_θ decreases

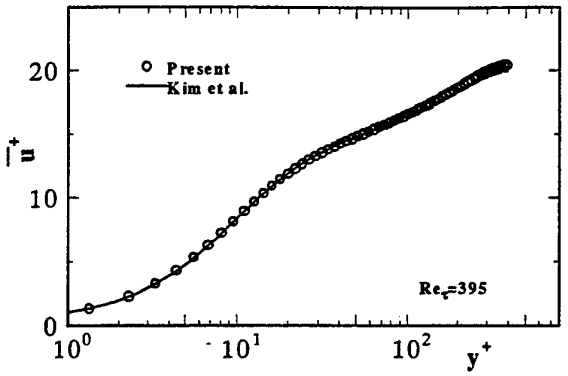

Figure 2: Mean velocity profile

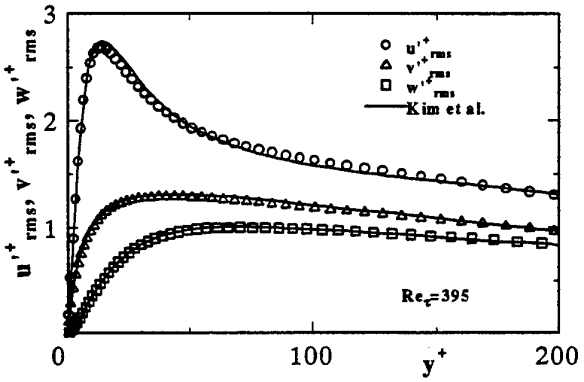

Figure 3: Rms of Reynolds normal stress

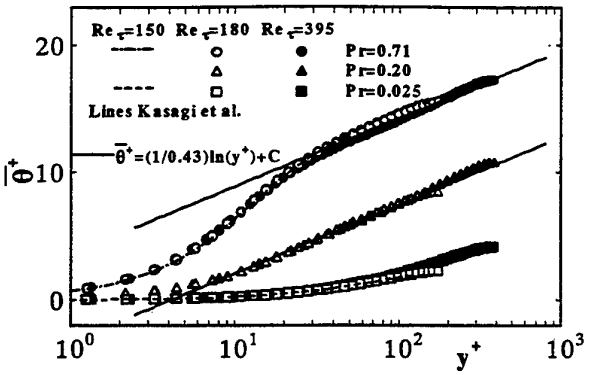

Figure 4: Mean temperature profile

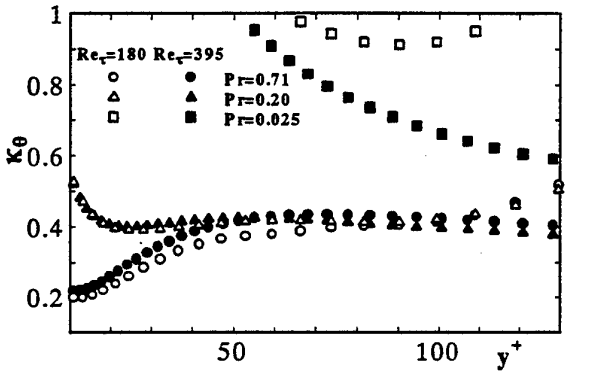

Figure 5: κ_θ of mean temperature

significantly after the plateau, which corresponds to the distinction between the logarithmic and wake regions. It is interesting to note that, in case of $Re_\tau = 395$, the values of κ_θ for $Pr = 0.71$ and 0.2 becomes roughly independent of Prandtl number for $y^+ > 50$. This means the semi-logarithmic plots of the mean temperature becomes parallel for $Pr > 0.2$, which can be confirmed in Fig. 4.

Kader [12] proposed $\kappa_\theta = 0.47$ independently upon Pr in his empirical correlation. The present DNS supports the independence; however, the value of the κ_θ itself is somewhat smaller than his proposal ($\kappa_\theta \simeq 0.42 \sim 0.45$) and is closer to the Karman constant of the mean velocity profile.

3.3 Wall-normal turbulent heat flux

Since the fully developed condition is assumed, the turbulent wall normal and the molecular heat fluxes satisfy the following relation.

$$q^+_{total} = \frac{1}{Pr}\frac{d\overline{\theta}^+}{dy^+} - \overline{v'^+\theta'^+} = 1 - \frac{\int_0^{y^+} \overline{u}_1^+ dy^+}{\langle \overline{u}^+ \rangle Re_\tau}, \quad (8)$$

which is equal to the total heat flux q^+_{total}. The total and the turbulent wall-normal heat fluxes are shown in Fig. 6. The peak of the turbulent heat flux increases with increase of the Re_τ and Pr. The peak arises at around $y^+ = 30 \sim 60$ for $Pr > 0.2$; while $y^+ > 50$ for $Pr = 0.025$.

The peak value of the turbulent wall-normal fluxes can be correlated as follows. Firstly, the total heat flux is expressed as

$$q^+_{total} = \frac{1}{Pr}\frac{d\overline{\theta}^+}{dy^+} - \overline{v'^+\theta'^+} = 1 - \frac{y^+}{Re_\tau} + \phi(y^+), \quad (9)$$

where $\phi(y^+)$ is a small correction function depending on the velocity profile. It can be empirically approximated as

$$\phi(y^+) = b\frac{y^+}{Re_\tau}\left(1 - \frac{y^+}{Re_\tau}\right)^2, \quad (10)$$

where b is an empirical constant of about 0.4. If the logarithmic profile is assumed for the mean temperature, then its gradient becomes

$$\frac{d\overline{\theta}^+}{dy^+} = \frac{1}{\kappa_\theta y^+}. \quad (11)$$

With use of Eqs. (10) and (11), Eq. (9) gives

$$-\overline{v'^+\theta'^+} = 1 - \frac{1}{\kappa_\theta Pr y^+} - (1-b)\frac{y^+}{Re_\tau} - 2b\left(\frac{y^+}{Re_\tau}\right)^2 + b\left(\frac{y^+}{Re_\tau}\right)^3. \quad (12)$$

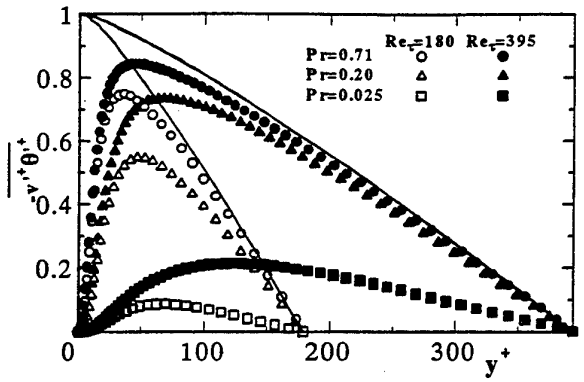

Figure 6: Total and turbulent heat fluxes

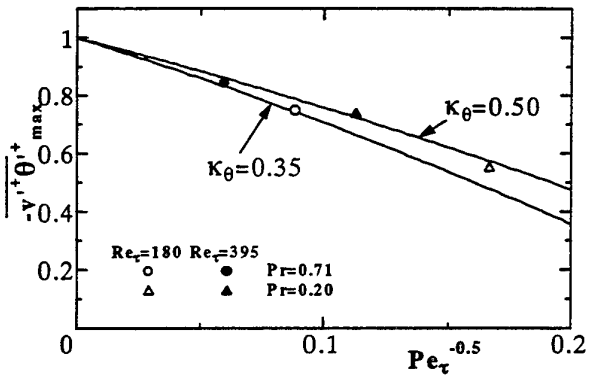

Figure 7: Peak value of wall-normal turbulent heat flux

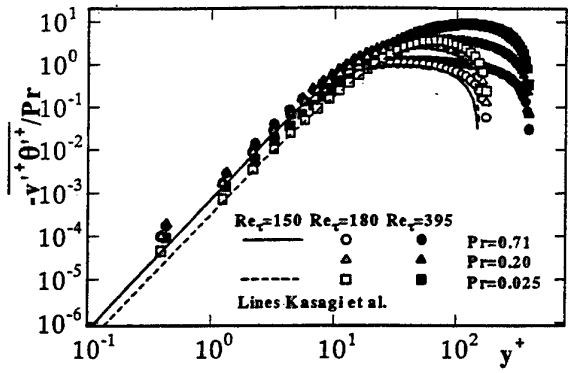

Figure 8: Logarithmic plot of wall-normal turbulent heat flux

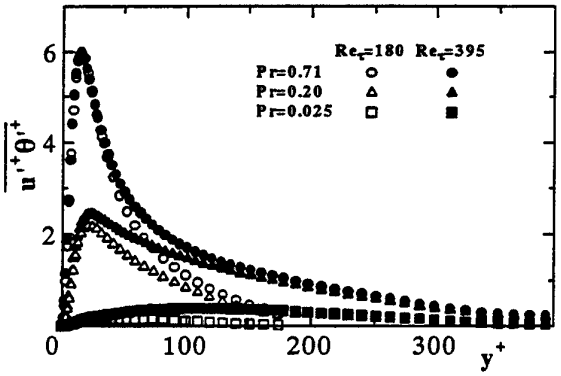

Figure 9: Streamwise turbulent heat flux

If the last two higher order terms are neglected for simplicity, the peak of $-\overline{v'^+\theta'^+}$ arises at

$$y^+{}_{max} = \sqrt{\frac{1}{(1-b)}\frac{Re_\tau}{\kappa_\theta Pr}}. \qquad (13)$$

Then the peak value becomes

$$-\overline{v'^+\theta'^+}_{max} \simeq 1 - 2\sqrt{\frac{1-b}{\kappa_\theta Pe_\tau}} - \frac{2b}{1-b}\frac{1}{\kappa_\theta Pe_\tau} + \frac{b}{(1-b)^{3/2}}\frac{1}{(\kappa_\theta Pe_\tau)^{3/2}}, \qquad (14)$$

where $Pe_\tau = Pr \cdot Re_\tau$ is the Peclet number. This correlation is compared with the DNS results in Fig. 7. The agreement is good.

The wall-normal turbulent heat flux is plotted again in Fig. 8 with an emphasis on the near wall region. It is expanded in terms of y^+ as

$$-\overline{v'^+\theta'^+} = Pr \cdot \overline{b_\theta c_2} \cdot y^{+3} + \cdots . \qquad (15)$$

The dependence of the correlation coefficient $\overline{b_\theta c_2}$ upon the Reynolds number is not large but still appreciable; i.e. $\overline{b_\theta c_2} \simeq 0.0008$ for $Re_\tau = 180$ and 0.001 for 395.

3.4 Streamwise turbulent heat flux

The streamwise turbulent heat flux is given in Fig. 9. Its peak is determined primarily by the Prandtl number and it increases with increase of Pr. The dependence of the peak value on the Reynolds number is already negligible for $Pr = 0.71$ but is still appreciable for $Pr = 0.2$ and 0.025. It is interesting to note that, in the central region of the channel, the streamwise heat flux is governed not by the Prandtl number but by the Reynolds number.

3.5 Temperature variance

The rms of the temperature variance is shown in Fig. 10 for various Re and Pr numbers. When the Prandtl number is enough large as $Pr = 0.71$, the peak value is not much dependent upon the Reynolds number. For a smaller Prandtl number, however, the peak increases as the Reynolds number does.

The temperature fluctuation can be expressed in the wall vicinity as

$$\theta'^+ = Pr \cdot (b_\theta y^+ + c_\theta y^{+2} + \cdots) . \qquad (16)$$

The ratio $\theta'^+{}_{rms}/Pr$ is plotted in Fig. 11. In case of a lower Re_τ of 180, it is dependent on Pr; that is, $b_\theta = 0.38$ for $Pr = 0.71$ and 0.34 for $Pr = 0.2$. ;

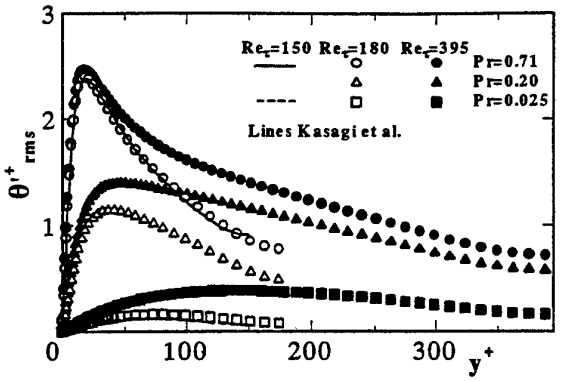

Figure 10: Rms of temperature variance

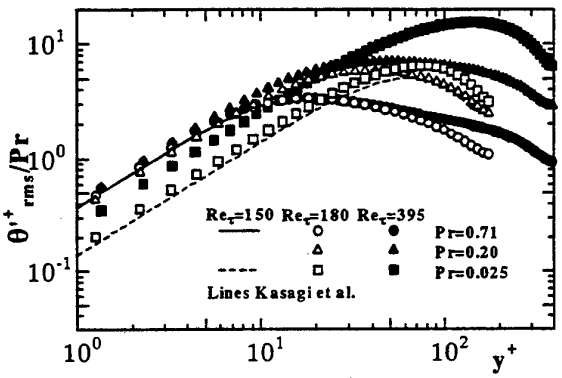

Figure 11: Ratio of θ'^+_{rms}/Pr

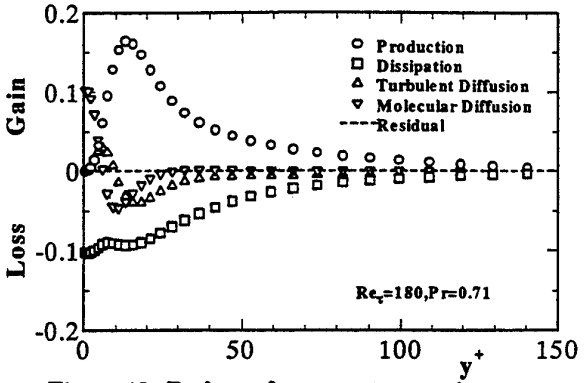

Figure 12: Budget of temperature variance

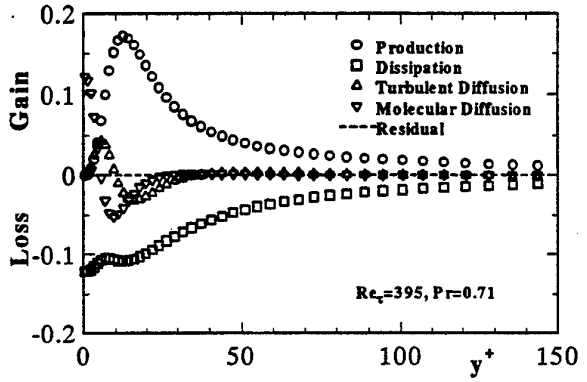

Figure 13: Budget of temperature variance

while, in the case of $Re_\tau = 395$, the coefficient $b_{\theta rms}$ is independent of Pr ($b_\theta = 0.42$) for $Pr > 0.2$ Thus the validity of the expansion of Eq. (16) is confirmed for a higher Rerynolds number as $Re_\tau = 395$.

3.6 Budget of transport equations

The budget of the transport equation for the temperature variance is given in Figs. 12 and 13 for $Re_\tau = 180$ and 395, respectively. Both the production and dissipation terms increase with increase of the Reynolds number. The present authors (Kawamura et al. [4,5]) examined a scaling low of the peak of the production term for the temperature variance P_θ and found that it can be scaled by P_θ/Pr and $Pr^{1/3}y^+$. As shown in Fig. 14, this scaling law is better satisfied with increase of the Reynolds number.

The budget for the wall-normal heat flux is shown in Figs. 15 and 16. It is well known that in the normal fluid ($Pr \geq 1$) the production term is balanced with the temperature pressure-gradient (TPG) term while the dissipation term is negligible. In case of $Pr = 0.2$, however, both the TPG and the dissipation terms contribute comparatively. It is interesting to note that, with increase of Reynolds number, the dissipation term stays unchanged while the TPG term increases to contribute more dominantly to the budget.

3.7 Turbulent Prandtl number and time scale ratio

The turbulent Prandtl number is an important quantity in the engineering heat transfer calculation. It is defined as

$$Pr_t = \frac{\nu_t}{a_t} = \frac{\overline{u'^+v'^+}}{\overline{v'^+\theta'^+}} \frac{\left(d\overline{\theta}^+/dy^+\right)}{\left(d\overline{u_1}^+/dy^+\right)}. \qquad (17)$$

There has been a long discussion on the dependence of Prandtl number upon the wall-normal distance y^+ and/or the molecular Prandtl number. Antonia-Kim [8]. found that the turbulent Prandtl number becomes independent of both y^+ and Pr as the wall is approached except for a very low Prandtl number. The present authors (Kawamura et al. [4,5].) confirmed it with an additional theoretical basis.

The turbulent Prandtl number is plotted in Fig. 17 including the present DNS of $Re_\tau = 395$. The wall asympotic value of Pr_t for $Pr > 0.2$ is certainly independent of y^+ and Pr irrespectively of the Reynolds number.

On the other hand, Pr_t of the low Prandtl number ($Pr = 0.025$) depends significantly upon the

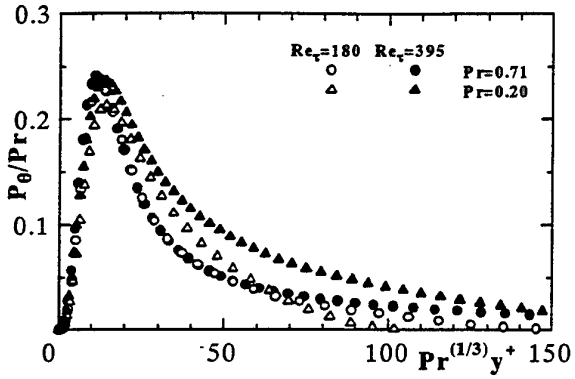

Figure 14: Production term P_θ for temperature variance

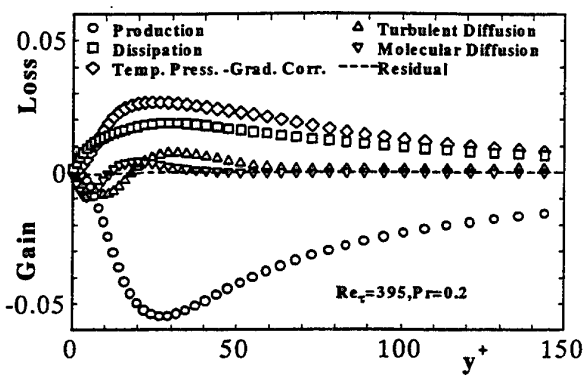

Figure 16: Budget of wall-normal turbulent heat flux

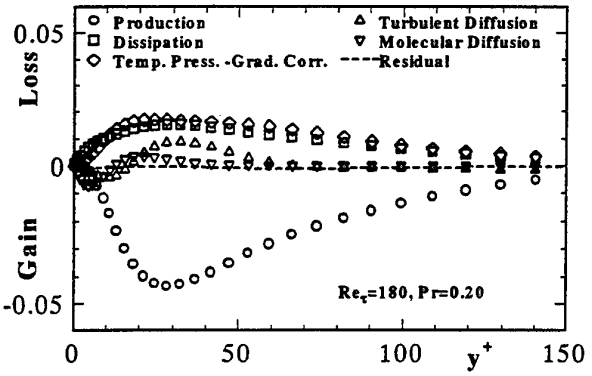

Figure 15: Budget of wall-normal turbulent heat flux

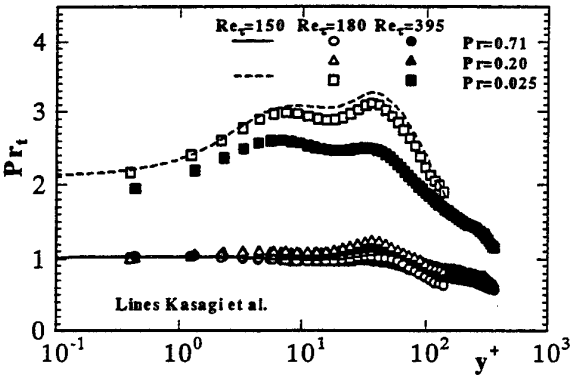

Figure 17: Distribution of turbulent Prandtl number

Reynolds number. It approaches to the normal value for a larger Pr. Thus it is indicated that the very high value of Pr_t for a low molecular Prandtl number fluid is caused also by the low Reynolds number effect.

The time scale ratio defined as

$$R = \frac{\overline{\theta'^2}\varepsilon}{2k\varepsilon_\theta} \tag{18}$$

is a quantity often used to estimate the dissipation rate of the temperature variance. Its wall asympotic value is exactly equal to the molecular Prandtl number. Figure 18 shows the distribution of the time scale ratio for several Prandtl numbers with $Re_\tau = 180$ and 395. Its wall value is indeed equal to Pr. The dependence upon the Reynolds number seems not so large for all the Prandtl numbers calculated.

3.8 Instantaneous velocity and temperature fields

The instantaneous velocity and thermal fields are visualized with the use of DNS data in Figs. 19 and 20. The visualized volume is one eighth of the computational domain ($2528 \times 790 \times 1264$ in the wall unit of (ν/u_τ)). Note that the fluid flows from the bottom left to the top right and that the sign of the temperature fluctuation is inversed ($T'^+ = -\theta'^+$) to meet an intuitive impression of the heating wall.

Figure 19 shows the instantaneous high and low velocity regions in case of $Re_\tau = 395$. When Reynolds number increases, the structures become highly intermittent in space. In case of a low Reynolds number, only a limited types of vortical structures are observed. On the other hand, with increasing Reynolds number, various shapes of the vortices appear. The well-known hairpin vortex is not observed, but many single vortices are dominant. Some of them look like the so-called banana vortex (Robinson [13]).

The elongated streaky structure is obtained. The low-speed streaks are much longer than high-speed ones as reported by Robinson [13]. The spanwise spacing of the low-speed streaks is approximately 100 wall units, which is in accordance with experimental knowledge. In addition, the low-speed streaks are elongated more than 1,000 wall units in the streamwise direction.

Figure 20 shows the instantaneous high and low temperature region for $Re_\tau = 395$ and $Pr = 0.71$. The thermal streaky structure has a strong resemblance to the momentum one.

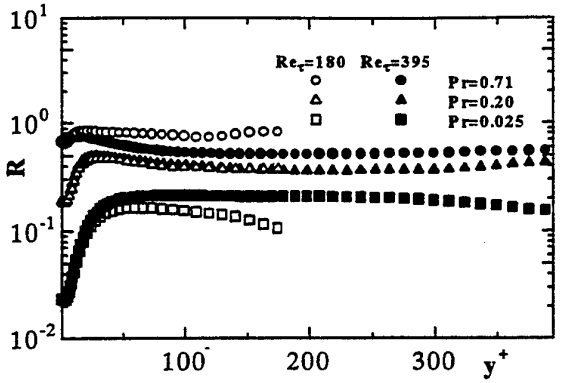

Figure 18: Distribution of time scale ratio

4 CONCLUDING REMARKS

The DNS of turbulent channel flow with scalar transport was performed for Reynolds number of Re_τ = 180 and 395. The molecular Prandtl number was 0.025, 0.2 and 0.71. In the mean temperature profile, the logarithmic and wake regions were better distinguished with increase of Re_τ. The temperature variance, streamwise and wall-normal heat fluxes were obtained and their expansion coefficient in the wall vicinity was examined. The turbulent Prandtl number (Pr_t) was calculated and found that its near-wall value was about unity independantly of both Re_τ and Pr of $Pr > 0.2$. The effect of the Reynolds number on Pr_t was more significant for a low molecular Prandtl number of 0.025. Instantaneous flow and temperature fields were visualized and their structures were compared for two different Reynolds numbers.

ACKNOWLEDGEMENTS

This simulation was performed with use of the Numerical Wind Tunnel (NWT) of National Aerospace Laboratory. The authors would like to acknowledge Mr. Ohsaka, a former graduate student, for his execution of DNS.

NOMENCLATURE

a_t	thermal eddy-diffusivity
b_i,c_i,d_i	coefficient of expansion
c_p	specific heat at constant pressure
k	turbulent kinetic energy
p	pressure
Pe_τ	Peclet number=$Pr \cdot Re_\tau$
Pr	molecular Prandtl number
Pr_t	turbulent Prandtl number
P_θ	production term of temperature

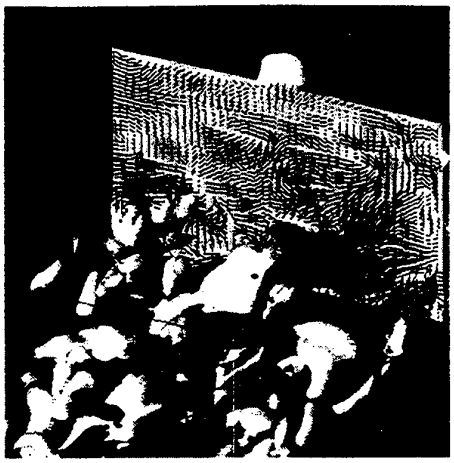
Figure 19: High and low speed streaks
$\langle Re_\tau = 395 \rangle$
($u'^+ < -3.5$; light-gray, $u'^+ > 3.5$; dark-gray,
$p'^+ < -3.5$; white)

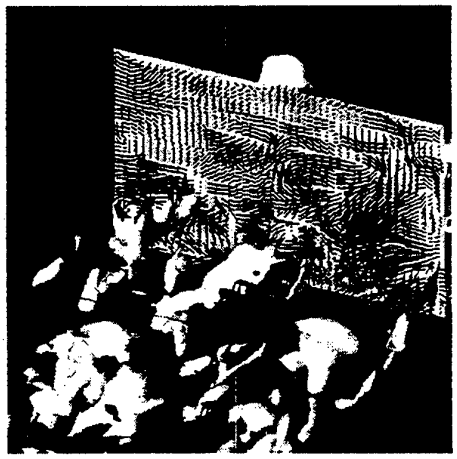
Figure 20: High and low temperature streaks
$\langle Re_\tau = 395 \rangle$
($T'^+ < -3.5$; dark-gray, $T'^+ > 3.5$; light-gray,
$p'^+ < -3.5$; white)

	variance
q_w	wall heat flux
q_{total}	total heat flux
R	time constant ratio
Re_τ	Reynolds number=$u_\tau \delta/\nu$
Re_m	Reynolds number=2 Re_τ $\langle \overline{u}^+ \rangle$
t	time
T	temperature
T_m	bulk mean temperature
T_τ	friction temperature
u_i, u, v, w	velocity component
u_τ	friction velocity=$\sqrt{\tau_w/\rho}$
x_1, x	streamwise direction
x_2, y	wall-normal direction
x_3, z	spanwise direction

Greak

δ	channel half width
ε	dissipation term of turbulent energy
ε_θ	dissipation term of temperature variance
κ_θ	Karman constant of mean temperature
θ	transformed temperature
ν	kinematic viscosity
ν_t	eddy-diffusivity
ρ	density
τ_w	statistically averaged wall shear stress

Superscript

$(\ )^*$	normalized by δ
$(\ )^+$	normalized by u_τ, ν and T_τ
$(\ )'$	fluctuation component
$\overline{(\ )}$	statistically averaged
$\langle\ \rangle$	averaged over channel section
$(\ )_{rms}$	root mean square

REFERENCES

1. Kim,J., Moin,.P., "Transport of passive scalars in a turbulent channel flow," in: *Turbulent Shear Flow* 6, 1989, pp. 85-96, Springer-Verlag, Berlin.

2. Kasagi, N., Tomita, Y., Kuroda, A., "Direct numerical simulation of passive scalar field in a turbulent channel flow," *Transactions of the ASME*, 1992, Vol. 114, pp.598- 606.

3. Kasagi, N., Ohtsubo, Y., 1993, "Direct numerical simulation of low Prandtl number thermal field in a turbulent channel flow," in: *Turbulent Shear Flow 6*, 1993, pp. 97-119, Springer-Verlag, Berlin.

4. Kawamura, H., Ohsaka, K., Yamamoto, K., "DNS of turbulent heat transfer in channel flow with low to medium-high Prandtl number fluid," *Proc. 11th Symp. Turbulent Shear Flows*, Grenoble, 1997, Vol. 1, pp. 8.7-8.12.

5. Kawamura, H., Ohsaka, K., Abe, H., Yamamoto, K., "DNS of turbulent heat transfer in channel flow with low to medium-high Prandtl number," *International Journal of Heat and Fluid Flow*, 1998, to be published.

6. Kim, J., Moin, P., Moser, R., "Turbulence statistics in fully developed turbulent channel flow at low Reynolds number," *Journal of Fluid Mechanics*, 1987, Vol. 177, pp. 133-166.

7. Kim, J., Moin, P., Moser, R., in the diskette of "Collaborative testing of turbulence models," , by P. Bradshaw, Stanford University, 1989.

8. Antonia, R., Kim, J., "Turbulent Prandtl number in the near-wall region of a turbulent channel flow," *Int. J. Heat Mass Transfer*, 1991, Vol. 34, pp.1905- 1908.

9. Kawamura, H., "Direct numerical simulation of turbulence by parallel computation," *10th Parallel CFD Conference*, Hsinchu, Taiwan, 1998.

10. Kawamura, H., "Direct numerical simulation of turnulence by finite difference scheme," in: *The Recent Developments in Turbulence Research*, 1995, pp.54-60, International Academic Publishers.

11. Kawamura H., Kondo Y., "Application of consistent finite difference scheme to DNS of turbulent heat transfer in channel flow," *Proc. of the 3rd KSME-ASME Thermal Eng. Conf.*, Kyongju, Korea, 1996, Vol. 1.,pp. 273-276.

12. Kader, B. A., "Temperature and concentration profiles in fully turbulent boundary layers," *Int. J. of Heat and Mass Transfer*, 1981, Vol. 24, pp. 1541-1544.

13. Robinson, S. K., "The kinematics of turbulent boundary layer structure," NASA TM-103859, 1991.

DNS OF SPANWISE TURBULENT HEAT TRANSFER IN A CHANNEL

Koji Matsubara*1, Mutsuo Kobayashi*1, Hiroshi Maekawa*1 and Kenjiro Suzuki*2

*1 Faculty of Engineering, Niigata Univ., Ikarashi 2-nocho 8050, Niigata 950-2181, Japan
*2 Department of Mechanical Engineering, Kyoto Univ., Kyoto 606-8501, Japan

ABSTRACT

Spanwise heat transfer in wall turbulence was studied in a turbulent channel flow having a linear spanwise variation of time-mean fluid temperature just the same as the spanwise variation of wall-temperature. Direct numerical simulation was performed for this flow geometry for four values of Prandtl number, Pr, ranging from 0.1 to 1.5. General trend of the spatial variation of the spanwise thermal eddy diffusivity for Pr=0.71 agrees well with the experimental data obtained by Maekawa et al. (1991). However, quantitative discrepancy was observed between the numerical and experimental results for the thermal eddy diffusivity in the near-wall region. Numerical results demonstrated that there is rough agreement between the values of eddy diffusivity ratio, $\varepsilon_{hz}/\varepsilon_{hy}$, and the Reynolds normal stress ratio, $\overline{w^2}/\overline{v^2}$, almost over the channel width, indicating the validity of the Launder's algebraic expression for the spanwise thermal eddy diffusivity. Comparison of the present results with the existing DNS data for wall-normal heat transfer in a channel uniformly heated wall suggested that spanwise heat transfer and wall-normal heat transfer are similar in both of the averaged feature of turbulent heat flux budget and instantaneous heat transfer mechanism.

1. INTRODUCTION

Spanwise or circumferential transfer of heat and mass in wall turbulent flows plays an important roll in many practical applications. Therefore, several experimental studies were performed for spanwise turbulent heat transfer[1-5], and some closure expressions were proposed for the spanwise turbulent heat flux or the spanwise thermal eddy diffusivity[3, 6, 7]. Early contributions to this topic were made by Black and Sparrow[1] and Quarmby and Quirk[2]. They studied experimentally non-axisymmetric transfer of passive scalar quantities in a circular pipe, and reported that the circumferential eddy diffusivities of heat and mass are much larger than their wall-normal counterparts in the vicinity of the wall. Maekawa and his colleagues[3-5] performed a series of experimental studies in an air flow turbulent boundary layer where the main-stream temperature was controlled to vary linearly in the spanwise direction. They measured distributions of spanwise thermal eddy diffusivity and related turbulence statistics across the boundary layer and drawn conclusions similar to those reported by previous workers. These experimental studies contributed to clarifying some fundamental aspects of spanwise heat transfer. However, quantitative accuracy of the existing experimental data is not still high enough to test the prediction performance of the existing turbulence models. For example, the distribution of spanwise thermal eddy diffusivity reported by Quarmby and Quirk[2] shows extremely wide scatter, and insufficient accuracy of the experimental data was thus suggested.

In the present study, direct numerical simulation (DNS) was performed for a turbulent channel flow having linear spanwise non-uniformity of time-mean fluid temperature equal to the spanwise variation of wall temperature. This flow system is somewhat artificial but offers a good arena for the discussion of the detailed features of spanwise heat transfer. The computational results for four cases of different values of Prandtl number are discussed in comparison with the experimental data for spanwise turbulent heat transfer and the DNS data for an ordinary wall-normal heat transfer in a channel with uniform wall heating.

2. COMPUTATIONAL METHOD

The computational domain and coordinate system presently used are shown in Fig. 1. The streamwise, wall-normal and spanwise coordinates are denoted by x, y and z, respectively. Velocity components along x-, y-

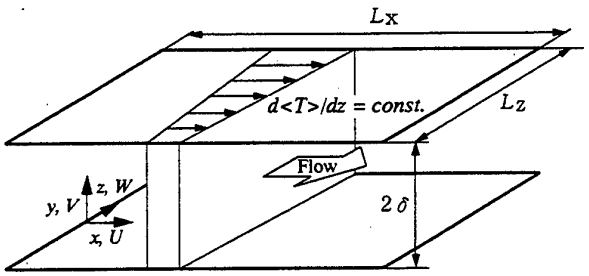

Fig. 1 Computational domain and coordinate system.

and z-directions are designated by U, V and W, respectively. The wall temperature, T_W, is assumed to be uniform in the streamwise direction but to vary linearly in the spanwise direction. The flow and thermal fields are assumed to be fully developed. In this situation, the time-mean fluid temperature, <T>, is uniform in the x- and y- directions but has a linear spanwise gradient equal to dT_W/dz. The working fluid is assumed to be a Newtonian fluid with constant properties. Temperature is treated as a passive scalar. The continuity, Navier-Stokes and energy equations used in the simulation are described, respectively, as

$$\nabla \cdot \mathbf{V}^+ = 0, \tag{1}$$

$$\frac{\partial \mathbf{V}^+}{\partial t^*} + (\mathbf{V}^+ \cdot \nabla)\mathbf{V}^+ = -\nabla P^+ + \frac{1}{Re}\nabla^2 \mathbf{V}^+ + \boldsymbol{i}, \tag{2}$$

$$\frac{\partial \Theta^*}{\partial t^*} + (\mathbf{V}^+ \cdot \nabla)\Theta^* = \frac{1}{RePr}\nabla^2 \Theta^* - W^+, \tag{3}$$

where variables are non-dimensionalized as

$$t^* = tU_\tau / \delta, \tag{4}$$

$$V^+ = V/U_\tau, \tag{5}$$

$$P^+ = P/(\rho U_\tau{}^2), \tag{6}$$

$$\Theta^* = \Theta/(\delta\, dT_W/dz). \tag{7}$$

A constant pressure gradient is provided to drive the channel flow, and its non-dimensional form corresponds to the last term on the right hand side of equation (2), $\boldsymbol{i}$. The temperature, T, is decomposed into the wall temperature, T_W, and its deviation from T_W, Θ. The last term on the right hand side of equation (3), $-W^+$, appears due to this decomposition. It is equivalent to $-W^+ d\langle T^*\rangle/dz^*$, where $d\langle T^*\rangle/dz^*$ is equal to unity under the present manner of normalization.

Spatial periodicity was assumed in describing the boundary conditions for the solved quantities at the inlet, outlet and side boundaries of the computational domain. On the wall, pressure was computed using the compatibility condition

$$\frac{\partial P^+}{\partial y^*} = \frac{1}{Re}\frac{\partial^2 V^+}{\partial y^{*2}} \tag{8}$$

derived from equation (2). The temperature fluctuation on the wall was fixed at zero as was done in the existing DNS performed by Kasagi and Ohtsubo[8] and Kim and Moin[9].

Fourth-order finite differencing is used for the discretization of all the spatial derivatives appearing in the equations (2) and (3). The finite differencing of the convection term in the Navier-Stokes equation is made following the consistent scheme developed by Kajishima[10] and Suzuki and Kawamura[11] with a modification to secure fourth-order accuracy. In the time integration of the resulting equations, the pressure terms are implicitly treated, and the other terms are evaluated by means of the Adams Bashforth method[12]. The Poisson equation derived from equations (1) and (2) is solved for the pressure. In the derivation of the Poisson equation, the continuity condition (1) was applied for the latest velocity components as was done in the fractional step method and in the MAC (Marker and Cell) method[13].

The initial value of the streamwise velocity was set by superimposing random fluctuation on the time-mean part obeying the wall law. Initial values of the other velocity components, pressure and temperature were all set to be zero. The computation was proceeded observing the first and second moments of the dependent variables. After the effect of artificial setting of the initial values fully vanished, ensemble averaging of the quantities was performed with respect to time and space. All the computed values of each quantity at every grid points in a plane at equal distance from the wall was counted in the averaging. The turbulence statistics obtained by this averaging are denoted with an over bar $\bar{(\ )}$ in the following discussion.

The adopted computational conditions are listed in Table 1. The Prandtl number, Pr, is changed in four steps from 0.1 to 1.5 keeping the Reynolds number, $Re(=U_\tau \delta/\nu)$, constant at 150. Grid points of the total number of 64x61x64 are allocated in the computational domain finely in the neighborhood of the wall. A smaller value of the time step is required for the case of Pr=0.1 to suppress the numerical instability more likely to occur for lower values of Pr.

3. RESULTS AND DISCUSSION

3.1 Flow field

The calculated flow field results are compared with the DNS database presented by Kasagi et al. for a turbulent channel flow of Re=150[14]. In the DNS of Kasagi et

Table 1 Computational condition.

Author	Present	Kasagi et al.
Re	150	150
Pr	0.1, 0.3, 0.71, 1.5	–
L_x/δ	7.85	15.7
L_z/δ	3.14	6.28
Grid number	64x61x64	128x96x128
Δx^+	18.4	18.4
Δy^+	1.03-9.51	0.08-4.9
Δz^+	7.36	7.36
Δt^+	0.03 for Pr=0.1 0.06 for others	0.12
Averaging time span	$3450\,\nu/U_\tau^2$	$4400\,\nu/U_\tau^2$

al., spectral method is used for the discretization of basic equations, and the grid resolution is finer than the present value as shown in Table 1. In Figs 2-4, the distributions of mean velocity, Reynolds shear stress and rms values of velocity fluctuations presently obtained are shown with DNS data obtained by Kasagi et al. for the same Reynolds number. In these figures, y^+ is the non-dimensional distance from the wall,

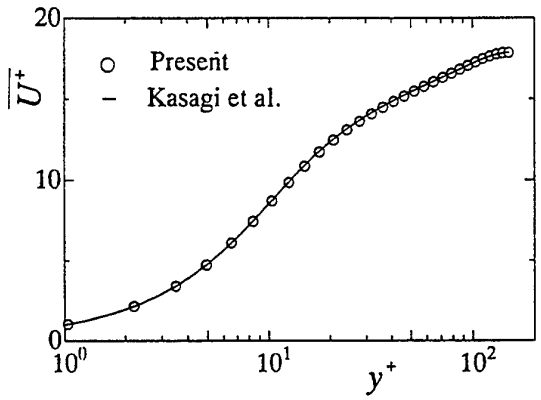

Fig. 2 Distribution of mean velocity.

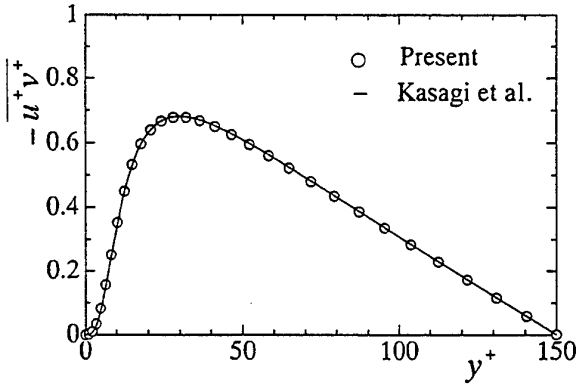

Fig. 3 Distribution of Reynolds shear stress.

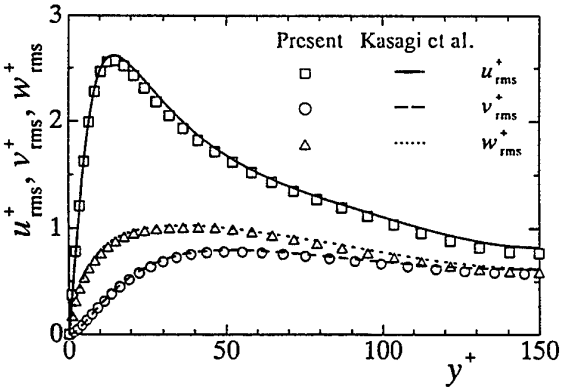

Fig. 4 Distributions of rms of velocity fluctuation.

yU_τ/υ, and y^+=150 corresponds to the channel center. Good agreement is found between the present results and the values taken from the DNS database by Kasagi et al. Slight discrepancy found between them suggests the possibility of the insufficient grid resolution of the present simulation. However, this discrepancy is small and it does not seriously degrade the following discussion of low-order turbulence statistical quantities.

3.2 Comparison with existing experimental data

In the flow system under discussion, non-zero component of turbulent heat flux is only the spanwise one, $\overline{w\theta}$. Since the spanwise gradient of time-mean temperature, d<T>/dz, is uniform throughout the flow field, distributions of $\overline{w\theta}$ and the corresponding thermal eddy diffusivity, ε_{hz}, are completely similar in shape. In Fig. 5, the calculated values of ε_{hz} for the case of Pr=0.71 and the kinematic eddy viscosity, ε_m are compared with experimental data for an air flow turbulent boundary layer reported by Maekawa et al.[3].

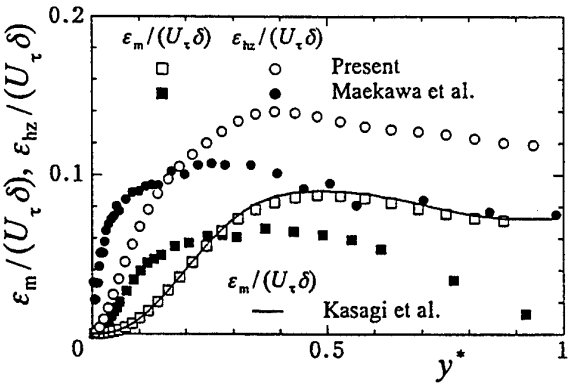

Fig. 5 Distributions of $\varepsilon_m/(U_\tau\delta)$ and $\varepsilon_{hz}/(U_\tau\delta)$.

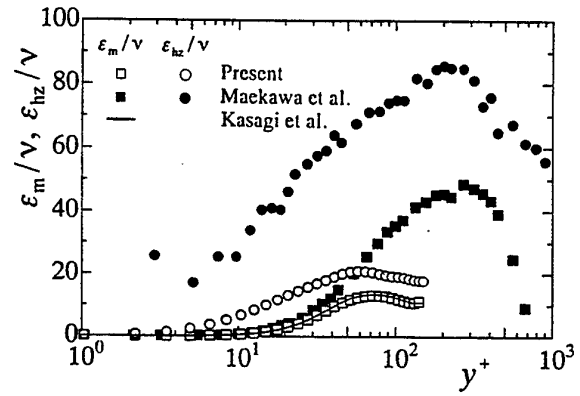

Fig. 6 Distributions of ε_m/ν and ε_{hz}/ν.

At the streamwise station where measured quantities are obtained, the Reynolds number based on U_τ and the boundary layer thickness is 770 and it is about five times larger than the value of Re of the present study. In Fig. 5, friction velocity is used as the velocity scale, and the channel half width or boundary layer thickness as the length scale in the non-dimensionalization. Despite of large difference of Reynolds number, following points are commonly observed in the calculated and measured values. (1) ε_{hz} and ε_m take peaks at almost the same position. (2) ε_{hz} is larger than ε_m over the channel width or boundary layer thickness, and the peak value of the former is about 1.5 times larger than that of the latter.

In Fig. 6, comparison is made again for ε_m and ε_{hz} but in an alternative way of non-dimensionalization, ε_m/ν and ε_{hz}/ν. These non-dimensional forms are suitable for observing the asymptotic behavior of ε_m and ε_{hz} toward the wall. In the vicinity of the wall, i.e. in the region of $y^+<30$, the calculated and measured values of ε_m show similar trend of variation to each other but quantitatively speaking remarkable discrepancy is found between both values of ε_{hz}. Near-wall behavior of the measured values of ε_{hz} is somewhat strange in a sense that it is considerably large even in the viscous sublayer, suggesting serious inaccuracy of the experimental data contained in the near-wall region.

3.3 Prandtl number effects

Figure 7 shows the distributions of ε_{hz} for various values of Prandtl number. Each distribution of ε_{hz} has a mild peak around $y^+=70$. There exists only a small difference between the distributions of ε_{hz} for the two cases of Pr=1.5 and Pr=0.71. However, when Pr is smaller than 0.71, ε_{hz} shows remarkable reduction with a decrease of Pr. As described later, these features of ε_{hz} reflect the characteristics in the budget of $\overline{w\theta}$.

In liquid metal turbulence, it is well known that the wall-normal thermal eddy diffusivity, ε_{hy}, is much smaller than that for fluids with Pr close to unity[8, 15-19]. According to Azer and Chao[15], temperature fluctuation induced in low Prandtl number turbulence rapidly decays due to large thermal diffusivity of the fluid. Additionally, it is also known that the change of ε_{hy} as well as that of ε_{hz} is not significant for the change of Pr exceeding its critical value[9, 20]. Therefore, the dependency of ε_{hy} and that of ε_{hz} on the value of Pr are very similar to each other.

In Fig. 8, comparison is made between the two kinds of correlation coefficients, $Q_{w\theta}$ and $Q_{v\theta}$. The latter is the DNS data calculated by Kim and Moin for the case of uniform wall heating at Re=180[9]. While the value of $Q_{v\theta}$ takes zero at the channel center, the value of $Q_{w\theta}$ is almost constant over the whole width of the channel. However, in the region of $y^+<100$, $Q_{w\theta}$ and $Q_{v\theta}$ are roughly equal to each other for the same value of Pr, and both of them increase slightly with the decrease of Pr.

As observed in Fig. 9, the temperature variance, $\overline{\theta^2}$, reduces as Pr is decreased. The reduction of $\overline{\theta^2}$ arises partly from the decrease in the production rate, $-\overline{w\theta}\, d\langle T\rangle/dz$. However, this effect is not major for Pr larger than 0.71 since $\overline{w\theta}$ is not substantially affected by the value of Pr in this range of Pr. Another possibility is the Prandtl number effect on the dissipation time scale of temperature fluctuation, τ_θ. Figure 10 shows the distribution of the time scale ratio, τ_θ/τ for four different values of Pr, where τ is the dissipation time scale of velocity fluctuation. As

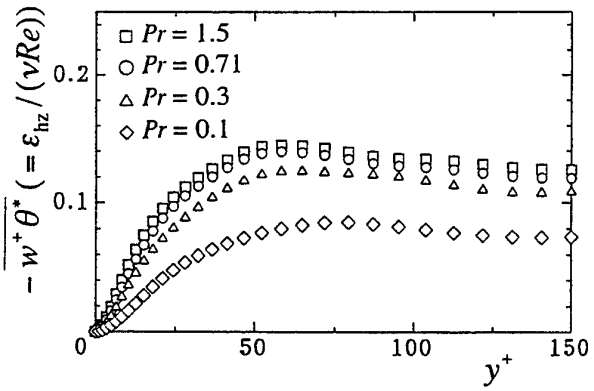

Fig. 7 Distributions of spanwise thermal eddy diffusivity [25].

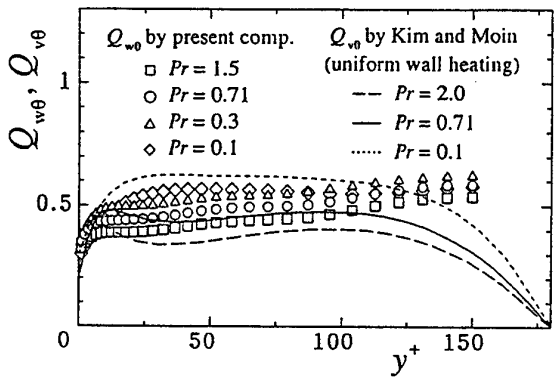

Fig. 8 Distributions of $Q_{w\theta}$ and $Q_{v\theta}$ [25].

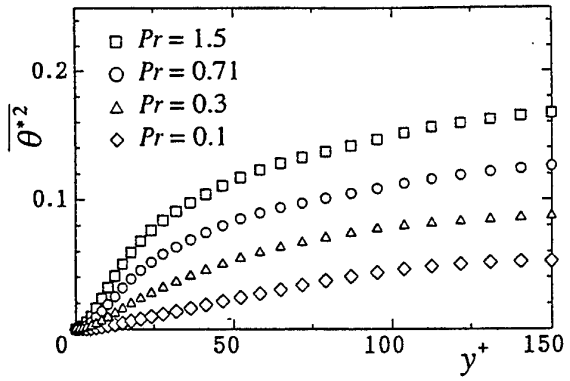

Fig. 9 Distributions of temperature variance [25].

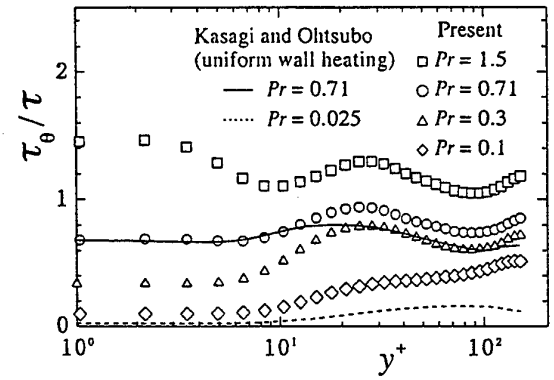

Fig. 10 Distributions of time scale ratio [25].

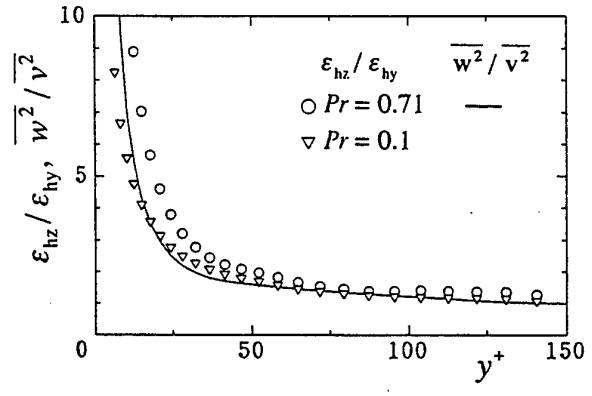

Fig. 11 Distributions of eddy diffusivity ratio [25].

indicated in the figure, time scale of temperature fluctuation becomes smaller with decrease of Pr. The result of Kasagi and Ohtsubo[8] for the case of heat transfer from uniformly heated walls is also plotted in Fig. 10. The temperature fluctuation is assumed to be zero at the wall in both computations. Thus, Taylor expansion of θ in respect to y=0 yields the relation of $\theta \propto y$ in the region very close to the wall. Similarly, in the same region $u \propto y$, $v \propto y^2$ and $w \propto y$ are obtained using continuity condition. From these relations, τ_θ / τ are theoretically deduced to asymptotically approach the value equal to Pr at positions very close to the wall, namely

$$\tau_\theta / \tau \rightarrow \mathrm{Pr} \quad \text{as } y^+ \rightarrow 0. \tag{9}$$

This is actually confirmed in Fig. 10.

Launder[6] examined the behavior of the eddy diffusivity ratio, $\varepsilon_{hz} / \varepsilon_{hy}$, assuming that the spanwise and wall-normal components of turbulent heat flux, $\overline{w\theta}$ and $\overline{v\theta}$ are in the local equilibrium and that related fluctuations, v, w, θ are of the local isotropy. Due to these assumptions, the pressure-temperature gradient correlation (P-TG) becomes a solitary term balancing with the production term in the budget of either of $\overline{w\theta}$ and $\overline{v\theta}$. As described later, this is confirmed to nearly hold in the case of Pr larger than 0.71 but does not hold for smaller values of Pr. This point will be discussed later in this section. Launder[6] approximated P-TG term so as to be proportional to the corresponding turbulent heat flux and derived

$$\varepsilon_{hz} / \varepsilon_{hy} = \overline{w^2} / \overline{v^2}. \tag{10}$$

Here, $\overline{w^2}$ and $\overline{v^2}$ are the spanwise and wall-normal components of the Reynolds normal stress, respectively. Figure 11 shows the eddy diffusivity ratio, $\varepsilon_{hz} / \varepsilon_{hy}$, for the two cases of Pr=0.1 and Pr=0.71, where the data of ε_{hy} is quoted from the DNS result presented by Kim and Moin[9]. The Reynolds number of the flow calculated by Kim and Moin is 180 and is slightly larger than the counterpart of the present study. The Reynolds normal stress ratio, $\overline{w^2} / \overline{v^2}$, is also plotted in the figure. The distribution of $\overline{w^2} / \overline{v^2}$ indicates that $\overline{w^2}$ decreases more gradually than $\overline{v^2}$ when approaching the wall. In the near-wall region, the value of $\varepsilon_{hz} / \varepsilon_{hy}$ depends on Pr and becomes smaller when Pr is decreased. However, in these Prandtl numbers, there is a rough similarity between the distributions of $\varepsilon_{hz} / \varepsilon_{hy}$ and the distribution of $\overline{w^2} / \overline{v^2}$. It is thus suggested that equation (10) approximately holds for the studied values of Pr.

Rogers et al. [7] performed the DNS of homogeneous turbulent shear flow with mean temperature gradients in each of the three orthogonal directions. In their simulation, periodicity condition of the flow and thermal fields was used for all the three directions, and decaying process of turbulence was obtained. In their result, the ratio of the spanwise and lateral components of thermal eddy diffusivity changes in time but asymptotically approaches the constant

value of approximately 1.6. This result almost agrees with the present result of $\varepsilon_{hz}/\varepsilon_{hy}$ in the central part of the channel $y^+>100$. Wang et al. [21] studied three-dimensional momentum diffusivity in a film cooling test surface and found that spanwise component of kinematic eddy viscosity takes larger value than its wall-normal component. This may imply that eddy viscosity ratio between spanwise and wall-normal components show the same trend as $\varepsilon_{hz}/\varepsilon_{hy}$. But, clear conclusion on the dependency of eddy viscosity ratio on the distance from the wall can not be drawn from the experimental data by Wang et al. because wide scatter of the measured values is contained in the distribution of the measured values.

In the case of the present study, the transport equation of $\overline{w\theta}$ can be written as

$$0=-\overline{w^{+2}}\frac{d<T^+>}{dz^+}-\left(1+\frac{1}{Pr}\right)\overline{\frac{\partial w^+}{\partial x_j^+}\frac{\partial \theta^+}{\partial x_j^+}}$$

Production Dissipation

$$-\frac{\partial}{\partial y^+}\left(\overline{v^+w^+\theta^+}\right)+\overline{p^+\frac{\partial \theta^+}{\partial z^+}}$$

Turbulent diffusion; Pressure temperature-gradient correlation

$$+\frac{\partial}{\partial y^+}\left(\overline{\theta^+\frac{\partial w^+}{\partial y^+}}+\frac{1}{Pr}\overline{w^+\frac{\partial \theta^+}{\partial y^+}}\right). \qquad (11)$$

Molecular diffusion

Figure 12 shows the computed magnitude of each term of equation (11) with the numerical residual of the equation. Since temperature is considered to be a passive scalar in this study, theoretically $\overline{w^2}$ and production rate of $\overline{w\theta}$ do not depend on Pr. Slight discrepancy found between the production rate obtained for Pr=0.1 and the counterpart of other cases arises from the fact that the calculated flow field for Pr=0.1 is not identical to the results of other cases due to different value of time step used for Pr=0.1. The following three features are commonly observed for all the studied cases of different Pr values. (1) Over the whole channel width except in the viscous sublayer ($y^+<5$), major terms of $\overline{w\theta}$ budget are the production rate, the pressure-temperature gradient correlation (P-TG) and the dissipation rate, and $\overline{w\theta}$ is thus nearly in the local equilibrium as Launder assumed in deriving equation (10). (2) The turbulent diffusion takes a mild peak around $y^+=10$, but its peak value is very small compared with the production rate over the whole channel width. (3) In the viscous sublayer, molecular diffusion and dissipation rate balance with each other.

As shown in Fig. 12, P-TG and dissipation rate have a sign opposite to the production term, and are supposed to be major terms suppressing excessive growth of turbulent heat flux. The term *destruction* is used to denote these processes. In all the cases, the dissipation rate is a dominant term of the total destruction of $\overline{w\theta}$ in the region of $y^+<10$. In the remaining region, P-TG and the dissipation are competitive processes for the destruction, and their

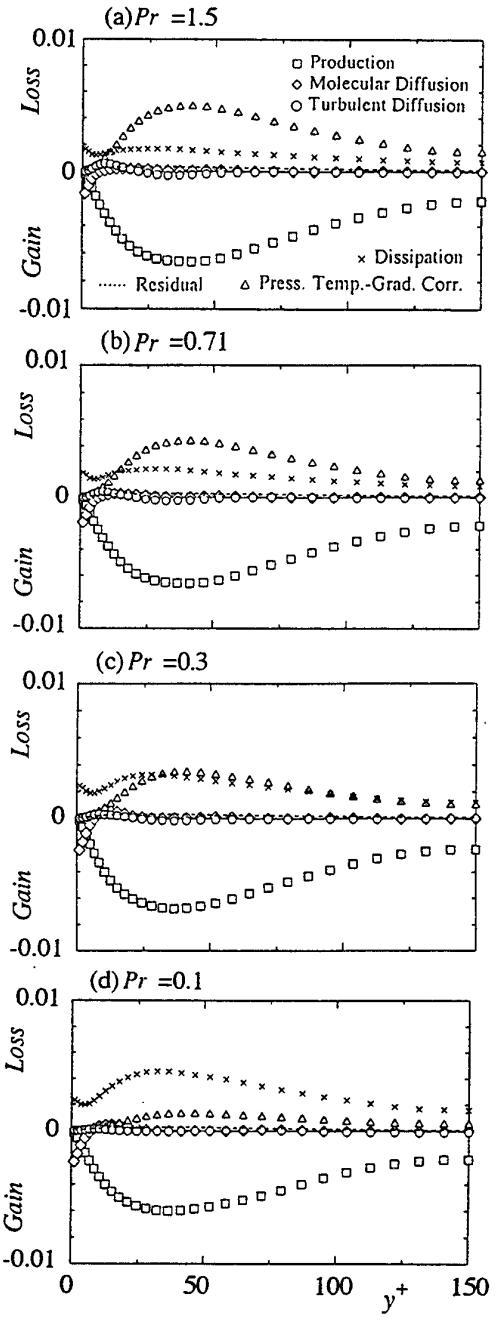

Fig. 12 Budgets of spanwise turbulent heat flux [25].

contributions to the total destruction vary with the change of Pr. In this region P-TG is distinctively larger than the dissipation rate for both cases of Pr=1.5 and Pr=0.71, which matches the Launder's assumption of local isotropy used in deriving equation (10). Since P-TG corresponds to the destruction through the turbulent mixing, it should be almost independent of Pr. This is consistent with the aforementioned feature of $\overline{w\theta}$ that its dependency on Pr is weak for Pr larger than 0.71. The contribution of the dissipation rate to the total destruction becomes larger with decreasing Pr, and becomes dominant over the whole channel width in the case of Pr=0.1. A similar trend was also reported by Kawamura[20] for the dissipation rate of wall-normal turbulent heat flux. Therefore, in low values of Pr local isotropy assumed by Launder does not hold for both $\overline{w\theta}$ and $\overline{v\theta}$ though equation (10) still gives good prediction. At the low values of Pr, the total destruction including the dissipation should follow the Launder's approximation originally made for P-TG, namely the total destruction should be roughly proportional to the corresponding turbulent heat flux. According to the discussion by Iida and Kasagi[20], the wave number range where the turbulent heat flux is dissipated shifts to the lower side with the decrease of Pr. This should lead to the shortening of life span of turbulent heat flux and thus to the decrease of the time scale of turbulent heat flux. This effect would cause the reduction of $\overline{w\theta}$ observed in the present computation.

3.4 Production and destruction of spanwise turbulent heat flux in instantaneous field

In Fig. 13, three-dimensional display of low-pressure regions of $p^+ \leqq -3.0$ is given by white blobs in the lower half of the computational domain having the volume of 1177.5x150x471 (wall units)^3. Low-pressure regions appear intermittently in space and some of them are elongated in x-direction. Figure 14 shows instantaneous velocity vector map in a y-z plain whose streamwise position is indicated in Fig. 13. In Fig. 14, corresponding pressure field calculated at the same instant is also shown by the change of gray tone level. Appearance of vortical fluid motion is observed at several locations in the velocity vector map, and their locations correspond well to the low-pressure region. In high-pressure regions, divergence-like fluid motion in the y-z plain appears, and streamwise velocity fluctuation, u should be decelerated. This suggests that energy transfer from u to v and that from u to w are statistically major processes in energy redistributions [14].

Discussion for the instantaneous process of

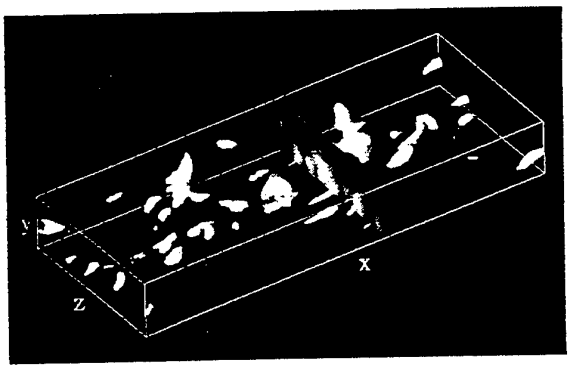

Fig. 13 Three dimensional display of low pressure region: white blobs, $p^+ \leqq -3.0$.

generating the spanwise turbulent heat flux is now made for the case of Pr=0.71. For this purpose, magnitude of each term in the transport equation of spanwise turbulent heat flux was studied at the same instant and in the same y-z plain as the ones discussed in Figures 13 and 14. In Fig. 15, for example, the distribution of the production rate, $-w^+2d\langle T^*\rangle/dz^+$, is shown. In the figure, positions of low- and high-pressure regions are indicated by the letters "L" and "H". Since $d\langle T^*\rangle/dz^+$ is equal to a positive constant 1/Re everywhere, instantaneous value of the production rate is negative everywhere in the channel or negative value of production contributes positively for generation of $\overline{w\theta}$. The production rate takes large negative values around upper and lower edges of the low-pressure regions where spanwise fluid motion is conspicuous due to the vortical fluid motion sitting in the low pressure region. High values of the production rate also appears around some parts of the high-pressure regions where spanwise velocity component also appears related to the divergence-like fluid motion mentioned above.

Instantaneous distribution of the dissipation rate of $\overline{w\theta}$ is shown in Fig. 16. Comparison of the distribution of the production rate with that of the dissipation rate reveals that positive value of the dissipation rate, i.e. destruction of turbulent heat flux, is located near the region where high negative value of the production rate is observed.

Instantaneous distribution of P-TG term is also shown in Fig. 17. The regions of positive P-TG, where the turbulent heat flux is destructed through turbulent mixing, are situated well at the low-pressure regions. This suggests that vortical fluid motion occurring in the low-pressure region plays an important roll not only for the production but also for the destruction of spanwise turbulent heat flux. On the other hand, in high-pressure regions, there is no clear distinction of the sign of P-TG.

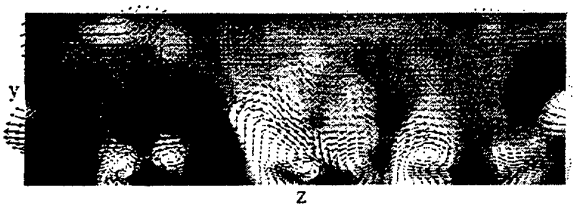

Fig. 14 Instantaneous velocity vectors and pressure fluctuation: gray to black, $p^+ = 0$ to 3.0; gray to white, $p^+ = 0$ to -3.0.

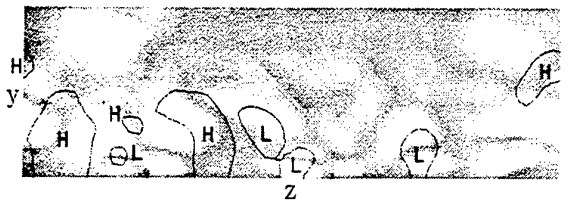

Fig. 15 Production for $\overline{w\theta}$: gray to white, $-w^{+2}d\langle T^+\rangle/dz^+ = 0$ to - 0.02.

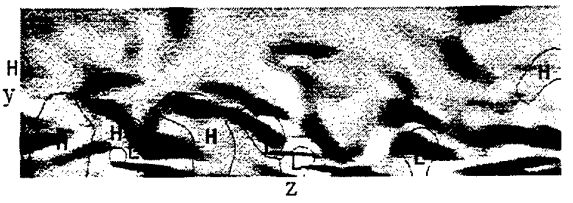

Fig. 16 Dissipation for $\overline{w\theta}$: gray to black, $-(1+1/Pr)\partial w^+/\partial x_j^+ \partial\theta^+/\partial x_j^+ = 0$ to 0.01; gray to white, $-(1+1/Pr)\partial w^+/\partial x_j^+ \partial\theta^+/\partial x_j^+ = 0$ to -0.01.

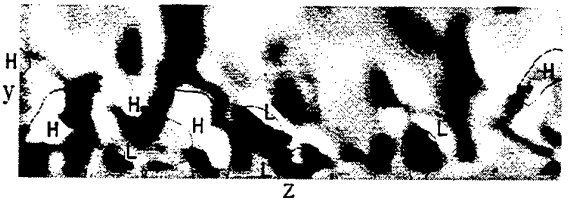

Fig. 17 P-TG for $\overline{w\theta}$: gray to black, $p^+\partial\theta^+/\partial z^+ = 0$ to 0.02; gray to white, $p^+\partial\theta^+/\partial z^+ = 0$ to -0.02.

Generation of temperature gradient in low-pressure region is schematically illustrated in Fig. 18. Clockwisely rotating vortex produces positive spanwise velocity in its upper edge region and negative spanwise velocity in its lower edge region. Each is assumed to be correlated respectively with negative and positive temperature fluctuation as is shown in the figure. These regions are entrained into the vortex and negative value

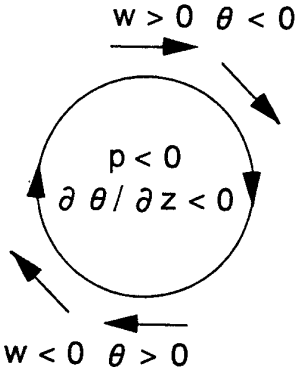

Fig. 18 Temperature gradient generation in a low-pressure region.

of spanwise temperature gradient is generated inside the vortex. This results in the positive correlation between the pressure fluctuation, which corresponds to the destruction of the spanwise turbulent heat flux due to the turbulent mixing. In Fig. 14, popularity of the clockwisely rotating vortex is observed to be much higher than the popularity of anti-clockwisely rotating vortex in low-pressure regions. But, statistically vortices of different rotating directions have the same popularity [23], and anti-clockwisely rotating vortex should also contribute destructing the turbulent heat flux in the same mechanism. Discussion for wall-normal heat transfer by Iida and Kasagi [24] suggests that destruction of spanwise turbulent heat flux and that of wall-normal component proceed in a similar manner.

4. CONCLUSIONS

Direct numerical simulation(DNS) was performed for the simple case of spanwise heat transfer in wall turbulence, namely a turbulent channel flow with a linear spanwise non-uniformity of time mean fluid temperature equal to the non-uniformity of the wall temperature. The present results for Prandtl number, Pr, ranging from 0.1 to 1.5 were compared with the existing DNS data for ordinary two-dimensional heat transfer in a channel flow with uniform wall heating. The following conclusions are derived.

(1) The spatial variation of the calculated spanwise thermal eddy diffusivity, ε_{hz}, generally agrees with experimental result by Maekawa et al. However, there is quantitatively wide discrepancy between the calculated and measured values of ε_{hz} in the vicinity of the wall.

(2) The spanwise thermal eddy diffusivity, ε_{hz}, shows remarkable reduction with decreasing of Pr. This reduction of ε_{hz} is quite similar to the behavior of the wall-normal thermal eddy diffusivity, ε_{hy}, in a channel flow with uniformly heated walls.

(3) The eddy diffusivity ratio $\varepsilon_{hz}/\varepsilon_{hy}$ is almost uniform away from the wall, but it changes steeply in the near-wall region. The distribution of $\varepsilon_{hz}/\varepsilon_{hy}$ for both Pr=0.71 and Pr=0.1 roughly agrees with the distribution of the Reynolds normal stress ratio, $\overline{w^2}/\overline{v^2}$. Therefore, the proposition of Launder $\varepsilon_{hz}/\varepsilon_{hy} = \overline{w^2}/\overline{v^2}$ nearly holds in a wide range of Pr.

(4) Since the Reynolds number treated in the present computation is comparatively low, not only the pressure-temperature gradient correlation (P-TG) but also the dissipation take part in the destruction of $\overline{w\theta}$. The contribution of the dissipation to the total destruction increases as Pr decreases. This trend of the dissipation is similar to the counterpart of $\overline{v\theta}$ previously reported in the case of uniform wall heating.

(5) For the case of Pr=0.71, instantaneous value of each term included in the transport equation of spanwise turbulent heat flux was displayed in a y-z plain and discussed in comparison with corresponding velocity and pressure fields. It was found that low-pressure regions accompanied by vortical flow motion plays a key roll for destruction of spanwise turbulent heat flux through turbulent mixing, i.e. P-TG. Discussion by Iida and Kasagi suggested that there is similarity between destruction mechanisms of spanwise heat transfer and wall-normal heat transfer.

NOMENCLATURE

C_p: specific heat at constant pressure [J/(KgK)]
$\boldsymbol{i}$: unit vector in x direction
k: turbulent kinetic energy [m^2/s^2]
L_x, L_z: computational domain size in x and z directions [m]
P: pressure deviating from P_x [Pa]
P_x: pressure component generating driving force [Pa] $=(\rho U_\tau^2/\delta)x+\text{const.}$
p: pressure fluctuation [Pa]
Pr: Prandtl number $=\rho C_p \nu/\lambda$
$Q_{\phi\psi}$: correlation coefficient $=|\overline{\phi\psi}|/(\phi_{rms}\psi_{rms})$
Re: Reynolds number $=U_\tau \delta/\nu$
T: temperature [K]
t: time [s]
$\boldsymbol{V}$: velocity vector [m/s] =(U, V, W)
U, V, W: velocities in x, y and z directions [m/s]
U_τ: friction velocity [m/s]
u, v, w: velocity fluctuation in x, y and z directions [m/s]
x, y, z: coordinates in streamwise, wall-normal and spanwise directions [m]
x_i: coordinate in i-th direction; x_1, x_2 and x_3 denote x, y and z, respectively [m]
Δt: time step [s]
Δx, Δy, Δz: grid spacings in x, y and z directions [m]
δ: channel half width [m]
ε: dissipation rate of k [m^2/s^3]
ε_{hy}: wall-normal thermal eddy diffusivity [m^2/s]
ε_{hz}: spanwise thermal eddy diffusivity [m^2/s] $=-\overline{w\theta}/(d<T>/dz)$
ε_m: kinematic eddy viscosity [m^2/s] $=-\overline{uv}/(d\overline{U}/dy)$
ε_θ: dissipation rate of $\overline{\theta^2}$ [K^2/s]
Θ: temperature deviating from T_W [K]
θ: temperature fluctuation [K]
λ: thermal conductivity [W/(mK)]
ν: kinematic viscosity [m^2/s]
ρ: density [K_g/m^3]
τ: dissipation time scale of velocity fluctuation [s] $=k/\varepsilon$
τ_θ: dissipation time scale of temperature fluctuation [s] $=\overline{\theta^2}/\varepsilon_\theta$

Superscripts and subscripts
$(\,)^+$: non-dimensionalization with U_τ, ν and ρ
$(\,)^*$: non-dimensionalization with U_τ, δ and dT_W/dz
$\overline{(\,)}$: ensemble average
$(\,)_W$: Wall

Miscellaneous
∇: nabla $=(\partial/\partial x^*, \partial/\partial y^*, \partial/\partial z^*)$
$<\,>$: time mean

REFERENCES

(1) Black, A. W. and Sparrow, E. M., Experiments on turbulent heat transfer in a tube with circumferentially varying thermal boundary conditions, Trans. ASME, J. Heat Transf., 1967, 89, 258-268.

(2) Quarmby, A. and Quirk, R., Measurements of the radial and tangential eddy diffusivities of heat and mass in turbulent flow in a plain tube, Int. J. Heat Mass Transfer, 1972, 15, 2309-2327.

(3) Maekawa, H., Kawada, Y., Kobayashi and M., Yamaguchi, H., An experimental study on the spanwise eddy diffusivity of heat in a flat-plate turbulent boundary layer, Int. J. Heat Mass Transf., 1991, 34(8), 1991-1998.

(4) Kawada, M., Maekawa, H., Kobayashi, M. and Saitoh, H., The effect of free-stream turbulence on spanwise eddy diffusivity of heat in a flat-plate turbulent

boundary layer, JSME Int. J., Ser. II, 1992, 35(4), 573-579.
(5) Kobayashi, M., Matsubara, K., Ohki, S. and Maekawa, H., Experimental study on a turbulent boundary layer with a constant temperature gradient for a spanwise direction, Trans. Jpn. Soc. Mech. Eng., Ser. B, (submitted), in Japanese.
(6) Launder, B. E., Heat and Mass Transport, Topics in Applied Physics ed. Bradshaw, Springer Verlag, 1978, 231-287.
(7) Rogers, M., Mansour, N. N. and Reynolds, W. C., An algebraic model for the turbulent flux of a passive scalar, J. Fluid Mech., 1989, 203, 77-101.
(8) Kasagi, N. and Ohtsubo, Y., Direct numerical simulation of low Prandtl number thermal field in a turbulent channel flow, Turbulent Shear Flows 8, ed. Durst, F. et al., Springer-Verlag, 1993, 97 119.
(9) Kim, J. and Moin, P., Transport of passive scalars in a turbulent channel flow, Turbulent Shear Flows 6, ed. Andre, J. C. et al., Springer-Verlag, 1989, 85-96.
(10) Kajishima, T., Convection properties of finite difference method for convection, Trans. Jpn. Soc. Mech. Eng., Ser. B, 1994, 60(574), 2058-2063, in Japanese.
(11) Suzuki, T. and Kawamura, H., Consistency of finite-difference scheme in direct numerical simulation of turbulence, Trans. Jpn. Soc. Mech. Eng., Ser. B, 1994, 60(578), 3280-3286, in Japanese.
(12) Peylet, R. and Taylor, T. D., Computational methods for fluid flow, Springer-Verlag, 1985.
(13) Canuto, C., Hussaini, M. Y., Quarteroni, A. and Zang, T. A., Spectral Methods in Fluid Dynamics, Springer-Verlag, 1988.
(14) Kasagi, N. et al., Data base No. 02302043 supported by the Ministry of Education Science and Culture (1992).
(15) Azer, N. Z. and Chao, B. T., A mechanism of turbulent heat transfer in liquid metals, Int. J. Heat Mass Transf., 1960, 1, 121-138.
(16) Suzuki, K., An approach to liquid metal turbulent heat transfer in a circular tube solving equation with local equilibrium assumption, Letters in Heat and Mass Transfer, 1982, 9(4), 245-254.
(17) Suzuki, K., Tohkaku, A. and Sato, T., Liquid metal turbulent heat transfer in concentric annuli, Proc. of 8th Int. Heat Transf. Conf., 1985, 3, 969-974.
(18) Suzuki, K. and Tohkaku, A., Liquid metal turbulent heat transfer in a circular tube, Heat Transfer Science and Technology, ed. Wang, B. X., Springer-Verlag, 1987, 261-268.
(19) Suzuki, K., Szmyd, J. S. and Ohtsuka, H., Liquid metal turbulent heat transfer in eccentric annuli, Proc. 9th Int. Heat Transf. Conf., 1990, 6, 299-304.
(20) Kawamura, H., DNS and LES of turbulent convective heat transfer, J. Heat Transf. Soc. Jpn., 1997, 36(141), 4-15, in Japanese.
(21) Wang, L., Tsang, H., Simon, T.W., Eckert, E.R.G., Measurements of mean flow and eddy transport over a film cooling surface, ASME Proceedings of the 31st National Heat Transfer Conference, 1996, 5, 71-79.
(22) Iida, O. and Kasagi, N., Direct numerical simulation of homogeneous isotropic turbulence with heat transport (Prandtl number effects), Trans. Jpn. Soc. Mech. Eng., Ser. B, 1993, 59(567), 3359 3364, in Japanese.
(23) Jeong, J., Hussain, F., Schoppa, W. and Kim, J., Coherent structures near the wall in a turbulent channel flow, J. Fluid Mech., 1997, 332, 185-214.
(24) Iida, O. and Kasagi, N., Redistribution of the Reynolds stress and destruction of the turbulent heat flux in homogeneous decaying turbulence, Proc. of Turbulent Shear Flows 9, 1993, (24-4)1-6.
(25) Matsubara, K., Kobayashi, M. and Maekawa, H., Direct numerical simulation of a turbulent channel flow with a linear spanwise mean temperature gradient - effects of Prandtl number - , Int. J. Heat Mass Transf. (Elsevier Science Ltd.), (to appear).

PREDICTION OF STRONGLY-HEATED INTERNAL GAS FLOWS

Donald M. McEligot[1,2,3], A. Mohsen Shehata[4] and Tomoaki Kunugi[3,5]

1. Idaho National Engineering and Environmental Laboratory / LMITCo, Idaho Falls, Ida. USA
2. University of Arizona, Tucson, Ariz., USA
3. Japan Atomic Energy Research Institute, Tokai, Ibaraki, Japan
4. Xerox Corporation, Webster, N. Y., USA
5. Tokai University, Hiratsuka, Kanagawa, Japan

ABSTRACT

The purposes of the present article are to remind practitioners why the usual textbook approaches may not be appropriate for treating gas flows heated from the surface with "large" heat fluxes and to review the successes of some recent applications of turbulence models to this case. Simulations from various turbulence models have been assessed by comparison to the measurements of internal mean velocity and temperature distributions by Shehata for turbulent, laminarizing and intermediate flows with significant gas property variation. Of about fifteen models considered, five were judged to provide adequate predictions.

1. INTRODUCTION

Gas cooling of heated surfaces offers the advantages of inherent safety, environmental acceptability, chemical inertness, high thermal efficiency and a high temperature working fluid for electrical energy generation and process heating. Consequently, helium and other gas systems are considered as coolants for advanced power reactors, both fission and fusion. Cooling of a gas is important in gas turbine engine and rocket propulsion systems. These applications have in common turbulent flow with significant gas temperature variation along and/or across the cooling channels.

The purposes of the present article are (1) to remind practitioners why the usual textbook approaches may not be appropriate for treating gas flows heated from the surface with "large" heat fluxes and (2) to review the successes (and failures) of some recent applications of turbulence models to this case. Some observations will also be pertinent to cooling of a gas as well. The main message is one of caution to thermal engineers, even for apparently simple cases.

There are enough effects induced by large heat fluxes so that, to concentrate on them and avoid further complications, this paper considers only steady state conditions in a simple geometry: the classical axisymmetric circular tube. The heated region is preceded by a flow development region which yields an approximately fully-developed turbulent velocity profile; heating is then by an approximately uniform wall flux, as from electrical resistance heating. No internal energy generation is treated. The case is further constrained to small tubes, low densities and/or microgravity applications so buoyancy effects are not important; that is, the situation represents *dominant forced convection*. As a first warning, Figure 1 demonstrates the dangers of blind application of recommended "general purpose," commercial computer codes for this limited case (a version of a popular commercial code has been used on a typical engineer's work station).

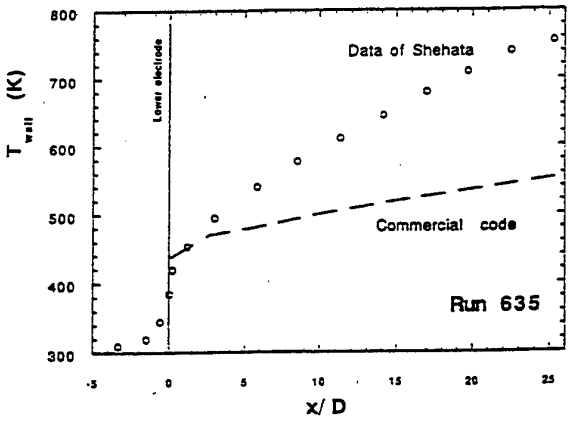

Figure 1 Numerical prediction from commercial general-purpose CTFD code, at conditions of Shehata's Run 635, compared to his measurements.

For a summary of Western studies to about 1982 on the effects of property variation on turbulent and laminar internal gas flows, the reader is referred to an earlier review by McEligot [1986]. While not all-inclusive and concentrating primarily on forced convection, this review can provide a useful introduction to the subject. The present study does not consider particle-laden gas flows; for studies of this promising technique, the reader is referred to the review of Hasegawa, Echigo and Shimizu [1986]. Reviews of mixed convection in vertical tubes are presented by Jackson and coworkers [Jackson, Cotton and Axcell, 1989; Cotton and Kerwin, 1995]. Useful reviews of the status of numerical prediction techniques for turbulent flows have been published by Nagano and Shimada [1995] and Iacovides and Launder [1995]. Nagano and Shimada relate modeling techniques to Direct Numerical Simulations (DNS) and their potential. Iacovides and Launder relate their study to applications for internal cooling passages of gas turbine blades, a complicated problem with some features of the present study; of particular interest is their conclusion

that "the first essential in modeling such flow is to adopt a low-Reynolds-number model for the sublayer region." The reader is referred to these reviews for general background on computational fluid dynamics (CFD), circa 1995.

In our terminology, the viscous layer is operationally defined to include both the so-called "linear" layer, where molecular effects dominate, and the next region where molecular effects are still significant but not dominant. For unheated flows, these regions typically extend to y^+ (= $y[g_c\tau_w/\rho]^{1/2}/\nu$) of about five and thirty, respectively. This usage follows that suggested by Bradshaw [1971]. Emphasis must often be centered on the viscous layer because it tends to provide the greatest uncertainty in predicting the convective thermal resistance [McEligot, 1986].

2. CONSTANT PROPERTY LIMIT

As will be seen later, simulations of some effects of strong heating of a gas involve the low-Reynolds-number turbulent range. In fact, Kawamura [1979] demonstrated nicely that adequate predictions of some phenomena with significant property variation were obtained when their results were also good in the low temperature-difference limit as the gas properties become effectively constant (his Figure 1). Therefore, it is appropriate that codes and their turbulence models be initially examined for fully-developed flow in a circular tube *with the constant properties idealization* to assess their capabilities to simulate low-Reynolds-number flows in the simplest case. In any event, most engineers would want both heat and momentum transfer to be handled adequately for constant properties before treating cases with property variation.

McEligot, Ormand and H. C. Perkins [1966] showed by measurements that for common gases the Dittus-Boelter correlation [1930], with the coefficient taken as 0.021 [McAdams, 1954], is valid to within about five per cent for Pr ≈ 0.7 and Reynolds numbers greater than about 2500. Thus, this correlation may be employed as a standard of comparison.

Mikielewicz [1994] conducted simulations of the predictive capabilities of a range of turbulence models for fully-developed flow in a circular tube with uniform wall heat flux and the constant properties idealization; eleven models were considered. The Reynolds number range covered was $4000 < Re < 6 \times 10^4$ and the Prandtl number used was 0.7, for air. His tabulated results are plotted in Figure 2. Based on his predictions for Nusselt number, several popular models could be immediately eliminated from further consideration. Some models do not even handle high-Reynolds-number flows well for heat transfer. Several k-ε models designed for use at low Reynolds numbers also gave poor results. At Re = 5000, the Jones and Launder version is over thirty per cent high and predictions by Lam and Bremhorst and by Shih and Hsu are over fifteen per cent above the correlation. The only model considered which gave acceptable results was that of Launder and Sharma; their predictions fall within the estimated experimental uncertainty in the Nusselt number over the full range.

Reasonable predictions have also been provided in the low-Reynolds-number range for this case by McEligot, Ormand and Perkins [1966], McEligot and Bankston [1969], Kawamura [1979], Torii et al. [1991], Ezato et al. [1997] and Nishimura and Fujii [Nishimura et al., 1997] and others. These calculations have covered a range of types of turbulence models, from modified mixing length approaches to a Reynolds stress model coupled to a two-equation model for heat transfer.

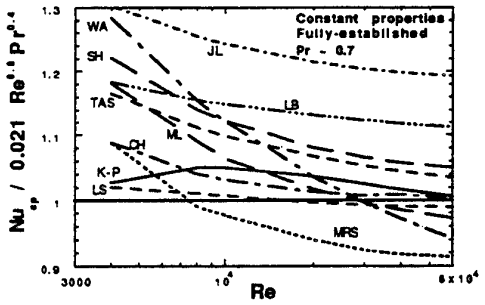

Figure 2. Simulations by Mikielewicz [1994] using various turbulence models (curve labeled KP is the Kurganov-Petukhov correlation).

3. EFFECTS OF LARGE HEAT FLUXES

The effects of temperature on the transport properties of helium are presented in Figure 3. From the perfect gas "law", one recalls that the density also varies significantly -- approximately inversely with the absolute temperature. These trends are typical of most common gases and of binary mixtures of gases; for the former, the Prandtl number is around 2/3 or 0.7, while for the latter in may be as low as 0.2 [McEligot, Taylor and Durst, 1977].

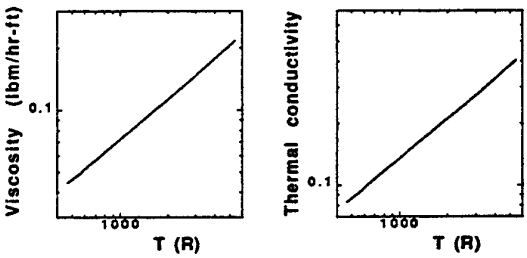

Figure 3. Transport properties of helium.

From Figure 3 it can be seen that the temperature dependencies of the viscosity and thermal conductivity can also be approximated by power laws

$$\mu/\mu_{ref} \approx (T/T_{ref})^a \text{ and } k/k_{ref} \approx (T/T_{ref})^b$$

for convenience in numerical predictions.

We consider the idealization of a uniform wall heat flux for convenience in the presentation. With

appropriate assumptions [McEligot, 1963], one can approximate the increase in bulk temperature along the tube as

$$(T_b/T_{in}) \approx 1 + 4\, q^+_{in}\, (x/D)$$

and the wall-to-bulk temperature difference as

$$((T_w - T_b)/T_{in}) \approx q^+_{in}\, Re^{1-a}\, Pr^{0.6}/C$$

The non-dimensional heating rate $q^+_{in} = q''_w/Gc_{p,in}T_{in} = q''_w A_{cs}/\dot{m}\, c_{p,in}T_{in}$ evolves naturally from non-dimensionalizing the governing equations and boundary conditions in pipe flow with an imposed wall heat flux distribution [Bankston and McEligot, 1970]. Property effects come in via the (non-dimensional) exponents in the power law representations. With "large" heat fluxes (large q^+), the resulting temperature range causes significant variation of the gas properties, invalidating the use of design relations such as the popular Dittus-Boelter correlation.

If one defines the Reynolds number based on bulk fluid properties as $Re = GD/\mu_b = 4\dot{m}/(\pi D\mu_b)$, then its value will continuously decrease as the axial distance increases with heating. The perfect gas approximation shows the bulk density likewise to decrease as x increases. From an integral continuity relationship for steady flow, $\dot{m} = \rho_b V_b A_{cs}$, one sees the velocity increases in the streamwise direction. That is, the flow accelerates spatially.

In strongly-heated, internal gas flows the pressure drop can be dominated by the induced acceleration as suggested by McEligot, Smith and Bankston [1970]. Assumptions and approximations involved are steady state, one-dimensional flow, constant cross section and low Mach number. The momentum equation then can be arranged in a non-dimensional form,

$$-\{2\rho_x g_c D_h (dp/dx)/G^2\} \approx 8q^+_x + 4f_{\tau,x} + 2(Gr^*_x/Re_x^2)$$

where the subscript x indicates evaluation of properties at the local bulk temperature. The Grashof number appearing in the body force term is defined as $Gr^*_x = gD_h^3/\nu_x^2$ and g is taken as directed opposite to the flow direction (i.e., upflow).

Thus, general effects of strong heating of a gas are variation of the transport properties, reduction of density causing acceleration of the flow in the central core, and - in some cases - significant buoyancy forces. Growth of the internal thermal boundary layer leads to readjustment of any previously fully-developed turbulent momentum profile, i.e., no truly fully-established conditions are reached because the temperature rises -- leading, in turn, to continuous axial and radial variation of properties such as the gas viscosity. For calculations, the property variation couples the momentum equation to the thermal energy equation so they must be solved "simultaneously."

In an application such as the High Temperature Engineering Test Reactor (HTTR) in Japan, or reduction of flow scenarios in other plants, another complication arises. To obtain high outlet temperatures, design gas flow rates are kept relatively low. For example, at the exit of the HTTR cooling channels, the Reynolds number is about 3500. In this range, the heat transfer parameters may appear to correspond to turbulent flow or to laminar flow or to an intermediate behavior, depending on the heating rate [Bankston, 1970], with consequent differences in their magnitudes (Figure 4). If the designer is to have confidence in a CTFD code, its turbulence model must demonstrate the "proper" predictions in these conditions. The situation where laminar values are measured at Reynolds numbers typifying turbulent flow is called "laminarization" by some authors [Perkins, 1975]. Several authors have developed approximate criteria for laminarization by heating using graphical correlations of the heating rate as $q^+_{in}\{Re_{in}\}$ [McEligot, 1963; Fujii et al., 1991] as in Figure 5; these have been shown by McEligot, Coon and Perkins [1970] to correspond to an acceleration parameter, $K_v = (\nu^2/V_b)/(dV_b/dx) \approx 4q^+_{in}/Re_{in}$, which varies approximately as $1/\dot{m}^2$.

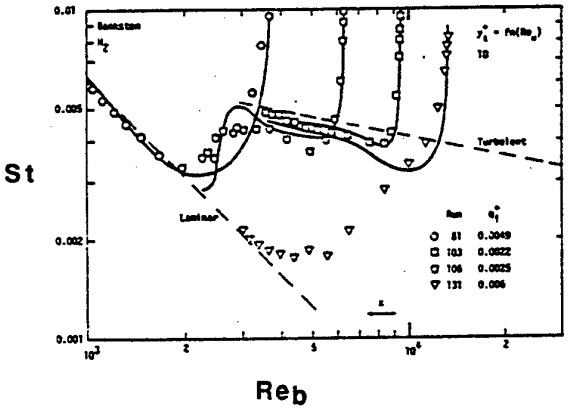

Figure 4. Measurements of Bankston [1965].

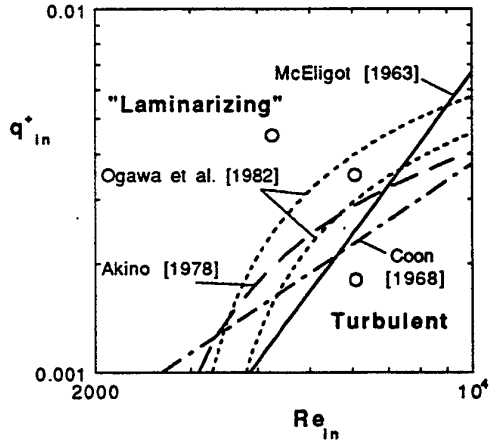

Figure 5. Suggested laminarization criteria [Ezato et al., 1997].

The difficulties in predicting wall temperatures and heat transfer parameters with strong heating and possible laminarization have been demonstrated strikingly by the data of Coon [McEligot, Coon and Perkins, 1970] and of Bankston [McEligot and Bankston, 1969]. Some of Bankston's measurements are shown in Figure 4 along with one attempt to match the data with a simple turbulence model. In this figure, the development is from right to left due to the axial variation of Reynolds number due to the heating; the dashed lines represent accepted empirical correlations for fully-established laminar and turbulent conditions with constant gas properties. One sees the local Stanton numbers decrease below the turbulent correlation for his runs 103 and 106 and then converge towards it downstream (as T_w/T_b approaches unity). For his run 131 the laminar prediction is approached at local Reynolds numbers near 4000.

4. RELATED WORK

Most of the early data for gas heating with significant property variation were obtained with circular tubes of small diameters so forced convection dominated [McEligot, 1986]. With test sections typically less than thirteen mm (D < 1/2 inch) probes could not be inserted for useful profile measurements and, therefore, the experiments could only provide integral wall parameters, such as local heat transfer coefficients and friction coefficients. These data gave initial tests of turbulence models accounting for temperature-dependent transport properties, as demonstrated by McEligot and Bankston [1969], Bankston and McEligot [1970] and Kawamura [1979]. For quasi-developed turbulent flow, experimental results were typified by the empirical correlations of McEligot, Magee and Leppert [1965],

$$Nu_b \approx 0.021\, Re_b^{0.8}\, Pr^{0.4}\, (T_w/T_b)^{-1/2}$$

and

$$(f_b / f_{cp}) \approx (T_w/T_b)^{-0.1}$$

In later studies, approximate agreement with such correlations has been taken as indication of normal turbulent behavior *with gas property variation.*

McEligot [1963] attempted to examine the effects of gas property variation in the laminar-to-turbulent transition region. He found conditions where the local Nusselt number diverged below the turbulent correlation shown above as the axial distance increased and the local Reynolds number thereby decreased. An approximate correlation for this transition was deduced. McEligot estimated flow regimes as turbulent, transitional or laminar based on agreement with the correlations; these studies *might* be considered to be the "discovery" of the process we now call laminarization by heating. Related measurements were obtained by Perkins and Worsoe-Schmidt [1965] and Bankston [1965] at higher temperature ratios during the same time period. Bankston [1966] pointed out that, for the transition or "reverse transition" regime, calculations of the acceleration parameter K_v gave values in the range that Kline et al. [1967] found corresponded to laminarizing conditions in unheated turbulent boundary layers.

Since the 1960s, measurements with larger test sections have been conducted by Hall and Jackson and colleagues at the University of Manchester to examine effects introduced by buoyancy forces aligned with or opposing the flow [Jackson, Cotton and Axcell, 1989]. These studies have led to criteria for significant buoyancy effects in turbulent flow.

By comparison to the thermal entry measurements of Perkins and Worsoe-Schmidt, of McEligot, Magee and Leppert and of Petukhov, Kirillov and Maidanik, Bankston and McEligot [1970] were able to examine the application of eleven algebraic turbulence models for high-Reynolds-number turbulent gas flows with properties varying strongly in both axial and radial directions. Best agreement was found with a van Driest mixing length model with the exponential term evaluated with wall properties,

$$\ell = 0.4\, y\, [\, 1 - \exp\{- y_w^+ / A^+\}\,]$$

where y_w^+ is defined unambiguously as $y(g_c\tau_w/\rho_w)^{1/2}/\nu_w$ and A^+ was taken as 26, as by van Driest. To accommodate low-Reynolds-number turbulent and laminarizing flows, McEligot and Bankston [1969] modified this model (described by Shehata and McEligot [1998]). This modification was developed by comparison to integral quantities, such as the local Stanton number, since internal profile measurements were not then available for guidance.

Most recent work on the topic of laminarization by heating has been conducted in Japan. Measurements of local heat transfer coefficients and friction factors for transitional and laminarizing flows have been obtained by Ogawa et al. [1982] and Ogawa and Kawamura [1986] with circular tubes. Local Nusselt numbers were measured for annuli by Fujii et al. [1991] and Torii et al. [1991]. The first investigator to succeed in applying an advanced turbulence model to laminarization by heating apparently was Kawamura [1979]. He concluded that a modified k-kL model gave good agreement with the experiments. Fujii et al. [1991] employed three types of turbulence models for comparisons to their measurements of strongly-heated turbulent gas flow in an annulus. Torii et al. [1991] and Torii and Yang [1997] applied modified k-ε models for predicting streamwise variation of heat transfer parameters in low-Reynolds-number turbulent and laminarizing flows in circular tubes and annuli. Torii et al. [1993] also attempted to apply the Reynolds-stress model of Launder and Shima to St{Re} data for a circular tube; they concluded that predictions were comparatively poor in the range of turbulent-to-laminar transition.

Since the flows are typically at low Reynolds numbers, it would appear that DNS techniques [Nagano and Shimada, 1995] would be ideal to predict situations such as laminarization induced by strong heating of a

gas. While Satake and Kunugi in Japan have been developing a DNS code for circular tubes for this purpose, results do not yet appear to be available with strong property variation. However, for the comparable quasi-developed problem in a two-dimensional channel, Dailey and Pletcher [1998] obtained successful Large Eddy Simulations (LES) employing a Smagorinsky subgrid-scale model with van Driest damping at the walls.

Turbulence models have generally been developed for conditions approximating the constant properties idealization. The few "advanced" turbulence models applied for high heating rates [Kawamura, 1979; Fujii et al., 1991; Torii et al., 1993; Torii and Yang, 1997] were developed without the benefit of velocity and temperature distributions in strongly-heated, dominant forced flow for guidance or testing. Thus, it is not certain whether the agreement with wall temperature data for moderate and strong wall heat fluxes, that was obtained in some cases with such models, was fortuitous or not. Before they can be applied with confidence to gas-cooled systems with high heat fluxes, predictions from turbulence models must be validated by comparison to careful measurements of the internal mean flow and thermal distributions for conditions with significant gas property variation.

5. MEASUREMENTS AVAILABLE

For dominant forced convection *with significant gas property variation* in low Mach number flow of common gases through a circular tube, apparently the only published profile data available to guide (or test) the development of predictive turbulence models have been K. R. Perkins's and Shehata's measurements of mean temperature distributions [Perkins, 1975] and mean velocity distributions [Shehata and McEligot, 1995] for this situation. Their careful measurements are now available to examine this problem and these can serve as the bases for evaluation of predictive techniques. Their experiments concentrated on three characteristic cases with gas property variation: turbulent, laminarizing and intermediate or "subturbulent" (as denoted by Perkins). To the authors's knowledge, the only numerical studies of "advanced" turbulence models for turbulent and laminarizing flows at high heating rates that utilized *internal* data have been those of Mikielewicz at Manchester and Ezato, Nishimura and Fujii in Japan recently.

The experiments of Shehata (and of Perkins) were conducted using an open flow system incorporating a vertical, resistively-heated, circular test section exhausting directly to the atmosphere in the laboratory. The experiment was designed to provide an approximately uniform wall heat flux boundary condition in a tube for ascending air, entering with a fully-developed turbulent velocity profile at a uniform temperature. The heated length was kept relatively short to permit high heating rates with Inconel as the material while possibly approaching quasi-developed conditions. Small single wire probes were introduced through the open exit in order to obtain pointwise temperature and velocity measurements. In addition to the usual difficulties of hot wire anemometry, the temperature range of his experiment introduced additional problems such as radiation corrections; these difficulties, their solutions and related supporting measurements are described by Shehata [1984] and Shehata and McEligot [1995]. Inlet Reynolds numbers ($Re_{in} = 4\dot{m}/(\Pi D\mu_{in})$) of approximately 6000 and 4000 were employed and attention was concentrated on three heating rates chosen to give significant variation of properties for conditions of predominantly forced convection which were considered to be "turbulent," "intermediate," and "laminarizing," respectively ($q^+_{in} \approx$ 0.0018, 0.0035 and 0.0045). The runs are labeled 618, 635 and 445 with the first digit identifying the inlet Reynolds number and the last two indicating the non-dimensional heating rate.

The length of the test section was chosen to permit measurements through and beyond the normal thermal entry region while attaining significant transport property variation, as exemplified by T_w/T_b and T_w/T_i, with common materials and gas. Wall temperatures reached 840 K (1510 R), the maximum wall-to-bulk temperature ratio was about 1.9 and the Mach number was less than 0.013, indicating that compressibility effects would have been negligible. At the entrance the buoyancy parameter Gr_q/Re^2 reached 0.53 for the highest heating rate and lower Reynolds number; it then decreased as x/D increased. The maximum wall-to-inlet temperature ratio was about 2.7, indicating that gas properties such as viscosity varied by a factor of two in the test section. Exit bulk Reynolds numbers were above 3000 in all cases, corresponding to turbulent flow if the test section had been adiabatic.

With the data of Perkins and of Shehata, detailed internal mean profiles for predominantly forced flow in a circular tube are now available for the following approximate conditions:

Re_{in}	q^+_{in}	Temperature	Velocity
8520	0.0010	X	
6020	0.0011	X	
6030	0.0018	X	X
6020	0.0035	X	X
6040	0.0045	X	
4260	0.0045	X	X
3760	0.0055	X	

Tabulations of these data and the boundary and initial conditions are available in the reports of Perkins [1975] and of Shehata and McEligot [1995]. From the graph of laminarization criteria by Fujii et al. [1991] as in Figure 5, one can see these measurements span a range from turbulent behavior at moderate heating rates to rapidly laminarizing flows. From those results further aspects of the development of the mean turbulence structure may also be deduced. For example, once one establishes agreement with measured U{y,x} and T{y,x} fields as in the next section, the distributions of ε/ν, $1/r_w$, $-\overline{uv}$, $-\overline{vt}$, etc. -- that are required for that

matching -- may be considered to be indirectly deduced data [Shehata and McEligot, 1995]. This approach could be thought to be an extension of the earlier technique of deducing eddy diffusivity profiles for simple fully-developed, adiabatic flows by fitting mean velocity profiles. That is, by adjustment of the turbulent models which give $-\overline{uv}$, $-\overline{vt}$, etc., the velocity and temperature distributions have been fit.

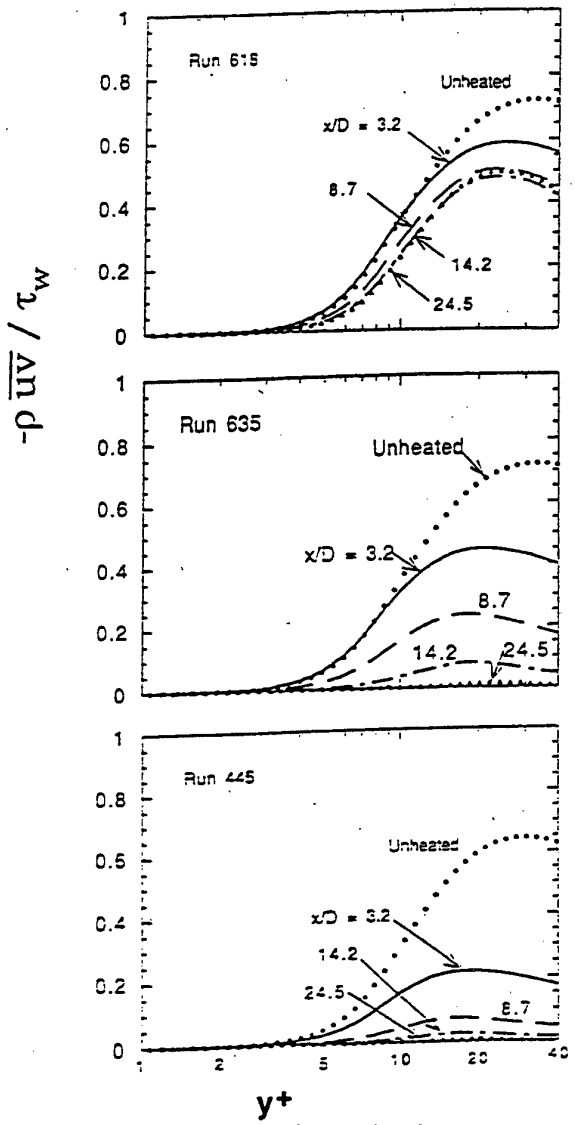

Figure 6 Axial behavior of Reynolds shear stress profiles as deduced from velocity and temperature measurements via numerical diagnostic technique [Shehata and McEligot, 1995].

The Reynolds shear stress or turbulent shear stress distributions, $-\rho\,\overline{uv}$, which are required in order to obtain agreement between predictions and measurements, are shown normalized by the local wall shear stress in Figure 6. For fully-developed, adiabatic turbulent flow the total shear stress, $\mu(\partial U/\partial y) - \rho\,\overline{uv}$, decreases linearly from the wall to the centerline. Therefore, across the viscous layer the normalized Reynolds stress increases from zero to approach the value for the total shear stress, as molecular effects become less important, and then follows this decreasing ramp-like function to zero at the centerline. For each of Shehata's runs, one can discern the beginning of this behavior in the adiabatic entry profile of $-\rho\,\overline{uv}/\tau_w$. With the significant heating of Runs 618 and 635, the deduced levels of these Reynolds stress profiles decrease from the entry to x/D ≈ 3.2, the first heated profile. For the "turbulent" run (618), the normalized Reynolds stress settles to an approximately constant profile from x/D ≈ 9 to 25 with slight variation. For the other two runs at higher heating rates, these profiles decrease to negligible values as the axial distance increases. For Run 445 the deduced reduction in the first few diameters is more severe than for Run 635; in a sense, Run 445 laminarizes more quickly (as might be expected for lower Re_i and higher q^+_i).

6. SIMULATIONS WITH GAS PROPERTY VARIATION

Mikielewicz [1994] examined eleven turbulence models developed for forced turbulent flow with the constant property idealization as discussed earlier. For fully-developed flow with constant properties at Reynolds numbers in the range 4000 < Re < 60,000, only the model by Launder and Sharma agreed with the Dittus-Boelter correlation for common gases (coefficient = 0.021) within its estimated experimental uncertainty over the full range; several k-ε models designed for low-Reynolds-number conditions gave poor agreement.

A number of turbulence models, developed for turbulent flows under conditions of uniform fluid properties, were applied by Mikielewicz for the purposes of simulating experiments with *strongly-heated, variable property* gas flows at low Reynolds numbers in a vertical circular tube [Shehata, 1984]. The selection of models included a mixing length model, eddy diffusivity models, a one-equation k model and two-equation models of k-ε type with low-Reynolds-number treatments; this selection is representative of models which have been widely used but obviously is not all-inclusive. Thermal energy transport was modeled using a turbulent Prandtl number with its value held constant (0.9).

To illustrate the predictions of *integral heat transfer*, Figure 7 presents the resulting wall temperature distributions for eight models for the three runs. For the thermal design engineer, these predictions are of key importance. In this figure the distance z/D is labeled from the start of the calculation, so the nominal start of heating (usually called x = 0) is at z/D = 14.8 and the near-uniform wall heat flux range is in the region 20 < z/D < 41. The expected sharp rise of wall temperature after the abrupt increase in wall heat flux (near z/D = 15) is demonstrated by all the models.

In Figure 7 the identification of the various models is via letter labels; the square symbols are the measurements from Shehata [1984]. For the lowest heating rate, "turbulent" Run 618, the trends from

model to model are approximately the same as for the results for fully-established heat transfer with constant properties that were presented in Figure 2; models which did not reproduce that condition well predict the behavior with property variation poorly as well. For the purpose of making quantitative comparisons, we examine the predictions at z/D ≈ 40 where the wall temperature is highest.

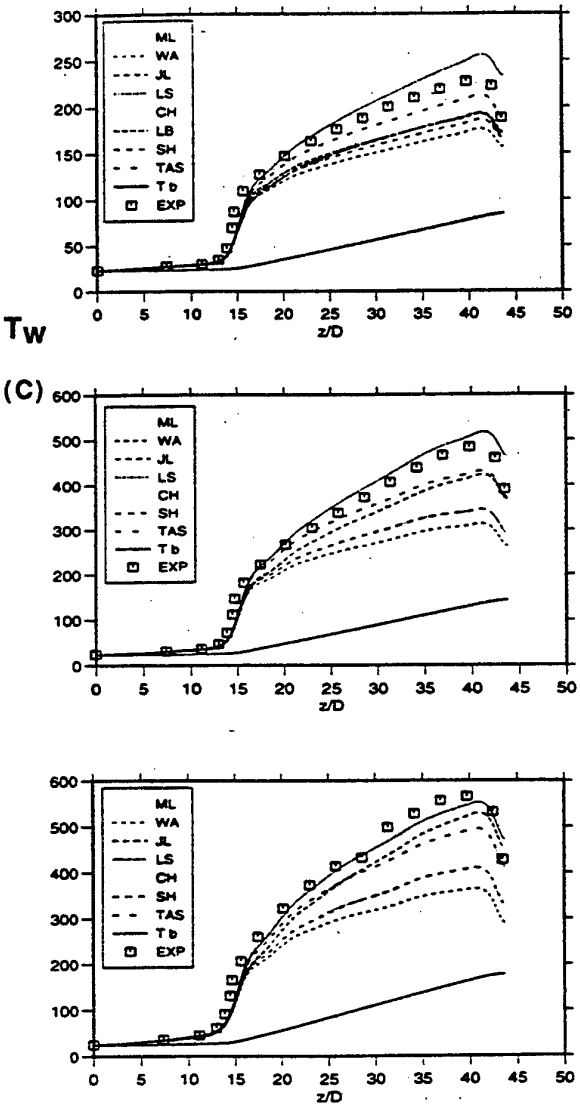

Figure 7 Simulations by Mikielewicz [1994].

The wall-to-bulk temperature difference is underpredicted by over forty per cent in the worst case. The discrepancy is thirty per cent in the case of one "low-Reynolds-number" k-ε model (SH), actually slightly worse than the "original" van Driest mixing length model. The low-Reynolds-number k-ε models of Jones and Launder and of Lam and Bremhorst gave approximately the same results as the mixing length model. Forecasts within twenty per cent of the measured values were yielded by Michelassi, Rodi and Scheurer, by Chien and by Thangam, Abid and Speziale. The model of Launder and Sharma (LS) did slightly better with a conservative overprediction of about thirteen percent.

Comparisons in the cases of the two higher heating rates discriminate amongst the models further. In general, the models showing poor agreement at the lower heating rate remained poor. Numerical difficulties were experienced using a couple models when they were applied under conditions of strongly varying properties and no results were produced. The one-equation model (WA) underpredicted the temperature difference by fifty per cent or more for such conditions. There were some differences in relative rankings of the models as the heating rate was increased and Reynolds number decreased. The JL model improved relative to the CH and TAS low-Reynolds-number k-ε models. At the lower Reynolds number, as one might expect, some of the low-Reynolds-number k-ε models performed better in comparison to the "original" van Driest mixing length model (which was developed for high Reynolds number flows). For strong heating of a gas with property variation, Mikielewicz concluded that the model of Launder and Sharma gave the best predictions overall.

Simulations are next assessed in terms of the *mean velocity and temperature profiles.* Figures 8 to 10 provide direct comparisons between predicted profiles and the data. Presenting velocities in the form of profiles of U/V_b avoids the uncertainties which would have been involved in the use of u_τ for non-dimensionalization. Presenting temperatures in the form T/T_{in} or $(T_w-T)/T_{in}$ checks agreement with the energy and mass balances as well as providing a picture of the development of the thermal layer. In general, the estimated uncertainty in local velocity measurement by Shehata was calculated to be in the range of eight to ten per cent, with the larger value being associated with measurements near the wall. The uncertainty in local temperature measurement was typically one or two percent of the absolute temperature. These estimates are believed to be conservative since comparisons between the integrated and measured total mass flow rates for each profile showed better agreement (three per cent or less, except near the exit in the runs with the two highest heating rates). In contrast to conventional wisdom, when there is significant *gas* property variation, a mass balance is primarily a test of the profile of the quotient $U\{y\}/T\{y\}$ and an energy balance checks the profile $U\{y\}$ (Shehata and McEligot [1995]).

The measured points nearest the wall correspond to values of y^+ from about 3 to 5, depending on the heating rate and station. The location $y/r_w = 0.1$ corresponds to $y^+ \approx 20$ for the entry profiles of Runs 618 and 635. At the last station, $y/r_w = 0.5$ is about $y^+ \approx 60$ and 30 for runs 618 and 445, respectively. A significant portion of the tube is therefore occupied by the viscous layer in all three runs.

The quantity T/T_{in} provides an indication of gas property variation both across and along the tube. In Run 618, T/T_{in} varies by about fifty per cent from the wall to $y/r_w = 0.5$ at the last station, so μ and k vary by about forty per cent in that region. In contrast, in run 445 they vary by more than that in the first three

diameters of the heated portion of the pipe. At the first station for each run, the velocity data points near the wall appear to be high relative to what would be indicated by extrapolation of the data further out, a common feature in such measurements (and a good reason for not determining u_τ by fitting to $u^+ = y^+$). Measurements at this location required the greatest insertion of the probe so some aspects of the data reduction are necessarily more uncertain there.

Overall agreement between the Launder Sharma predictions of internal distributions by Mikielewicz and the measurements by Shehata was encouraging though close examination revealed some detailed discrepancies. In such cases there were corresponding differences between predictions of integral parameters and data. Generally, however, the predictions of velocity and temperature profiles are considered to provide a satisfactory description of the observed behavior.

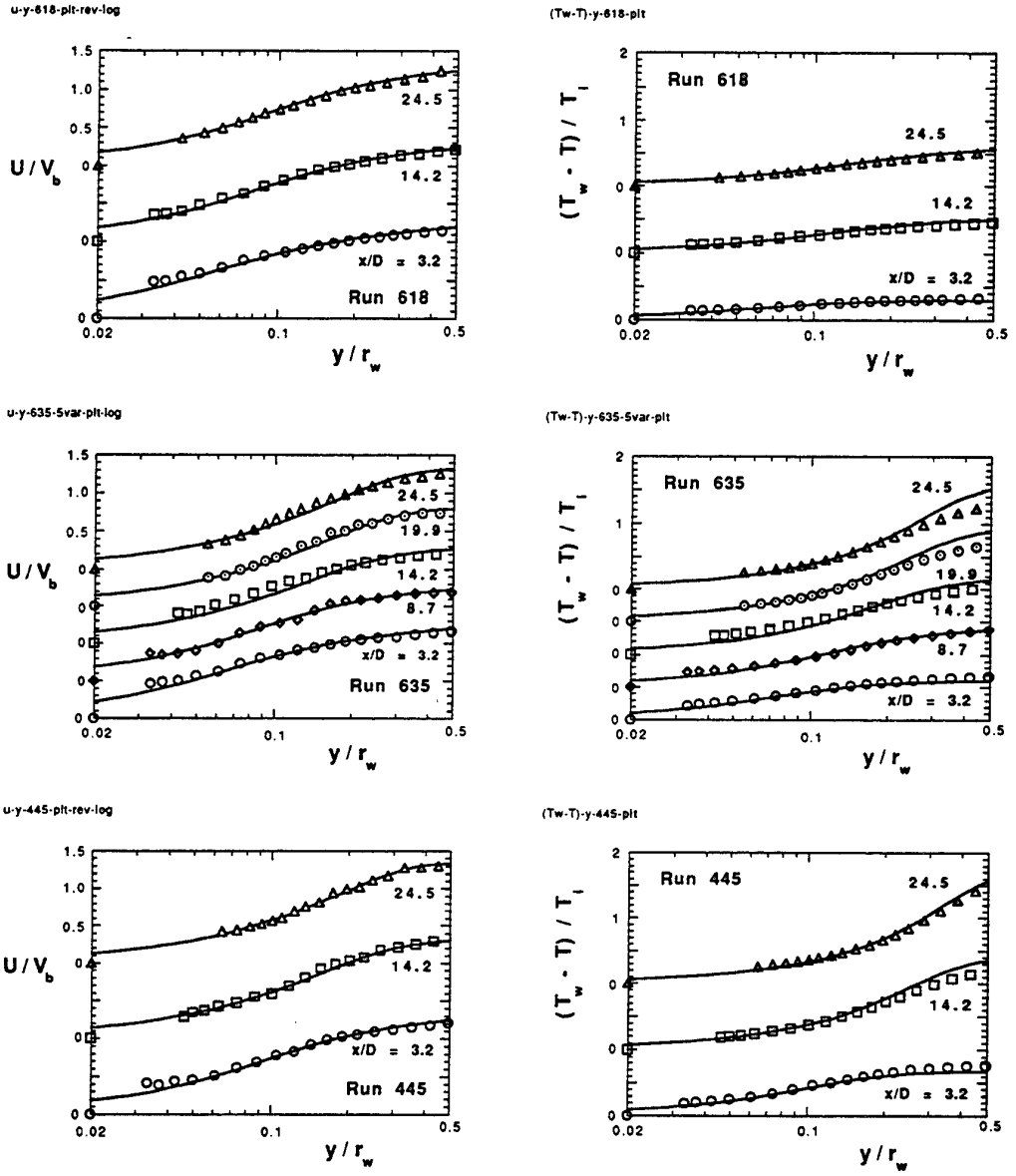

Figure 8 Simulations from modified van Driest model compared to data [Shehata and McEligot, 1998].

In addition to documenting the first mean velocity distributions for these difficult cases, the study by Shehata and McEligot [1998] demonstrated that the simple *modified van Driest model* (developed from wall data alone by McEligot and Bankston [1969]) predicts the mean internal profiles (Figure 8) and non-dimensional pressure drop reasonably well overall. However, Bates et al. [1974] have demonstrated that this model is not appropriate for flows with large buoyancy effects.

Figure 8 presents the comparison between predictions and data for the viscous layer in forms equivalent to wall coordinates while avoiding the uncertainty introduced by the determination of the wall shear stress. In wall coordinates the velocity profile is particularly sensitive to the uncertainty of τ_W since it

appears in the numerator for y^+ and the denominator for u^+. By using the semi-log axes the presentation is concentrated on the viscous layer. For the temperature profiles, $t^+_w = (T_w\text{-}T)\rho_w u_{\tau,w} c_{p,w}/q''_w$ is represented by $(T_w\text{-}T)/T_i$. These comparisons of predictions and measurements are more direct (and more severe) than using wall coordinates based on a wall shear stress which has been fitted in the viscous layer.

As $t^+\{y^+\}$ normally shows the same trends as $u^+\{y^+\}$ in fully-established, constant-property flow, the profiles of $(T_w\text{-}T)/T_i$ approximate the trends of U/V_b here. Even when the examination concentrates on the near wall region, Runs 618 and 445 (lowest and highest q^+) are predicted well by the modified van Driest model through the viscous layer. (At $x/D \approx 24.5$, $y^+_w \approx 30$ corresponds to $y/r_w \approx 0.26$ for Run 618 and to $y/r_w \approx 0.5$ for 445.)

For Run 635 the velocity predictions agree reasonably well within the viscous layer for all but the profile at $x/D \approx 14$ (at this location, $y^+_w \approx 30$ corresponds to $y/r_w \approx 0.32$ for this run). Non-dimensional temperature profile agreement is approximately the same at this location, underpredicted for $y/r_w < \sim 0.2$ and then overestimated. Further downstream the non-dimensional temperature agrees well for $y/r_w < \sim 0.2$ then diverges for higher values (at $x/D \approx 24.5$, $y/r_w \approx 0.2$ corresponds to $y^+_w \approx 16$, which would be about halfway across the viscous layer in unheated flow). Shehata and McEligot [1995] show that $-\rho\overline{uv}/\tau_w$ is predicted to be less than 0.1 at $x/D >$ 14 there in this heated flow (Figure 6) -- so this good agreement near the wall would be a consequence of molecular transport dominating. For temperature distributions these trends continue downstream while agreement of the velocity distribution appears to improve at $x/D \approx 20$ and 24.5. Interpreting this observation in terms of energy transport, one could say that the model predicts a lower rate of turbulent transport than observed from the wall region to the core, starting between $x/D \approx 9$ and 14; *one* explanation could be overprediction of the effective viscous layer thickness at these local conditions. Conceptually, one could adjust the function $A^+\{Re\}$ or other features of a turbulence model to accommodate these details (in fact, Perkins [1975] did improve prediction of $T\{r,x\}$ for "subturbulent" runs by revising $A^+\{Re\}$ at low Reynolds numbers). Figure 8 demonstrates that the *modified* van Driest model does correlate the mean velocity and temperature measurements fairly well overall even for Run 635, the most difficult of the three to predict.

For Run 445, temperature predictions generally look good throughout, despite the fluid property variation being greatest for that case. This result is probably because molecular transport increases in importance once the laminarizing process has begun and so the uncertainties in the turbulence modeling are of less significance. While the mean velocities are slightly high in the central region for $x/D \approx 14$ and 25, they are within the (conservative) estimated experimental uncertainties. Whereas the temperature profiles show close agreement at the thermal entrance and exit, the profile at $x/D \approx 14$ also exhibits the discrepancies seen for Run 618, i.e., overprediction near the wall and underprediction in the core.

The *k-ε turbulence model* of Abe, Kondoh and Nagano [1994], developed for forced turbulent flow between parallel plates with the constant property idealization, has been successfully extended by Ezato [1997] to treat strongly-heated gas flows at low Reynolds numbers in vertical circular tubes. For thermal energy transport, he adopted the turbulent Prandtl number model of Kays and Crawford [1993]. No constants or functions in these models were readjusted.

Under the idealization of constant fluid properties, predictions for fully-established conditions agreed with the Dittus-Boelter correlation for common gases (coefficient = 0.021) within about five per cent for $Re > 3200$. Predicted friction coefficients were about five per cent higher than the Drew, Koo and McAdams [1932] correlation in this range. Below $Re \approx$ 2000 both predictions agreed with theoretical laminar values within about one per cent. The local thermal entry behavior, $Nu\{x/D\}$, was further confirmed by comparison to the measurements of H. C. Reynolds [1968] for $Re \approx 4180$ and 6800.

The capability to treat forced turbulent flows with significant gas property variation was again assessed via calculations at the conditions of experiments by Shehata. Predictions forecast the development of turbulent transport quantities, Reynolds stress and turbulent heat flux, as well as turbulent viscosity and turbulent kinetic energy. Results suggest that the run at the lowest heating rate behaves as a typical turbulent flow, but with a reduction in turbulent kinetic energy near the wall. For the highest heating rate all turbulence quantities showed steady declines in the viscous layer as the axial position increased - representative of conditions called laminarizing. For the intermediate run, predictions showed the same trends as the highest heating rate but occurred more gradually with respect to axial distance. These observations are consistent with empirical criteria for these regimes, expressed in terms of $q^+_{in}\{Re_{in}\}$. No direct measurements are available to confirm or refute these turbulence distributions; they must be assessed by examination of the mean velocity and temperature distributions that result from these predictions of the turbulent transport quantities.

Figure 9 provides direct comparisons of the predictions to measured profiles. Run 618 shows a slight overprediction of the velocity profile at $z/D \approx 25$ but otherwise all profiles are good. (In Ezato's calculations, the quantity z represents the distance from the nominal start of heating.) Run 445 predictions look good throughout despite having the largest fluid property variation; again, this result probably occurs because molecular transport increases in importance once the laminarizing process has begun. So if one wishes the most sensitive test of a turbulence model for low-Reynolds-number flows with gas property variation, conditions like those of Run 635 may be key.

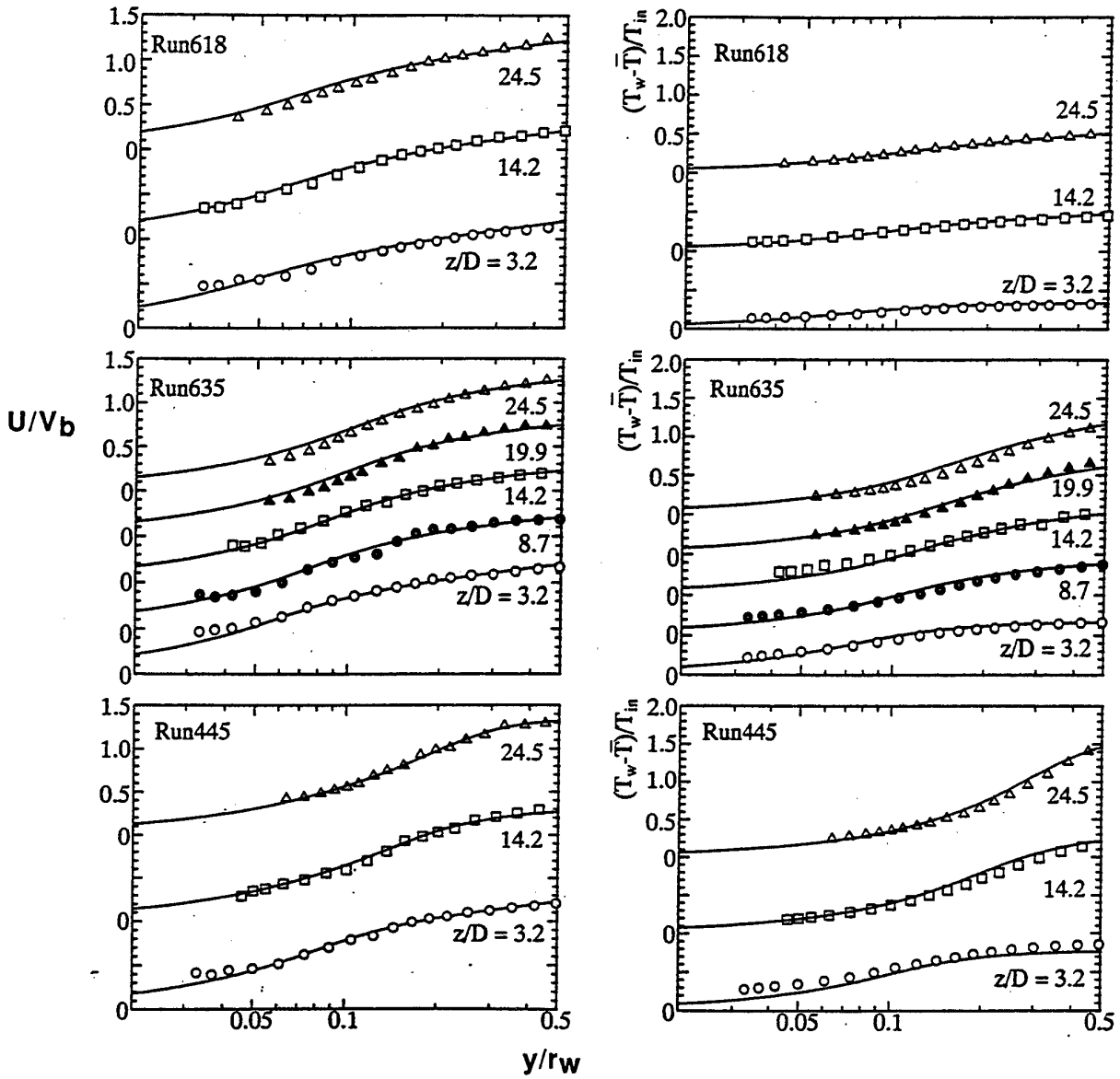

Figure 9 Simulations from k-ε model by Ezato compared to data [Ezato et al., 1997].

For Run 635 agreement between calculations and data is good for the first three stations. Then at $z/D \approx 20$ and 25 the velocity is overpredicted near the wall and at $z/D \approx 25$ the quantity $(T_w - T)/T_{in}$ is overpredicted in the range $0.1 < y/r_W < 0.25$ (corresponding approximately to $8 < y^+ < 20$), i.e., $T\{y\}$ is *under*predicted. In the viscous layer, a higher velocity is caused by a lower value of μ_t, which also leads to a higher thermal resistance in the layer; this higher thermal resistance would interfere with thermal energy transport beyond the region leading, in turn, to lower temperatures further from the heated wall. If one wishes to improve the model further, these observations could provide a starting point. For the present purposes, the level of agreement seen is considered satisfactory.

Overall agreement between the predictions and the measured velocity and temperature profiles is good, establishing confidence in the values of the forecast turbulence quantities -- and the model which produced them. Most importantly, the model also yields predictions which compare well to the measured wall heat transfer parameters and the pressure drop. Thus, thermal design engineers should find calculations based on the turbulence model used by Ezato to be satisfactory for forced low-Reynolds-number turbulent flows with significant gas property variation.

Figure 10 describes the axial flow development after the start of heating in non-dimensional terms, $U/V_b\{x\}$ and linear coordinates. Circles represent Shehata's measurements.

The first set of thermal entry data is for the *"low" heating rate* conditions characterized as *turbulent* by Perkins [1975]. The reference control parameters

were $Re_i \approx 6000$ and $q^+ \approx 0.0018$ (i.e., *Run 618*), leading to an acceleration parameter of about 1.2×10^{-6}. The non-dimensional radius of the unheated upstream section is about $r^+ = y^+_c \approx 200$. It is expected that the heat transfer parameters would correspond to turbulent predictions, with allowance for a reduction in local Nusselt number (typically of the order of $(T_W/T_b)^{-1/2}$)) due to the gas property variation along the tube and across the viscous layer. Figure 10a presents the momentum development axially in terms of mean profiles at 3.17, 14.2 and 24.5 diameters. Obtaining the *mean streamwise velocity data* was the main objective of Shehata's work since Perkins [1975] was unable to obtain meaningful velocity measurements in his attempts with an impact tube.

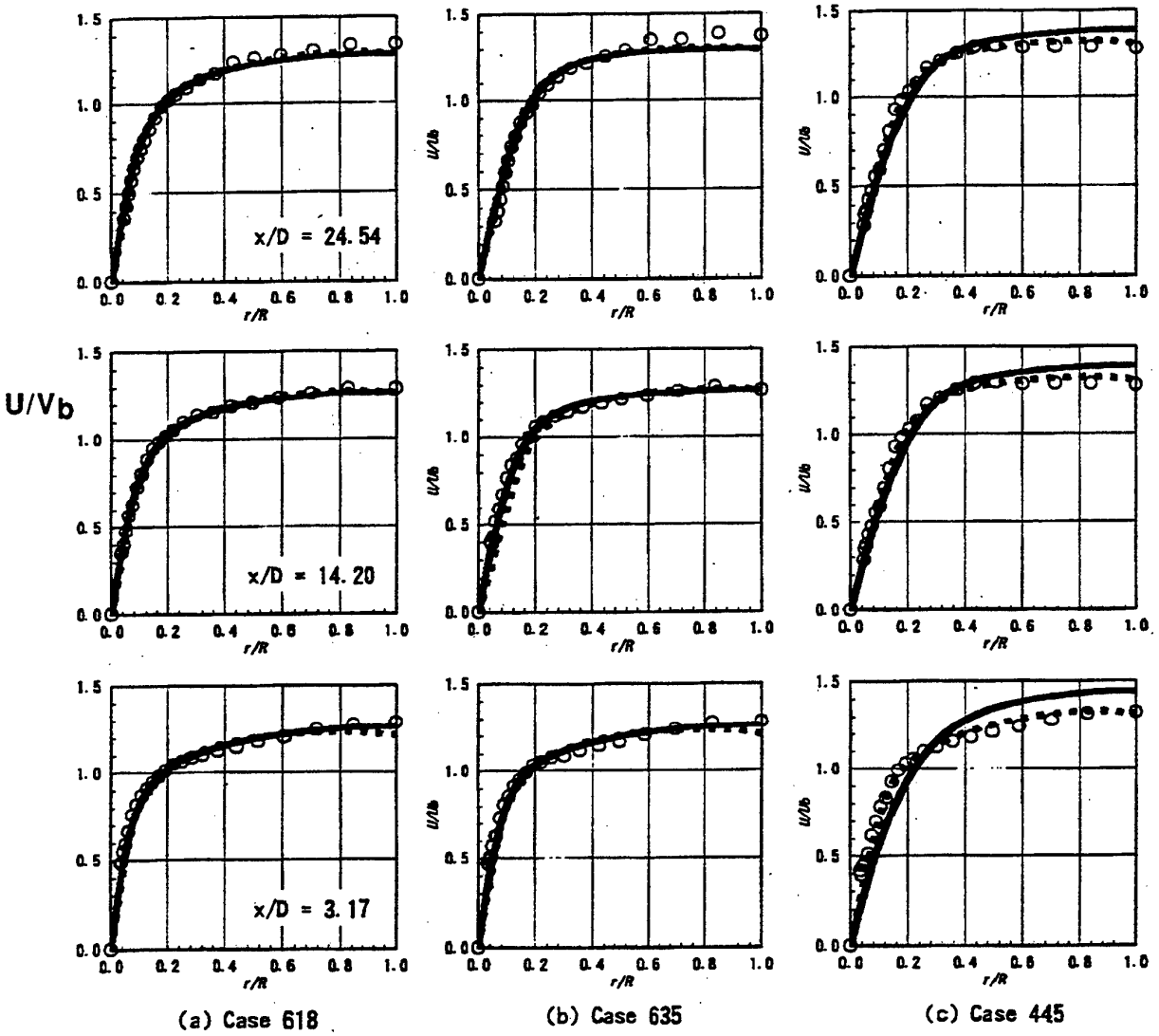

Figure 10 Simulations of Reynolds stress model by Nishimura (solid lines) and k-kL-$\overline{uv}$ model by Fujii (dashed lines) compared to data of Shehata [Nishimura et al., 1997].

Velocity profiles appear representative of normal, developed turbulent flow in a circular tube, as expected. As the flow progresses downstream, the gradient at the wall decreases with the progressive decrease in Reynolds number. No surprises are evident. For these results a thermal boundary layer thickness is operationally defined as the distance from the wall beyond which there is no observable difference from the inlet temperature. At x/D = 3.17, the thermal boundary layer reached about forty per cent of the tube radius. By 14.2 diameters, the thermal boundary layer already extended to the centerline and the profile was typical of a developed turbulent flow, distinguished by a high gradient near the wall (most of the thermal resistance) and a well mixed flow in the interior. The last profile was qualitatively the same, with an increase in level corresponding to the higher bulk temperature. The temperature data of Perkins [1975] behave in much the same way as those of Shehata. Variations between the two are mainly due to minor differences in the heating rates and inlet Reynolds numbers.

The second set of data is at the *intermediate heating rate* (Re_i still 6000 and $q^+ \approx 0.0035$) which was described as *subturbulent* by Perkins [1975]. The acceleration parameter was about 2×10^{-6} along most of the tube. This set has almost twice the heating rate and K_v as the first set, while having the same inlet flow rate. For these conditions, Perkins has shown that the integral heat transfer parameters do not agree with turbulent, variable properties correlations *nor* with laminar, variable properties numerical predictions.

The first three temperature profiles indicated that the thermal boundary layer reached the centerline near x/D = 9 or 10. Near the wall the temperature profile was near linear over a substantial region. This near-linear region grew thicker as the flow progressed downstream, reaching $y/r_w \approx 0.25$ by the last station. Although significant thermal resistance appeared distributed across a large portion of the cross section, a near flat profile was still evident in the central region at the last three locations. This last observation implies that turbulent mixing was not suppressed there (it was not a case of being outside the thermal boundary layer, since the centerline temperature was above $T_w/T_i = 1$).

The last set of runs is at the *highest non-dimensional heating rate* and lowest inlet flow rate ($Re_i \approx 4000$ and $q^+ \approx 0.0045$ ---> *Run 445*). These conditions were categorized as being on the borderline between subturbulent and *laminarizing* flow by Perkins (his Figure 8). The acceleration parameter K_v exceeds 3.5×10^{-6}, which is considered by Sreenivasan [1982] and others as near a critical value for laminarization to set in. The measurements at 3.17 diameters showed that the thermal boundary layer had grown to $y/r_w \approx 0.4$ by this distance. Presumably this growth was partially a consequence of upstream axial conduction and axial thermal radiation to the tube wall of the "unheated" entry region, as is evident in earlier Figure 7. By x/D = 14.2 the thermal boundary layer again filled the tube. The temperature profile started to take a parabolic shape, except in the central region where the effects of turbulent mixing still appeared significant. At x/D = 24.5, the measured temperature profile resembled a parabola more closely. One recalls that the analytic profile for fully established laminar flow with constant properties is a fourth-order parabola [Kays and Crawford, 1980] - but, in these data, viscosity and thermal conductivity vary by factors of about two and at this Reynolds number a laminar flow would require a longer distance to become fully established. However, Perkins [1975] did demonstrate that a *laminar, variable properties* calculation - starting from the existing turbulent velocity profile in the entry - *could provide reasonable predictions* of the mean temperature distribution for comparable conditions. The mean velocity profiles in the wall region (Figure 10c) show a near Blasius shape while progressing downstream. In the central region, starting at about half the radius, the profiles are almost flat for the measurements at x/D ≈ 14.2 and 24.5, indicating high turbulent mixing, effects of acceleration, reduced shear stress and/or buoyancy effects there.

Fujii "extended" his *k-kL-*$\overline{uv}$ *model* from the annular case to treat flow in circular tubes. Since his model evolved from the one by Kawamura, it is expected that his results would be comparable to those of Kawamura. *Nishimura* utilized a *Reynolds stress model* (RSM) from Shima *with turbulent heat flux and thermal energy fluctuation equations*; the heat flux equations contain two extra terms to take account of anisotropy of turbulence and velocity turbulence-thermal energy gradient production for the pressure-temperature fluctuation gradient correlation terms [Nishimura, Fujii et al., 1997]. For fully-established, constant-property gas flows, the two turbulence models agreed with accepted correlations of friction and heat transfer in laminar and turbulent regimes and forecast a transition within the Reynolds number range from 2000 to 2400.

To assess their predictive capabilities, simulations from the models of Fujii and Nishimura are compared to the velocity measurements of Shehata in Figure 10. For cases 618 and 635, the results from the two models agree closely with one another and with Shehata's measurements. Only at the last station do the predictions appear to be slightly lower in the central region of the flow, but these deviations are within the estimated experimental uncertainties. For Run 445 the two models do predict observable differences. At the first station the RSM already shows a more laminar appearance for the velocity profile than the k-kL-$\overline{uv}$ model does and at the two later stations the velocity gradient near the wall is slightly less than for the k-kL-$\overline{uv}$ model. For this laminarizing run, the k-kL-$\overline{uv}$ model of Fujii et al. represents the measurements better than the RSM does. However, with the exception of the last station, the differences between the RSM results and the data are still within the estimated experimental uncertainties in general. Agreement of the pressure drop predictions with the experiment is good except in Run 445 where the RSM simulation is about ten per cent low. For the axial wall temperature distributions, the only situation where the results of the two models differ significantly is laminarizing Run 445 where the RSM appears slightly better. In summary, the comparisons to measurements are generally acceptable, giving one confidence in the results predicted for the turbulence quantities which were not measured directly.

7. CONCLUDING REMARKS

The purposes of the present article are (1) to remind practitioners why the usual textbook approaches may not be appropriate for treating gas flows heated from the surface with "large" heat fluxes and (2) to review the successes (and failures) of some recent applications of turbulence models to this case. These objectives have been met to some extent.

Results have been primarily considered for *dominant forced convection* at the conditions of the experiments of Shehata and of Perkins, for cases involving significant variation of density, viscosity and thermal conductivity along and across a circular tube. Examination concentrated on three situations for vertical upflow, labeled "turbulent," "subturbulent" or

intermediate and "laminarizing." From the measurements the following observations may be inferred concerning the mean turbulence quantities:

- o the heating disturbed the incoming flow almost immediately in the thermal entry
- o the "turbulent" run recovered to an approximately self-preserving condition
- o in the other two runs, the quantities continued to decrease axially until they were much less than the molecular effects

Simulations of the low-Reynolds-number internal flows were made using about fifteen turbulence models. After preliminary examination treating the gas properties as constant, the ability of the models to handle strongly-heated flows was assessed via calculations at the conditions of experiments by Shehata. Possible effects of buoyancy forces at these conditions were considered and it was concluded that forced convection dominated the heat transfer parameters. Numerical predictions forecast the development of turbulent transport quantities, Reynolds stress and turbulent heat flux, plus mean velocity and temperature distributions, wall heat transfer parameters and pressure drops. In contrast to earlier approaches of other investigators, validation focused on comparisons to the measurements of the developing mean velocity and temperature fields.

One may conclude that existing low-Reynolds-number turbulence models and commercial codes should be used with *caution* for

- o low-Reynolds-number, fully-established, *constant-property* flow and
- o strongly-heated, internal gas flows

For strongly-heated turbulent or laminarizing gas flows, five models were found to give reasonable agreement with the internal profile measurements of Shehata:

- o van Driest model as modified by Bankston and McEligot [1969]
- o k-kL-uv model of Fujii, Akino, Hishida, Kawamura and Sanokawa [1991]
- o k-ε model of Launder and Sharma [1974] as calculated by Mikielewicz [1994]
- o k-ε of Abe, Kondoh and Nagano [1994] by Ezato and Kunugi [1997]
- o Reynolds stress model of Shima by Nishimura [1997]

Since the model of Fujii et al. was derived from the earlier model of Kawamura [1979], it is expected that Kawamura's model would provide good simulations but, to our knowledge, it has not yet been tested directly by comparison to profile measurements. The modified van Driest model is not recommended for conditions with significant buoyancy effects [Bates et al., 1974].

ACKNOWLEDGEMENTS

The study reported was supported by the Long Term Research Initiative and Laboratory Directed Research and Development Programs of the Idaho National Engineering Laboratory / Lockheed Martin Idaho Technologies Company under DoE Idaho Field Office Contract DE-AC07-94ID13223 and by the Japan Atomic Energy Research Institute. The experiments of Dr. Shehata were funded by the Office of Naval Research, the National Science Foundation and the University of Arizona. During part of the effort, Prof. McEligot received support as a JAERI Distinguished Foreign Scientist. To all we are extremely grateful. By acceptance of this article for publication, the publisher recognizes the U. S. Government's (license) rights in any copyright and the Government and its authorized representatives have unrestricted right to reproduce in whole or in part said article under any copyright secured by the publisher.

NOMENCLATURE

{ }	function of
A_{cs}	cross-sectional area
c_p	specific heat at constant pressure
D	tube diameter; D_h, hydraulic diameter
g	acceleration of gravity
g_c	units conversion factor, e.g., 1 kg m /(N s^2)
G	mean mass flux, $\dot{m} / A_{cs}$
h	convective heat transfer coefficient, $q''_w/(T_w-T_b)$
k	turbulent kinetic energy, thermal conductivity
l	mixing length
L	turbulent length scale
$\dot{m}$	mass flow rate
p	pressure
q''_w	wall heat flux
r	radial coordinate; r_w, tube wall radius
T	absolute temperature
u_τ	friction velocity, $(g_c \tau_w / \rho_w)^{1/2}$
U	time-mean streamwise velocity component
v	local radial velocity component
V	time-mean radial velocity component
V_b	bulk or mixed-mean streamwise velocity
x	axial coordinate measured from nominal start of heating
y	coordinate perpendicular to the wall
z	axial location

Non-dimensional quantities

f, f_τ	friction factor, $2 \rho_b g_c \tau_w / G^2$
Gr_q	local Grashof number based on heat flux, $g D^4 q''_w /(\nu_b^2 k_b T_b)$
Nu	Nusselt number, e.g., hD/k
Pr	Prandtl number, $c_p\mu/k$
q^+	heat flux parameter, q''_w/Gc_pT; q_i^+, based on inlet conditions, $q''_w/Gc_{p,in}T_{in}$
Re	Reynolds number, $4 \dot{m} / \Pi D \mu$; $Re_{w,m}$, modified wall Reynolds number, $V_b D / \nu_w$
y^+	wall distance coordinate, $y (g_c\tau_w/\rho_w)^{1/2} / \nu_w$

Greek symbols

ε	dissipation of turbulence kinetic energy;
μ	absolute viscosity
ν	kinematic viscosity, μ/ρ
ρ	density
τ	shear stress; τ_w, wall shear stress

Subscripts

b	evaluated at bulk or mixed-mean temperature (or enthalpy)
cp	constant property idealization
i, in	inlet
w	wall, evaluated at wall temperature

REFERENCES CITED

Abe, K., T. Kondoh and Y. Nagano, 1994. A new turbulence model for predicting fluid flow and heat transfer in separating and reattaching flows -- I. Flow field calculations. *Int. J. Heat Mass Transfer*, 37, pp. 139-151.

Bankston, C. A., 1965. Fluid friction, heat transfer, turbulence and inter-channel flow stability in the transition from turbulent to laminar flow in tubes. Sc.D. thesis, Univ. New Mexico.

Bankston, C. A., 1966. Personal communication, Los Alamos Scientific Laboratory, 4 November.

Bankston, C. A., 1970. The transition from turbulent to laminar gas flow in a heated pipe. *J. Heat Transfer*, 92, pp. 569-579.

Bankston, C. A., and D. M. McEligot, 1970. Turbulent and laminar heat transfer to gases with varying properties in the entry region of circular ducts. *Int. J. Heat Mass Transfer*, 13, pp 319-344.

Bates, J. A., R. A. Schmall, G. A. Hasen and D. M. McEligot, 1974. Effects of buoyant body forces on forced convection in heated laminarizing flows. *Heat Transfer 1974* (Proc., 5th Intl. Heat Transfer Conf., Tokyo), vol. II, pp. 141-145.

Cotton, M. A., and P. J. Kerwin, 1995. A variant of the low-Reynolds-number two-equation turbulence model applied to variable property mixed convection flows. *Int. J. Heat Fluid Flow*, 16, pp. 486-492.

Dailey, L. D., and R. H. Pletcher, 1998. Large eddy simulations of constant heat flux turbulent channel flow with property variations. AIAA paper 98-0791.

Drew, T. B., E. C. Koo and W. M. McAdams, 1932. The friction factor in clean round pipes. *Trans., A.I.Ch. E.*, 38, pp. 56-72.

Dittus, F. W., and L. M. K. Boelter, 1930. Heat transfer in automobile radiators of the tubular type. *Pub. in Engrg.* (Univ. California), 2, pp. 443-461.

Ezato. K., A. M. Shehata, T. Kunugi and D. M. McEligot, 1997. Numerical predictions of transitional features of turbulent gas flows in circular tubes with strong heating. Paper FEDSM97-3304, ASME Fluids Engr. Conf., Vancouver, B. C.

Ezato. K., A. M. Shehata, T. Kunugi and D. M. McEligot, 1997. Numerical predictions of local transitional features of turbulent forced gas flows in circular tubes with strong heating. Tech. rpt. JAERI-Research 97-029, Japan Atomic Energy Research Institute, Tokai.

Fujii, S., N. Akino, M. Hishida, H. Kawamura and K. Sanokawa, 1991. Experimental and theoretical investigations on heat transfer of strongly heated turbulent gas flow in an annular duct. *JSME International J., Ser II*, 34, No. 3, pp. 348-354.

Hasewaga, S., R. Echigo and A. Shimizu, 1986. Convective and radiative heat transfer of flowing gaseous-solid suspensions. *Handbook of heat and mass transfer, Volume 1: Heat transfer operations* (Ed.: N. P. Cheremisinoff), Houston: Gulf Publishing Co., pp. 523-557.

Kline, S. J., W. C. Reynolds, F. A. Schraub and P. W. Rundstadler, 1967. The structure of turbulent boundary layers. *J. Fluid Mech.*, 30, pp 741-773.

Jackson, J. D., M. A. Cotton and B. P. Axcell, 1989. Studies of mixed convection in vertical tubes. *Int. J. Heat and Fluid Flow*, 10, pp. 2-15.

Kawamura, H., 1979. Analysis of laminarization of heated turbulent gas using a two-equation model of turbulence. Proc., 2nd Intl. Symp. Turb. Shear Flow, London, pp. 18.16-18.21.

Kays, W. M., and M. E. Crawford, 1993. *Convective heat and mass transfer, 3rd ed.* New York: McGraw-Hill.

Launder, B. E., and B. I. Sharma, 1974. Application of the energy-dissipation model of turbulence to the calculation of flow near a spinning disc. *Lett. Heat Transfer*, 1, pp. 131-138.

McAdams, W. H., 1954. *Heat transmission, 3rd ed.* New York: McGraw-Hill, p. 219.

McEligot, D. M., 1963. The effect of large temperature gradients on turbulent flow of gases in the downstream region of tubes. Ph.D. thesis, Stanford Univ. Also TID-19446.

McEligot, D. M, 1986. Convective heat transfer in internal gas flows with temperature-dependent properties. *Adv. Transport Processes*, 4, pp 113-200.

McEligot, D. M., and C. A. Bankston, 1969. Turbulent predictions for circular tube laminarization by heating. ASME paper 69-HT-52.

McEligot, D. M., C. W. Coon and H. C. Perkins, 1970. Relaminarization in tubes. *Int. J. Heat Mass Transfer*, 9, pp. 1151-1152.

McEligot, D. M., P. M. Magee and G. Leppert, 1965. Effect of large temperature gradients on convective heat transfer: The downstream region. *J. Heat Transfer*, 87, pp. 67-76.

McEligot, D. M., L. W. Ormand and H. C. Perkins, 1966. Internal low Reynolds number turbulent and transitional gas flow with heat transfer. *J. Heat Transfer*, 88, pp 239-245.

McEligot, D. M., S. B. Smith and C. A. Bankston, 1970. Quasi-developed turbulent pipe flow with heat transfer. *J. Heat Transfer*, 92, pp. 641-650.

McEligot, D. M., M. F. Taylor and F. Durst, 1977. Internal forced convection to mixtures of inert gases. *Int. J. Heat Mass Transfer*, 20, pp. 475-486.

Mikielewicz, D. P., 1994. Comparative studies of turbulence models under conditions of mixed convection with variable properties in heated vertical tubes. Ph.D. thesis, Univ. Manchester.

Nagano, Y., and M. Shimada, 1995. Computational modeling and simulation of turbulent flows. *Computational Fluid Dynamics Review 1995* (Ed.: M. Hafez and K. Oshima), Chichester: John Wiley & Sons, pp. 695-714.

Ogawa, M., and H. Kawamura, 1986. Experimental and analytical studies on friction factor of heated gas flow in circular tube. *J. At. Energy Soc., Japan*, 28, No. 10, pp. 957-965 (in Japanese).

Ogawa, M., H. Kawamura, T. Takizuka and N. Akino, 1982. Experiment on laminarization of strongly heated gas flow in a circular tube. *J. At. Energy Soc., Japan*, 24, No. 1, pp. 60-67 (in Japanese).

Perkins, K. R., 1975. Turbulence structure in gas flows laminarizing by heating. Ph.D. thesis, Univ. Arizona.

Reynolds, H. C., 1968. Internal low-Reynolds-number, turbulent heat transfer. Ph.D. thesis, Univ. Arizona. Also DTIC AD-669-254.

Shehata, A. M., 1984. Mean turbulence structure in strongly heated air flows. Ph.D. thesis, Univ. Arizona.

Shehata, A. M., and D. M. McEligot, 1995. Turbulence structure in the viscous layer of strongly heated gas flows. Tech. report INEL-95/0223, Idaho National Engineering Laboratory.

Shehata, A. M., and D. M. McEligot, 1998. Mean turbulence structure in the viscous layer of strongly-heated internal gas flows. Measurements. *Int. J. Heat Mass Transfer*, in press.

Torii, S., A. Shimizu, S. Hasegawa and M. Higasa, 1993. Numerical-analysis of laminarizing circular tube flows by means of a Reynolds stress turbulence model. *Heat Transfer - Japanese Research*, 22, pp. 154-170.

Torii, S., A. Shimizu, S. Hasegawa and N. Kusama, 1991. Laminarization of strongly heated annular gas flows. *JSME International J., Ser II*, 34, No. 2, pp. 157-168.

Torii, S., and W.-J. Yang, 1997. Laminarization of turbulent gas flow inside a strongly heated tube. *Int. J. Heat Mass Transfer*, 40, pp. 3105-3117.

The Modification of Quasi-streamwise Vortices in Liquid Turbulent Flow in a Duct by the Injection of Polymer Solution

Yoshimichi HAGIWARA, Takayuki OKUDA, Mitsuru TANAKA and Susumu MURAI

Department of Mechanical and System Engineering,
Kyoto Institute of Technology, Japan

ABSTRACT

Flow visualisation and heat transfer experiments were carried out for quasi-streamwise vortices generated by the intermittent protrusion of a wing into a water turbulent duct flow with the injection of water or the polymer solution. The newly-developed vortex generator was found to be effective for the intermittent generation of the quasi-streamwise vortices in a downstream region. It was shown that the streamwise vortices and heat transfer related to the vortices were attenuated noticeably by a dilute polymer solution injected in the upstream region.

1 INTRODUCTION

The drag reduction and the reduction of the heat transfer coefficient associated with the drag reduction of water turbulent duct flow, by adding a small amount of specific polymer, has been focused on recently. This is mainly because these reductions are expected to be of great advantage in large urban primary heating circuits (1, 2).

In order to understand the effects of a polymer solution on near-wall turbulence, Tiederman *et al.* (3) conducted experiments on a water turbulent channel flow by the injection of a polymer solution into near-wall region from a transverse slot in one wall. They determined that the transverse spacing of streaks increased and the average bursting rate decreased in the downstream region. The injected polymer solution was not uniformly mixed with the main flow in the region under observation. No experimental data have been obtained for the effect of the injected polymer solution on the heat transfer in the turbulent duct flow.

The present authors carried out a direct numerical simulation with cluster models of beads and springs in a thin layer inside the buffer layer in a turbulent channel flow, and showed continuous attenuation of vorticities of the quasi-streamwise vortices (QSVs) in a coherent structure (4).

In the present study, the effects of injecting a polymer solution from a transverse slot on the quasi-streamwise vortices were examined experimentally. Since QSVs are observed irregularly in space and time in near-wall regions, the direct comparison of the dimension of QSVs' is difficult. Then, a small vortex generator was developed and used in order to obtain intermittent quasi-streamwise vortical motion in a specific downstream region. Flow visualisation and image processing were carried out for the vortical motion. The fluid temperature was also measured at a point inside the thermal boundary layer near the heated wall around the vortex generator.

2 EXPERIMENTAL METHOD

2.1 Apparatus

Figure 1 shows the apparatus. A total of 0.05 m^3 water stored in a tank ⑪ was introduced into a horizontal duct ④ through an upstream chamber ①, a honeycomb straightener ② and a contraction nozzle ③. The duct was made of acrylic plates and had a rectangular cross section of H=12 mm in height and W=100 mm in width. The other chamber ⑩ was connected to the downstream end of the rectangular duct. A valve for the control of the main flow rate and a small pipe to exhaust air were fixed to this chamber.

Either water or a dilute aqueous solution (about 100 ppm) of polyethylene glycol (Wako Pure Chemical Industries Ltd. Japan; average molecular weight is in the range of 3.5 to 4.0 $\times 10^6$) in an overhead bottle of 1000 cm^3 ⑤ was introduced via a transverse slot 15 mm in transverse length and 1.0 mm in streamwise width ⑥. The fluid was introduced into the main flow at an angle of 45° with respect to the wall. The slot was located 1316 mm (=110H) downstream from the inlet of the duct. The flow rate of the injected liquid was adjusted by a valve. The solution of polyethylene oxide was held in another tank for an hour for hydration before filling the overhead bottle.

A vortex generator ⑧ was placed 84 mm (=7H) downstream from the transverse slot.

2.2 Vortex generator

Figure 2 illustrates the detail of the vortex generator. The vortex generator consisted of a wing with an iron pipe, an electromagnet, and a timer. The wing was made of stainless steel plate 3.8 mm in width and 0.3 mm in thickness. The lower surface of the plate was angled at 30 degrees to the flow. The angle between the slit and the duct axis, and hence the angle of attack for the wing to the main flow, was 15 degrees. When the timer was off the lowest part of the wing was inserted from a slit 5 mm in length and 1.2 mm in

width on the upper wall of the test section. The maximum protrusion of the wing tip, h, was 1.5 mm from the inner wall surface. When the timer was on the electromagnet withdrew the iron pipe, and the wing was withdrawn. The duration and the interval of the timer were varied so that the wing was inserted for predetermined intervals. The wing insertion works as a trigger of streamwise vortices, and the effect of the wing to the main flow field is expected to be kept minimal. Note that the inserted wing does not work as half-delta wings on a wall do for the purpose of generation of streamwise vortices effective for heat transfer augmentation (for example, Torii *et al.* (5)).

2.3 Flow visualisation and image processing

To facilitate flow visualisation near the upper wall, a small amount of white dye was mixed with the injected liquid to obtain streak lines. The images of the visualised flow were recorded into a Hi8 videotape by a CCD camera module (SONY XC-77-RR with a total pixel number of 768 × 493 and signal-to-noise ratio of 56 dB) and a VCR (SONY CVD1000 with a horizontal resolution more than 400 lines per frame). The camera module was positioned below the duct.

A halogen lamp provided the source of light. A flat light guide made of 320 aligned optical-fibres and a cylindrical lens was used to provide a uniform region of light, 10 mm × 160 mm. The light illuminated the flow horizontally from outside the test section.

The images stored in the video tape were replayed and converted into digital images by a PCI-bus-type frame grabber and a personal computer.

2.4 Heat transfer

A thermal boundary layer was formed along the upper wall around the slit through which the wing was inserted. This thermal boundary layer was formed by replacing part of the upper wall by a transparent heater of area 100 mm × 100 mm. The heater consists of a metal deposited onto a base glass plate 0.5 mm thick and a cover glass plate of identical size. An alternating current was imposed on the deposited metal in order to form a thermal field under the condition of uniform heat flux. The thermal field is basically stable.

Fluid temperature was measured by a CC (T-type) thermocouple 0.076 mm diameter at the position of 30 mm downstream of the insertion slit of the wing (See Fig. 2). The thermocouple was Teflon-coated except at the measuring point. The coated part of the thermocouple was attached by an adhesive to a metal stem 0.7 mm diameter. The stem was fixed to a supporting pipe. The supporting pipe can be moved in its axial direction, allowing the thermocouple to be traversed normal to the heater. The distance between the location of the thermocouple junction (the temperature measuring point) and the lower surface of the heater, y_θ, was measured by a microscope on a traverse stage. The distance was fixed at 0.5 mm in the present study. The streamwise distance of the temperature measuring point from the upstream edge of the heater (the leading edge of the thermal boundary layer), x_θ, was 80 mm. The thermoelectromotive force of the thermocouple was recorded on a chart with a pen recorder.

2.5 Experimental conditions

The experiments were carried out under the condition where the main water flow rate was 1.6×10^2 cm^3/s. The Reynolds number based on the hydraulic diameter and the mean velocity was 2.5×10^3. The friction velocity, u^*, was estimated to be 1.0 cm/s from the computational results of turbulent channel flow and the maximum velocity measured by flow visualisation using tracer particles in the main flow. The flow rate of the injection fluid was either 0.1 cm^3/s or in the range of 0.15 ~ 0.2 cm^3/s.

The nondimensional value of the maximum height of the wing tip is shown in Table 1. The tip was inside the buffer layer. The protrusion period, T, and the duration of protrusion, t, in the period were adjusted by changing the resistance in the timer. T, t adopted in the present study and their nondimensional values are also shown in Table 1. The longer protrusion period of case 2 was longer than the average life cycle of QSV in near-wall turbulence, $T_{LC} \sim 100\nu/u^{*2}$ (ν is the kinematic viscosity) (6), and the intermittency cycle for the minimal flow unit in near-wall turbulence, $T_I \sim 33H^2/Q$ (Q is the volumetric flow rate per unit width) ~ $260\nu/u^{*2}$, determined by Jiménez and Moin (7).

The heat flux q_w was 11 kW/m^2. Total heat loss due to conductive heat transfer from the glass plate of the heater to the duct wall and natural convection heat transfer from the cover glass plate of the heater to the ambient air was estimated at most 3 percent of the total electric power. The heat loss was therefore considered to be negligible. The temperature measuring point was at $y_\theta^+ = 4.4$ and $x_\theta^+ = 700$.

3 RESULTS AND DISCUSSIONS

3.1 Non-insertion condition

Observations were made under three conditions in which fluid was introduced through the slot but the wing was not inserted.

3.1.1 Water injection under lower flow rate condition

When the wing was not inserted, the dye in the injected water formed a thin white layer in the region from 0.5 to 1 mm below the upper wall ($4.4 < y^+ < 8.8$). This dye layer was considered to be in the near-wall zone in the buffer layer of wall turbulence. The dye layer was generally found to be stable, but occasionally in an unstable state. The average period of the unstable state was longer than 10

seconds. The unstable state was caused by extremely-large-scale turbulence of the main flow.

3.1.2 Water injection under higher flow rate condition

When the flow rate of injected water was increased, the dye formed a thicker layer and the layer was located further below the upper wall compared with that aforementioned. The dye layer was estimated to be in the far-wall zone in the buffer layer.

There were large-scale fluctuations in the concentration of the dye observed. The rotation of the nonuniform concentration of dye, whose axis was in the streamwise direction, was seen. This is caused by the quasi-streamwise vortices of the main flow occurred in the observed region or upstream region.

Small-scale fluctuation in the transverse edge of the dye layer was also observed particularly near the slot. This is a result of difference between high velocity of the injected fluid from the slot and the low velocity of the main flow.

3.1.3 Polymer solution injection under higher flow rate condition

When the polymer solution was injected in the case of higher flow rate condition, the frequency of the large-scale fluctuation of dye concentration decreased. This shows the attenuation of coherent structures by polymers. This is in agreement with the experimental results by Tiederman *et al.*(2). The small-scale fluctuation of the dye layer edge in the transverse direction was also observed to be attenuated by the polymer.

3.2 Continuous protrusion of the wing

Observations were made under two conditions in which fluid was introduced through the slot and the wing was inserted.

3.2.1 Water injection under lower flow rate condition

A white streak was observed to be in an almost steady state downstream from the trailing edge of the wing. This is the result of dye being trapped upstream side of the wing and then released. No noticeable disturbance of the streak was found. This means that the continuous protrusion of the wing does not generate large-scale disturbance in the main flow.

The temperature measuring point was located between the thin layer of injected fluid and the heated wall. The difference between fluid temperature at the measuring point and that outside the thermal boundary layer, θ, was 1.7 degree. The nondimensional temperature difference, θ^+ (= $\theta \rho Cp\, u^* / q_w$; ρ is water density and Cp is the specific heat of water at constant pressure), was 6.5. Temperature fluctuation was in the range of 0.9 ~ - 0.9 K.

3.2.2 Polymer solution injection under lower flow rate condition

The white dye layer was found to be similar to that in case of water injection.

θ was 3.4 K, and the range of the temperature fluctuation decreased to 0.6 ~ - 0.6 K. These show that lumps of fluid with a high temperature remained near the heater. This proves that the transport of fluid lumps by near-wall turbulence was retarded by polymer solution. This is in agreement with the experimental data of heat transfer reduction by a polymer (for example, reference 2).

3.3 Periodical insertion of the wing

Observations were made under two conditions in which fluid was introduced through the slot and the wing was inserted periodically.

3.3.1 Water injection under lower flow rate condition

Figure 3 shows a typical snapshot of the images captured. The dye flowed from left to right. Part of the slit of wing insertion is seen on the left side of the figure. Noticeable fluctuations synchronized with the period insertion of the wing were observed for the white dye layer: On the successive images during the wing insertion, the white streak released from the wing appeared first in front of the dye layer, then moved towards downward direction, and finally approached the day layer changing its direction towards the upward. This fluctuation indicated that clockwise vortical motion, whose axis is in the streamwise direction, was generated. The clockwise vortical motion is in agreement with that generated from the half-delta wing (5).

A dark region following the white streak was also observed through the period of wing withdrawal. This region is a result of dye trapping at the side of the wing. The average dimension of the dark region in the transverse direction was 6.5 mm, which is $54\nu/u^*$. This is about 50 percent larger than the core dimension of QSV (8).

θ was 1.4 K, and lower than that of continuous protrusion of the wing. This shows that the vortical motion of water enhanced near-wall heat transfer.

3.3.2 Polymer solution injection under lower flow rate condition

Figure 4 shows a typical snapshot of the images captured in case of polymer solution. Some streaks showed no fluctuation, and the other streaks indicated smaller-scale fluctuation with slower motion in the transverse direction than that observed in case of water injection. The mean transverse dimension of the dark region decreased to 4.2 mm. These show that the vorticity of the motion was reduced. This means that the streamwise vortical motion was attenuated noticeably by polymer solution.

θ was 3.4 degree in the case of a polymer solution. The attenuation of heat transfer associated with the streamwise vortical motion is clearly found.

4 CONCLUSION

The flow visualisation was carried out for quasi-streamwise vortices generated by the intermittent protrusion of the wing in a water turbulent duct flow with the injection of water or the polymer solution. The main conclusions obtained are as follows:

(1) The intermittent protrusion of the wing was effective for the generation of the quasi-streamwise vortices in a specific region.
(2) The streamwise vortices were attenuated noticeably by a dilute polymer solution injected in the upstream region.
(3) The heat transfer due to the quasi-streamwise vortices was attenuated by the polymer solution.

5 NOMENCLATURE

Cp : specific heat of water at constant temperature
H : height of horizontal duct
h : maximum height of wing tip
q_w : wall heat flux
T : period of wing insertion
t : duration of wing insertion
u^* : friction velocity
W : width of horizontal duct
x : streamwise distance
y : normal distance from upper wall

ρ : density of water
θ : difference between temperature at the measuring point and that out of thermal field

Subscript
θ : thermal field

Superscript
$+$: nondimensional value

6 REFERENCES

(1) Singh, R. P., Drag Reduction and shear stability mechanisms, *Encyclopedia of Fluid Mechanics*, vol. 9, 1990, pp.425-480, Gulf Publishing Co..
(2) Inaba, H. *et al.*, Flow drag and heat transfer reduction of water flow with fibrous material and polymer in a straight pipe, *Proc. 10th Symp. on Transport Phenomena*, vol. 1, 1997, pp. 133 - 138.
(3) Tiederman, W.G. *et al.*, Wall-layer structure and drag reduction, *J. Fluid Mechanics*, 1985, vol. 156, pp. 419-437.
(4) Hagiwara, Y. *et al.*, A numerical simulation on the heat transfer attenuation due to tangled polymers in a liquid turbulent channel flow, *Proc. 11th Heat Transfer Conference*, 1998, to appear.
(5) Torii, K. *et al.*, Mechanism of heat transfer augmentation by longitudinal vortices in a flat plate boundary layer, *Heat Transfer 1994* (ed. by G.F. Hewitt), vol. 6, 1994, pp. 123 - 128.
(6) *Computational Fluid Dynamics of Turbulent Flow* (in Japanese), (ed. by H. Daiguji, Y. Miyake and A. Yoshizawa), 1998, p. 239, University of Tokyo Press.
(7) Jiménez, J. and Moin, P., The minimal flow unit in near-wall turbulence, *J. Fluid Mechanics*, 1991, vol. 225, 1991, pp. 213 - 240.
(8) Kim, J., Investigation on heat and momentum transport in turbulent flows via numerical simulations, *Transport Phenomena in Turbulent Flows: Experiment and Numerical Simulation* (ed. by M. Hirata, N. Kasagi), 1988, pp. 157 - 170, Hemisphere Publishing Co.

Table 1 height and protrusion period of wing

case	h [mm]	h^+	T [s]	T^+	t [s]	t^+
1	1.5	13	0.6	53	0.1	9
2	1.5	13	2.0	1.7×10^2	1.0	88

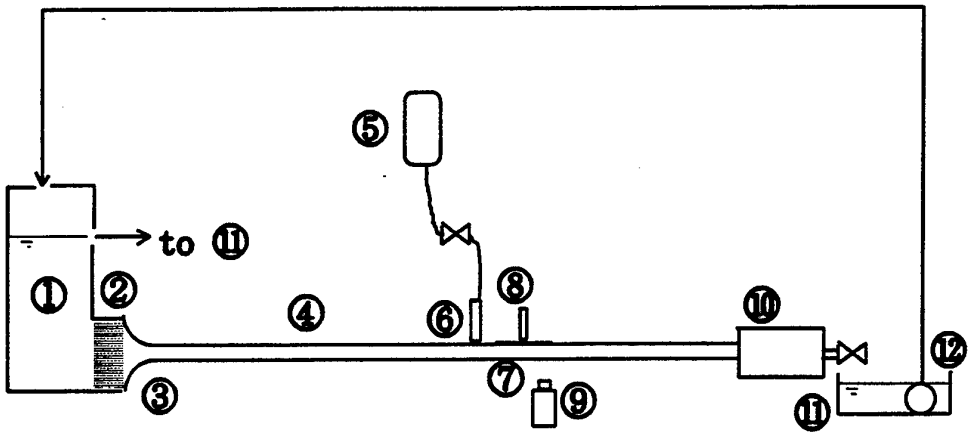

① Upstream chamber ② Honeycome ③Contraction nozzle ④ Rectangluar duct ⑤ Overhead bottle
⑥ Injection slit ⑦ Test section ⑧ Vortex generator ⑨ CCD camera module
⑩Downstream chamber ⑪ Tank ⑫ Pump

Figure 1 Apparatus

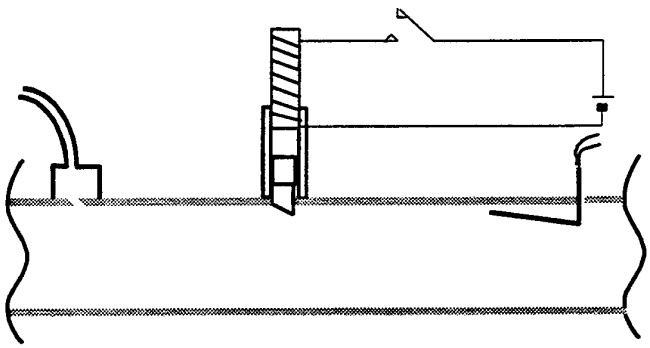

① Duct wall ② Wing (Stainless steel plate) ③ Iron pipe
④ Electromagnet ⑤ Timer ⑥ Injection slot ⑦ Thermocouple

Figure 2 Injection slot, vortex generator and thermocouple

Flow direction →

Figure 3 A typical image of injected water with dye

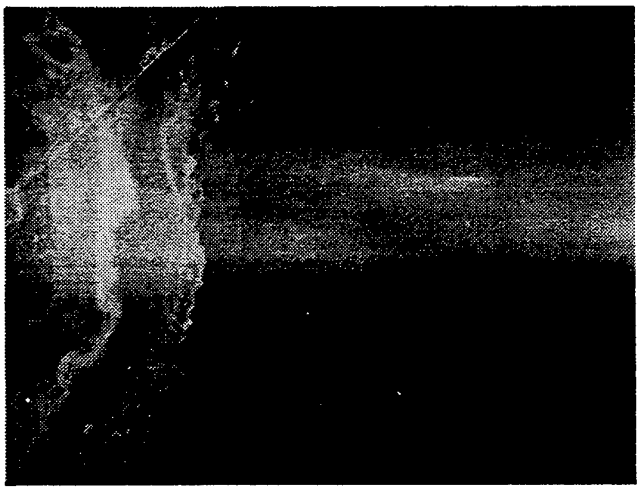

Flow direction →

Figure 4 A typical image of injected polymer solution with dye

New Observations in transitional Flat Plate Boundary Layers : Measurement and Visualisation

Cun Biao Lee

State Key Laboratory of Atmospheric Boundary Layer Phys. & Atmospheric Chemistry, Inst. of Atmospheric Phys.
Chinese Academy of Sciences, Beijing 100029, P. R. China
State Key Laboratory of Turbulence Research of Beijing University, Beijing 100871, P. R. China

ABSTRACT

This report draws on transition in flat plate boundary layer. Results are obtained as follow: 1. Very clear pictures of the formation and the development of the butterfly-like structures rather than Λ-structures in the K-regime of boundary layer transition are observed. 2. A process of multiple re-connection of the Λ-vortex which is the part of the butterfly-like structure with formation of a set of ring-like vortices is visualised for the first time. 3. The wave -like structure is also observed both in the external edge of the boundary layer and the near wall region even far downstream.

1. INTRODUCTION

The problem of the onset of the turbulence in flat plate boundary layer has attracted the attention of many investigators for more than a century. Despite its complexity, interest in laminar-turbulent transition has increased during the past a few decades owing to the importance in both fundamental and applied aspects of fluid mech. Theoretical studies in this field are discussed in the books by Craik(1985) and Zhigulyov & Tumin (1987) and reviews in both theoretical and experimental fields by Nayfeh(1987), Herbert(1987), Reed & Saric(1989), Fasel(1990), Kleiser & Zang(1991) and Kachanov(1994). After the famous experiments by Schubauer & Klebanoff (1956) and Klebanoff et al. (1962) it is well known that the nonlinear wave development at later stages farther downstream is characterised by the appearance of powerful flashes of disturbances on the velocity oscilloscope traces in the specific form of narrow spikes. The other extremely careful experiments performed by Kachanov et al.(1989) (see also Kachanov 1994) provide firm evidence that shows existence of multi-spikes on the velocity oscilloscope traces. In the work by Kachanov(1994), some new hypotheses have been suggested for comprehension the formation of the spike and multi-spikes on the time traces. The boundary layer structures are composed of the tooth-like structures in the near wall region, spike-solitons in the external edge of boundary layer and chaotic flows in the middle of the boundary layer. Very recently, a new possible physical path from laminar to turbulence in both natural and controlled transition has been suggested by Lee[1993,1995a,b; 1996a,b,c,d; 1997a,b,1998; Lee et al.1998a,b) and Borodulin et al.(1998). In this paper we concentrate on giving experimental observations at later stage of the non-linear breakdown of the boundary layer in controlled transition and trying to give direct evidence which is used to show a possible physical mechanism for the multi-spike formation.

2. EXPERIMENTAL TECHNIQUES AND FACILITIES

A description of the experiment set-up and procedure used to process the data is presented as before(Lee et al 1998a,b). The experiments are conducted in new established low turbulence level water channel in State Key Laboratory of Turbulence Research of Beijing Univ., at a free stream velocity U_∞=17.0cm/s with turbulence level less than 0.2% measured by several persons from China, Japan and Russia. A flat plate having a chord length 1.8m, a span of 0.8m and a thickness of 15mm is used. The leading edge is composed of two semi-cycles. The plate is mounted in the test section normally under zero degree angle of attack. The model had almost a zero steam-wise and span-wise pressure gradient far enough from the

leading edge.

A disturbance generator is a crack of a length of 150mm and a width of 1mm on the working side through which water is pumped in and out periodically at the frequency of 2 Hz. The water case which is connected both the crack and the two tubes is on the opposite side. The loudspeaker past on the top of a round barrel and the two tubes are mounted on the out side of the bottom. So the instability wave has the frequency of 2Hz and the amplitude of this disturbance is of 1.6% of the free stream speed. The source is mounted at a distance x=200mm from the leading edge of the plate. The development of the disturbances in the boundary layer and the structure of the mean flow are investigated by means of a set of instatement based on Kanomax hot.wire anemometer. The hot films are made from TSI and the sensitive part of the probe is 2mm. The data processing is carried out by 586-computer.

The experimental data is acquired from the positions of x=248mm to 700mm. At each spatial point, three characteristics are measured: the mean values of a stream-wise U-component of the mean flow velocity, the amplitude and phase of the u-component of the velocity disturbance filtered at fundamental frequency. Distributions of all measured characteristics along the downstream(x), normal to wall (y) and span-wise(z) co-ordinate have been measured.

The hydrogen bubble technique is used to visualise the flow structures very carefully. The flow structures at positions from x=250mm to 700mm with a step of 50mm and from y=0.5mm to 6mm with a step of 0.5mm.

3. THE MEAN FLOW

Normal-to-wall profiles of the U/Uo without generator are shown in Fig. 1. These profiles are taken in the locations of x=300mm, 400mm, and 600mm for z=0. All this results prove in excellent agreement with the Blasuis profile. The maximum deviation of the experiment points from the theoretical curve is less than ±1%.

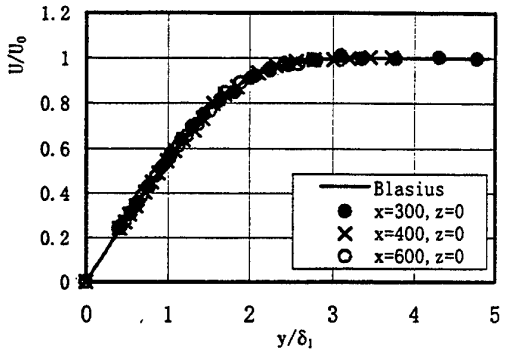

Fig.1 The Blasuis Profiles

The distributions of the free stream velocities in stream-wise and span-wise are shown in Fig.2.

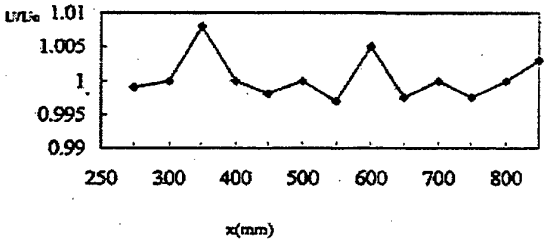

Fig.2(a) Stream-wise distributions of free stream

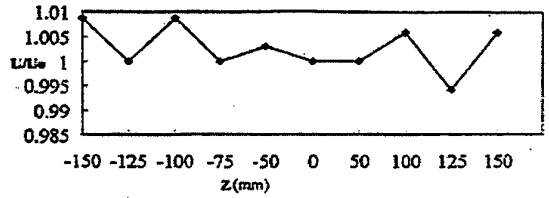

Fig.2(b) Span-wise distributions of free stream

Normal-to-wall profiles of U/δ with generator in peak position z=0) and in a place far from the peak position are shown in Fig.3. These results prove the difference compared with the Blasuis ones.

4. EXPERIMENTAL RESULTS

During the first stage, in the region of relatively low local Reynolds number, instability waves (i.e. boundary layer eigen oscillations, usually called Tollmien-Schlichting waves) are generated. Fig.4 shows the typical T-S wave. The wave length is of about 50 mm. The so-called Λ-structures are obtained very clearly by means of the visualisation from the plan-view shown in Fig. 5. The shape of the

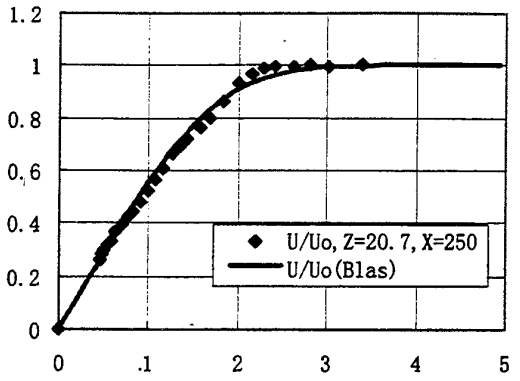

Fig.3 The profiles of velocity with generator

flow structures is strongly dependent on the position of the hydrogen bubble line. If we put the hydrogen bubble wire near to the wall, the structures are different from the pictures in Fig. 5, the butterfly-like structures are visualised in Fig.6(a). The head part of the ∧-structure disappears and a new rhombus-like structure presents in the center of the peak position. If we put the hydrogen bubble line slightly higher in y-direction, the ∧-structures and rhombus-like structures inside the ∧-structures are separately to be seen (Fig.6(b)). If the hydrogen bubble line is put very near to the wall, a low-speed streak presents in the peak position (see Fig.7). Besides the low-speed streaks, a long-streak present in the peak position. A closure vortex is formed which is combined with the low-speed streak and the ∧-structure. It is beyond doubt that the ∧-structure is the part of the perfect coherent flow structures. Inside the butterfly-like structures, a new structure exists exactly(see Fig.6). These structures have the features such as waves. In near wall region of the boundary layer, this wave-like property downstream at x=500mm is very clearly to be shown in Fig.8. In this figure the long-streak appears nearly in the centre of the butterfly-like structure (peak position and the semi-rhombus-like structure appear in the two sides of the long-streak periodically at the frequency of 2 Hz the semi-rhombus in other side above the long-streak in the peak position is not clear to be seen because of the weak of the light). It is beyond doubt that the ∧-structure can not induce this kind of structure. Because of the features of the stability and periodicity of this structure, it is considered as a solitary wave named as one of the solitons-like coherent structures (CS-solitons) which are the same as that observed by Lee (1995b) and in the work by Hama et al.(1963). As described in a study (Lee 1998), Hama did not pay enough attention to study the structure which he called kink because the solitons-like coherent structures (CS-solitons) are unknown at that time. Why do the CS-solitons just appear in few studies clearly? Two reasons are seen: 1. The studies by means of the flow visualisation are not as popular as that by means of the hot wire measurement. 2. The boundary layers are not thick enough as that in the works(Hama et al 1963, Lee1995) in that thick boundary layer is very convenient for side-view of the flow visualisation.

Fig.4 Plan-view of the typical T-S wave in transitional boundary layers (rate 1:2.5 and x from 248mm, y=1.5mm)

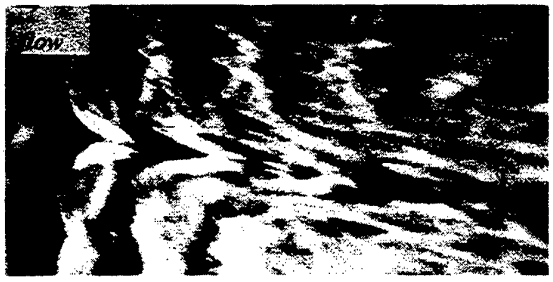

Fig.5 Plan-view of the typical ∧-structure in transitional boundary layer (rate 1:3.3; x=350mm, y=2mm)

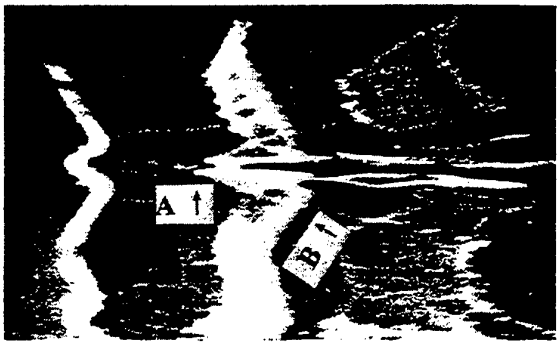

Fig.6(a) Plan-view of the butterfly-like structure and its evolution(rate1:3.3; x from 350, y=1.0)

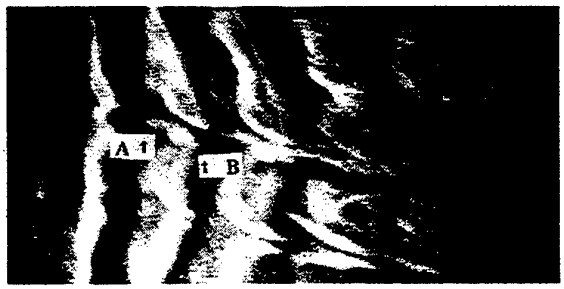

Fig6(b) Plan-view of the butterfly-like structure and its evolution(rate1:3.3; x from 350, y=1.5)

Fig.7 Plan-view of the long streak and the low-speed streaks (rate1:5; X from 300, y=0.5) (see Arrows)

Fig.8 The semi-rhombus-like structure(A↑) and long streak in peak position (rate 1:3.3; x from 430, y=0.5)

A set of the ring-like vortices (4 or 5), which appears periodically at the same frequency of T-S wave, associated with one Λ-structure (part of the closure vortex) is observed experimentally for the first time. The process for the formation of the set of ring-like vortices is obviously to be seen in the Fig.9. The typical x-distance between the two ring-like vortices is about 10mm. These visual results are very agreement with the measurement results (Kachanov1994, Fig.30) and our very recent results obtained both in Beijing and in Novosibrisk (Lee et al.1998a,b; Borodulin et al. 1998). In Fig.10 the typical set of the oscilloscope traces measured at various disturbances from the wall is shown. In Fig.10(a), the CS-solitons present on time traces of U-component of velocity. In the near wall region the fluctuations at low frequency(2Hz) and high amplitude are generated by the CS-soliton (See Fig.6) rather than $\wedge$-vortex suggested in former works. It is necessary to go back to see the Figs.6, and 7. The spatial scale of CS-solitons in X-direction is much higher than that of the $\wedge$-structures in peak position It is easy to calculate the time scale of both CS-solitons and $\wedge$-vortex in x-direction in peak position from Fig.6 by means of hydrogen bubble time line technique (Kline et al. 1967). Roughly, the time scale and the amplitude of CS-solitons are much higher than that of the $\wedge$-vortex in X-direction in peak position because the trace of the $\wedge$-vortex does not appear in peak position in Fig.6. Because of the same features of the low frequency fluctuations at different y-position (The frequency is of 2 Hz and the phases of them for different time trace in different y-position are nearly the same in value), the results in Fig.10(a) are considered as the behaviours of the CS-solitons at different y-position. In Fig.10(b) the positive and negative multi-spikes, which are induced by the set of ring-like vortices and the closure vortex, appear periodically. The number of these spike-pair (each has one positive and one negative spike) is 5 or 6 which is one more higher than that of the ring-like vortices. The closure vortex combined $\wedge$-structure and low-speed streak can generate another one spike-pair. Because a ring-like vortex can generate one spike-pair on time trace of U-component of velocity (The left hand side of the spike is generated by the right hand side of the vortex and vice verse), and because a plane where a ring-like vortex appear is inclined at more than 45 degrees to the wall, the pair is not always present on any time traces of the velocity in fixed y-position. In the near wall

region, it represents on the right side on the time traces in one period because the localised flow velocity is affected just by left part of the ring-like vortex. In the middle layer, the spike-pair exists on the time trace (see Fig.10(b) and Kachanov 1994, Fig.30).

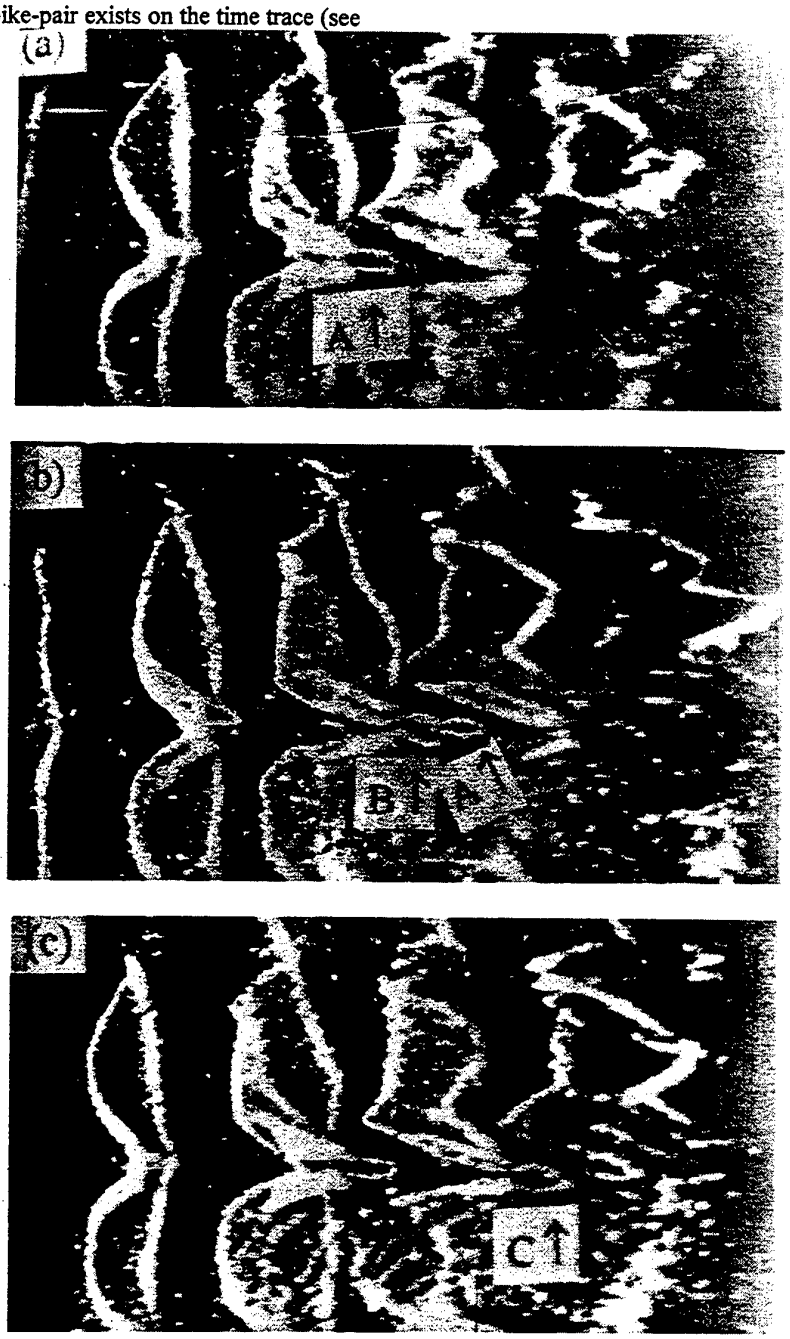

Fig.9 The formation of the ring-like vortices
(rate 1:2; and x from 430, y=1.0)
(a) 1st ring-like vortex formation (A↑) (t= 0 s)
(b) 2nd ring-like vortex formation (B↑) (t=0.166s)
(c) 3rd ring-like vortex formation (C↑) (t=0.291s)

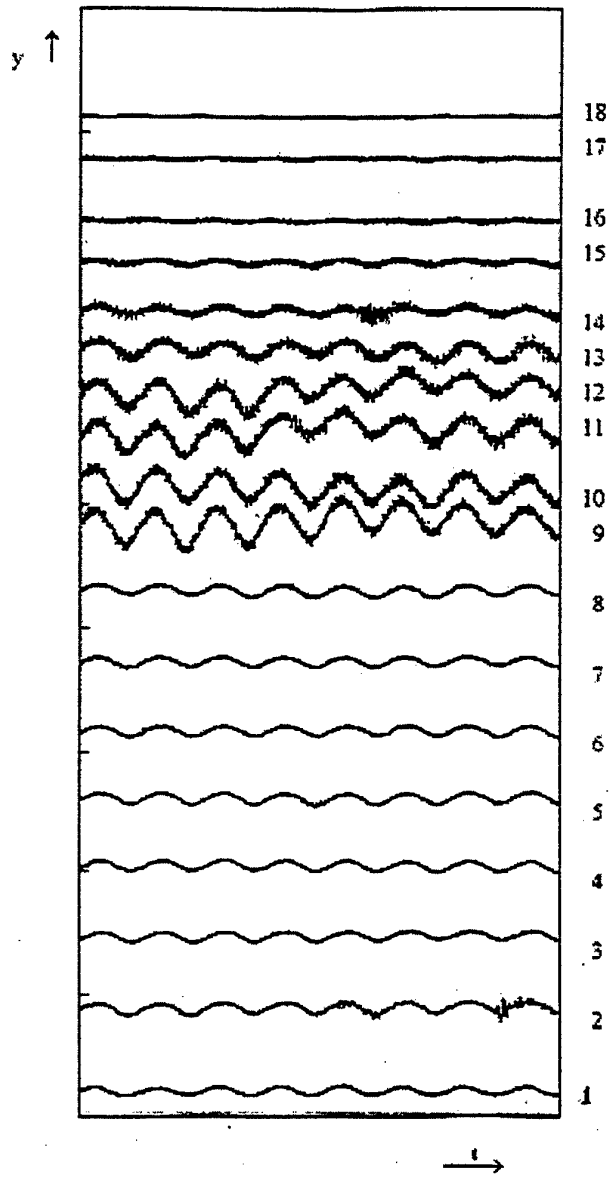

Fig10(a) Oscillaosocope traces of velocity disturbances at various distances from the wall at x=400.
1,2, .. . for y/δ=0.042, 0.069, 0.095, 0.12, 0.145, 0.208, 0.247, 0.344, 0.382, 0.42, 0.47, 0.519, 0.57, 0.62, 0.67, 0.795, 0.832, 1.025

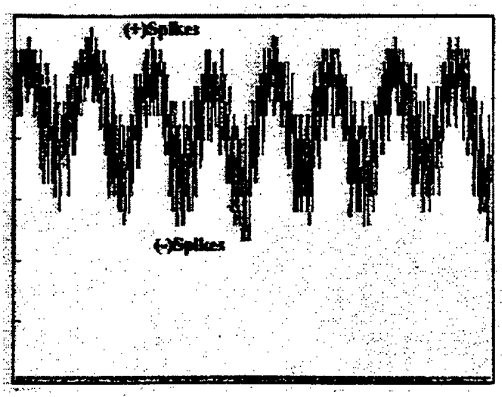

Fig10(b) Oscilloscope traces of velocity disturbances at x=400, y/δ=0.42

Several features are seen from the above experimental facts: 1. The solitary wave present not only in the near wall region but also in the external edge of the boundary layer. 2. Traces with single, double, etc. spikes are observed in the time traces which influence the time traces in the near wall region and the external edge of the boundary layer and these kinds of multi-spikes are response to the set of the ring-like vortices one by one.

Three questions should be answered: what are the differences between the CS-solitons by Borodulin & Kachanov and Lee? What are the differences between the CS-solitons by Lee and a fundamental wave (T-S wave)? What is the relation between the CS-solitons by Lee and turbulent spot? CS-solitons suggested by Lee are the typical three-dimensional wave packets although they have the same frequency of the T-S wave. The span-wise distributions of the amplitudes of the CS-solitons (the amplitude here is defined as half of the fluctuation amplitude on time traces), obtained at different y-position, are seen in Fig.11. The graph shows strong span-wise localisation of the CS-soliton. Fig. 12 shows the same results as in Fig. 9 at x=500mm and z=0. Both the visual results and the experimental measurement results show that the existence of the CS-solitons from initial stage to the later stage of transition and to the nearly developed turbulence.

it becomes easy to answer the second question because the fig.9 is obtained. The CS-solitons suggested by Borodulin & Kachanov represent the multi-spikes on time traces of velocity which are induced by the set of ring-like vortices in the above session.

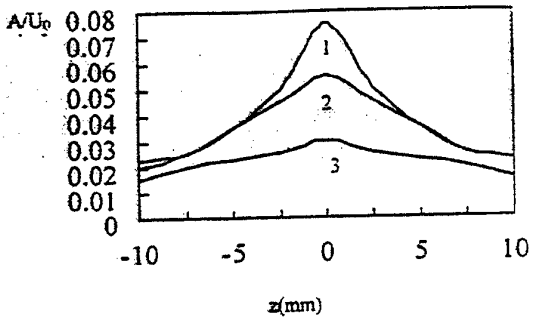

Fig.11 Span-wise distributions of the amplitudes of the CS-solitons at different y-positions 1,2,3 for y=0.62, 1.42, 2.4.

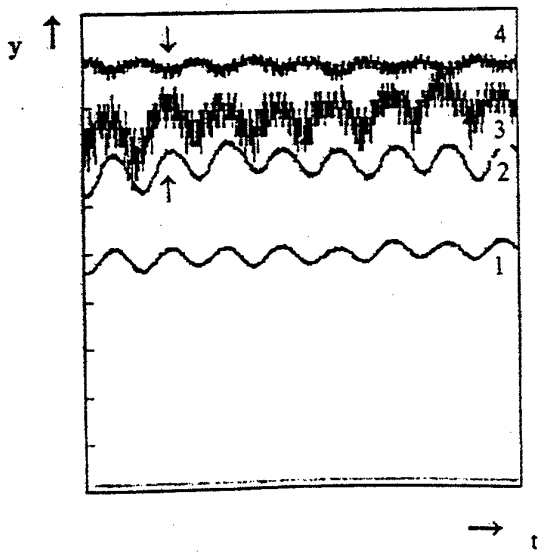

Fig12(a) Fig10(a) Oscilloscope traces of velocity disturbances at various distances from the wall at x=500
1,2, .. . for y=0.4, 2.3, 3.4, 8.2

It is well known that the turbulent spot presents at the later stage of transition. Very recently, Kachanov (1994) suggested a transitional path called without turbulent spot transition. Some other researchers suggested another path called direct to turbulent spot transition As a result of the wave resonance among T-S waves (Kachanov 1994), the three-dimensional wave structures present at the initial stage to the later stage of transition. It has some features such as the solitary wave. As described by Lee (1996a,1998), this kind of wave structure can generate spike and you can find it on time trace of velocity in the work by Kachanov(1994). In other words, no exact evidence in the present paper can be used to confirm there exist so-

called without turbulent spot transition Because of no detailed visualised results at the initial stage about this structure, the clear pictures of this structure is mainly obtained at later stage of transition. At this time, so-called turbulent spot is formed. Because of the importance of this structure in transitional boundary layer and because the fact that it was found in other flow fields, it is well reasoned that we call this structure as one of the CS-soliton. Furthermore, Lee (1998) supposed that this structure is the source where the determination of the flow fields appears. The so-called direct to turbulent spot transition appears in some studies in which the boundary layer is thick enough (Hama 1963, Lee 1995b, 1998). .In the viewpoint of Lee (1998), there does not exist a basic physical difference between so-called direct to turbulent spot transition and other boundary layer transition in boundary layer.

It is necessary to take time to discuss the measurement results in Fig.12 and in Fig.30 by Borodulin & Kachanov (Kachanov1994). The peaks" with nearly same phase on time traces of velocity in near wall region and in external edge of boundary layer are in opposite direction (see Arrows in the figure). In the near wall region, the convection velocity of the CS-solitons is higher than that of environment flows so that the flow speed become high when the CS-solitons fly through. Because in the external edge of boundary layer the environment flow speed is higher than that of the convection speed of the CS-solitons, the flow speed is decreased when the CS-solitons pass through.

Both Figs.10 and 12 demonstrate one more interesting fact: Spikes are always observed in regions between pairs of counter-rotating vortices. Exactly spike-pairs, each of which consists of one positive and one negative spike, have the form of a ring-like vortex with an axis of asymmetry directed along the x- co-ordinate. Strong rotation of these ring-like vortices result in large local negative and positive values of the central steam-wise flow velocity which appear as spike-pairs in an oscilloscope trace when the vortices fly past a fixed hot-film probe.

Thus, experimental studies (which correlate very well with numerical experiments by Rist 1990,1992, and private communication between Kachanov and Rist)show that the CS-solitons suggested by Borodulin & Kachanov (Kachanov1994), which are different from the CS-solitons by Lee (1995,1996), represent the typical ring-like vortices. The spikes move downstream together within the external part of the boundary layer with the same velocity and remain essentially unchanged even far downstream.

5. POSSIBLE PHYSICAL MECHANISM FOR THE FORMATION OF THE SET OF RING-LIKE VORTICES

The time difference between the presentations of the neighbouring ring-like vortices are equal in value to that of neighbour spikes. On the surface (see Fig.9) this kind of the ring-like vortices is separated from the tip of the Λ-structure and two legs of the vortex are reconnected into a closed ring-like vortex. This physical process was suggested by Kachanov for several times(1997 private communication). The present experiments show the formation of the kind of first ring-like vortex is not directly separated from the tip of the Λ-structure. Fig. 13 shows the formation process of first ring-like vortex which demonstrates that this structure is directly separated from the border of the solitary wave inside the butterfly -like structure. Why can we see the evolution of flow structures just from one picture instead of several pictures such as in Fig.9? The periodical features of flow structures should be mentioned again. All detailed information for this process is clearly to be seen in video. For the second, third, and etc. ring-like vortex, the physical mechanism for their formation is not very clear now. Maybe, they have the same physical mechanism for their formation as that of the first ring-like vortex. It is beyond doubt that direct experimental evidence is necessary. Fig.14 shows the conceptual sketches of the flow structure formation. In fig.14(a) the formation of the CS-soliton and the high-shear layer along the border of the CS-soliton at initial stage of transition is given which is the same as in natural transition (Lee1997a,b,c; 1998). Then the closure vortex is formed because of mass conservation and lower convection velocity of the CS-soliton. Fig.14(b) shows the 1st ring-like vortex formation along the border of the CS-soliton again because of the secondary or higher instability (Herbert 1988). At this moment the closure vortex is separated from the CS-solitons. Fig.14(c) shows presentation of the 2nd ring-like vortex along the border of CS-soliton and the head of 1st ring-like vortex meets the tip of the

closure vortex because the head part of this vortex appears in a place where the y-position is higher than that of the tip-of closure vortex so that it has higher convection velocity. After interaction between the head of the 1st ring-like vortex and the tip of the closure vortex, the rotation speed of the 1st ring-like vortex is increased then it is separated from the tip and flies downstream at high speed. The 3rd, 4th and 5th ring-like vortex are formed along the border of the CS-soliton step by step. Their evolution is supposed as similar as that of the 1st ring-like vortex. All these are shown in Fig.14(d) and (e).

Fig.13 Head part of 1st ring-like vortex (Arrow B)separated from CS-solitons (Arrows A) (rate 1:3.3)

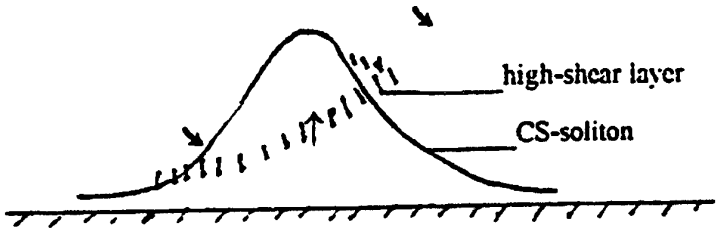

Fig.14(a) Formation of the CS-soliton and the high-shear layer

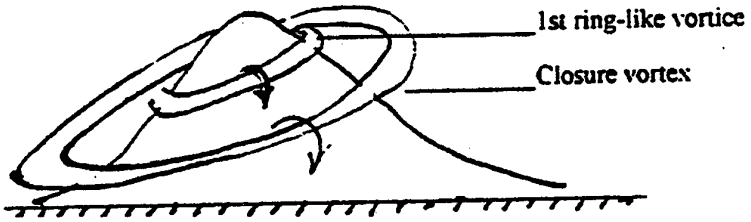

Fig14(b) Closure vortex formation, separated from the borders of the CS-solitons and the 1st ring-like vortex formation

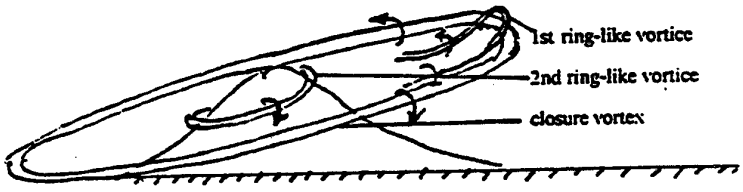

Fig14(c) 2nd ring-like vortex formation and the 1st ring-like vortex meet the tip of the closure vortex

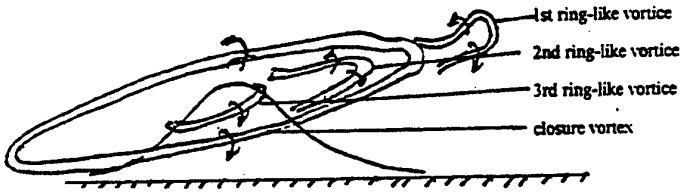

Fig14(d) 3rd ring-like vortex formation and the 1st ring-like vortex separated from the tip of of the closure vortex

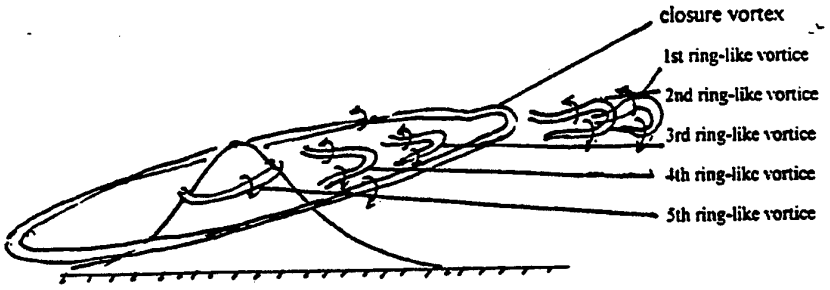

Fig14(e) Set of ring-like vortices formation

Furthermore, it is necessary to repeat to mention the results of the vortex -ring formation along the border of the CS-solitons in natural transition (Lee 1997a,b,c; 1998). Two reasons are very important to explain the high-shear layers and the vortex-ring formation along the borders of the CS-solitons: mass conservation and low convection speed of the CS-solitons. On the right hand side of the CS-soliton, the flow sweeps down from the free stream to the its right side. In order to conserve mass, the flow above CS-soliton would sweep down to their right side. Otherwise the vacuum region would be formed. The flow upstream the CS-soliton would sweeps down to the near wall region on their left hand side. Finally, the high-shear layer and the vortex-ring formed along the border of the CS-soliton. As mentioned by Lee(1997a,1998a,b,c), the process for the vortex-ring formation along the border of the CS-soliton appears in the work by Hama et al.(1963) which was also found by Lee(1997a,b). For the 2nd, 3rd, 4th and 5th ring-like vortex, it is supposed that they have the same physical process such as the first ring-like vortex which is considered as the secondary instability or higher instability of the border of the CS-soliton.

In order to understand the present results deeply, more detailed information is necessary. Because the hydrogen-bubble technique strongly dependants on the place where the line is mounted, it should be paid more attentions to check the flow structures and determine the properties.

6. LONG-STREAK IN TRANSITIONAL BOUNDARY LAYERS

A long-streak (See Fig.7) in transitional boundary layer are different from that in developed turbulent boundary layer (Kline et al. 1967, Lian 1990) in some aspects: 1.The long-streaks in transitional boundary layer present in the near wall region and in the peak position But the long-streaks in developed turbulent boundary layer appear in the region where the interface often appears(Lian 1990) and the stream-wise vortex often happen between the high-speed streak and the low-speed streak. 2. The long-streak in transitional boundary layer represents the features of the CS-solitons. The direct evidence shows the formation of the long-streak in the region of near to the wall is given in Fig.15. Arrows A and B demonstrate the evolution of the form of the CS-soliton into a long-streak, which still has the features of CS-soliton. The reason for that long-streak behaves the features of the CS-solitons is not difficult to be explained. In the near wall region the fact of the fluctuations of U-component of velocity at low frequency and high amplitude makes the streak here longer. In other word, the streak has not only a convection velocity but an oscillatory velocity at high

amplitude. Then the streak should spread both upstream and downstream and the long-streak should be formed. From figs.15 and 6, it is clear to be found that the time scales of the head part of $\wedge$-structure and the CS-soliton in X-direction in peak position by means of both Taylor Formula and hydrogen bubble time line technique. It offers us a solid evidence which is used to show that the time traces at low frequency and high amplitude in Fig.10 are generated by CS-solitons instead of $\wedge$-structures.

Fig.15 Formation of the long-streak: from the shape of rhombus-like(A↑) to long streak (B↑) (rate 1:3.3)

7. DISCUSSION

It is necessary to pay more attentions to understand the present time traces and the time traces by Borodulin & Kachanov (see Kachanov 1994, Fig.30). Because of the sensitive length of the probe is two times large than that used by Kachanov in Novosibirsk. The amplitude of the spikes is not as high as that obtained in former work by Kachanov. Because of the same reason, the present probe is very convenient to be used to measure the large scale structures such as CS-solitons. From the near wall region to the external edge of the boundary layer, the CS-solitons present periodically in the time traces.

Actually, the time traces just represent the features of a wave. It is very difficulty to distinguish wave and vortex from the time trace. Flow visualisation becomes very important in order to distinguish the characteristics of a flow structure and obtain full field information.

8. CONCLUSIONS

Based on the above experimental observation, it is concluded that the multi-spikes, which are observed in the range of one period of the fundamental wave, in transitional flat plate boundary layer is generated by a set of ring-like vortices and the closure vortex. For the first ring-like vortex, the present experimental results show it is separated from the solitary wave -like structure inside the butterfly-like structure rather than separated from the tip of the $\wedge$-structure. The $\wedge$-structure is part of the perfect butterfly-like structure from the initial stage of the transition to the nearly developed turbulent flow. Inside the butterfly-like structure, the solitary wave, which had been suggested in works (Lee 1995b; 1996a,b,c,d; 1997a,b; 1998) and in work by Hama many years ago, is observed which presents in total boundary layer thickness. Otherwise, the observation of the set of ring-like vortices during one period of fundamental wave makes it possible to explain the physical process for the formation of the multi-spikes in the time traces measured by Borodulin &Kachanov.

This work was guided by Prof. Kachanov, Y.S., Dr. Borodulin, V. I. and Dr. Gaponenko, V.V. (Russian Academy of Sciences).

We would like to thank Prof. Q. D. Wei (Dean of the State Key Laboratory of Turbulence Research of Beijing University) and Mr. Du, X. T. for their helps during our experiment. Thanks also go to Prof. Z. M. Jin (Head of Mech. Department of the Chinese NSF) for his very kind support. This joint project was supported by Chinese NSF, RFBR under grant No.96-01-001c (Russian Foundation for Basic Research), Wang K.-C. Foundation and Chinese National Foundation special for Post Doctor.

9. REFERENCES

(1) Borodulin, V. I., Gaponenko, V. R., Kachanov, Y. S., Lee, C. B. Experimental investigation of the spatial flow structure at late stages of laminar-turbulent transition in a boundary layer. 1998, Proc. of Int. conference on Mechods of Aerophysical Research. Novosibirsk: Inst. Theor. & Applied Mech.

(2) Craik, A. D. D. Wave Interactions and Fluid Flows. 1985. Cambridge, Cambridge Univ. Press. .

(3) Fasel, H. Numerical simulation of instability and transition in boundary layer flows. See Arnal &

Michel, 1990, pp587-598.
(4) Hama, F. R., Nautant, J. Detailed flow-field observations in the transitional process in a thick boundary layer. Proc. of Heat Transfer & Fluid Mech. Inst. 77-93, 1963, Stanford Univ. Press.
(5) Herbert, T. Secondary instability of boundary layers. Annu. Rev. Fluid Mech., 1988, **20**,487-526.
(6) Kachanov, Yu. S. Physical mechanism of laminar-boundary-layer transition. Annu. Rev. Fluid Mech.1994, **26**, 411-482.
(7) Klebanoff, P. S., Tidstrom, K. D. & Sargent, L. M. The three dimensional nature of boundary layer instability , J. Fluid Mech.1962, **12**,1-34.
(8) Kleiser, L., Zang, T. A. Numerical simulation of transition in wall -bounded shear flows. Annu. Rev. Fluid Mech., 1991, **23**, 495-537.
(9) Kline, S. J., Reynolds, W. C., Schraub, F. A. Runstaller, W. P. J. Fluid Mech. 1967, **30**, 741-73.
(10) Lee, C. B. Some new results in turbulent boundary layer / shock wave interactions. Proc. IUTAM Symp. On Non-linear Instability of Nonparallel flows. 1993, 213-31. Springer-Verlag.
(11) Lee, C. B. A study of shock wave system / turbulent boundary layer interaction.1995a, Exps. In Fluids, 143-49.
(12) Lee, C. B. Transition in Accelerated Boundary Layers. Ph.D. Dissertation of Beijing Univ. of Aero. & Astro. 1995.
(13) Lee, C. B. On the Instability of the Borders of the CS-solitons and the formation of the Eddy, Chinese Sci. & Tech. Letts. 1996, **2(2)**, 67(1996a): 2(4), 137(1996b) (see also Proc. of ICTAM 6, 210, Kyoto(1996c), Japan).
(14) Lee, C. B. From CS-soliton to Eddy, Proc. of 10th National Symp. on Hydrodynamics, 1996d, 741-745, Ocean press(in English).
(15) Lee, C. B. Comparison Between The Natural Transition and Controlled Transition. Proc. of 3rd International Conference of Experimental Fluid Mech., Moscow, 1997a, in press.
(16) Lee, C. B. 1997b New features of CS-solitons and formation of the vortices, Proc. 7th Asian congress of Fluid Mech., Dec 8-12,1997, Chennai, 445-447(also accepted by Phys. Letts A).
(17) Lee, C. B. Recent Development in the Study of Transition and Turbulence. Chinese J. of Fluid Measurement, 1998a , 12(1), 8-28.
(18) Lee, C. B. Borodulin, V. I., Gaponenko, V. R., Kachanov, Y. S. 1998a Combined study of mechanisms of evolution and Breakdowm of coherent structures in transitional boundary layer at controlled condition. Proc. of Int. conference on Mechods of Aerophysical Research. Novosibirsk: Inst. Theor. & Applied Mech.
(19) Lee, C. B., Kachanov, Y. S., Borodulin, V. I., Gapoonenko, V. V., Some new results in transitional boundary layers. Chinese Sci. & Tech. Letts. 1998b, 4(2),270(in Chinese).
(20) Lian, Q. X. J. Fluid Mech. 215, 101-20.
(21) Nayfeh, A. H. Non-linear stability of boundary layers. AIAA paper,1987, No.87-0044
(22) Reed, H. L., Saric, W. S. Stability of Three-Dimensional Boundary Layers. Annu. Rev. Fluid Mech. 1990, 21,235-84
(23) Schubauer, G. B., Klebanoff, P. S., Contibutions on the mechanism of boundary layer transition. NACA Rep.1956, No.1289.
(24) Zhigulyov, V. N., Tumin, A. M. Origin of Turbulence. Dynamic Theory of Generation and Development of the Instabilities of Boundary Layers. Novosibrisk, Nauka Publ., Sib. Div. 1987, 282pp, (In Russian).

Session 2

Vertical Mixed and Natural Convection

EXPERIMENTAL INVESTIGATION OF TURBULENT MIXED CONVECTION HEAT TRANSFER IN A VERTICAL ANNULUS FOR AIDING FLOWS

P.Poškas, B. Jazbutis

Lithuanian Energy Institute, Kaunas, Lithuania

ABSTRACT

We present our experimental results of a study on turbulent mixed convection heat transfer in a vertical annulus d_1/d_2 = 0.372 for aiding air flows. The experiments were performed with outer and inner tubes only with one-side heating at the boundary condition close to q_w = const.

1 INTRODUCTION

Turbulent mixed convection in vertical tubes has been studied for few decades (see for ex. [1, 2]). It was revealed that in a heated downward flow, where forced convection and free convection are in opposition (opposing flows) buoyancy forces cause an enhancement of the turbulence of the flow, and the heat transfer is higher than for forced convection. For upward flow in heated tubes (aiding flows) local heat transfer can be significantly lower than for forced flow as a result of a partial laminarisation of the flow. With increasing of the effect of buoyancy, when the free convection component becomes dominant, heat transfer for aiding flows also becomes enhanced.

Data on turbulent mixed convection heat transfer in vertical channels of other cross sections are very limited. There are some publications on mixed convection heat transfer in flat channels (see for ex. [3]). This is true for annuli, too.

Say, [4] is a study of average heat transfer from the inner tube of an annulus with the diameter ratio of d_1/d_2= 0.742. Aiding and opposing flows were steadied in an annular water flow. The decrease of the heat transfer was observed in both situations under the effect of thermal gravity. This is in contradiction to investigations in circular pipes, which indicates that the heat transfer rate increases under opposing flow conditions.

Very interesting results were presented in [5], where mixed convection heat transfer from inner smooth and rough tubes of annulus d_1/d_2= 0.49 was investigated. It was shown that with the effect of buoyancy the heat transfer increases in opposing flows. It decreases and after that recovers for aiding flows. Differences between mixed convection heat transfers from smooth and rough surfaces were revealed. But the channel was rather short (x/d till 28), so it was not possible to demonstrate all effects of mixed convection.

We have not found any publications on turbulent mixed convection heat transfer from the outer wall of the annulus.

We present in this study the results of an experimental investigation of turbulent mixed convection heat transfer from inner and outer wall of vertical annulus d_1/d_2= 0.372 for aiding flows. The experiments were performed with outer and inner tubes only with one-side heating at boundary condition close to q_w = const.

2 EXPERIMENTAL TECHNIQUE

Investigations were performed on an open-loop wind tunnel (Fig. 1). Atmospheric air from compressor (1), from witch mechanical impurities and moisture were removed, was supplied at about 20 MPa to high pressure receivers (2) and then through a moisture separator (3) to pressure reducers (4, 5). The pressure reducer (5) dropped the air pressure to 0.7 MPa and this lower-pressure air flowed to the low-pressure receiver (6). After that the air through one of three parallel lines with double flowmetering orifices (7) of different cross sections was supplied to test section (8), from which it was vented into the atmosphere through a throttling valve (9). A special air line to the test section was used when the air flowrate was less than 25 kg/h. In this case the air was supplied to the test section through the control valve (10) and the flowmeter (12), capable of measuring air flowrate between 1 to 25 kg/h. The principal component of this flowmeter was a nozzle generating a flow with a uniform velocity profile. Reducers, the control valve (10), the bypass valve (9), and the throttling slide valve controlled the air pressure and flowrate.

The calorimeter tube in the test section was heated by direct current. Type PSM-1000 electromechanical converters (13) generated this current. The current was controlled by varying the voltage to the excitation winding of the converter and was measured on the basis of the value of U on shunt (14). The high stability of the so generated current and therefore the stability of the heat evolved to the air were due to the use of a negative-feedback electronic control.

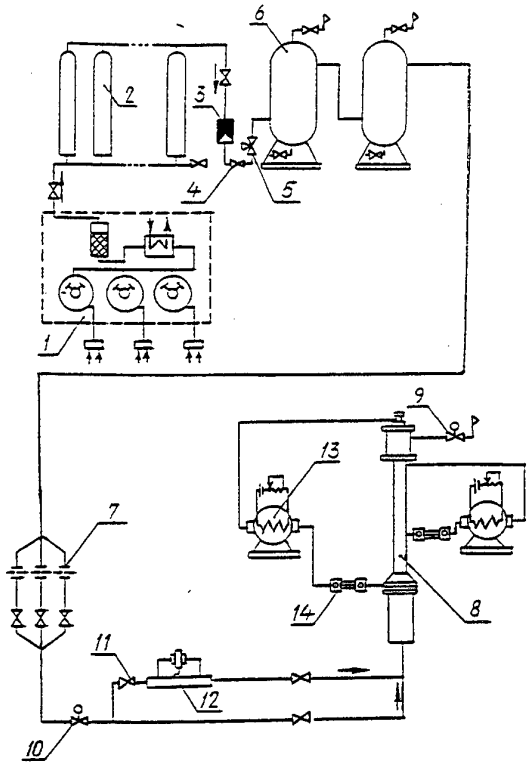

Figure 1.Test rig.

The 2145-mm-long annulus with a 1400 mm electrically heated part was formed by a polished stainless steel outer tube (2), 29.75 mm in outer diameter, a precision made wall thickness of 0.8 mm, and by a replaceable inner tube (1), coaxial in the outer tube (Fig. 2). The axially fixed internal stainless steel pipe had external diameter of 10.47 mm, wall thickness of 0.4 mm. Both tubes could serve as calorimeters (1400 mm long). So, the experiments were performed with annulus $d_1/d_2 = 0.372$ only with one-side heating at boundary condition close to q_w = const.

To reduce heat losses to the surroundings, the 1600-mm heated length of the annulus was placed in a vacuum chamber (3) and surrounded by six cylindrical reflecting screens made of 0.15-mm polished stainless steel sheets. The screens were suspended from the vacuum chamber cover (5). The upper end of the outer tube was soldered to the cover of the discharge chamber, its housing was welded to the cover of the vacuum chamber. Its lower end was soldered to the elongation stub located at the bottom of the vacuum chamber, which by means of a connecting ring and a bellows provided compensation for thermal expansion. The outer tube was maintained in a stressed state by a spring and was held coaxial with the vacuum chamber by means of a Teflon ring.

Current to the outer tube was supplied from the upper copper current-distributing ring, through the

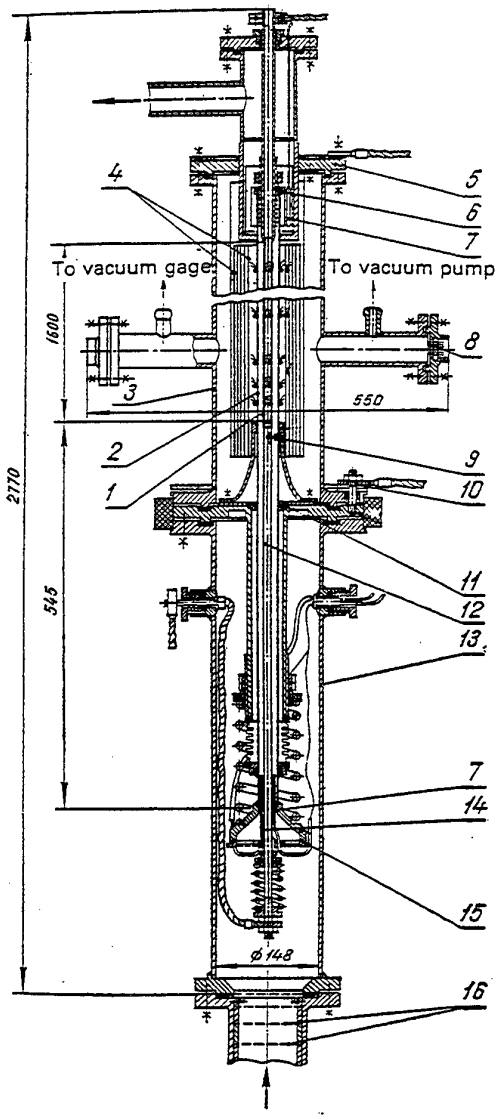

Figure 2.Test section.

vacuum-chamber cover and the walls and bottom of the discharge chamber. It was led out from the lower current-distributing ring, along bronze pins, the bottom of the vacuum chamber, flexible copper busbars, and a copper ring soldered to the tube.

The inner tube was suspended in the center of the outer tube. Centering was provided in three sections: at the inlet, at the outlet, and prior to the heated length, where three 0.8-mm-diameter centering pins with Teflon insulating tips were placed. The spring held the inner tube in a stretched state and compensated for longitudinal thermal deformations. The current was supplied to the inner tube through the hollow upper busbar and central bar (12), its diameter always equal to that of the inner tube.

To stabilize the emissivity, the tubes were subject to 2-hour roasting in air at 1090 K.

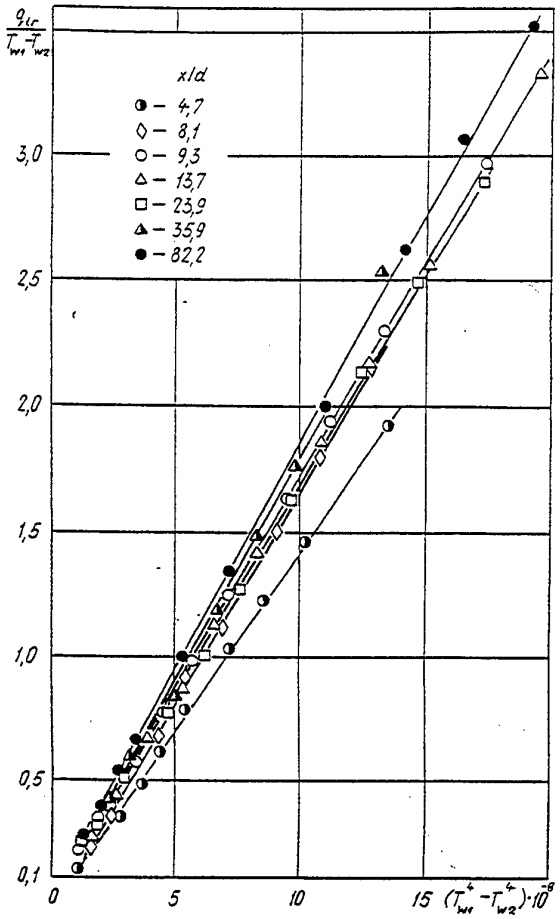

Figure 3. Radiation heat fluxes between the tubes for different x/d.

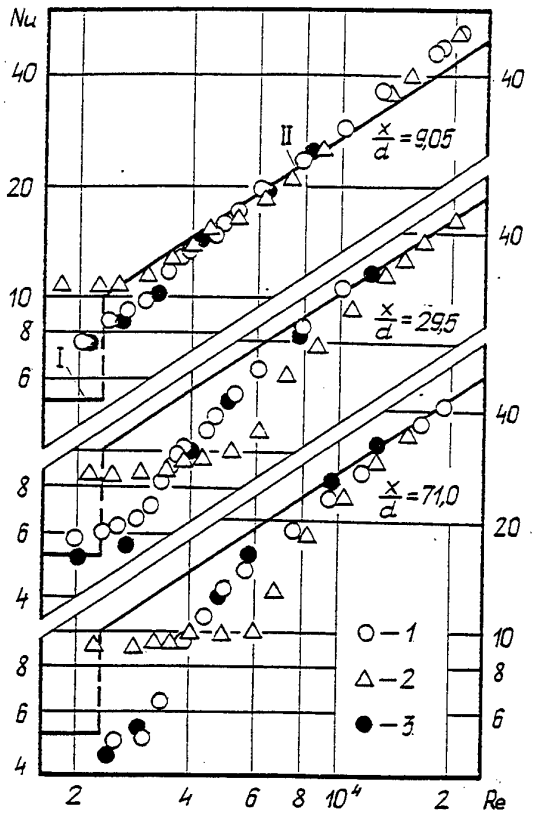

Figure 4. The behavior of Nu vs Re for the outer tube of an annulus at different x/d: 1.2 - upward flow for p ≈ 0.1 MPa and p ≈ 0.7 MPa, respectively, 3 - downward flow at p ≈ 0.7 MPa. The heat flux parameter q^{+}_{in} ≈ 0.0005 - 0.0003, I – for laminar flow /6/, II - for turbulent flow / 7/.

The chromel-alumel thermocouples were contact-welded at the outer surface of the outer tube and on the inner surface of the inner tube. They were positioned on opposite sides of the perimeter in 22 locations along the annulus. They were made of 0.2- to 0.3-mm wires, coated with heat-resistant insulation. The thermocouples were used for measuring the temperature as well as for determining the voltage drop along the tube. The locations of thermocouples on both tubes were identical only when neither of the tubes were heated. In the remaining cases they were shifted relative to one another due to thermal expansion. A correction for this was made in the test data.

The cooling air was supplied to inlet chamber (13) through flow equalizing meshes (16). It then flowed smoothly through a narrowing down transition piece of the annulus, passed the non heated hydrodynamic entrance length, and, through the perforated end of the outer tube, was exhausted to the mixing device of the discharge chamber. The air was removed through an outlet, located in the upper part of the discharge chamber. The pressure was measured only in two points – at the annulus inlet and in the vacuum chamber.

The air temperature was measured by thermocouples in several locations of the discharge chamber and at the start of the hydrodynamic entrance region. The heat losses to the surroundings were measured by placing eight thermocouples along the first reflecting screen.

All the electric signals from thermocouples, as well as from instruments measuring the voltage drops along the tubes and shunts, were measured by means of an automatic data acquisition system.

The reference parameters for Re, Nu and Gr numbers were local bulk flow temperature and velocity, entrance pressure and equivalent diameter.

As we see this study was performed with an annulus of relatively small diameters d_1 and d_2 but using a 0.7 MPa airflow pressure. This allowed us to cover rather wide ranges of buoyancy parameters. Tentative experiments showed a week effect of buoyancy at atmospheric pressure of the air in such channel.

To define the heat flux through the vacuum-shield and radiation flux between inner and outer tubes special

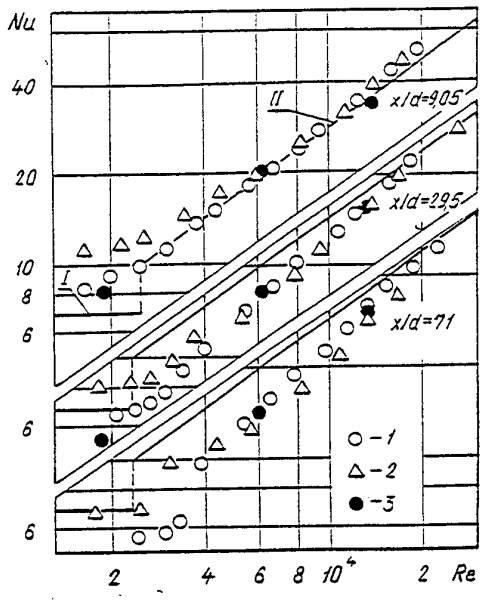

Figure 5. The behavior of Nu vs Re on the inner tube for different x/d: notations as in Fig.4.

calibration tests were performed with vacuum not only in the space of six cylindrical reflecting screens but also between the tubes of the annulus. In this case only the inner tube was heated. The heat emitted by the inner tube was transferred by radiation to the outer calorimeter tube, and was sinked by radiation across the vacuum insulation layer.

The measurements in this case covered the temperatures of the inner T_{w1} and outer T_{w2} tubes, of the first reflecting screen T_{s1}, power of the electric current, and voltage drop along the inner tube, with the account of the heat conduction along each of the tubes. Wall temperatures covered were from 100 C to about 600 C in steps of 50 C.

The test points for each circumference of measurement were interpreted in coordinates:

$$\frac{q_{lr}}{T_{w1}-T_{w2}} = f[(\frac{T_{w1}}{100})^4 - (\frac{T_{w2}}{100})^4]$$

between the inner and outer tube, and in

$$\frac{q_{lr}}{T_{w2}-T_э} = f[(\frac{T_{w2}}{100})^4 - (\frac{T_э}{100})^4]$$

between the outer tube and a reflecting screen. Fig.3 illustrates the test points for the above relations. A conclusion follows from the experiment, that the relations is close to linear for variable heating rates, and some relation with the dimensionless length x/d is evident. Numerical values of the test points were approximated for each circumference by a second –

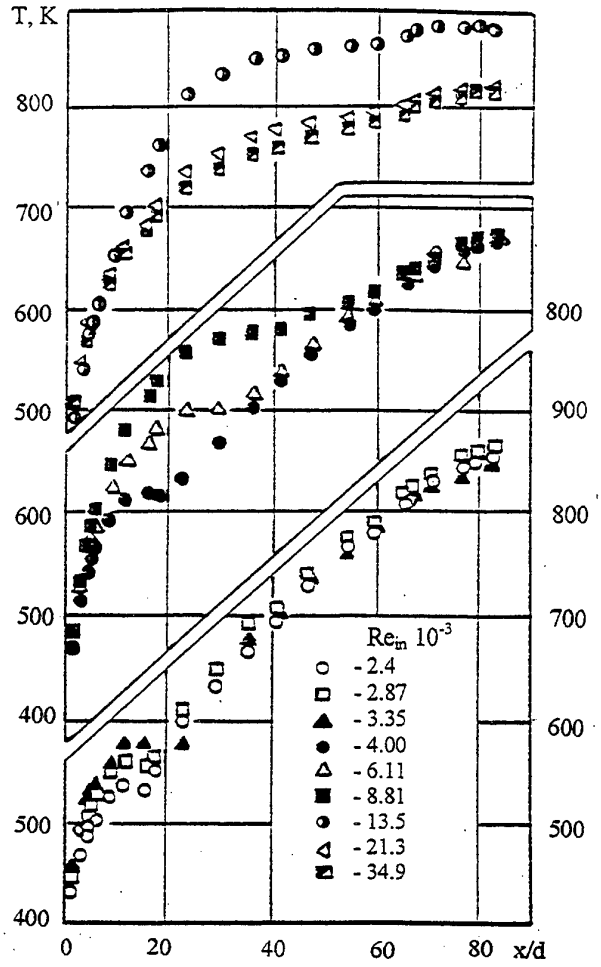

Figure 6. The variation of temperature of the outer - tube wall for different Re.

order polynomial. This yielded the corresponding relations for the calculation of the radiation heat fluxes q_{lr} in main experiments.

3 RESULTS AND DISCUSSION

Mixed - convection heat transfer was studied at air pressures p about 0.7 Pa. In the absence of any prediction of turbulent heat transfer in annular channels for forced convection in the low range of Re, the tests were also performed at air pressures close to the atmospheric one, for a minimum free convection effect.

Fig.4 and 5 illustrate the behavior of Nu vs Re at different distances from the start of heating of the inner and the outer tubes $d_1/d_2 = 0.372$. Note a higher effect of thermal gravity on the outer wall, than on the inner one, for the same Re. One more observation is that the effect of thermal gravity increases with an increase of x/d. For x/d about 9 and Re over 4000, the heat transfer at p about 0.1 and 0.7 MPa is actually the

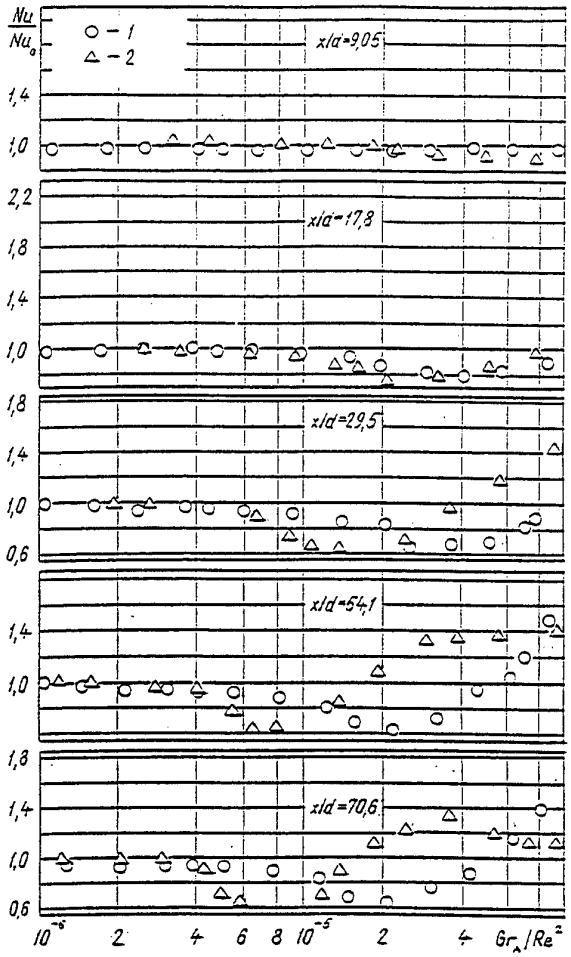

Figure 7. Relative heat transfer from the outer tube of an annulus for different heat loads: $1 - q^{+}_{in} \approx 0.0007 - 0.0004$, $2 - q^{+}_{in} \approx 0.0006 - 0.003$.

same, but for higher x/d a decrease of turbulent heat transfer is evident at higher pressures because of the thermal gravity force effect. At p about 0.1 MPa the heat transfer is actually the same for either downward or upward flow of air. This speaks for the absence of any effect of thermal gravity on forced convection heat transfer.

The behavior of the wall temperature along the tube is demonstrated in Fig.6. Local maxima of temperature are noted at specific values of Re, same as in a hollow pipe. The maxima are more evident at higher heat loads. Besides, they are more pronounced on the outer tube.

Relative heat transfer as a function of the buoyancy parameter Gr_A/Re^2, with the heat transfer at p = 0.1 MPa as a reference, that is for forced heat transfer, is demonstrated in Fig.7. Same as for a hollow single pipe, the heat transfer decrease is related to x/d. The large the x/d, the more evident the heat transfer decrease. A stratification of the test points may be noted for different heat loads, and is especially evident on the location of the minimum heat transfer.

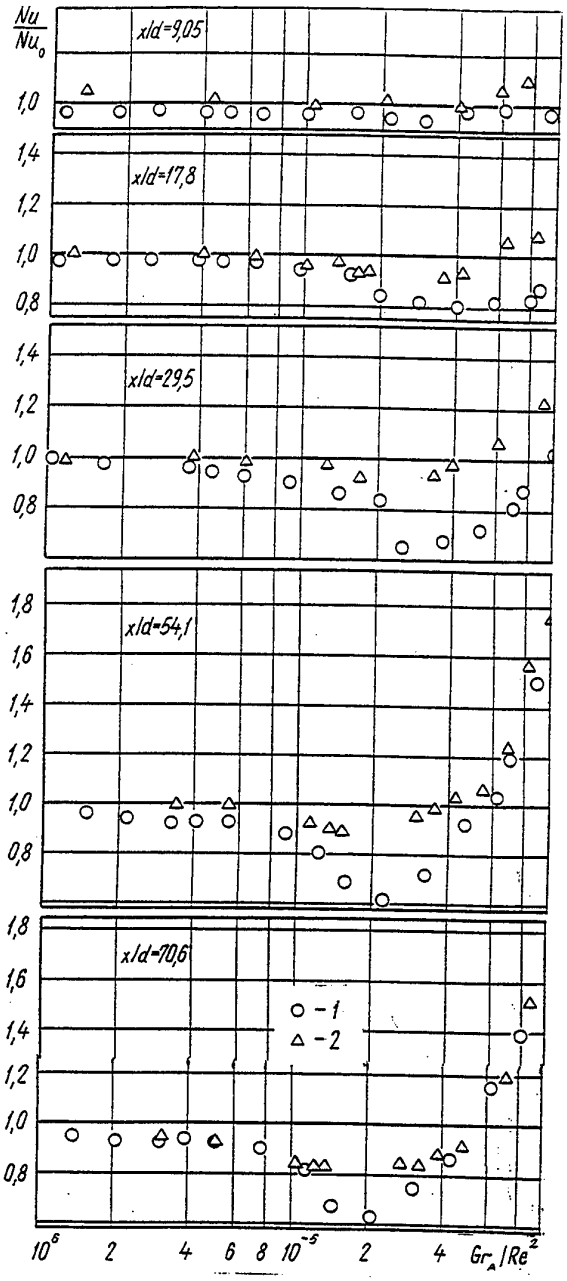

Figure 8. A comparison of the relative heat transfer from inner (2) and outer tubes of the annulus d_1/d_2 = 0.372 for low heat loads.

A comparison of the relative heat transfer from the outer and the inner tubes of annular channels shows for arbitrary x/d and configurations of the channels, a more significant decrease of the heat transfer from the outer tube, than from the inner one, Fig.8.

For the outer tube of an annular channel d_1/d_2 = 0.372, the maximum decrease of the heat transfer equals 40% of the corresponding heat transfer of a pure forced convection. For the inner tube of the same annulus the decrease is less, about 20%. A similar

situation is observed at higher heat loads. As it was demonstrated in many papers the maximum decrease of the heat transfer in vertical hollow pipes is 50-60 %.

CONCLUSIONS

Experiments of mixed turbulent convection in a vertical annulus for aiding flows lead to the following conclusions:

1. The behavior of the heat transfer on either the outer or the inner tube of the annulus, under thermal gravity is similar to that in a vertical tube. That is, for weak effects of thermal gravity the heat transfer rate is lower, than for forced convection heat transfer, but is restored at higher effects of thermal gravity.

2. When only the inner tube of the annulus is heated, the effect of thermal gravity is lower, than for only the outer tube heated and in both cases it is lower than for vertical pipe.

NOMENCLATURE

c_p	Specific heat, J/kg K
d	Hydraulic diameter of annulus, m
d_1, d_2	Diameters of the inner and outer cylinders forming the annulus, respectively, m
q	Heat flux density, W/m^2
$q^+=q_w/\rho u c_p T_f$	Heat flux parameter
T	Temperature, K
u	Bulk velocity, m/s
x	Distance from start of heating, m
ρ	Density, kg/m^3
$Gr_A=Gr_q/4RePr$	Grashof number defined by the longitudinal gradient of the bulk temperature of the fluid
Gr_q	Grashof number defined by the heat flux specified on the surface
Gr_A/Re^2	Buoyancy parameter
Nu	Nusselt number
Pr	Prandtl number
Re	Reynolds number

SUBSCRIPTS

0	Refers to forced convection
1	Refers to inner wall of an annulus
2	Refers to outer wall of an annulus
in	Refers to the conditions at the inlet
f	Refers to the flow
p	Refers to the constant pressure
w	Refers to wall conditions

REFERENCES

(1) Jackson, J. D., Cotton, M. A. and Axcell B. P. Review: studies of mixed convection in vertical tubes. Int. J. Heat and Fluid Flow, 1989, 10, pp.2-15.

(2) Vilemas, J. V., Poskas, P. S. and Kaupas, V. E. Local heat transfer in a vertical gas-cooled tube with turbulent mixed convection and different heat fluxes. Int. J. Heat Mass Transfer, 1991, vol. 35, No. 10, pp. 2421-2428.

(3) P. Poskas, J. E. Adomaitis, J. Vilemas, G. Bartkus. Development of turbulent heat transfer over the length of vertical flat channel under a strong influence of buoyancy. Proc. 10th Int. Heat Transfer Conf., Brighton, UK, 1994, vol. 5, pp. 555-560.

(4) Bohne, D. and Obermeier, E. Combined free and forced convection in a vertical and inclined cylindrical annulus. Proc. 8th Int. Heat Transfer Conf. San Francisco, 1986, vol. 3, pp. 1401-1406.

(5) Jackson, J. D., Romero, E., Li, J., Axcell, B. P. The influence of transverse rib- roughness on mixed convection heat transfer to water in an annulus. Proc. 2nd World Conf. On Experimental Heat Transfer, Fluid Mechanics and Thermodynamics, Dubrovnik, Yugoslavia, 1991.

(6) Petukhov, B. S. Heat transfer and hydraulic drag in tubes for laminar flow. M., 1967, 411 p. (in Russian).

(7) Petukhov, B. S., and Royzen, L. I.. Correlations for heat transfer in annuli. Teplofizika Vysokikh Temperatur, 1974, No. 12(3), pp 565 – 569 (in Russian).

FEATURES OF DYNAMIC AND HEAT STRUCTURE OF FREE CONVECTION BOUNDARY LAYER NEAR VERTICAL HEATED SURFACE

Yu.S. Chumakov and S.B. Nikolskaja

Department of Hydroaerodynamics
State Technical University of St.-Petersburg, Russia

ABSTRACT

The object of the study is the free convection boundary layer formed on the vertical isothermally heated plane surface.The results of the experimental study of the free convection boundary layer structure are shown. The boundaries of the dynamic and heat viscous sublayers are determined. The existence of the dynamic and heat layers of buoyancy force are proved. The boundaries of the above said layers are determined. The empirical ratios to describe the distribution of the longitudinal velocities and temperatures along these layers are hereby represented. The experimental study of such flows is very difficult since the flow velocities are very low (not above 60 cm/s), the turbulence degree is high (up to 30%) and the flows are non-isothermal. The latter makes difficult the use of hot wire anemometer method to measure the free convection flow velocity.

1 EXPERIMENTAL UNIT

A generator of the free convection flow is a vertical aluminium plate as wide as 90 cm and as high as 4.95 m. From the back side of the plate there are 25 heaters which are controlled by the electronic system which is able to keep the set heat regime for a long time (6-8 hours). When setting any regime to each of 25 sections the different laws of the surface heating, in particular the constant surface temperature, can be simulated by the surface height. Due to the considerable height of the plate there can be obtained all the three flow regimes such as laminar, transitive and developed turbulent up to Grashof number 4.5×10^{11}. To transfer the sensor in the air flow a coordinate mechanism is created. This coordinate mechanism provides the precision of the shift along the vertical coordinate about 1 cm and along the normal coordinate with regard to the surface (it means across the boundary layer) about 1 micrometer. The shift along the normal coordinate is remote controlled. In addition, the measurement of the flow parameters in one section of the boundary layer is totally automated thanks to the use of the specially designed equipment and computer software.

In the course of the experiment there were measured the average and fluctuation temperature components. All the measurements were made by using he resistance thermometer and the hot wire anemometer. As a sensor a tungsten wire of 5 micrometers diameter and 3-4 mm length was used. It is known that when using the hot wire anemometer to measure the velocity in non-isothermal flow the influence of the temperature should be taken into account to decode the hot wire anemometer readings. To our opinion, almost all the existing methods of the thermal compensation can not be used for this free convection flow which is featured by low average velocities and high turbulence degree as it was above noted. Therefore, a new method of thermal compensation by the actual temperature was developed. Without describing this method in detail it should be only noted that unlike other methods of the thermal compensation by the average temperature, in this method the readings of the hot wire anemometer which correspond to the actual temperature in the given point of the area are decoded taking into account the actual temperature in this point.

All the measurements were made at the constant surface temperature which is 70°C. The air temperature at the exterior border of the boundary layer was constant and equal to 25-26°C up to the height 2 meters and then it was being increased and reached 27-28°C when the height reached 5 meters.

2 CALIBRATION UNIT

To carry out a new method of the velocity determination a special calibration unit was designed. The main principle of the unit operation is a regular sensor movement at the set velocity in the stationary non-isothermal air. This unit can calibrate the sensors at the velocity from 1 to 50 cm/s and the temperature from 20 to 80°C.

In literature various methods of the sensor calibration are described. In the most part of these methods the flow moves past a stationary sensor. In this work another method is used. It's the sensor who moves at a set constant velocity past the stationary air. The operation of such a calibration unit can be outlined as follows: a small truck with the fixed sensor goes by the horizontal lines . This truck is put in motion by the electric motor via the reduction box which can change the truck speed. The motor and reduction box are remote controlled

The sensor goes about a horizontal tube axis. The truck speed is determined by the time during which the truck passes the basis distance. To create non-isothermal flow, the air in the tube is heated with the use of infrared emission. A special study was made to determine the influence of the heater power and the heating time on the temperature distribution in the tube.

For the simultaneous measurement of the velocity and the temperature there was used the two wire sensor: the hot wire measures the velocity and the cold one measures the temperature. These two tungsten wires were located at the dimension 3.5 mm each from other and perpendicular to the axis of the tube. Such a design of the sensor eliminates the influence of the hot wire on the cold one.

The calibration consisted in obtaining the measurements sufficient for the statistic treatment at different sensor movement velocities by the unevenly heated stationary air. The sensor calibration time is about 2 hours. After recording all the required measurements the computer data treatment is carried out. For the further use of the obtained data the calibration results are provided as a ratio of the hot wire anemometer voltage to the flow velocity. The parameter is the air temperature.

It is very important to note that when using a measurement procedure like this, there is a thermal compensation of the readings of the hot wire anemometer by the actual temperature value. This is one of the key features of the measurement in this work.

3 ANALYSIS OF EXPEREMENTAL DATA

3.1 Profiles of average values of longitudinal velocity and temperature within the transitive region

It is commonly known that the profiles of average velocities and temperature depends a lot on the flow regime in the boundary layer. For example, based on our data, in the case of the turbulent flow regime the profiles of the longitudinal velocity component become more filled compared to such profiles in the laminar flow regime, and the exterior region of the boundary layer (i.e. the region from the maximum of the average velocity to the exterior layer boundary) is more than 90% of the total layer thickness. The thickness of the boundary layer at the unit was varied within the range 2-3 cm in the lower part of the plate (Grashof number Gr_x was about $10^5 \div 10^8$) to 20 cm in the upper part of the plate ($Gr_x \approx 10^{10} \div 10^{11}$).

First of all, the results obtained for the region of the transition of the laminar regime to the turbulent one are subject to the analysis. This region is still hardly studied, mainly because of the measuring difficulties which are due to big intermittence and intensive fluctuations. A method of the thermal compensation of the hot wire anemometer by the actual temperature used in this work does not depend on the intensity of the fluctuations. This made possible to make measurements in the transitive region.

Fig.1 and 2 show the evolution of the longitudinal velocity and temperature profiles in the boundary layer transitive region. The data are given for more convenience as dependencies of non-dimensional velocity U_S ($U_S = U/(g\beta\Delta Tx)^{1/2}$) and temperature Θ ($\Theta = (T - T_\infty)/\Delta T$) on non-dimensional coordinate η ($\eta = y \cdot Gr_x^{1/4}/x$). Where g is gravitational acceleration, β is volume expansion coefficient, $\Delta T = T_W - T_\infty$ is difference of surface temperature T_W and air temperature T_∞ beyond the boundary layer, x is longitudinal coordinate along the surface, $Gr_x = g\beta\Delta Tx^3/\nu^2$ is Grashof number. Fig.1-a and 2-a demonstrate that the average velocity and temperature profiles are very close to the laminar profiles even at Grashof numbers $3 \cdot 10^9$ - for $U_S(\eta)$ and $1.9 \cdot 10^9$ for $\Theta(\eta)$. At the same time, based on other flow characteristics, the transition processes have already started developing. Especially, the increase of the fluctuation intensity is evident. I.e. if the start of the profile characteristics change is used as a criterion of the transition start, then the transition slows down. More intensive fluctuations do not still result to the change of the average characteristics.

Fig.1-b and 2-b show the change of the velocity and temperature profiles, respectively, in the middle of the transitive region. The lines show conventionally the boundaries of this change, i.e. the profiles characteristic of the laminar and developed turbulent regions. Fig.1-c and 2-c below demonstrate the laminar and turbulent profiles in full in order to show how they change. The analysis of the experimental data represented on the figures shows that the boundary layer becomes thicker in the transitive region very fast, the velocity maximum is decreased and the slope of the temperature profile near the surface is fast increased.

The value of Grashof number corresponding to the end of the transitive region when the profiles become like for the turbulent regime turns out to be lower than the value of Grashof number determined based on other characteristics. In other words, at the beginning of the transitive region the average velocity and temperature profiles start slightly changing with significant conservatism, but coming down to the end of this region the profiles become very fast like for the developed turbulent flow regime. In this case the fluctuation characteristics are relaxed at some distance

along the plate to the constant value corresponding to the developed turbulent regime.

3.2 Region of «Buoyancy Force Layer»

In work [1] based on the theoretical analysis of the free convection boundary layer equations the following supposition was made: there is a specific region named by the authors as «Buoyancy Force Layer». Using the expertimental data [2] the authors obtained the empirical dependencies for the average velocity and temperature in this region. Unfortunately there are only a few works which paid their attention to the Buoyancy Force Layer.

In the present work the systematic study of the average velocity and temperature profiles was made in the purpose to determine the buoyancy force layer and its boundaries as well as to get more accurate empirical coefficient values in velocity and temperature dependencies. A region where the below dependence is correct is hereinafter called as «heat buoyancy force layer»:

$$\Theta = A_T + B_T \cdot \left(y/\eta_{in}\right)^{-1/3}$$
$$\text{at} \qquad h_{T1} \le y \le h_{T2}\ , \qquad (1)$$

A region where the below dependence is correct is hereinafter called as "dynamic buoyancy force layer»:

$$U/U_{in} = A_U + B_U \cdot \left(y/\eta_{in}\right)^{1/3}$$
$$\text{at} \qquad h_{U1} \le y \le h_{U2}\ . \qquad (2)$$

Where: h_{T1}, h_{T2} and h_{U1}, h_{U2} are the boundaries of these two regions, respectively, $U_{in} = (g\beta\Delta Ta)^{1/3}$ and $\eta_{in} = (g\beta\Delta Ta^{-2})^{-1/3}$ are the scales of the velocity and length, where a is a kinematics heat conductivity coefficient.

As a result of the treatment of the experimental velocity and temperature profiles according to the dependencies (1) и (2) the boundaries of the heat and dynamic layers of buoyancy force and empirical coefficients of these dependencies were determined. Fig.3 shows the dependence of coefficients A_T and B_T on Grashof number. It is evident from the figure that these values have almost constant values ($A_T \approx -0.24$, $B_T \approx 1.25$) along all the turbulent region and neighboring transitive region ($Gr_x = 7 \cdot 10^9 \div 5 \cdot 10^{11}$). Unfortunately there are almost no literature data on the values of the coefficients A_T and B_T. However, these values were determined in the works [1] ($A_T = -0.35$, $B_T = 1.45$) and [3] (-0.36 and 1.42, respectively). In order to get more rich comparison data basis in the present work the proper treatment of the temperature profiles obtained in [4,5] was made, the coefficients of dependence (1) were determined. The obtained results as well as the data of [1,3], are demonstrated on Fig.3.

The average longitudinal velocity profiles were analyzed and the values of the coefficients A_U and B_U were determined the same way. The dependence of these coefficients on Grashof number is shown on Fig.4. This figure also shows the only one value of these coefficients given in literature (-9.3 and 12.3, respectively) obtained in [1]. This figure also notes the results of the study of the velocity profiles measured in [4,5-7]. It is interesting to note that the region of the linear dependence of the velocity on the value $\left(y/\eta_{in}\right)^{1/3}$ may be found also in the transitive region and even in the laminar flow region (see Fig.4) that is not correct for the same region for the case of the temperature profile. This raises some doubts in how the dynamic buoyancy force layer is peculiar of the free convection flow. Therefore, this is matter of interest to determine the boundaries of the buoyancy force layer and, as a result, of its role in the structure of the free convection boundary layer.

The analysis of the obtained results show that the boundaries of the heat and dynamic layers of buoyancy force do not coincide: the dynamic layer is very thin. It is about at 0.4 - 2.5 mm from the wall. The heat layer is significantly thicker and located farther from the wall (from 2.0 mm to 12.0 mm). If taking into account that the coordinate of the average velocity maximum at the turbulent flow regime is 8 - 9 mm, then the heat layer of buoyancy force covers fully the maximum velocity region.

Fig.5 shows the coordinates of the boundaries of heat viscous sublayer (δ_T) and buoyancy force layer (h_{T1} and h_{T2}) depending on the distance x along with the plate. Fig.6 shows the coordinates of the boundaries of dynamic buoyancy force layer (h_{U1} and h_{U2}) and dynamic viscous sublayer (δ_U). It is evident from Fig.5 that while the turbulent regime is developed, the heat layer of buoyancy force starts being formed near the heat viscous sublayer. Actually there is no buffer zone between these two layers. Fig.6 shows absolutely another situation: viscous sublayer completely laps **a** very thin dynamic layer of buoyancy force. In this case the flow regime does not influence very much the boundaries of the buoyancy force layer. Apparently, the following conclusion can be made: the dynamic layer of buoyancy force does not play any important role in the structure of the free convection boundary layer. On the contrary, the heat layer of buoyancy force is the definite region peculiar just to the turbulent flow regime. This layer is located just above the heat viscous sublayer and covers the region of the maximum average velocity. Its boundaries are constant at the turbulent flow regime. The dependence of the

temperature on the transversal coordinate in the heat layer of buoyancy force for the Grashof number values $Gr_x = 7 \cdot 10^9 \div 5 \cdot 10^{11}$ can be described with the following empirical dependence:

$$\Theta = 1.25 \cdot \left(y/\eta_{in}\right)^{-1/3} - 0.24$$

$$\text{at} \qquad 0.40 \le \left(y/\eta_{in}\right)^{-1/3} \le 0.74. \qquad (3)$$

3.3 Profiles of velocity and temperature component fluctuations

When studying the velocity and temperature component fluctuation in free convection flows first of all the following factor attracts attention: the fluctuation intensity in such a kind of flows is very high. The intensity of temperature fluctuations $I_T = (\overline{t^2})^{1/2}/\Delta T$ in the developed turbulent flow region may achieve about $0.14 \div 0.18$, and the intensity of longitudinal velocity fluctuations $I_U = (\overline{u^2})^{1/2}/U_m$ is from 0.20 to 0.30 and based on some data (for example, [8]) it even achieves 0.40. Obviously, the process of the fluctuation characteristics measurement in such a kind of flows is very difficult. Some special methods of measurements are required. As above noted, the method of thermal compensation by actual temperature used in this work limits neither non-isothermal degree nor fluctuation intensity. Using this method the measurements of the fluctuation velocity and temperature components in the transitive and turbulent flow regions were made.

Fig.7 shows the distribution of the temperature fluctuation intensity compared to the results of various works. The agreement of the data of this work and other works should be noted. The intensity I_T reaches its maximum value at the point $\zeta \approx 0.7$ ($\zeta = y \cdot Nu_x/x$). The dimensional value of this coordinate is 4 mm from the wall. There is some difference only in data of this work and [6], where a thermocouple was used to measure temperature.

This situation with the velocity fluctuation measurements is far different. Fig.8 represents the distribution of the value I_U. Fig.9 shows the intensity of the fluctuation of normal velocity component $I_V = (\overline{v^2})^{1/2}/U_m$ compared to the data of other works. The significant difference in the results of present work and the most part of other works is obvious. This difference is not only in quantity but also in quantity.

Based on our data the maximum of the velocity fluctuations in the turbulent region is recorded near the wall - between the boundary of the viscous sublayer and the coordinate of the average velocity maximum. The coordinate of the maximum velocity fluctuation intensity is $\zeta \approx 0.8 \div 0.9$. The dimensional value of this coordinate is about 5 mm from the surface. This point is a little bit farther from the wall than the coordinate of maximum I_T. Such a location of the region of maximum values I_U and I_V, to our opinion, does not contradict with physical property of flow. In fact, near the wall the gradient of the average temperature is high, and, as a result, the buoyancy force is also high. At the same time the gradient of the average velocity is also high due to the inhibiting effect of the wall on the flow in this region. Therefore, it seems to be reasonable that the maximum generation of the turbulence occurs near the boundary of the viscous sublayer in the region of high velocity and temperature gradients. However, Fig.8,9 demonstrate that based on the data of the most authors the fluctuation maximum is, on the contrary, in the external region where the velocity and temperature fluctuations are considerably lower. It should be noted that in this region on the plots built by the data of present work there is some plateau. Naturally, in the external part of the boundary layer the flow slows down when contacting with the external motionless air. But it is still an open question why many authors show the fluctuation maximum exactly at this point and not in the internal region of the boundary layer.

To our opinion, the analysis of such results shall take into account the features of the velocity measurement methods used by various authors. In particular, the results of [4] are obtained with the use of hot wire anemometer with analogous thermal compensation. In this case some errors which always take place, when any model is used to describe the heat exchange between the anemometer hot wire and air, may result in errors in thermal compensation. This will inevitably influence the result of the velocity measurement. Data [6-7,9] are obtained with the use of **LDV.** This method is known to have a lot of disadvantages in measuring in the region of high velocity and temperature gradients. It should be noted that the results which are in quality close to our data are obtained in [2], where the hot wire anemometer was used to measure the velocity. In [2] the signal treatment was made in digital form. For the present work the discrete signal treatment was applied: all the frequencies existing in the flow are recorded without distortion. This discrete signal treatment in addition to the thermal compensation by the actual temperature are the key reasons of the difference in the near wall results.

The results of the measurement of the intensity profiles of longitudinal velocity $I_U(y)$ and temperature $I_T(y)$ component fluctuation in the transitive region of the boundary layer are shown on Fig.10,11. These figures show that at the beginning of the transitive region the intensity profiles have two maximums: the one is near the external boundary of the

viscous sublayer and the other one is in the average velocity maximum zone. Then, while downstream the boundary later is developed, two maximums becomes one big maximum, and the profiles of fluctuation intensity $I_U(y)$ и $I_T(y)$ becomes like for the turbulent regime. Unfortunately the available literature provides only two references about the work when the similar measurements in the transitive region were made. In work [8] when measuring in air the authors also noted the formation of two maximums on the profile $I_U(y)$ in the transitive region. The authors of [10] remarked the similar phenomena when making the experiments in water. However, the information in [8,10] is not sufficient to make any conclusions on the location of these maximum with regard to the boundary layer regions.

In present work the measurements of the turbulent shear stress $\tau_{xy} = -\rho\overline{uv}$ and two components of the turbulent heat flux vector ($q_x = -\rho c_p \overline{ut}$ и $q_y = -\rho c_p \overline{vt}$) were made. Fig.12 represents the results of the measurements of the longitudinal turbulent heat flux q_x. For the comparison with the experimental results of other authors the data of present work are given as a correlation coefficient $R_{UT} = \overline{ut}/(\overline{u^2 t^2})^{1/2}$ (as the most results available in the literature are presented in such a form) and as a correlation $\overline{ut}$ referred to the constant scale. This figure and all the other figures show by the abscissa the maximum values of the fluctuation intensity of the temperature I_{Tm} and the longitudinal velocity I_{Um} as well as the maximum value of the average velocity value U_m in this section of the boundary layer. The analysis of the data given on Fig.12 shows good agreement of the data of this work with the one of most works.

The turbulent shear stress profiles τ_{xy} measured in present work are shown on Fig.13 along with the data available in the literature. It should be noted that the results of the present work are similar to the ones of most authors. However, there is a significant difference near the wall. This is caused by the same reasons which are mentioned above referred to the analysis of the flow fluctuation characteristics. The plots show very well that the coordinate of the average velocity maximum is much closer to the wall than the coordinate where the turbulent shear stress becomes equal to 0.

The shear stress τ_{xy} depends on the sign of the derivative of the average velocity by the normal coordinate ($\tau_{xy} \propto \partial U/\partial y$). Hence, in the free convection boundary layer the sign of the turbulent shear stress shall change. The experimental data of present work and the results of the works [9,11] are not in conflict with the said factor. On the contrary, the data [5] under which the turbulent shear stress is always negative, are doubtful. Apparently, the reason of the difference in results of [5] and most data in the near wall region is that the authors of [5] used analogous thermal compensation of hot wire anemometer signal. The data of work [12] seems to be also questionable: under these data. The Reynolds stress is positive along all the thickness of the turbulent boundary layer. It should be noted that the velocity component V which is normal to the surface was not measured in [12] but calculated.

Fig.14 demonstrates the distribution of the transversal turbulent heat flow q_y compared to the results of other works. In the near wall region the results of present work are much differed not only in quantity but also in quality from the results of other authors.

This work is conducted thanks to the financially assistance by the Russian Funds of the Fundamental Research Study (project: 96-02-19461).

REFERENCES

1. George W.K., Capp S.P. A theory for natural convection boundary layer next to heated vertical surfaces, Int. J. Heat Mass Transfer, 1979, V.22, N 6, p.813-826.

2. Smith R.R. Characteristics of turbulence in free convection flow past a vertical plate, Ph.D. Thesis, Queen Mary College, Univ. of London, 1972.

3. Siebers D.L., Maffat R.F., Schwind R.G. Experimental, Variable Properties Natural Convection From a Large, Vertical Flat Surface, J. Heat Transfer, 1985, v. 107, N 1.

4. Tsuji T., Nagano Y. Caracteristics of a turbulent natural convection boundary layer along a vertical flat plate, Int. J. Heat Mass Transfer, 1988, V.31, N 8, p.1723-1734.

5. Tsuji T., Nagano Y. Turbulence measurements in a natural convection boundary layer along a vertical flat plate, Int. J. Heat Mass Transfer, 1988, V.31, N 10, p.2101-2111.

6. Miyamoto M., Okayama M. An experimental study of turbulent free convection boundary layer in air along a vertical plate using LDV, Bull. JSME, 1982, V.25, N 209, p.1729-1736.

7. Cheesewright R., Ierokipiotis E.G. Velocity measurements in a natural convection boundary layer, Proc. 7th Int. Heat Transfer Conf., Munich, FRG, 1982, V.2, NC31, p.305-309.

8. Miyamoto M., Katoh Y., Kurima J., Taguchi Y. Characteristics of free-convection boundary layer in

transition region along vertical plate, Trans. JSME, Ser.B, 1994, V.60, N 571, p.971-976.
9. Miyamoto M., Kajino H., Kurima J., Takanami I. Development of turbulence characteristics in a vertical free convection boundary layer, Proc. 7th Int. Heat Transfer Conf., Munich, FRG, 1982, V.2, NC31, p.323-328.
10. Jaluria Y., Gebhart B. On transition mechanisms in vertical natural convection flow, J. Fluid Mech., 1974, V.66, N 2, p.309-337.
12. Hishida M., Nagano Y., Tsuji T., Kaneko I. Turbulent boundary layer of natural convection along a vertical flat plate, Trans. JSME, Ser.B, 1981, V.47, N 419, p.1260-1268.
12. Doan K.S., Coutanceau J. Structure d'un ecoulement de convection naturelle-transition et turbulence etablie, Acta Astronautica, 1981, V.8, p.123-160.
13. Griffiths E., Davis A.H. The transmission of heat by radiation and convection, British Food Investigations Board, Dept. Sci. and Ind. Res., London, 1922, Spec. Rept. N 9, 18p.
14. Cheesewright R., Natural Turbulent Convection Along Vertical Plate. J. Heat Transfer, 1968, v. 90, N 1.
15. Hoogendoorn C.J., Euser H. Velocity profiles in turbulent free convection boundary layers, Proc. 6th Int. Heat Transfer Conf., Toronto, 1978, V.2, p.193-198.
16. Cheesewright R., Mirzai M.H. The correlation of experimental velocity and temperature data for a turbulent natural convection boundary layer, Proc. 2nd U.K. National Conf. Heat Transfer, Glasgow, 1988, C140/88, p.79-89.

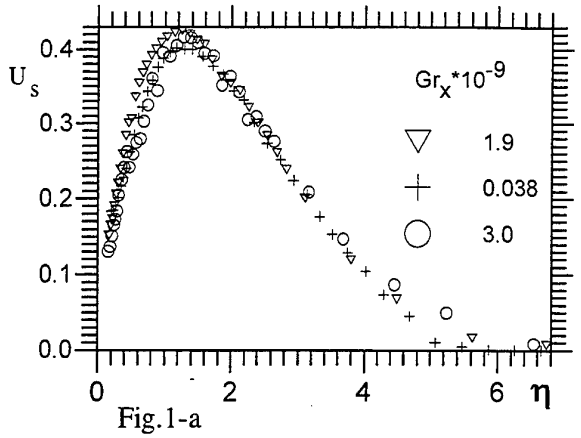

Fig.1-a

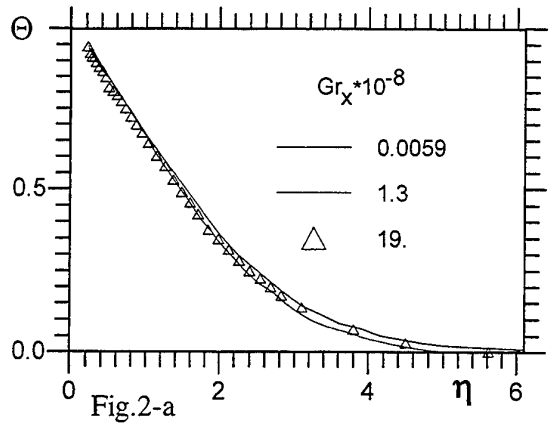

Fig.2-a

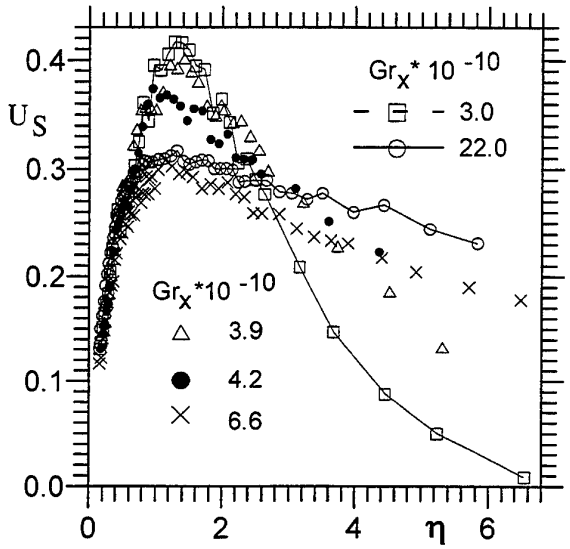

Fig.1-b

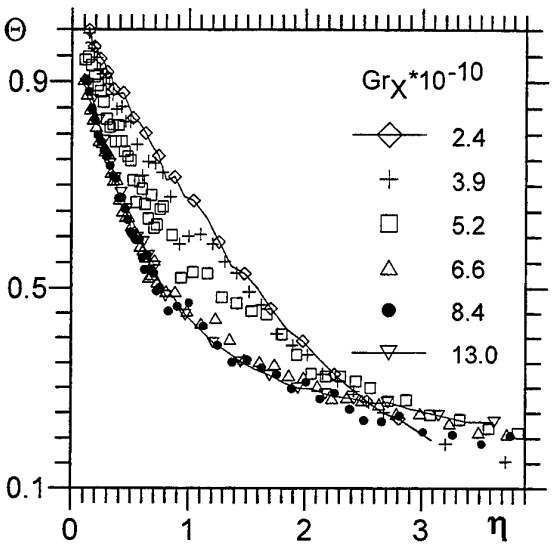

Fig.2-b

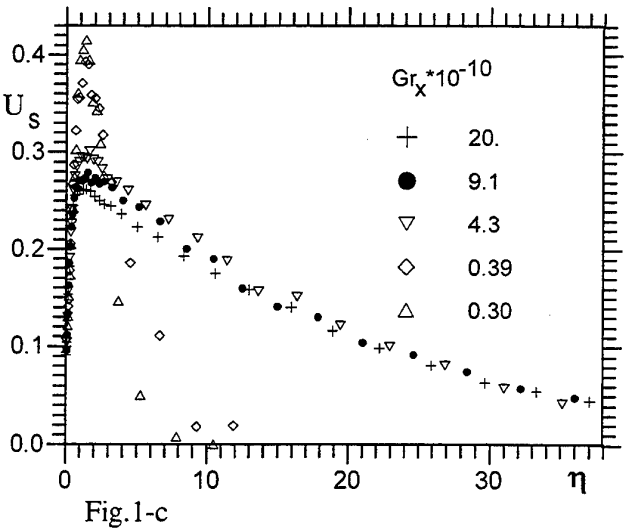

Fig.1-c

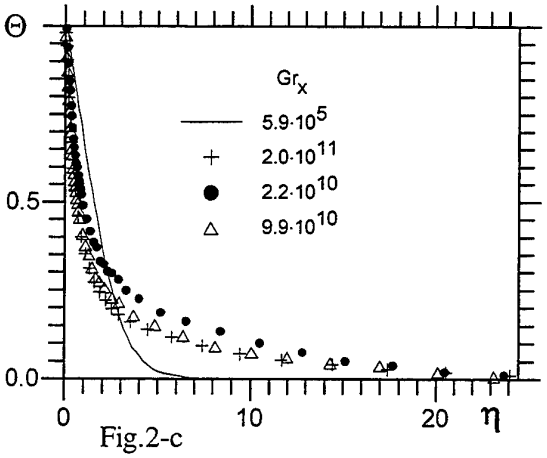

Fig.2-c

Figure 1

Figure 2

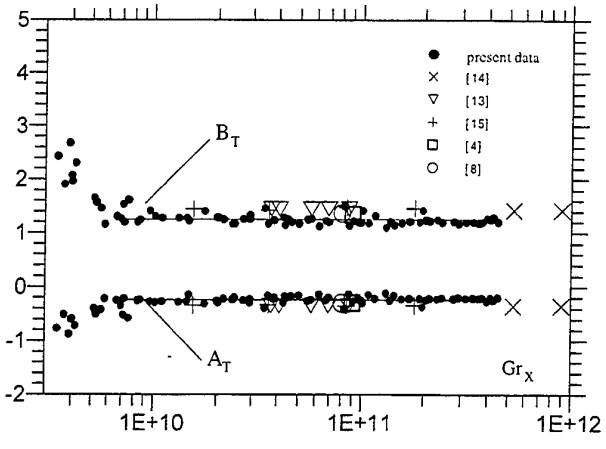

Figure 3

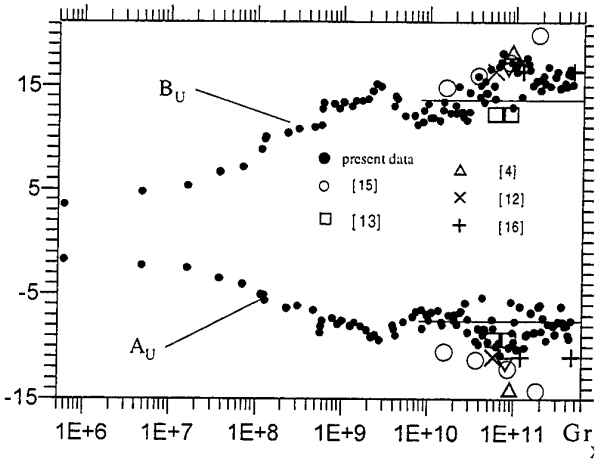

Figure 4

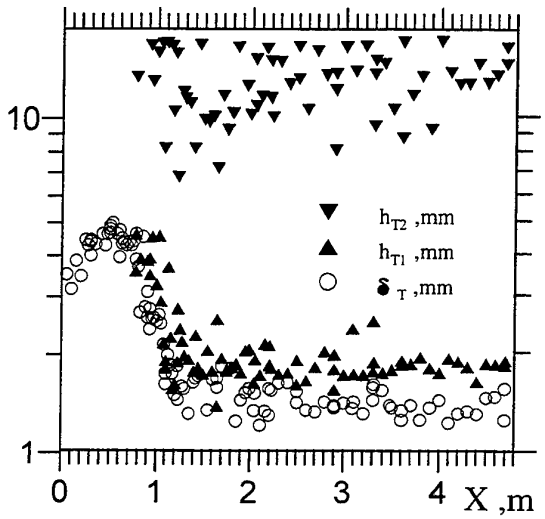

Figure 5

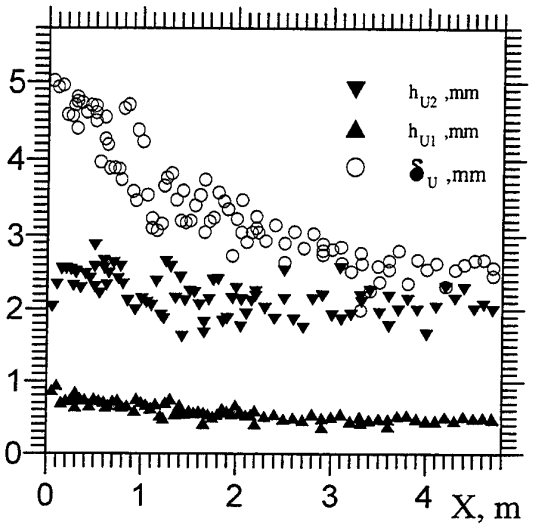

Figure 6

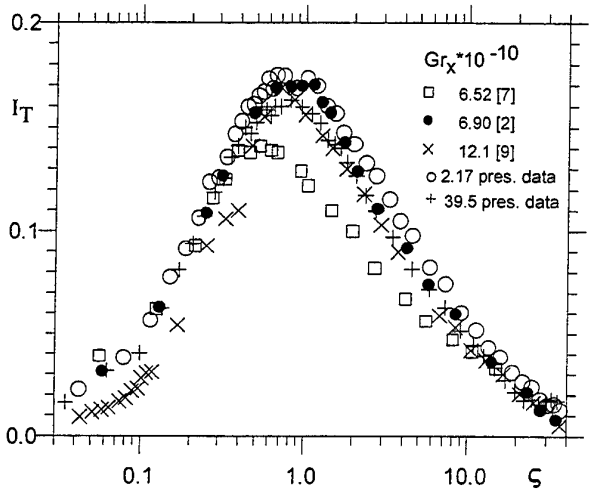

Figure 7

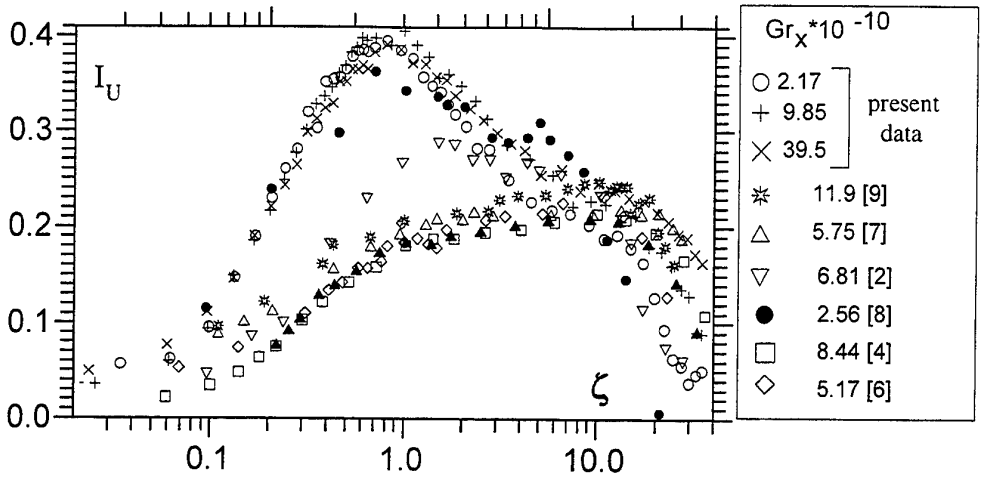

Figure 8

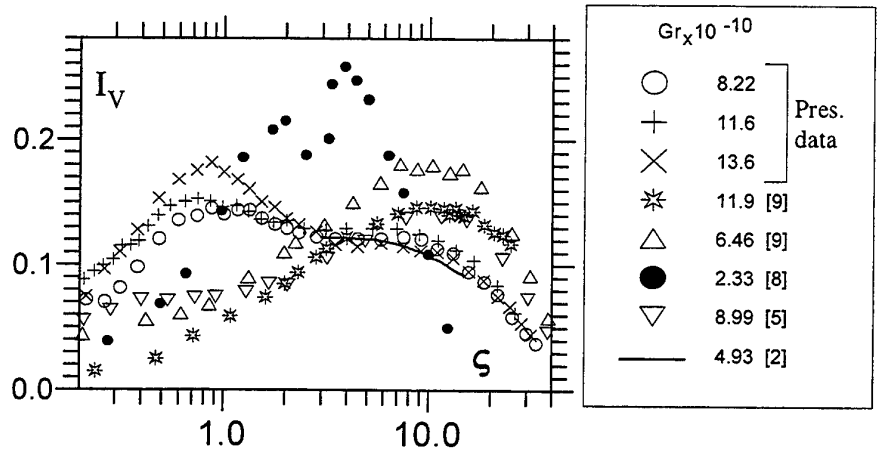

Figure 9

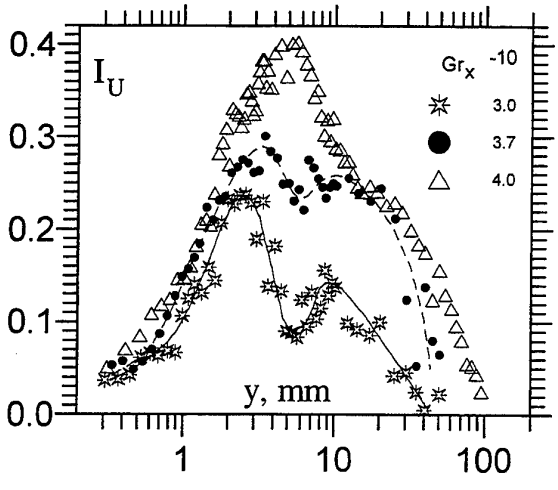

Figure 10

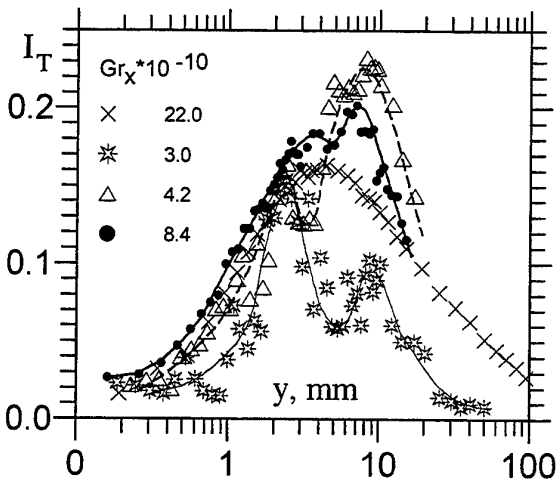

Figure 11

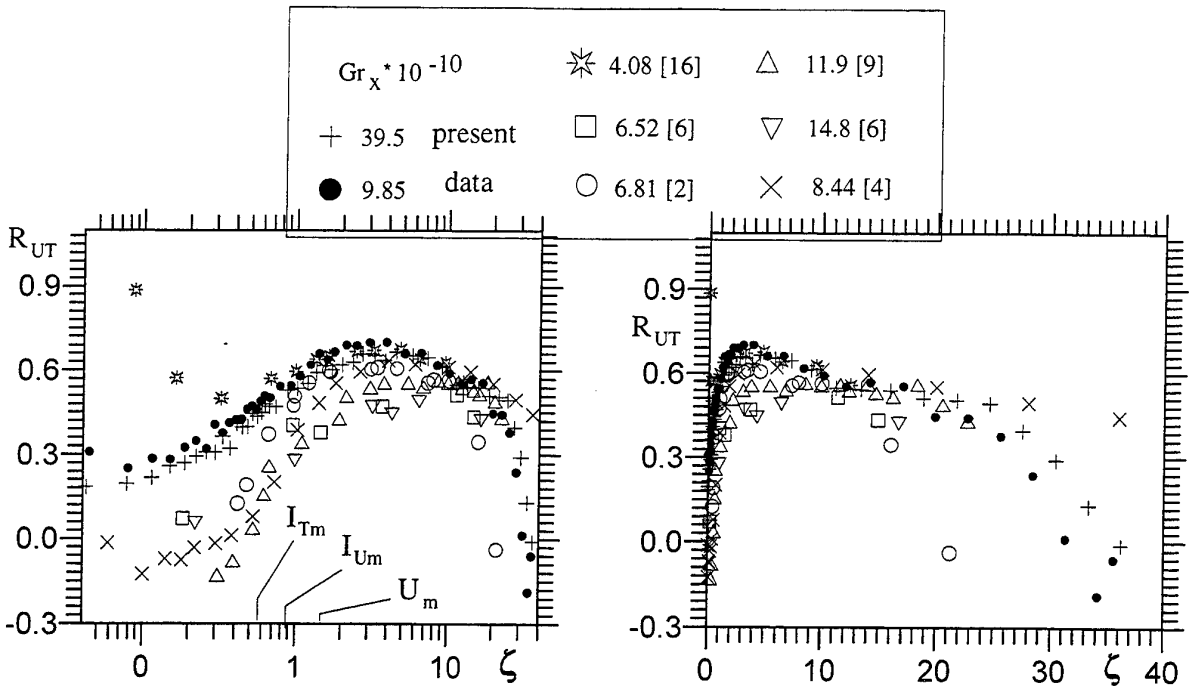

Figure 12

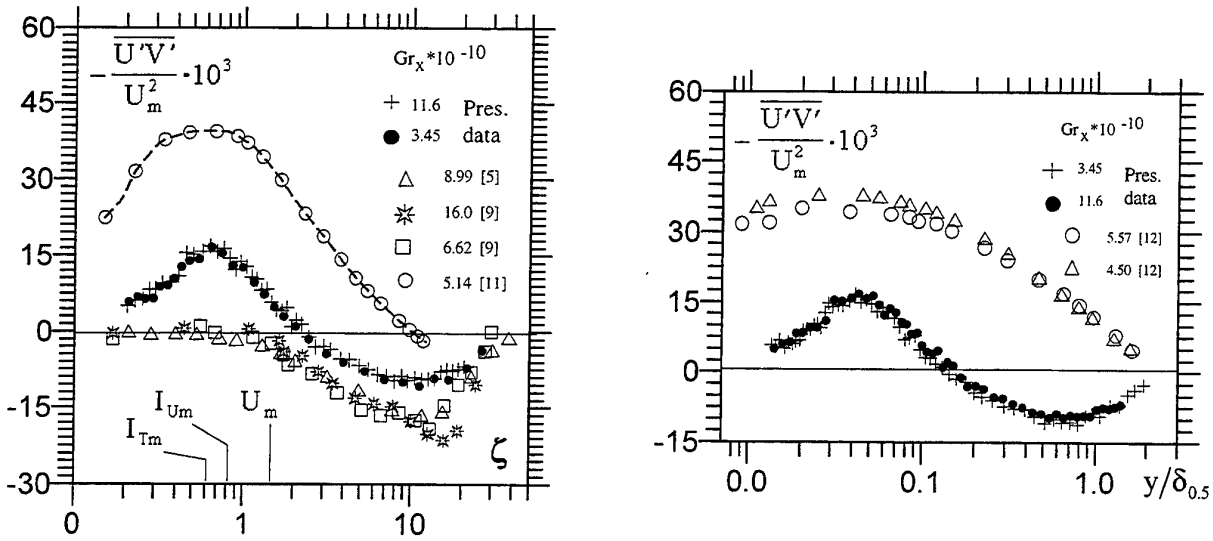

Figure 13

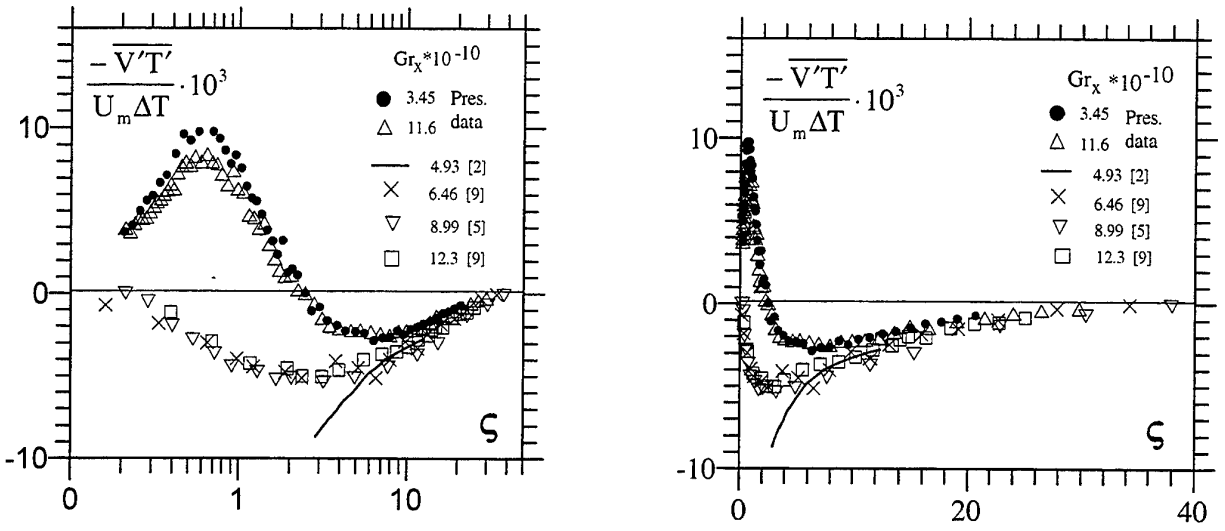
$\frac{-\overline{V'T'}}{U_m \Delta T} \cdot 10^3$
$Gr_x * 10^{-10}$
3.45 Pres.
11.6 data
4.93 [2]
6.46 [9]
8.99 [5]
12.3 [9]
ς
10
0
-10
0
1
10
20
40

Figure 14

VARIABLE PROPERTY MIXED CONVECTION : LOW-REYNOLDS-NUMBER AND STRAIN PARAMETER EDDY VISCOSITY MODEL RESULTS

M.A. Cotton, J.O. Ismael[1] and P.J. Kirwin[2]

School of Engineering
University of Manchester
Manchester M13 9PL
U.K.

ABSTRACT

Turbulent flow in vertical heated pipes may be strongly modified from the forced convection condition by the action of buoyancy. Such 'mixed convection' flows may be complicated further as a consequence of other effects due to the temperature dependence of fluid properties. In the investigation reported here comparisons are made between experimental data and two eddy viscosity models : the well-established k-ϵ model of Launder and Sharma (1) and the recent 'strain parameter' (or k-ϵ-S) model of Cotton and Ismael (2).

1 MIXED CONVECTION AND VARIABLE PROPERTY INFLUENCES

The heat transfer regime of turbulent mixed convection arises where a forced flow is significantly affected by buoyancy forces. Consideration is given here to flow in a heated vertical passage. In such a configuration buoyancy forces cause changes to the shear stress and velocity profiles in the region of the heated surface, thereby also altering the turbulence production and diffusion processes of the flow. Heat transfer characteristics are in consequence different from those of a forced convection flow at the same Reynolds and Prandtl numbers. In ascending flow it is found that heat transfer effectiveness, quantified in terms of Nusselt number, may be either impaired with respect to forced convection values (at lower levels of buoyancy influence) or enhanced (at higher levels of buoyancy influence). The maximum impairment condition corresponds to a situation where partial laminarization of the flow has occurred. (Heat transfer effectiveness in descending flow is enhanced through the regime.) Experimental, analytical, and computational studies of turbulent mixed convection are discussed in the monograph of Petukhov and Polyakov (3) and the review paper of Jackson et al. (4).

A dimensionless group known as the 'buoyancy parameter', Bo, is used here to characterize the extent of buoyancy influence. The buoyancy parameter was developed in the semi-empirical analysis of Hall and Jackson (5) and is written here in the form quoted by Jackson et al. (4):

$$Bo = 8 \times 10^4 \frac{Gr}{Re^{3.425} Pr^{0.8}} \qquad (1)$$

Variable property effects other than those associated with buoyancy become significant where the temperature variations in a flow are large. An appropriate dimensionless measure of axial temperature variation is provided by the 'heat loading parameter', q^+:

$$q^+ = \frac{\dot{q}}{\rho U_b c_p \theta_b} = \frac{D}{4\theta_b} \frac{d\theta_b}{dx} \qquad (2)$$

A marked axial variation of temperature will produce significant bulk acceleration of the flow and attendant influences on turbulence. A second variable property effect arises in consequence of the radial variation of temperature. An increase in kinematic viscosity with temperature in an air flow will act to reduce local turbulent Reynolds number and hence the diffusivity of the flow. This effect is particularly important in wall regions where turbulent Reynolds number is low and temperature high. Rearrangement of the definitions of Nusselt number and q^+ yields

$$\frac{\theta_w - \theta_b}{\theta_b} = \frac{RePr}{Nu} q^+ \qquad (3)$$

Now, in the absence of effects due to mixed convention and axial property variation discussed above, $Nu \sim Re^{0.8}$ in a thermally fully-developed region. Hence,

---

(1) Present address: Department of Manufacturing and Engineering Systems, Brunel University, Uxbridge UB8 3PH, U.K.

(2) Present address: Perkins Technology Ltd., Peterborough PE1 5NA, U.K.

neglecting a relatively weak Reynolds number dependence, Equation (3) indicates that q^+ may also serve as a measure of normalized wall-to-bulk temperature variation.

In the present work comparison is made with experimental data for ascending air flows in vertical pipes. Figures 1 and 2 are in the form of 'maps' showing the range of buoyancy influence and heat loading encompassed by the datasets of Carr et al. (6), Steiner (7), Polyakov and Shindin (8), Shehata and McEligot (9), and Vilemas et al. (10). Ten individual sets of data for Nusselt number development have been selected here from the measurements of Steiner (S1 to S4), Shehata and McEligot (SM1 to SM3), and Vilemas et al. (VPK12, VPK11, and VPK10). Table 1 details the values of Bo and q^+ prevailing at the start of heating in these cases. The values of heat loading parameter are relatively low in Steiner's data (i.e. low only in relation to the data selected from References (9) and (10)). At higher values of q^+, it is seen that the data of Shehata and McEligot and of Vilemas et al. are arranged in Table 1 to give a monotonic increase in Bo. For purposes of comparison with the results below, the final column of Table 1 gives approximate values of Nusselt number for fully-developed, constant property forced convection heat transfer as estimated from the equation $Nu_o = 0.022\ Re^{0.8}\ Pr^{0.5}$ (Kays and Leung (11)). The data are discussed further in § 4, and more detailed accounts of the conditions of the individual experimental runs may be found in the original works and the summary tables of Kirwin (12).

2 AN OUTLINE OF THE STRAIN PARAMETER MODEL

2.1 High-Reynolds-number approaches

Conventional high-Reynolds-number k-ϵ models determine the Reynolds shear stress in a flow with a principal strain rate $\partial U/\partial y$ as

$$-\overline{uv} = C_\mu \frac{k^2}{\epsilon} \frac{\partial U}{\partial y} \qquad (4)$$

Equation (4) viewed in 'structural' terms advances a linear relationship between $-\overline{uv}/k$ and $(k/\epsilon)\ \partial U/\partial y$, the latter expression representing the product of the local strain rate and the local large-scale turbulence timescale. Dimensional analysis shows only that $-\overline{uv}/k = F[(k/\epsilon)\ \partial U/\partial y]$ and therefore, still working in *high*-Reynolds-number terms (i.e. disregarding viscous effects), a damping function may introduced to Equation (4):

$$-\overline{uv} = C_\mu\ f\left[\frac{k}{\epsilon}\frac{\partial U}{\partial y}\right] \frac{k^2}{\epsilon}\frac{\partial U}{\partial y} \qquad (5)$$

The importance of $(k/\epsilon)\ \partial U/\partial y$ in characterizing near-wall turbulence has been established by Lee et al. (13).

It is seen below that the group also arises as a limit that results from a more general approach which seeks to provide a representation of the strain history of a flow.

2.2 Effective total strain concepts

Under conditions of high strain rate, or short periods of straining, the instantaneous Navier-Stokes equations may be linearized and thus reduced to the formal approximation known as 'Rapid Distortion Theory' (RDT), see for example Hunt and Carruthers (14). A result of RDT applied to homogeneous flows with strain rate $\partial U/\partial y$ is that the ensemble-averaged structural ratio $-\overline{uv}/k$ at time t depends upon total strain, $\alpha(t)$:

$$\alpha(t) = \int_0^t \frac{\partial U}{\partial y}(\tau)\ d\tau \qquad (6)$$

Maxey (15) sought to extend the concept of total strain to have utility beyond RDT conditions : in order to do this, however, account must be taken of the finite eddy timescale, or 'lifetime', which is of order k/ϵ. The approach adopted by Maxey was to introduce an ad hoc equation for α :

$$\frac{\partial \alpha}{\partial t} = \frac{\partial U}{\partial y} - \frac{\alpha}{T_D} \qquad (7)$$

where T_D is a large-scale turbulence timescale (associated below with k/ϵ). α determined as the solution of Equation (7) becomes an *effective* total strain, recovering Equation (6) where RDT is applicable, and asymptoting to $T_D.\partial U/\partial y$ under slowly changing conditions. Thus $T_D.\partial U/\partial y$, or $(k/\epsilon)\partial U/\partial y$, may now be viewed as the total strain truncated on eddy lifetime.

The present modelling approach, which is based upon the work of Maxey (15) and the earlier study of Townsend (16), adopts a 'strain parameter', S, as the subject of a third scalar transport equation (complementing the conventional k- and ϵ-equations). In application to an inhomogeneous flow in simple shear the S-equation reads

$$\frac{DS}{Dt} = \frac{k}{\epsilon}\left[\frac{\partial U}{\partial y}\right]^2 + \frac{\partial}{\partial y}\left[\frac{\nu_t}{\sigma_s}\frac{\partial S}{\partial y}\right] - \frac{S}{(k/\epsilon)} \qquad (8)$$

Now, material fluid elements arriving at a given point by different paths will experience different strain histories. Thus, following Townsend (16), the diffusive term of Equation (8) is included on the basis that "qualitatively, the variations of path affect the mean total strain in much the same way as an eddy diffusivity of the mean total or the effective strain". Lumley et al. (17) advance an equation for inverse timescale (or strain rate) with features similar to those of Equation (8). In their Figures 2.4.1 and 2.4.2 they provide a graphic illustration of the properties of such equations by which a point "is influenced by an integral back along the mean streamline through the point, with a spreading zone of influence and a fading memory".

S determined as the solution of Equation (8), or alternatively as the solution of Equation (18) in the present set of calculations, acts to modify the model constitutive equation via its action as the independent variable of the principal damping function, cf. Equation (5) and Equation (12). A fuller discussion of different effective total strain approaches and the present k-ϵ-S strain parameter model is provided by Cotton and Ismael (2). The reader might also be interested in the notion of effective total strain modelling as developed by Mankbadi and Liu (18).

3 MEAN FLOW AND TURBULENCE MODEL EQUATIONS

3.1 Mean flow equations

The flow is taken to be axi-symmetric and swirl-free, and the thin shear approximations are applied. The mean flow equations of continuity, momentum, and energy are written below in cylindrical polar coordinates:

$$\frac{1}{r}\frac{\partial}{\partial r}(\rho r V) + \frac{\partial(\rho U)}{\partial x} = 0 \qquad (9)$$

$$\frac{1}{r}\frac{\partial}{\partial r}(\rho r UV)+\frac{\partial}{\partial x}(\rho U^2)=-\frac{dp}{dx}+\frac{1}{r}\frac{\partial}{\partial r}\left[r\left[\mu\frac{\partial U}{\partial r}-\rho\overline{uv}\right]\right]-\rho g \qquad (10)$$

$$\frac{1}{r}\frac{\partial}{\partial r}(\rho r Vh)+\frac{\partial}{\partial x}(\rho Uh)=\frac{1}{r}\frac{\partial}{\partial r}\left[r\left[\frac{\lambda}{c_p}\frac{\partial h}{\partial r}-\rho\overline{vh}\right]\right] \qquad (11)$$

3.2 Turbulence model equations

Equation (4), with $\partial U/\partial y$ replaced by $\partial U/\partial r$, gives the basic high-Reynolds-number form of the constitutive equation applicable to the present problem.

A variety of low-Reynolds-number modifications of the basic scheme introduce a viscous damping term to the right of Equation (4). The first of these was proposed by Jones and Launder (19) and incorporated a damping function $f_\mu(Re_t)$. A variant of that scheme advanced by Launder and Sharma (1) has been widely applied and is adopted here as a 'benchmark' against which the k-ϵ-S model is examined. The large number of alternative k-ϵ schemes which achieve damping through the use of viscosity-dependent functions has provided the stimulus for several comparative studies of these models : an early work by Patel et al. (20) examined the application of two-equation models to various boundary layer flows, and Cotton and Kirwin (21) and Jackson and Mikielewicz (22) have more recently focused on mixed convection applications. The latter two works found the Launder and Sharma model to be superior to other models tested, and this is also (the rather more general) picture to emerge from the results of other comparative studies. A fundamental reason for the relative success of the Launder and Sharma model by comparison with other two-equation closures is that the scheme avoids any reference to *non-local* parameters, i.e. groups involving wall distance. (Nonetheless, details of model tuning also play a role: for example, Jackson and Mikielewicz found the Launder and Sharma model to be more accurate than the Jones and Launder model which differs only in the prescription of the damping function and the values of $C_{\epsilon 1}$ and $C_{\epsilon 2}$, Equation (16).)

An even more fundamental question, and the one that originally prompted the present developments, concerns the true role of viscosity as an agent responsible for 'damping'. The issues raised in § 2.1, and the modelling concepts discussed in § 2.2 do not involve viscosity; it remains the case, however, that as a wall is approached and $Re_t \rightarrow 0$, account must be taken of the viscous properties of a turbulent flow. The present approach is, in fact, a combined strain parameter/low-Reynolds-number strategy, although effective reduction of C_μ is achieved <u>not</u> primarily by a viscosity-dependent variable (except at extremely low Re_t), but instead by the use of a damping function $f_s(S)$, where S is the strain parameter introduced in § 2.2. The extent to which viscous damping is relegated to secondary importance may be judged from Equation (14a) which gives $f_\mu = 0.9$ at $Re_t = 50$, corresponding to $y^+ < 10$ in an isothermal wall-bounded flow. The tuning of the constants and functions of the present model was undertaken primarily by reference to Direct Numerical Simulation data for isothermal channel flows (see Reference (2)); to a lesser degree account was also taken of data for mixed convection flows.

Some further discussion of the detailed features of the Launder and Sharma and present models may be found in Cotton and Ismael (2). In this paper, however, we now proceed to state the full equations of both models as applied to the flows under consideration. Thus, the constitutive and k- and $\tilde{\epsilon}$-equations for the Launder and Sharma (hereafter 'LS') and present

models, and the function f_S and the S-equation (for the present model only) read as follows:

$$-\rho\overline{uv} = \mu_t \frac{\partial U}{\partial r} \; ; \quad -\rho\overline{vh'} = \frac{\lambda_t}{c_p}\frac{\partial h}{\partial r}; \qquad \mu_t = C_\mu f_s(S) f_\mu(Re_t) \frac{\rho k^2}{\tilde{\epsilon}} \tag{12}$$

where

$$f_s = \frac{2.88}{1+0.165S}\left(1 - 0.55 \exp\left[-(0.135S + 0.0015S^3)\right]\right) \tag{13}$$

$$f_\mu = 1 - 0.3 \exp\left[-0.02Re_t\right] \quad \text{(14a - present model)}$$

$$f_\mu = \exp\left[\frac{-3.4}{(1 + Re_t/50)^2}\right] \quad \text{(14b - LS)}$$

$$\frac{D(\rho k)}{Dt} = \mu_t\left[\frac{\partial U}{\partial r}\right]^2 + \frac{1}{r}\frac{\partial}{\partial r}\left[r\left[\mu + \frac{\mu_t}{\sigma_k}\right]\frac{\partial k}{\partial r}\right] - \rho\epsilon \tag{15}$$

$$\frac{D(\rho\tilde{\epsilon})}{Dt} = C_{\epsilon 1}\frac{\tilde{\epsilon}}{k}\mu_t\left[\frac{\partial U}{\partial r}\right]^2 + \frac{1}{r}\frac{\partial}{\partial r}\left[r\left[\mu + \frac{\mu_t}{\sigma_\epsilon}\right]\frac{\partial \tilde{\epsilon}}{\partial r}\right] - C_{\epsilon 2} f_2 \rho \frac{\tilde{\epsilon}^2}{k} + C_{\epsilon 3}\frac{\mu\mu_t}{\rho}\left[\frac{\partial^2 U}{\partial r^2}\right]^2 \tag{16}$$

where

$$f_2 = 1.0 \quad \text{(17a - present model)}$$

$$f_2 = 1 - 0.3 \exp(-Re_t^2) \quad \text{(17b - LS)}$$

$$\frac{D(\rho S)}{Dt} = \frac{\rho k}{\tilde{\epsilon}}\left[\frac{\partial U}{\partial r}\right]^2 + \frac{1}{r}\frac{\partial}{\partial r}\left[\frac{r\mu_t}{\sigma_s}\frac{\partial S}{\partial r}\right] - \frac{\rho S}{(k/\tilde{\epsilon})} \tag{18}$$

Turbulent Prandtl number, σ_t is set to 0.9 throughout the present study. In both models $C_\mu = 0.09$, $\sigma_k = 1.0$, $C_{\epsilon 1} = 1.44$, and $C_{\epsilon 2} = 1.92$. σ_ϵ and $C_{\epsilon 3}$ take the values 1.3 and 2.0 in the LS model; values of 1.21 and 0.9 are adopted in the present model. In Equation (18) $\sigma_s = 6.0$. All calculational variables are set to zero at the pipe wall (except enthalpy, which has a wall heat flux boundary condition); all variables have zero gradient at the axis (except that V = 0).

Density is determined from the ideal gas equation of state. Dynamic viscosity, thermal conductivity, and specific heat capacity are obtained from polynomials in temperature. Numerical solution of the equations is obtained using a parabolic finite volume/finite difference scheme with very fine near-wall resolution. Kirwin (12) details the variable property functions and numerical procedures.

4 RESULTS

Comparison is made with the measurements of Nusselt number development made by Steiner (7), Shehata and McEligot (9), and Vilemas et al. (10). The general features of these datasets were discussed above in § 1.

Steiner (7) reported experimental data for the ascending flow of air in a vertical, uniformly heated pipe. The test section was 60 diameters in length and was preceded by an unheated development section of 30 diameters. The data of Steiner encompass a fairly wide range of buoyancy influence, with Bo at the start of heating varying by a factor of almost 20 between Cases S1 and S4 (Table 1 and Figure 1). The increase of buoyancy influence over the series was achieved while maintaining the ratio of Grashof to Reynolds number approximately constant. Temperature at the start of heating is constant between the four runs as, more approximately, is the ratio $\dot{q}/U_b$ (reflecting Gr/Re) and there is therefore only a modest variation in the heat loading parameter (Table 1 and Figure 2). Hence, to a first approximation, the variation of buoyancy influence may be examined in isolation from variable heat loading effects. It should be observed nonetheless that the values of q^+ are not low in absolute terms : significant variable property influences are therefore present in Steiner's data and the use of a constant property formulation of the model equations would be questionable. Comparison of the two models with data is made in Figures 3 to 6. The case of lowest buoyancy influence, Figure 3, shows the present model to be in better agreement with the data than the LS model. In Figures 4 to 6 the position is reversed, although in Figure 4 the discrepancies between both sets of calculations and data are comparable, and in the final case the two computed distributions of Nusselt number are similar. It should be noted finally that there are two sources of uncertainty in Steiner's data: firstly, there is no scale on the abscissa of the graph presented in Reference (7), although it seems probable that the data lie in the region $0 \leq x/D \leq 60$ (the length of the

heated section). Secondly, the Nusselt number data of Steiner have here been re-scaled using local bulk thermal conductivity because it appears that the reported experimental points are based upon the value prevailing at the start of heating.

The second set of data for ascending air flow is that of Shehata and McEligot (9). The heated section was 29 diameters in length with an upstream unheated section of 50 diameters. The experimental apparatus was designed to produce a uniform wall heat flux, although in fact there was some variation in $\dot{q}$ due to end conduction effects. Shehata and McEligot supplied data which allowed the calculation of the local wall heat flux over the 14.5 diameters preceding the nominal start of heating. The figures below therefore depict 14.5 diameters of indirect heating (due to heat conduction in the wall) followed by a test section of 29 diameters (including a short downstream section where end conduction effects are significant). The experimental conditions investigated by Shehata and McEligot are in the main characterized by relatively low buoyancy influence and high loading (Table 1 and Figures 1 and 2). Thus, the most important physical effects are those associated with variable properties and bulk acceleration, rather than buoyancy forces (as confirmed by a test reported by Kirwin (12) which demonstrated that the body force term of Equation (10) could be 'switched off' with little effect on the computed values of Nusselt number). The present and LS models are shown with Shehata and McEligot's measurements in Figures 7 to 9. Attention is focused on the directly-heated test section, $x/D \geq 14.5$. Figure 7 reveals the LS model to be closer to the experimental points from $x/D = 14.5$ up to $x/D \simeq 25$; over the remainder of the test section the present model is in closer agreement with data. In Figure 8 the LS model results are generally below the data, whereas the present model generates values of Nusselt number higher than those measured. Figure 9 shows that both models return heat transfer levels higher than the data, the LS values being closer to measurements. A consistent trend emerges in all three cases whereby the present model computes Nu values higher than the LS model; throughout these comparisons both models are in acceptable agreement with data, apart from a single possible exception which arises in Figure 9 where the present model is compared against Shehata and McEligot's Case SM3.

The final dataset to be considered here is that of Vilemas et al. (10) (in fact results from a more comprehensive dataset supplied by Poškas (23) are used here). The experimental arrangement consisted of a heated length of 110 diameters with an unheated section of 69 diameters prior to the start of heating. An approximately uniform wall heat flux boundary condition was imposed; $\dot{q}$ has been taken to be precisely uniform in the current computations (in relation to the data of Shehata and McEligot (9) above, Kirwin (12) demonstrated that sensitivity to non-uniformities in wall heat flux is restricted to the entry and exit regions of a test section). Vilemas et al. reported results for twelve test cases; here we select three cases at relatively high heat loading and moderate-to-high levels of buoyancy influence (Table 1 and Figures 1 and 2). Nusselt number development is shown in Figures 10 to 12. The data show striking recoveries in Nusselt number which are attributable to the influence of buoyancy following an initial region of thermal development. As buoyancy influence increases in the sequence from Figure 10 to Figure 12 the axial location at which Nusselt number recovery occurs moves progressively upstream. (There is no evidence of local recovery in the data of Shehata and McEligot, a fact that is presumably due to the relatively low values of Bo imposed on a shorter test section. Steiner's Case S4, Figure 6, has a very similar value of Bo to Case VPK11, Figure 11. Here there is a slight hint of recovery, but the disparity in q^+ values must also be borne in mind.) Turning to the accuracy with which the LS and present models reproduce the measurements of Vilemas et al., while neither model is in excellent agreement with data, both are seen to capture the broad patterns of Nusselt number development. It is clear that neither model accurately resolves the local recoveries apparent in the experimental distributions of Nusselt number (this being the case especially in Figure 10); in Figure 12 the LS model is more accurate in the determination of the x/D location at which recovery occurs.

5 CLOSING REMARKS

The present turbulence modelling study of mixed convection air flows has made comparison with the experimental data of Steiner (7), Shehata and McEligot (9), and Vilemas et al. (10). The experimental data were obtained over different ranges of buoyancy influence, characterized by the buoyancy parameter of Equation (1), and heat loading, quantified by Equation (2). The low-Reynolds-number k-ϵ model of Launder and Sharma (1) has been selected as an established closure for the computation of turbulent mixed convection flows against which the 'strain parameter', or k-ϵ-S model, of Cotton and Ismael (2) has been examined. The k-ϵ-S model combines the concept of 'effective total strain' as developed by Townsend (16) and Maxey (15) with familiar elements of k-ϵ closure.

Ten individual mixed convection cases have been examined here, and in the complete study comparison has been made with over 20 cases. The results of Figures 3 to 12 show the performance of the LS and present models to be comparable, with, if anything, the LS model emerging as the marginally more accurate formulation. In an isolated case shown in Cotton and Ismael (2, 24) (namely Vilemas et al. Case VPK3) the LS model is significantly closer to data than the k-ϵ-S

scheme. The case is, however, exceptionally sensitive to prescribed conditions: Kirwin (12) found that a 2% change in bulk velocity could alter Nusselt number computed using the LS model by 20%. This sensitivity is due to the Reynolds number dependence of the buoyancy parameter (Equation (1)) and to the particular value of Bo in Case VPK3 (which is associated with a region in which heat transfer levels vary rapidly with the buoyancy parameter).

The question of the relative importance of the roles played by the turbulence response to the mean field (here characterized by the strain parameter), and viscous effects (quantified in terms of turbulent Reynolds number) is not yet resolved. In terms of the present model, impairment of heat transfer is associated both with *high* values of S (giving low f_S) and *low* values of Re_t (giving low f_μ). The latter dependence assumes increased significance under laminarizing conditions because, although Equation (14a) is active in the model only for very low values of Re_t, precisely such low values arise where the flow is laminarescent (and mixed convection computations are then sensitive to model detail at that level). Further work needs to be done in order to address various questions related to turbulence modelling along the lines pursued here : while some 'successes' have been recorded, it is also the case that shortcomings as discussed here and elsewhere (References (2), (24), and (25)) have emerged.

Case	Fig.	Bo	q^+	Nu_o
S1	3	0.117	1.02×10^{-3}	40.2
S2	4	0.276	8.69×10^{-4}	28.8
S3	5	0.801	1.16×10^{-3}	22.2
S4	6	2.11	1.30×10^{-3}	16.8
SM1	7	0.0641	1.79×10^{-3}	19.6
SM2	8	0.125	3.51×10^{-3}	19.6
SM3	9	0.376	4.58×10^{-3}	14.8
VPK12	10	0.420	1.68×10^{-3}	52.4
VPK11	11	2.14	2.18×10^{-3}	32.5
VPK10	12	6.81	2.66×10^{-3}	24.1

Table 1 Conditions at the start of heating in the experiments of Steiner (1971), Shehata and McEligot (1995), and Vilemas et al. (1992); also approximate values of Nu_o

Acknowledgements

Partial support for this study was provided by EPSRC and DERA under Research Grant GR/H74247 and also by EPSRC via the provision of a Research Studentship.

Nomenclature

Bo	buoyancy parameter, Equation (1)
c_p	specific heat capacity at constant pressure
$C_{\epsilon 1}$, $C_{\epsilon 2}$, $C_{\epsilon 3}$	constants in Equation (16)
C_μ	constant in constitutive equation
D	pipe diameter
D_ϵ	$2\nu(\partial k^{1/2}/\partial y)^2$
f, f_s, f_μ	damping functions
f_2	function in Equation (16)
F	general function
g	acceleration due to gravity
Gr	Grashof number, $\beta g \dot{q} D^4/\lambda\nu^2$
h	specific enthalpy
k	turbulent kinetic energy
Nu	Nusselt number, $\dot{q}D/\lambda(\theta_w-\theta_b)$
p	pressure
Pr	Prandtl number, $c_p\mu/\lambda$
$\dot{q}$	wall heat flux
q^+	heat loading parameter, Equation (2)
r	radial coordinate
Re	Reynolds number, U_bD/ν
Re_t	turbulent Reynolds number, $k^2/\nu\,\tilde{\epsilon}$
S	strain parameter, Equations (8) and (18)
t	time
T_D	timescale, Equation (7)
U,V	mean velocities in x-, r-directions
u,v	fluctuating velocities in x-, r- (or y-) directions

x	streamwise coordinate
y	Cartesian cross-stream (wall-normal) coordinate
y^+	$y\sqrt{\tau_w/\rho}\,/\nu$

Greek

α	total strain, Equation (6)
β	coefficient of volumetric expansion, $1/\theta$
δ_{ij}	Kronecker delta
ϵ	rate of dissipation of k
$\tilde{\epsilon}$	modified dissipation variable, ϵ-D_ϵ
θ	absolute temperature
λ	thermal conductivity
μ	dynamic viscosity
ν	kinematic viscosity, μ/ρ
ρ	density
σ_t	turbulent Prandtl number, $c_p\mu_t/\lambda_t$
σ_k, σ_ϵ, σ_s	turbulent Prandtl number for diffusion of k,ϵ,S
τ	'dummy' time variable; shear stress

Subscripts

b	bulk
t	turbulent
w	wall
0	forced convection

Superscripts

-	time-average (or ensemble-average)
'	fluctuating

REFERENCES

(1) Launder, B.E. & Sharma, B.I. Application of the energy-dissipation model of turbulence to the calculation of flow near a spinning disc. *Lett. Heat Mass Transfer*, 1974, **1**, 131-138.

(2) Cotton, M.A. & Ismael, J.O. A strain parameter turbulence model and its application to homogeneous and thin shear flows. To appear in *Int. J. Heat Fluid Flow*, 1998.

(3) Petukhov, B.S. & Polyakov, A.F. *Heat Transfer in Turbulent Mixed Convection*, (ed. B.E. Launder), 1988 (Hemisphere).

(4) Jackson, J.D., Cotton, M.A. & Axcell, B.P. Studies of mixed convection in vertical tubes. *Int. J. Heat Fluid Flow*, 1989, **10**, 2-15.

(5) Hall, W.B. and Jackson, J.D. Laminarization of turbulent pipe flow by buoyancy forces. ASME Paper 69-HT-55, 1969.

(6) Carr, A.D., Connor, M.A. & Buhr, H.O. Velocity, temperature, and turbulence measurements in air for pipe flow with combined free and forced convection. *ASME J. Heat Transfer*, 1973, **95**, 445-452.

(7) Steiner, A. On the reverse transition of a turbulent flow under the action of buoyancy forces. *J. Fluid Mech.*, 1971, **47**, 503-512.

(8) Polyakov, A.F. & Shindin, S.A. Development of turbulent heat transfer over the length of vertical tubes in the presence of mixed air convection. *Int. J. Heat Mass Transfer*, 1988, **31**, 987-992.

(9) Shehata, A.M. & McEligot, D.A. Turbulence structure in the viscous layer of strongly heated gas flows. Idaho National Engineering Laboratory Report INEL-95/0223, 1995.

(10) Vilemas, J.V., Poškas, P.S. & Kaupas, V.E. Local heat transfer in a vertical gas-cooled tube with turbulent mixed convection and different heat fluxes. *Int. J. Heat Mass Transfer*, 1992, **35**, 2421-2428.

(11) Kays, W.M. & Leung, E.Y. Heat transfer in annular passages - hydrodynamically developed turbulent flow with arbitrarily prescribed heat flux. *Int. J. Heat Mass Transfer*, 1963, **6**, 537-557.

(12) Kirwin, P.J. Investigation and development of two-equation turbulence closures with reference to mixed convection in vertical pipes. Ph.D. thesis, University of Manchester, 1995.

(13) Lee, M.J., Kim, J. & Moin, P. Structure of turbulence at high shear rate. *J. Fluid Mech.*, 1990, **216**, 561-583.

(14) Hunt, J.C.R. & Carruthers, D.J. Rapid distortion theory and the 'problems' of turbulence. *J. Fluid Mech.*, 1990, **212**, 497-532.

(15) Maxey, M.R. Distortion of turbulence in flows with parallel streamlines. *J. Fluid Mech.*, 1982, **124**, 261-282.

(16) Townsend, A.A. Entrainment and the structure of turbulent flow. *J. Fluid Mech.*, 1970, **41**, 13-46.

(17) Lumley, J.L., Berkooz, G., Elezgaray, J., Holmes, P., Poje, A. & Volte, C. Fundamental aspects of incompressible and compressible turbulent flows. In *Simulation and Modeling of Turbulent Flows* (eds. T.B. Gatski et al.), 1996, 5-78 (Oxford).

(18) Mankbadi, R.R. & Liu, J.T.C. Near-wall response in turbulent shear flows subjected to imposed unsteadiness. *J. Fluid Mech.*, 1992, **238**, 55-71.

(19) Jones, W.P. & Launder, B.E. The prediction of laminarization with a two-equation model of turbulence. *Int. J. Heat Mass Transfer*, 1972, **15**, 301-314.

(20) Patel, V.C., Rodi, W. & Scheuerer, G. Turbulence models for near-wall and low Reynolds number flows: a review. *AIAA J.*, 1985, **23**, 1308-1319.

(21) Cotton, M.A. & Kirwin, P.J. A comparative study of two-equation turbulence models applied to turbulent mixed convection in vertical pipes. In *Proc. 5th International Symposium on Refined Flow Modelling and* Turbulence Measurements, Paris (eds. P.-L. Viollet et al.), 1993, 375-382 (Presses Ponts et Chaussées).

(22) Jackson, J.D. & Mikielewicz, D.P. Computational studies of buoyancy-influenced flow of air in a vertical pipe. In *Engineering Turbulence Modelling and Experiments 3*, Heraklion (eds. W. Rodi & G. Bergeles), 1996, 349-358 (Elsevier).

(23) Poskas, P.S. Personal communication, 1991.

(24) Cotton, M.A. & Ismael, J.O. A 3-equation transported strain parameter model of turbulence and its application to turbulent mixed convection. In *Turbulence, Heat and Mass Transfer 1*, (eds. K. Hanjalić & J.C.F. Pereira), 1995, 184-189 (Begell House).

(25) Cotton, M.A. & Ismael, J.O. Some results for homogeneous shear flows computed using a strain parameter model of turbulence. In *Proc. 10th Symposium on Turbulent Shear Flows*, Pennsylvania State University (eds. F. Durst et al.), 1995, 26.7-26.12.

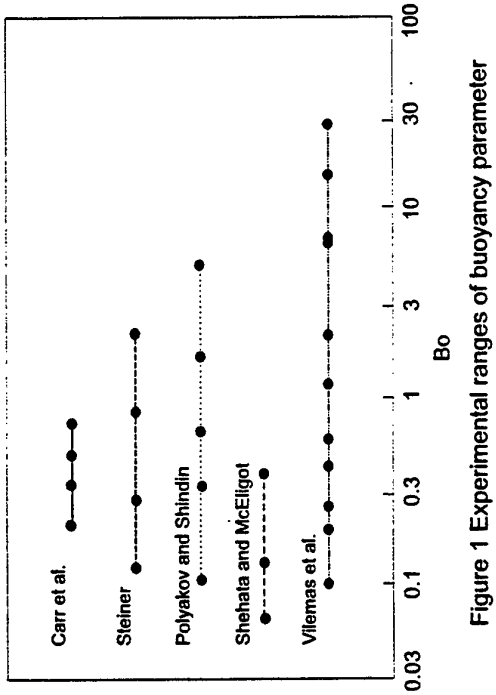

Figure 1 Experimental ranges of buoyancy parameter

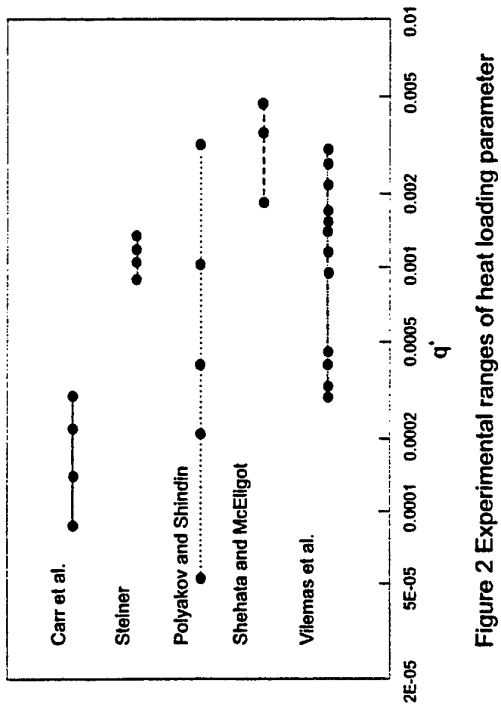

Figure 2 Experimental ranges of heat loading parameter

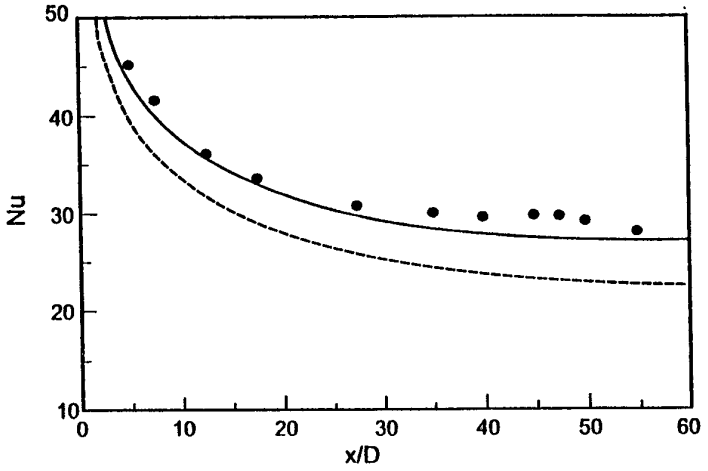

Figure 3 Steiner Case S1
(•Data; - Present model; ---LS model)

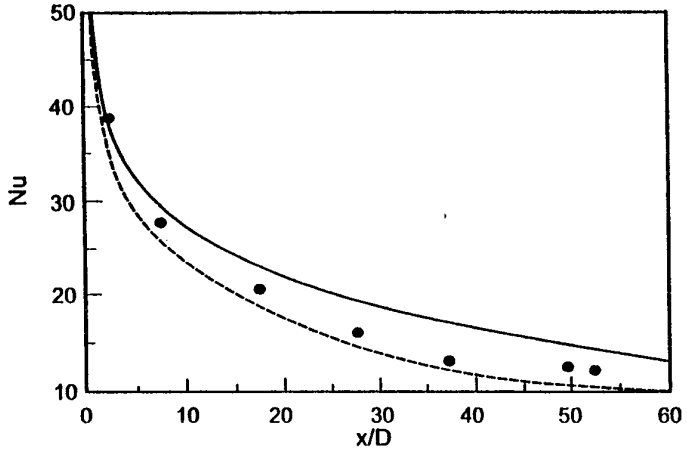

Figure 4 Steiner Case S2
(•Data; - Present model; ---LS model)

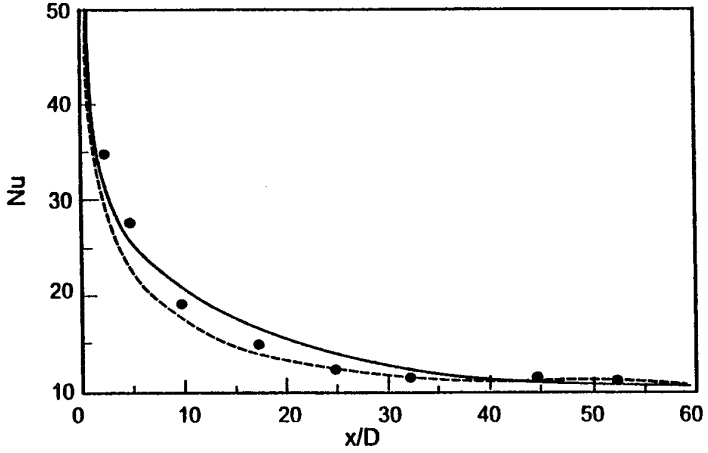

Figure 5 Steiner Case S3
(•Data; - Present model; ---LS model)

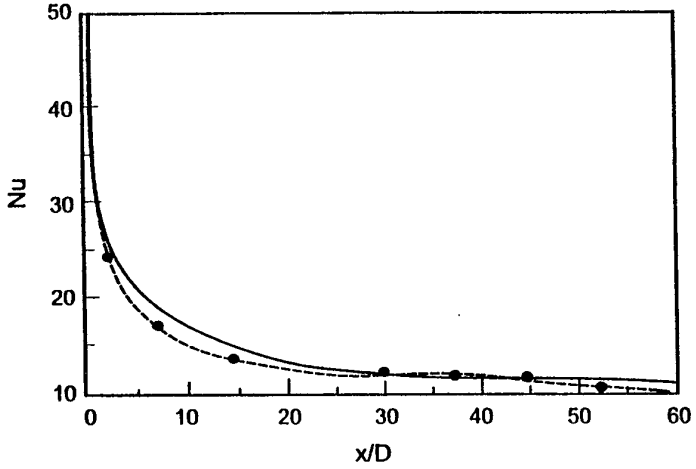

Figure 6 Steiner Case S4
(• Data; - Present model; ---LS model)

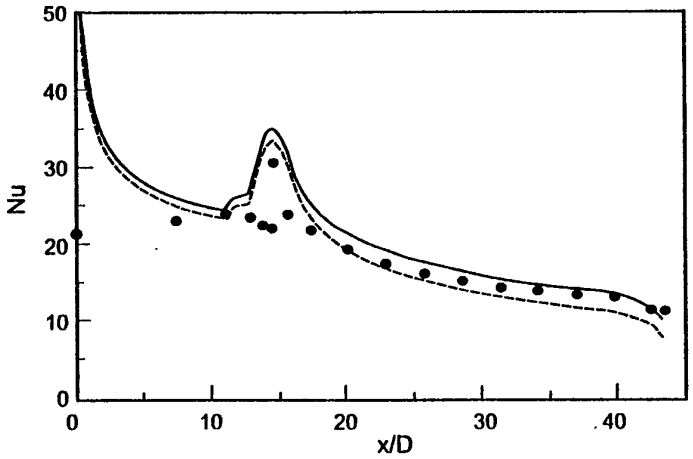

Figure 7 Shehata and McEligot Case SM1
(• Data; - Present model; ---LS model)

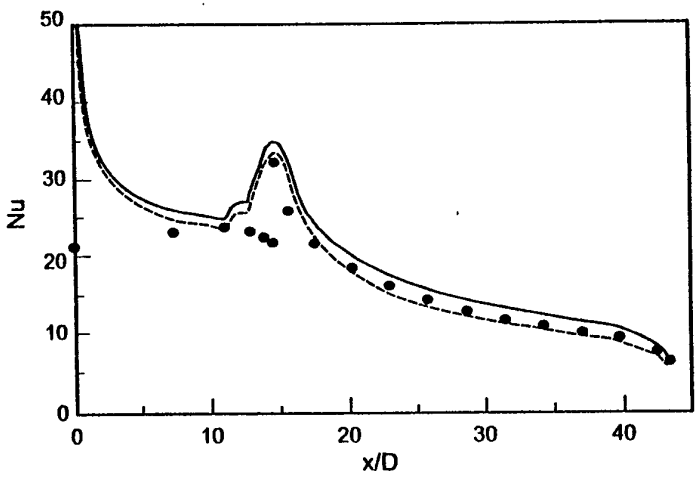

Figure 8 Shehata and McEligot Case SM2
(• Data; - Present model; ---LS model)

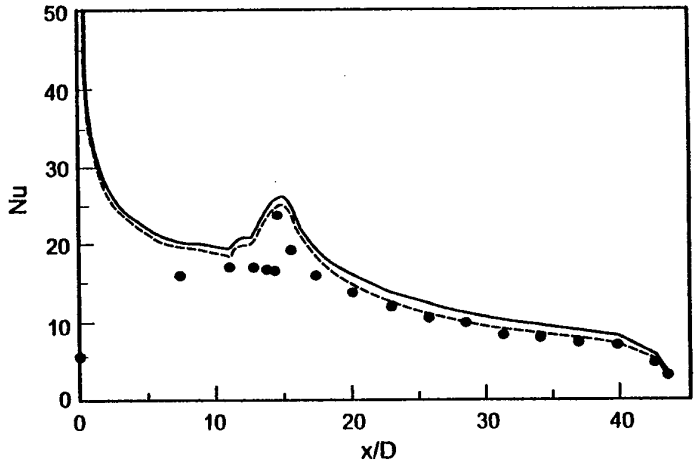

Figure 9 Shehata and McEligot Case SM3
(• Data; - Present model; ---LS model)

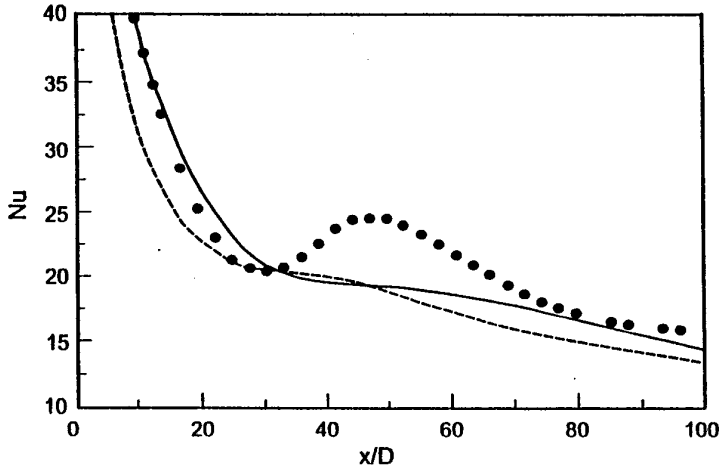

Figure 10 Vilemas et al. Case VPK12
(• Data; - Present model; ---LS model)

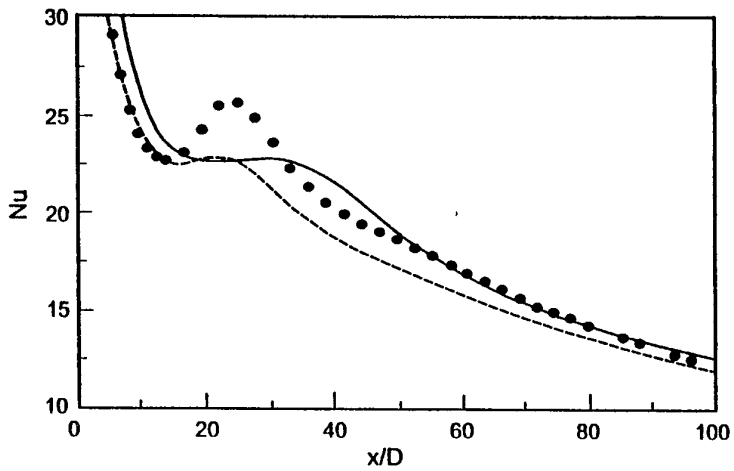

Figure 11 Vilemas et al. Case VPK11
(• Data; - Present model; ---LS model)

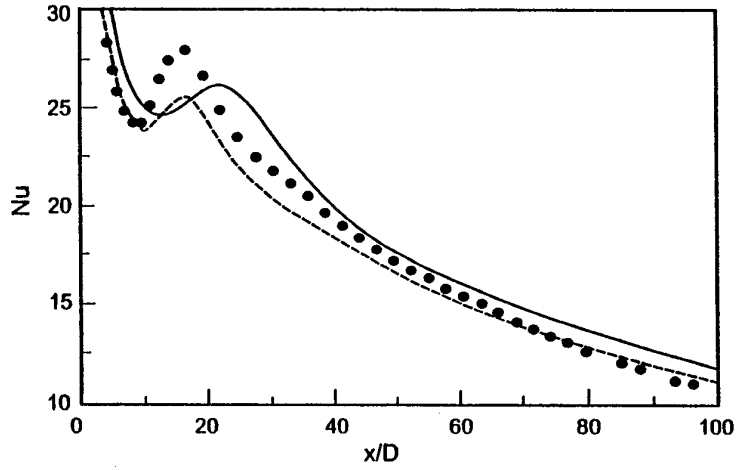

Figure 12 Vilemas et al. Case VPK10
(• Data; - Present model; ---LS model)

BUOYANCY-INFLUENCED TURBULENT HEAT TRANSFER TO AIR FLOWING VARIABLE PROPERTY IN A UNIFORMLY HEATED VERTICAL TUBE

Jiankang Li and J.D. Jackson

School of Engineering
University of Manchester, U.K.

ABSTRACT

A detailed experimental study is reported of buoyancy-influenced variable property turbulent convection for the case of air flowing in a uniformly heated vertical tube. Experiments were conducted with both upward and downward flow. For each case, the conditions covered ranged from forced convection with negligible influences of buoyancy to mixed convection with dominant influences of buoyancy.

The results obtained serve to reinforce and extend the existing picture of mixed convection heat transfer in vertical tubes. For downward flow, (the buoyancy-opposed case), the influence of buoyancy is to enhance turbulence production and improve the effectiveness of heat transfer. Fully developed thermal conditions are readily achieved and data can be satisfactorily correlated in terms of the local values of Nusselt, Reynolds and Grashof number and well fitted by a simple equation based on a semi-empirical model of turbulent mixed convection.

For upward flow (the buoyancy-aided case), modest influences of buoyancy cause turbulence production to be reduced and the development of a partially or even fully laminarised flow condition to occur with impaired effectiveness of heat transfer. An excellent description of the conditions under which complete laminarisation occurs and the extent to which heat transfer effectiveness is then reduced is provided by the semi-empirical model referred to above. Stronger influences of buoyancy cause the flow to develop in such a way that, after being reduced, turbulence production recovers as a result of the velocity profile becoming inverted in the core region. Complete laminarisation is then avoided. The distribution of Nusselt number is non-uniform, falling in the thermal entry region, reaching a minimum, then rising to a maximum and finally falling steadily again. This behaviour can be readily explained by the fact that in the experiments reported here the axial variations of temperature were large enough under certain conditions to cause considerable variation of fluid properties. As a consequence, both Grashof number and Reynolds number decreased significantly with distance along the tube. Thus, buoyancy influences became weaker and also the flow became less turbulent. Further increase in the strength of buoyancy influences causes the non-uniformity of Nusselt number to be concentrated more and more upstream and the effectiveness of heat transfer to be enhanced in relation to that for forced convection under corresponding conditions.

1 INTRODUCTION

Motion of the fluid in a convective heat transfer system can either be produced applying a pressure difference through the action of a fan or pump or simply by applying heat, causing the fluid density to become non-uniform and hence and modifying the gravitational body force field. The heat transfer process in a situation where the motion is generated by an externally applied pressure field is referred to as forced convection. That in a system where the flow is generated entirely as a result of the application of heat is called free convection. In situations where both mechanisms operate simultaneously, the process is called mixed convection.

As a consequence of its practical importance, turbulent mixed convection in vertical passages has been a topic of continuing interest to researchers (see for example, papers by Steiner (1), Easby (2), Carr, Connor and Buhr (3), Polyakov and Shindin (4), Jackson and Fewster (5), Vilemas, Poskas and Kaupas (6)). A number of detailed reviews of mixed convection research have been published, see for instance Jackson and Hall (7) and Jackson et al (8)). The influences of buoyancy on heat transfer which have been observed in the studies referred to above, and others, can be summarised as follows. In heated downward flow, where buoyancy forces oppose the gradient, there is a general enhancement of turbulent diffusion with the result that heat transfer coefficients are higher than for forced convection alone. In contrast, for upward flow in heated tubes, influences of buoyancy can lead to impairment of turbulent diffusion. Heat transfer coefficients are then lower than those for forced convection. Partial or even complete laminarization of the flow can occur. With increase in the strength of buoyancy influence complete laminarization is avoided, turbulence production recovers and heat transfer can even become enhanced in relation to forced convection. In the limit of very strong buoyancy influences, heat transfer coefficients for both ascending and descending flows become similar.

A physical explanation of the influences of buoyancy outlined above was given by Hall and Jackson (9). They argued that for upward flow, in a heated tube the reduction of shear stress due to buoyancy in the near-wall region of the boundary layer would result in turbulence production being diminished and the diffusion of heat impaired. By comparing the reduction of shear stress across the buoyant wall layer with the wall shear stress they arrived at a criterion for laminarization of flow due to

buoyancy influences.

A simple semi-empirical model of fully developed turbulent mixed convection based on these ideas was developed by Jackson (10) and used by Jackson and Fewster (5) as a framework for correlating and fitting their experimental data. Details of the model can be found in Jackson and Hall (7). As further experimental data have become available the model has been refined. The present version (see Jackson and Buyukalaca (15)) is

$$\frac{Nu}{Nu_f} = \left[1 \pm 2.5x10^5 \frac{Gr^*}{\mathrm{Re}^{3.425}\,\mathrm{Pr}^{0.8}} \left[\frac{Nu}{Nu_f} \right]^{-2} \right]^{0.46} \quad (1)$$

In this equation the Nusselt number for mixed convection Nu is normalised using the value Nu_f for forced convection for the same flow rate. The local values of Grashof number Gr^* and Reynolds number Re and combine together with the Prandtl number Pr to form a buoyancy parameter $Gr^*/Re^{3.425}Pr^{0.8}$. The negative sign in Equation 1 refers to the buoyancy-aided case and the positive sign to the buoyancy opposed case). The model does not take account of inertia effects and these are certainly present as the flow develops in a pipe under the influence of buoyancy. As such , the model is most likely to be successful in describing mixed convection in the downstream region, where a fully developed conditions is being approached. Apart from utilising local values of Re and Gr^* the model does not take account of the variable property effects which arise where the axial and radial variations of fluid temperature are large. Figure 1 shows the variation of Nusselt number ratio with buoyancy parameter predicted by the model. For values of $Gr^*/Re^{3.425}Pr^{0.8}<5x10^{-7}$, Nusselt number is predicted to be within 5% of the forced convection value. The predicted modification of the effectiveness of heat transfer by buoyancy is quite consistent with what is observed in practice. For the buoyancy-opposed case (heated downward, flow) systematic enhancement of heat transfer with increase of buoyancy parameter. For the buoyancy-opposed case (heated upward flow), impairment of heat transfer is predicted, which develops very sharply at a value of $Gr^*/Re^{3.425}Pr^{0.5}$ of about 10^{-6} , is predicted. This is followed by recovery of heat transfer effectiveness in relative terms with further increase of buoyancy influence.

Although the general pattern of behaviour in turbulent mixed convection is now quite well documented, there is still a need for further data to reinforce the existing picture and provide a better basis for the validation of computational models. The complicating effect of variable fluid properties on mixed convection still needs to be clarified.

In this paper, a detailed experimental study of buoyancy-influenced turbulent convection is reported for both ascending and descending flows of air in a long uniformly heated vertical tube. The experiments covered a wide range of conditions from forced flow with negligible influence of buoyancy to mixed convection with dominant influences of buoyancy. Effects of variable fluid properties are significant and evident in some of the results.

2 EXPERIMENTAL APPARATUS

2.1 General Arrangement of the Test Facility

Figure 2 shows the general arrangement of the test facility. It was designed for operation with either forced or naturally induced flow of air through the test section. The present paper is concerned with experiments which were conducted with forced flow. The figure shows the arrangement for the case of upward flow with an unheated hydrodynamic development section present. Air from the laboratory was delivered by a blower through a flexible duct to the entry box, inside of which there was a honeycomb arrangement to straighten the flow. The flow rate was controlled using two valves situated downstream of the blower, one on the pipe leading to the test section and the other on a by-pass line. The air flowed from the entry box into the bellmouth intake where a uniform inlet velocity profile was generated. The flow then developed in a lone unheated hydrodynamic development section to the fully developed condition at the inlet to the heated section. After passing up the heated section the air was finally exhausted into the laboratory at the top through a flow metering nozzle.

Experiments were also conducted without an unheated section present and also using a modified arrangement which provided downward flow in the test section. The flow rate could either be measured either by using a hot film probe positioned centrally in the throat of the bellmouth intake or by means of the nozzle metering arrangement at outlet. The hot film probe was calibrated in situ using the nozzle.

2.2 Test Section

The heated section was the same for each of the configurations studied. It consisted of a stainless steel tube of inside diameter of 76.1 mm, wall thickness 1.9 mm, and length 7.87 m, which was resistively heated using alternating current supplied from the mains by a variable voltage system. Fifty-eight chromel-alumel thermocouples were attached to the outside surface of the heated tube by resistance welding at forty three axial measuring locations almost equally spaced along the heated length. At five of these locations, four thermocouples were attached 90° apart around the circumference to enable the uniformity of temperature to be checked. Detailed measurements of the tube wall thickness were made using an ultrasonic thickness gauge and the electrical resistance of the tube was carefully measured as a function of temperature. Thus, the local rate of heat generation within the wall could be estimated precisely from a knowledge of the power input and wall temperature. The heated section was heavily lagged with low conductivity fibre insulation material on the outside and calibration experiments were conducted to measure the rate of heat loss to the surroundings under steady

conditions. The unheated hydrodynamic development section, which was of length 3.085m, was also made from stainless steel tube of inside diameter 76.1 mm.

2.3 Data acquisition system

The data acquisition system consisted of a Solartron 7060 microprocessor digital voltmeter (DVM), eight Solartron 7010 minate analogy scanners and an IBM-AT personal computer system implemented with a GPIB-IEEE-488.2 interface board. Software for the system was written to suit the experiment for monitoring conditions, data acquisition and processing.

3 RESULTS AND DISCUSSION

3.1 Forced Convection conditions

In order to quantify the extent to which buoyancy forces influence the heat transfer process it is necessary to establish a reliable buoyancy-free, forced convection base for comparison. In the present study we have chosen to utilise a well-established correlation equation for this purpose. This was carefully adjusted to fit values of Nusselt number for forced convection determined from experimental data obtained using our test section. The equation used is that due to Petukhov et al (12) for variable property forced convection heat transfer to gases in smooth uniformly heated tubes with hydrodynamically developed turbulent flow at entry but developing thermal conditions. It consists of three parts, a semi-empirical, constant property correlation equation relating Nusselt number to Reynolds number and Prandtl number for fully developed flow and heat transfer, and further equations giving factors which take account of thermal development and variable property effects. The constant property correlation equation takes the form

$$Nu_{p_{cp}} = \frac{\mathrm{Re}\,\mathrm{Pr}\left(\frac{f}{8}\right)}{1.07+\frac{900}{\mathrm{Re}}-\frac{0.63}{(1+10\,\mathrm{Pr})}+12.5\sqrt{\frac{f}{8}}\left(\mathrm{Pr}^{\frac{2}{3}}-1\right)} \qquad (2)$$

In which $f = \left[1.82\log_e\left(\frac{\mathrm{Re}}{8.0}\right)\right]^{-2}$ for $10^4 \le \mathrm{Re} < 5\times10^6$

or $f = 0.316\,\mathrm{Re}^{-0.25}$ for $4000 < \mathrm{Re} < 10^4$

The equation for the factor which describes thermal development is

$$C_{\mathrm{Therm}} = 1.0+0.48\left[1.0+\frac{3600}{\mathrm{Re}\sqrt{x/D}}\right]\frac{\exp(-0.17x/D)}{(x/D)^{0.25}} \qquad (3)$$

As can be seen, this is only weakly dependent on Reynolds number. Its variation with x/D is shown in Figure 3(a).

The equations, which describe the variable property effect are too lengthy to quote here. They depend on x/D, the ratios Tw/Tb and Tb/Tb_{in} and the property variation characteristics of the gas. Figure 3(b) shows correction factors for air calculated using the equations. They are plotted against x/D for a range of value of Tw/Tb. The strong dependence of the factor on x/D for large values of Tw/Tb should be noted. Petukhov et al claimed that their equation was able to reproduce the very extensive body of data which is available on variable property gas heat transfer to within 6%. Values of Nusselt number for forced convection determined using data from the present study agree very well with the Petukhov et al correlation equation for Re>20000. However, for lower values of Reynolds number the equation over predicts our values slightly. The discrepancy increases systematically with reduction of Reynolds number. To take account of this, correction factors which are dependent on both x/D and Reynolds number have been carefully established in the course of the present study. The maximum modification needed was only about 7% (for details see Li (13)). Figures 4(a), (b), (c) and (d) show examples of comparisons between distributions of Nusselt number from experiments made in the course of the present study for conditions under which buoyancy influences were negligible with those calculated using the equation of Petukhov et al. It can be seen that the agreement is excellent. On the basis of such comparisons we are confident that the modified version of the Petukhov et al equation provides a reliable forced convection base against which our mixed convection results can be compared.

3.2 Mixed convection

3.2.1 Downward flow results

A detailed programme of experiments was completed for the downward flow case, during which heat input and flow rate were systematically varied giving values of Grashof number and Reynolds number at inlet in the ranges $4 \times 10^6 < Gr^* < 6 \times 10^8$ and $1{,}000 < Re < 35{,}000$, respectively. As a result, the value of the parameter $8\times10^4 Gr^*/Re^{3.425}Pr^{0.8}$, at inlet varied in the range 0.006 to 40. Such values cover conditions from forced flow with negligible influence of buoyancy through to buoyancy dominated flow. Complete details of the experiments and results can be found in Li (13). Here, we present a selection of the experimental results which serve to illustrate the important features and trends.

Typical profile of wall temperature is shown in Figure 5. For higher Reynolds numbers (see for example Figure 5(a)), the wall temperature distributions are very similar in appearance to what would be obtained for conditions of forced convection. However, a local maximum and a local minimum appear on the wall temperature profiles near the inlet when the Reynolds number is very low (see Figure 5(b)). An explanation of this anomalous behaviour will be given later.

Figure 6 shows distributions of Nusselt number for downward flow mixed convection along with the corresponding once for forced convection calculated using the correlation equation of Petukhov et al. If can be seen that, with increase of buoyancy parameter, heat transfer becomes more and more enhanced, compared with forced convection. As was mentioned earlier, this is the established trend in the case of buoyancy-opposed turbulent mixed convection in vertical tubes.

It is of interest to consider the axial distribution of Nusselt number in relation to that for forced convection. Initially the two coincide but as the thermal layer grows and buoyancy influence develop they diverse. The enhancement of Nusselt number due to buoyancy remains rather uniform on the thermal layer thickness reaches a steady value and a fully developed mixed convection heat transfer situation is achieved. Some non-uniformity of buoyancy influence is evident as Reynolds number is reduced see Figure 6(g) and (h). this is due to the fact that under such conditions a significant reduction of buoyancy parameter occurs as the bulk temperature increases with x/D. Striking non-uniformity of behaviour is found at very low Reynolds number (Re<4,000), as can be seen from the results shown in Figure 7 and in the plots of normalised Nusselt number shown on Figure 8, (The forced convection Nusselt number Nu_f used for normalisation purposes was calculated using the modified Petukhov et al equation). For relatively small buoyancy influences (line 3 in Figures 8(a) and 8(b)), the Nusselt number variation first shows a sharp decrease down to a level lower than the forced convection value. Then there is a rapid increase to a maximum value after which there is a further decrease before the distribution finally becomes more or less established at large x/D. With increase of Grashof number at the same Reynolds number, this non-uniformity simply becomes concentrated nearer and nearer to the inlet of the test section (see lines 1 and 2 in Figures 8(a) and 8(b)). This unusual, behaviour is due to the thermal entry effects and strong buoyancy influences acting in combination. The motion of fluid in the near wall region is retarded by buoyancy even near start of heating when such influences are significant, as is the case in the results under consideration. This decreases convection but also leads to enhanced turbulence production. The net effect is that the thermal development occurs more rapidly than otherwise would have been the case. So, Nusselt number falls rapidly at first. However as the thermal layer grows in thickness a stage is reached where the production of additional turbulence due to the increased buoyancy of the layer becomes considerable and Nusselt number then starts to increase and then stabilises once the thermal development is completed. This explains the localised peaking of wall temperature near the start of heating under conditions of low flow rate seen in Figure 5(b).

The approach adopted here to characterise buoyancy influences in mixed convection and correlate data is to plot normalised Nusslt number Nu/Nu_f against a buoyancy parameter which combines Reynolds number, Grashof number and Prandtl number in the form $Gr^*/(Re^{3.425}Pr^{0.8})$. Other buoyancy parameters have been proposed (see, for example, Petukhov and Strigin (14), Easby (2), and Polyakov and Shindin (4)). In a fairly recent study, Buyukalaca (15) compared the extent to which the various buoyancy parameters correlated his data for heated downward flow of water. He found that the combination of Gr^*, Re and Pr in the form $Gr^*/(Re^{3.425}Pr^{0.8})$ was the most successful one (see Jackson and Buyukalaca (11)). Figure 9 shows the present data for downward flow presented in terms of Nu/Nu_f and $G_r^*/Re^{3.425}Pr^{0.8}$ for downstream locations with x/D in the range $40 < x/D < 91$. The solid line on the figure is from the semi-empirical model of Jackson and Hall (Equation (1)). It can be seen that relative heat transfer increases systematically with increase of buoyancy parameter. The data are satisfactorily correlated when presented in this form. For locations well downstream the results are represented particularly well by equation (1).

3.2.2 Upward flow results

A further detailed programme of mixed convection experiments was completed for the case of upward flow with an unheated development section. Again the conditions covered ranged from forced convection with buoyancy-negligible influence through to buoyancy dominated mixed convection. The Reynolds number Re was varied from 2000 to 38000 and the Grashof number Gr^* from 4×10^6 to 6×10^8, giving values of the parameter $8 \times 10^4 Gr^*/Re^{3.425}Pr^{0.8}$ from 0.001 to 35. Figures 10 (a) to (h) show distributions of Nu with x/D for a range for upward flow mixed convection for progressively stronger influences of buoyancy. Also shown are the corresponding distributions for forced convection calculated using the correlation of Petukhov et al. Figure 10(a) to (c0 show the development of impaired heat transfer with complete laminarisation being approached in case (b0 and reached in case (c). With further increase of buoyancy influence a local minimum is followed by a maximum and then the Nusselt number falls. The velocity profile develops under the influence of buoyancy and becomes inverted in the core region. The eventual fall in Nusselt number is as sociated with the fact that in all cases the Reynolds number falls as the bulk temperature rises. Axial variation of viscosity plays a part in the manner in which Nu various with x/D. With increase of buoyancy influence the local peak on the Nusselt number distribution becomes concentrated more and more upstream as the development of the velocity profile occurs more and more rapidly. Laminarisation is avoided and eventually enhancement of heat transfer occur.

Figure 11 shows comparisons of Nusselt number distribution for upward and downward flow and Figure 12 shows relative heat transfer for some upward flow results for a range of conditions. It is apparent that, compared with the corresponding forced convection value, Nusselt number for upward can be either reduced by buoyancy, unchanged or increased. This is the established picture of buoyancy-influenced turbulent heat transfer in a vertical tube for the buoyancy-aided case. The difference between heat transfer for upward and downward flow is greatest for conditions where complete laminarisation of the flow

develops in the upward flow case. With further increase of buoyancy influence heat transfer recovers for that case and eventually becomes enhanced in relative terms. When this happens the upward and downward flow results come closes together.

Figure 13 show results from experiments with and without an unheated development section. This figure illustrates the fact that the values of Nusselt number for a configuration without an unheated development section are slightly higher than those with one for conditions where buoyancy influences are relatively weak 9see line 1 in Figure 13). However, where buoyancy influences are stronger, the results for the two cases become identical (lines 1 and 2 in Figure 13). This is because the velocity profile is then strongly modified by buoyancy on entering the heated section so its form at entry becomes unimportant.

Figures 14 and 15 show the experimental results for x/D=26.9 and 90.3 respectively in terms of Nusselt number ratio plotted against buoyancy parameter. Also shown on each figure is the distribution predicted by the semi-empirical model (equation (1). For x/D=26.9 the experimental values normalised Nusselt number first decrease gradually with increase of buoyancy parameter above a value of about 0.02 and then increase for values above about 0.2. The maximum impairment of heat transfer is about 40%. The agreement between the experimental data and the semi-empirical model is poor for this value of x/D. For axial locations further downstream the impairment of heat transfer occurs more sharply. From Figure 15 it can be seen that for x/D=90.3 a very sudden decrease of the normalised Nusselt number occurs at a buoyancy parameter value of about 0.1. This is well described by the semi-empirical model (equation (1)). This predicts a gradual decrease of normalised Nusselt number in the region of weak buoyancy influences ($B_o<0.08$) and then a very sudden decrease followed by steady recovery enhancement of leading to enhancement of relative heat transfer with further increase of buoyancy parameter. Some differences between the experimental data points and the model prediction are evident in the recovery region but nevertheless the model describes the data extremely well. The fact that it performs less well in describing the data for smaller values of x/D is not surprising since inertia effects are neglected in the analysis and so it is most likely to be applicable where fully developed conditions are approached.

Figures 16 and 17 show values of Nu/Nu_f from results where the distributions of Nu exhibit a local minimum and maximum. The values of Nu_{min}/Nu_f and Nu_{max}/Nu_f are plotted against the buoyancy parameter It can be seen that these are correlate quite well when presented in this form. The local minimum and maximum values of Nu/Nu_f increase steadily with increase of buoyancy parameter. This was also found to be the case by Rouai (16) and Vilemas et al (6). It is also found that the values of x/D at which the minimum and maximum values of Nu are achieved also correlate on the same basis.

4 CONCLUSIONS

1. The results presented here reinforce and extend the existing picture of mixed convection heat transfer in tubes. For heated downward flow (buoyancy-opposed flow), buoyancy forces enhance the turbulent diffusion properties of the flow, causing the heat transfer to be more effective than for forced convection alone. For heated upward flow (buoyancy-aided flow), heat transfer can be either impaired, or enhanced by such forces depending on the strength of the buoyancy influence.
2. For downward flow, striking variations of local Nusselt number can occur near the inlet under conditions of low Reynolds number. Nusselt number first decreases rapidly, then increases sharply and this is followed by a further decrease. These anomalous variations are associated with the interaction between thermal development and buoyancy influences.
3. For upward flow either partial or complete laminarisation of the flow can be caused by buoyancy influences. Nusselt number is weakly dependent on Reynolds number for large x/D under conditions where the flow is laminarised and has a value just below 10. For conditions of stronger buoyancy where complete laminarisation is avoided local heat transfer exhibits non-monotonic behaviour. Axial variations of Gr^* and Re due to density and viscosity changing significantly with x/D have an influence on this.
4. The general behaviour of buoyancy-influenced heat transfer for upward flow without an unheated development section is similar to that with an unheated section present. Local Nusselt numbers for both cases are virtually identical under strongly buoyancy influenced conditions. However, with relatively weak buoyancy-influences Nusselt number for the case without an unheated development section is slightly higher than that with one.
5. Downward flow mixed convection data correlate quite well in terms of normalised Nusselt number and buoyancy parameter. Some x/D effects are evident in the results for x/D<40. The semi-empirical model describes the experimental mixed convection heat transfer data very well for x/D>40.
6. For upward flow, a sudden decrease in relative Nusselt number at a value of buoyancy parameter of about 0.09 is evident in the data and is well predicted by the semi-empirical model. In general, the quantitative agreement between the semi-empirical model and the experimental data is very satisfactory for locations sufficiently well downstream that fully developed conditions are approached.

NOMENCLATURE

B_o buoyancy parameter, $\frac{8x10^4 Gr^*}{Re^{3.425} Pr^{0.8}}$

D inside diameter of test section

g acceleration due to gravity

Gr^* Grashof number based on wall heat flux, $\beta g D^4 q_w/(k_f \nu^2)$

h heat transfer coefficient, $q_w/(T_w - T_b)$

k thermal conductivity of air

Nu Nusselt number, hD/k

Nu_f forced convection Nusselt number

Pr Prandtl number, $c_p \mu / k_f$

q_w wall heat flux

Re Reynolds number, $w_b d/\nu$

T_b bulk temperature of fluid

T_w wall temperature

w_b bulk velocity

x axial position

Greek letters

β coefficient of volume expansion

μ dynamic viscosity

ν kinematic viscosity, μ/ρ

ρ density of air

REFERENCES

(1) Steiner, A., On the reverse transition of turbulent flow under the action of buoyancy forces, J. Fluid Mech, 1971, Vol.47, Part 3, pp.71-75

(2) Easby, J.P., The effect of buoyancy on flow and heat transfer for a gas passing down a vertical pipe at low turbulent Reynolds numbers, Int. J. Heat and Mass Transfer, 1978, Vol. 21, pp. 791-801.

(3) Carr, A.D., Connor M.A. and Buhr H.O., Velocity, temperature and turbulence measurements in air pipe flow with combined free and forced Convection, Trans. ASME, J. Heat Transfer, 1973, Vol. 95, pp.445-452

(4) Polyakov, A.F. and Shindin, S.A., Development of turbulent heat transfer over the length of vertical tubes in the presence of mixed air convection, Int. J. Heat Mass transfer, 1988, Vol.31, pp.987-992.

(5) Jackson, J.D. and Fewster, J., Enhancement of turbulent heat transfer due to buoyancy for downward flow of water in vertical tubes, Heat Transfer and Turbulent Buoyant Convection, Seminar of International Centre for Heat and Mass Transfer, Dubrovnik, Yugoslavia, 1976 (eds. Spalding, D.B. and Afgan, N.), Hemisphere Publishing Corporation, Washington D.C., pp. 759-775.

(6) Vilemas, J.V., Poskas, P.S. and Kaupas, V.E., Local heat transfer in a vertical gas-cooled tube with turbulent mixed convection and different heat fluxes, Int. J. Heat Mass Transfer, 1992, Vol.35, No.10, pp 2421-2428.

(7) Jackson, J.D. and Hall, W.B., Influences of buoyancy on heat transfer to fluids flowing in vertical tubes under turbulent conditions, Turbulent Forced Convection in Channels and Bundles Theory and Applications to Heat Exchangers and Nuclear Reactors, 1979, Vol.2, (eds. Kakac, S. and Spalding, D.B.), Advanced Study Institute Book, pp. 613-640.

(8) Jackson, J.D., Cotton, M.A. and Axcell, B.P., Studies of mixed convection in vertical tubes, Int. J. Heat and Fluid Flow, 1989, Vol. 10, No. 1, pp. 2-15.

(9) Hall, W.B. and Jackson, J.D., Laminarization of a turbulent pipe flow by buoyancy forces, ASME Paper, 1969, No. 69-HT-55.

(10) Jackson, J.D., Mixed forced and free convection – the influence of buoyancy on heat transfer in vertical pipes. Paper presented in Session V, Euromech-72 Meeting, Salford University, UK, March 1976.

(11) Jackson, J.D. and Büyükalaca, O., Correlation of heat transfer data for buoyancy-opposed turbulent mixed convection in a vertical tube, Eurotherm Meeting No. 32 on Heat Transfer in Single Phase Flows, 1993, Oxford University, U.K.

(12)Petukhov, B.S. and Kurganov, V.A. and Gladuntsov, A.I., Turbulent heat transfer in tubes to gases with variable physical properties, Heat and Mass Transfer, 1972, Vol.1, pp.117-127, Izd. ITMO AN BSSR, Minsk (in Russian).

(13)Li, J., Studies of Buoyancy-influenced convective heat transfer to air in a vertical tube, Ph.D. Thesis, 1994, University of Manchester

(14) Petukhov, B.S. and Strigin, B.K., Experimental investigation of heat transfer with viscous inertial-gravitational flow of a liquid in vertical tubes. Teplofizika Vysokikh temperatur, 1968, Vol. 6, No. 5, pp. 933-937.

(15)Büyükalaca, O., Studies of convective heat transfer to water in steady and unsteady pipe flow. Ph.D. Thesis 1993, University of Manchester.

(16)Rouai, N.M., Influences of buoyancy and imposed flow transients on turbulent convective heat transfer in a tube. Ph.D. Thesis, 1987, University of Manchester.

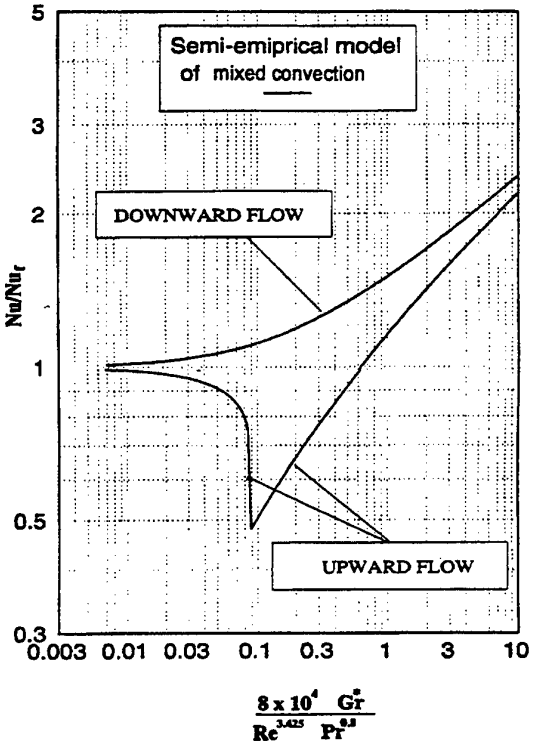

Figure 1 Model of Jackson and Hall

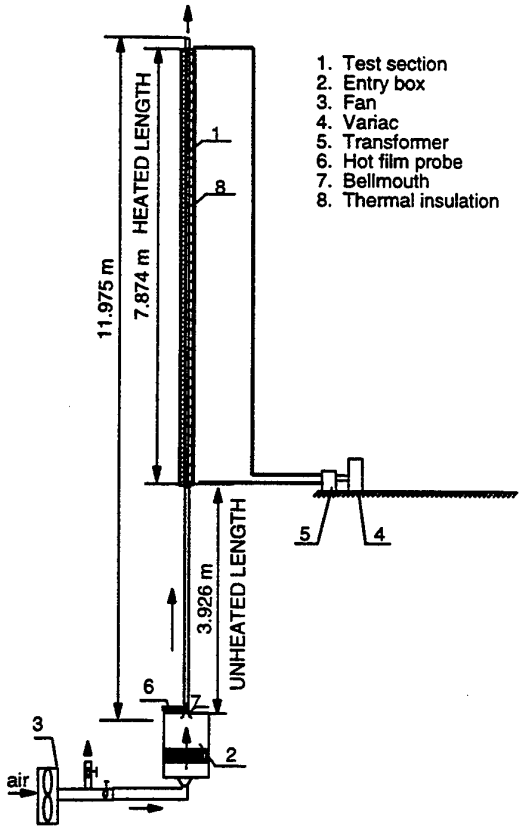

Figure 2 General arrangement of test facility (upward flow with unheated development section present)

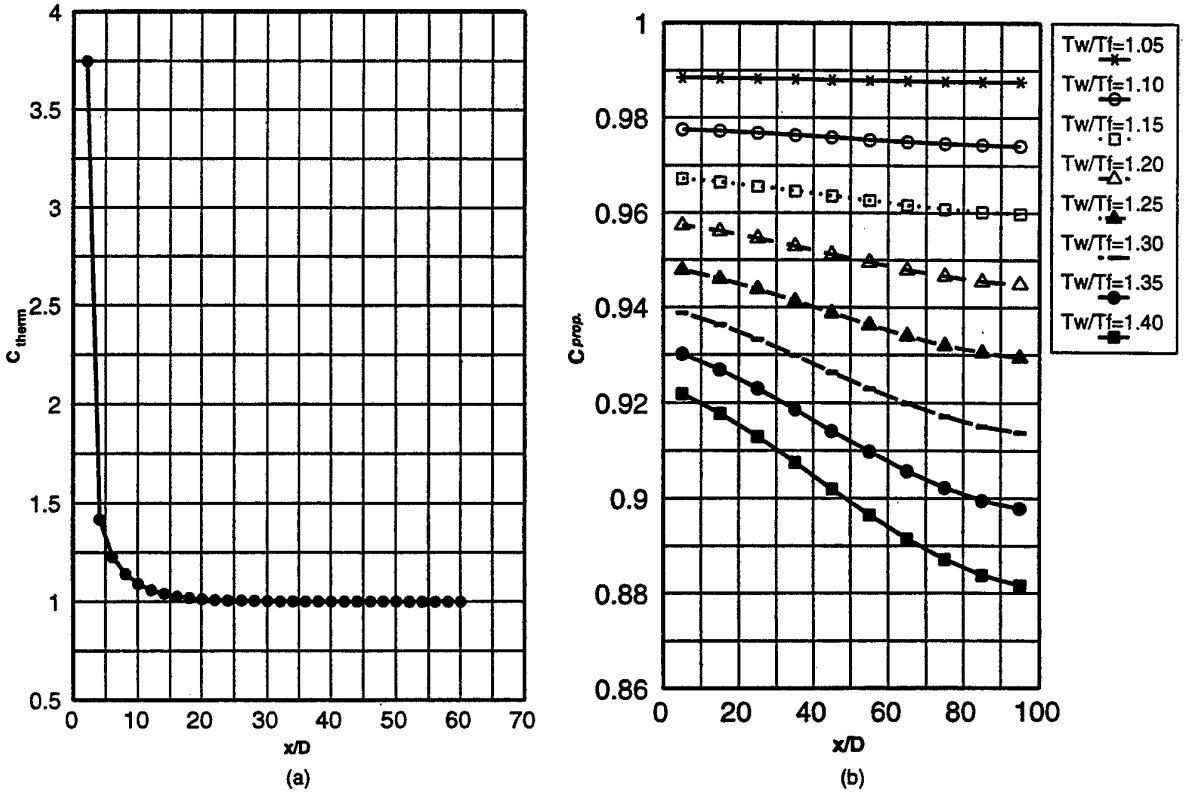

Figure 3 Correction factors for (a) thermal entry and (b) variable property effects in the forced convection correction equation of Peturchov et. al.

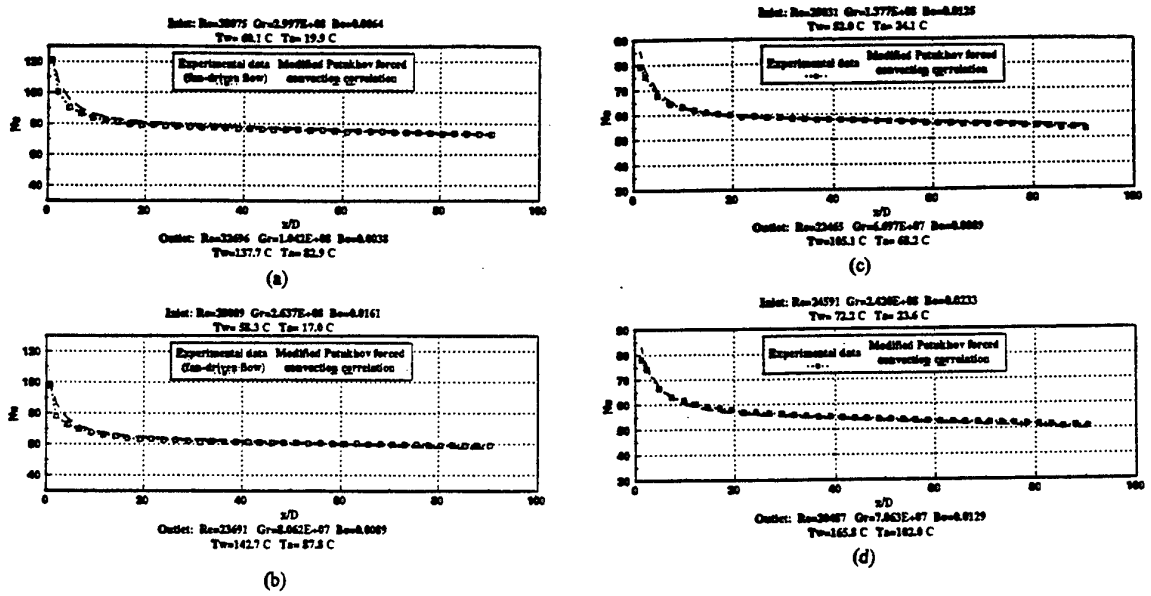

Figure 4 Comparison between Nusselt number distributions for conditions of forced convection from experiment and the modified Petukhov et al correlation equation ((a) and (b) – upward flow, (c) and (d) – downward flow)

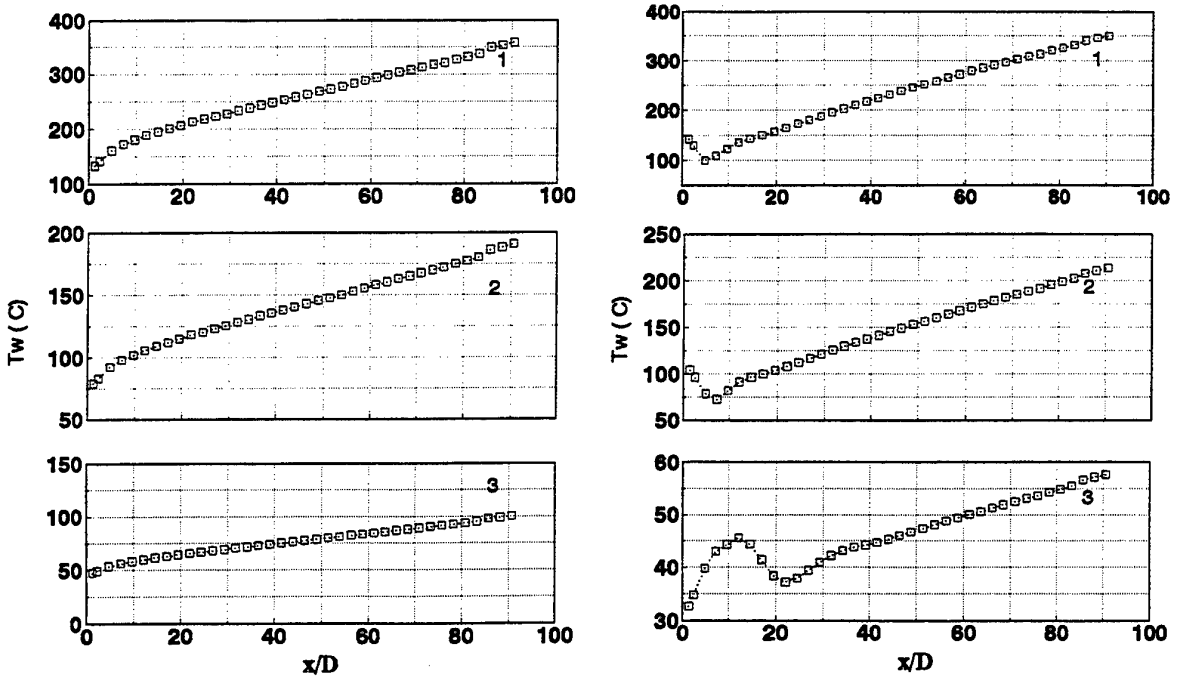

Figure 5 Local wall temperature distribution for downword flow with an unheated development section (a) Re: 20,000 (b) Re: 2,900

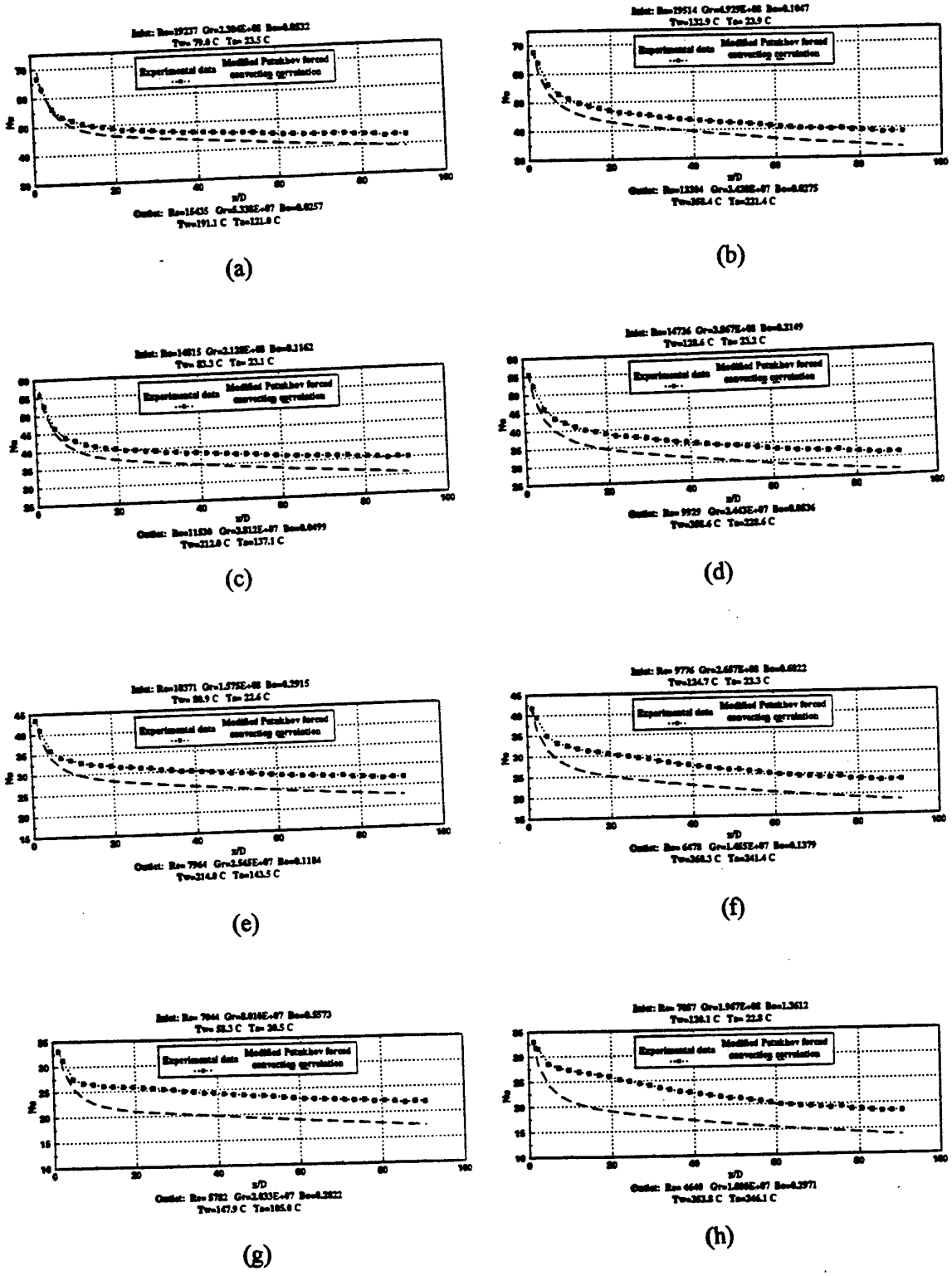

Figure 6 Local Nusselt number distributions for downward flow mixed convection

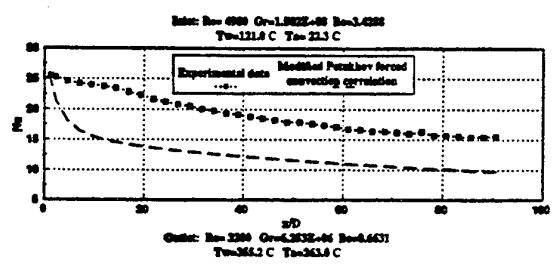

(a)

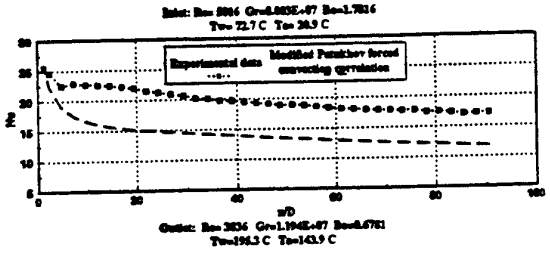

(b)

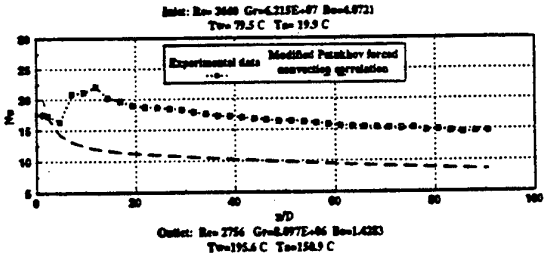

(c)

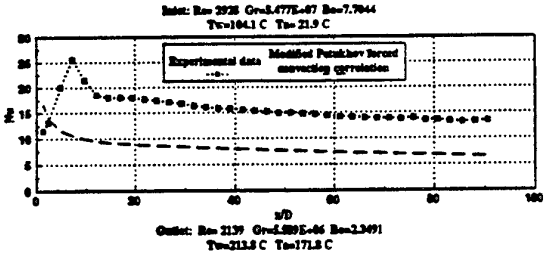

(d)

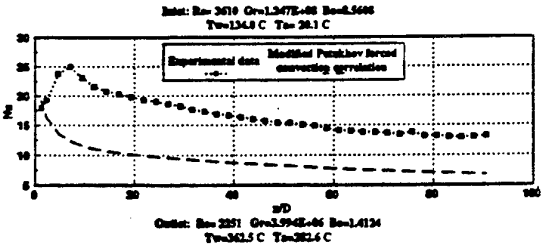

(e)

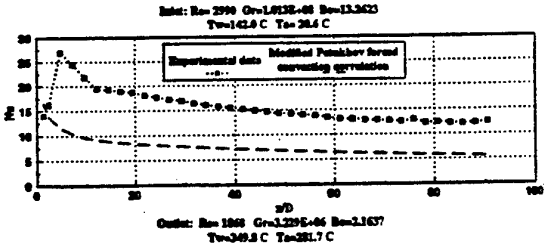

(f)

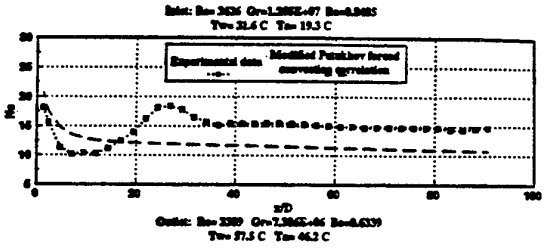

(g)

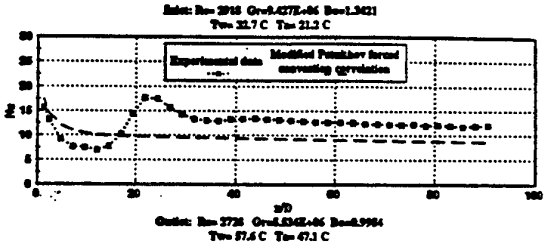

(h)

Figure 7 Local Nusselt number distributions for downward flow mixed convection

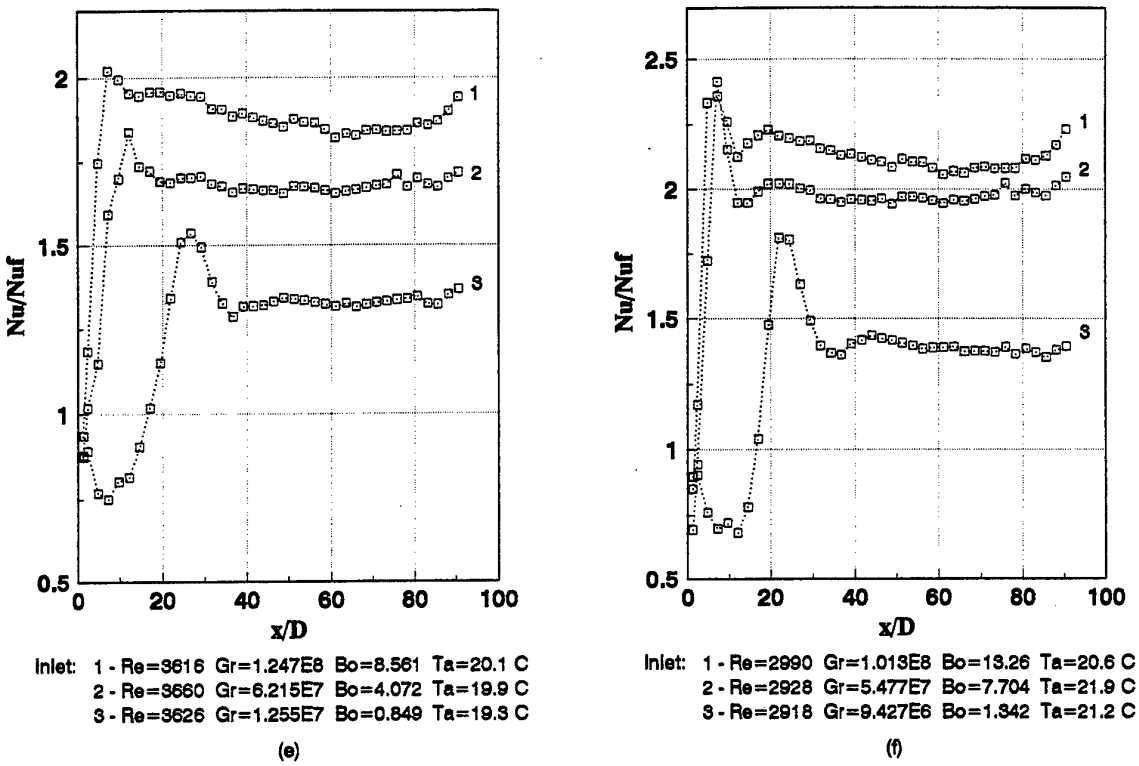

Figure 8 Distribution of normalised Nusselt number for downward flow mixed convection

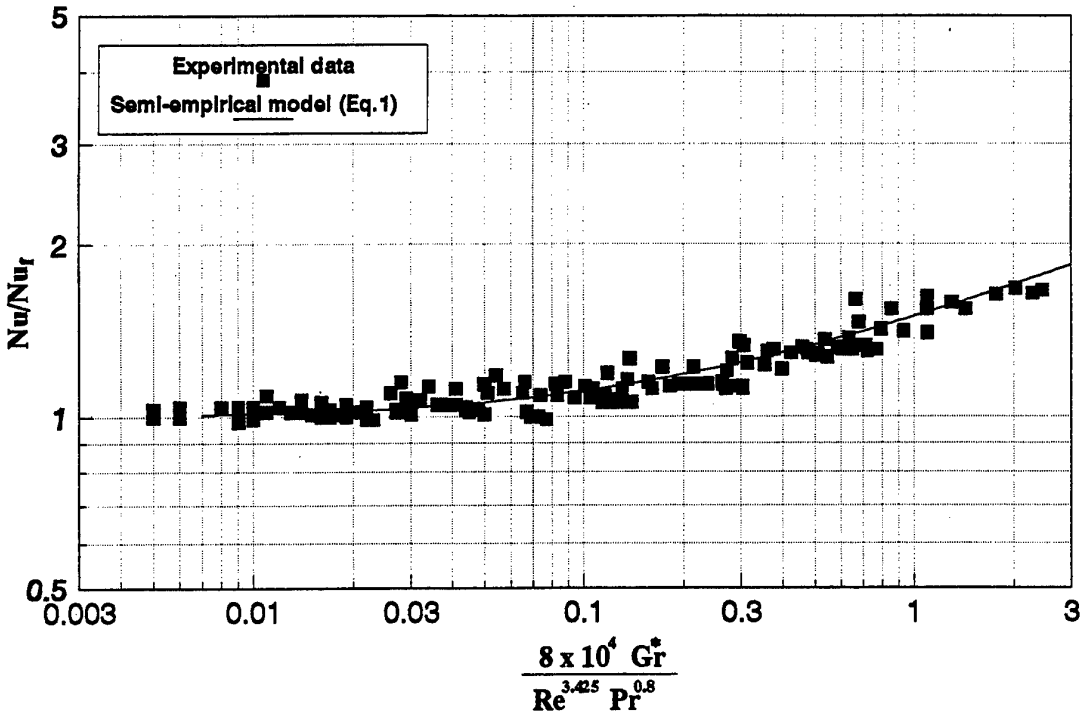

Figure 9 Downward flow mixed convection for downstream conditions (x/D = 41.5 to 90.5)

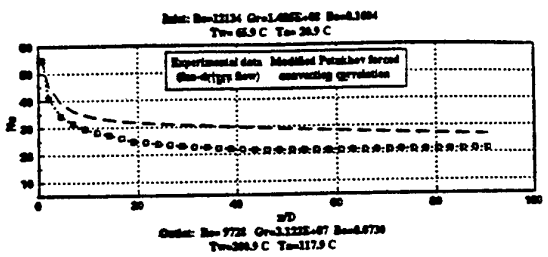

(a)

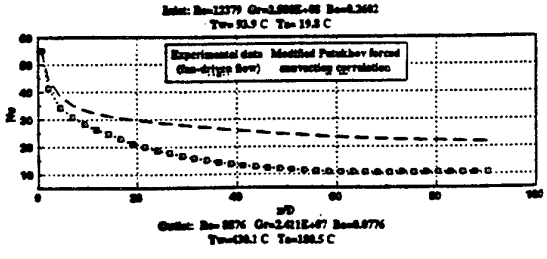

(b)

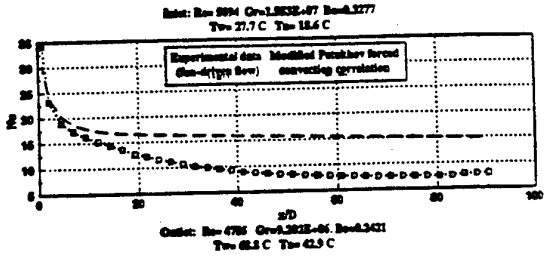

(c)

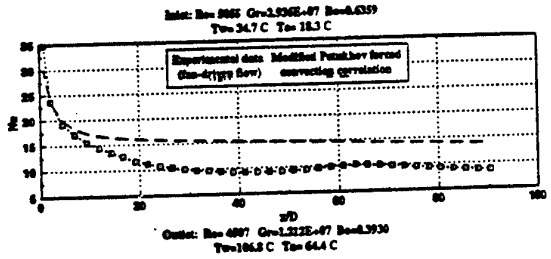

(d)

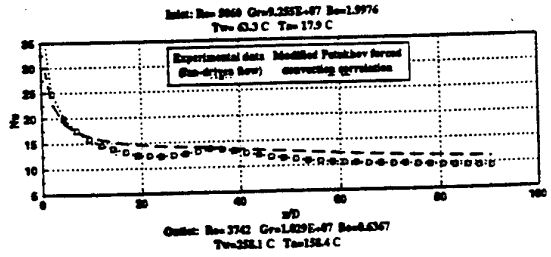

(e)

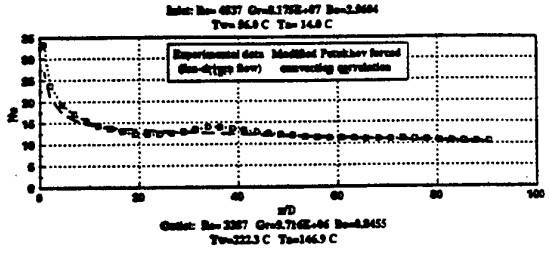

(f)

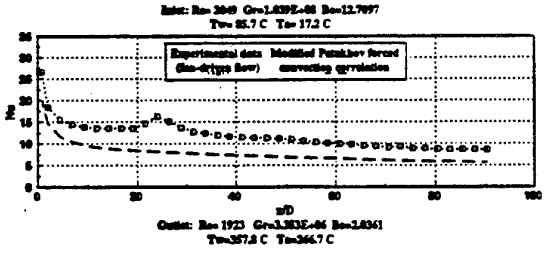

(g)

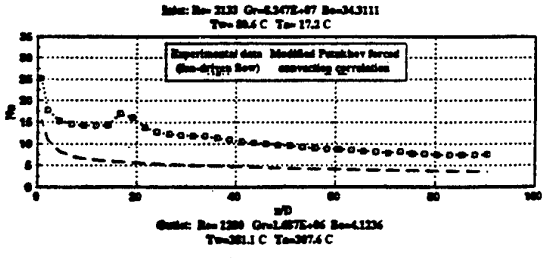

(h)

Figure 10 Local Nusselt number distributions for upward flow mixed convection

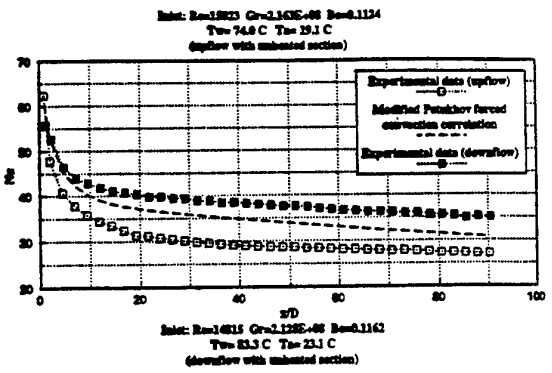

(a)

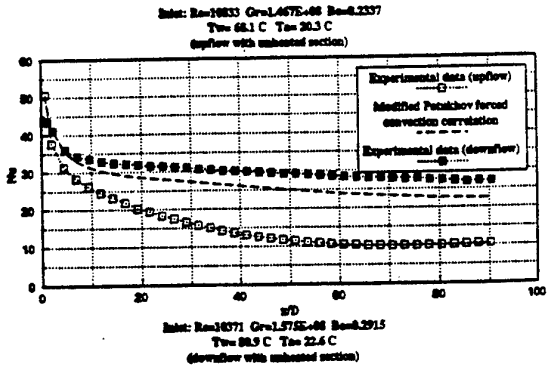

(b)

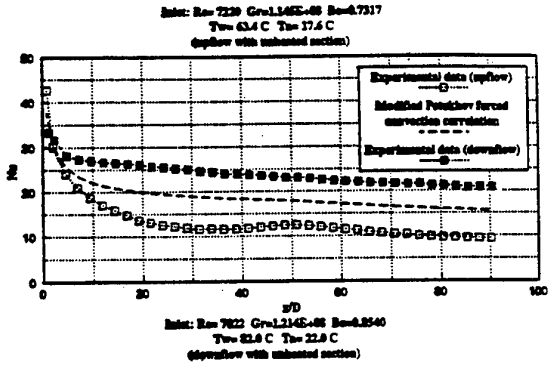

(c)

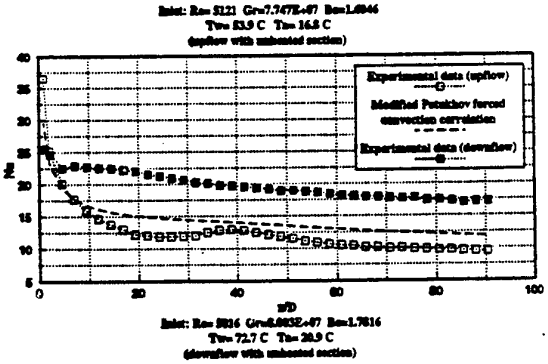

(d)

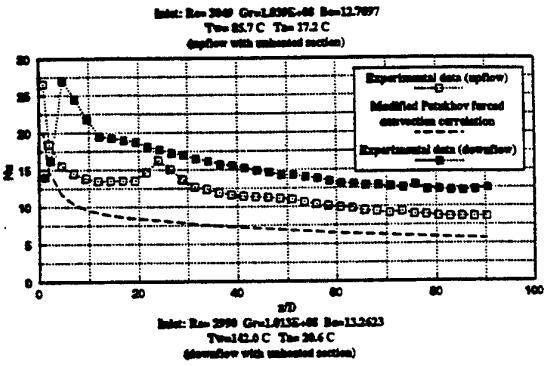

(e)

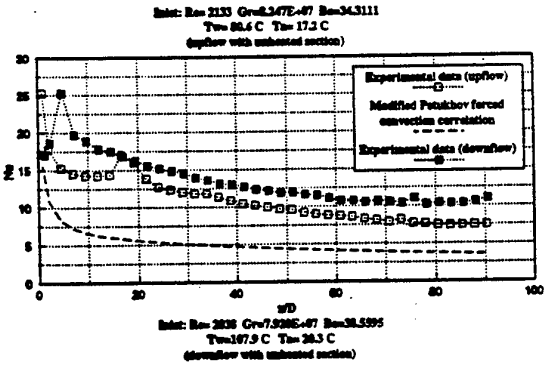

(f)

Figure 11 Comparison between Nusselt numbers for upward and downward flow mixed convection

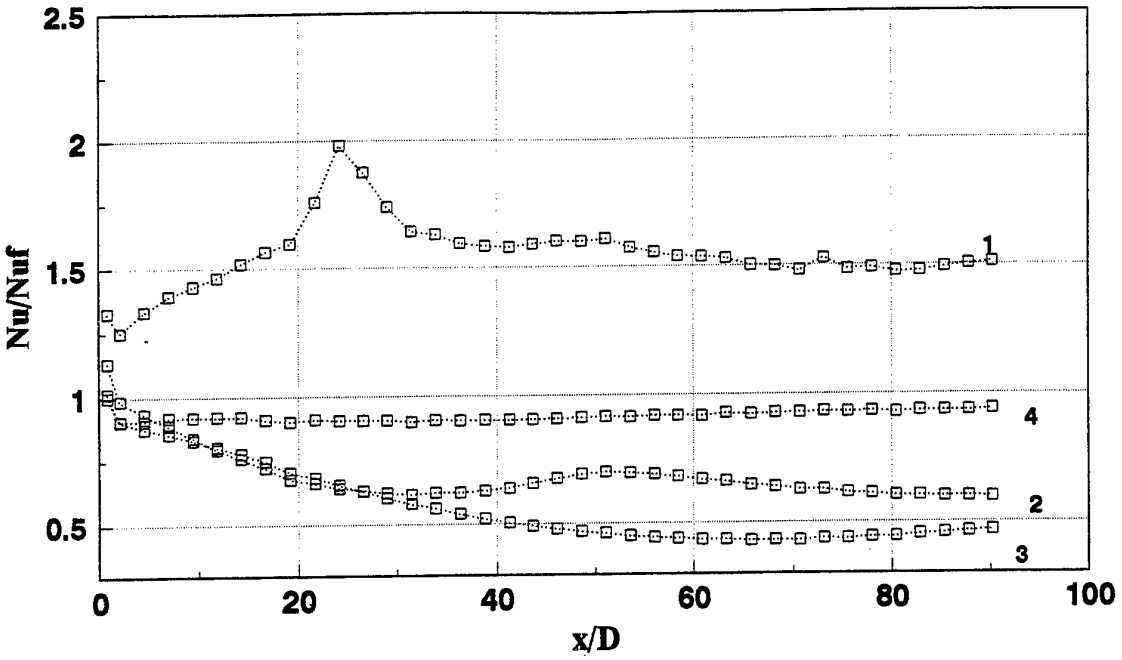

Inlet: 1 - Gr=1.039E8, Re=3049, Bo=12.71, Ta=17.2 C 3 - Gr=1.467E8, Re=10833, Bo=0.234, Ta=20.3 C
2 - Gr=1.145E8, Re=7220, Bo=0.732, Ta=17.6 C 4 - Gr=1.714E8, Re=16886, Bo=0.060, Ta=21.4 C

Figure 12 Distribution of normalised Nusselt number for upward flow

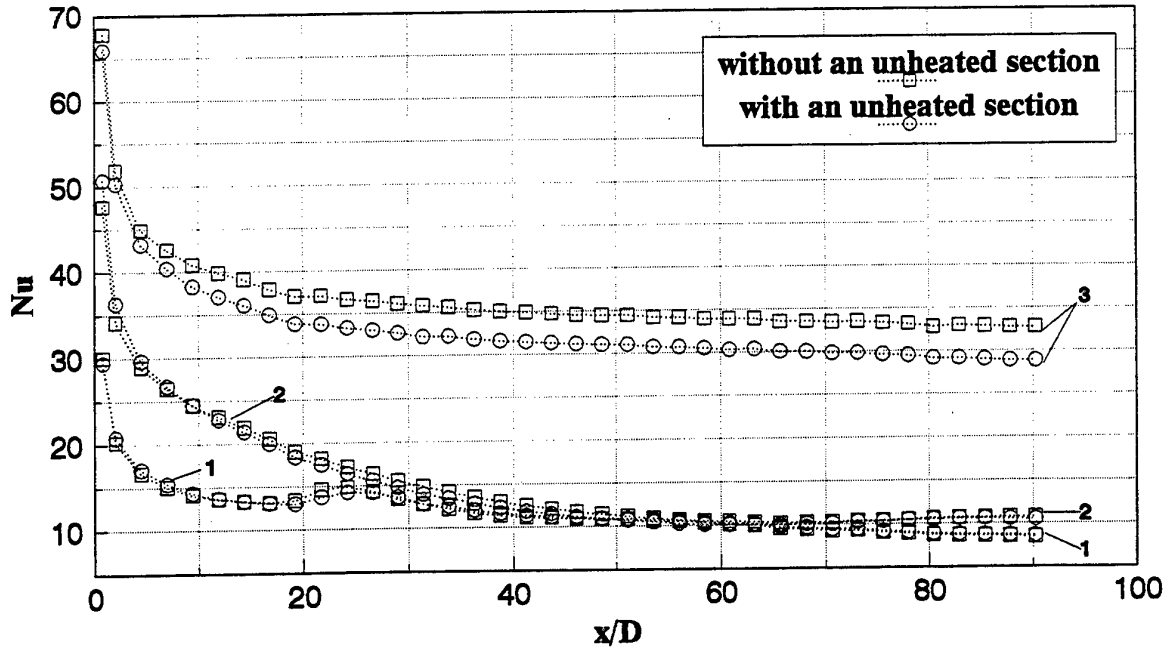

Inlet: 1 - Gr=8.105E7, Re=3773, Bo=4.786, Ta=22.3 C 2 - Gr=1.190E8, Re=9486, Bo=0.299, Ta=22.0 C
3 - Gr=2.249E8, Re=16087, Bo=0.093, Ta=23.0 C

Figure 13 Nusselt number distribution for upward flow with and without an unheated development section

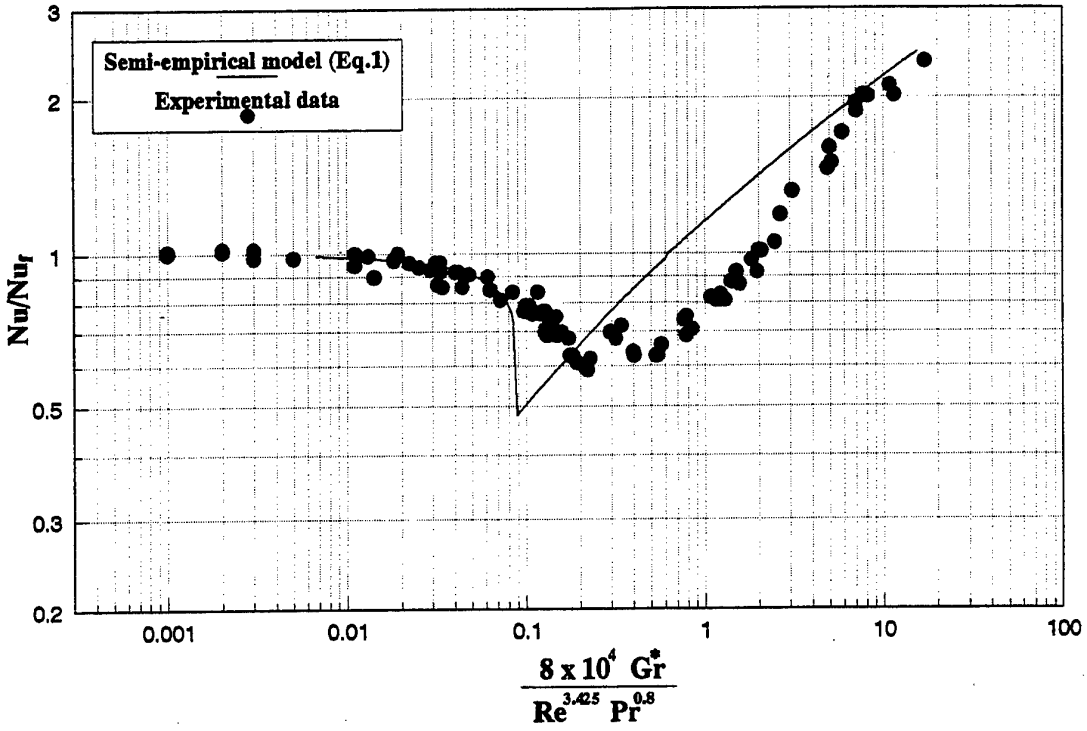

Figure 14 Upward flow mixed convection for x/D = 26.6

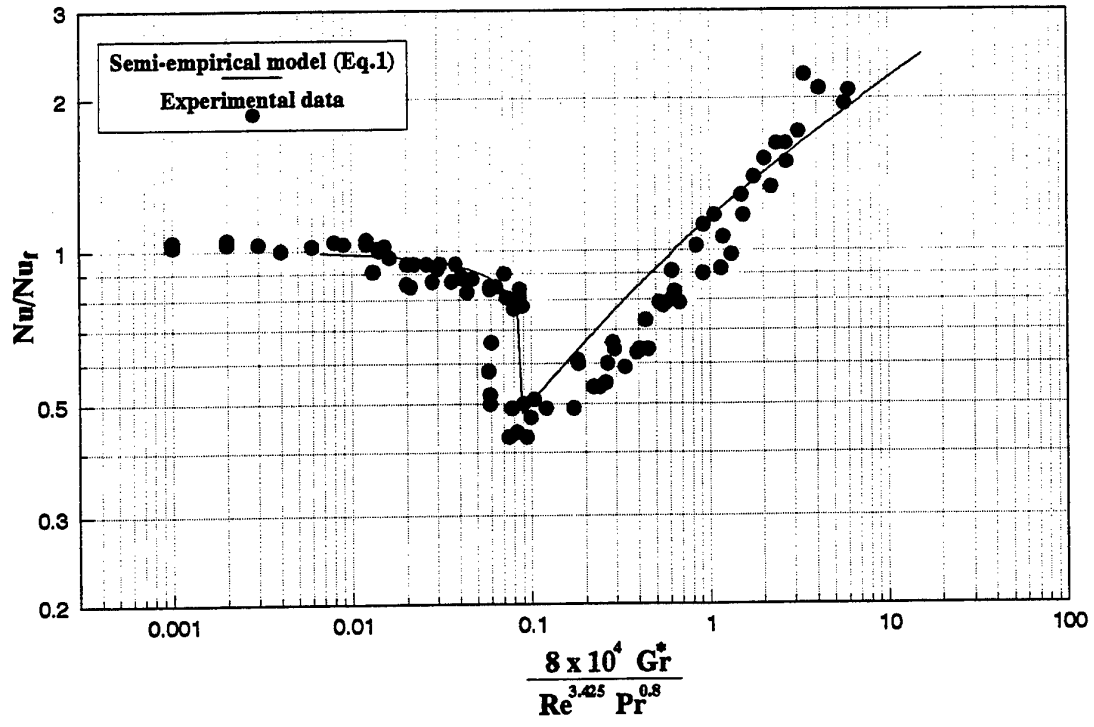

Figure 15 Upward flow mixed convection for x/D = 90.3

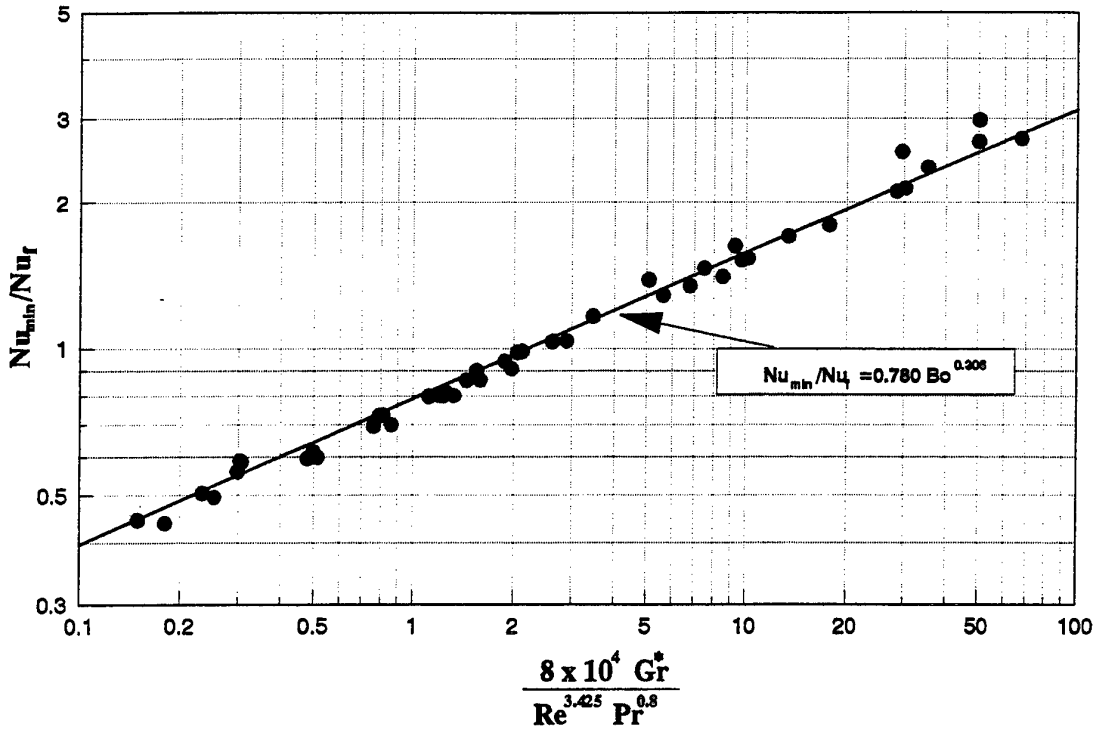

Figure 16 The first minimum value of Nu/Nuf at various axial locations for upward flow with an unheated development section

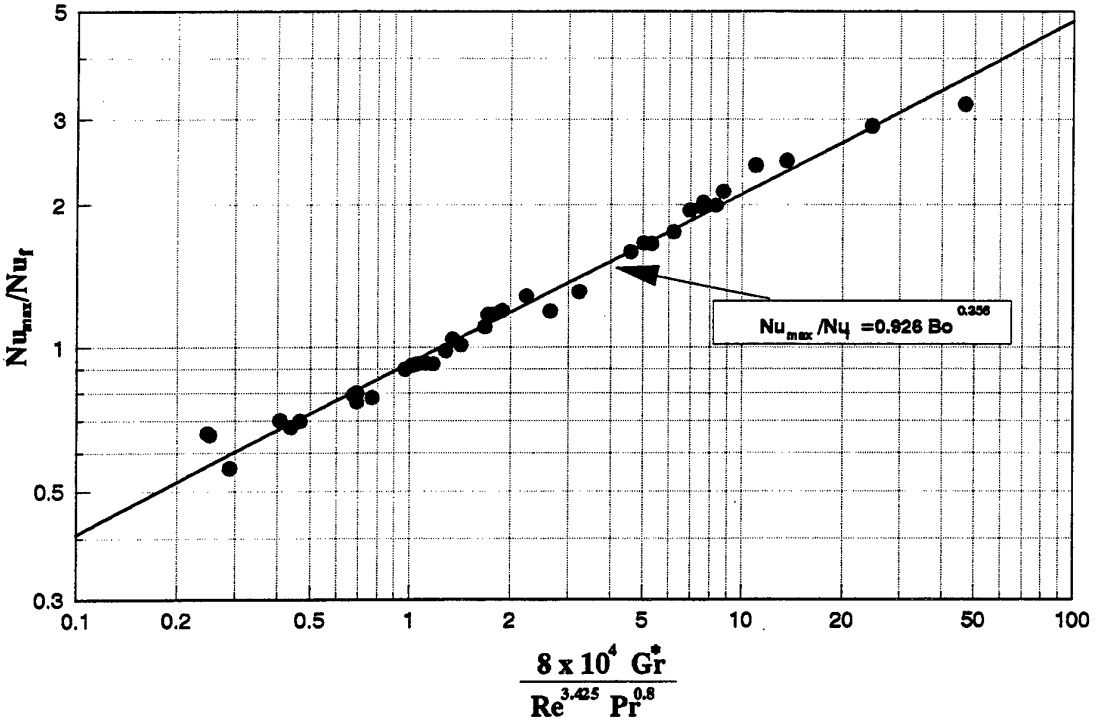

Figure 17 The first maximum value of Nu/Nuf at various axial locations for upward flow with an unheated development section

Session 3

Flow with Interfaces

TURBULENT TRANSPORT PROCESSES ACROSS FLUID-FLUID INTERFACES

V. De Angelis and S. Banerjee

Department of Chemical Engineering
University of California Santa Barbara
Santa Barbara, California

ABSTRACT

The mechanisms governing turbulent heat and mass transfer across fluid-fluid interfaces are difficult to unravel because measurements and full simulations are difficult to perform due to interface motion and deformation. Recent developments in laser anemometry and particle imaging/tracking methods, as well as in direct numerical simulation techniques, now allow investigations of transport processes between two turbulent streams separated by a wavy interface. While this is a subset of the more general problem, in which the interface shape can assume configurations in the form of slugs, plugs, dispersed bubbles etc., nevertheless the insight gained from investigations of transport processes across wavy interfaces is still valuable for more complex multiphase flows.

This paper briefly discusses experimental and numerical investigations that indicate qualitative similarity between turbulence structures, in the vicinity of a continuous interface, to those in wall turbulence – if the shear rates correspond. There are of course detailed differences, which depend on the interfacial tension, fluid densities and viscosities for the gas and liquid streams. At atmospheric conditions, and restricting consideration to the wave scales important for scalar transfer (capillary waves), the differences are primarily on the liquid side. The liquid-side tangential turbulent fluctuations peak right at the interface, whereas on the gas side they peak a small distance away – much like in wall turbulence. In some sense, the liquid therefore sees the interface much like a slip surface, whereas the gas sees it much like a wavy solid wall. Furthermore, the patterns of shear stresses and pressure are primarily controlled by the quasi-streamwise vortical structures on the gas-side, with their associated sweeps and ejections. Quasi-streamwise vortices also arise near the interface on the liquid side, but the associated sweeps and ejections do not correlate with the interfacial shear stress pattern. Low-speed-high speed streaky regions are also seen near the interface on both sides, with their spanwise spacing scaling with kinematic viscosity and friction velocity (defined for each side as the square root of the ratio between the interfacial shear stress and the fluid density). Ejection and sweep frequencies also scale with the same parameters.

Turning now to heat and mass transfer mechanisms, they are primarily controlled by the sweeps, with ejections playing an important role in a certain range of Schmidt numbers on the gas side. An understanding of the dominant mechanisms allows a simple parametrization of the scalar transfer velocity on each side, which compares well with experiments and direct numerical simulations. Capillary waves appear to have little effect on the parametrizations for scalar transfer velocity. More of a wave effect is seen for scalar transfer from a solid wavy wall arising from flow separation and reattachment around the crests in a wave train. Such separation does not appear to occur for capillary waves at a mobile interface and this explains the small effect seen. While these results pertain primarily to scalar transfer between separated streams there are indications that they carry over to more complex flow regimes if the length scales of the interfacial structures are of the order or larger than capillary waves.

1 INTRODUCTION

Turbulence structure at boundaries govern high Reynolds number transport processes and must be elucidated for applications in the process and power industry, as well as in several atmospheric and environmental problems. A number of investigations have dealt with the phenomena that occur near solid boundaries. Work by Kline et al[1] and many others have shown that streaks of low-speed/high-speed fluid form near the wall, and that these break down periodically in a spectacular phenomenon called a "burst", in which fluid is ejected from the wall layer with significant wall-normal velocities. These "ejections", and the associated "sweeps" that follow account for nearly 80% of the Reynolds stresses observed in boundary layers. Typical spanwise spacing of the streaks are $\lambda_w^+ \sim 100$, where λ_w^+ is the non-dimensional spanwise spacing – the non dimensionalizing variables being the shear velocity, $u_{\tau w} = \sqrt{\tau_w/\rho}$ and the kinematic viscosity, ν. Rashidi and Banerjee [2], amongst others, have shown that, at sufficiently high Reynolds number, inner variables give a non-dimensional time between bursts $T_{\tau w} = (u_{\tau w}^2/\nu)\overline{T}_w \sim 90$.

In contrast to this understanding of the main features of turbulence near solid boundaries, albeit with many outstanding questions regarding the reasons for the phenomena, very little was known about turbulence near fluid-fluid boundaries till recently. This, in spite of the importance of near-interface phenomena in determining mass and heat transfer rates in a variety of contacting equipment like gas absorbers

and condensers, as well in geophysical problems like gas transfer at the air-sea interface.

We do know that at fluid-fluid interfaces the mass transfer coefficient, β, varies as the 1/2 power of the molecular diffusivity, D, whereas at solid boundaries β varies roughly as the 2/3 power of D. Obviously molecular effects are more important at solid boundaries, where turbulence is damped more than it is near clean, mobile interfaces.

The importance of the problem has led to many models for mass and heat transfer starting with that of Lewis and Whitman[3] which postulates a film of stagnant fluid near the interface, giving $\beta \propto D$, which is, however, incorrect. Higbie [4] suggested a "penetration" or "surface renewal" model to correct the dependence on D. This results in $\beta \cong (D/\overline{\tau})^{1/2}$ where $\overline{\tau}$ is the average time between "surface renewals". These models capture some features of the phenomena, but do not incorporate the effect of the underlying hydrodynamics since the parameter, $\overline{\tau}$, is left unspecified.

Fortescue and Pearson[5] proposed that the time between renewals could be approximated by a scale related to the integral time and velocity scales of the far field turbulence suggesting that $\overline{\tau} \cong \Lambda_\infty/\sqrt{\overline{u'^2}}$, where Λ_∞ is the integral length scale and $\sqrt{\overline{u'^2}}$ is the r.m.s. velocity fluctuations. When the the bulk turbulence was grid-generated, they obtained good agreement with experiments for the mass transfer coefficient at free (unsheared) surfaces.

At about the same time Banerjee et al.[6], and subsequently Lamont and Scott[7], suggested that the time between renewals was related, however, to the Kolmogorov time scale, proposing $\overline{\tau} \cong \sqrt{\nu/\epsilon}$, where ϵ is the turbulence dissipation rate.

Unlike the model of Fortescue and Pearson where the renewals are thought to be mainly due to the large eddies, Banerjee focused on the small eddies in the viscous dissipation range. Both of these so-called large and small-eddy models predicted the data against which they were compared rather well. The controversy continued for some time until Banerjee[8] used a theory due to Hunt and Graham[9] to calculate the surface divergence spectrum and developed the following analytical expression for the effect of eddy Reynolds number on scalar transfer rates in the absence of interfacial shear.

$$\frac{\overline{\beta} Sc^{0.5}}{u'_\infty} \cong \frac{C}{Re_T}(0.3(2.38Re_T^{3/4} - 2.14Re_T^{2/3}))^{1/4} \quad (1)$$

Here $\overline{\beta}$ is the mass transfer rate, Sc is the Schmidt number equal to ν/D, u'_∞ is the far-field integral velocity scale of the turbulence, C is a constant of the order 1, and Re_T is an eddy Reynolds number based on the far-field integral velocity scale, length scale and kinematic viscosity.

Banerjee[8] clarified that the "large eddy" model of Fortescue and Pearson[5] held for relatively low values of the Reynolds number, $Re_T = u_\infty(2\Lambda_\infty)/\nu$, whereas the "small eddy" model of Banerjee et al.[6] held for high values of Re_T.

It should be noted that the theory proposed in Banerjee[8] only applies strictly to far-field turbulence that is homogeneous and isotropic, and at an unsheared gas-liquid interface *i.e.* , there is no wind stress imposed. In most practical situations, however, shear is imposed on the interface and the situation is further complicated by the formation of waves. Very little was known about such problems until recently.

The present study is aimed toward a better understanding of such phenomena via direct numerical simulation (DNS), *i.e.* solving the full time-dependent 3-D Navier-Stokes equations without any closure model. This DNS aims to calculate the mean statistical properties of turbulence on both sides of the near-interface region, clarify mechanisms related to the coupling fluxes between the phases, with particular regard to the role of turbulence structures (*i.e.* their appearance and evolution in the immediate neighborhood of the fluid-fluid interface) and to develop scalar transfer parametrizations based on the physical insight gained from the DNS.

Before discussing the results we use the Lewis-Whitman[3] film theory to approximate the scales controlling the various transport processes to ensure the correct level of resolution.

Consider, as a scale-limiting case, transfer of sparingly soluble gases such as carbon dioxide and methane at the ocean surface. At wind speeds below those at which wave breaking occurs, typical gas transfer velocities, controlled by the liquid side, are $\sim$O(10 cm/hr). Since molecular diffusivities of such gases in water are $\sim$O(10^{-5} cm^2/s), it follows from film theory that the main concentration changes occur in layers $\sim$O(10^{-2} mm) in thickness. For moisture transfer on the air side, transfer velocities are $\sim$O(1 cm/s) and diffusivities are $\sim$O(0.1 cm^2/s) so that concentration changes occur over regions of $\sim$O(1 mm).

These scales are also of the order that would be expected in typical industrial applications.

Thus scalar transfer occurs over scales that are at most affected by capillary waves. It therefore becomes possible to examine the controlling processes by DNS over a domain size of the order of several capillary waves, and in isolation from surface deformations that are larger in scale.

Both lab-scale experiments and direct numerical simulation may therefore be used to understand the controlling mechanisms. These are now discussed briefly. A brief description of the numerical scheme used to compute the velocity and scalar fields in the DNS is also given in the Appendix.

The typical flow geometry, investigated as a canonical problem is shown in Figure 1. Gas flows contercurrent to the liquid flow. The interface for moderate wind speed, $\sim$O(3-6 m/s), forms capillary waves that have amplitude of roughly a millimiter. Before discussing the effect of waves, however, we examine the turbulence structures on the liquid and gas side in the simpler situations in which the interface is kept

flat.

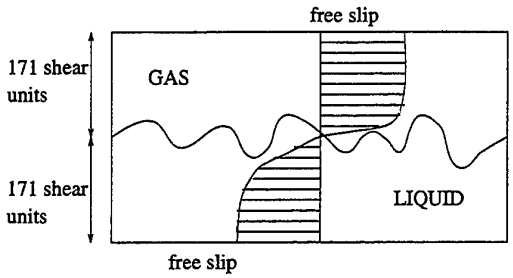

Figure 1: Geometry of the Simulation

2. GAS-LIQUID FLOW ACROSS FLAT GAS-LIQUID INTERFACES

Consider now experimental conditions set to keep the liquid Froude number low and the gas velocity low enough to be well away from Kelvin-Helmhotz instabilities. A non-wavy surface can be obtained even when quite high shear rates are imposed, as shown by Rashidi and Banerjee[2].

They visualize the liquid side flow, using a microbubble tracer technique, in a situation in which there is a wall at the bottom of the liquid stream. The high-speed, low-speed streaks seen by many investigators are found near the wall. However similar structures are also seen at high enough shear rates at the interface – whereas at low shear rate the interface structure looks patchy. Clearly there is a shear rate at which transition occurs, but once streaks are established in the near interface region, the similarity between the bursts seen in the vicinity of the wall and of the interface is remarkable. This is shown in Figure 2, representing a side view of the liquid stream, with gas on the top going contercurrent to the liquid.

Figure 2: Bursts from the liquid surface for contercurrent flow

Quantitative similarities were also found by Rashidi and Banerjee[2]. If the interfacial streak spacing is non-dimensionalized with the interfacial shear rate, then $\lambda_I^+ \sim 100$, where $\lambda_I^+ = \lambda_I u_{\tau i}/\nu$. Thus the interfacial streak spacing scales in the same way as the wall streak spacing, provided one uses the interfacial shear stress to obtain the velocity scale. Furthermore the period between bursts is seen to scale in the same way as at the wall, i.e. $\overline{T}_{BI}^+ \cong 90$.

The criterion for transition from the patchy structures seen at no shear, to the streaky structures was clarified through direct numerical simulations by Lam and Banerjee[10]. They showed that the criterion for formation of streaky regions near a boundary depends on a non-dimensionalized mean shear rate (representing the ratio between shear and Reynolds stresses) which must be greater than one. Later the finding regarding interfacial bursts and streaks was confirmed by Komori et al.[11].

Even if the qualitative picture seems the same at a sheared interface and at a solid boundary, there are detailed differences between the two cases that will play a role in mass and heat transfer processes.

Lombardi et al.[12] did a simulation assuming a flat interface. They resolved about 170 shear-based units, h^+, on each side of the interface, where h^+ is based on the interfacial shear velocity, $u_{\tau i}$.

Runs at different density ratios (R^2) between the fluids were performed. The gas and liquid were coupled through continuity of velocity and stress boundary conditions at the interface.

The interfacial plane itself showed regions of high shear stress and low shear stress, with low shear stress regions corresponding to the low speed regions and the high shear stress to the high speed regions. The low shear stress regions are streaky in nature with high shear stress islands. At the edges of the high shear stress regions, vortices are seen to spin up on both sides of the interface. These are initially in the plane normal to the interface but subsequently are stretched in the quasi-streamwise direction by the mean flow. These quasi-streamwise vortices are known to play a major role in the ejection-sweep processes observed in wall turbulence, and they do the same at the gas-liquid interface.

At this point it is worth considering how the high shear stress regions form. This can be clarified by considering a quadrant analysis of the velocity field over the interface in which velocity fluctuations in each quadrant of the Reynolds stresses are correlated with shear stress at the interface. In the first quadrant both the streamwise and interface normal velocity fluctuations are positive. In the second, the streamwise component is negative but the interface normal component is positive. This corresponds to an ejection of low speed fluid. In the third quadrant both the streamwise and the interface-normal velocity fluctuations are negative, and in the fourth the streamwise component is positive whereas the interface-normal component is negative. The fourth quadrant then corresponds to a sweep in which high-speed fluid is brought towards the interface. Consider now the correlation of each quadrant of such velocity fluctuations with the interfacial shear stress shown in Figure 3 (top) on the gas side. It is clear that sweeps, i.e., in the fourth quadrant, lead to the high shear stress regions whereas ejections lead to the low shear stress regions. This is what is observed in wall turbulence at a solid boundary and therefore the gas sees the liquid surface much like a solid boundary.

However, if we look at Figure 3 (bottom), it is immediately clear that no such correlation exists on the liquid side. In fact, all the quadrants have similar

behavior with regard to the shear stress regions that occur below the high speed sweeps on the gas side, i.e., the motions that bring high speed fluid from the outer regions to the interface on the gas side, lead to the high shear stress at the interface. Conversely, ejections on the gas side which take low speed fluid away from the interface into the outer flow, strongly correlate with low shear stress regions. The liquid does not behave in this way and does not dominate the pattern of shear stress on the interface.

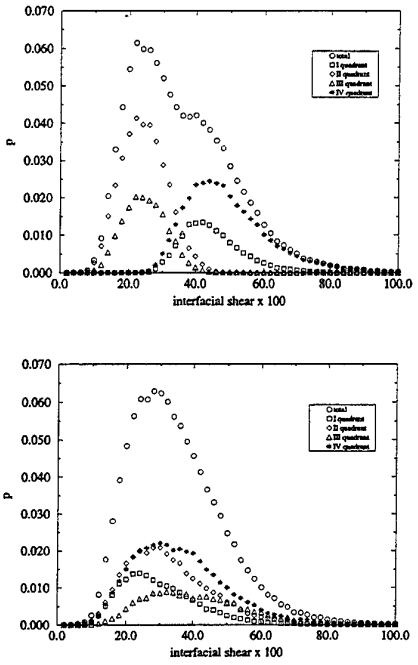

Figure 3: Probability of strongly coherent events classes according to quadrant as a function of interfacial shear stress in the region over which the events occur top: gas; bottom: liquid

The difference between the gas and the liquid phases in the near interface region is further clarified by observing the velocity fluctuations on each side of the interface as shown in Figure 4. The top portion of the figure is for the gas whereas the bottom figure is for the liquid. The gas, as is evident, behaves much like flow over a solid wall. The fluctuations are almost identical to that at a solid boundary, in all directions – streamwise, spanwise, and wall-normal. On the other hand, the liquid, as evident from the bottom figure, has the largest fluctuations in the streamwise and spanwise directions right at the interface itself. It sees the interface virtually as a free slip boundary, except for the mean shear. As a consequence, vertical fluctuations vary as the first power of normal distance, and the square of the normal distance, on the liquid and gas sides, respectively.

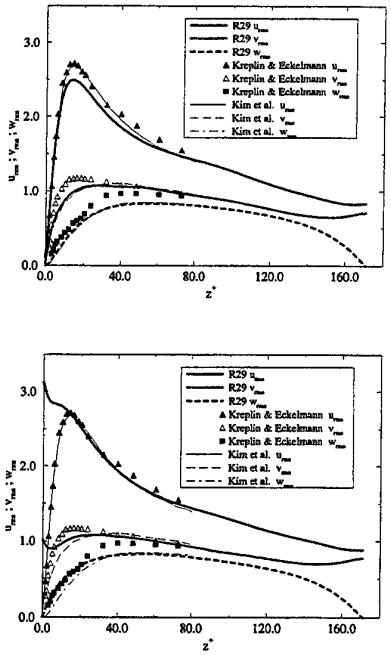

Figure 4: Results from direct numerical simulation on rms velocity fluctuations, top: gas; bottom: liquid

These observations are of some importance for the scalar flux on the gas and liquid sides. The mass transfer velocity β^+ is defined as:

$$\beta^+ = \frac{1}{\sqrt{2ReSc}(c_o - c_b)} \frac{du}{dx_3}$$

$$c_b = \frac{\int_0^{2h} \overline{u_1 c} dx_3}{\int_0^{2h} \overline{u_1} dx_3} \qquad (2)$$

where $\frac{du}{dx_3}$ is the nondimensional gradient at the interface and c_b and c_o are the bulk and interface concentrations. Mass transfer takes place at the interface by conduction only, therefore it is enhanced when bulk fluid is conveyed to the interface region, e.g. by sweeps. We extend the quadrant analysis and look at the correlation of the Reynolds stress – and therefore of the turbulence structure, in the various quadrants with the instantaneous value of mass transfer velocity β^+ at the interface.

Results are reported in Figure 5 for Sc=1 and Sc=100 on the gas side and liquid sides. In all the cases, except for Sc=100 on the gas side, IV quadrant events (sweeps) are seen to generate the highest values of the mass transfer velocity.

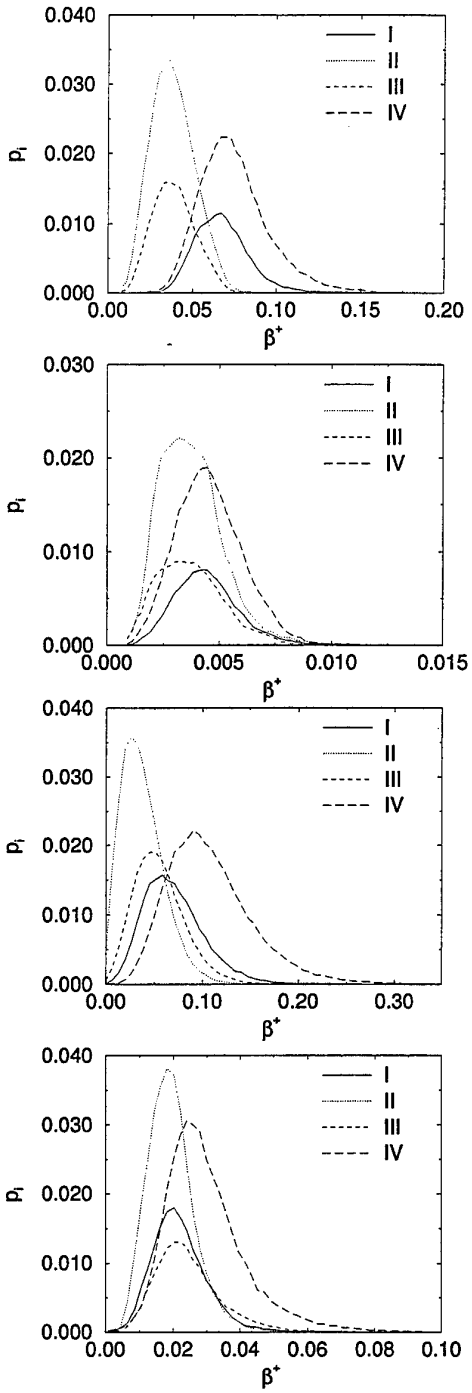

Figure 5: Prob. of strongly coherent events according to quadrant as a function of interfacial flux, β^+, in the region over which the events occur from top: gas Sc=1; Sc=100; liquid Sc=1; Sc=100

This is evident when looking at the probability of such an event to occur (f_p) and at the fraction of the total flux through the interface associated with it (f_h), as in Table I. On the liquid side the sweeps carry a larger fraction of mass flux ($\sim$ 0.50), than their probability ($\sim$ 0.30). On the liquid side the interface can be efficiently renewed by sweeps, because the horizontal fluctuations are unimpeded. On the gas side the situation in modified by the different boundary conditions. At low Sc number, sweeps and Quadrant I events are seen to be the most efficient for scalar transfer, but when the Sc number increases, and the thermal boundary layer becomes thin, sweeps cannot efficiently penetrate the concentration layer and the role of ejections becomes important as in the Sc=100 case. The vertical velocity fluctuations very close to the interface decrease fast (as $\sim x_3^2$) and limit the mass fluxes.

Table I: Reynold stress and total heat fraction corresponding to II and IV quadrants.

Sc (gas)	1	100	Sc (liq)	1	100
f_p in II	0.36	0.38	f_p in II	0.29	0.32
f_p in IV	0.33	0.32	f_p in IV	0.34	0.37
f_h in II	0.25	0.34	f_h in II	0.15	0.20
f_h in IV	0.46	0.36	f_h in IV	0.52	0.52

In Figure 6 we show a comparison between the DNS results and the prediction of surface renewal theory on the liquid side for Sc=56. Surface renewal theory hypothesizes that the mass fluxes across the interface are enhanced by sweeps of fluid, that bring fresh bulk fluid close to the interface. When a sweep impacts the interface the mass transfer coefficient reaches a maximum and then decaies in time as the near interface fluid saturates, till the region is eventually refreshed by the next sweep.

In the bottom of the figure the Reynolds stress and the vertical fluctuating velocity are shown as time proceeds. When they are both negative, a sweep is impacting the interface. In the center figure the corresponding mass transfer velocity is shown and compared to the values predicted by surface renewal theory. The top figure shows the total mass flux over time. The dotted curve in the center and top figures are computed using, respectively:

$$\sqrt{\frac{D}{\pi t}} \text{ and } 2\sqrt{\frac{Dt}{\pi}} \ . \tag{3}$$

It appears that the mass transfer velocity increases when a sweep is present on the interface. The decay of the mass transfer velocity appears to be faster than $t^{-1/2}$. It should be noticed, however, that the sweep effect persists at the interface and travels with the liquid mean velocity, therefore its effect propagates further along the interface, leaving the point of observation. This means that in a Lagrangian frame, the DNS is closer to the surface renewal theory.

To clarify this point, in Figure 7 we report the contour of the Reynolds stress (bottom) and of the mass transfer velocity (top). The vertical axis is time, and the horizontal the x_1 position. The graph describes how a sweep moves along a line parallel to the streamwise direction, as time passes. The arrows indicate a sweep event and the corresponding mass transfer velocity. The sweeps appear to survive for more than 300 wall units, and the patch of high mass flux moves with it.

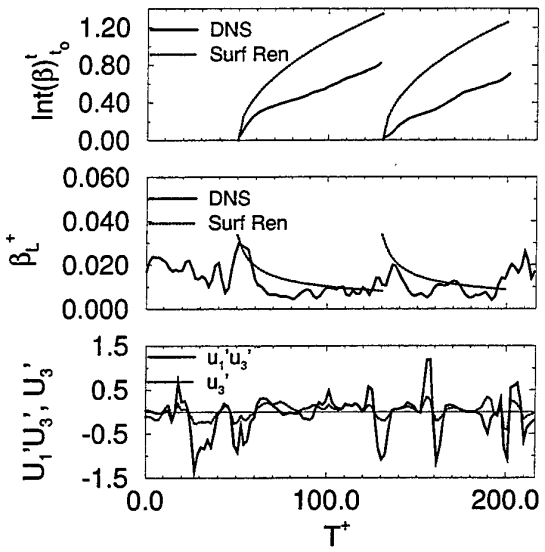

Figure 6: DNS and Surface Renewal theory

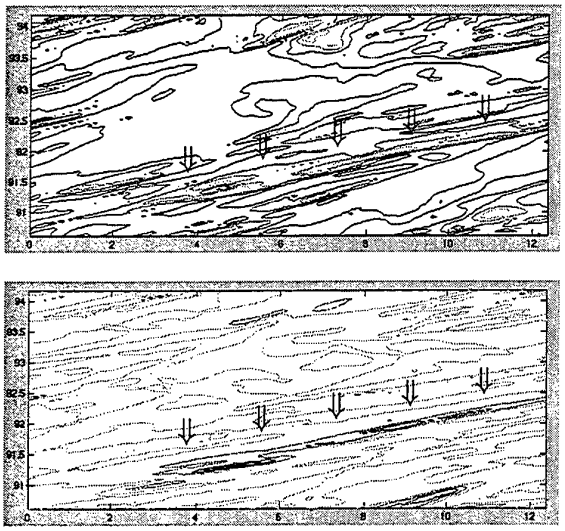

Figure 7: Streaks and β^+ moving at different x_1 locations (horizontal axis), as time progresses (vertical axis)

Based on the results of the quadrant analysis, a model based on surface renewal theory seems appropriate for liquid side mass transfer. Sweeps are seen to control the mass transfer process, and the time history of β^+ in Figure 6 also supports this hypothesis.

On the gas side, at first glance, it seems that this assumption would be less well founded. In fact we find that all large vertical (interface-normal) velocity fluctuations are responsible for high mass transfer rates. Large vertical fluctuations are, however, mainly related to the bursting process thus also supporting parametrizations based on surface renewal-type models with both sweeps and ejections being important.

The values of β^+ are shown in Figure 8 for the gas and the liquid, and in fact the high Sc number cases are in excellent agreement with correlations proposed by Banerjee [13, 8], based on surface renewal theory. Banerjee assumed that ejections/sweeps (the burst cycle) dominated mass transfer at high Schmidt numbers, and since these events scale with the friction velocity, he was able to derive, for the gas side and the liquid side, respectively, nondimensional mass transfer coefficients:

$$\beta_g^+ = 0.07 \text{ to } 0.09 Sc^{-2/3} \quad (4)$$

$$\beta_l^+ = 0.108 \text{ to } 0.158 Sc^{-1/2} \quad (5)$$

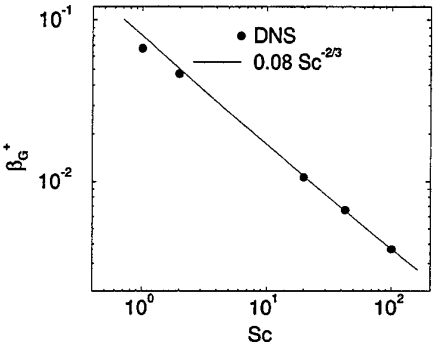

a)

Figure 8.a: β^+ as function of Sc. gas

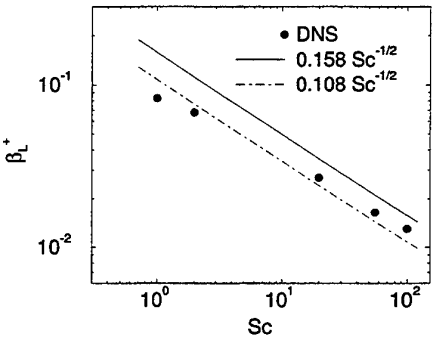

b)

Figure 8.b: β^+ as function of Sc. liq.

Support for these correlations comes also from experiments, some of them performed after the correlations where proposed. For the liquid side, equation (5) is compared with wind-wave tank data for SF_6 transfer rates from Wanninkhof and Bliven[14] in Figure 9. Again the agreement is good noting that u_* is probably somewhat over estimated as the form drag was not separated out. For the gas side the lower bound of equation (4) is compared with the moisture transfer data of Ocampo-Torres et al.[15] in Figure 10. The agreement, again, is good.

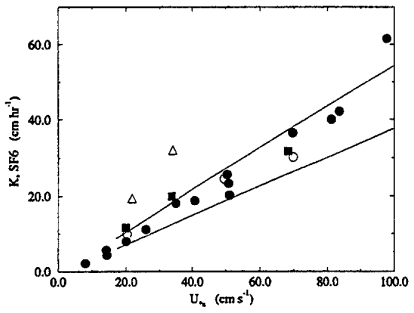

Figure 9: Comparison of Equation (5) with the data by Wanninkhof and Bliven

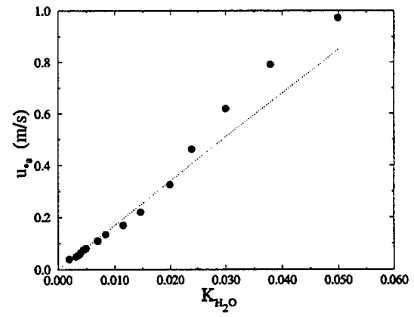

Figure 10: Mass transfer coefficient v.s. u_* (Ocampo-Torres et al) compared with Equation (4)

3 GAS FLOW OVER WAVY WALL

We now examine in more detail what happens when the boundary is wavy. As pointed out earlier the gas sees the liquid virtually as a solid wall because the liquid has high inertia. Therefore, it is interesting to examine the case where the waves form a no-slip boundary. The wavelengths of the profile considered are comparable to that of capillary waves. Therefore this case can elucidate some of the effects on gas side mass and momentum transfer, that will then help in understanding the full problem of gas and liquid interacting across a deforming interface.

Table II: Matrix of runs performed.

Case	a/λ	$\lambda/2h$	h^+	a
S1	0.025	2.09	85.5	8.95
S2	0.050	1.04	85.5	8.95

The parameters of the simulation are shown in Table II, in which a is the amplitude of the (sine) wave and λ is the wavelength. A detailed analysis of the velocity field and its statistics can be found in De Angelis *et al.* [16]. It is worth summarizing some of the characteristics of the flow. In Figure 11 the average streamlines over one period for the S1 case, and over two periods for the S2 case, are shown. In the first case the mean profile does not show recirculation, in the second case the flow separates behind the crest and recirculates in the valleys of the wave train.

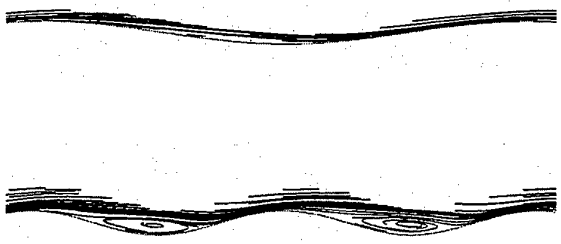

Figure 11: Streamlines of the av velocity. S1 top, S2 bottom

We find that the streaky structure and quasi-streamwise vortices repeat somewhat regularly over the wavy surface. The quasi-streamwise vortices were identified using a scalar indicator related to the streamline rotation, Ω_1, defined using the complex eigenvalues of the velocity gradient tensor. In Figure 12 the iso-contours of positive and negative Ω_1 are shown for the S1 and the S2 cases. In the S1 case most of the quasi-streamwise vortices initiate after $x/\lambda = 0.5$, *i.e.* after the reattachment point. In the S2 case they initiate after $x/\lambda = 0.7$, again after the reattachment point. In the S2 case it is evident that the quasi-streamwise vortices are always generated at the region of favorable pressure gradient and that they extinguish in the next reattachment point where they are replaced by new vortices arising from the wall region.

A simple scenario for the phenomena can be developed from these considerations. Fluid impacts the wall at the reattachment point, and the kinetic energy associated with it, in part redistributes to the spanwise direction, and in part generates high shear stress in the region downstream of the reattachment point. A very thin, but energetic layer of streaky (low speed-high speed) fluid develops and propagates over

the crest of the wave and over the recirculation region, transported by the mean flow. When the next reattachment point is approached, this streaky region is carried by the fluid stream and impacts the wall. The process then starts again. The quasi-streamwise vortices are generated in the region after the reattachment point and they are also transported by the mean flow till they are replaced by new streamwise vortices coming from the next reattachment region.

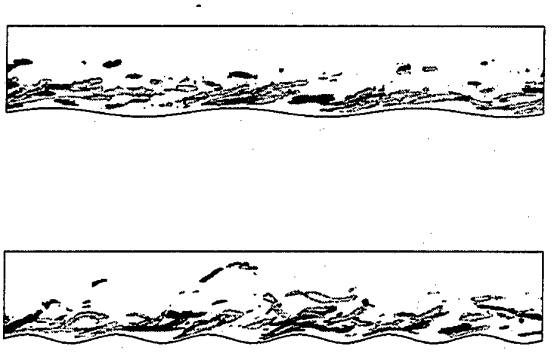

Figure 12: Iso-contours of Ω_1. S1 top, S2 bottom

The wave steepness affects the mass transfer velocity β^+. The value of β^+ is shown in Figure 13 for cases S1 and S2 and compared to the results obtained for a flat wall. Over the range of Sc numbers investigated, β^+ is seen to increase with wave steepness. This phenomenon has been observed experimentally[17], in attempts to obtain heat transfer augmentation.

The dependence on the steepness of the wave profile is more evident as the Sc number increases. This can be explained as follow. For low Sc number the quadrant analysis shows that sweeps and Quadrant I events control the mass transfer. Sweeps are in turn related to the shear velocity that decreases with wave steepness. On the other hand, the vertical motion over the wave can bring flow closer to the boundary and help mass transfer. These two contrasting effects do not compensate, and β^+ increases with steepness. When the Sc number increases, sweeps are not longer controlling the mass transfer process, which is now limited by vertical fluctuations, and benefits more from the induced vertical fluid motion over the wave.

The vertical flow motion over the wave acts in the same way as the sweep-ejection cycle. The flow can penetrate closer to the boundary and renew it more efficiently. The part of the pressure drop that goes into form drag, on these scales promotes mass transfer, generating inrushes and outrushes of flow.

These findings do not contrast with the generally accepted view that only the friction velocity has to be accounted for when parametrizing β^+. The wave amplitude of our simulation is $\sim$ few millimeters. The length scale on which inrushes and outrushes take place is similar to the length scale of sweeps and ejections, and their influence on the mass transfer is to be expected.

In the ocean, waves have lengths in the order of meters. The vertical flow induced by these long waves are irrelevant for mass transfer. They happen on scales much bigger than the mass flux length scales, and they cannot affect β^+. From our analysis it emerges that in such situations only the friction drag, and the form drag over capillary waves, are relevant for the modeling of β^+.

We should notice that for the simulations reported the form drag amounts only to a small part of the total drag. Specifically, 10% of the total drag in the S1 case, and 18% in the S2 case goes into form drag.

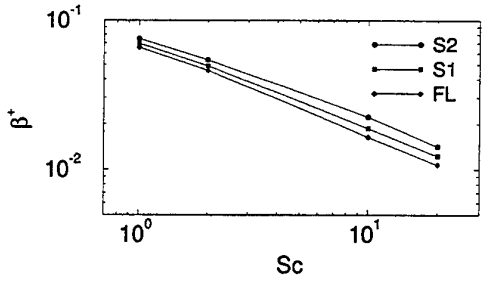

Figure 13: β^+ as a function of Sc

4 GAS-LIQUID FLOW NEAR DEFORMING INTERFACES

When the interface is free to deform two new parameters enter into analysis: the Weber number (We) and Froude number (Fr), defined in the Appendix.

The numerical method, also discussed briefly in the Appendix, cannot handle wave breaking so We and Fr have to be chosen carefully. This limits the shear velocity $\sim$ 0.3 m/s on the gas side which implies for an air-sea problem a 10 m wind velocity of about 8 m/s. In any case, the cases considered are listed in Table III together with 10 m and 5 m wind velocities.

Table III: Matrix of runs performed.

Case	Fr_τ	We_τ	$u_{\tau g}$	U_5	U_{10}
D1	1.410^{-4}	3.610^{-3}	0.18	4.4	5.5
D2	3.910^{-4}	5.010^{-3}	0.26	5.5	7.4
D3	5.710^{-4}	5.710^{-3}	0.29	6.0	8.1

The wave amplitudes in these cases are less than 2 mm and the wavelength about 4 to 5 cm. The computational domain dimensions are roughly 16 cm in the streamwise direction, 8 cm in the spanwise direction and 2 cm in the interface-normal direction. The domain size is therefore sufficient to capture capillary wave effects.

Before we discuss the results, we note that these are complicated and delicate simulations because there are three very different time scales. If R is

the square root of the density ratio between the two fluids, the turbulence time scale on the gas side is R time smaller than on the liquid side, and the time-period of waves is significantly greater than the turbulence time scale on the liquid side. This problem is therefore very stiff. Also the final wave spectrum depends upon the initial wave-shape assumed, to some extent, because of the non-linearity of the problem.

In the three cases in Table III, the waves appear to have reached a equilibrium amplitude and steepness. A snapshot of the interface shape is shown in Figure 14, for the three cases. The interface shape becomes more three-dimensional as the wind speed increases, and the amplitude, of course, increases. If the shear stress pattern on the interface is observed, high shear stress regions can be seen over the wave crests, and low shear stress regions over the valleys, as the shear stress pattern is dominated by the gas side. Also the typical streaky structures are similar to those observed in the flat interface case.

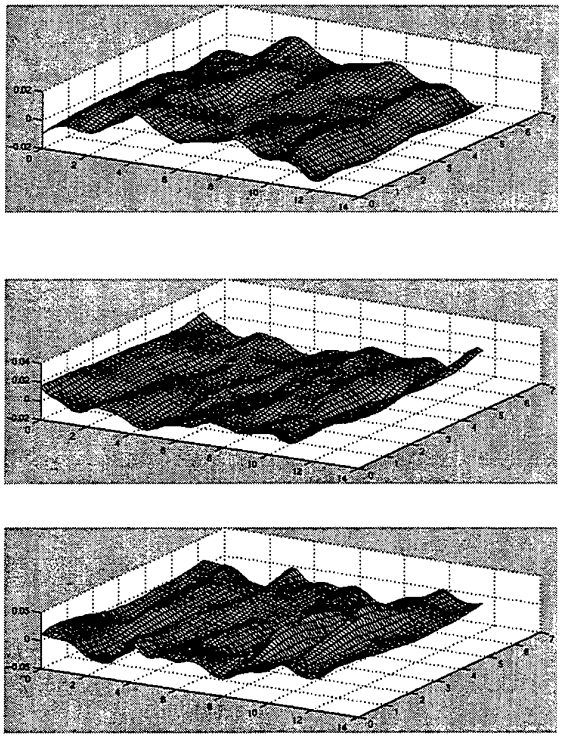

Figure 14: Interface shape, gas on the top, going from left to right, liquid on the bottom, going from right to left. From top to bottom, cases D1, D2, D3

Turning now to scalar transfer, we do not observe significant changes in the value of β^+ on the gas and liquid side compared to the flat interface case. Changes are of O(5-10%) which is within the statistical error. Having said this, we do observe a slight trend. The value of β^+ on the liquid side is seen first to increase and then to decrease with wave amplitude. On the gas side we observe no significant change. The values are shown in Table IV.

Table IV: β^+ for Sc=2.

Case	Gas	Liquid
FL	0.043	0.065
D1	0.044	0.071
D2	0.041	0.077
D3	0.040	0.075

The modest increase of β^+ for small wave amplitude on the liquid side has also been observed by Komori et al.[11] in wind-wave tank experiments. Komori at al.[11] observed first a slight increase of β^+ with wave amplitude and then a drop.

5 CONCLUSION

Mass transfer across gas-liquid interfaces has been studied. For flow over a flat interface the effect of the Schmidt number has been investigated. Also the effect of the turbulence structure on the mass fluxes has been studied. It has been found that large vertical (interface-normal) velocity fluctuations dominate the gas side flux whereas sweeps control the liquid side flux. Both these scale with the friction velocity and support parametrizations proposed previously (equations (4) and (5)).

For gas flow over a wavy wall mass transfer augmentation has been observed, the interface-normal motion being enhanced by the sinusoidal form of the boundary. However for waves formed on a mobile interface, the value of β^+ is not significantly affected, indicating that the parametrizations in equations (4) and (5) are still valid. It appears that such parametrizations also carry over to more complex multiphase flows e.g. bubble columns where a group in Tolouse[18] has shown that equation (5) holds for the liquid side mass transfer. This is probably because the length scales associated with the sweeps are much smaller than the bubble size and the mean interface structures are similar to those in separated flows.

6 APPENDIX

6.1 Velocity field calculation

The mass and the momentum balance for an incompressible Newtonian fluid can be written as:

$$\begin{cases} \nabla \cdot \mathbf{u} = 0 \\ \frac{\partial \mathbf{u}}{\partial t} + \mathbf{u} \cdot \nabla \mathbf{u} = -\nabla p + \frac{1}{Re} \nabla^2 \mathbf{u} \end{cases} \quad (6)$$

The Reynolds Number based on the shear velocity is given by:

$$Re = \frac{\rho u_\star h}{\nu} \; ; \; u_\star = \sqrt{h\Pi} \quad (7)$$

where $u_\star$ is the effective shear velocity, Π is the mean pressure gradient that drives the flow and h is half the average length in the vertical direction. The dimensions of the domain are $(l^+_{x_1}, l^+_{x_2}, l^+_{x_3}) =$

$(4\pi h^+, 2\pi h^+, 2h^+)$ where $h^+ = \sqrt{2}Re$ and $Re = 60.4$. The boundary conditions are periodic in the x_1 and x_2 directions. The flow geometry is shown in Figure 1, for the case of gas and liquid interacting across a deforming interface. The boundary conditions in the x_3 direction are as follows: at the interface the flow on the gas and liquid is constrained to satisfy continuity of velocity and stresses, *i.e.*

$$\begin{cases} \frac{1}{Re}((\underline{\underline{\tau}}_l - \underline{\underline{\tau}}_g)\cdot\mathbf{n})\cdot\mathbf{n} + p_g - p_l - \\ \frac{1}{We}\nabla\cdot\mathbf{n} + \frac{1}{Fr}f = 0 \\ ((\underline{\underline{\tau}}_l - \underline{\underline{\tau}}_g)\cdot\mathbf{n})\cdot\mathbf{t_i} = 0 \ , \ i = 1,2 \\ \mathbf{u}_l = \mathbf{u}_g \end{cases} \tag{8}$$

where the subscripts l and g stand for gas and liquid respectively, $\underline{\underline{\tau}}$ is the stress tensor, p the dynamic pressure, f is a measure of the vertical displacement of the interface with respect to the mid plane, and $\mathbf{n}$ and $\mathbf{t_i}$ are the normal and tangential directions. The quantities We and Fr are the Weber and Froude numbers defined as:

$$We = \frac{\rho h u_*^2}{\gamma} \ ; \ Fr = \frac{u_*^2 \rho}{gh(\rho_l - \rho_g)} \tag{9}$$

where γ is the interfacial tension (assumed constant) and g is the gravitational acceleration. On the outer boundaries free slip is assumed, so no turbulence generation occurs there.

The evolution of the interface is computed from the kinematic condition, that it is applied at the end of the liquid half step.

$$\frac{\partial f}{\partial t} + \mathbf{u}\cdot\nabla f = 0 \tag{10}$$

We use a nonorthogonal transformation to map the 3D, time-varying domain into a parallelepiped, and a projection method to discretize the flow equations. A modification of the fractional time step method introduced by Temam[19] is used, with two intermediate steps. Details can be found in De Angelis et al. [16], where the algorithm is discussed for flow over a wavy wall.

The only new element in the algorithm used here compared to [16] is related to the way boundary conditions are satisfied. We use a fractional time-step technique. On the liquid side continuity of stress is imposed using the stresses computed on the gas side at the previous half time step, also the continuity equation is explicitly enforced. We obtain therefore a 4x4 system of linear equations in the unknowns $du_i/d\xi_i$, $i = 1...3$ and p. On the gas side the velocity at the boundary is taken equal to the velocity of the liquid at the previous half time step.

Care has to be taken in choosing the required pressure boundary conditions. For the solution on the gas side, we used the usual zero-normal-gradient boundary condition, $\partial p/\partial\mathbf{n} = 0$ at the interface, that we found to perform well in the case of flow over a wavy wall. This is possible because when the velocity field is computed on the gas side, $\mathbf{u}_{gI}^{n+1/2} = \mathbf{u}_{lI}^n$ is used at the interface. The gas is therefore boundary fitted to the domain.

On the liquid side it is not appropriate to use this boundary condition, because the velocity field at the end of the liquid half step, is not boundary fitted. Instead we use as a boundary condition for p, the pressure that satisfies the normal stress balance on the interface.

A pseudospectral solver is used to finally solve equation (7).

6.2 Concentration field calculation

The evolution of a passive scalar field is governed by the equation:

$$\frac{\partial c}{\partial t} + \nabla\cdot(\mathbf{u}c) = \frac{1}{\mathrm{Sc\ Re}}\nabla^2 c + \frac{\mathrm{Q}}{\mathrm{Sc\ Re}} \tag{11}$$

where Sc is the Schmidt number. Boundary conditions are periodic in the x_1 and x_2 directions. In the x_3 direction $c = 1$ on one boundary and $c = 0$ on the other. The first boundary condition conforms to the usual chemical engineering assumption that the interfacial concentration is the equilibrium concentration at given pressure and temperature. The term Q represents a source term, that can be either zero or constant[20].

In order to resolve the concentration field for high Sc numbers a very fine grid is required. Given the maximum number of nodes allowed, this can be achieved by remapping the Chebyshev collocation points, to concentrate grid points in the interface region. This approach has two drawbacks. Sufficient resolution is not guaranteed in the coarsened regions, and the resulting transformation is non linear, complicating the solution of equation (11). We use, instead, a very simple linear mapping to stretch the scalar boundary layer into a domain that is suitable for use of Chebyshev polynomials, *i.e.* $L_{\mathrm{scalar}} = aSc^{-s}L_{\mathrm{velocity}}$, where s=1/2 and s=1/3 respectively on the liquid and gas sides, as suggested by equations (4) and (5). We then introduce a fictitious internal boundary within the fluid region resolved for the velocity field calculations.

This is possible because, as we mentioned in the introduction, the main concentration changes take place in length of order of millimeters on the gas and liquid sides, whereas domain length scales are $\sim$O(cm).

The presence of the source term is necessary at low Sc number. In a real situation, say heat transfer across pipe walls, the temperature gradient decreases linearly in the boundary-normal direction, x_3, because the heat is convected away by the mean flow. In a numerical simulation in which periodic boundary conditions are used in the streamwise direction, the mass flux remains constant in the x_3 direction, because what "exits" from one edge of the domain, "enters" from the other.

As a consequence the concentration profile shows significant gradients in the x_3 direction. The definition of the bulk concentration is meaningless in

this case. This problem was also reported by Calmet and Magnaudet[21]. They solved the problem by resorting to an ingenious – but somewhat ambiguous – graphical construction to compute the bulk concentration that would correspond to a linear decreasing mass flux (in the wall-normal direction), based on the results for the constant-flux profile.

We use a different approach. In order to obtain a linear flux in the x_3 direction it is sufficient to use a source term, Q, in the scalar diffusion-advection equation, (11). A constant source term is consistent with periodic boundary conditions in the two horizontal direction, and results in a total mass flux linearly decreasing in the x_3 direction, see Moin and Kim[20] and Teitel and Antonia[22].

For Sc=1 and Sc=2, in the case in which the source term is zero, the value of the mass transfer velocity is substantially lower than what is predicted by equation (4) and measured in experiments, see for example Kader and Yaglom[23]. The data are reported in Table V. Previous numerical simulations in which Q=0 was used, predicted a value of $\beta^+ = 0.52$ for Sc=1[24] – in agreement with our own DNS results for this case.

Table V: β^+ for small Sc numbers.

Sc	gas Q=0	gas $Q \neq 0$	liq Q=0	liq $Q \neq 0$
1.0	0.053	0.067	0.067	0.083
2.0	0.040	0.047	0.059	0.068

When a source term is introduced, the value of β^+ increases significantly, and lies just below the prediction of equation (4), as expected from experiments[23].

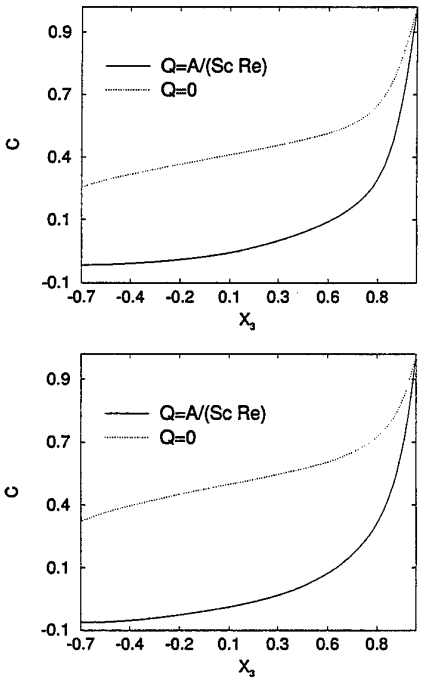

Figure 18: Average concentration profiles for $Q = 0$ and $Q \neq 0$.

The concentration profiles for $Sc = 1$ on the gas and liquid sides are shown in Figure 18, and it can be clearly observed how in the case in which the source term is zero, considerable concentration gradients exist in the center of the domain, whereas the concentration profile appears flat when $Q \neq= 0$.

LIST OF SYMBOLS

β	mass transfer velocity (m/s)
β^+	non-dimensional mass transfer velocity
ϵ	dissipation rate
h	half-domain depth
h^+	domain depth based on u_τ
λ^+	non-dimensional streak spacing
Λ_∞	integral length scale
R	square root of gas/liquid density ratio
Re_T	eddy Reynolds number
Re	Reynolds number based on u_τ and h
Q	source term in scalar transport equation
$\overline{T}$	time between bursts
T_τ	non-dimensional time between bursts
$\overline{\tau}$	time between surface renewals
τ_w	wall shear
τ_I	interface shear
$u_{\tau w}$	wall shear velocity
$u_{\tau I}$	interface shear velocity
$\sqrt{\overline{u'^2}}$	r.m.s. velocity fluctuations

References

[1] S.J. Kline, W.C. Reynolds, F.A. Schraub, and P.W. Runstadler. The structure of turbulent boundary layers. *J. Fluids Mech.*, 70:741, 1978.

[2] M. Rashidi and S. Banerjee. The effect of boundary conditions and shear rates on streaks formation and breakdown in turbulent channel flow. *Phys. Fluid*, A2:1827, 1990.

[3] W.K. Lewis and W.G. Whitman. The principles of gas absorption. *Ind. Eng. Chem.*, 16:1215, 1924.

[4] R. Higbie. The rate of absorption of a pure gas into a still liquid during short period of exposure. *Trans. Am. Inst. Chem. Eng.*, 31:365, 1935.

[5] G.E. Fortescue and J.R.A. Pearson. On gas absorption into a turbulent liquid. *Chem. Eng. Science*, 22:1163, 1967.

[6] S. Banerjee, E. Rhodes, and D.S. Scott. Mass transfer through falling wavy liquid films in turbulent flow. *Ind. Eng. Che. Fundamentals*, 7:22, 1968.

[7] J.C. Lamont and D.S. Scott. An eddy cell model of mass transfer into the surface of a turbulent liquid. *AIChE J.*, 16:1215, 1970.

[8] S. Banerjee. Turbulence structure and transport mechanisms at interfaces. *Proceedings of the Ninth International Heat Transfer Conference, Jerusalem, Israel*, pages 395–417, 1990.

[9] J.C.R. Hunt and J.M.R. Graham. Free stream turbulence near plane boundaries. *J. Fluids Mech.*, 84:209, 1978.

[10] K. Lam and S. Banerjee. On the condition of streak formation in a bounded turbulent flow. *Phys. Fluid*, A4(2):306–320, 1992.

[11] S. Komori, R. Nagaosa, and Y. Murakami. Turbulence structure and mass transfer across a sheared air-water interface in wind-driven turbulence. *Journal of Fluid Mechanics*, 249:161–83, 1993.

[12] P. Lombardi, V. De Angelis, and S. Banerjee. Direct numerical simulation of near-interface turbulence in coupled gas-liquid flow. *Physics of Fluids*, 8(6):1643–65, 1996.

[13] S. Banerjee. A note on turbulent mass transfer at high schmidt numbers. *Chemical Engineering Science*, 26(6):989–90, 1971.

[14] R.H. Wanninkhof and L.F. Bliven. Relationship between gas exchange, wind speed, and radar backscatter in a large wind wave tank. *J. of Geophys. Res.*, 96(C2):2785–2796, 1991.

[15] F.J. Ocampo-Torres, F.J. Donelan, J.M. Woollen, and J.R. Koh. Laboratory measurements of mass transfer of carbon dioxide and water vapor for smooth and rough flow conditions. *Tellus Series B*, 46:16, 1994.

[16] V. De Angelis, P. Lombardi, and S. Banerjee. Direct numerical simulation of turbulent flow over a wavy wall. *Physics of Fluids*, 8(8):1643–65, 1997.

[17] S. Saniei, N.; Dini. Heat transfer characteristics in a wavy-walled channel. *Transactions of the ASME. Journal of Heat Transfer*, 115(3):788–92, 1993.

[18] A. Cockx, M. Roustan, A. Line, and G. Hebrard. Modelling of mass transfer coefficient k_l in bubble columns. *Trans IChemE*, 73-A:627, 1977.

[19] R. Temam. *Navier-Stokes Equations*. North-Holland, Amsterdam, 1979.

[20] J. Kim and P. Moin. Transport of passive scalars in a turbulent channel flow. *Turbulent Shear Flow 6*, Springer-Verlag, Berlin:85–96, 1989.

[21] I. Calmet and J. Magnaudet. Large-eddy simulation of high-schmidt-number mass transfer in a turbulent channel flow. *Physics of Fluids*, 9(2):438–55, 1997.

[22] M. Teitel and R.A. Antonia. Heat transfer in fully developed turbulent channel flow: comparison between experiment and direct numerical simulations. *International Journal of Heat and Mass Transfer*, 36(6):1701–6, 1993.

[23] B.A. Kader and A.M. Yaglom. Heat and mass transfer laws for fully turbulent wall flows. *International Journal of Heat and Mass Transfer*, 15(12):2329–51, 1972.

[24] S.L. Lyons, T.J. Hanratty, and J.B. McLaughlin. Direct numerical simulation of passive heat transfer in a turbulent channel flow. *International Journal of Heat and Mass Transfer*, 34(4):1149–61, 1991.

Session 4

Separating, Impinging and Recovering Flows

DISSIMILARITY BETWEEN HEAT TRANSFER AND MOMENTUM TRANSFER IN A DISTURBED TURBULENT BOUNDARY LAYER WITH INSERTION OF A ROD

K. Inaoka, J. Yamamoto and K. Suzuki

Department of Mechanical Engineering
Kyoto University, Kyoto 606-8501, Japan

ABSTRACT

Numerical computation was carried out for a turbulent boundary layer disturbed by a square rod based on a concept of decomposing each quantity into its three components, i.e. time mean, periodical and stochastic ones, respectively. The effect of stochastic fluctuation of velocity and temperature on the time mean and periodically changing parts of flow and thermal fields was modeled with a $k-\varepsilon$ type turbulence model. Obtained results of heat transfer coefficient agree well with the experimental data with a modified LS model. Reduction of skin friction coefficient is obtained simultaneously. Therefore, generation of the dissimilarity between momentum transfer and heat transfer in the studied boundary layer was predicted. Discussion is developed for the washing action exerted by a spanwise vortex and its role of generating the dissimilarity.

1 INTRODUCTION

In a flat plate turbulent boundary layer disturbed by a cylinder mounted normal to the flow direction and detached from the plate, reduction of skin friction of the flat plate was found to appear in the region downstream the inserted cylinder where significant enhancement of heat transfer was observed [1]. This opposite direction of change of heat transfer against the one of momentum transfer was called dissimilarity. Later, structural study of turbulence was made near the wall with octant analysis[2] in the similar disturbed turbulent boundary layer in which the dissimilarity was generated. It was clarified in the study that hot outward and cold wallward interactions were intensified more strongly than sweep and ejection were intensified[3]. Such interactive fluid motions are the motions classified into the first and third quadrants in u-v plane where u and v are the streamwise and wall-normal components of velocity fluctuation, respectively. Thus, these two interactive fluid motions contribute negatively to momentum transfer. On the other hand, such an intensified wallward interaction was found more likely to be cold one, i.e., the one characterized by negative temperature fluctuation, than to be hot one, namely the one characterized by positive temperature fluctuation. Additionally, the intensified outward interaction is more likely to be hot than to be cold. Therefore, the two types of interactive fluid motions were regarded to contribute positively to heat transfer and result in generating the dissimilarity.

Similar larger fractional contribution from the first and third quadrants of u-v plane were separately reported also for a few types of organized unsteady laminar flows[4],[5],[6]. In these works, the washing action to be exerted by a spanwise vortex was found to be responsible for the generation of spontaneous dissimilarity which can lead to the dissimilarity between the time mean heat transfer and momentum transfer. Recently, selective intensification of such interactive fluid motions was related to the periodical velocity and temperature fluctuations produced by the Karman vortex shed from a square rod in case of a turbulent channel flow [7] or the from a cylinder in the case of a disturbed turbulent boundary layer[8]. de Souse et al.[8] also suggested that the washing action is also important in the generation of the dissimilarity in a disturbed turbulent boundary layer.

The present article discusses the above topics from an approach different from the previous ones. An effort is made to see if the dissimilarity can be predicted numerically. For this purpose, an unsteady flow numerical computation is carried out for a flat plate turbulent boundary layer disturbed by a square rod by making use of a $k-\varepsilon$ type turbulence model. The adopted numerical scheme is developed from the computation code for an unsteady laminar boundary layer disturbed by a square rod[9], and the shedding of the Karman vortex from the inserted square rod is computed one by one. The discussion will be developed on the results to be obtained and attention is paid to the roles of the Karman vortex and the washing action exerted by a vortex appearing near the wall.

2 FEATURES OF DISSIMILARITY AND FLOW GEOMETRY TO BE STUDIED

As discussed in the INTRODUCTION, skin friction coefficient C_f and heat transfer coefficient h as well as turbulence quantities have been measured intensively in a turbulent boundary layer disturbed by a cylinder[3],[10]. Some results on C_f and h are cited from Suzuki et al.[3] in Figures 1(a) and 1(b). Recently, similar experiments were done for the case where a square rod was inserted into a turbulent boundary layer[11]. This is to make the

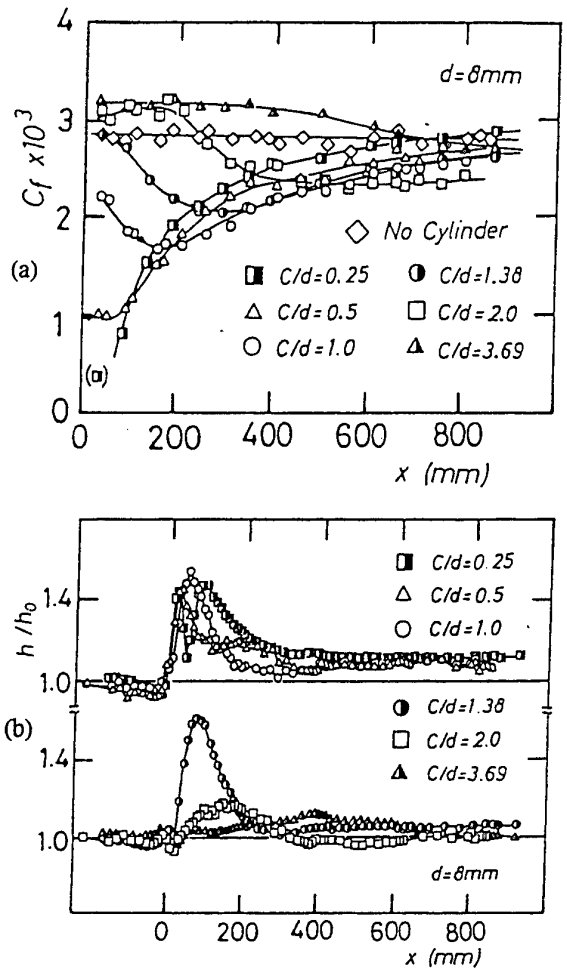

Figure 1 Distribution of C_f and h/h_0 in a turbulent boundary layer disturbed by a cylinder[3].

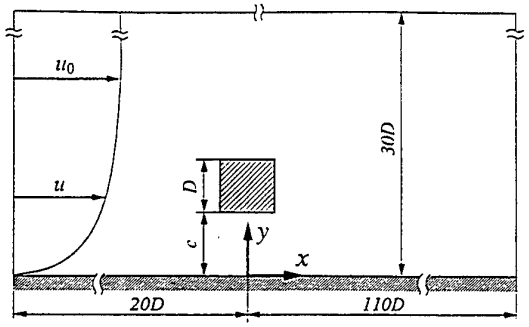

Figure 2 Computational domain and coordinate system.

geometry of an inserted body more convenient to attach a splitter plate and see if its attachment is effective to suppress the Karman vortex and, therefore, to suppress the dissimilarity. From a view point of grid point allocation in a numerical computation, a square rod is preferable as a body to insert in the turbulent boundary layer. Therefore, the present numerical computation will be made for this geometry shown in Figure 2.

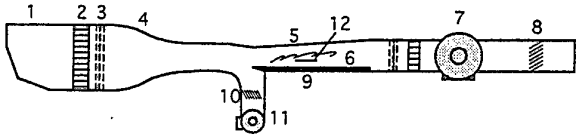

1 Entrance
2 Honeycomb
3 Screen
4 Contraction chamber
5 Upper wall
6 Test section
7 Main blower
8,10 Flow controller
9 Plate
11 Suction blower
12 Inserted body

Figure 3 Schematic view of the wind tunnel.

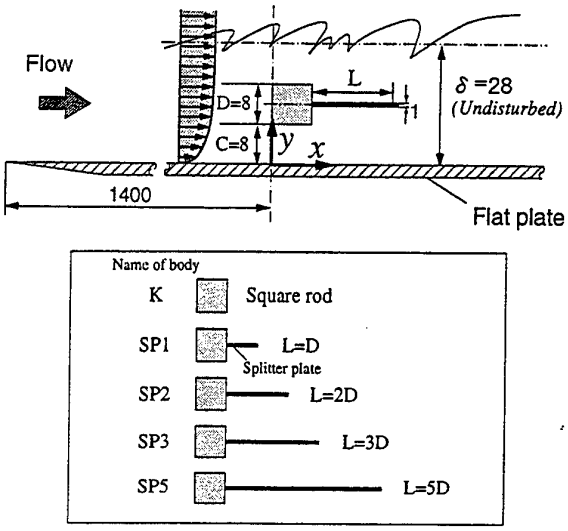

Figure 4 Geometry of the flow system, coordinate system and geometric parameters[11].

Description of the experimental apparatus and results to be compared with the present numerical computation will be briefly made in the following. Some features of the dissimilarity to be discussed later are also demonstrated here.

Figure 3 illustrates a used low speed wind tunnel. A flat plate was located at the bottom of the wind tunnel of the cross section of 380mm x 380mm. Uniformity of free stream velocity was secured at the leading edge of the flat plate by drawing the boundary layer developed on the upstream part of the tunnel floor with a blower 11. The free stream velocity was kept at 14m/s and streamwise uniformity of static pressure was established by adjusting the geometrical position of the tunnel ceiling. As is shown in Figure 4, a square rod of 8mm thickness was mounted at a streamwise position of 1400mm downstream from the flat plate leading edge in a manner keeping the space between the rod and the flat plate at 8mm. The thickness of the approaching boundary layer was measured to be 28mm at the insertion station of the rod unless it was inserted. The square rod was positioned parallel to the flat plate and normal to the free stream. Therefore, the studied flow is statistically two-dimensional. In some experiments, a

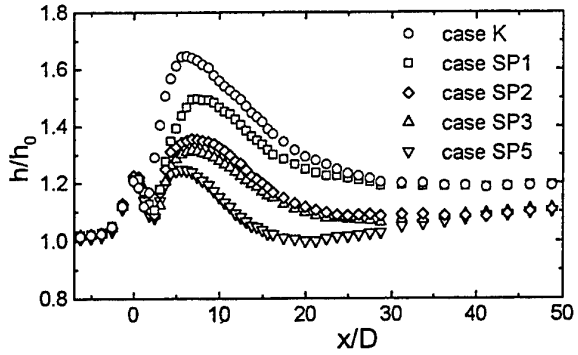

Figure 5 Streamwise distribution of h/h_0.

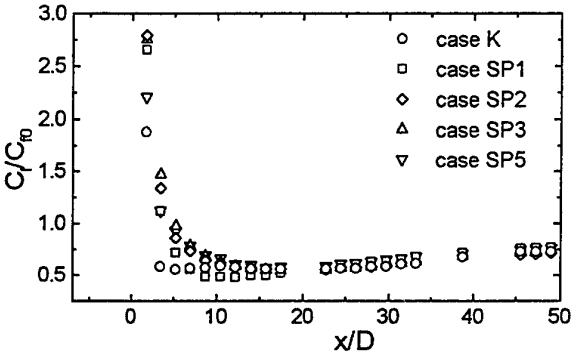

Figure 6 Streamwise distribution of C_f / C_{f0}.

splitter plate of different length was attached to the square rod. Attachment of the splitter plate did not significantly affect the value of skin friction coefficient. However, lengthening the splitter plate resulted in the suppression of the Karman vortex and was observed to noticeably change the value of heat transfer coefficient. Thus, the degree of the dissimilarity can be controlled by changing the length of the attached splitter plate.

Figures 5 and 6 illustrate the streamwise distribution of the measured heat transfer coefficient and skin friction coefficient, respectively. h_0 in the figure indicates the value of the heat transfer coefficient for a normal flat plate boundary layer without insertion of any body. It is clear that heat transfer is enhanced by the insertion of the square rod (case K) but that skin friction coefficient is less affected by the attachment of splitter plate. The results of the present numerical computation is compared in the following with the experimental results of this case K.

It is observed that enhancement of heat transfer becomes less pronounced with the elongation of the splitter plate. In contrast to this, skin friction coefficient does not change noticeably with the change of the splitter plate length. Figure 7 shows the power spectra for streamwise component of velocity fluctuation for several cases of different length of the splitter plate. The spectra were measured at a position near the flat plate at the streamwise location near the square rod. Peak of the spectrum becomes less remarkable with lengthening of

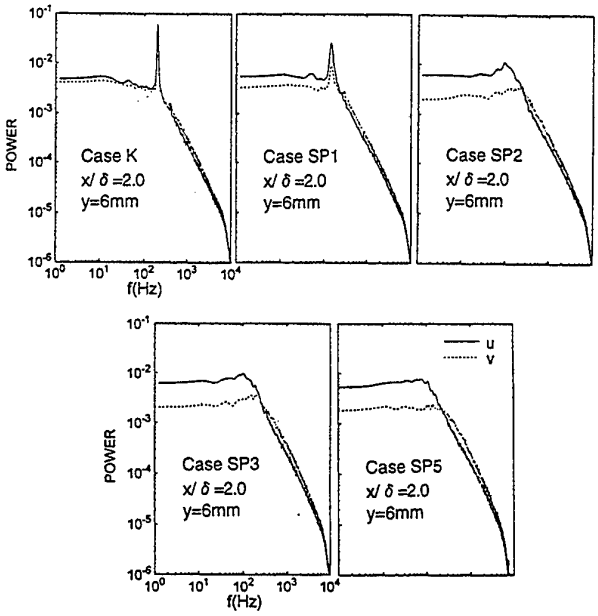

Figure 7 Power spectrum of u and v.

the splitter plate. Especially, no peak is observable in the spectrum for the case of the longest splitter plate. In this case, heat transfer is least enhanced. Therefore, the Karman vortex or its accompanying periodical fluctuation is concluded to play an important role in generating the dissimilarity. In this sense, three component decomposition of a quantity, namely decomposition into time mean value, periodical part and stochastic part of fluctuation, is needed in the numerical computation to succeed in the prediction of the generation of dissimilarity. This was also pointed out by Yao et al. in their paper on a turbulent channel flow disturbed by an inserted square rod[7].

In the experiments on a turbulent boundary layer disturbed by a cylinder, de Souza et al. showed that the Karman vortex shed from the lower half of the inserted body disappears in a short distance and that another vortex shed from the upper half keeps a much longer life[8]. It was also observed in their experiments that the latter vortex approaches to the flat plate and that it exerts a washing action to the flat plate surface. This washing action was confirmed to be the generation mechanism of the dissimilarity, as was concluded by Suzuki et al. in a series of numerical studies of an unsteady channel flow partially blocked with a square rod[4],[5].

3 COMPUTATIONAL METHOD AND PROCEDURES

The following three components decomposition is adopted for a velocity component in x_i direction, u_i, pressure p and temperature θ:

$$u_i = \overline{u}_i + \tilde{u}_i + u_i' = \langle u_i \rangle + u_i' \quad (1)$$

$$p = \overline{p} + \tilde{p} + p' = \langle p \rangle + p' \quad (2)$$

$$\theta = \overline{\theta} + \tilde{\theta} + \theta' = \langle \theta \rangle + \theta' \quad (3)$$

where $\overline{\ }$ denotes the time mean value of a quantity, $\tilde{\ }$ designates the periodical part of the fluctuation of the quantity and $'$ the turbulent stochastic component of the fluctuation of the quantity. $\langle\ \rangle$ denotes the phase average.

The governing equations for u_i may be written as follows[12].

$$\frac{\partial u_i}{\partial x_i} = 0 \quad (4)$$

$$\frac{\partial u_i}{\partial t} + u_j \frac{\partial u_i}{\partial x_j} = -\frac{\partial p}{\partial x_i} + \frac{1}{Re}\frac{\partial^2 u_i}{\partial x_j \partial x_j} \quad (5)$$

where t is time and Re is the flow Reynolds number. Substituting Eqs.(1)-(3) into Eq.(5), taking into account of Eq.(4) and then phase averaging, one obtains the following equation for $\langle u_i \rangle$.

$$\frac{\partial \langle u_i \rangle}{\partial t} + \langle u_j \rangle \frac{\partial \langle u_i \rangle}{\partial x_j} = -\frac{\partial \langle p \rangle}{\partial x_i} + \frac{1}{Re}\frac{\partial^2 \langle u_i \rangle}{\partial x_j \partial x_j} - \frac{\partial}{\partial x_j}\langle u_i' u_j' \rangle \quad (6)$$

The third term of the right hand side of the above equation is modelled with a turbulence model as was made in the references (13)-(18). Here are used two types of low Reynolds number version of the $k-\varepsilon$ turbulence models, i.e., Launder-Sharma model (hereafter referred as LS model) [19] and Kato-Launder model (hereafter referred as KL model) [20] but with a little modification, namely;

$$-\langle u_i' u_j' \rangle = \nu_t \left(\frac{\partial \langle u_i \rangle}{\partial x_j} + \frac{\partial \langle u_j \rangle}{\partial x_i} \right) - \frac{2}{3}\delta_{ij}\langle k \rangle \quad (7)$$

where $$\nu_t = C_\mu f_\mu \frac{\langle k \rangle^2}{\langle \hat{\varepsilon} \rangle},$$

$$C_\mu = 0.09,\ f_\mu = \exp\left\{ \frac{-3.4}{\left(1 + R_t/50\right)^2} \right\},\ R_t = \frac{\langle k \rangle^2}{\nu \langle \hat{\varepsilon} \rangle} \quad (8)$$

Phase averaged turbulent kinetic energy $\langle k \rangle$ and the rate of its dissipation $\langle \varepsilon \rangle$ are determined from the following transport equations with reference to the LS model:

$$\frac{\partial \langle k \rangle}{\partial t} + \langle u_j \rangle \frac{\partial \langle k \rangle}{\partial x_j} = \frac{\partial}{\partial x_j}\left\{ \left(\nu + \frac{\nu_t}{\sigma_k} \right) \frac{\partial \langle k \rangle}{\partial x_j} \right\} + P_k - \left(\langle \hat{\varepsilon} \rangle + D \right) \quad (9)$$

$$\frac{\partial \langle \hat{\varepsilon} \rangle}{\partial t} + \langle u_j \rangle \frac{\partial \langle \hat{\varepsilon} \rangle}{\partial x_j} = \frac{\partial}{\partial x_j}\left\{ \left(\nu + \frac{\nu_t}{\sigma_\varepsilon} \right) \frac{\partial \langle \hat{\varepsilon} \rangle}{\partial x_j} \right\} + C_{\varepsilon 1} f_1 \frac{\langle \hat{\varepsilon} \rangle}{\langle k \rangle} P_k - C_{\varepsilon 2} f_2 \frac{\langle \hat{\varepsilon} \rangle^2}{\langle k \rangle} + E \quad (10)$$

where

$$P_k = \nu_t S^2,\ S = \sqrt{\frac{1}{2}\left(\frac{\partial \langle u_i \rangle}{\partial x_j} + \frac{\partial \langle u_j \rangle}{\partial x_i} \right)^2},$$

$$D = 2\nu \left(\frac{\partial \sqrt{\langle k \rangle}}{\partial x_j} \right)^2,\ \langle \hat{\varepsilon} \rangle = \langle \varepsilon \rangle - D,$$

$$E = 2\nu\mu_t \left(\frac{\partial^2 \langle u_i \rangle}{\partial x_j \partial x_i} \right)^2,\ f_1 = 1.0,\ f_2 = 1.0 - 0.3\exp\left(-R_t^2\right),$$

$$C_{\varepsilon 1} = 1.14,\ C_{\varepsilon 2} = 1.92,\ \sigma_k = 1.0,\ \sigma_\varepsilon = 1.3 \quad (11)$$

$\hat{\varepsilon}$ is the isotropic part of the dissipation rate. Adoption of $\hat{\varepsilon}$ as a variable simplifies the wall boundary condition of the dissipation rate since $\hat{\varepsilon} = 0$ at the wall.

In order to reduce the excessive production of $\langle k \rangle$ in the stagnation regions due to an unrealistic simulation of the normal turbulent stresses in LS model, KL model was proposed to replace the production expression P_k by

$$P_k = \nu_t S\Omega,\ \Omega = \sqrt{\frac{1}{2}\left(\frac{\partial \langle u_i \rangle}{\partial x_j} - \frac{\partial \langle u_j \rangle}{\partial x_i} \right)^2} \quad (12)$$

Similarly, energy equation can be expressed with $\langle \theta \rangle$ as follows:

$$\frac{\partial \langle \theta \rangle}{\partial t} + \langle u_j \rangle \frac{\partial \langle \theta \rangle}{\partial x_j} = \frac{1}{RePr}\frac{\partial^2 \langle \theta \rangle}{\partial x_j \partial x_j} - \frac{\partial \langle u_i' \theta' \rangle}{\partial x_j} \quad (13)$$

$$-\langle u_i' \theta' \rangle = \frac{\nu_t}{Pr_t}\frac{\partial \langle \theta \rangle}{\partial x_i} \quad (14)$$

Unsteady flow Prandtl number was assumed to be constant in this study, namely $Pr_t = 0.9$.

Fully implicit forms of finite difference equivalents of the above mentioned equations were solved numerically along the time axis. For the finite-differencing of the governing equations, a central finite-differencing scheme was used for the diffusion terms. For the convection terms, the third-order upwind scheme (QUICK) was applied in case of the momentum equation but the central finite-differencing scheme in cases of the $\langle k \rangle$, $\langle \hat{\varepsilon} \rangle$ and energy equations. For the pressure evaluation, the SIMPLE algorithm was employed. The alternating direction implicit (ADI)

Table 1 Conditions for computation.

u_0	14.0 m/s
D	8 mm
Re_D	7075
$Re_{x'}$	1.24×10^6
δ_0	25 mm
c/D	1.0

method was also combined.

The geometry treated in the present study is illustrated in Figure 2, together with the coordinate system to be used below. A square rod is mounted in a flat plate turbulent boundary layer in a position normal to the flow direction and detached from the flat plate. The conditions for which computation is made are shown in Table 1. In the present study, main stream velocity u_0 (=1.4m/s) and rod size D(=8mm) were kept constant and the square rod was introduced at the location of streamwise Reynolds number $Re_{x'}=1.24\times10^6$. The inlet and outlet boundaries of the computational domain were located at $20D$ upstream and $110D$ downstream from the cylinder position, respectively. The free stream boundary was located at y=$30D$. 200×110 grid points were allocated non-uniformly in the computational domain with fine grid meshes near the flat plate and the square rod. Especially, more than two grid points were allocated within the viscous sublayer in order to evaluate quantities near the flat plate. The upstream boundary condition for the streamwise velocity $\langle u\rangle$, was given as follows;

$$\begin{aligned} u^+ &= y^+ && (y^+ \le 5)\\ u^+ &= 5.0+5.0\ln(y^+/5.0) && (5<y^+\le 30)\\ u^+ &= 2.44\ln y^+ + 5.0 + 2.44\Pi W(y/\delta) && (30<y^+) \end{aligned} \tag{15}$$

where $W(y/\delta)=2\sin^2(\pi y/2\delta)$,

$$\Pi = 0.596,\quad y^+=\frac{u^* y}{\nu},\quad u^+=\frac{u}{u^*} \tag{16}$$

In order to determine other quantities such as $\langle v\rangle$, $\langle k\rangle$, $\langle\hat{\varepsilon}\rangle$ and $\langle\theta\rangle$ at the upstream boundary, preliminary steady computation was made for a normal undisturbed flat plate turbulent boundary layer in the smaller region of $-30\le x/D\le-17.5$. As for the upstream boundary condition for that preliminary calculation, $\langle v\rangle$ was assumed to be zero, $\langle k\rangle$ and $\langle\hat{\varepsilon}\rangle$ were given by the DNS results [19], and $\langle\theta\rangle$ was given by the experimental data obtained by the above mentioned wind tunnel.

At the downstream boundary, gradients of all quantities were assumed to be zero in x direction. At the free stream boundary, the streamwise velocity and the cross-stream velocity were set to be u_0 (=14m/s) and zero, respectively. The gradients of the other quantities were also set to be zero in y direction. At the solid boundary, no-slip condition was used. The square rod was treated to be thermally insulated and uniform heat flux was assumed at the flat plate surface.

The above set of equations was numerically solved and the time mean Nusselt number and time mean skin friction coefficient were calculated and compared with the experimental data discussed in the above.

4 NUMERICAL RESULTS AND DISCUSSIONS

Here is discussed the obtained numerical results in comparison with the experimental data. Figure 8 shows the streamwise distributions of time mean Nusselt number $\overline{Nu}$ and Figure 9 those of time mean skin friction coefficient $\overline{C_f}$. In these figures, both values are normalized with the respective counterparts of the undisturbed boundary layer. It is observed in Figure 8 that the present numerical results with LS model for the time mean values of Nusselt number agree fairly well with the experimental data over a wide range of streamwise length while those with KL model do not agree with the experimental data. Although the numerical results with LS model for the time mean values of skin friction coefficient take larger value than unity in the region near downstream of the rod, reduction of skin friction is obtained at the position $x/D \ge 9$ as is actually observed experimentally. Thus, the

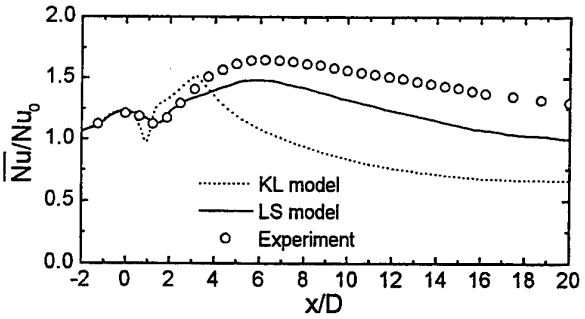

Figure 8 Streamwise distribution of Nusselt number.

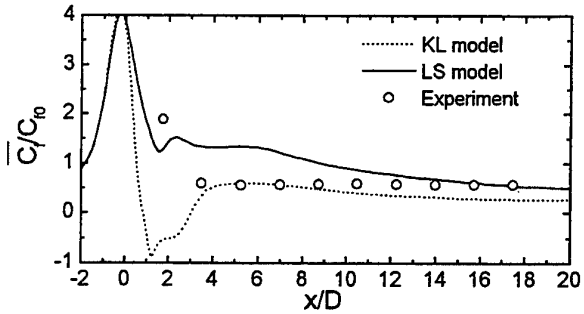

Figure 9 Streamwise distribution of skin friction coefficient.

generation of the dissimilarity was found to be reasonably predicted over a wide range of streamwise length with the LS model though it is weak in the region just downstream of the rod. This was achieved first time only through the present type of unsteady flow computation based on the three component decomposition approach. Such success has never been achieved with steady flow computation employing a few

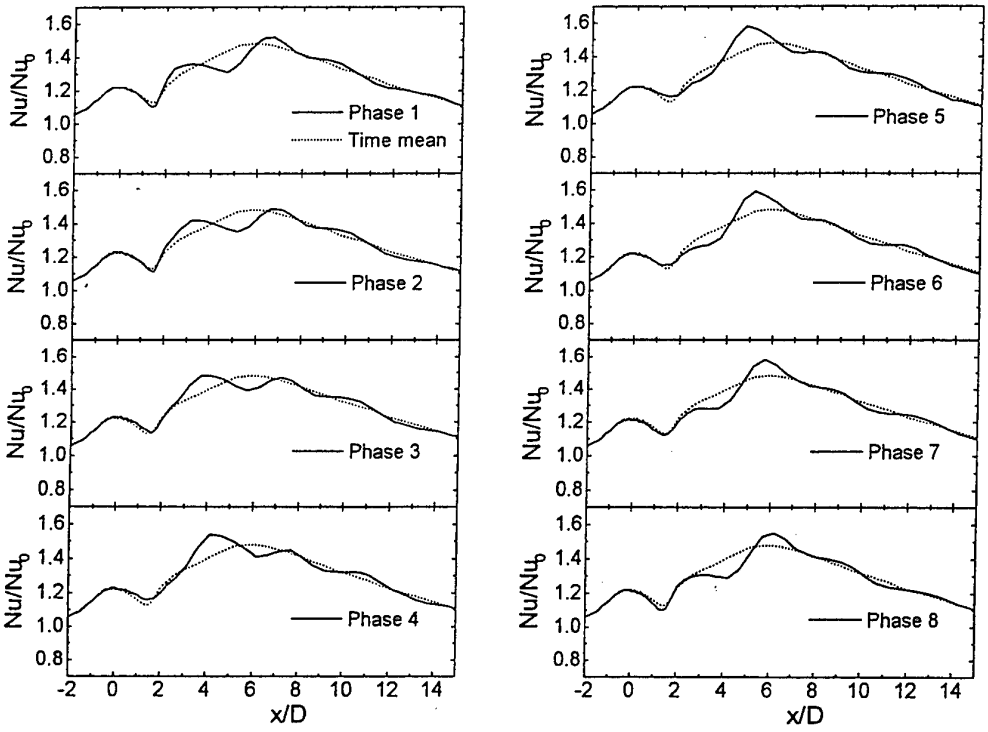

Figure 10 Streamwise distributions of instantaneous Nusselt number.

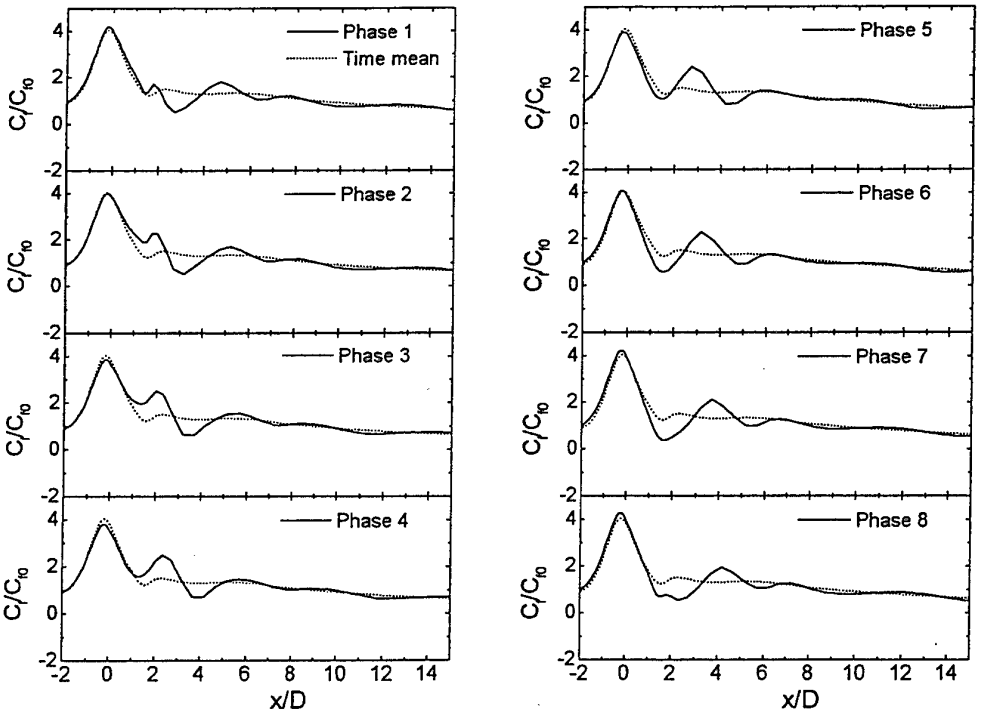

Figure 11 Streamwise distribution of instantaneous skin friction coefficient.

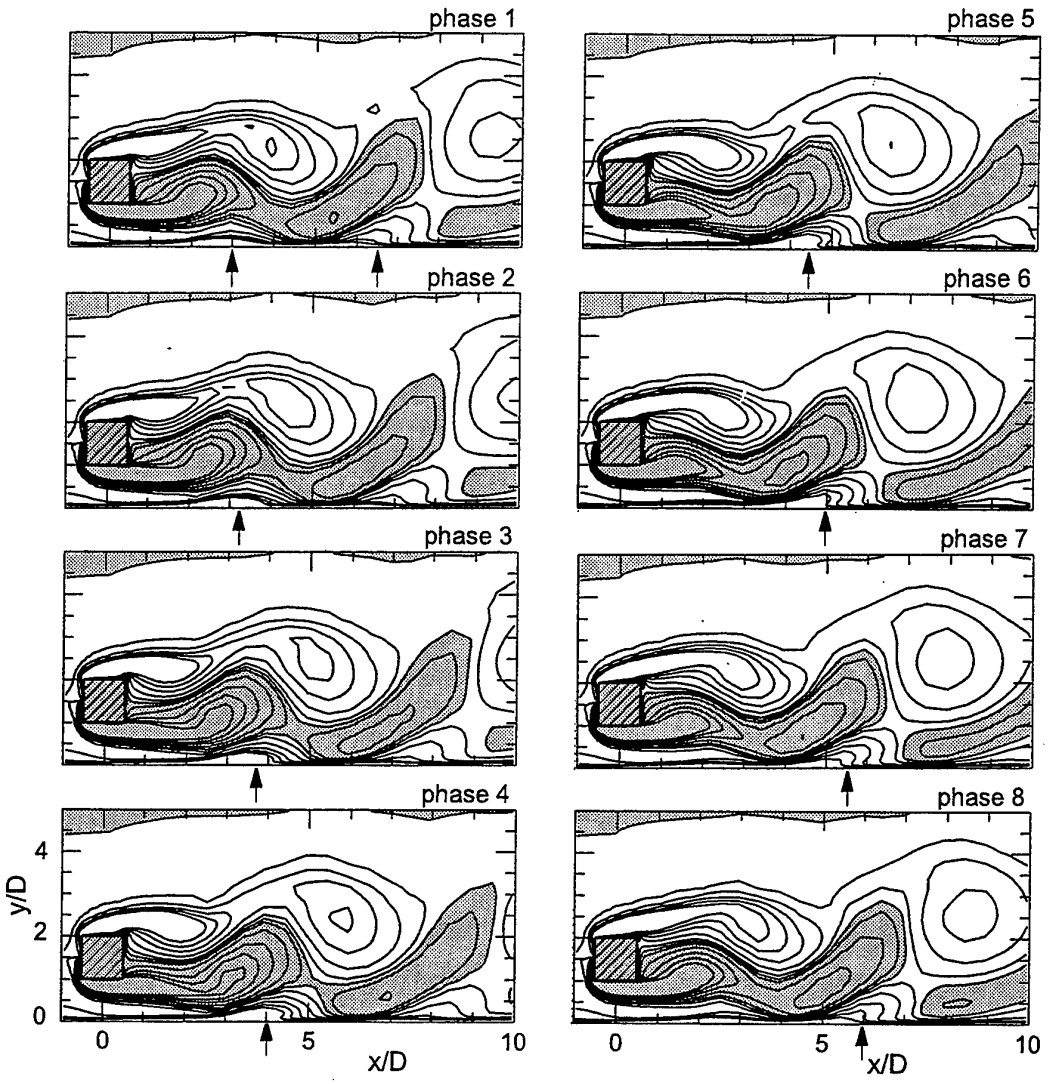

Figure 12 Instantaneous maps of the vorticity contours (Shaded parts: vorticity is positive).

different turbulence models in attempts by the group of the present author. Although the results of the skin friction coefficient with KL model agree with the experimental data better than those with LS model, unreasonable results were observed in the Nusselt number distribution. Thus, the discussion will be concentrated on the generation mechanism of the dissimilarity predicted by the LS model in the following.

As will be mentioned later, flow and thermal fields change in a highly periodic manner accompanied by a Karman-like vortex shed from the square rod. Therefore, in order to investigate the instantaneous flow and thermal field structures, several quantities were sampled at each instant corresponding to one eighth of a period of the velocity fluctuation. Figure 10 shows the streamwise distributions of instantaneous Nusselt number Nu and Figure 11 those of instantaneous skin friction coefficient C_f. In each frame of these figures, instantaneous distributions of Nusselt number and skin friction coefficient are shown with solid lines together with their time mean values illustrated by dotted lines. Time change of Nu and C_f distributions are observed in these figures. Similar to the distribution of $\overline{Nu}$, Nu has two or three peaks in distribution at each instant. While its first peak appears at almost the same position close to the square rod, its second peak changes its position from one phase to another, i.e., the second peak position moves downstream with an elapse of time. The same feature of time variation is clearly observed in the distribution of C_f. In these figures one interesting feature can be observed. Namely, heat transfer enhancement is generated at positions where the reduction of the skin friction coefficient is observed. This means that instantaneous dissimilarity between heat transfer and momentum transfer is locally generated. This instantaneous dissimilarity appears at an upstream position of x/D=3.0 at the instant of phase1 and moves downstream with an elapse of time. Because of such instantaneous dissimilarity can be ob-

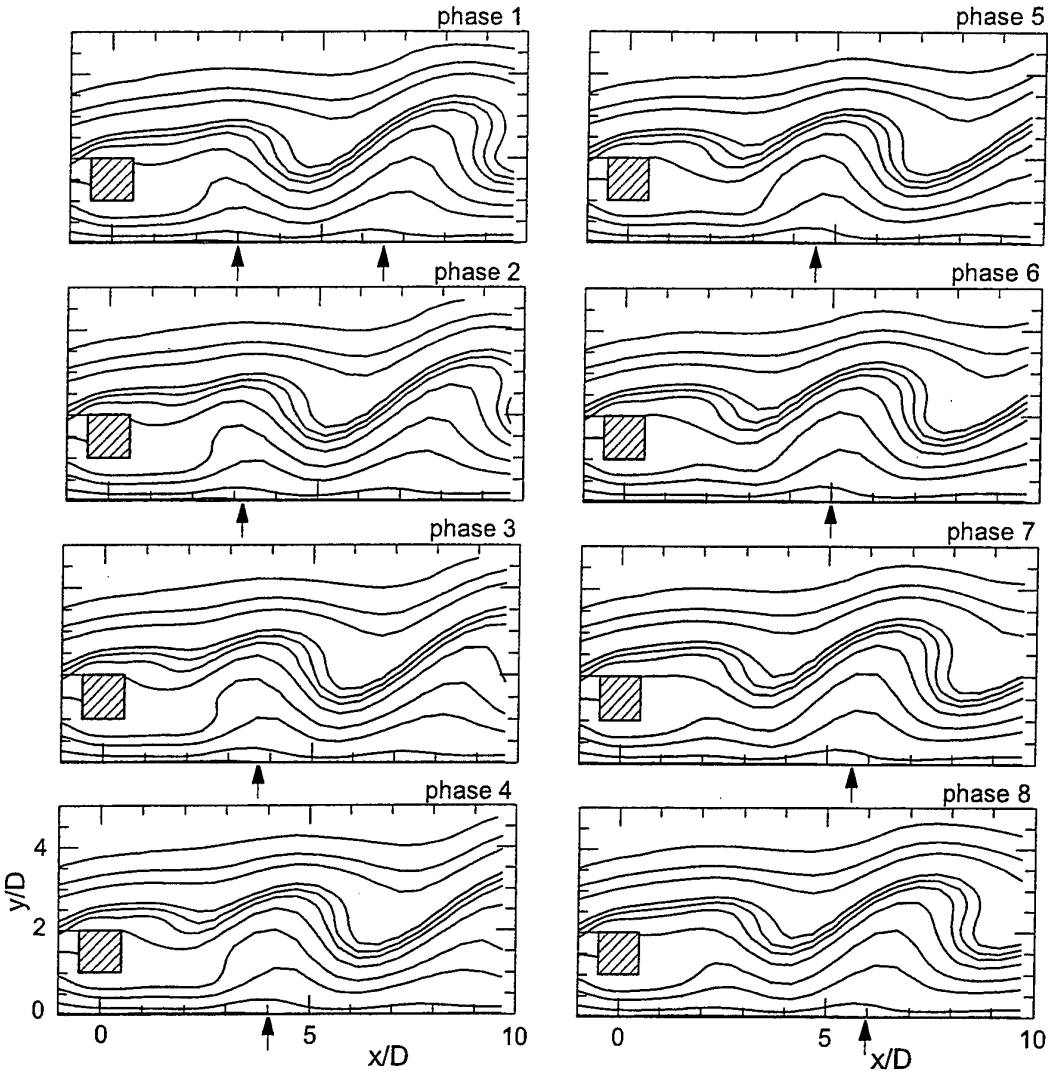

Figure 13 Instantaneous maps of the temperature contours.

served at every instant, it should contribute to the time mean dissimilarity found in Figures 8 and 9.

Figures 12 and 13 respectively show the instantaneous maps of the vorticity and temperature contours, which were sampled at the same instant as the for each frame of Figures 10 and 11. In Figure 12, the shaded parts correspond to the regions where vorticity is positive and the unshaded parts to those where it is negative. The arrow in the figure represents the peak position of instantaneous Nusselt number or the position where the dissimilarity exists. Time dependent behavior of the Karman vortex shed from the square rod can be observed in these figures but it is strongly distorted by the effect of the shear existing in the boundary layer. Negative-vorticity region (hereafter called NS region), which is formed in the upper half of the near wake of the square rod, rotates clockwisely entraining cooler fluid from the outer region of the turbulent boundary layer downward toward the flat plate while it moves downstream with an elapse of time (phase1→phase4). Simultaneously, this NS region drives the positive-vorticity region (hereafter called PS region) upward (phase3→phase7). The PS region is formed in the lower half of the near wake of the square rod, although NS region itself is disconnected by the PS region at the phase1 of the next period. Since this NS region supplies the cooler fluid from the outer region of the boundary layer toward the wall and the PS region ejects the hotter fluid from near wall region toward the outer region, their periodical motions basically enhance the wall heat transfer.

The above mentioned motions of the PS and NS regions produce another important unsteady behavior of the flow. Namely, high-vorticity wall region develops near the flat plate surface is intensified in vorticity at the location beside the rod due to the flow acceleration occurring in the space between the rod and the flat plate. Figure 14 shows the magnified view of the instantaneous maps of the vorticity contour near the flat plate, which were sampled at the same instant as that of

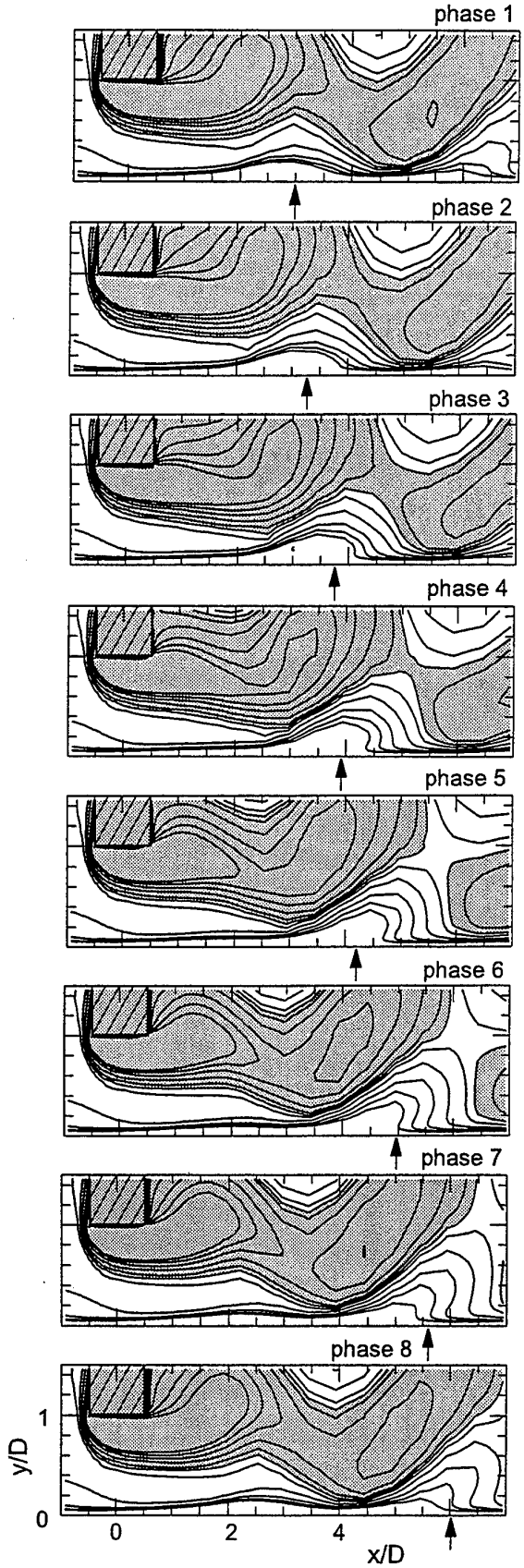

Figure 14 Instantaneous maps of the vorticity contours (Shaded parts: vorticity is positive).

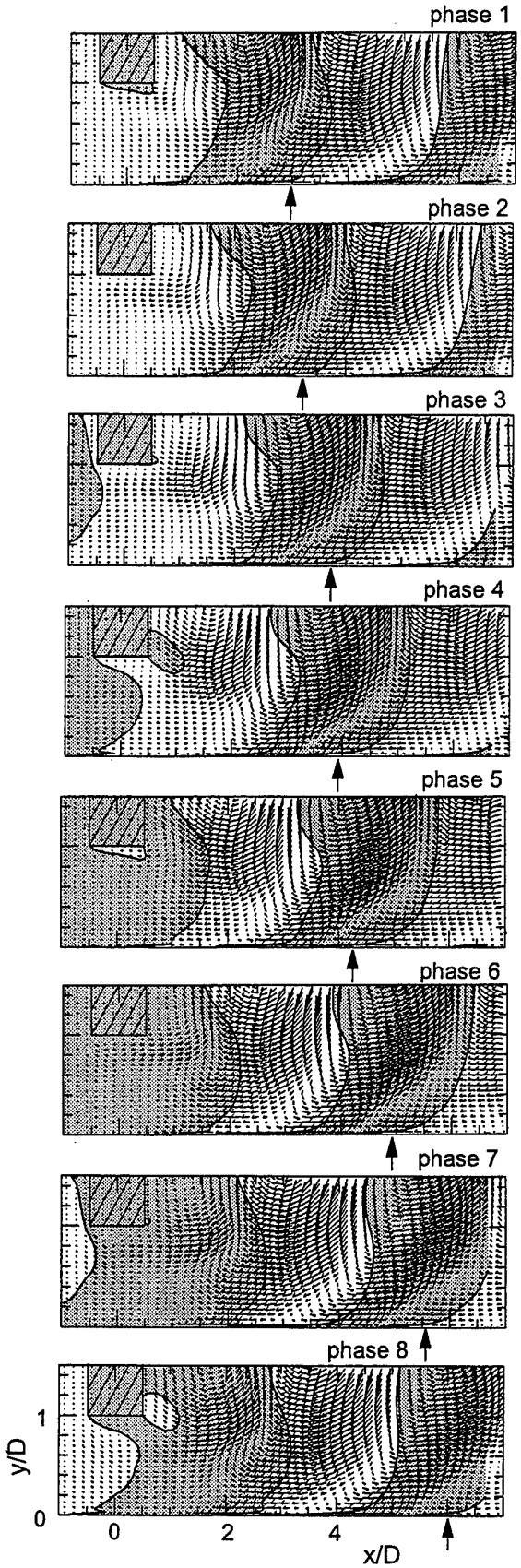

Figure 15 instantaneous distribution of the fluctuating velocity vector, $\tilde{u} - \tilde{v}$ (Shaded parts: hotter than time mean temperature).

Figure 12. It is clearly observed that, assisted by the motion of the PS and NS regions, the tip of this high-vorticity wall layer is lifted just around streamwise position indicated by an arrow where the instantaneous dissimilarity is attained. This periodically lifted wall high-vorticity layer (hereafter called NW tongue) induces clockwise fluid motion around it and plays an important role on the generation of the instantaneous dissimilarity.

Figure 15 shows the instantaneous distribution map of the fluctuating velocity vector, $\tilde{u}-\tilde{v}$, together with the instantaneous temperature fluctuation, $\tilde{\theta}$, sampled at the instant same as that of the previous figures. In Figure 15, the shaded parts indicate the region where $\tilde{\theta}$ is positive and unshaded parts the region where it is negative. It is clearly observed in this figure that clockwise fluid motion is induced in the region where the lift of the tip of the NW tongue is observed in Figure 14. Around there, region of cooler fluid or of negative temperature fluctuation exists at positions near the flat plate. Thus, this clockwise fluid motion entrains fresh and cooler fluid into the near wall region below the NW tongue from its downstream side so that heat transfer enhancement is achieved there. Since this fluid motion entrains the fluid into the near wall region from the downstream side, it temporarily reduces the streamwise velocity along the wall so that skin friction reduction occurs there. At the upstream side of its fluid motion, appearance of an intense upflow from the near-wall region to the outside is observed. The upflow is effective in pumping out the hot fluid, which has exchanged heat with the wall surface. It prevents the excess heating of the wall and is thus effective in enhancing the heat transfer, too. This clockwise fluid motion is clearly observed to lie just above the peak position of Nu indicated by an arrow, and it is the washing action of a spanwise vortex appearing near the wall discussed for a different type of unsteady flows in the references[4),(5),(9)]. This washing action of the vortex appearing near the wall is concluded to be the direct cause of the generation mechanism of the dissimilarity predicted in the present study. Supply of cooler fluid from the outer region and ejection of hotter fluid toward the outer region by the NS and PS regions discussed above play the role to keep fluid temperature around NW tongue cool.

On the other hand, such entrainment of cooler fluid and pumping out of the heated fluid caused by the washing action exerted by the vortex are characterized by $\tilde{u}<0$, $\tilde{v}<0$ and $\tilde{\theta}<0$, and $\tilde{u}>0$, $\tilde{v}>0$ and $\tilde{\theta}>0$, respectively. Thus, they are classified into the elementary fluid motions equivalent to the "cold wallward interaction" and "hot outward interaction" of turbulent elementary fluid motions. They contribute negatively to momentum transfer but positively to heat transfer and thus result in generating the dissimilarity. Figures 16 and 17 respectively show the spatial distribution of the contours of an instantaneous product between the fluctuating velocities, $-\tilde{u}\tilde{v}$, and of that between lateral fluctuating velocity and temperature fluctuation, $\tilde{v}\tilde{\theta}$. In these figures, the shaded parts indicate the region where the value is positive and unshaded parts the region where it is negative. From these figures, such interactive fluid motions are confirmed to be produced in the near-wall region around the position indicated by an arrow. $-\tilde{u}\tilde{v}$ takes negative value but $\tilde{v}\tilde{\theta}$ takes positive value just downstream the positions specified by arrows. Thus, two types of interactive fluid motions are confirmed to be periodically intensified with relation to the washing action. Therefore, as was suggested by de Souza et al[8], selective intensification of such interactive fluid motions observed in a disturbed turbulent flow should be related to the washing action periodically exerted by a vortex near the wall.

5 CONCLUDING REMARKS

Numerical computation was carried out for a turbulent boundary layer disturbed by a square rod based on a concept of decomposing each quantity into its three components, i.e. time mean, periodical and stochastic ones. The effect of stochastic fluctuation of velocity and temperature on the time mean and periodically changing parts of flow and thermal fields was modeled with a $k-\varepsilon$ type turbulence model.

Obtained results of heat transfer coefficient with LS model agree well with the experimental data while that with KL model do not agree with them. In the results obtained with the LS model, reduction of skin friction coefficient is observed, therefore, generation of the time mean dissimilarity between momentum transfer and heat transfer in the studied boundary layer can be predicted. Unfortunately, dissimilarity remains weak in the region just downstream of the square rod. This time mean dissimilarity results from the occurrence of the instantaneous dissimilarity. Generation mechanism of the instantaneous dissimilarity is strongly related to the behavior of the Karman vortex, i.e., high vorticity region shed from the square rod periodically intensifies the wall vorticity layer in the region downstream of the square rod. The downstream tip of the wall vorticity layer lifted from the wall induces a clockwise motion producing the effects called washing action. The washing action supplies cooler fresh fluid into the near-wall region from the downstream side and ejects the hotter fluid toward outside from the wall region, and therefore, generates the dissimilarity there. This washing action can fairly well explain the experimental results that the selective intensification of two types of interactive fluid motions was observed.

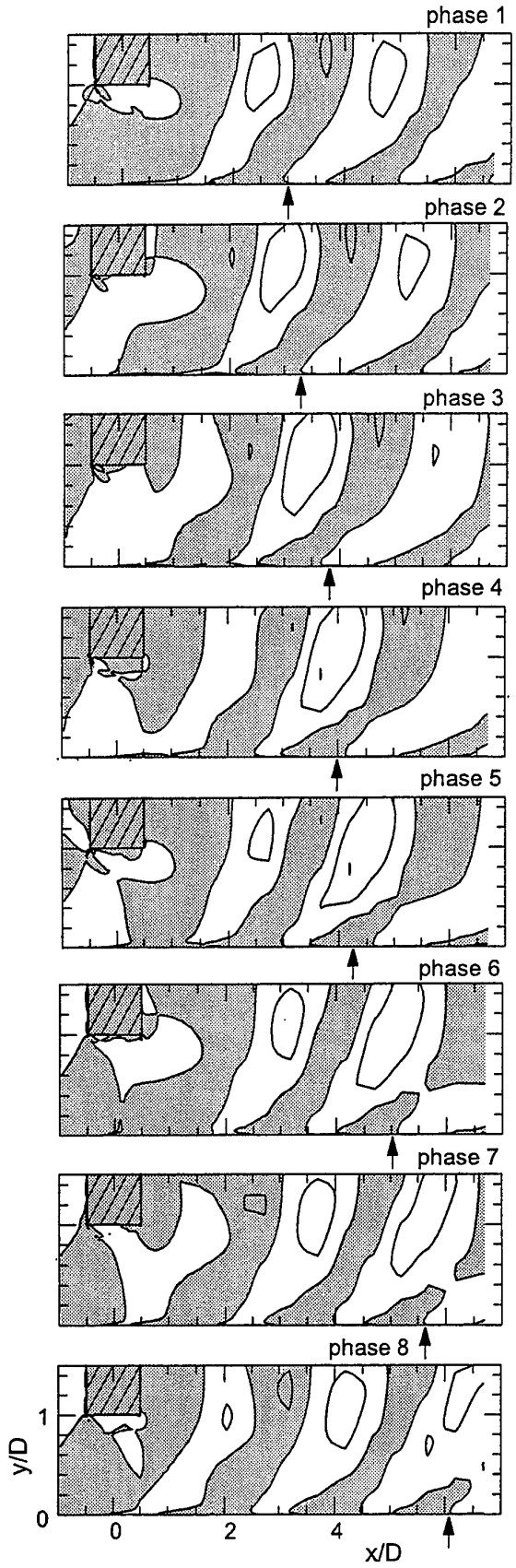

Figure 16 Instantaneous maps of $-\tilde{u}\tilde{v}$
(Shaded parts: the value of $-\tilde{u}\tilde{v}$ is positive).

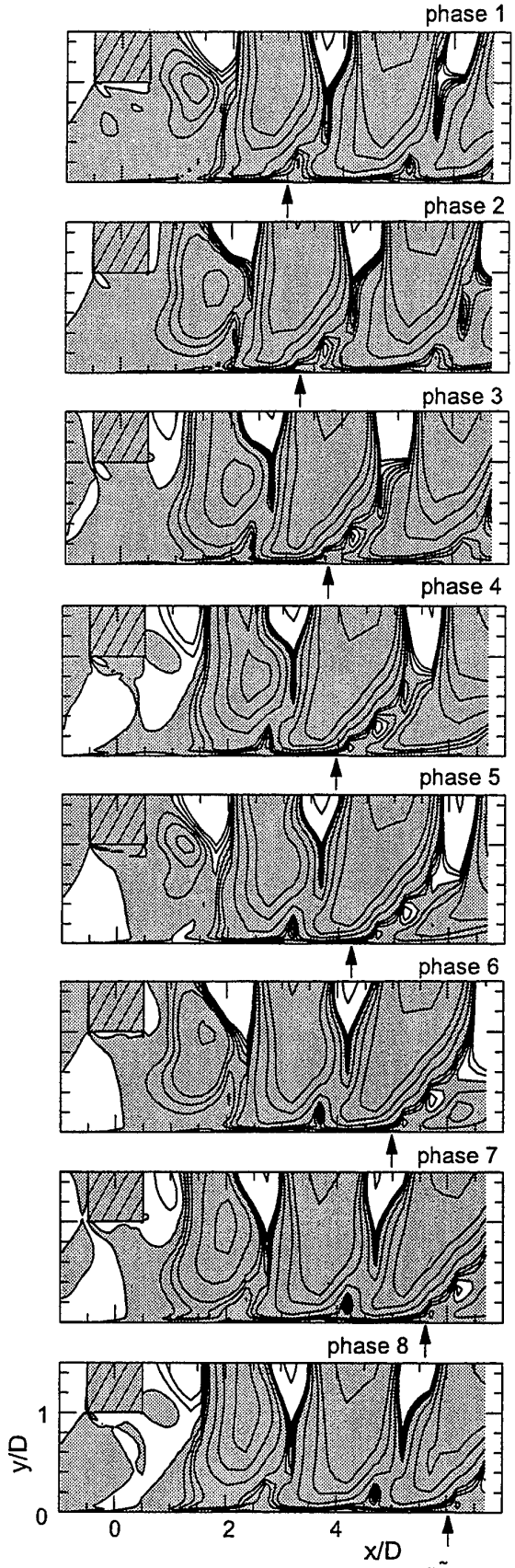

Figure 17 instantaneous maps of $\tilde{v}\tilde{\theta}$
(Shaded parts: the value of $\tilde{v}\tilde{\theta}$ is positive).

REFERENCES

(1) Y. Kawaguchi, T. Y. Matsumori and K. Suzuki, Structural study of momentum and heat transfer in the wall region of a disturbed turbulent boundary layer, Proc. Ninth Biennial Symposium on Turbulence, 1984, pp.28.1-28.10.

(2) S. S. Lu and W. W. Willmarth, Measurements of the structure of the Reynolds stress in a turbulent boundary layer, J. Fluid Mechanics, 60-3, 1973, pp. 481-511.

(3) H. Suzuki, K. Suzuki and T. Sato, Dissimilarity between heat and mass transfer in a turbulent boundary layer disturbed by a cylinder, Trans. JSME B, 54-503, 1988, pp. 1716-1722 (in Japanese).

(4) K. Suzuki and H. Suzuki, Unsteady heat transfer in a channel obstructed by an immersed body, Annual Review of Heat Transfer, 5, 1994, pp. 177-206, Begell House Inc.

(5) K. Suzuki and H. Suzuki, Instantaneous structure and statistical feature of unsteady flow in a channel obstructed by a square rod, Int. J. Heat and Fluid Flow, 15-6, 1994, pp. 426-437.

(6) K. Suzuki, G.N. Xi, K. Inaoka, Y. Hagiwara, Mechanism of heat transfer enhancement due to self-sustained oscillation for an in-line fin array, Int. J. Heat and Mass Transfer, 37-1, 1994, pp. 83-96.

(7) M. Yao, M. Nakatani, M. Okuda, K. Suzuki, Wavelet analysis of the velocity and temperature signals measured in a channel obstructed by a square rod, Proc. 10th Symp. on Turbulent Shear Flows, 1995, pp. 28.19-28.24.

(8) F. de Souza, J. Delville, J. Lewalle and J.P. Bonnet, On the large scale organization of a turbulent boundary layer disturbed by a circular cylinder, Proc. 11th Symp. Turbulent Shear Flows, Vol.3, 1997, pp. 33.25-33.30.

(9) K. Inaoka, J. Yamamoto and K. Suzuki, Heat transfer characteristics of a flat plate laminar boundary layer disturbed by a square rod, 5th Int. Conf. Advanced Comp. Methods in Heat Transfer, Heat Transfer 98' (to be presented).

(10) K. Suzuki, H. Suzuki, Y. Kikkawa, H. Kigawa and Y. Kawaguchi, Heat transfer and skin friction of a flat plate turbulent boundary layer disturbed by a cylinder - The effect of cylinder diameter and clearance between the cylinder and the flat plate, Turbulent Shear Flows 7, (ed. F. Durst et al.), 1991, pp.119-135.

(11) K. Inaoka, M. Matsui and K. Suzuki, Flow and heat transfer characteristics of a turbulent boundary layer disturbed by a square rod (Control of vortex shedding by means of a splitter plate), Proc. 2nd Int. Symp. on Turbulence, Heat and Mass Transfer (ed. by K. Hanjalic and T.W.J. Peters), 1997, pp.95-104, Delft University Press.

(12) W.C. Reynolds and A.K.M.F. Hussain, The mechanics of an organized wave in turbulent shear flow, Part 3: Theoretical models and comparisons with experiments, J. Fluid Mechanics, 54-2, 1972, pp. 263-288.

(13) J. Cousteix, A. Desopper and R. Houdeville, Structure and development of a turbulent boundary layer in an oscillatory external flow, Turbulent Shear Flows, 1979, pp. 154-171, Springer-Verlag.

(14) H. Ha Minh, J.R. Viegas, M.W. Rubesin, D.D. Vendrome and P. Spalart, Physical analysis and second-order modelling of an unsteady turbulent flow: The oscillating boundary layer on a flat plate, Proc. 7th Symp. Turbulent Shear Flows, 1989, pp.11.5.1-11.5.6.

(15) J.M. MacInnes, R.W. Claus and P.G. Huang, Time-dependent calculation of a forced mixing layer using a $k-\varepsilon$ turbulence model, 1989, Proc. 7th Symp. Turbulent Shear Flows, pp. 11.4.1-11.4.6.

(16) R. Franke and W. Rodi, Calculation of vortex shedding past a square cylinder with various turbulence models, Proc. 8th Symp. Turbulent Shear Flows, 1991, pp. 20.1.1-20.1.6.

(17) M. Kato and B.E. Launder, The modelling of turbulent flow around stationary and vibrating square cylinders, Proc. 9th Symp. Turbulent Shear Flows, 1993, pp. 10.4.1-10.4.6.

(18) G. Bosch and W. Rodi, Simulation of vortex shedding past a square cylinder near a wall, Proc. 10th Symp. Turbulent Shear Flows, 1996, pp. 4-13-4-18.

(19) B.E. Launder and B.I. Sharma, Letters in Heat and Mass Transfer, Vol. 1, 1974, pp. 131-138.

(20) N.N. Mansour, J. Kim and P. Moin, Reynolds-stress dissipation-rate budgets in a turbulent channel flow, J. Fluid Mech., Vol.194, 1988, pp.14-44.

PREDICTION OF HEAT TRANSFER IN TURBULENT STAGNATION FLOW WITH A NEW SECOND-MOMENT CLOSURE

T.J. Craft

Department of Mechanical Engineering
UMIST
Manchester, UK

ABSTRACT

The paper describes the application of a recently proposed low-Reynolds-number stress transport model to calculate the flow and heat transfer from an axisymmetric jet impinging normally onto a heated flat plate. Two different jet discharge heights, of 2 and 6 jet diameters are considered. Overall agreement with the experimental data is encouraging, but at the higher discharge height it is shown that weaknesses in capturing the initial jet development have some adverse effects on the subsequent radial wall jet behaviour.

1 INTRODUCTION

Flows involving impingement are widely used in industrial heating, cooling and drying processes, because of the high heat-transfer rates which can be achieved between the fluid and the impingement surface.

In practical applications, a wide variety of configurations can be found, including impingement onto non-planar surfaces, multiple jet impingement and oblique impingement, all of which present some additional modelling challenges. The present study, however, concentrates on the relatively simple case of a single axisymmetric jet impinging normally onto a flat heated plate.

Despite the geometrical simplicity of a single jet impinging normally onto a wall, there are, nevertheless, a number of quite complex aspects of the flow physics which have to be captured if the flow is to be predicted numerically. In the stagnation region there is almost irrotational straining of the mean flow, and the Reynolds stress component normal to the wall is actually *larger* than those parallel to it, in marked contrast to the situation in a simple boundary layer flow. There are also significant streamline curvature effects as the incoming jet is deflected by the wall and, although the flow does revert to a shear flow away from the stagnation point, the radial wall jet so formed is by no means a simple flow to predict.

The combination of the above physical phenomena means that, despite its importance in engineering applications, stagnation heat-transfer is notoriously badly predicted by most turbulence models which have, primarily, been developed for shear flows parallel to walls. However, the challenging physics and the geometrical simplicity also combine to make the impinging jet an ideal flow to study when testing and developing new turbulence model formulations.

Craft et al [1] reported calculations of the impinging jet flows studied experimentally by Cooper et al [2] and Baughn et al [3] using a variety of different turbulence models. They showed that both the Launder-Sharma k-ε scheme [4] and a basic, linear, second-moment closure significantly overpredicted the stagnation heat transfer. By employing a stress model with a cubic, realizable, pressure-strain model and an appropriate "wall-reflection" model, better predictions were obtained, although the computed variation of the stagnation Nusselt number with Reynolds number was not entirely in agreement with experimental data. Since these stress models were only valid for high Reynolds number regions, they were both used in conjunction with the Launder-Sharma k-ε model covering the near-wall region, and some discrepancies, particularly in the heat-transfer predictions, may have been attributable to the rather simple near-wall modelling.

Building on earlier work at UMIST [5,6], Craft & Launder [7] reported further development of the above realizable stress transport model, extending it by introducing low-Reynolds-number effects and "inhomogeneity" corrections to account for the presence of walls. One important aspect of the model was that it contained no geometry-specific quantities such as wall-normal distances or vectors, which have conventionally been employed to account for wall-blocking effects, and which seriously limit the applicability of models to complex wall topographies. Some encouraging initial results in shear and shear-free boundary layers were reported, although when applied to the impinging jet, the stagnation heat transfer was seriously overpredicted as a result of the model returning large turbulence lengthscales in this region.

Craft [8] reported additional refinements to the model, and obtained reasonable agreement with experimental and direct numerical simulation (DNS) data for a number of separating and reattaching flows. Amongst the additional elements built into

this model was a lengthscale correction term, based on that proposed by Iacovides & Raisee [9], in the ε equation, which improved predictions around reattachment points, and might be expected to bring similar improvements at stagnation points. This term again contained no explicit wall distance, and could, therefore, be applied to arbitrary geometries.

Because of the importance of impingement heat transfer, there are many experimental measurements available in the literature. Reviews and references to a number of studies can be found in [10,11,12]. However, many studies have not been ideal for use in validating turbulence models because of uncertainties in the inlet conditions or other aspects of the flow. In the present study, the dynamic field measurements of Cooper et al [2] and corresponding heat transfer measurements of Baughn et al [3] are used for comparison. These two experiments employed the same geometrical set-up and, moreover, the jet exit conditions were well defined since a long section of tubing was used to ensure that fully-developed pipe flow was attained towards the exit.

The following sections outline the details of the present Reynolds stress model, describe the numerical implementation, and present and discuss the results.

2 MODELLING DETAILS

The Reynolds stress transport equations can be written as

$$\frac{D\overline{u_i u_j}}{Dt} = P_{ij} + \Pi_{ij} - \varepsilon_{ij} + d_{ij} \qquad (1)$$

where the production term

$$P_{ij} = -(\overline{u_i u_k}\partial U_j/\partial x_k + \overline{u_j u_k}\partial U_i/\partial x_k) \qquad (2)$$

does not require any modelling, Π_{ij} represents the sum of the pressure-strain and pressure-diffusion processes, ε_{ij} is the dissipation and d_{ij} represents diffusion of the stress as a result of the triple moments and viscous action.

The models employed for the unclosed processes are those proposed by [8], which are summarised below.

2.1 Pressure-Correlation Model

The pressure correlation, Π_{ij} is split into a redistributive and a non-redistributive part by

$$\Pi_{ij} = \phi^*_{ij} - \overline{u_i u_j}/k\, d^p_k \qquad (3)$$

where $d^p_k = -(1/\rho)\partial(\overline{pu_k})/\partial x_k$ is the pressure-diffusion of the turbulent kinetic energy. Such a division was found to be advantageous by Craft & Launder [7], since the redistributive part, ϕ^*_{ij}, shows the same qualitative behaviour in both near-wall and near-surface flows.

The redistributive part of Π_{ij} is modelled as

$$\phi^*_{ij} = \phi^*_{ij1} + \phi^*_{ij2} + \phi^{inh}_{ij1} + \phi^{inh}_{ij2} \qquad (4)$$

where the modelled forms for ϕ^*_{ij1} and ϕ^*_{ij2} (detailed in Table 1) are based on the high Reynolds number forms of ϕ_{ij1} and ϕ_{ij2} described by Craft et al [13], but with the addition of some turbulent Reynolds number dependent damping functions.

The coefficients c_2 and c'_2 in ϕ^*_{ij2} have been taken as functions of the strain and vorticity parameters S and Ω as described by Craft [8], who found that this brought improvements to the predictions of a number of homogeneous strain fields, including axisymmetric expansion. This latter case is particularly relevant to the present calculations since the strain field on the stagnation line in the impingement region does quite closely resemble an axisymmetric expansion flow. Figure 1 shows the predicted development of the stress anisotropies in a homogeneous axisymmetric expansion flow, for a range of strain parameters S'. The computations are started from an initially isotropic turbulence and the figure shows the subsequent time development of the stress anisotropies which can be seen to be in good agreement with the DNS data of Lee & Reynolds [14], particularly at the higher strain rates.

Some additional "inhomogeneity corrections" (ϕ^{inh}_{ij1} and ϕ^{inh}_{ij2}) are also included in the pressure-strain model, and these are summarised in Table 2. ϕ^{inh}_{ij1} is designed to return the correct near-wall and near-surface distribution of the stresses in the absence of any mean strain effects. It does this partly by employing the "normalized lengthscale gradient" d^A_i defined as

$$d^A_i = \frac{N^A_i}{0.5 + (N^A_k N^A_k)^{0.5}} \qquad (5)$$

where

$$N^A_i = \frac{\partial(k^{1.5}A^{0.5}/\varepsilon)}{\partial x_i} \qquad (6)$$

As shown in [7], this quantity can be used to identify regions and the direction of strong inhomogeneity in the flow, such as is found near a wall or surface.

The ϕ^{inh}_{ij2} correction acts to enhance the damping of the wall-normal stress component very close to a stagnation point. However, the main near-wall correction to ϕ_{ij2} is achieved by employing an "effective velocity gradient" in the expression for ϕ^*_{ij2}, based on earlier explorations carried out by Launder & Tselepidakis [5] and Launder & Li [6]:

$$\left.\frac{\partial U_i}{\partial x_j}\right|_{eff} = \frac{\partial U_i}{\partial x_j} + c_1 l d^A_k \frac{\partial^2 U_i}{\partial x_k \partial x_j} \qquad (7)$$

with the lengthscale l taken as

$$l = \min(k^{3/2}/\varepsilon, 20(\nu^3/\varepsilon)^{1/4}) \qquad (8)$$

in order to limit the effect of the correction at large distances from the wall, and the coefficient

$$c_I = 0.7(A(1-A))^{1/2}\min(S/6, 1.0) \qquad (9)$$

The reason for the dependence of c_I on the strain parameter S is to limit the influence of the term in regions where the velocity gradients are small but the second derivatives are large. Without such a limit equation (7) leads to excessively large effective velocity gradients around the position of the velocity maximum in the radial wall jet, resulting in too much damping of the turbulence, particularly in the initial wall jet development region of the flow.

The correlation between fluctuating pressure and velocity, $\overline{pu_k}$, appearing in d_k^p, is modelled as

$$\overline{pu_k} = -\rho(0.5d_k + 1.1d_k^A)(\nu\varepsilon k A A_2)^{1/2} \times [c_{pd1}A_2 + c_{pd2}R_t^{-1/4}\exp(-R_t/40)] \qquad (10)$$

with $c_{pd1} = 1.0 + 2.0\exp(-R_t/40)$ and $c_{pd2} = 0.4$ which was designed to give a reasonable fit to the available DNS data.

2.2 Dissipation Tensor Model

The form of the dissipation tensor model, ε_{ij}, employed can be written as

$$\varepsilon_{ij} = (1-f_\varepsilon)(\varepsilon'_{ij} + \varepsilon''_{ij} + \varepsilon'''_{ij})/D + {}^2\!/_3 f_\varepsilon \varepsilon \delta_{ij} \qquad (11)$$

where

$$\begin{aligned}
\varepsilon'_{ij} &= \varepsilon\frac{\overline{u_iu_j}}{k} + 2\nu\frac{\overline{u_lu_n}}{k}\frac{\partial\sqrt{k}}{\partial x_l}\frac{\partial\sqrt{k}}{\partial x_n}\delta_{ij} \\
&\quad + 2\nu\frac{\overline{u_lu_i}}{k}\frac{\partial\sqrt{k}}{\partial x_j}\frac{\partial\sqrt{k}}{\partial x_l} + 2\nu\frac{\overline{u_lu_j}}{k}\frac{\partial\sqrt{k}}{\partial x_i}\frac{\partial\sqrt{k}}{\partial x_l} \\
\varepsilon''_{ij} &= \varepsilon\left[2\frac{\overline{u_lu_k}}{k}d_k^A\delta_{ij} - \frac{\overline{u_lu_i}}{k}d_j^A - \frac{\overline{u_lu_j}}{k}d_i^A\right]d_l^A \\
\varepsilon'''_{ij} &= c_{\varepsilon s}\nu k\left(\frac{\partial\sqrt{A}}{\partial x_k}\frac{\partial\sqrt{A}}{\partial x_k}\delta_{ij} + 2\frac{\partial\sqrt{A}}{\partial x_i}\frac{\partial\sqrt{A}}{\partial x_j}\right) \\
D &= (\varepsilon'_{kk} + \varepsilon''_{kk} + \varepsilon'''_{kk})/(2\varepsilon) \qquad (12)
\end{aligned}$$

and the coefficients are taken as $c_{\varepsilon s} = 0.3$, $f_\varepsilon = A^{1.5}$.

Far away from a wall, the function f_ε ensures that the model returns close to isotropic dissipation, $\varepsilon_{ij} = {}^2\!/_3\varepsilon\delta_{ij}$. Somewhat closer to a wall, ε'_{ij} is designed to return $\varepsilon_{ij} \propto \varepsilon\overline{u_iu_j}/k$, as indicated by the DNS data of Kim et al [15]. Much closer to a wall, where the gradients of $\sqrt{k}$ become large, the remaining terms in ε'_{ij} act to ensure that the wall-limiting values of Launder & Reynolds [16] are correctly predicted:

$$\frac{\varepsilon_{11}}{\overline{u_1^2}} = \frac{\varepsilon_{33}}{\overline{u_3^2}} = \frac{1}{4}\frac{\varepsilon_{22}}{\overline{u_2^2}} = \frac{1}{2}\frac{\varepsilon_{12}}{\overline{u_1u_2}} = \frac{\varepsilon}{k} \qquad (13)$$

The ε''_{ij} term improves the behaviour of the shear stress dissipation, ε_{12}, in the buffer region, whilst the final term, ε'''_{ij} yields good agreement with the free-surface data of Perot & Moin [17].

2.3 Turbulent Diffusion Model

Craft [8] proposed an algebraic model for the triple moments, which was found to improve predictions of separating and reattaching flows as well as some shear-free boundary layers. This form has been retained in the present calculations, although for the particular flows studied here it does not result in significant improvements over a simpler gradient-diffusion type of model. The formulation is based on an algebraic simplification of the triple moment transport equations, which can be written as

$$\frac{D\overline{u_iu_ju_k}}{Dt} = P^1_{ijk} + P^2_{ijk} + \phi_{ijk} + d_{ijk} - \varepsilon_{ijk} \qquad (14)$$

where the production terms

$$P^1_{ijk} = -\overline{u_iu_j}\frac{\partial\overline{u_ku_l}}{\partial x_l} + \overline{u_iu_k}\frac{\partial\overline{u_ju_l}}{\partial x_l} + \overline{u_ku_j}\frac{\partial\overline{u_iu_l}}{\partial x_l} \qquad (15)$$

$$P^2_{ijk} = -\overline{u_iu_ju_l}\frac{\partial U_k}{\partial x_l} - \overline{u_iu_ku_l}\frac{\partial U_j}{\partial x_l} - \overline{u_ku_ju_l}\frac{\partial U_i}{\partial x_l} \qquad (16)$$

are exact.

The Millionshtchikov [18] approximation is employed to express the fourth order moments appearing in the diffusion term d_{ijk} in terms of second moments:

$$d_{ijk} = -\frac{\partial}{\partial x_l}(\overline{u_iu_j}\,\overline{u_ku_l} + \overline{u_iu_k}\,\overline{u_ju_l} + \overline{u_ku_j}\,\overline{u_iu_l}) \qquad (17)$$

and ε_{ijk} is modelled as $-2\varepsilon\overline{u_iu_ju_k}/k$ from a simplification of the form proposed by Kawamura et al [18].

The pressure correlations ϕ_{ijk} are modelled as

$$\phi_{ijk} = \phi_{ijk1} + \phi_{ijk2} + \phi^{inh}_{ijk} \qquad (18)$$

where

$$\begin{aligned}
\phi_{ijk1} &= -c_{t1}\varepsilon\overline{u_iu_ju_k}/k \\
\phi_{ijk2} &= -c_{t2}P^2_{ijk} \\
&\quad + c'_{t2}\left(\overline{u_iu_ju_l}\frac{\partial U_l}{\partial x_k} + \overline{u_iu_ku_l}\frac{\partial U_l}{\partial x_j} + \overline{u_ku_ju_l}\frac{\partial U_l}{\partial x_i}\right) \\
\phi^{inh}_{ijk} &= c_{tw}\left(\frac{\partial\overline{u_iu_n}}{\partial x_r}\delta_{jk} + \frac{\partial\overline{u_ju_n}}{\partial x_r}\delta_{ik} \right. \\
&\quad \left. + \frac{\partial\overline{u_ku_n}}{\partial x_r}\delta_{ji}\right)\overline{u_lu_r}d_l^A d_n^A \qquad (19)
\end{aligned}$$

represent a return to isotropy term, a mean-strain dependent term, and an inhomogeneity related term respectively, and the coefficients are taken as

$$c_{t1} = 4.2 \quad c_{t2} = 0.8 \quad c'_{t2} = 0.2A \quad c_{tw} = 0.5$$

The algebraic model for the triple moments is then obtained by simply neglecting the convection terms on the left hand side of equation (14).

2.4 Dissipation Rate Equation

The dissipation rate is obtained by solving a transport equation for the "homogeneous" dissipation rate, $\tilde{\varepsilon}$, defined as

$$\tilde{\varepsilon} = \varepsilon - 2\nu(\partial\sqrt{k}/\partial x_j)^2 \qquad (20)$$

which can be written as

$$\begin{aligned}\frac{D\tilde{\varepsilon}}{Dt} &= c_{\varepsilon 1}\frac{\tilde{\varepsilon}P_{kk}}{2k} - c_{\varepsilon 2}\frac{\tilde{\varepsilon}^2}{k} - c'_{\varepsilon 2}\frac{(\varepsilon-\tilde{\varepsilon})\tilde{\varepsilon}}{k} \\ &+ \frac{\partial}{\partial x_l}\left(\left(\nu\delta_{lk} + c_\varepsilon\overline{u_l u_k}\frac{k}{\varepsilon}\right)\frac{\partial\tilde{\varepsilon}}{\partial x_k}\right) \\ &+ c_{\varepsilon 3}\nu\overline{u_i u_j}\frac{k}{\varepsilon}\frac{\partial^2 U_k}{\partial x_i \partial x_l}\frac{\partial^2 U_k}{\partial x_j \partial x_l} + Y_E \qquad (21)\end{aligned}$$

The $c'_{\varepsilon 2}$ term in equation (21) is included to return the correct near-wall behaviour of $\tilde{\varepsilon}$, whilst the term Y_E is a lengthscale correction based on the proposal of Iacovides & Raisee [9], which can be written as

$$Y_E = c_{\varepsilon l}\frac{\tilde{\varepsilon}^2}{k}\max\{F(F+1)^2, 0\} \qquad (22)$$

where

$$\begin{aligned}F = \left\{\frac{\partial l}{\partial x_j}\frac{\partial l}{\partial x_j}\right\} &- c_l\left[1-\exp(-B_\varepsilon R_t)\right] \\ &- B_\varepsilon c_l R_t \exp(-B_\varepsilon R_t) \qquad (23)\end{aligned}$$

$$l = k^{3/2}/\varepsilon \qquad B_\varepsilon = 0.1069 \qquad c_l = 2.55 \qquad (24)$$

The term is designed to drive the lengthscale towards that which would be prescribed in the Wolfshtein [20] 1-equation model. In the present calculations, its main effect is to reduce the predicted lengthscale around the stagnation point. The remaining model coefficients in the $\tilde{\varepsilon}$ equation are summarized in Table 3.

2.5 Heat-Transfer Modelling

In the outer region, away from the impingement plate, transport equations were solved for the scalar fluxes, using the model described in Craft et al [13]. However, this is a high-Reynolds-number model, and so it was interfaced to a generalized gradient diffusion hypothesis model (GGDH, Daly & Harlow [21]) in the near-wall region:

$$\overline{u_i\theta} = -c_\theta\frac{k}{\varepsilon}\overline{u_i u_j}\frac{\partial\Theta}{\partial x_j} \qquad (25)$$

with coefficient $c_\theta = 0.25$. The switch between models was effected along a fixed grid line, corresponding roughly to where the turbulent Reynolds number was around 150. In practice, since the heat-transfer is dominated by the near-wall behaviour, the above algebraic near-wall heat flux model was far more influential on the results than the outer flux transport model.

3 NUMERICAL DETAILS

The calculations were performed with a suitably modified version of the TEAM computer code (Huang & Leschziner [22]). This is a finite volume solver which employs a cartesian grid with a fully staggered storage arrangement for the variables, and obtains the solution via an iterative process, using the SIMPLE pressure correction algorithm [23]. Leonard's QUICK scheme [24] is used for convection of mean quantities, and the PLDS scheme [23] for turbulence quantities.

Figure 2 shows the computational domain adopted. On the entrainment and outflow boundaries, the pressure was set to zero, and the velocity normal to the boundary was obtained from continuity. For cells where there was inflow into the domain, the turbulence quantities on the boundary were set to zero, whilst a zero gradient was applied where the flow was leaving the domain.

The experiments of Cooper et al [2] and Baughn et al [3] employed a long length of tubing to ensure that the incoming jet was fully-developed. For the present study a separate calculation was carried out using a version of the parabolic PASSABLE code (Leschziner [25]) to obtain predictions of fully-developed pipe flow at the required Reynolds numbers. These results were then interpolated onto the jet inlet of the impinging jet calculation domain.

For the case with a jet discharge height $H/D = 2$, an 80 (axial) by 70 (radial) grid was employed, with grids cells clustered near the wall and the shear layer of the incoming jet. When computing the higher discharge height case of $H/D = 6$, the number of axial nodes was increased to 100. These grid densities had been shown in the earlier work of [1] to produce grid-independent results.

When calculating the thermal field, the incoming jet was at the ambient air temperature, and a constant heat flux was applied through the impingement plate.

4 RESULTS AND DISCUSSION

Predicted mean velocity profiles across the wall jet at various radial positions are shown in Figure 3 for the case of a jet discharge height $H/D = 2$ and a Reynolds number of 23000. Corresponding shear stress and rms velocity profiles are shown in Figures 4 and 5. As can be seen, good agreement with the experimental data of [2] is achieved, although at larger radial distances the turbulence energy appears to be

slightly overpredicted towards the outer edge of the jet. Of particular note for present purposes are the turbulence levels along the stagnation line $r/D = 0$ in Figure 5. As shown in [1], the Launder-Sharma k-ε model, and even a widely-used stress transport model, overpredict the rms velocity by a factor of 3 or more in this region, resulting in significant overprediction of the stagnation heat transfer. The present model does return the correct turbulence levels in the stagnation region and, as can be seen in Figure 6, the heat-transfer predictions are thus also in good agreement with the data of [3]. At slightly larger radial distances of $r/D \approx 2$ the model does predict a small secondary peak in the Nusselt number, although not as large as that measured experimentally.

Also shown in Figure 6 are predictions of the Nusselt number obtained without the lengthscale correction term Y_E of equation (22). As commented earlier, the term has a significant influence at the stagnation point, reducing the heat-transfer levels down to those found experimentally.

At a higher Reynolds number of 70000 the mean and rms velocity profiles show a similar level of agreement with the data. The Nusselt number predictions shown in Figure 7 are also in good agreement with the measurements of [3], and the secondary peak at around $r/D \approx 2$ is better predicted in this instance.

At large radial distances, Figures 6 and 7 show that both the experiments and model predictions return a Nusselt number which scales with $Re^{0.7}$. In the stagnation region, the experiments show a dependence closer to $Re^{0.5}$, which is fairly well predicted by the model also.

In the cases considered so far, with $H/D = 2$, the incoming jet does not undergo much development before it impinges on the heated plate. When H/D is increased to 6, however, there is more mixing and spreading of the jet before it impinges on the wall. Consequently, the predictions of the wall jet region depend not only on the accuracy of the impingement zone modelling, but also on the ability of the model to capture the initial development of the incoming jet.

Figure 8 shows mean velocity profiles across the wall jet for $H/D = 6$ at a Reynolds number of 70000, and corresponding shear stress profiles are shown in Figure 9. In this case the velocity peak is slightly underpredicted and, although this underprediction decreases at larger radial distances, the jet appears to be spreading somewhat too rapidly. The rms velocities shown in Figure 10 indicate that there is still significant damping of the turbulence in the near-wall impingement zone. However, at larger distances from the wall the turbulence levels are overpredicted, and it is this that leads to the underprediction of the wall jet velocity maximum and the excessive spreading of the radial jet in its early stages.

The predicted Nusselt number distribution shown in Figure 12 is in fairly good agreement with the data of [3], although it is slightly overpredicted at radial distances up to $r/D \approx 2$. At a lower Reynolds number of 23000 the predicted Nusselt number levels are in slightly better overall agreement with the data, as shown in Figure 13.

To shed some further light on the prediction of the incoming jet development, Figure 14 shows contours of the predicted turbulent kinetic energy. It can be seen that there is quite rapid initial mixing at the edge of the incoming jet, and it is this which leads to high turbulence levels in the jet as the impingement region is approached. Interestingly, if the same model is used to compute the fully-developed axisymmetric free jet, it returns quite good agreement with the data, very similar to that reported with an early high-Reynolds-number version of the model by [26]. Thus, it appears that it is the development region of the axisymmetric jet which requires some more attention, and which should be investigated with a view to further model refinement.

5 CONCLUSIONS

The low-Reynolds-number stress model tested in the present impinging jet applications has been found to lead to reasonably good agreement of both the dynamic field and the heat-transfer with experimental measurements. In particular, the stagnation heat-transfer levels, which are notoriously overpredicted by many commonly-used models, are captured with a fairly good degree of accuracy.

Overall agreement with the data is better at lower discharge heights, since at the higher value of $H/D = 6$ the initial jet development is not entirely captured by the model, resulting in rather high turbulence levels in the jet as it approaches the impingement region. Some further modelling refinement is therefore suggested to improve the predictions of this developing jet region.

Acknowledgements

The author would like to thank the Royal Society of London for funding the work through a University Research Fellowship.

Nomenclature

A_2, A_3	stress anisotropy invariants.
A	Lumley's flatness parameter.
a_{ij}	Reynolds stress anisotropy.
D	jet diameter.
d_{ij}	diffusion of $\overline{u_i u_j}$.
d_{ijk}	diffusion of triple moments.
d_k^p	pressure diffusion of k.
d_i^A	normalized lengthscale gradient.

H	jet discharge height.
k	turbulent kinetic energy.
k_o	initial turbulence energy.
N_i^A	lengthscale gradient.
Nu	Nusselt number.
P_{ij}	production rate of $\overline{u_i u_j}$.
P^1_{ijk}, P^2_{ijk}	production terms of triple moments.
Pr	molecular Prandtl number
p	fluctuating pressure.
Re	bulk Reynolds number.
R_t	turbulent Reynolds number,$k^2/(\nu\varepsilon)$.
r	radial distance.
S_{ij}	mean strain tensor.
Ω_{ij}	mean vorticity tensor.
S, Ω, S_I	strain and vorticity invariants.
S'	strain rate in homogeneous expansion.
t	time.
U_i	mean velocity components.
u_i	fluctuating velocity components.
$\overline{u_i u_j}$	Reynolds stresses.
$\overline{u_i \theta}$	turbulent heat fluxes.
x_i	coordinate directions.
Y_E	lengthscale correction term.
y	distance from wall.
ε	dissipation rate of k.
$\tilde{\varepsilon}$	"homogeneous" dissipation rate.
ε_{ij}	dissipation rate of $\overline{u_i u_j}$.
ϕ^*_{ij}	redistributive pressure-strain term.
ϕ_{ijk}	pressure-correlation terms in triple moment equations.
Θ	mean temperature.
ρ	fluid density.
ν	kinematic viscosity.
Π_{ij}	pressure correlations in $\overline{u_i u_j}$ equations.

References

1. Craft, T.J., Graham, L.J.W., Launder, B.E. "Impinging jet studies for turbulence model assessment. Part 2: An examination of the performance of four turbulence models", *Int J. Heat Mass Transfer*, 1993, **36**, 2685-2697.

2. Cooper, D., Jackson, D.C., Launder, B.E., Liao, G.X. "Impinging jet studies for turbulence model assessment. Part 1: Flow field measurements", *Int J. Heat Mass Transfer*, 1993, **36**, 2675-2684.

3. Baughn, J.W., Yan, X.J., Mesbah, M. "The effect of Reynolds number on the heat transfer distribution from a flat plate to a turbulent impinging jet" *ASME Winter Meeting*, November 1992.

4. Launder, B.E., Sharma, B.I. "Application of th energy-dissipation model of turbulence to the calculation of flow near a spinning disc" *Lett. Heat Mass Transfer*. 1974, **1**, 131.

5. Launder, B.E., Tselepidakis, D.P. "Contribution to the modelling of near-wall turbulence", in *Turbulent Shear Flows 8*, 1993, Springer, Berlin.

6. Launder, B.E., Li, S-P. "On the elimination of wall-topography parameters from second-moment closure", *Phys. Fluids*, 1994, **6**, 999.

7. Craft, T.J., Launder, B.E. "A Reynolds stress closure designed for complex geometries", *Int J. Heat Fluid Flow*, 1996, **17**, 245-254.

8. Craft, T.J. "Developments in a low-Reynolds-number second-moment closure and its application to separating and reattaching flows", To appear in *Int. J. Heat Fluid Flow*.

9. Iacovides, H., Raisee, M. "Computation of flow and heat transfer in 2D rib roughened passages" Proc. 2nd Int. Symposium on Turbulence, Heat and Mass Transfer (ed. K. Hanjalic, T.W.J. Peeters), Delft, 1997.

10. Martin, H. "Heat and mass transfer between impinging gas jets and solid surfaces" *Adv. in Heat Transfer*, 1977, **13**, 1.

11. Goldstein, R.J., Franchett, M.E. "Heat transfer from a flat surface to an oblique impinging jet", *ASME J. Heat Transfer*, 1988, **110**, 87.

12. Jambunathan, K., Lai, E., Moss, M.A., Button, B.L. "A review of heat transfer data for single circular jet impingement" *Int. J. Heat Fluid Flow*,

13. Craft, T.J., Ince, N.Z., Launder, B.E. "Recent developments in second-moment closure for buoyancy-affected flows", *Dynamics of atmospheres and oceans*, 1996, **23**, 99-114.

14. Lee, M.J., Reynolds, W.C. "Numerical experiments on the structure of homogeneous turbulence", *Report TF-24*, Mech. Eng. Dept., Stanford University.

15. Kim, J., Moin, P., Moser, R. "Turbulence statistics in fully-developed channel flow at low Reynolds number", *J. Fluid Mech.*, 1987, **177**, 133-166.

16. Launder, B.E., Reynolds, W.C. "Asymptotic near-wall stress dissipation rates in a turbulent flow" *Phys. Fluids*, 1983, **26**, 1157.

17. Perot, J.B., Moin, P. "Shear free turbulent boundary layers: physics and modelling", *Report TF-60*, Mech. Eng. Dept., Stanford University, 1993.

18. Millionshtchikov, M.D. *C.R. Acad. Sci. SSSR*, 1941, **32**, 619-621.

19. Kawamura, H., Sasaki, J., Kobayashi, K. "Budget and modelling of triple moment velocity correlations in a turbulent channel flow based on DNS" Proc. 10th Turbulent Shear Flows Symposium, Pennsylvania State University, 1995.

20. Wolfshtein, M. "The velocity and temperature distribution in one-dimensional flow with turbulence augmentation and pressure gradient" *Int J. Heat Mass Transfer*, 1969, **12**, 301-318.

21. Daly, B.J., Harlow, F.H. "Transport equations in turbulence", *Phys. Fluids*, 1970, **13**, 2634.

22. Huang, P.G., Leschziner, M.A. "An introduction and guide to the computer code TEAM", *UMIST Mech. Eng. Rep. TF/83/9*, 1983.

23. Patankar. S.V. *Numerical Heat Transfer and*

Fluid Flow, 1980, McGraw-Hill.
24. Leonard, B.P. "A stable and accurate convective modelling procedure based on quadratic upstream interpolation" *Comp. Meths. Appl. Mech. Engrg.*, 1979. **19**, 59.
25. Leschziner, M.A. "An introduction and guide to the computer code PASSABLE", *UMIST Mech. Eng. Rep. TF/82/11*, 1982.
26. Craft, T.J., Launder, B.E. "A new model for the pressure/scalar-gradient correlation and its application to homogeneous and inhomogeneous free shear flows", Proc. 7th Turbulent Shear Flows Symposium, 1989, Stanford.

$$
\begin{aligned}
\phi^*_{ij1} &= -c_1\tilde{\varepsilon}[a_{ij} + c_1'(a_{ik}a_{kj} - 1/3 A_2\delta_{ij})] - \tilde{\varepsilon} f_A' a_{ij} \\
\phi^*_{ij2} &= -0.6\,(P_{ij} - 1/3\delta_{ij}P_{kk}) + 0.3 a_{ij}P_{kk} \\
&\quad - 0.2\left[\frac{\overline{u_k u_j}\;\overline{u_l u_i}}{k}\left[\frac{\partial U_k}{\partial x_l} + \frac{\partial U_l}{\partial x_k}\right] - \frac{\overline{u_l u_k}}{k}\left[\overline{u_i u_k}\frac{\partial U_j}{\partial x_l} + \overline{u_j u_k}\frac{\partial U_i}{\partial x_l}\right]\right] \\
&\quad - c_2\left[A_2\,(P_{ij} - D_{ij}) + 3a_{mi}a_{nj}\,(P_{mn} - D_{mn})\right] \\
&\quad + c_2'\left\{\left(\frac{7}{15} - \frac{A_2}{4}\right)(P_{ij} - 1/3\delta_{ij}P_{kk})\right. \\
&\qquad + 0.1\left[a_{ij} - 1/2\,(a_{ik}a_{kj} - 1/3\delta_{ij}A_2)\right]P_{kk} - 0.05 a_{ij}a_{lk}P_{kl} \\
&\qquad + 0.1\left[\left(\frac{\overline{u_i u_m}}{k}P_{mj} + \frac{\overline{u_j u_m}}{k}P_{mi}\right) - 2/3\delta_{ij}\frac{\overline{u_l u_m}}{k}P_{ml}\right] \\
&\qquad + 0.1\left[\frac{\overline{u_l u_i}\;\overline{u_k u_j}}{k^2} - 1/3\delta_{ij}\frac{\overline{u_l u_m}\;\overline{u_k u_m}}{k^2}\right]\left[6D_{lk} + 13k\left[\frac{\partial U_l}{\partial x_k} + \frac{\partial U_k}{\partial x_l}\right]\right] \\
&\qquad \left. + 0.2\frac{\overline{u_l u_i}\;\overline{u_k u_j}}{k^2}\,(D_{lk} - P_{lk})\right\}
\end{aligned}
$$

where $D_{ij} = -(\overline{u_i u_k}\partial U_k/\partial x_j + \overline{u_j u_k}\partial U_k/\partial x_i)$ and

$$c_1 = 3.1 f_A f_{Rt} A_2^{0.5} \quad c_1' = 1.1 \quad f_{Rt} = \min((R_t/160)^2, 1) \quad f_A' = A^{0.5} f_{Rt} + A(1 - f_{Rt})$$

$$f_A = \begin{cases} (A/14)^{1/2} & A < 0.05 \\ A/0.7^{1/2} & 0.05 < A < 0.7 \\ A^{1/2} & A > 0.7 \end{cases}$$

$$c_2 = \min(0.55(1 - \exp(-A^{1.5}R_t/100)), 3.2A/(1+S))$$

$$c_2' = \min(0.6, A) + 3.5(S - \Omega)/(3 + S + \Omega) - 2S_I$$

$$S = (k/\varepsilon)(1/2 S_{ij}S_{ij})^{1/2} \quad \Omega = (k/\varepsilon)(1/2\Omega_{ij}\Omega_{ij})^{1/2} \quad S_I = S_{ij}S_{jk}S_{ki}/(1/2 S_{lk}S_{lk})^{1.5}$$

$$S_{ij} = \frac{\partial U_i}{\partial x_j} + \frac{\partial U_j}{\partial x_i} \quad \Omega_{ij} = \frac{\partial U_i}{\partial x_j} - \frac{\partial U_j}{\partial x_i}$$

$$a_{ij} = \overline{u_i u_j}/k - 2/3\delta_{ij} \quad A_2 = a_{ij}a_{ij} \quad A_3 = a_{ij}a_{jk}a_{ki} \quad A = 1 - 9/8(A_2 - A_3)$$

Table 1: Model forms for ϕ^*_{ij1} and ϕ^*_{ij2}.

$$\phi_{ij1}^{inh} = f_{w1}\frac{\varepsilon}{k}(\overline{u_l u_k}d_l^A\delta_{ij} - 3/2\overline{u_i u_k}d_j^A - 3/2\overline{u_j u_k}d_i^A)d_k^A$$
$$+ f_{w2}\frac{\varepsilon}{k^2}\overline{u_l u_n}(\overline{u_n u_k}d_k^A\delta_{ij} - 3/2\overline{u_i u_n}d_j^A - 3/2\overline{u_j u_n}d_i^A)d_l^A$$
$$+ f_{w3}\nu\left(a_{il}\frac{\partial\sqrt{k}}{\partial x_l}\frac{\partial\sqrt{k}}{\partial x_j} + a_{jl}\frac{\partial\sqrt{k}}{\partial x_l}\frac{\partial\sqrt{k}}{\partial x_i} - 2/3 a_{nl}\frac{\partial\sqrt{k}}{\partial x_l}\frac{\partial\sqrt{k}}{\partial x_n}\delta_{ij} - 4/3 a_{ij}\frac{\partial\sqrt{k}}{\partial x_l}\frac{\partial\sqrt{k}}{\partial x_l}\right)$$
$$+ f'_{w1}\frac{k^2}{\varepsilon}\left(\overline{u_k u_l}\frac{\partial\sqrt{A}}{\partial x_k}\frac{\partial\sqrt{A}}{\partial x_l}\delta_{ij} - 3/2\overline{u_i u_k}\frac{\partial\sqrt{A}}{\partial x_k}\frac{\partial\sqrt{A}}{\partial x_j} - 3/2\overline{u_j u_k}\frac{\partial\sqrt{A}}{\partial x_k}\frac{\partial\sqrt{A}}{\partial x_i}\right)$$

$$\phi_{ij2}^{inh} = f_I k\frac{\partial U_l}{\partial x_n}d_l^A d_n^A\,(d_i^A d_j^A - 1/3 d_k^A d_k^A\delta_{ij})$$

with coefficients

$$f_{w1} = 0.9 + 0.5A^{1/2} + 1.6f'_{Rt} \qquad f_{w2} = 0.1 + 0.8A_2 f''_{Rt} \qquad f_{w3} = 2.5A^{0.5} \qquad f'_{w1} = 0.22 \qquad f_I = 2.5f_A$$

$$f'_{Rt} = \min(1, \max(0, 1 - (R_t - 55)/20)) \qquad f''_{Rt} = \min(1, \max(0, 1 - (R_t - 50)/200))$$

Table 2: Model forms for ϕ_{ij1}^{inh} and ϕ_{ij2}^{inh}.

$c_{\varepsilon 1}$	$c_{\varepsilon 2}$	$c'_{\varepsilon 2}$	$c_{\varepsilon 3}$	$c_{\varepsilon l}$	c_ε	A_{2d}
1.0	$\frac{1.92}{1+0.7AA_{2d}^{0.5}}$	1.0	0.5	0.5	0.18	$\min(A_2, 0.4)$

Table 3: Coefficients employed in the $\tilde{\varepsilon}$ equation

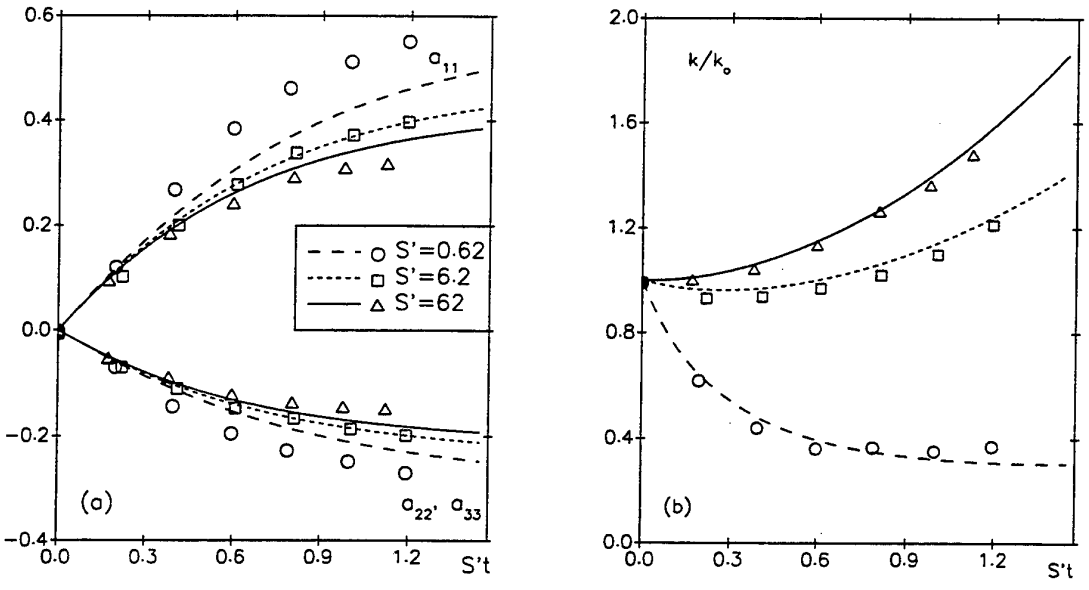

Figure 1: Development of (a) stress anisotropy and (b) turbulent kinetic energy in a homogeneous expansion at different strain rates, $\partial U_1/\partial x_1 = -2\partial U_2/\partial x_2 = -2\partial U_3/\partial x_3 = -2/\sqrt{3}S'$.

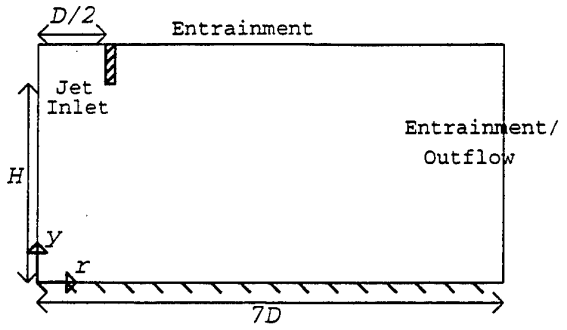

Figure 2: Impinging jet computational domain

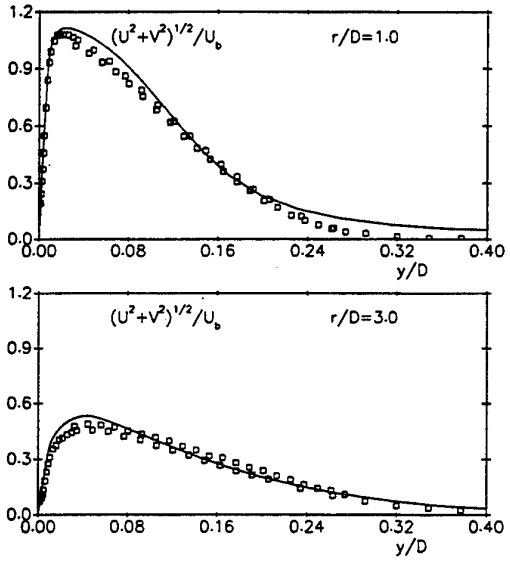

Figure 3: Mean velocity profiles in the radial wall jet for $H/D = 2$, $Re = 23000$.

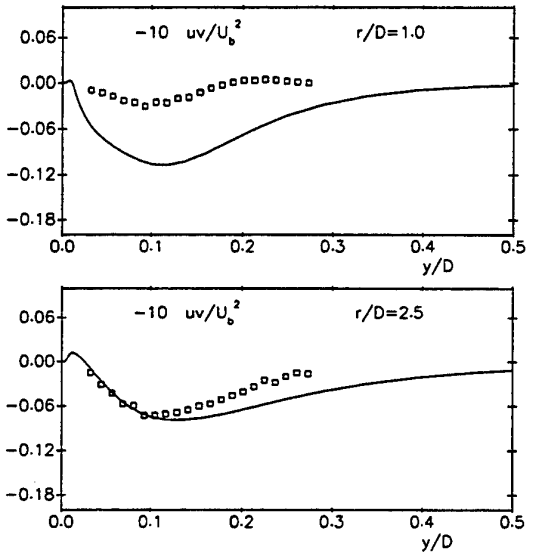

Figure 4: Shear stress profiles in the radial wall jet for $H/D = 2$, $Re = 23000$.

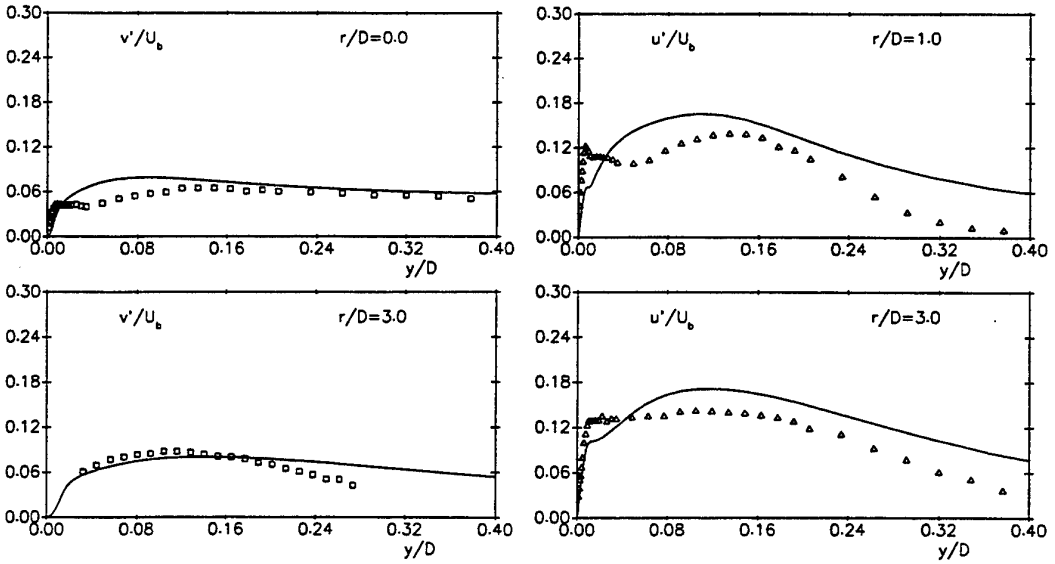

Figure 5: Rms velocity profiles in the radial wall jet for $H/D = 2$, $Re = 23000$. v' is normal to the wall, u' in the streamwise direction.

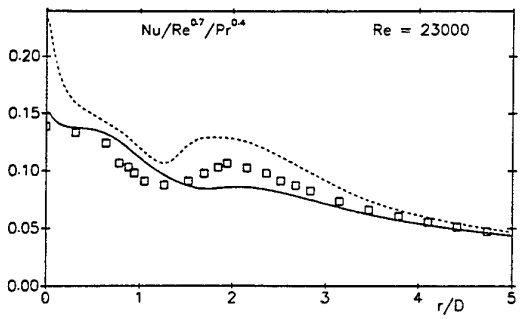

Figure 6: Nusselt number distribution for the case $H/D = 2$, $Re = 23000$. Solid line: present model, broken line: without Y_E term.

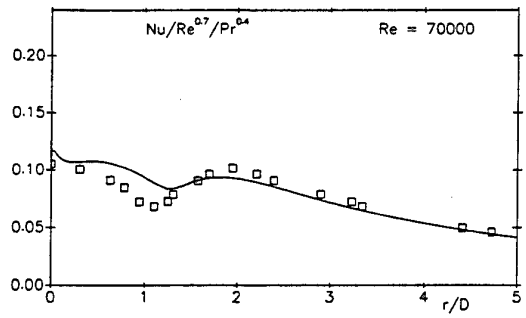

Figure 7: Nusselt number distribution for the case $H/D = 2$, $Re = 70000$.

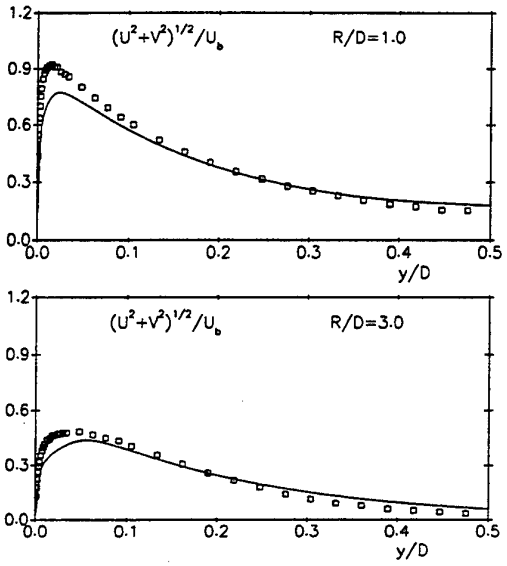

Figure 8: Mean velocity profiles in the radial wall jet for $H/D = 6$, $Re = 70000$.

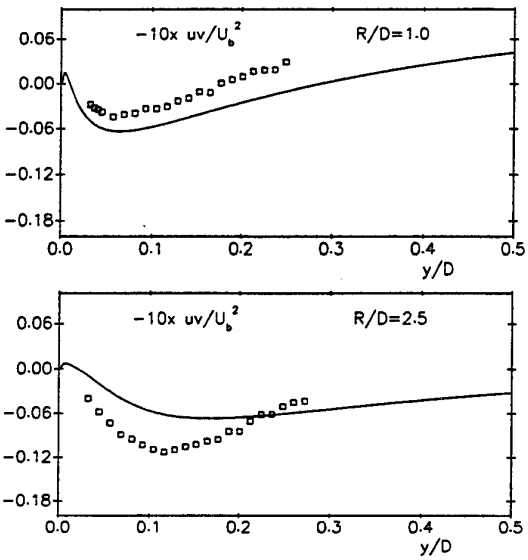

Figure 9: Shear stress profiles in the radial wall jet for $H/D = 6$, $Re = 70000$.

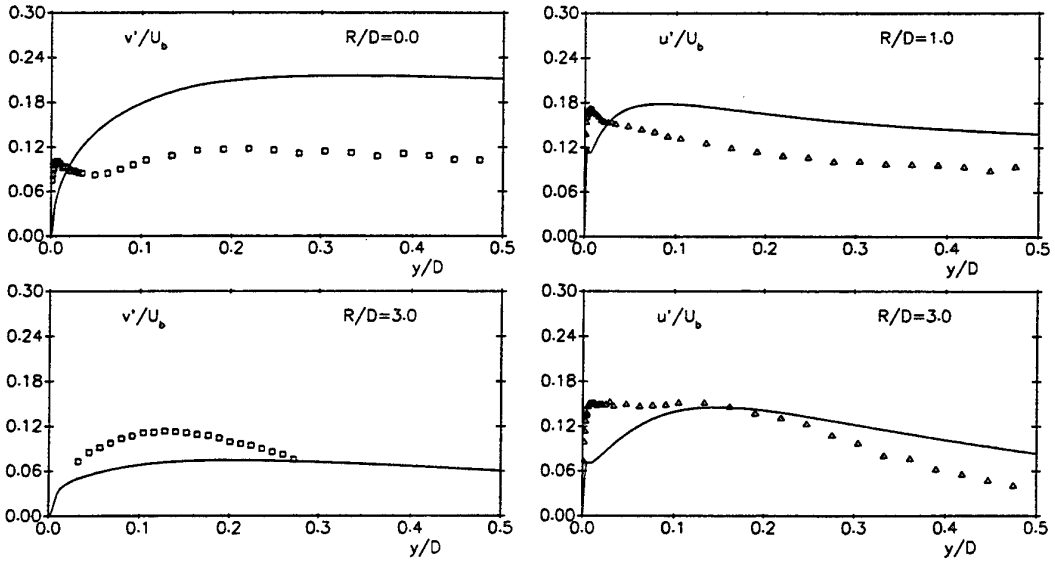

Figure 10: Rms velocity profiles in the radial wall jet for $H/D = 2$, $Re = 23000$. v' is normal to the wall. u' in the streamwise direction.

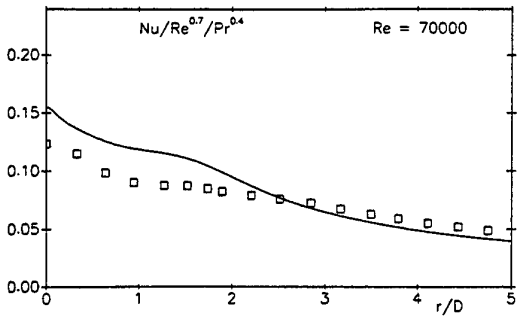

Figure 11: Nusselt number distribution for the case $H/D = 6$, $Re = 70000$.

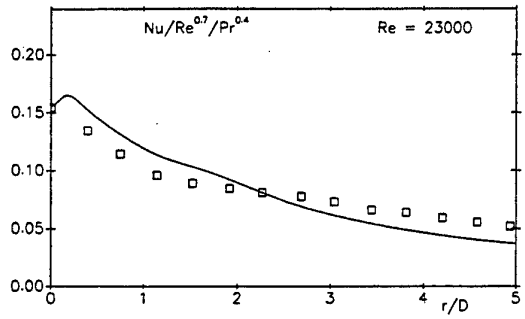

Figure 12: Nusselt number distribution for the case $H/D = 6$, $Re = 23000$.

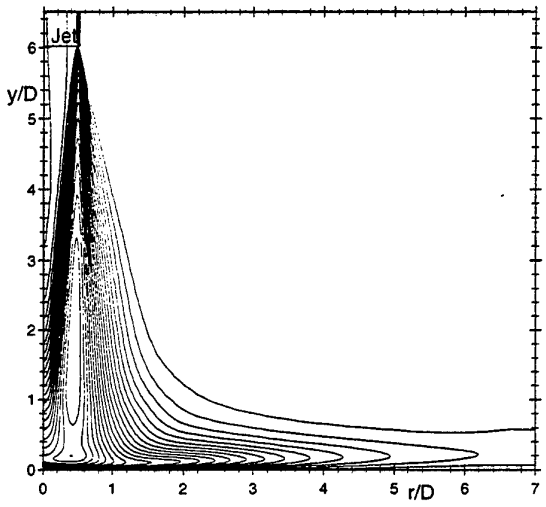

Figure 13: Turbulent kinetic energy contours for the case $H/D = 6$, $Re = 70000$.

SURFACE HEAT TRANSFER AND FLOW STRUCTURES OF STEADY AND FULLY PULSED RADIAL REATTACHING JETS

K. Bremhorst and N.D. Agnew

Department of Mechanical Engineering
The University of Queensland
Brisbane, Queensland, 4072,
Australia

ABSTRACT

Radial jet reattachment results in a region of flow on the surface to which a radial jet positioned near it attaches, where higher heat transfer rates are obtained than with in-line jets impinging normal to the surface. Flow pulsing was used in an attempt to increase heat transfer. Measurements showed no improvement over the steady case. Velocity measurements near the surface show that pulsing reduces the wall velocity gradient. Reynolds shear stresses relative to the exit jet momentum were also found to be lower than for the steady case. Computations with the basic k-ε model failed to predict a secondary flow region and gave only limited success in the prediction of pressure coefficients and Nusselt numbers.

1 INTRODUCTION

Many drying processes use jet impingement for transport of heat and mass in order to speed the process. Examples can be found in the paper industry where the wet sheet is dried as it passes between rollers of the production process. One method is to use in-line jets which direct a jet of hot air normal to the paper. A more recent innovation which has already found industry acceptance uses radial jet reattachment flow in order to increase transfer rates (1). While surface heat transfer characteristics are well documented (1) and (2), the flow processes are not well understood and no satisfactory modelling of such flows has been published.

Radial jet reattachment (RJR) flow is obtained when a radial jet operates sufficiently near a surface so that the entrainment by the jet causes it to deflect and attach to the surface. This results in a flow similar to that of a backward facing step except that the equivalent of a backward facing wall does not exist and more importantly perhaps, the flow is axisymmetric and diverging between the nozzle and the surface. The resultant jet leads to a reattachment circle where the stagnation streamline meets the surface. A cross-section of such a flow with the coordinate system to be used, is shown in Fig. 1.

Further improvements in heat transfer are being sought. Pepper, (3), adapted the whistler nozzle (4) to the in-line jet in order to obtain unsteady flow as it is known from the earlier work (5) that introduction of flow unsteadiness, leads to an increase in entrainment. Fully pulsed jet flow (6) is also known to give significant increases in entrainment, although consistent with Taylor's entrainment hypothesis, it is found that the increase in entrainment is directly proportional to the jet's momentum (6).

Flow visualization of the steady RJR nozzle flow (7) showed that the reattachment circle is not steady or closed at all times. Instead, it consists of periodic blowouts at random locations around the reattachment zone. This is distinctly different from the stagnation point of an in-line jet and was thought to be a contributing feature of the higher surface heat transfer experienced with RJR flow. Due to the trapped fluid within the reattachment curtain, a small area under the nozzle has low heat transfer rates. If fluid in that area can be removed periodically, a further increase in heat transfer was thought to be possible.

It was postulated that by use of a fully pulsed RJR flow which leads to periodic destruction of the reattachment curtain and its renewal, it should be possible to obtain considerable gains due to the increased temperature gradients at the wall with every cycle of fluid renewal.

The purpose of this paper is to report experimental results of investigations into steady and fully pulsed RJR flow produced by pulsing the mass flow to the radial jet nozzle in order to yield a periodically reattaching flow. Results of simple modelling are also presented together with an examination of the velocity field.

2 EXPERIMENTAL EQUIPMENT

A crucial aspect of any jet flow studies is the initial condition of the jet as determined by the nozzle details. For the results reported here, a nozzle with an internally shaped flow path as shown in Fig. 1 was used (9). Hot-wire anemometer measurements at the exit of the nozzle verified that a near ideal top hat

profile existed. The exit root mean square turbulence level was less than 7% of the mean exit velocity even for the largest exit gap.

Air was supplied to a plenum chamber through filters from a compressed air source. At the outlet of the plenum chamber, a rotating valve consisting of two geared counter-rotating rollers allowed full pulsing of the flow. A variable speed motor connected to the rollers was used to control the frequency of pulsation. Different sets of rollers gave different on:off ratios. A timing signal was generated by use of a fixed light beam and slotted disc attached to the roller When the rollers were fully open and not rotating, a smooth flow passage existed resulting in the steady RJR flow. The exit velocity time history for pulsed operation approximated a half sinusoid squared.

Flow rate was measured with a sonic nozzle thus preventing pressure fluctuations from the pulsing valve propagating upstream and affecting flow rate readings (9). In the case of laser Doppler anemometer measurements, a venturi injector nozzle introduced seed particles into the air supply just upstream of the plenum chamber. The latter was sized to maintain pressure fluctuations during a pulsing cycle at or below 3% of the mean pressure.

Surface heat transfer measurements were performed on a heated INCONEL 600 sheet of 0.0254 mm thickness held on to a perspex table by a vacuum. This construction minimized heat losses. The foil was heated with a 50 amp 5 volt dc power supply.

Local heat transfer coefficients were obtained from

$$h_{loc} = \frac{(q''_{gen} - q''_{rad} - q''_{con})}{(T_h - T_{ad})}$$

where T_h is the surface temperature when the foil is heated and T_{ad} is the adiabatic surface temperature. The foil surface was painted matte black to ensure ideal black body radiation. Both temperatures were measured with a MIKRON 6T62 infrared thermographic system with a maximum temperature resolution of 0.025 °C giving an accuracy of better than ±0.5% over its operating range. The heat fluxes, q″, represent generation of heat within the foil, radiant loss of heat from the surface of the foil and heat loss from the foil by conduction to its support base respectively. From the local heat transfer coefficient values, area averages could be obtained to any radius.

Velocity field measurements were conducted with a TSI 3-beam argon-ion laser Doppler anemometer system with polarisation to achieve separation of channels. A 40 MHz Bragg cell was used for frequency shifting to maintain an adequate number of fringe crossings to avoid fringe bias during the high velocity section of the pulse.

Signal processing was by means of two TSI 1990A counter type processors interfaced with an IBM compatible PC. Sample-hold processing was employed to remove velocity bias while Doppler burst validation was performed with a 1% accuracy for 1:2 time comparisons. Sample rates to ensure minimal velocity bias were selected according to the following criterion (10).

$$\dot{N} T_u > 5$$

where $\dot{N}$ is the data rate and T_u is the integral time scale of the flow.

3 SURFACE HEAT TRANSFER

Local Nusselt numbers (11) for the RJR case can be integrated to yield the area averaged Nusselt numbers shown in Figs. 2(a)-(c). The smaller on:off ratio is seen to give the least favorable result irrespective of the size of surface over which the averages are formed. Some degree of pulsing frequency dependency is evidenced in all cases.

From the two results at N=2/3, it is seen that the steady jet result was approached for the closer spacing between nozzle and surface. None of the three cases led to average Nusselt numbers higher than the steady case although, for the case of Fig. 2(b), indications are that if lower frequencies of pulsation had been possible, the steady case may be exceeded. Due to the low thermal inertia of the thin heating foil, lower frequencies could not be tested as the surface temperature fluctuates with the pulsations. The larger frequency dependency for this case is probably due to the time taken to establish a reattachment curtain and the vortex flows within it. The increase in Nusselt number with decreasing distance between nozzle and surface suggests that further increases may be possible by bringing the nozzle still closer to the surface.

The effect of a one pixel shift of surface temperature readings with the imaging equipment is shown in Fig. 2(a) at the lowest frequency where some fluctuation of surface temperature was already evident. Repeatability of readings is demonstrated by the repeat result for 45 Hz in Fig. 2(c). Neither effect is seen to be significant in the final result.

Measurements were also taken with an in-line nozzle without the radially reattaching feature, Fig.2(d). Pulsing is seen to make little difference to the average Nusselt number relative to the steady case but levels are well below those of the RJR flow.

Although only low subsonic flow existed, measured adiabatic surface temperatures varied across the surface for any given jet setting. This demonstrates the sensitivity of the thermal imaging equipment as well as the lack of radial conduction in the thin foil.

4 SIMULATION OF STEADY RJR FLOW

Notwithstanding the well documented shortcomings of the simple k-ε model for separated and impinging flows, an attempt was made to model one of the above RJR flows. The relevant equations are shown in Appendix A where C_μ=0.09, $C_{1\varepsilon}$=1.44, $C_{2\varepsilon}$=1.92, σ_k=1.0 and σ_ε=1.3. A turbulent Prandtl number, σ_T, of 0.86 was used to relate the eddy viscosity, ν_t, and eddy diffusivity.

In order to obtain a reattachment zone which is independent of the size of the computational domain, the flow field was solved to r/r_o=10 in the radial direction and to x/r_o=7 in the axial direction. Zero gradient boundary conditions were used along the open boundaries together with the no-slip condition at the wall. A wall function was included at the surface in order to speed up calculations using PHOENICS Ver. 2.0.

The predicted heat transfer result is shown in Fig. 3 and is compared with experimental data. Remarkably good agreement is noted for the location of the peak which corresponds to the reattachment line. For part of the region underneath the nozzle and the recirculation zone, predictions match measurements quite well but the region further downstream in the wall jet region as well as the level of the peak show significant disagreement between experiment and prediction.

Rather than extend computations to the pulsed case with the same model, a more detailed investigation of the flow field is presented to discover where shortcomings of the modelled results may exist for the steady case and to also obtain a better understanding of the velocity field for pulsed flow prior to further modelling.

5 VELOCITY FIELD INVESTIGATION

5.1 Mean velocity field

The predicted velocity field is summarized in the vector plot of Fig. 4. The reattachment region is seen clearly. Use of measured mean axial and mean radial velocities (11) leads to the qualitative flow representation of Fig. 5 which holds for both the steady and pulsed RJR flows, although for the latter it applies only in the later part of the cycle once the attached flow has been reestablished. From Fig. 5 it is seen that a secondary vortex exists which is absent in the predicted results of Fig. 4.

Corresponding pressure coefficients are given in Fig. 6 where a small radial shift between measured and predicted results is noted as well as a difference in the peak values. The predicted values in the centre region beneath the nozzle (r/r_o<1) are below the measured values thus indicating stronger suction than actually exists. This and the lower peak value at the reattachment point ($r/r_o\approx$3.1) indicate that the model does not yield the full recovery of pressure observed by measurement. The model is also unable to reproduce the low pressure peak within the stagnation region.

Comparing the radial and axial velocity fields for N=1/3 and 2/3, shows little variation from the steady case (11). In all cases, reattachment occurs near r/r_o=3.1 and a surface vortex is found together with a secondary recirculation region in the space between the nozzle and the surface. Only small variations with pulsing frequency were observed. The above results indicate little difference between the steady and pulsed RJR flows.

Extension of mean radial velocity measurements to the near wall region where the flow is essentially parallel to the wall, highlights a significant difference between the two types of flows, Figs. 7(a-c). The data were obtained in single channel mode in order to allow the measuring volume of the LDA to be brought almost to the solid surface. The radial measurement planes are located within the recirculation zone, near the stagnation or reattachment region and well outside of the recirculation region.

The limited data show a clear frequency dependency but more importantly, show that relative to the steady jet, wall damping of pulsations leads to a significant reduction in mean velocity parallel to the wall. A consequence of this is a reduction of mean velocity gradient at the wall which in turn will affect heat and mass transfer. This feature is a key indicator of why pulsed surface heat transfer Nusselt numbers for the range of pulsations studied, are not above those for the steady case.

5.2 Fluctuating velocity field – time means

Averaging over many pulses at a given point in the pulse, permits phase averaged means and phase averaged root mean squares of velocity fluctuations to be obtained. The latter can then be averaged over a cycle to give the average root mean square turbulence level at any point. This is the shear generated or intrinsic turbulence which is comparable to that of a steady flow. Figs. 8(a)-(c) illustrate the case of steady and pulsed jet intrinsic turbulence levels. Considerable similarity is noted between the two cases both in distribution and in level. The similarity also applies to the radial component, (9).

Transport by turbulence is through the Reynolds shear stresses. Figs. 9(a)-(c) show that unlike the normal stresses, these are different for steady and pulsed flow with the pulsed cases being significantly lower than for the steady one. Normalisation on jet exit momentum is used on the basis that jet momentum determines turbulent shear stresses as already found to be the case for pulsed free jets (6). The reduced level of the shear stresses for the pulsed cases is further

evidence of a reduction of transport by the small scale motions.

5.3 Fluctuating velocity field – phase averaged

From a modelling perspective, it is expected that quasi-steady state behavior results if the time scale of pulsation is large relative to the time scales of the turbulence. The flow behavior is then expected to be like a steady flow but with varying mass flow rate. On that basis, it is useful to consider flow variables as a function through the pulse, that is, phase averages. (9) gives a comprehensive set of phase averaged turbulence quantities of which the most instructive are reproduced in Figs. 10-12. In order to facilitate comparison of measured turbulence levels with those of steady, free jets, components of root mean square intrinsic turbulence are normalized on the mean velocity magnitude, $VMAG_\tau$, given by

$$VMAG_\tau = \sqrt{(U_\tau^2 + V_\tau^2)}.$$

In order to keep data files of LDA signals within reasonable bounds, some scatter of phase averages has to be accepted. In spite of this, trends of the data are readily visible. Under the nozzle, the mean velocity at any instant through the pulse is very small, hence turbulence intensities are high. Prior to reattachment, a finite mean velocity exists during the "on" part of the cycle thus giving somewhat reduced turbulence intensity. A further reduction in mean velocity exists at the reattachment radius but near the wall at x/X_p=0.33. This is near the stagnation point where a high turbulence level is observed. Much higher turbulence intensities exist during the deceleration and "off" part of the cycle when the periodic velocity is very small.

From Figs. 10 and 11 it is seen that for the "on" part of the cycle where turbulence intensities similar to those of free jets or in boundary layers can be expected if the flow is quasi-steady, the turbulence intensities and hence k, are much higher than for corresponding steady flows. This is consistent with findings in fully pulsed jets (6, 12) for which the intrinsic turbulence intensity is higher than that found in steady jets. The intrinsic covariances of Fig. 12 are particularly uncertain but the same trends seen above are still visible.

For each section of flow, turbulence intensities are higher than those found in similar steady flows. While qualitatively, the present flow would be expected to act like a quasi-steady one due to the very low Strouhal numbers (<0.005 based on exit slot width and exit velocity), the higher intrinsic turbulence level leads to modelling difficulties (13) which still remain to be resolved.

6 CONCLUSIONS

Radial jet reattachment flow has associated with it a significantly higher surface heat transfer than in-line jets impinging normally to a surface. This has found use in the paper drying industry where even higher heat transfer rates are desired. Attempts to improve the surface heat transfer even further by periodic renewal of the trapped fluid in the recirculation zone under the nozzle, did not yield further improvements above those of the steady RJR flow although the heat transfer rates were a strong function of the length of the "on" period for the pulsed flow with a longer on period giving better heat transfer results.

Simple k-ε modelling of the flow with a turbulent Prandtl number to give surface heat transfer, led to reasonable predictions of surface heat transfer but results indicated that improvements in modelling are required.

Detailed velocity field measurements for the steady and fully pulsed RJR flow led to the realization that the pulsing effect does not penetrate the wall region fully thus leading to a reduced velocity gradient in the wall region and hence leading to a reduced temperature gradient.

Turbulence measurements indicated a lower relative turbulent shear stress which is consistent with the reduced heat transfer. Normal intrinsic turbulent stresses, even in regions where the flow more closely resembles free jet flow, were found to be higher for the pulsed jet than for the steady jet. This aspect was previously found to lead to significant flow modelling difficulties (13).

7 ACKNOWLEDGMENTS

The authors wish to thank Professor R.H. Page, Texas A&M University, College Station, Texas for his generous assistance which made collection of the heat transfer data possible and Mr. T. Gruber, his student, for assistance with operation of the thermographic system.

8 NOMENCLATURE

b - nozzle slot width
D - in-line jet exit diameter
f - frequency of pulsation
H - distance of in-line jet from surface
k - turbulent kinetic energy = $\frac{1}{2}\overline{u_i u_i}$
M_s, M_p - steady jet momentum, pulsed jet momentum
N - on:off ratio for pulsed flow
Nu - Nusselt number
P - static pressure
Pr - Prandtl number
r - radial direction
r_o - radial distance to nozzle exit plane

T - fluid temperature
U - mean axial velocity (positive direction is from nozzle to surface)
U_τ - phase averaged mean axial velocity
u - velocity fluctuation
u_I - axial intrinsic velocity fluctuation
u_I' - root mean square intrinsic velocity, phase or pulse averaged
$\overline{uv_I}$ - intrinsic covariance, phase or pulse averaged
V, V_τ, v_I' - as for U, U_τ and u_I' but in radial direction
V_o - nozzle exit velocity
x - axial coordinate
X_p - distance between nozzle and surface

9 REFERENCES

(1) Page, R.H. and Kiel, R., Utilization of a radial jet reattachment (RJR) for industrial drying, Proceedings of Forum on Industrial Application of Fluid Mechanics, 1990, 100, 71-77, ASME FED

(2) Ostawari, C. and Page, R.H., Convective heat transfer from a radial jet reattachment, AIChE Symposium Series, Heat Transfer, San Diego, 1992, **88**, 189-197

(3) Pepper, F., The self oscillating jet impingement nozzle, Studienarbeit, Texas A&M University, Department of Mechanical Engineering, College Station, Texas, May, 1993

(4) Hill, Jr. W.G. and Greene, P.R., Increased turbulent jet mixing rates obtained by self-excited acoustic oscillation, Journal of Fluid Engineering, Trans. ASME, 1977, **99**, 520-525

(5) Crowe, S.C. and Champagne, F.H., Orderly structure in jet turbulence, Journal of Fluid Mechanics, 1971, **84**, 547-591

(6) Bremhorst, K. and Hollis, P.G., Velocity field of an axisymmetric pulsed, subsonic air jet, AIAA Journal, 1990, **28**, 2043-2049

(7) Agnew, N.D., An investigation of radial reattachment using laser Doppler anemometry and flow visualization, Undergraduate thesis, Department of Mechanical Engineering, The University of Queensland, St. Lucia, Brisbane, Australia, 1991

(8) Page, R.H., Axisymmetric gas jets: surface impingement phenomena, 14th Canadian Congress of Applied Mechanics, CANCAM'93, Queen's University, Kingston, Ontario, 30 May – 3 June 1993, **1**, 10-19

(9) Agnew, N.D., An investigation into fully pulsed radial jet reattachment, Ph.D. thesis, The University of Queensland, St. Lucia, Brisbane, Australia, 1996

(10) Winter, A., Graham, L.J.W., and Bremhorst, K., Effects of velocity bias in LDA measurements using sample and hold processing, Experiments in Fluids, 1991, 11, 147-152

(11) Bremhorst, K. and Agnew, N.D., An investigation into the fully pulsed radial reattaching jet, FED-Vol. 237, 1996 Fluids Engineering Division Conference, 1996, Vol. 2, 589-594, ASME

(12) Bremhorst, K., Gehrke, P.J. and He, S., Measured Reynolds stress distributions and energy budgets of fully pulsed round free jets and comparisons with k-ε model predictions, 11th Symposium on Turbulent Shear Flows, Institut. National Polytechnique, Universite Joseph Fourier, Grenoble, Sept. 8-10, 1997, Vol. 22.1 - 22.6

(13) Graham, L.J.W. and Bremhorst, K., Application of the k-ε turbulence model to the simulation of a fully pulsed free air jet, Trans. ASME, Journal of Fluids Engineering, 1993, 115, 1, 70-74

APPENDIX A – EQUATIONS

For incompressible flow, invoking the Boussinesq relationship and the eddy viscosity relationship of

$$\nu_t = \frac{C_\mu k^2}{\varepsilon}$$

Momentum

$$U_j \frac{\partial U_i}{\partial x_j} = -\frac{1}{\rho}\frac{\partial P}{\partial x_i} + \frac{\partial}{\partial x_j}\left(\nu \frac{\partial U_i}{\partial x_j} - \overline{u_i u_j}\right)$$

Energy

$$U_i \frac{\partial T}{\partial x_i} = \frac{\partial}{\partial x_i}\left[\left(\frac{\nu}{Pr} + \frac{\nu_t}{\sigma_T}\right)\frac{\partial T}{\partial x_i}\right]$$

k-transport

$$U_i \frac{\partial k}{\partial x_i} = \frac{\partial}{\partial x_i}\left[\frac{\nu_t}{\sigma_k}\frac{\partial k}{\partial x_i}\right] + \nu_t\left(\frac{\partial U_i}{\partial x_j} + \frac{\partial U_j}{\partial x_i}\right)\frac{\partial U_i}{\partial x_j} - \varepsilon$$

ε-transport

$$U_i \frac{\partial \varepsilon}{\partial x_i} = C_{1\varepsilon}\nu_t \frac{\varepsilon}{k}\left(\frac{\partial U_i}{\partial x_j} + \frac{\partial U_j}{\partial x_i}\right)\frac{\partial U_i}{\partial x_j} + \frac{\partial}{\partial x_i}\left(\frac{\nu_t}{\sigma_\varepsilon}\frac{\partial \varepsilon}{\partial x_i}\right) - C_{2\varepsilon}\frac{\varepsilon^2}{k}$$

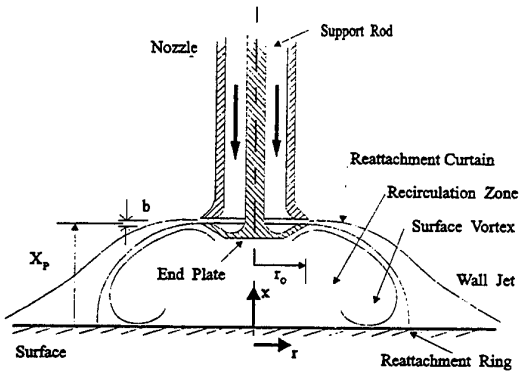

Fig. 1 – Radial jet reattachment and coordinate system, r_o=21.7 mm

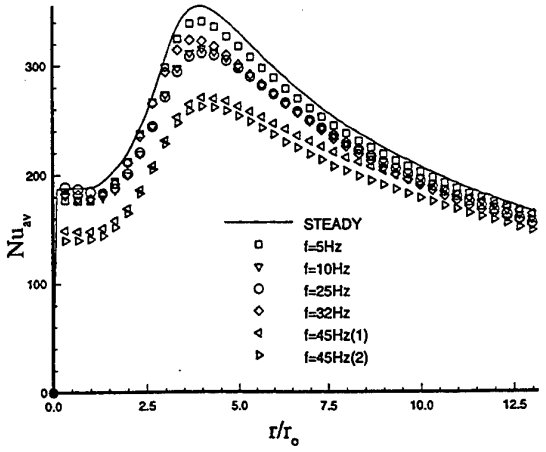

Fig. 2(b) - Average Nusselt number with RJR (b=2.5 mm, X_p=24 mm, V_o=48 m/s, N=2/3)

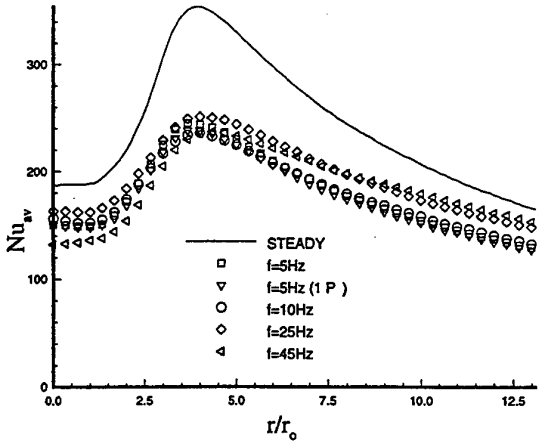

Fig. 2(a) – Average Nusselt number with RJR (b=2.5 mm, X_p=24 mm, V_o=48 m/s, N=1/3)

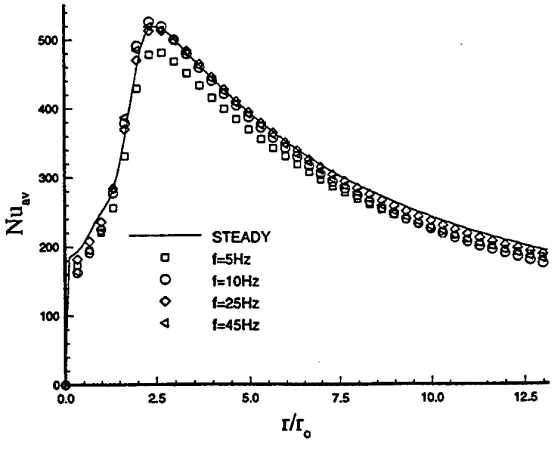

Fig. 2(c) - Average Nusselt number with RJR (b=2.5 mm, X_p=10 mm, V_o=48 m/s, N=2/3)

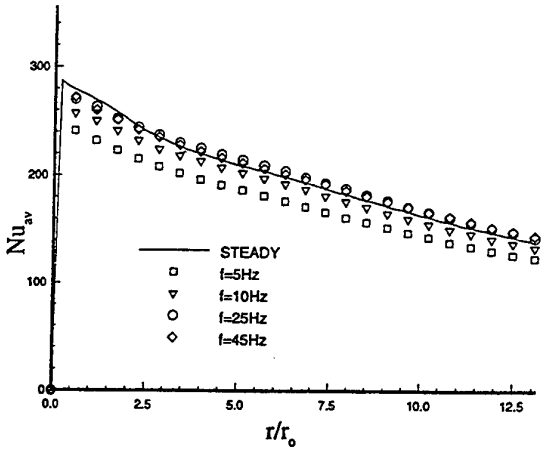

Fig. 2(d) - Average Nusselt number with in-line nozzle (H=6D, V_o=48 m/s, N=2/3)

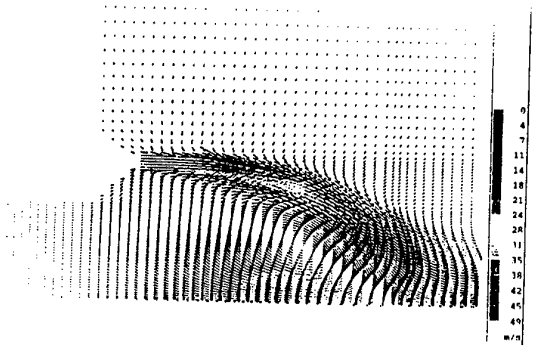

Fig. 4 – Predicted velocity field of steady RJR flow

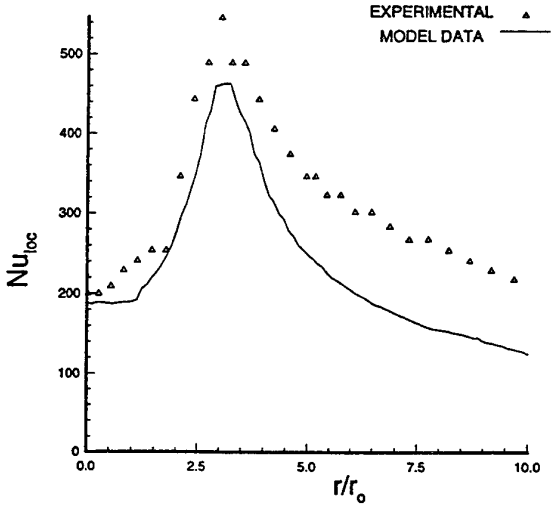

Fig. 3 – Comparison of predicted and experimental local Nusselt numbers for steady RJR flow.

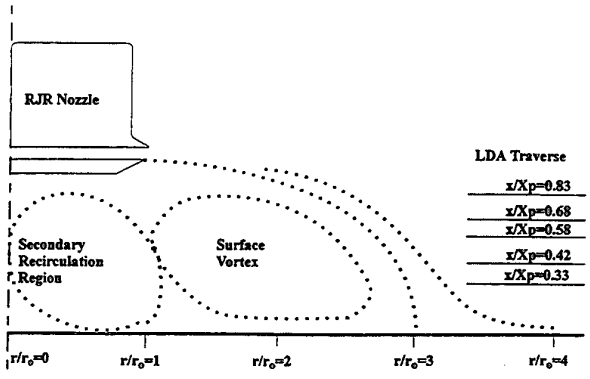

Fig. 5 – Flow field deduced from U and V measurements – steady and pulsed flows are similar

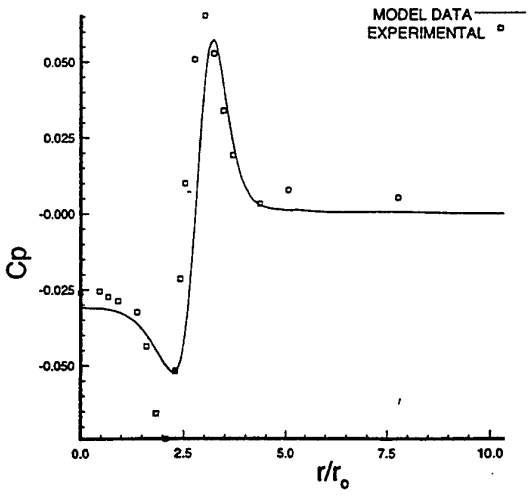

Fig. 6 – Pressure coefficient distribution at surface for steady RJR flow (b=2.5 mm, X_p=24 mm, V_o=48 m/s)

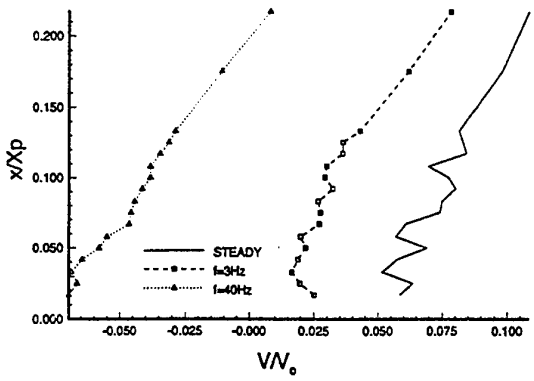

Fig. 7(b) – Mean radial velocity – V_o=48 m/s, b=2.5 mm, X_p=24mm, r/r_o=3.14

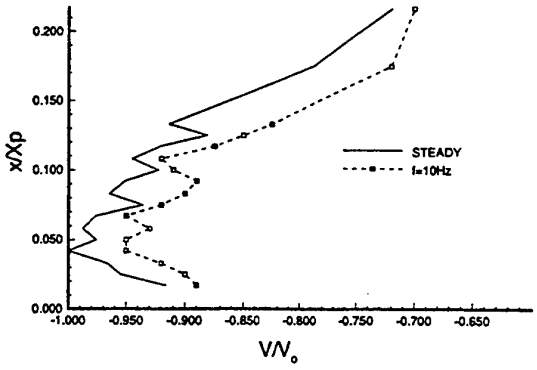

Fig. 7(a) – Mean radial velocity – V_o=48 m/s, b=2.5 mm, X_p=24mm, r/r_o=2

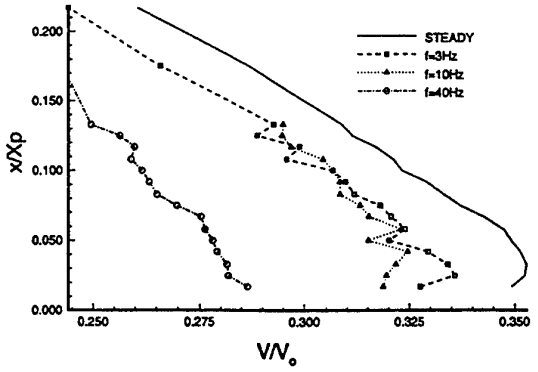

Fig. 7(c) – Mean radial velocity – V_o=48 m/s, b=2.5 mm, X_p=24mm, r/r_o=4.8

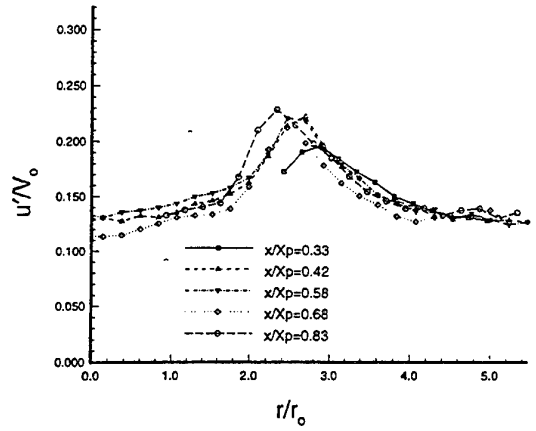

Fig. 8(a) – Intrinsic turbulence intensities for steady RJR flow - V_o=48 m/s, b=2.5 mm, X_p=24mm

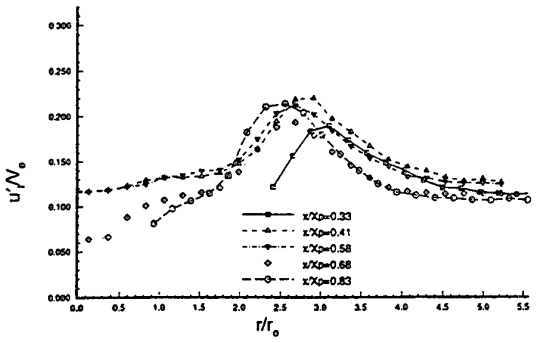

Fig. 8(c) – Intrinsic turbulence intensities for pulsed RJR flow - V_o=48 m/s, b=2.5 mm, X_p=24mm, 10 Hz pulsation frequency and N=2/3

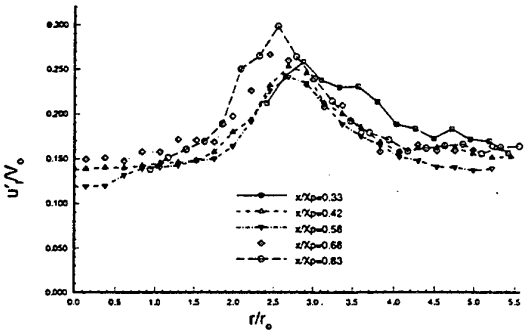

Fig. 8(b) – Intrinsic turbulence intensities for pulsed RJR flow - V_o=48 m/s, b=2.5 mm, X_p=24mm, 10Hz pulsation frequency and N=1/3

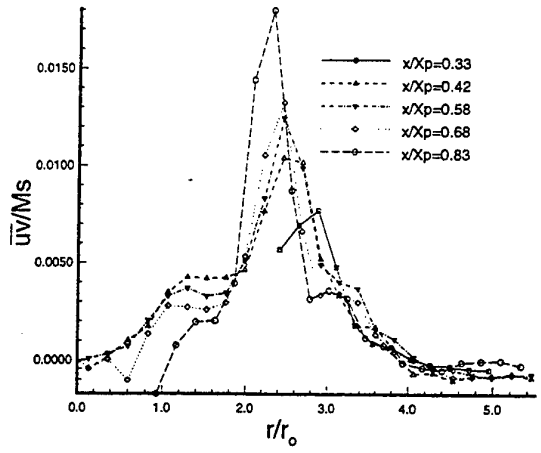

Fig. 9(a) – Intrinsic Reynolds shear stress for steady RJR flow - V_o=48 m/s, b=2.5 mm, X_p=24mm

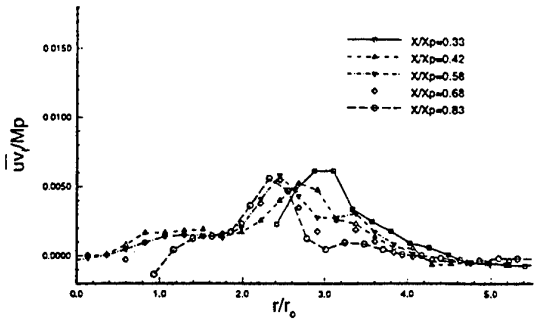

Fig. 9(c) – Intrinsic Reynolds shear stress for pulsed RJR flow - V_o=48 m/s, b=2.5 mm, X_p=24mm, 10Hz pulsation frequency and N=2/3

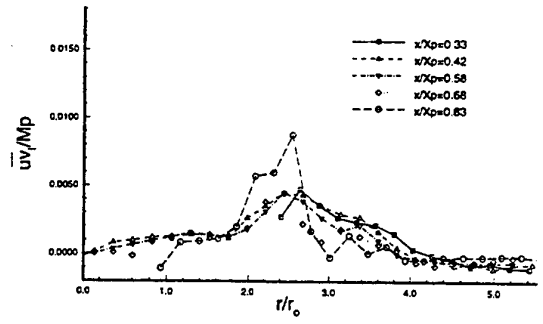

Fig. 9(b) – Intrinsic Reynolds shear stress for pulsed RJR flow - V_o=48 m/s, b=2.5 mm, X_p=24mm, 10Hz pulsation frequency and N=1/3

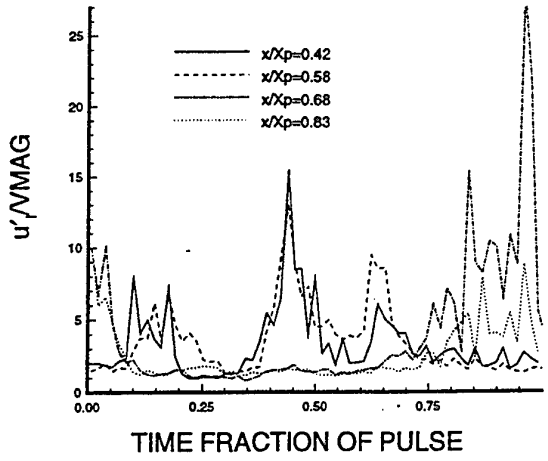

(a) At nozzle radius, r/r_o=1.0

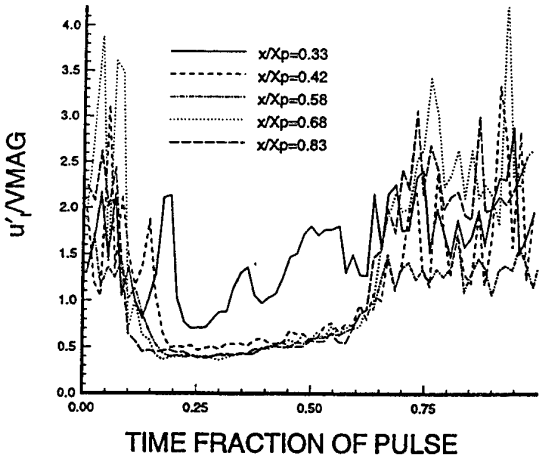

(c) Near reattachment region, r/r_o=3.1

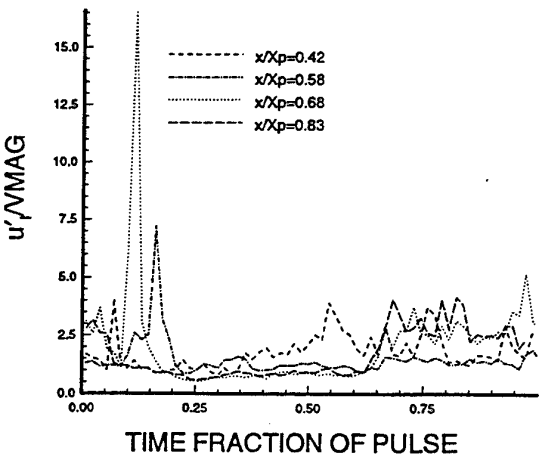

(b) Just inside reattachment region, r/r_o=2.4

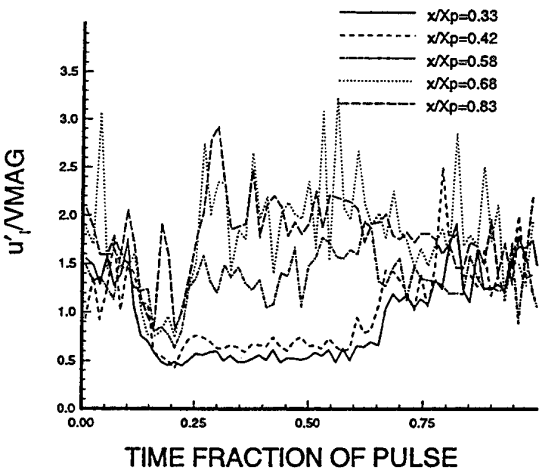

(d) In the wall jet region, r/r_o=4.5

Fig. 10 – Ensemble averaged axial intrinsic turbulence - V_o=48 m/s, b=2.5 mm, X_p=24mm, 10Hz and N=2/3

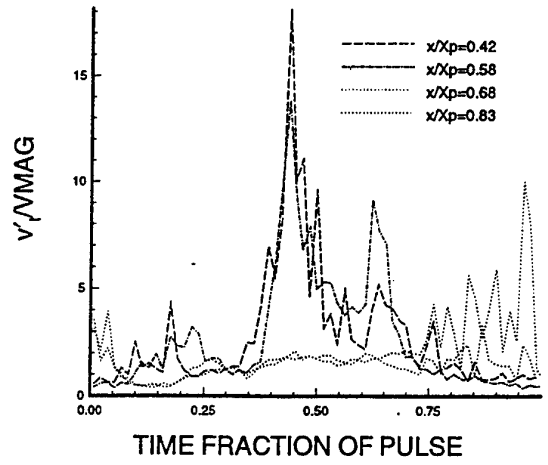

(a) At nozzle radius, r/r_o=1

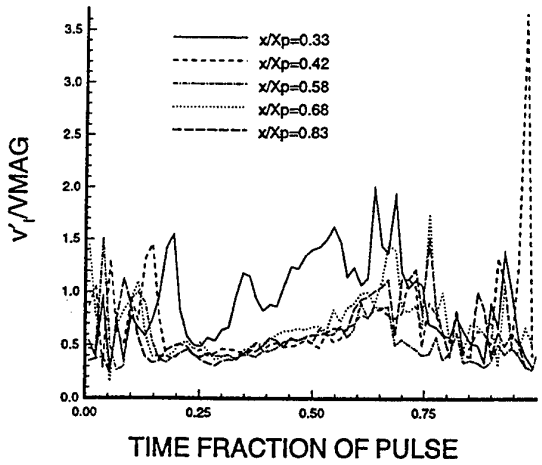

(c) Near reattachment region, r/r_o=3.1

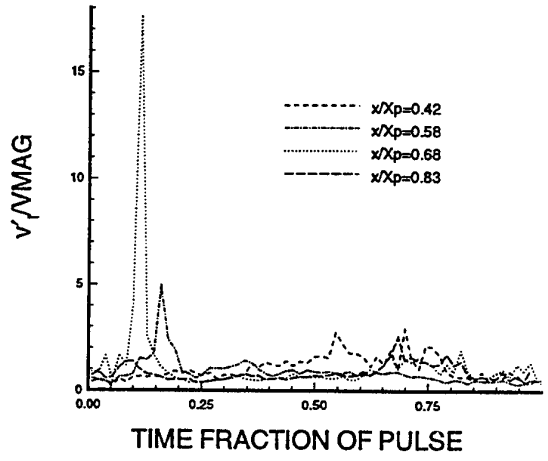

(b) Just inside reattachment region, r/r_o=2.4

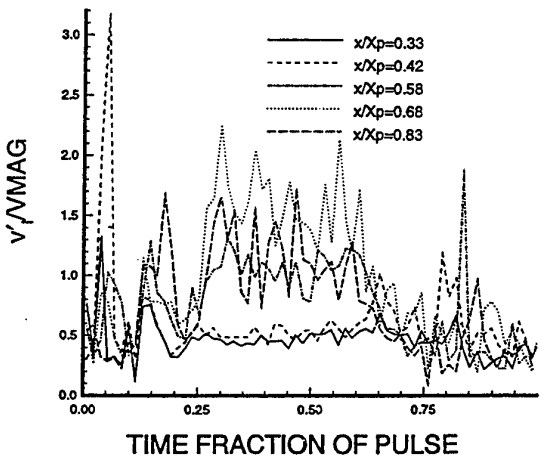

(d) In the wall jet region, r/r_o=4.5

Fig. 11 – Ensemble averaged radial intrinsic turbulence - V_o=48 m/s, b=2.5 mm, X_p=24mm, 10Hz and N=2/3

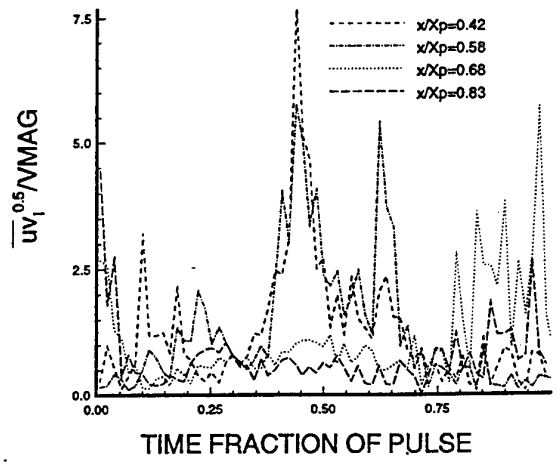

(a) At nozzle radius, r/r_o=1.0

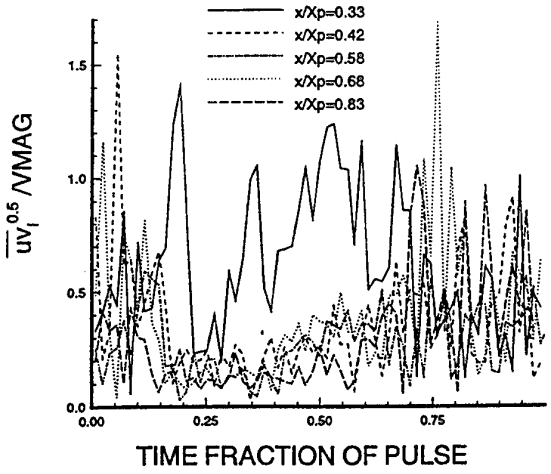

(c) Near reattachment region, r/r_o=3.1

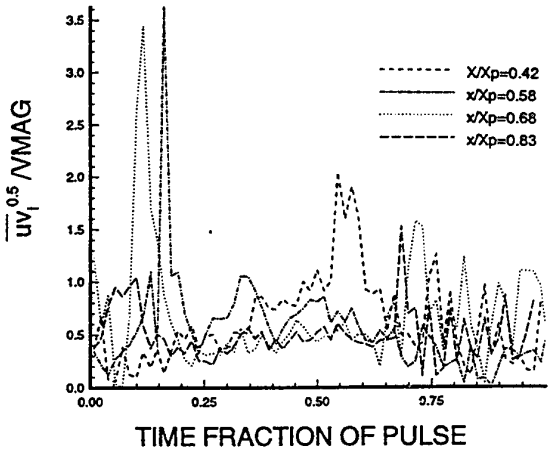

(b) Just inside reattachment region, r/r_o=2.4

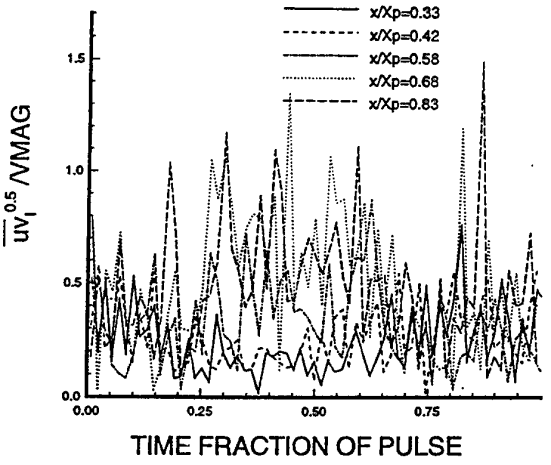

(d) In the wall jet region, r/r_o=4.5

Fig. 12 – Ensemble averaged covariance of intrinsic turbulence - V_o=48 m/s, b=2.5 mm, X_p=24mm, 10Hz and N=2/3

COMPUTATION OF ENHANCED TURBULENT HEAT TRANSFER IN A CHANNEL WITH PERIODIC RIBS

W.B.Tsai*, W.W. Lin*, C.C. Chieng†

Department of Engineering and System Science
National Tsing Hua University,
Hsinchu, Taiwan, R.O.C.
*Department of Mathematics
†Corresponding person

ABSTRACT

This study performs numerical computations on the heat transfer and fluid flow behavior in a rectangular channel flow with streamwise-periodic ribs mounted on one of the principal wall. Several different low Reynolds number models are employed in the numerical predictions, which are $k-\varepsilon$ models of Launder & Sharma (LS), Chien (CH), Lin, $k-\omega$ model and Durbin's $k-\varepsilon-v^2$ model. The numerical results shows that all these models can predict the flowfield reasonable well, and the inclusion of Yap term in the $\varepsilon-$equation can further improve the prediction in all $k-\varepsilon$ models, and $k-\varepsilon-v^2$ model. However, these models behave differently in heat transfer computations. $k-\omega$ model leads to too low level of heat transfer and turbulence. Lin's model with Yap term predicts the heat transfer level best among all $k-\varepsilon$ models. Durbin's model with extra $\overline{v^2}$, f equations and Yap term has the best performance.

1. INTRODUCTION

Repeated rib-turbulators created in flow passage at periodic intervals can enhance the removal of heat transfer. The flow separation zones ahead and after the ribs increase the turbulence and heat transfer levels significantly. It is of practical importance and employed in blade and other cooling applications. Computations of flow and heat transfer through ribbed passage need appropriate turbulence models and most of the computations employed high-Re models of turbulence with the wall function approach. The exceptions were the works of Taylor et al [1], and Iacovides et al [2]. Iacovides et al's work suggested the necessity of the use of low-Re models of near-wall turbulence. He tested both the effective viscosity models and second moment closure models and indicated the needs of tests of more refined low-Re models. Present work compare the predictions by different low-Re turbulence models in wider range : $k-\varepsilon$ models of Launder and Sharma (LS) [3],Chien (CH) [4], Lin [5], Durbin's $k-\varepsilon-v^2$ model [6], and $k-\omega$ model [7]. Besides, for separated flow, the excessively high levels of near wall turbulence in most turbulence model must be taken care, so that the effect of the addition of a correction term to the $\varepsilon-$equation [8] is studied also.

In this paper, numerical computations on the heat transfer and fluid flow behavior in a rectangular channel with streamwise-periodic ribs mounted on one of the principal walls are performed based on the flow measurements by Drain & Martin [9] and heat transfer measurements by Liou et al [10]. The calculations will demonstrate the performance of these models by comparing the measurements and numerical predictions.

2. GOVERNING EQUATIONS

In this study, the time-dependent, Reynolds-averaged, incompressible Navier-Stokes equations are employed. The equations can be written in cartesian tensor notation as follows:

Continuity equation :

$$\frac{\partial U_i}{\partial x_j}=0$$

Momentum equations :

$$\frac{\partial(\rho U_i)}{\partial t}+\frac{\partial \rho U_i U_j}{\partial x_j}=\beta\delta_{ii}-\frac{\partial \hat{P}}{\partial x_j}+\frac{\partial}{\partial x_j}[\mu(\frac{\partial U_i}{\partial x_j}+\frac{\partial U_j}{\partial x_i})-\rho\overline{u_i u_j}]$$

The Reynolds stress can be approximated by adopting

Boissineq approximation within the framework of eddy viscosity :

$$-\rho\overline{u_i u_j} = \mu_t\left(\frac{\partial U_i}{\partial x_j}+\frac{\partial U_j}{\partial x_i}\right)-\frac{2}{3}\delta_{ij}k$$

where μ is the molecular viscosity and μ_t is the turbulent viscosity.

In the fully developed region, the pressure drop per pitch is a constant, i.e. $P(x+Pi,y)=P(x,y)-\beta\cdot Pi$, where Pi is the pitch length. If we define

$$\hat{P}(x,y)=\beta x+P(x,y)$$

then we have the following relations :

$$\hat{P}(x+n\cdot Pi,y)=\hat{P}(x+(n-1)\cdot Pi,y)=\cdots=\hat{P}(x,y)\ ,$$

where n is an integer and $\hat{P}$ repeats itself from pitch to pitch.

Energy equation :

$$\frac{\partial(\rho\hat{T})}{\partial t}+\frac{\partial(\rho U_i\hat{T})}{\partial x_i}=\frac{\partial}{\partial x_i}\left[\left(\frac{\mu}{\mathrm{Pr}}+\frac{\mu_t}{\mathrm{Pr}_t}\right)\frac{\partial\hat{T}}{\partial x_i}\right\}-\rho U_i\gamma\delta_{il}$$

where Pr is the Prandtl number, Pr_t is the turbulent Prandtl number and γ is the temperature gradient which is defined as

$$\gamma=\frac{T(x+Pi,y)-T(x,y)}{Pi}$$

Turbulence properties

There are numerous versions of $k-\varepsilon$ turbulent models in the low Reynolds number form. According to the evaluations of two-equation turbulence for near wall and low Reynolds number form by Patel, Rodi, Scheuerer [11] for tests with a variety of boundary layer flows, the $k-\varepsilon$ models of Launder-Sharma, Chien, Lam and Bremhorst [12], and the $k-\omega$ model of Wilcox and Rubesin [13] were found considerably better than the other 4 models. Therefore, these models are selected for the present study. Besides, Lin [5] proposed an improved model based on direct numerical simulation data and he claimed that the model not only conform with the near wall characteristics but also posses the correct asymptotic behavior in the vicinity of the wall. The application of Lin's model produces correctly the skin friction and near wall heat transfer coefficient for a two-dimensional backward-facing step. In addition to these models, Durbin [6] proposed a $k-\varepsilon-\overline{v^2}$ model for computing non-equilibrium, or complex, turbulent flows. In his model, the velocity scale for turbulent transport toward the wall is $\overline{v^2}$, not k. Extra two parameters $\overline{v^2}$ and f, need to be solved via $\overline{v^2}$ transport equation and an elliptic relaxation equations for f. Good agreement between experiment and predictions are obtained for turbulent separated flows over a backstep, in a plane diffuser, and around a triangular cylinder [6], and jet impinging onto a pedestal using a revised model [14]. Brief descriptions of the transport equations of turbulent properties for various models are given as follows :

- $k-\varepsilon$ model

$$\frac{\partial(\rho k)}{\partial t}+\frac{\partial(\rho U_j k)}{\partial x_j}=\frac{\partial}{\partial x_j}\left[\left(\mu+\frac{\mu_t}{\sigma_k}\right)\frac{\partial k}{\partial x_j}\right]+\Pi_k-\rho\overline{u_i u_j}\frac{\partial U_i}{\partial x_j}-\rho(\bar{\varepsilon}+\hat{\varepsilon})$$

$$\frac{\partial(\rho\bar{\varepsilon})}{\partial t}+\frac{\partial(\rho U_j\bar{\varepsilon})}{\partial x_j}=\frac{\partial}{\partial x_j}\left[\left(\mu+\frac{\mu_t}{\sigma_\varepsilon}\right)\frac{\partial\bar{\varepsilon}}{\partial x_j}\right]+\Pi_{\bar{\varepsilon}}-\rho C_{\varepsilon 1}f_1\frac{\bar{\varepsilon}}{k}\overline{u_i u_j}\frac{\partial U_i}{\partial x_j}-\rho C_{\varepsilon 2}f_2\frac{\bar{\varepsilon}^2}{k}+E$$

where

$$\mu_t=\rho C_\mu f_\mu\frac{k^2}{\bar{\varepsilon}}$$

The constants and damping functions for the models of Launder-Sharma (LS) [3], Chien (CH) [4], and Lin [5] in the above equations are listed in table 1. The dissipation rate of turbulent energy ε , can be decomposed into two part, i.e. $\varepsilon=\bar{\varepsilon}+\hat{\varepsilon}$, and $\bar{\varepsilon}$ is the dependent variable of the transport equation. The extra term, denoted by E, can better represent the near wall behavior.

- $k-\omega$ model

$$\frac{\partial(\rho k)}{\partial t}+\frac{\partial(\rho U_j k)}{\partial x_j}=\frac{\partial}{\partial x_j}\left[(\mu+\sigma^*\mu_t)\frac{\partial k}{\partial x_j}\right]+\rho(P_k+D_k)$$

$$\frac{\partial(\rho\omega)}{\partial t}+\frac{\partial(\rho U_j\omega)}{\partial x_j}=\frac{\partial}{\partial x_j}\left[(\mu+\sigma\mu_t)\frac{\partial\omega}{\partial x_j}\right]+\rho(D_\omega+P_\omega+C_\omega)$$

where

$$\mu_t=\rho\alpha^*\frac{k}{\omega}$$

$$P_k=\alpha^*\frac{k}{\omega}\Omega^2,\ D_k=-B^*\omega k,\ P_\omega=\alpha\alpha^*\Omega^2,$$

$$C_\omega=\max\{0,\frac{\sigma_{il}}{\omega}\left(\frac{\partial k}{\partial x}\frac{\partial\omega}{\partial x}+\frac{\partial k}{\partial y}\frac{\partial w}{\partial y}\right)\},\ D_\omega=-B\omega^2$$

$$\sigma^*=1,\sigma=0.6,R_k=6,R_\beta=8,R_\omega=2.2,$$

$$\alpha_0^*=0.025,\ \mathrm{Re}_t=\frac{\rho}{\mu}\frac{k}{\omega},\ \alpha^*=\frac{R_k\alpha_0^*+\mathrm{Re}_t}{R_k+\mathrm{Re}_t},$$

$$\alpha=\frac{1}{2}\frac{R_\omega\alpha_0+\mathrm{Re}_t}{(R_\omega+\mathrm{Re}_t)\alpha^*},\ \alpha_0=0.1,\ B=0.075,$$

$$B^* = 0.09 + \frac{\frac{5}{18}+(\frac{Re_t}{R_\beta})^4}{1+(\frac{Re_t}{R_\beta})^4},$$

$$\Omega^2 = (\frac{\partial u}{\partial y} + \frac{\partial v}{\partial x})^2 + 2[(\frac{\partial u}{\partial x})^2 + (\frac{\partial v}{\partial y})^2].$$

- Durbin's mode

$$\frac{\partial(\rho k)}{\partial t} + \frac{\partial(\rho U_j k)}{\partial x_j} = \frac{\partial}{\partial x_j}[(\mu + \frac{\mu_t}{\sigma_k})\frac{\partial k}{\partial x_j}] + P_k - \rho\varepsilon$$

$$\frac{\partial(\rho\overline{v^2})}{\partial t} + \frac{\partial(\rho U_j \overline{v^2})}{\partial x_j} = \frac{\partial}{\partial x_j}[(\mu + \frac{\mu_t}{\sigma_k})\frac{\partial \overline{v^2}}{\partial x_j}] + \rho k f - \rho\overline{v^2}\frac{\varepsilon}{k}$$

$$\frac{\partial(\rho\varepsilon)}{\partial t} + \frac{\partial(\rho U_j \varepsilon)}{\partial x_j} = \frac{\partial}{\partial x_j}[(\mu + \frac{\mu_t}{\sigma_\varepsilon})\frac{\partial \varepsilon}{\partial x_j}] + \frac{\rho C_{\varepsilon 1} P_k - \rho C_{\varepsilon 2}\varepsilon}{T}$$

$$L^2\nabla^2 f - f = (1-C_1)\frac{[\frac{2}{3}-\frac{\overline{v^2}}{k}]}{T} - C_2\frac{P_k}{k},$$

$$\mu_t = \rho C_\mu \overline{v^2} T.$$

where

$$\sigma_k = 1.0, \sigma_\varepsilon = 1.3, C_{\varepsilon 1} = 1.3 + \frac{0.25}{[1+(\frac{d}{2\ell})^2]^4},$$

$$C_{\varepsilon 2} = 1.9, C_\mu = 0.19, C_L = 0.3, C_\eta = 70,$$

$$\ell = \frac{L}{C_L}, \quad C_1 = 1.4, \quad C_2 = 0.3,$$

d: distance to the closest boundary,

$$L = C_L \max(\frac{k^{1.5}}{\varepsilon}, C_\eta(\frac{\nu^3}{\varepsilon})^{\frac{1}{4}}),$$

$$T = \max(\frac{k}{\varepsilon}, 6(\frac{\nu}{\varepsilon})^{\frac{1}{2}}).$$

- Boundary conditions :

In the inlet and outlet of the calculated flow domain, the periodic behavior leads to the periodic boundary conditions, i.e.

$$U_i(0,y) = U_i(Pi,y), \quad k(0,y) = k(Pi,y),$$

$$\hat{P}(0,y) = \hat{P}(Pi,y), \quad \hat{T}(0,y) = \hat{T}(Pi,y)$$

these conditions are valid for all the turbulent models used.

The no-slip boundary condition is applied at the surfaces of the rib and the walls of the channel for all the models . The turbulent kinetic energy k is equal to zero at all these solid walls for all models. For the models of Launder-Sharma, Chien, and Lin, $\tilde{\varepsilon}$ is set to zero at wall boundaries. As for Durbin's model, periodic boundary conditions are applied on variables of ε, $\overline{v^2}$ and f, zero is assigned for $\overline{v^2}, f$, k at solid walls, and the equation as

$$\varepsilon(y) = 2\upsilon\frac{k}{y^2} \text{ as } y \to 0 \cdot$$

is used for ε near the wall. For $k-\omega$ model, periodic boundary condition is applied on ω, and the following asymptotic equation, i.e.

$$\omega(y) \to \frac{2\mu}{B^*\rho y^2} \quad y \to 0 \cdot$$

Is applied near the solid wall.

- **Yap term :**

It is well known that the energy dissipation equation of turbulence model, in particular the low Reynolds number $k-\varepsilon$ model, produce too large turbulence length scale for separated flows. Therefore excessively high levels of near-wall turbulence and heat transfer are obtained. Yap [8] introduced a term into the ε - equation to reduce the departure from the local-equilibrium length scale in wall turbulence. The correction term is expressed as

$$YC = \max\{0.83\frac{\rho\varepsilon^2}{k}(\frac{k^{1.5}}{\varepsilon}\frac{1}{2.55Y} - 1)(\frac{k^{1.5}}{\varepsilon}\frac{1}{2.55Y})^2, 0\}$$

This Yap Term is added to the $\varepsilon-$equation for the above turbulence models so that better predictions on flow and heat transfer characteristics can be expected.

3. NUMERICAL METHODS

The governing equations are discretized in finite volume approach with staggered grid arrangement. Hybrid scheme is employed for convective terms and central difference method for diffusion terms. PISO algorithm [15] is employed to couple the velocity and pressure, where the pressure correction equation is derived from the continuity equation and momentum equations. The difference equations can be expressed as

$$A_P\phi_P = A_E\phi_E + A_W\phi_W + A_N\phi_N + A_S\phi_S + b$$

where the subscript P indicate the P-th control volume, E represent the node located at the east of the P-th node, and W, N, S located at the west, north, and south respectively. Then the above equations can be combined together into a linear system, named $A\phi = b$, where A is a sparse and penta-diagonal matrix. The Bi-CGSTAB method [16] with the ILU or MILU preconditioners are applied to solve the matrix system. This numerical method had been demonstrated fast and

stable convergence in computations for turbulent separation flows [17].

4. RESULTS AND DISSCUSSION

The computed fluid mean flow profiles are compared with the measurement of Drain & Martin [9] who performed Laser-Doppler velocimetry (LDV) measurements of fully developed water flow in a rectangular duct with one surface roughened by a periodic rib structure. The Reynolds number based on the channel height is 3.72×10^4, the ratio of rib and channel height is 0.2 (h/H=0.2), and the rib pitch-to-pitch height ratio ($PR = Pi/h$) is 7.2. Figure 1 plots the ribbed channel geometry and the calculation domain. Since the passage is long enough for repeating flow conditions to prevail over each rib interval, the numerical flow domain cover only one rib interval and periodic flow boundary conditions are applied. The result predicted here are obtained using 107×126 grid system, in which the first grid nodes next to the wall was placed at $y^+ \le 0.3$.

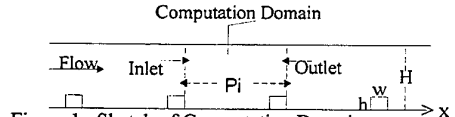

Figure 1 : Sketch of Computation Domain
(w=h, H/h=5, PR=Pi/h=7.2)

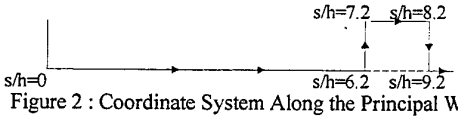

Figure 2 : Coordinate System Along the Principal Wall

For this problem, the separation bubble downstream of the rib extends over almost half the rib interval and a smaller bubble exists ahead of the rib. Figure 2 illustrates the physical coordinate system along the ribbed wall for the following figures. Figure 3(a) compares the measured mean velocity profiles with the computed profiles by Launder and Sharma's model. The computations compute the main feature of the flow field with somewhat different sizes of separation bubble ahead of the rib (s>0) and thicker boundary layer on the top surface of the rib (s/h>7.2). In this figure, there are four profiles of streamwise velocity distribution are shown, namely, s/h=3.18, s/h=4.32, s/h=7.3, and s/h=7.7 respectively, where the positions at s/h=7.3 and s/h=7.7 are located above the rib. This figure shows that the mean velocity profiles fit the experimental data well at most of the height levels, y/H, except at the surface wall. For this case, the reattachment point is occurred approximately at s/h $\doteqdot$ 4.32, and computed separation bubble is larger than the measured one. Moreover, at s/h=7.3, the computed boundary layer is thicker than the measured layer. Figure 3(a) also shows that the addition of the Yap term in the $\varepsilon-$equation improves the prediction of the reversed flow field using Launder-Sharma's model. Figure 3(b) plots the flow field obtained by Chien's model. Differing from the previous model, a smaller separation bubble is obtained in this model. Similar to the model of Launder-Sharma, computed boundary layer on the top of the rib is thicker than the measured value. Again, the addition of the Yap term in the $\varepsilon-$equation improves the prediction of the velocity profile at all four stations. Similar to Chien's model, smaller separation bubble is observed as the velocity profile at s/h=3.18, s/h=4.32 indicates (Figure 3(c)) and slower developments of the velocity profiles are shown at s/h=7.3, s/h=7.7 if Lin's model is applied. The addition of Yap term only slightly change the numerical results, because Lin's model posses the correct turbulence properties already in the vicinity of the wall. Durbin's model predicts the velocity profiles as good as the Chien's and Lin's models, although extra terms of $\overline{v^2}$ and f are calculated to evaluate the time averaged properties (Figure 3(d)). Besides, Yap term is also in need to achieve better prediction as $k-\varepsilon-v^2$ model is used. Wilcox [18,19,20,21] performed a series of computations and demonstrated that the $k-\omega$ model was accurate for boundary layers with adverse pressure gradient and suggested that the use of $k-\omega$ model for studying transition and surface roughness effect. In this case, it is found that the predicted profiles at various locations fit the measured profiles well, and slightly improvement is observed as compared to those predicted profiles in the above four $k-\varepsilon$ models without the Yap term. Since Yap term is an addition term of $\varepsilon-$equation, the addition of Yap term in $k-\omega$ model is not applied. In conclusion, the addition of Yap term in the models of Launder-Sharma, Chien, Lin, and Durbin improves the velocity computation by enlarging the separation bubble after the rib, and reduce the boundary layer thickness at the top surface of the rib. It implies that the action of adding Yap term corrects the turbulence length scale near the wall and takes care the non-local-equilibrium of the flow.

The computed local Nusselt number is compared with the experiment of Liou et al [10]. The real time holographic interferometry technique was employed to measured the time-dependent temperature field in the ribbed duct. The flowfield with Reynolds number of 1.26×10^4 was reported. The computation domain

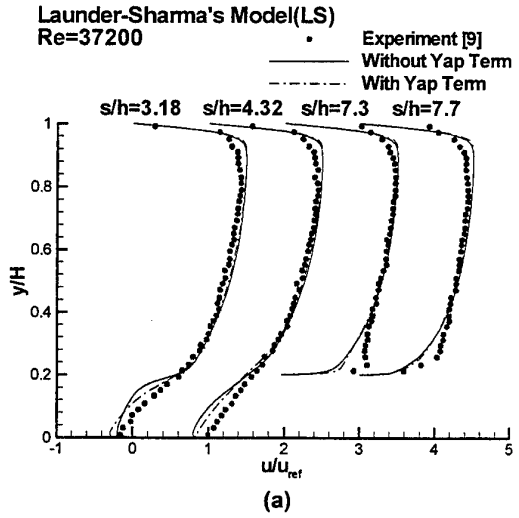

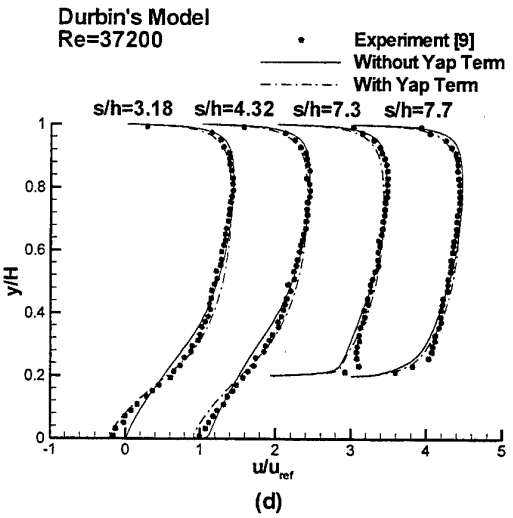

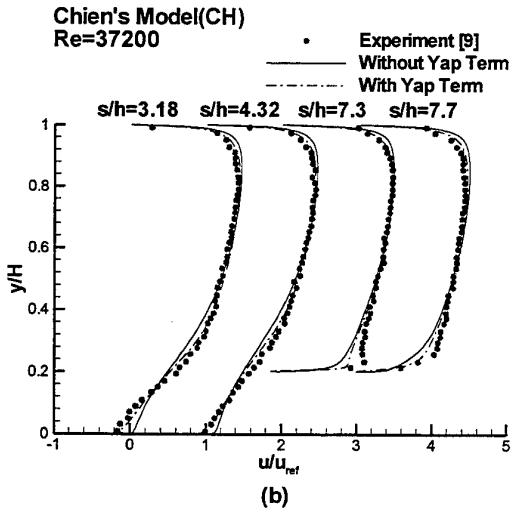

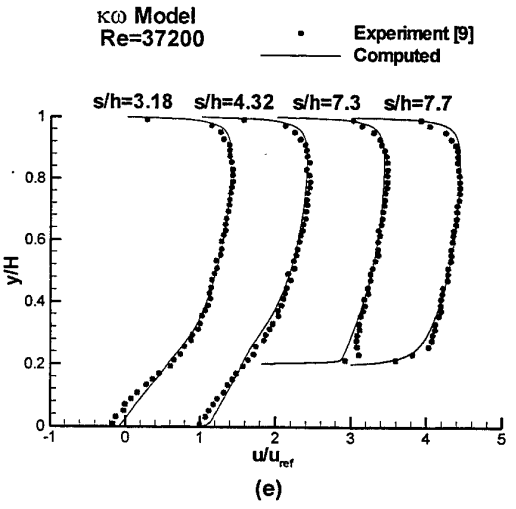

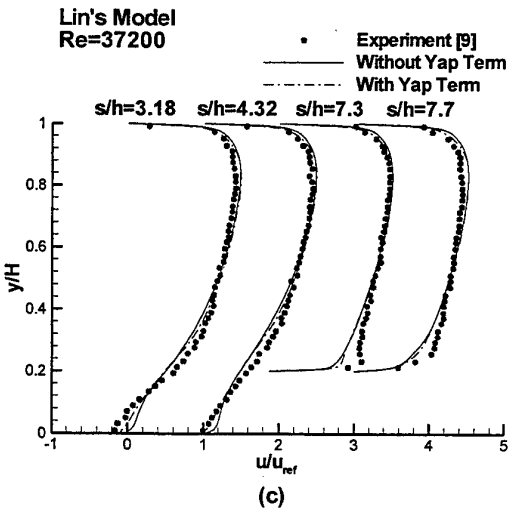

Figure 3: Streamwise Velocity Profiles Using
(a) : Launder-Sharma's model
(b) : Chien's model
(c) : Lin's model;
(d) : Durbin's model
(e) : $k-\omega$ model

and grid system are the same as the previous work. The first grid point next to the wall is located at $y^+ < 0.1$ at this Reynolds number. Figures 4(a) to 4(e) present the measured and computed Nusselt number distribution (where $Nu_s = 0.023\mathrm{Re}^{0.8}\mathrm{Pr}^{0.4}$) by various turbulence models. Figure 4(a) shows that the model of Launder-Sharma greatly over-predicts the Nusselt number level if the Yap term is not included, and the level of Nusselt number distribution is lowered down to the level of measurement in most part of the axial locations if the Yap term is included. Even with the

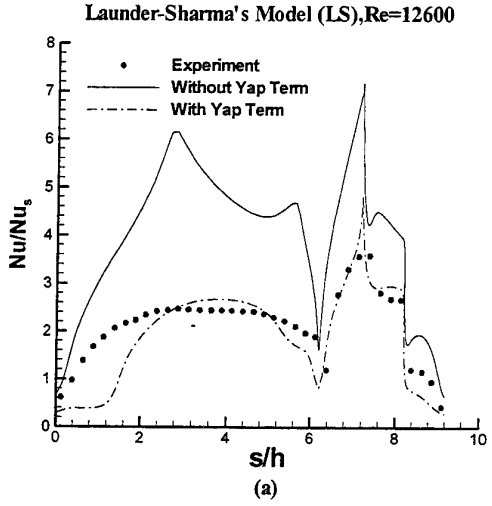

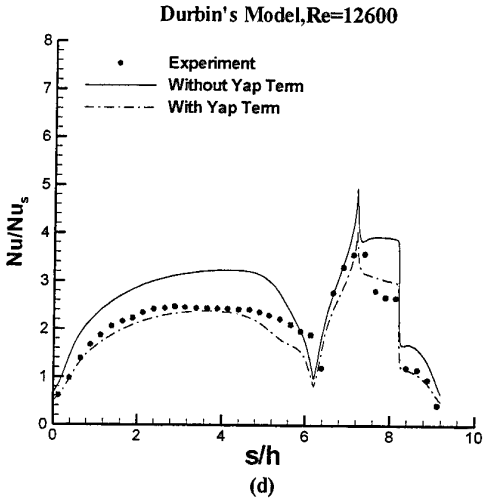

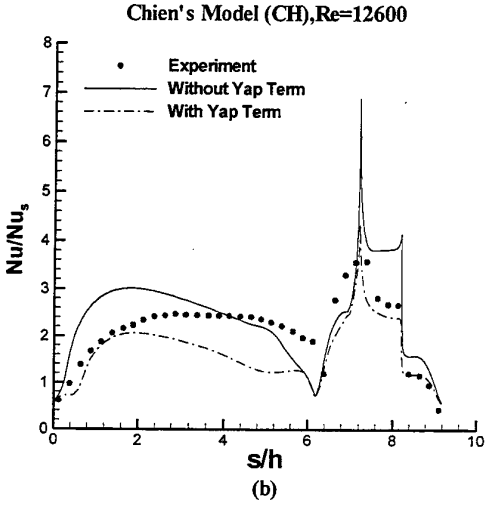

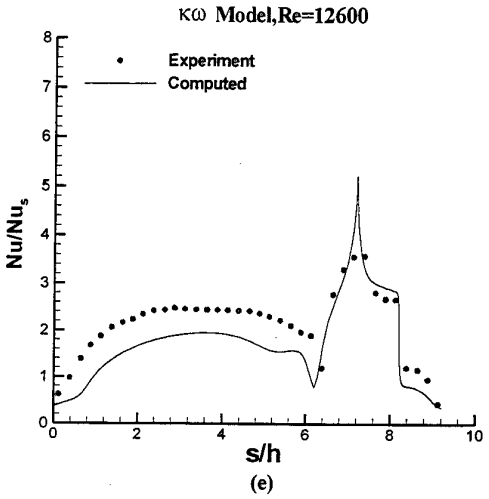

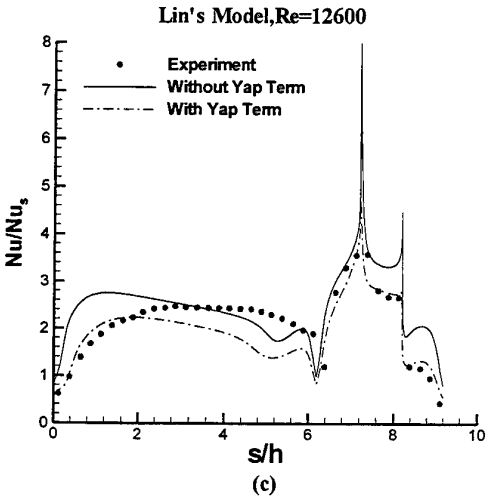

Figure 4 : Local Nusselt number Distribution using
(a) : Launder-Sharma's model
(b) : Chien's model
(c) : Lin's model
(d) : Durbin's model
(e) : $k-\omega$ model

Yap term, serious discrepancy between the measurement and computation is observed near the upstream corner ($s/h=0.$), where heat transfer level is seriously under-estimated. The same discrepancy occurs at the corner before the rib ($s/h=6.2$). However, it is interested to note that, the computed heat transfer coefficient fits well with measured distribution on all surfaces of the rib if LS model with Yap term is employed. Figure 4 (b) indicates that the Nusselt number level predicted by Chien's model is on the measurement level with different shapes if the Yap term

is not included, and the predicted level is somewhat lower than the measured level after the flow recirculation zone (s/h$\approx$1.6) if the Yap term is employed in this model. The over all Nusselt number distribution pattern along s is fairly agreed to the measurement with some discrepancy. Lin's model obtains the Nusselt number distribution with improvement both in distribution shape and magnitude (Figure 4(c). With Lin's model and Yap term, the heat transfer level is correctly calculated starting from the upstream corner (s/h=0), but, the level is gradually under-estimated as the flow goes more downstream (s/h$\approx$2.0), however, the heat transfer coefficient on the rib surface are correctly predicted. With extra parameters of $\overline{v^2}$ and f, Durbin's model obtains the Nusselt number level higher than the measured level along the wall and on the surfaces of the rib without the Yap term in the $\varepsilon-$equation, but the distribution shape is much improved. The prediction of the heat transfer level is reduced to the measured level in most part if the Yap term is appended to the $\varepsilon-$equation. Although the $k-\omega$ model predicts the flowfield well in the case of Re=37200, under-prediction of heat transfer level with uniform discrepancy from the measured level is observed downstream the rib, s/h=0 to 6 (Figure 4(e)). Good prediction of the heat transfer level on all faces of the rib is achieved. These Nusselt number distributions using various turbulence models reveal that Durbin's model with the Yap term in $\varepsilon-$equation provides the best simulation in local Nusselt number distribution. In concluding , these turbulence models can predict same good flowfield well as shown in Figure 3, but give large variations of heat transfer predictions. Lin's model is the best among $k-\varepsilon$ models. Durbin's $k-\varepsilon-v^2$ model offers some further improvement, and $k-\omega$ model do not yield the desired level of heat transfer coefficient.

Since the $k-\varepsilon$ models use $\mu_t=\rho C_\mu f_\mu k^2/\tilde{\varepsilon}$ as the eddy viscosity, the high values of k in the flowfield lead to high heat transfer predictions. The function of Yap term in $\varepsilon-$equation is mainly reducing the excessive turbulent energy so that the heat transfer level can be reduced. The behavior of heat transfer computations can be viewed and explained by the contour of turbulent kinetic energy. Figure 5(a) plots the computed turbulent kinetic energy contours using Launder-Sharma's model and shows three locations of peak values : at s/h=0, s/h=2.5 and 6.2 with y/H=1. Two points (at s/h=0 and 6.2 with y/H=1) are singular points. The levels of turbulent kinetic energy are greatly reduced especially at flowfield near the rib and wall as the Yap term is applied (Figure 5(b)). Also, the contour pattern is greatly changed and only two locations of peak values are observed. Lin's model tends to correct the prediction of near wall turbulence and the turbulent kinetic energy is concentrated near the wall surfaces (Figure 5(c)), however, it does not consider the local non-equilibrium at the flowfield and over-predicts the level with non-smooth pattern, therefore, the inclusion of Yap term which considers the non-equilibrium phenomena cuts down the turbulent kinetic energy level and smoothes out the distribution (Figure 5(d)). The improving turbulence very close to the wall can explain why Lin's model with Yap term best predicts the heat transfer coefficient among all $k-\varepsilon$ models employed. Figure 6(a) plots the turbulent kinetic energy contours calculated by Durbin's model, smooth distributions are observed. It may justify the role of $\overline{v^2}, f$ terms. The adoption of Yap term in $\varepsilon-$equation again reduce the levels of turbulence significantly near the rib and wall surface. The correct distribution of turbulent kinetic energy yields the correct heat transfer level. The computed turbulence using $k-\omega$ model also shows smooth contours (Figure 7) with levels much lower than levels using $k-\varepsilon$ models without Yap term. The low level of turbulence leads to low level of heat transfer.

5. CONCLUSIONS

In this study, various versions of ow-Reynolds number turbulence models are used to compute the flow and heat transfer in two dimensional rectangular channel flow with ribbed passage. All the low-Re models tested exhibit the similar performance on the calculation of flowfield, but behave very differently on the calculations of heat transfer characteristics. Lin's model with Yap term leads to best prediction on heat transfer level among all $k-\varepsilon$ models tested because his model adopted the Taylor microscale in the damping functions and the inclusion of the pressure diffusion terms in both the k and ε equations. His modification gives the correct behavior in the vicinity of the wall. The near-wall treatment of $\overline{v^2}-f$ system of equation helps Durbin's model performing even better than Lin's model on the calculation of heat transfer. $k-\omega$ model underestimates the heat transfer prediction and needs improvement.

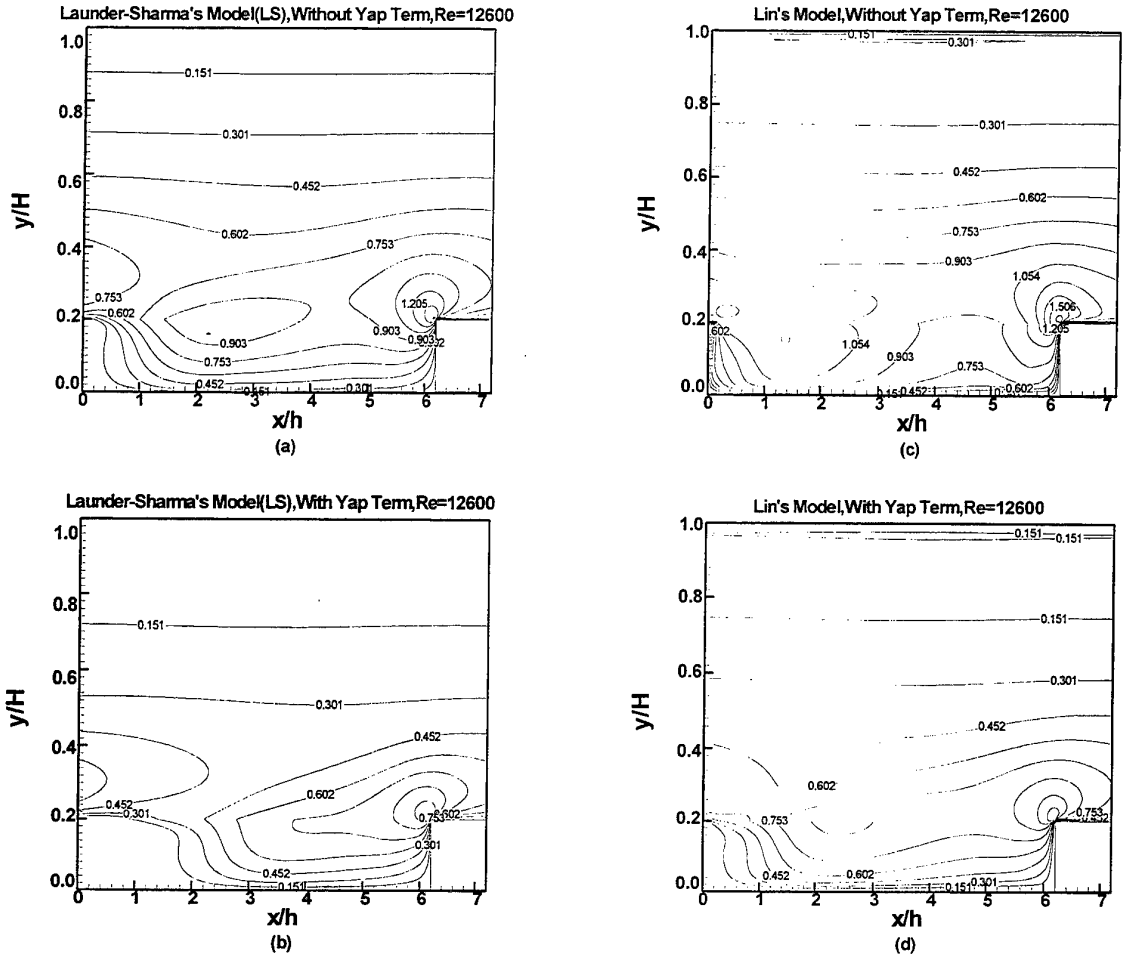

Figure 5: turbulent kinetic energy using

(a) : Launder-Sharma's model without Yap term

(b) : Launder-Sharma's model with Yap term

(c): Lin's model without Yap term

(d) : Lin's model with Yap term

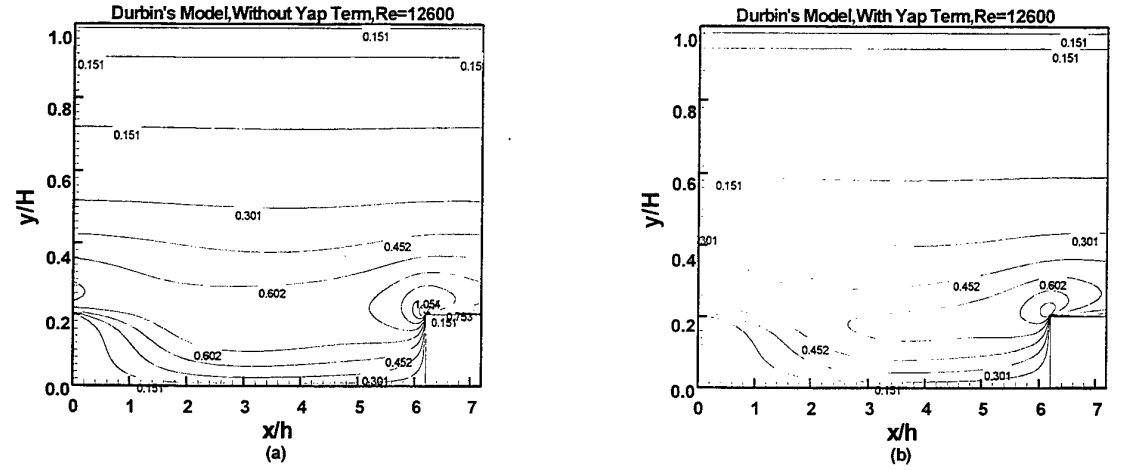

Figure 6 : Turbulent kinetic energy contour using

(a) : Durbin's model without Yap term,

(b) : Durbin's model with Yap term

Code	LS	CH	Lin
C_μ	0.09	0.09	0.09
f_μ	$\exp(-\frac{3.4}{(1+0.02R_t)^2})$	$1-\exp(-0.0115y^+)$	$1-\exp(-\frac{y_\lambda}{100}-\frac{8y_\lambda^3}{1000})$
σ_k	1.0	1.0	$1.4-1.1\cdot\exp(-\frac{y_\lambda}{10})$
$\sigma_{\tilde{\varepsilon}}$	1.3	1.3	$1.3-\exp(-\frac{y_\lambda}{10})$
$\prod_k$	0	0	$-\frac{1}{2}\frac{\partial}{\partial x_j}(\upsilon\frac{k}{\varepsilon}\frac{\partial\hat{\varepsilon}}{\partial x_j})$
$\prod_{\tilde{\varepsilon}}$	0	0	$-\frac{\partial}{\partial x_j}(\upsilon\frac{\tilde{\varepsilon}}{k}\frac{\partial k}{\partial x_j})$
$\hat{\varepsilon}$	$2\upsilon(\frac{\partial\sqrt{k}}{\partial y})^2$	$2\upsilon\frac{k}{y^2}$	$2\upsilon(\frac{\partial\sqrt{k}}{\partial y})^2$
E	$2\upsilon\upsilon_t(\frac{\partial^2U_i}{\partial x_j\partial x_k})^2$	$-2\upsilon(\frac{\tilde{\varepsilon}}{y^2})\exp(-0.5y^+)$	0
f_1	1	1	1
f_2	$1-0.3\exp(-R_t^2)$	$1-0.22\exp(-\frac{R_t^2}{36})$	$1-0.22\exp(-\frac{R_t^2}{36})$
$C_{\tilde{\varepsilon}1}$	1.44	1.35	1.44
$C_{\tilde{\varepsilon}2}$	1.92	1.8	1.92
R_t	$R_t=\frac{k^2}{\upsilon\tilde{\varepsilon}}$	$R_t=\frac{k^2}{\upsilon\tilde{\varepsilon}}$	$R_t=\frac{k^2}{\upsilon\tilde{\varepsilon}}$
		$y^+=\frac{yU_\tau}{\upsilon}$	$y_\lambda=\frac{y\sqrt{\tilde{\varepsilon}}}{\sqrt{\upsilon k}}$

Table 1 : The constants and functions in Launder-Sharma's(LS), Chien's(CH), and Lin's low Reynolds number models.

Nomenclature

h	rib height	t	time
H	Channel height	U	axial mean velocity
k	turbulent kinetic energy	V	transverse mean velocity
Nu	local Nusselt number	w	rib width
P	pressure	x	axial coordinate
$\hat{P}$	reduced pressure	y	transverse coordinate
Pi	rib pitch	β	Pressure gradient
PR	rib pitch-to-pitch ratio, Pi/h	γ	temperature gradient
Pr	Prandtl number	ε	dissipation rate of turbulent kinetic energy
Re	Reynolds number, $\mathrm{Re}=U_{ref}H/\upsilon$	μ	molecular dynamic viscosity
T	temperature	μ_t	turbulent dynamic viscosity
$\hat{T}$	reduced temperature	υ	kinetic viscosity

6. Reference

(1) Taylor, C. ,Xia J. Y., Medwell J. O. and Morris W. D., "Numerical simulation of three-dimensional turbulent flow and heat transfer within a multi-ribbed cylindrical duct." ASME Paper 91-GT-8, Int. Gas-Turbine and Aero Congress, Orlando, Florida, 1991.

(2) H. Iacovides, M. Raisee, "Computation of flow and heat transfer in 2-D rib roughened passages", 2nd Int. Symposium on Turbulence, Heat and Mass Transfer. Delft, The Netherland, june 9-12. 1997, pp. 21-30.

(3) Launder B.E. and Sharma B.I., "Application of the energy-dissipation model of turbulence to the calculation of flow near a spinning disc", Letrs in Ht Mass Trans., 1, 1974, pp. 131-138.

(4) Chien, K. Y., "Predictions of Channel and Boundary Layer flows with a Low-Reynolds Number Turbulence Model", AIAA Journal, 1982, vol. 20, No. 1, pp. 33-38.

(5) C. B. Hwang, and C. A. Lin, " Improved Low-Reynolds-Number $k-\widetilde{\varepsilon}$ Model Based on Direct Numerical simulation Data", AIAA Journal, 1998, vol. 36, No. 1, pp. 38-43.

(6) P. A. Durbin, "Separated Flow Computations with the $k-\varepsilon-v^2$ Model", AIAA Journal, 1995, vol. 33, No. 4, April, pp. 659-664.

(7) Wilcox, D. C. and Rubesin, W. M., " Progress and in Turbulence Modeling for Complex Flow Fields Including Effects of Compressibility", 1980, NASA Tech. Paper 1517.

(8) Yap C. R., "Turbulence heat and momentum transfer in recirculating and impinging flows", phD Thesis, Department of Mech. Engnrg, Faculty of Technology, University of Manchester, 1987.

(9) L. E. Drain and S. Martin, "Two Component velocity measurements of turbulent flow in a ribbed-wall flow channel", Int. Conf. On Laser Anenometry-Advances and Application, Manchester, U. K. 1985, pp. 99-112.

(10) Tong-Ming Liou, Jenn-Jiang Hwang and Shih-Hui Chen, "Simulation and measurement of enhanced turbulent heat transfer in a channel with periodic ribs on one principal wall", Int. J. Heat Mass Transfer, 1993, vol. 36, No. 2, pp. 507-517.

(11) V. C. Patel, W. Rodi, and G. Scheuerer, "Turbulence Models for Near-Wall and Low-Reynolds Number Flow: A Review", AIAA Journal, 1985, Vol. 23, No. 9, September, pp. 1308-1319.

(12) Lam, C. K. G. and K. Bremhorst, " A modified form of the $k-\varepsilon$ model for Predicting Wall Turbulence", J. of Fluid Engrg., Trans. of ASME, 1981, vol. 103, pp. 456-560.

(13) Wilcox, D. C. and Rubesin, W. M., "Progress in Turbulence Modeling for Complex Flow Fields Including Effects of Compressibility", NASA Tech. Paper 1517, 1980.

(14) Durbin, P.A., Y. Shabany, S. Parneix, M. Behmia, "Connections of Lagrangian Dissipation Theory to Heat Transfer", 2nd Int. Symposiumon Turbulence, Heat and Mass Transfer, Delft, The Netherlands, June, 1997, pp. 47-54.

(15) Issa, R. I. "Solutions of Implicitly Discretized Fluid flow Equations by Operator-Splitting", J. of Comp. Physics, 1985, vol. 62, pp. 40-65.

(16) Van Der Vost, "Bi-CGSTAB : A fast and smoothly converging Variant of Bi-CG for the solution of Non-symmetric Linear Systems", SIAM J. of Sci. Stat. Comp. 1992, Vol. 13, No. 2, pp.631-644.

(17) W. B. Tsai, W.W. Lin, C. C. Chieng, "Effectiveness of Preconditioning Bi-CGSTAB Algorithm in Solving Turbulent Flow", vol. 10, Preceeding of the Tenrh International Conference, Swansea, U. U. 21-25 July, 1997.

(18) Wilcox D. C., "Turbulence Modeling for CFD", 1993a, DCW Industries, Inc., La Canada, CA.

(19) Wilcox D. C., "A Two-Equation Turbulence Model for Wall-Bounded and Free-Shear Flows", AIAA Paper93-2905. 1993b.

(20) Wilcox D. C., "Comparison of Two-Equation Turbulence Model for Bound Layers with Pressure Gradients", AIAA Journal, 1993, Vol. 31, No. 8, pp. 1414-1421.

(21) Wilcox D. C., "Simulation of Transition with a Two-Equation Turbulence Model", AIAA Journal, 1994, Vol. 32, No. 2, pp. 247-255.

HEAT TRANSFER IN RELAXATION ZONE AFTER A LOCAL CLOSED SEPARATION OF VARIOUS TYPE

E.Ya. Epik, L.E. Yushyna and T.T. Suprun

Institute of Engineering Thermophysics of National Academy of Sciences of Ukraine (IET NASU), Ukraine

ABSTRACT

The results of the experimental study of the velocity and temperature characteristics and turbulence structure are presented for the relaxating flow downstream of a separation of various types in case of low free stream turbulence $Tu_e \approx 0.2$ % and velocities of an external flow $U_e \approx 5$ - 10 m/s. The type of a separation (laminar, transitional or turbulent) is adjusted by the shape of an inlet edge of the plate and the length of an intercepter, installed in the test section of the wind tunnel. Due to the approach, developed and broadly used in IET NASU in investigations of complex transport processes, turbulent viscosity at an outer edge of a dynamic boundary layer is chosen as a main determining criterion for diagnostics of a separation type and its intensity as well as for calculation of heat transfer after a turbulent separation. The measurements confirm extremely slow recovery to a "classical" turbulent boundary layer after various types of a separation. They also demonstrate the dissimilarity of an internal structure and different rates of recovery in a hydrodynamic and thermal boundary layer in relaxation zone both in an inner region and at an outer part of a boundary layer.

1 INTRODUCTION

For many years due to wide spread in industrial and environmental engineering the great attention has been paid to transport processes in a boundary layer developing in the presence of a closed local separation. Extensive studies were devoted to the separation itself and the recovering flows downstream of the separation region (1-11).

Despite numerous attempts to penetrate into the mechanism of a separation and distortions caused by it in an internal structure of a dynamic and thermal boundary layer in zones of reattachment and relaxation, many aspects of these complex flows remain unknown and unpredictable. Thus there are no reliable recommendations for determination of reattachment length and height; there are absent the universal criteria for estimation of the separation intensity; there are limited data on transformation of velocity and temperature turbulence in relaxation zone, etc.

Most the experiments and calculations were made for momentum transport. The problems connected with the influence of a separation on heat transfer remain obscure. Generally the number of experimental investigations on hydrodynamics substantially exceeds those on heat transfer, numerical simulation predominating over the experiments. Questions, concerning the memory (or relaxation) after a closed separation, are not widely studied especially in the important case when surface heat transfer occurs.

Thus far it is not clear: how can the typical dimensions of the relaxation zone be defined and predicted; how does the highly distorted turbulence around reattachment re-organize itself towards the more usual boundary layer forms; how can the intensity of a separation in terms of subsequent effects on the developing after it a boundary layer be characterized; how can the type of a separation (laminar, transitional or turbulent) be diagnosed, etc.? The lack of the experimental information restricts the possibilities of calculation methods as well as an extension of new phenomenological approaches for description of main features of a separation itself and relaxation zone after it.

That is why for many years in IET NASU the experimental investigations of heat transfer and hydrodynamics have been carried out for separated flows (7,8,10,12, etc.). The experiments presented here are specially designed for the flow downstream of reattachment rather than the separation region itself. The experimental arrangements are described in the following section and subsequent sections contain some of the results.

It is necessary to note that the presented results do not pretend to universal correlations or generalization. Their goal is to emphasize the common problems of the relaxating flow in the process of its very slow recovery to a "classical" turbulent boundary layer after a separation of different type without superposition of another additional factors (for example, free stream turbulence or longitudinal pressure gradient) which influence intensity and dimensions of a separation itself. One can use these results for comparison, calculations, working out corresponding turbulence models, etc., taking into account that in relaxation zone an analysis and estimation of course of transport process and its intensity, influenced by a separation, is directly connected with the choice of the reference

conditions. Some aspects of this problem are discussed below.

2 EXPERIMENTAL ARRANGEMENT

The experiments were conducted in the typical low-velocity open type wind tunnel T-5 IET NASU with a test section of 120x120x800mm (Figure 1). The confuser (designed by Lespinar's curve with contraction 9) ensured the smooth passage to the test section. Damping chamber had 5 identical sections with deturbulizing grids and filters. The level of flow turbulence was varied by 10 mm thick perforated plates (PP) with perforation diameter 13.5mm placed at the inlet to the wind tunnel confuser.

The experiments, the results of which are presented below, were specially carried out without turbulence generator (PP0). In this case the natural turbulence level in the initial section of the tunnel was about 0.2% and a "pure" separation of different type and intensity "worked" as a generator of turbulence in a boundary layer. The intensity of a separation was adjusted by the shape and thickness of the plate inlet edge; by the values of mean velocity of an external flow; by the height of an interceptor located in the end of test section on its top wall. The changes of height of an interceptor caused the essential redistribution of pressure near the inlet edge, however the streamwise pressure gradient along the rest of the plate part was practically absent. Thus there were realized flows without and with a separation of different types and intensity near the inlet edge of the plate. In the experiments designated as PP0-0, PP0-25 and PP0-60 the latter figures corresponded to the height of the interceptor in mm.

The plate under study, the leading edge of which was rounded off by a radius of 1.5mm (2h=3mm) or was blunt (2h=7.5mm), was installed in the tunnel test section at height of 20mm above its bottom wall, i.e. the upper (working) and low surfaces of the plate were streamlined asymmetrically.

The main plate part of thickness of 10mm and length of 770mm was made of cloth-based laminate (textolite). Heat transfer was explored by electrocalorimetry, using six surface ribbon-type heaters with individual power control, glued along the plate. The inlet plate part of the length of 30mm was made from brass. Additional heating of the inlet part provided simultaneous development of thermal and dynamic boundary layers. Due to the combination of the electrocalorimetrical method on the main part of the plate with additional heating of its inlet part, the boundary conditions were approximately $t_w \approx$ const and $q_w \approx$ const at x<30mm and x>30mm respectively.

Parameters of velocity and temperature turbulence were measured by the DISA-55M hot-wire system with 1μ and 5μ probes; coefficients of friction were determined by modified Clauser's method in turbulent boundary layer (k=0.4 and C=5.1) or on the basis of velocity profiles. The length of the reattachment region was determined by method developed in IET NASU and based on changing thermoanemometer signal in this region. Results of thermal and aerodynamic measurements carried out in the range of x=50-600mm were processed on IBM-486 personal computer.

The research program involved an experimental study of local values of friction and heat transfer coefficients, velocity and temperature profiles, their characteristic thicknesses and shape parameters as well as distributions of velocity and temperature fluctuations and their spectral composition.

Characteristics of five cases under study are given in the Table. As seen from the Table, the following types of a separation were observed in experiments: turbulent of various intensity (cases 4 and 5), transitional (case 3) and laminar (case 2). In case 1 the separation was absent.

Table

Case	1	2	3	4	5
Des.	PP0-60	PP0-25	PP0-25	PP0-0	PP0-0
Inlet edge, mm	rounded 2h=3	rounded 2h=3	rounded 2h=3	rounded 2h=3	blunt 2h=7.5
U_e, m/s	10	5	10	10	10
x_r, mm	-	25	10	10	30
$\nu_{t\delta r} / \nu$	0	5	20	36	62
Type of separation	without separation	laminar	trans.	turbulent	turbulent
Symbols: dynamic	□	+	○	△	×
thermal	-	-	●	▲	-

For diagnostics of the type of a separation and its intensity the common approach, developed in IET NASU for the estimation of transport processes intensification in any boundary layer, influenced by different external factors including free stream turbulence, was used (13). Due to this approach dimensionless turbulent viscosity at an outer edge of a dynamic boundary layer $\nu_{t\delta} / \nu$ is one of the main parameters responsible for the transport properties of a wall boundary layer. In case of generation of turbulence by a separation turbulent viscosity $\nu_{t\delta r} / \nu$ in the section of reattachment ($x \approx x_r$) was chosen as such parameter. As seen from the Table, at $\nu_{t\delta r} / \nu \approx 5$ a laminar separation took place. With the $\nu_{t\delta r} / \nu$ growth a transitional separation was developed and at last at $\nu_{t\delta r} / \nu > 30$ a turbulent separation arose. Thus the given

parameter can be used for the approximate diagnostics of a separation type (of course in combination with another diagnostic methods and first of all with the most reliable of them, based on an analysis of mean velocity profiles). The problems connected with determination of turbulent viscosity at an outer edge of a dynamic boundary layer will be discussed in the section 3.5.

3 EXPERIMENTAL RESULTS

Before the description of the experimental results we would remind of the following circumstances. We have no for an object to obtain the universal recommendations for calculation of intensity of transport processes (friction or heat transfer) or universal correlations and criteria in the relaxation zone after a separation of different nature. Our main aim is to present experimental, to some extent, inconclusive data about variations of the most important characteristics of the dynamic and thermal boundary layer first of all for zone of "slow" relaxation where recovery to a "classical" turbulent boundary layer took place irrespective of a separation type. Due to approximate estimation, in case of a turbulent separation the beginning of this zone corresponds~$3.3x_r$, whereas the end is not known because it has not been achieved in any investigation, devoted to characteristics of relaxation zone. To some extent it is connected with such "curious" fact that the outer flow recovers substantially slower than the inner one (11) and a separation manifests itself as a generator of an external turbulence (7,10). We did not attempt to use the dimensionless parameters involving the length of reattachment taking into account uncertainty of its determination (10).

3.1 Coefficients of friction and heat transfer

Generalizing the experimental data on transport processes in zone of relaxation after a separation, the current coordinate $(x - x_r)$ is usually used as a determining geometrical size. As it was shown in (10), it is correct only for turbulent separation at reasonably high Reynolds numbers, when $x_r / h \approx \text{const}$, i.e. at $Re_h \geq 10^4$. In given experiments the x_r / h values changed nonmonotonously (see the Table). Therefore Reynolds number Re^{**} based on a momentum thickness was chosen to present data on friction and heat transfer. In our opinion this choice is rather successful because as it will be shown below local Reynolds number Re^{**} quite satisfactorily correlates the integral changes in structure of the dynamic and thermal boundary layers, caused by a separation.

Variations of local coefficients of friction and heat transfer are presented in Figures 2 and 3. To compare with a "classical" boundary layer the following dependencies were used (13, 14):
for laminar boundary layer:

$$C_{f0} = 0.44\,Re^{**-1} \tag{1}$$

$$St_0 = 0.365\,Re^{**-1} \tag{2}$$

for turbulent boundary layer:

$$C_{f0} = 0.027[1 + 0.05(\lg Re^{**} - 3.3) + 0.1(\lg Re^{**} - 3.3)^2]\,Re^{**-0.268} \tag{3}$$

$$St_0 = 0.0157\,Re^{**-0.25} \tag{4}$$

The equation (3) was recommended in (13) taking into account the influence of low Reynolds numbers on the wake parameter values.

As seen from Figures 2 and 3 when a separation is absent a typical laminar-turbulent transition takes place (case 1, PP0-60). After a laminar boundary layer, characterized by the decrease of coefficients of friction and heat transfer, the latter substantially increase in the region of transition with further declining in a turbulent boundary layer. The points of the start (Re^{**}_{st}) and end (Re^{**}_{end}) of a dynamic and thermal transition practically coincide, the length of transition (estimated as usual by relation of $Re^{**}_{end} / Re^{**}_{st}$) being ~ 2.6. These data agree with the known features of laminar-turbulent transition described for example in (15).

Cases 2 and 3 are identical from the point of view of their geometry (PP0-25) but differ by velocities ($U_e \approx 5$ and 10m/s), i.e. first of all by turbulent viscosities at an outer edge of a dynamic boundary layer ($\nu_{t\delta r} / \nu \approx$ 5 and 20).

In case 2 after a laminar separation the pseudolaminar boundary layer develops and transforms into the quasiturbulent-like boundary layer through the bypass transition. The distributions of friction coefficients along the plate $C_f = f(Re^{**})$ are nonmonotonous which is one of the main indications of any transition, whereas the distributions of heat transfer coefficients exhibit an obvious tendency to disappearance of nonmonotonicity of the variation $St = f(Re^{**})$.

As the result of the appearance of the pseudolaminar or quasiturbulent boundary layer the bypass transition can start and end at higher

C_f and St values than those in initial "classical" laminar or turbulent boundary layer.

In case 3 after a transitional separation the bypass transition begins immediately without a stage of a pseudolaminar boundary layer. The variations of coefficients of friction and heat transfer become monotonous despite the presence of bypass transition, after which the quasiturbulent-like boundary layer follows.

Such unusual forms of bypass transition were first observed in (16) and named "upper". In our opinion the origin of "upper" bypass transition in a boundary layer owing only to the presence of a laminar or transitional separation at comparatively low free stream turbulence is an important fact for engineering. It is obvious that it is impossible to predict without special experiments the described effects of a separation type on the development of boundary layers and intensity of transport processes in zone of relaxation using even the very modern theories and turbulence models.

In cases 4 and 5 (PP0-0) at $U_e \approx 10$ m/s after a turbulent separation in zone of "fast" relaxation ($x / x_r < 3.3$) the global growth of friction coefficients takes place whereas the heat transfer coefficients being substantially higher than in "classical" turbulent boundary layer decline. In zone of "slow" relaxation the very long quasiturbulent-like boundary layer develops along the remaining part of the plate under study. In described cases turbulent viscosity at an outer edge of a dynamic boundary layer is rather high ($\nu_{t\delta r} / \nu \approx 36$ and 62 respectively), under other equal conditions determined by the mean velocity and length of interceptor, the values of viscosity as well as the intensity of a turbulent separation depending only on a shape of inlet edge (rounded off or blunt). For these two cases as it will be shown below the similarity equations to calculate heat transfer are suggested, using approach developed in IET NASU.

3.2 Velocity and temperature profiles

Velocity and temperature profiles are presented at x=const. In our opinion the analysis of experimental data in such form is preferable for direct comparison of the characteristics of boundary layers after different types of a separation, irrespective of the values of dimensionless lengths based on x_r or h and their combinations with x.

Figure 4 demonstrates the velocity profiles in wall law coordinates. At x=50mm two characteristic parts of the velocity distributions can be distinguished for case 1 (without a separation) and case 2 (laminar separation): a wall zone where $u^+ = y^+$ and a buffer zone between the wall zone and an external flow. The logarithmic law region is completely absent. Such profiles are typical for laminar and pseudolaminar boundary layers (13,15).

In case 3 the appearance of a transitional separation promotes the expansion of the buffer zone on both sides, but the profile remains far from a turbulent one. In three cases described the diffuser effect is not observed in distributions of velocity at x=50mm.

The substantial distortion of the velocity profiles takes place in cases 4 and 5 after a turbulent separation. It results in an expansion of the buffer zone in the region of lower y^+ and appearance of the usual for diffuser flows "loop" in the wake zone, enveloping the outer part of a dynamic boundary layer. Although the validity of the logarithmic law is questionable near a separation (see, e.g. (2,4,5,11)), we use the following equation (5) for analysis of the obtained data and determination of friction coefficients by modified Clauser's method:

$$u^+ = 2.5 \ln y^+ + 5.1 \qquad (5)$$

Along the zone of "slow" relaxation the existence of the region of the logarithmic law validity is experimentally confirmed by the given data: the velocity profiles become similar to those for quasiturbulent boundary layer differing in the values of wake parameters (13).

The transformation of temperature profiles is not identical to those for the velocity profiles described above. The experiments in a thermal boundary layer carried out for cases 3 and 4 show that near a separation at x=50mm as well as along the relaxation zone up to x=600mm all the temperature profiles lie below the usual relation (17):

$$\Theta^+ = 2.12 \ln y^+ + 3.5 \qquad (6)$$

This is an evidence of nonuniversality of the temperature profiles in wall law coordinates. The tendency to universality of temperature profiles is observed only in coordinates $\Theta - y / \delta_t$ within the range of x under study. This fact confirms the conservative reaction of a temperature field to the effects of a different nature, including a separation.

3.3 Characteristic thicknesses of boundary layers, shape parameters

After a separation of various types the thicknesses of a dynamic and thermal boundary layer (determined as usual by conditions $U_\delta = 0.99 U_e$ or $\Theta_\delta = 0.99 \Theta_e$) substantially exceed the ones in a "classical" turbulent layer (Figure 5), however the

rate of their growth varies along the relaxation zone. In all cases under study in the presence of separation the thicknesses of a dynamic and thermal boundary layers change monotonously, their values practically coinciding. The monotonous changes are also peculiar to momentum and enthalpy thicknesses. A different behaviour is observed for displacement thicknesses: in case of a turbulent separation: their changes become nonmonotonous. Generally in a thermal boundary layer the values δ_t^* and δ_t^{**} are less than δ^* and δ^{**} in dynamic one. This fact confirms the different character of the recovery in a dynamic and thermal boundary layer particularly in an inner and outer parts in zone of relaxation.

The distributions of shape parameters H and H_t (Figure 6) reflect the features of changes of characteristic thicknesses (displacement, momentum and enthalpy) described above. In case 1 when a separation is absent the main variations of H (from 2.59 to 1.48 at x=50 and 600mm respectively) take place in the zone of laminar-turbulent transition owing to changes of flow regimes in a dynamic and thermal boundary layer. The quoted figures correspond to a "classical" laminar and turbulent (at comparatively low Reynolds numbers) boundary layer. In case 2 after a laminar separation in region of development of a pseudolaminar boundary layer the values of H falls to 2.13 (at x=50mm) and approaches to the same mentioned above at x=600mm for a turbulent boundary layer. In case 3 a transitional separation causes the similar changes with lower values of H=1.9 at x=50mm. It is necessary to note that in all three cases the diffuser effect at x=50mm was not revealed in velocity profiles, i.e. the changes of H near reattachment are connected only with the separation type, i.e. the flow regimes in a separation region. Otherwise after a turbulent separation in cases 4 and 5 the H values at x=50mm (H=1.79) indicate on the diffuser effect; at x=600mm the H values are slightly lower (H=1.38) in comparison with previous cases what is connected with the development of a quasiturbulent-like boundary layer. As shown in (13) the development of pseudolaminar or quasiturbulent boundary layers accompanies by decrease of the H values.

In a thermal boundary layer for cases 3 and 4 under study the distributions of H_t are completely similar to H (in particular H_t=1.85 and 1.74 at x=50mm declining to 1.45 at x=600mm).

In our opinion one can take into account unpredictable changes of the characteristic thicknesses of a dynamic and thermal boundary layer in calculations of transport processes in complex flows and approbations of calculating models.

3.4 Velocity and temperature fluctuations

Analysis of longitudinal velocity fluctuation profiles permits to conclude that a separation of flow being the powerful wall generator of turbulence manifests itself first of all in the deformation of an outer edge of a dynamic boundary layer (Figure 7). Thus in cases 5 and 4, when a turbulent separation of different intensity takes place, at an outer edge of a dynamic boundary layer the level of turbulence reaches to 7.7 and 5.1% at x=50mm declining to 2.8 and 2.0% at x=600mm despite a low free stream turbulence (Tu_e=0.2%). Such high values of turbulence are typical for external turbulized flows when turbulence is generated by special grids or perforated plates. Comparatively high levels of turbulence at the outer edge of a dynamic boundary layer are also observed in cases 2 and 3 for a laminar and transitional separation.

The usual decay laws for free stream turbulence after grids or another types of turbulence generators can be successfully used for an outer edge of a boundary layer (10). On the basis of these laws it is possible to calculate the changes of kinetic turbulence energy, characteristic scales and turbulent viscosity, the latter decreasing along the zone of relaxation (10).

Another character of turbulence variations at an outer edge is observed for case 1 when a separation is absent and along the plate the growth of turbulence and turbulent viscosity takes place. Energy of fluctuations firstly increases linearly and then exponentially right up to maximum (to the end of a laminar-turbulent transition); only in a turbulent boundary layer it begins to decrease.

At that time for both cases 3 and 4 under study the level of temperature fluctuations at the outer edge of a thermal boundary layer is substantially lower than the level of velocity fluctuations (in all 1.3 and 1.6% at x=50mm and 0.8-0.9% at x=600mm for cases 3 and 4). This evidences a weakening of the correlation between fluctuations of velocity and temperature at an outer edge of the boundary layers along the relaxation zone.

Distributions of the longitudinal component of velocity fluctuations near the reattachment at x=50mm (Figures 8 and 9) show that in cases 5 and 4 after a turbulent separation there are two maxima of longitudinal fluctuations: the first of them is situated near the wall ($y^+ \approx 13$) and the second is shifted into the outer region ($y/\delta \approx 0.6$ and 0.4). The most part of turbulence energy is concentrated in the second maximum

($u' / U_e \approx 19$ and 15% respectively). In the relaxation zone the second maxima gradually disappear and the fluctuation distributions become quasiturbulent-like with one maximum near the wall.

In cases 3 and 2 after a transitional or laminar separation the distribution of fluctuations factually has only one maximum reaching to $u' / U_e \approx$ 13-14% at $y^+ \approx 13$-14. These figures are typical for the first maximum of all four cases as well as for a "classical" turbulent boundary layer.

In case 1 when a separation is absent there is the growth of fluctuation energy along the plate with one maximum at $y / \delta \approx 0.4$. Such location of maximum of fluctuation energy indicates the existence of a pseudolaminar boundary layer (13).

Temperature fluctuations (Figure 10) are distributed through the thickness of a thermal boundary layer in another manner. In cases 4 and 3 after a turbulent and transitional separation near reattachment at x=50mm they have only one maximum ($t' / (t_w - t_e) \approx 17$ and 13%, $t' / t^* \approx 0.9$) which practically lies on the wall ($y^+ < 4$). Along the relaxation zone the maximum shifts from a wall to $y^+ \approx 13$, at x=600mm the values of $t' / (t_w - t_e)$ decreasing to 10-12% and otherwise of t' / t^* increasing to 1.3-1.7. Note that in coordinates $t' / (t_w - t_e) - y / \delta_t$ profiles of fluctuation are close to universal. So, the field of temperature fluctuations forms earlier than velocity one, i.e. the length of a thermal and dynamic relaxation is different.

3.5 Calculations of heat transfer

The method of calculation of heat transfer is developed for the zone of "slow" relaxation ($x / x_r > 3$) in cases 5 and 4 when a turbulent separation takes place.

As it was pointed above, the approach of IET NASU assumes that the type of a separation as well as the enhancement of heat transfer in the relaxation zone is determined by dimensionless turbulent viscosity at an outer edge of a dynamic boundary layer in the section of reattachment ($x = x_r$). The values of this viscosity can be calculated on the basis of an "energy-dissipation" turbulence model by two methods.

The first and the simplest of them suggests using the decay law of longitudinal fluctuations at an outer edge of the developing after a separation dynamic boundary layer. As our experience shows the description of this decay law can be made in a similar manner as it is accepted for free stream turbulence after generators of turbulence as grids or perforated plates installed directly in the test sections or before the confusers of the wind tunnels respectively.

The second method requires the measurements not only of longitudinal fluctuation energy but its spectral composition to determine the dissipation.

Two methods of determination of turbulent viscosity at the outer edge in the section of reattachment described above can be successfully used in the cases of low free stream turbulence when its scale does not influence on the developing boundary layers. As shown in studies of IET NASU (7,8,10,12,13, etc.) in cases of high free stream turbulence and its large relative scales so called "overlayer" arises between an outer edge of a dynamic boundary layer and turbulized external flow. In overlayer an attenuation of transport properties of the external flow takes place. It results in an anisotropy at an outer edge of a dynamic boundary layer and requires the development of new schemes of calculation or modification of existing ones, taking into account the scale influence described above. Problem is actual in case of high free stream turbulence arising in passage part of power equipment.

In the first approximation in zone of "slow" relaxation after a turbulent separation at $x / x_r > 3.3$ (cases 5 and 4) at $Re^{**} = const$ the current values of heat transfer coefficients (St) can be calculated by the following relation:

$$St / St_0 = 1 + 0.2(\nu_{t\delta r} / \nu)^3 \qquad (7)$$

where the St_0 values are determined from equation (4) for a "classical" turbulent boundary layer. The relation (7) contains also the turbulent viscosity ν_{t_0} generated near the wall in a turbulent boundary layer and calculated on the basis of known recommendation, for example:

$$\nu_{t_0} = 0.0168 U_e \delta^* \qquad (8)$$

It is necessary to note that the choice of reference conditions is very important in generalization of experimental results. The relation (7) has been obtained at $Re^{**} = const$.

The comparison of data under the reference condition $Re^{**} = const$ in fact leads to a virtual overstating of coefficients of heat transfer intensification St / St_0 (due to the growth of a momentum thickness with strengthening a turbulent separation) and as a consequence to the shift of the used reference dependence (4) into the range of higher Re^{**}. However in our opinion such choice is rather grounded by local presentation of experimental data when many uncertainties connected with the initial conditions

are excluded owing to use of momentum thickness (not current length x) as a determining dimension.

3.6 Filtration properties

A deep insight into the mechanism of development of a boundary layer after a separation is given by so called filtration coefficient: the ratio of the spectral power at the given point in the boundary layer, $E_u(n)$, to its value at the outer edge of the boundary layer, $E_u(n)_\delta$, at the same frequency, n.

The distributions of filtration coefficients for the longitudinal component of velocity fluctuations after a turbulent separation in the beginning of zone of "slow" relaxation at x=50mm (Figure 11, case 4) indicate the existence of the one-directed flow of the kinetic turbulence energy directed from the boundary layer into the external flow at all frequencies. The maxima of local energies are located at $y/\delta \approx 0.4$, as it takes place for integral energy of fluctuations, i.e. practically coincide with the position of the second maximum in distributions of longitudinal fluctuations. Such behaviour of filtration coefficients is typical for the flows with a longitudinal unfavourable pressure gradient (12).

After a transitional separation the energy transfer into the external flow is also observed at all frequencies, however the character of coefficient filtration distributions is another. In range of low and moderate frequencies the maxima of local energies are placed near the wall ($y^+ \approx 13$), and coincide with the same for the integral energy, whereas at high frequencies they shift up to $y/\delta \approx 0.3$ from wall. Thus a pseudolaminar boundary layer or weak diffuser effect manifest themselves only at high frequencies, because they are practically absent in the changes of another characteristics (in the first turn in the velocity distributions at x=50mm).

In both cases described above at x=600 mm there is only the drain of energy into the external flow, maxima of local energies at all frequencies being located at $y^+ \approx 13$, what confirms an existence of a turbulent or quasiturbulent-like boundary layer along the zone of "slow" relaxation.

4 CONCLUSION

The presented results of the experimental study of the characteristics of the relaxating flow downstream of a separation of various types confirm the validity of approach developed in IET NASU for estimation of transport properties of complex flows. Due to this approach turbulent viscosity at the outer edge of a dynamic boundary layer in the section of reattachment $\nu_{t\delta r}/\nu$ was chosen as the basic criterion determining in the first approximation the type of a separation (laminar, transitional or turbulent) and its intensity. The latter were adjusted both by flow regime (the values of mean velocity) and by geometric (the shape of an inlet edge of a plate and height of an interceptor) parameters. The experiments were specially carried out at low free stream turbulence ($Tu_e \approx 0{,}2\%$), i.e. under conditions when a "pure" separation was arisen and "worked" as generator of turbulence in a developing after it boundary layers.

As shown when a separation was absent ($\nu_{t\delta r}/\nu \approx 0$) a typical laminar-turbulent transition took place along a plate surface. The growth of $\nu_{t\delta r}/\nu$ to ~5 caused a laminar separation promoting after it the emergence of the bypass transition and further development of a quasiturbulent-like boundary layer. At $\nu_{t\delta r}/\nu \approx 20$ a transitional separation as well as at $\nu_{t\delta r}/\nu > 30$ a turbulent separation of different intensity also transformed to the quasiturbulent-like boundary layers. In the latter case at Re^{**}=const the enhancement of heat transfer was described by the similarity equation (7) based on the ratio of turbulent viscosity at an outer edge of a boundary layer in the section of reattachment to turbulent viscosity in a "classical" turbulent boundary layer ($\nu_{t\delta r}/\nu_{t0}$).

The measurements confirmed an extremely slow recovery to a "classical" turbulent boundary layer with various rates of this gradual process in an inner and outer parts of the boundary layers. Causing the powerful structural changes near the wall, a separation "works" first of all as a generator of an external turbulence; that is why the length of relaxation in an outer part of the boundary layers is substantially longer than in an inner one. Moreover the relaxation zone of a thermal boundary layer is shorter than of hydrodynamic one due to conservative reaction of thermal boundary layers to different disturbances including a separation.

The measurements also broadened the existing ideas about untraditional and to some extent unpredictable transformation of many important characteristics of a dynamic and thermal boundary layer in relaxation zone, concerning the distributions of heat and friction coefficients, mean velocities and temperatures, characteristic thicknesses, shape parameters, fluctuations of velocity and temperature, their spectral composition, etc.

The analysis of power spectra permitted to conclude that memory effects manifest themselves differently depending on frequency: at some frequencies the main features of prehistory

preserve when at others they disappear. In our opinion this fact is very important and demands further experimental investigations for penetration into the internal mechanism of relaxation and improvement of existing turbulence models..

We thank the INTAS for support in the framework of project "Pan-European Network on Flow, Turbulence and Combustion".

NOMENCLATURE

C_f	friction coefficient
H, H_t	shape parameters
t	mean temperature
t'	rms temperature fluctuation
t^*	dynamic temperature
U	mean axial velocity
u^*	velocity of friction
u^+	dimensionless velocity, U / u^*
u'	rms longitudinal fluctuation
x	distance along a plate
y	distance normal to a plate
y^+	dimensionless coordinate, yu^* / ν

Greek

δ, δ_t	boundary layer thicknesses
δ^*, δ_t^*	displacement thicknesses
δ^{**}	momentum thickness
δ_t^{**}	enthalpy thickness
ν	viscosity
Θ, Θ^+	dimensionless temperature $(t_w - t)/(t_w - t_e)$, $(t_w - t)/t^*$

Criteria

Re^{**}	Reynolds number
St	Stanton number

Subscripts

e	external flow
r	point of reattachment
t	turbulent, thermal
w	wall
δ	outer edge of the boundary layer
0	$Tu_e = 0$

REFERENCES

(1) Chang, P.K. Separation of flow, 1970, 300p. (Pergamon Press, London-N.Y.)
(2) Bradshaw, P., Wong, F.Y.F. The reattachment and relaxation of a turbulent shear flow, J. Fluid Mech., 1972, 52, pt.1, pp.113-135
(3) Eaton, J.K., Johnston, J.P. Review of research on subsonic turbulent attaching flows, AIAA J., 1981, 19, No.9, pp.1093-1100
(4) Ruderich, R., Fernholz, H.H. An experimental investigation of a turbulent shear flow with separation, reverse flow, and reattachment, J. Fluid Mech, 1986, 163, pp.283-322
(5) Castro, I.P., Haque, A. The structure of a turbulent shear layer bounding a separation region, J. Fluid Mech., 1987, 179, pp.439-478
(6) Simpson, R.L. Turbulent boundary layer separation, Ann. Rev. Fluid Mech., 1981 , pp.205-234
(7) Dyban, E.P., Epik, E.Ya., Yushyna, L.E. Influence of turbulence of external flow on the development of boundary layer behind the separated region, Prom. Teplotechnika, 1991, 13, No.2, pp.3-10 (in Russian)
(8) Dyban, E.P., Epik, E.Ya., Yushyna, L.E. Spectral characteristics of boundary layer behind the separation, Prom. Teplotechnika, 1991, 13, No. 3, pp.12-19 (in Russian)
(9) Jovic, S. An experimental study on the recovery of a turbulent boundary layer downstream of reattachment, Engineering Turbulence Modelling and Experiments 2, 1993, pp.509-517 (Elsevier)
(10) Dyban, E.P., Epik, E.Ya., Yushyna, L.E. Heat transfer on the surface of longitudinally streamlined bodies in the presence of closed separation and external flow turbulization, 10-th International Heat Transfer Conf., Brighton, UK, 1994, 3, pp.211-216
(11) Castro, I.P., Epik, E.Ya. Boundary layer relaxation after a separated region, Tenth Symposium on Turbulent Shear Flows, Pennsylvania, USA, 1995, 6p.
(12) Dyban, E.P., Epik, E.Ya. Internal structure of turbulent boundary layer at unfavorable pressure gradient and increased turbulence of external flow, Energetika, Lietuvas Moksly Akademija, 1992, No. 3, pp.110-118
(13) Dyban, E.P., Epik, E.Ya. Heat mass transfer and hydrodynamics of turbulized flows, 1985, 296p. (Nauk.Dumka, Kiev, in Russian)
(14) Kutateladze, S.S., Leontiev, A.I. Heat transfer and friction in turbulent boundary layer, 1987, 287p. (Energoatomizdat, Moskow, in Russian)
(15) Epik, E.Ya., Suprun, T.T., Yushyna, L.E. The influence of turbulence on the mechanism of heat transfer and selective properties of bypass transition, 2-nd International Symposium on Turbulence, Heat and Mass Transfer, Delft, Netherlands, 1997, pp.243-252
(16) Dyban, E.P., Epik, E.Ya., Suprun, T.T., Kuimov, S.V. Heat transfer of plate in the presence of laminar-turbulent transition and increased turbulence of the external flow, 1 Int. Symposium on Turbulence, Heat and Mass Transfer, Lisbon, Portugal, 1994, P.I.12.1-P.I.12.4
(17) Dyban, E.P., Epik, E.Ya. Thermal boundary layer in turbulized flows with an unfavorable pressure gradient, Prom. Teplotechnika, 1987, 11, No.6, pp.40-49 (in Russian)

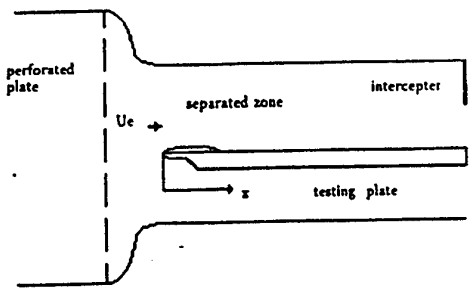

Figure 1 Sketch of the experimental arrangement

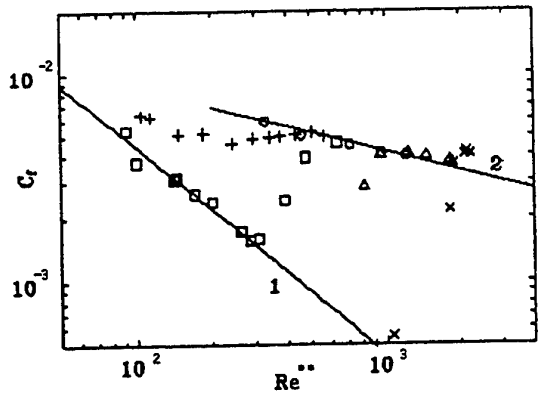

Figure 2 Friction coefficients versus Re^{**}
1-eq. (1); 2-eq. (3)

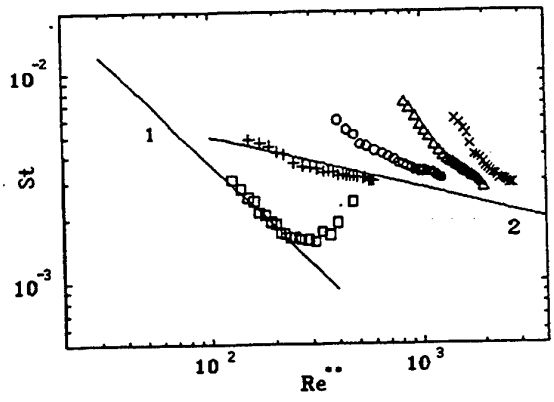

Figure 3 Heat transfer coefficients versus Re^{**}
1-eq. (2); 2-eq. (4)

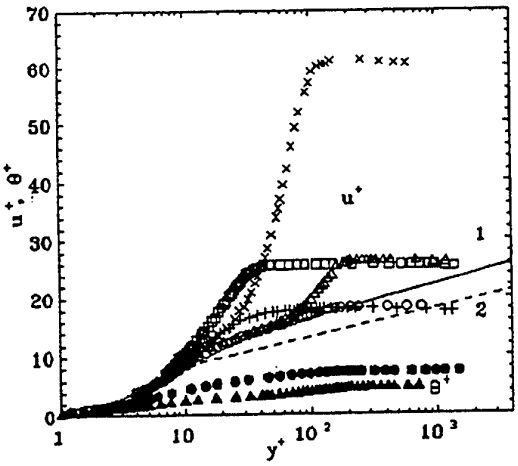

Figure 4 Distributions of velocity and temperature at x=50 mm
1-eq. (5); 2-eq. (6)

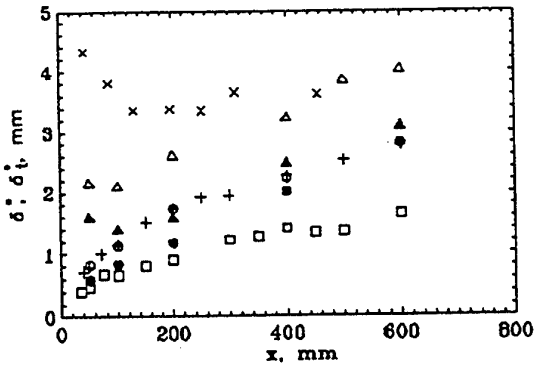

Figure 5 Displacement thicknesses in dynamic and thermal boundary layer

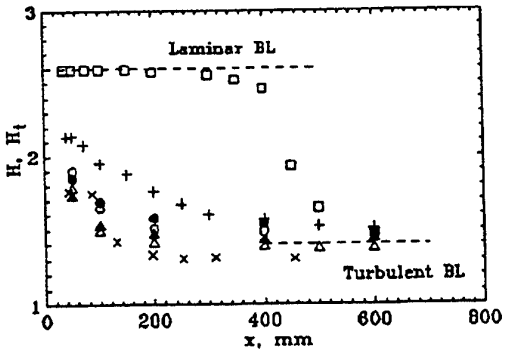

Figure 6 Shape parameters in dynamic and thermal boundary layer

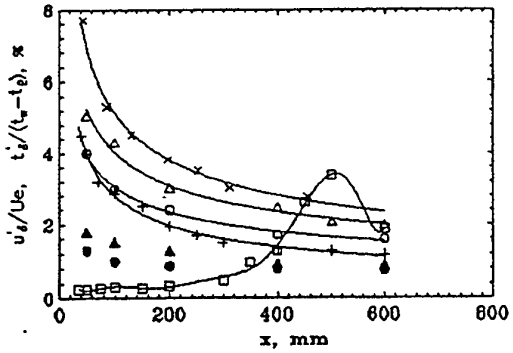

Figure 7 Fluctuations of velocity longitudinal component and temperature at an outer edge of boundary layer

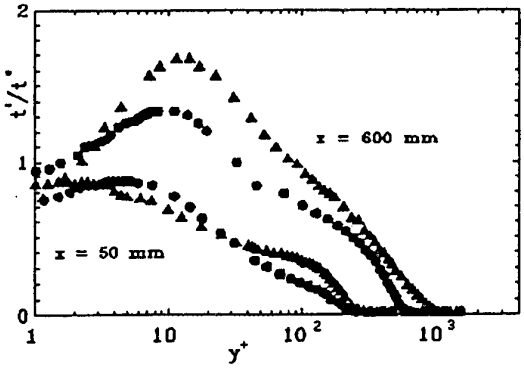

Figure 10 Distributions of temperature fluctuations

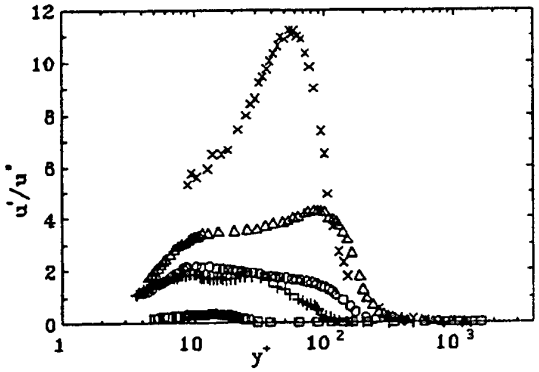

Figure 8 Distributions of longitudinal fluctuations at x=50 mm

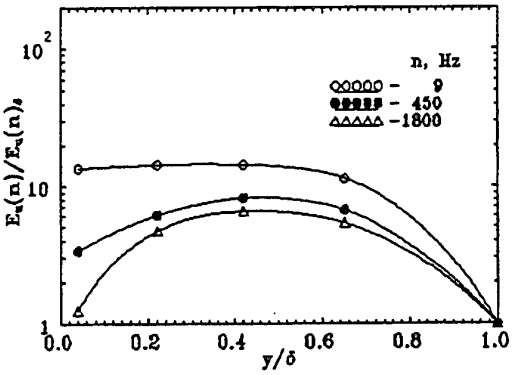

Figure 11 Filtration coefficients after turbulent separation at x=50 mm

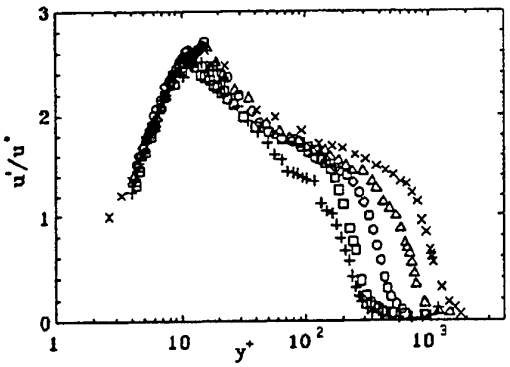

Figure 9 Distributions of longitudinal fluctuations at x=600 mm

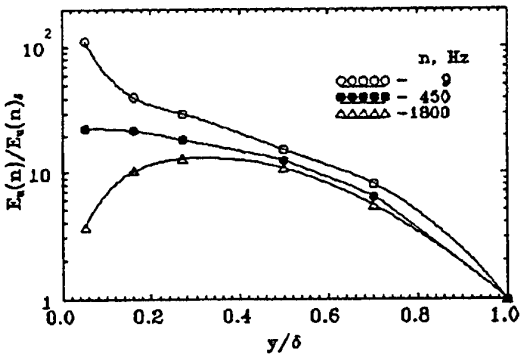

Figure 12 Filtration coefficients after transitional separation at x=50 mm

BUOYANCY-OPPOSED TURBULENT WALL JET FLOW DOWN A VERTICAL PLANE SURFACE

S. He, Z. Xu and J.D. Jackson

Manchester School of Engineering
University of Manchester, U.K.

ABSTRACT

Some results are presented from a program of research concerned with generic studies of thermal convection. The work was initiated to produce detailed measurements of the velocity, turbulence and temperature fields in buoyancy opposed plane wall jet flow. A large scale experimental facility consisting of a water flow loop with a test section in the form of a vertical rectangular channel having transparent walls has been constructed and equipped with advanced instrumentation for Particle Image Velocimetry, Laser Dopplor Anemometry and whole field thermal measurements. Detailed measurements of the temperature field together with preliminary measurements of the flow field using PIV are presented and discussed along with the results of CFD simulations. It has been found that the flow and temperature fields are highly unsteady. The effect of the presence of buoyancy is to restrict the penetration of the jet into the slowly ascending counter current flow and also to stabilize it.

1 INTRODUCTION

The turbulent plane, buoyancy-opposed vertical wall jet has been identified as having some key elements of flows encountered in certain nuclear reactor systems where hot fluid is diverted down the inside surface of the pressure vessel into a space containing colder stationary fluid. A similar flow situation can be produced in the early stages of the development of a fire in an enclosure, where a ceiling jet spreads outwards from the point of impingement and is turned downwards at the top corners of the room. With such applications in mind, a detailed program of generic thermal convection studies has been initiated at Manchester University to produce measurements of velocity, turbulence and temperature in turbulent buoyancy-opposed plane wall jet flow. A large scale experimental facility using water as the working fluid has been constructed and equipped with advanced instrumentation for the Particle Image Velocimetry (PIV), Laser Doppler Anemometry and measurements of the whole temperature field in such flows. The aim is to obtain a better understanding of the mechanisms involved in turbulent, buoyancy-influenced wall jet flow and to produce detailed information on both thermal and flow fields for use as a benchmark to establish trust in the CFD codes which are used in industry for simulating such flows. In this paper, we report some initial results obtained using the new test facility. CFD simulations of the flow system being studied are presented. These were made to help with the design and planning of the experiment. They are followed in the paper by some preliminary measurements made using PIV which show features of the instantaneous flow structures. Finally, some detailed measurements of the thermal field are presented and discussed.

A plane wall jet is formed by injecting a stream of fluid along a wall into fluid which is either at rest or moving slowly. The velocity field consists of two distinct flow regimes – an inner region where the flow resembles that of a conventional wall shear flow and an outer region where the flow has features similar to that of a free shear layer. Much research effort has been directed at such problems since the pioneering work of Glauert (1). A critical review of experimental studies on isothermal wall jets prior to 1981 can be found in Launder and Rodi (2). Recent studies have been directed at more complicated flow situations. Examples include the work Padmanabham and Gowda (3,4) and Sinclair et al (5), in which studies of three-dimensional wall jets are reported. Buoyant jets and/or plumes have been the subject of particular attention, for the obvious reason that in reality most jets are released into an environment of different density. Over ninety experimental studies of vertical buoyant jets were reviewed by Chen and Rodi (6). However, only one of these studies, Turner (7), was classified as a 'negative buoyancy jet'. In that study, the behavior of jet and plume flows were investigated and compared. Later, Goldman and Jaluria (8) reported a more detailed investigation of the effect of opposing buoyancy on the flow in free jets and wall jets using flow visualization with smoke and hot-wire anemometry. The penetration distance was found to be rather dependent on the discharge Froude number *Fr*. This work was subsequently extended to include consideration of mixed convection flow due to a buoyant wall jet turning downwards at a corner by Kapoor and Jaluria (9).

Recently Gogineni and Shih (10) have reported observations of whole flow field structures in plane wall jets using flow visualization and the PIV technique. The interaction between the inner and outer layers has been studied. The jet flow was found to start

to show transition from the laminar condition to the turbulent one when Reynolds number based on the exit mean velocity and channel width was greater than 2200. Hsiao and Sheu (11) investigated qualitatively and also quantitatively the behavior of double-row vertical structures in the near field region of a plane wall jet using flow visualization and hot-wire techniques.

Finally, it is of interest to note the studies of Balachandar et al (12) and Volchkov et al (13) of a wall jet injected into an approaching flow. The flow configuration studied was in some respects similar to the present one but no significant buoyancy influences were involved. The effects on the flow pattern of jet to background flow velocity ratio were investigated. It was found that the influence of the counter current flow on the jet flow appeared to be weak when the velocity ratio was greater than about 10.

2 THEORETICAL BACKGROUND

Figure 1 illustrates the two-dimensional buoyancy-opposed vertical plane wall jet flow considered here. As shown in the figure, hot fluid is injected downwards along a wall into a slowly ascending colder fluid. The jet flow eventually turns upwards and is removed along with the upward flowing colder fluid from the top of the test section. The non-dimensional parameters describing such a flow situation certainly include the jet Reynolds number (based on mean velocity U_0 at the injection location and slot width D) and the discharge Froude number Fr (the ratio of inertial to buoyant forces). The Froude number can be defined in terms of initial momentum flux M_0 and the weight deficit W_0 as,

$$Fr = \frac{M_0 U_0}{W_0 D} \qquad (1.)$$

where $M_0 = 2\int_0^\infty \rho_0 U_0^2 dx$ and $W_0 = 2g\int_0^\infty (\rho_a - \rho_0) U_0 dx$.

For the case of uniform profile of velocity and density at the jet, the Froude number can be expressed as,

$$Fr = \frac{U_0^2}{gD(\rho_a - \rho_0)/\rho_0}. \qquad (2.)$$

Another important parameter is the ratio of the jet velocity to the ascending flow velocity U_0/U_a. As mentioned earlier, the effect of this on the jet flow has been investigated by Balachandar et al (12) and Volchkov et al (13). In the present study, we have kept this ratio relatively large so as to guarantee that for most of the cases studied, the effect of buoyancy dominates that of the counter flow.

3 COMPUTATIONAL STUDY

Pre-test numerical simulations of the buoyant wall jet flow considered here have been conducted using the computer code FEAT, a finite element CFD package, which is widely used in the UK nuclear industry. The code was developed for studying general flow, heat transfer and thermal stress problems. It has the feature of being interactive – the user can monitor and interact with the solution process at virtually all stages. High order convection schemes are used in the FEAT code, which guarantee that numerical diffusion is minimised in the solution, thus avoiding problems which are commonly encountered when using CFD codes employing finite volume methods.

The FEAT code is designed for conditions of uniform fluid properties. The effects of buoyancy are included in the momentum equations using the Boussinesq approximation. The energy equation is solved coupled with the continuity equation and the momentum equations to update the buoyancy term. In the standard version of the code, various turbulence models, including two-equation eddy viscosity models, are available for use. In our simulations, the standard k-ε turbulence model (Smith (14)) has been employed. (The equations actually solved in the FEAT code are those for q and f, the square root of the turbulence kinetic energy and the frequency of the large scale turbulence motions, respectively. Extra source terms are added to the q and f equations to accommodate other models chosen by the user). Wall functions are used in the near-wall region. A non-uniformly distributed mesh was employed in the present calculations.

4 EXPERIMENTAL FACILITY AND INSTRUMENTATION

The test section used in the present experimental study is a vertical passage of height 2.3m having a rectangular cross section 0.3m x 1.2m with transparent walls to enable optical measurements to be made. As shown in Figure 1, a plane jet of heated water passing downwards through the 18 mm space between a glass plate and one wall, is injected into a slowly ascending flow of colder water, supplied at the bottom of the test section through a carefully designed flow conditioning arrangement. The jet flow eventually turns upwards and is removed from the top of the test section along with the upward flowing colder fluid. The flow can be considered as a confined two-dimensional buoyant plane wall jet. The width of the test section is 15 times that of the wall jet gap and the aspect ratio of the test section is 4:1. Figure 2 shows a schematic diagram of the flow loop. The heating and cooling systems have been designed with a capacity to deliver and remove a maximum power of 108kW. This enables experiments to be made covering values of Froude number as low as 30 while the Reynolds number based on the jet gap and jet velocity can be varied between 3000 and 10000.

Figure 3 shows details of the instrumentation. The temperature distribution on the wall down which the jet flows is measured using 11 fixed thermocouples. The temperature distribution within the entire flow field is measured using a traversable thermocouple rake having 21, fast response, thermocouples (wire diameter 0.076 mm) mounted on it. The thermocouple signals are connected to a 60 channel computer controlled scanning system connected to a Solartron DVM system. The data from the DVM are transferred to a PC for further processing to obtain mean and fluctuating components of temperature. The computer controlled data acquisition system is also used to measure the electrical power delivered to the heaters and the flow rates of both the jet and ascending fluid.

Figure 3(b) shows sketches of the optical arrangement for the Particle Image Velocimetry (PIV) which is being used for whole velocity field measurement. A 4 Watt Argon-ion laser provides the light source. The laser beam is brought to the side of the test section (about 2 metres away from it) using a mirror and lens arrangement, where it is split into a sheet, about 600mm wide and 1.5mm thick, using a cylindrical glass rod. A rotating disk placed before the rod chops the light into pulses. Two image recording methods are available in the present arrangement, one involving a CCD camera and one a film camera. In the first arrangement, a camera of resolution of 752 (H) x 582 (V) is connected to an image grabber card installed on the PC, which is used for data processing and storage. This enables Digital Particle Image Velocimetry (DPIV) measurements to be made. Due to the limitation of the resolution of the CCD camera, the maximum view area for DPIV measurement is only about 100x80mm^2, whereas the area of interest in the flow field is much larger, typically, 300x800mm^2. Consequently, in the present investigation, the DPIV arrangement is currently being mainly used for monitoring purposes. The second recording method involves the use of a Nikon film camera and a Nikon 35mm film Scanner (Coolscan II). The scanner has a maximum resolution of 106 pixels per millimeter. When an area of flow of 600x300mm^2 is covered per frame, this gives a resolution of 0.16 mm physical distance per pixel.

Figure 3(c) shows a two-color, two-component, fibre optic Laser Doppler Anemometry (LDA) system, incorporating two Burst Spectrum Analysers, which is available with the test facility. This will be used to make measurements of instantaneous local velocity from which information about the turbulence (second and higher moments) can be obtained.

5 RESULTS AND DISCUSSION

5.1 Computational results

Figure 4 shows velocity, turbulence and temperature distributions, from pre-test simulations made using the computer code FEAT. Results are presented for two typical cases (a buoyancy-free flow and a buoyancy-influenced flow). These computations were performed to help with the planning of the experiments. The results exhibit some interesting features. It can be seen that both the penetration and the lateral spread of the jet are predicted to be significantly reduced in the buoyant flow case. The velocity gradients in both the mixing layer and the near-wall region are greater in this case and the flow above the jet is shifted laterally to the right, which results in a region of considerable streamline curvature being produced. The turbulence kinetic energy levels are quite different in the two cases, the contours providing pictures which again illustrate the reduction in penetration and lateral spread in the buoyancy-influenced case. The values are more than 30% higher for the buoyant jet case because additional turbulence is generated in the mixing region. The temperature field is greatly altered as well. A feature which is evident in both the non-buoyant and buoyant cases is that, the temperature variation is highly concentrated in the flow stagnation region.

5.2 The instantaneous flow structure

5.2.1 Flow visualization

The PIV arrangement described earlier has been used for flow visualization. For such studies the chopper is removed. By suitably choosing the shutter speed of the camera, the trace of the seeding particles can provide a good indication of the instantaneous flow pattern. Pictures have been obtained for both the isothermal jet flow and buoyant jet flow cases at various values of Froude number.

The results indicate that the flow is highly unsteady under isothermal flow conditions. The instantaneous flow patterns obtained vary significantly and are in general very different from the mean flow pattern predicted by the computer simulation. The main stream flow , usually a distorted pattern of that from the simulation, can normally be identified, but the exact shape changes constantly. The penetration of the jet varies by as much as a quarter. Large scales vortices can be seen to be superimposed on the 'main flow structure' and they sometimes penetrate much further down than the main structure does.

The influence of buoyancy on flow structure has been clearly demonstrated by the flow visualisation studies. Jet penetration is found to be reduced in the buoyant jet cases when the Froude number is moderate (<80). The lateral spread of the jet is also reduced. These trends are clearly consistent in qualitative terms with those exhibited by the CFD simulations. An interesting observation, concerning the influence of the buoyancy, is that the flow is much more stable in the buoyant jet case than in the isothermal one. The main flow pattern is much better defined and the superimposed random vortices are much less frequently seen. The reason appears to be that the

relatively dense ascending flow prevents the lighter hot jet from interacting freely with it and therefore keeps the two streams rather separate. Temperature measurements presented later seem to support this view.

5.2.2 Preliminary results from PIV measurements

Figure 5 shows velocity vector plots for two different times for an isothermal jet flow (Re=3000) obtained using PIV with the film camera. Both auto-correlation and particle tracking schemes are used in order to extract velocity vectors from the quadruply exposed films.

The flow structure shown in the velocity vector plots is very typical. In frame A, the jet main steam flow penetrates fairly deep down but much less deep in Frame B. In both cases, large scale vortices can be seen in places. Both are clearly very different from the mean flow field yield by the computer simulations.

5.3 Mean temperature field

Local fluid temperature was measured using the traversable rake of twenty-one equally spaced thermocouple junctions, which were arranged horizontally 12.5 mm apart. The rake was traversed vertically to cover the whole flow field. Measurements were made every 100mm in the region where the temperature gradients were small and every 10mm where they were large. A summary of the experimental conditions is shown in Table 1.

Figures 6(a) and 6(b) show temperature contours for two typical cases one with strong buoyancy influence and one with a much reduced influence. Measurements obtained using the fixed thermocouples were combined with those obtained using the traversable rake in order to produce temperature contours over the whole flow field. It can be seen from the figures that the jet penetrated much deeper into the ascending counter-current flow in the case of larger Froude number (smaller buoyancy effect). It is also interesting to note that the area of relatively large temperature gradient spreads more widely in the case of smaller buoyancy influence. When such influences are strong, such as for the case shown in Figure 6(b), temperature falls quickly within a very limited region at the frontier of the jet.

As mentioned earlier in this paper, the flow is very unsteady for the case of isothermal or flow with small buoyancy influence. The frontier of the jet oscillates over a fairly large region and large scale vortices appear frequently and penetrate further downwards. These features combine to help the energy transfer process in the region and result in a rather smoothed temperature variation over a relatively larger region. When the influence of buoyancy is strong, the flow is stabilised and the jet frontier maintains a relatively steady level. The convection effect through large vortices disappears and the primary mixing of the two streams is restricted to a smaller region.

Figure 7 shows the temperature distribution along the wall down which the jet flows. The temperature difference T_w-T_c has been normalised using the temperature difference T_h-T_c between the hot jet flow and the cooler incoming ascending flow. The trend is clear. The smaller the Froude number, the more sharply the temperature falls. It is however of interest to see that the temperature variation is similar in all cases before this sharp fall occurs. This could imply that the early development of the jet is not much influenced by the buoyancy even when such effect is strong.

Figure 8 shows the variation of normalised jet penetration distance with the Froude number. The penetration distance is arbitrarily defined here as the distance between the jet exit location and the one where the maximum excess temperature *(T-Tc)/(Th-Tc)* is less than 2 %. Also shown in the figure is the curve calculated using the correlation obtained by Goldman and Jaluria (1). The normalised penetration clearly increases with Froude number in both cases but the absolute value is very different. In this connection it should be noted that both the jet considered in the present study and that considered by Goldman and Jaluria were in a confined space but the geometries were different. Some effect of the particular configuration on the penetration distance is to be expected.

5.4 The instantaneous temperature

The time variation of the instantaneous temperature of the fluid at several vertical locations (for the horizontal location x=241mm) with a Froude number 84 is shown in Figure 9. It can be seen from the figure that the time variation of the instantaneous temperature is very different at the various levels. It is instructive to compare this figure with the temperature contour plot shown in Figure 6(a). At level y=100mm, the fluid from the two steams (hot jet and ascending flows) are clearly well mixed and the time variation of the temperature is typical of what one might encounter in a turbulent flow. The amplitude of the variations of temperature at the next three levels is very violent and the patterns differ markedly. The temperature switches between two levels, one close to the temperature of the hot jet and one to that of the colder ascending flow. The percentage of time which the temperature stays at the higher level is greater at a higher level (y=500mm) and less at a lower level (y=640mm). Consequently, the mean temperature shown in Figure 6(a) is just a nominal value. In reality, the fluid does not actually take such a value at all. In this region, the wall adjacent to the jet is subjected to large variations of temperature. This could lead to large fluctuations of thermal stress. The temperature variations discussed above are consistent with the observations made earlier on the basis of the flow visualisation studies – it is

apparent that the frontier of the jet flow oscillates over a relatively large region. At a fixed location, one feels the jet intermittently reaching it. At level y=700mm or lower, the temperature of the fluid is basically equal to the temperature of the incoming ascending flow with very small fluctuations.

Figure 10 shows plots of the histograms of the variation of fluid temperature at various vertical and horizontal locations. The histogram distribution concentrates to a single value at y=100mm and it remains much the same at y=300mm but spreads slightly out. Further down from the exit of the jet, the distribution spreads significantly and a second peak appears. This is centred at the temperature of the colder ascending flow and is very concentrated, which reflects the fact that ascending flow is a rather slow laminar flow.

Figure 11 shows the intermittence of jet fluid arrival at certain location for two typical flow situations. This was calculated by adding up the area under the histogram above a certain temperature, which was chosen to distinguish between the two streams. For the case shown in Figure 10, for example, 26 was chosen as the dividing temperature. Figure 11(a) shows the vertical variations of the intermittence at several x locations for the higher Froude number condition. It can be seen that in this case the vertical variations of intermittence are similar at the various x locations. It takes a distance of 200mm for the intermittence to reduce from 90% to 10%, which indicates a large spread of the mixing region. For the case with a smaller Froude number (Figure 11(b)), the vertical variation of intermittence is very different at various x locations. It remains very near to unity up to about y=300 in the region near to the jet (small x), after which it reduces quickly to nearly zero within a distance of about 100mm. This confirms what was noted earlier that the jet flow with small Froude number has a much smaller mixing region. It can be seen that the intermittence starts to reduce immediately below the jet level for locations further away from the jet (larger x) and that the variation is rather slow. This indicates that the jet flow is restricted laterally near to the jet exit. This can also be seen from the contour plot of the mean temperature shown in Figure 6(b).

Figure 12 shows the root mean square temperature fluctuations t' for the case of high and low Froude number respectively. The variation of t' is similar at different x locations for the case of the higher Froude number. It is fairly uniform and takes values around unity in the region of high intermittence but remains low in the region of low intermittence. It can be seen from Figure 12(b) that for the case of low Froude number the RMS temperature fluctuation peaks in a relatively small mixing region. Beyond this region it is similar to that in the case of higher Froude number, although the temperature difference in the flow region is much higher in this case. This again suggests that the mixing process is restricted to a more localised region in the case of lower Froude number.

6 CONCLUDING REMARKS

A detailed program of generic thermal convection studies has been initiated at Manchester to produce detailed measurements of velocity, turbulence and temperature in buoyancy opposed turbulent wall jet flow in water. A large scale experimental facility has been constructed and equipped with advanced instrumentation for Particle Image Velocimetry (PIV), Laser Doppler Anemometer and measurement of the whole temperature field. Some initial results for a buoyancy-opposed vertical turbulent wall jet flow are reported.

Both flow visualisation studies and the thermocouple measurements of the temperature field show that the wall jet flow is highly unsteady. The instantaneous flow structure is very different from that indicated by the mean flow pattern yielded by CFD simulations. The frontier of the jet oscillates over a large region and this contributes significantly to the mixing of the hot jet flow and the ascending colder flow. The fluid temperature in the mixing region oscillates between the temperature of the hot jet flow and the colder ascending flow. Therefore, in practice thermal stresses on the wall in the jet mixing region may be an important issue. The effect of the buoyancy is to restrict the penetration of the jet. It also has the effect of stabilising it. Further detailed study on the flow field is needed in order to understand such flows more fully.

ACKNOWLEDGEMENTS

The work is supported by a research contract on 'Generic Studies of Thermal Convection' funded by the UK Nuclear Industry Management Committee (IMC). The authors wish to acknowledge the contribution made by Dr. J Song to the design and construction of the test facility and are grateful to Dr. T Wu for assistance provided in the preparation of the material included in the paper.

REFERENCES

1. Glauert, M.B. (1956) The wall jet. *J. Fluid Mech.*, vol. 1, pp625-643.
2. Launder, B.E. and Rodi, W. (1981) The turbulent wall jet. *Prog. Aerospace Sic.*, vol. 19, pp81-128.
3. Padmannabham, G. and Gowda, B.H.L. (1991) Mean and turbulence characteristics of a class of three-dimensional wall jets – part 1: mean flow characteristics. *ASME J. Fluids Engineering*, vol. 113, pp620-628.
4. Padmannabham, G. and Gowda, B.H.L. (1991) Mean and turbulence characteristics of a class of three-dimensional wall jets – part 2: turbulence

characteristics. *ASME J. Fluids Engineering*, vol. 113, pp629-634.
5. Sinclair, J.R., Slawson, P.R. and Davidson, G.A. (1990). Three-dimensional buoyant wall jets released into a coflowing turbulent boundary layer. *ASME J. Fluids Engineering*, vol. 112, pp356-362.
6. Chen, C.J. and Rodi, W. (1980) Vertical turbulent buoyant jets – a review of experimental data. Pergamon Press.
7. Turner, J.S. (1966) Jets and plumes with negative or reversing buoyancy. *J. Fluid Mech.*, vol. 26, part 4, pp770-792.
8. Goldman, D and Jaluria, Y (1986) Effect of opposing buoyancy on the flow in free and wall jets. *J. Fluid Mech.*, vol. 166, pp41-56.
9. Kapoor, K. and Jaluria, Y. (1991) Mixed convection flow due to a buoyant wall jet turning downward at a corner. In *Mixed Convection Heat Transfer,* ASME, HTD-vol.163, pp119-128.
10. Gogineni, S. and Shih, C. (1997) Experimental investigation of the unsteady structure of a transitional plane wall jet. *Experiments in Fluids*, vol 23, pp121-129.
11. Hsiao, F.B. and Sheu, F.B. (1994) Double row structures in the near field region of a plane wall jet. *Experiments in Fluids*, vol.17, pp291-301.
12. Balachandar, R., Robillard and Ramamurthy, A.S. (1992) Some characteristics of counter flowing wall jets. *ASME J. Fluids Engineering*, vol 114, pp554-558.
13. Volchkov, E.P., Lebedev, V.P., Nizovtsev, M.I. and Terekhov, V.I. (1995) Heat transfer in a channel with a counter-current wall jet injection. *Int. J. Heat and Mass Transfer*, vol.38, pp2677-2687.
14. Smith, R.M. (1984) A practical method of two-equation turbulence modelling using finite-elements. Int. J. Num. Meth. Fluids, vol.4, pp321-336.

NOMENCLATURE

D	jet width
Fr	Froude number
g	gravitational acceleration
M	momentum flux
Re	Reynolds number based on the mean velocity at the jet exit and the jet width
T	temperature
x	horizontal co-ordinate
y	vertical co-ordinate
U	mean velocity
W	weight deficit

Greek symbols

ρ	density

Subscripts

$_0$	jet exit
$_a$	ambient
$_c$	colder fluid (ascending flow)
$_h$	hot fluid (at jet exit)
$_w$	wall

Table 1. Experimental conditions

Test	Re	Power (kW)	Fr	Jet mass flow rate (kg/s)	Flow rate of the ascending flow (kg/s)	$T_h - T_c$ (°C)
A	3000	36	84	3.6	4	4
B	3000	72	42	3.6	4	7.4
C	3000	100	30	3.6	4	10.8

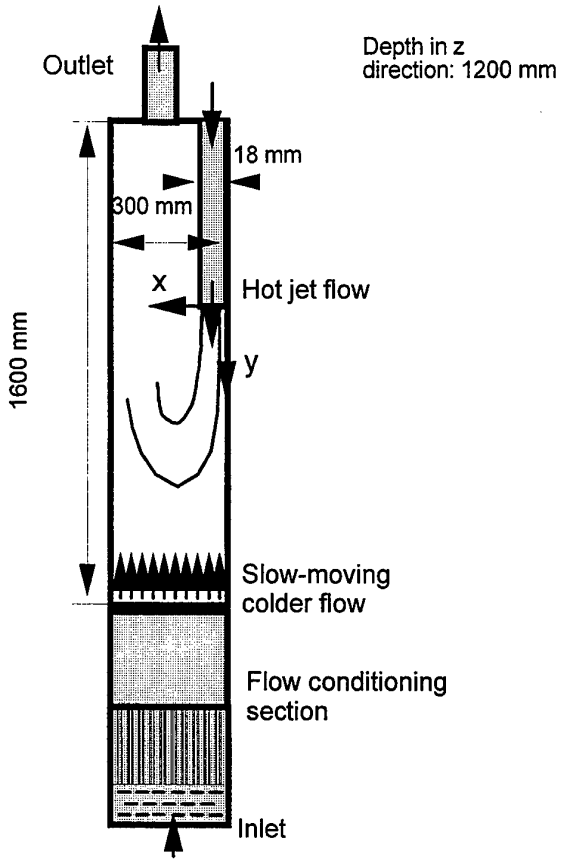

Figure 1 Test Section (Side View)

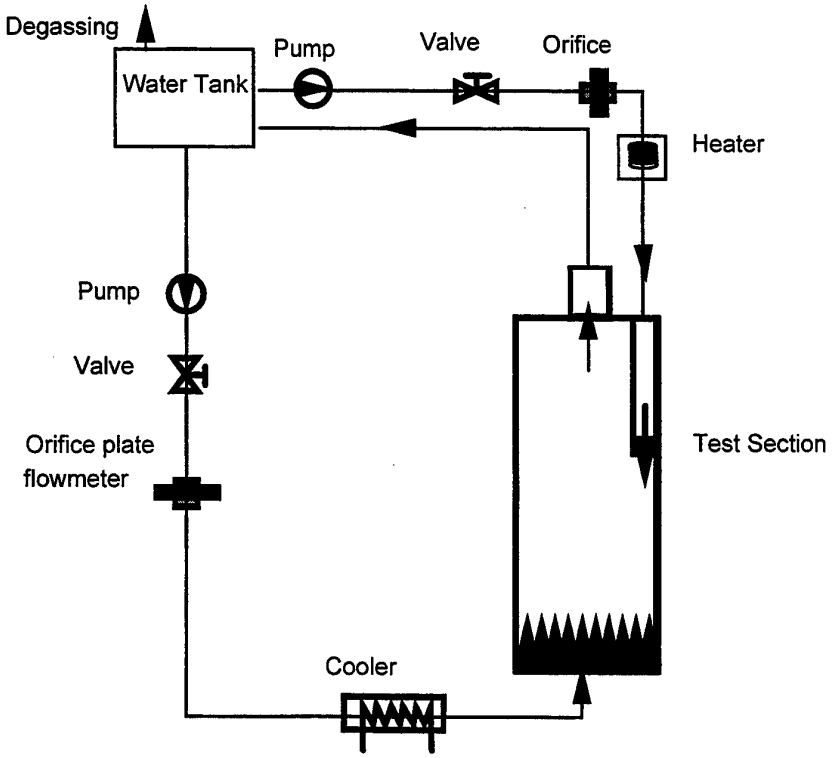

Figure 2 Flow Loop

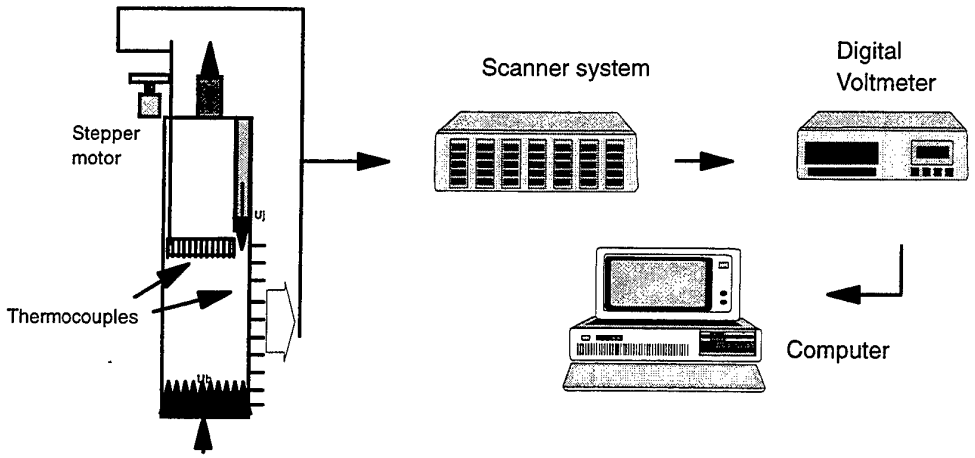

(a) Temperature Measurement System

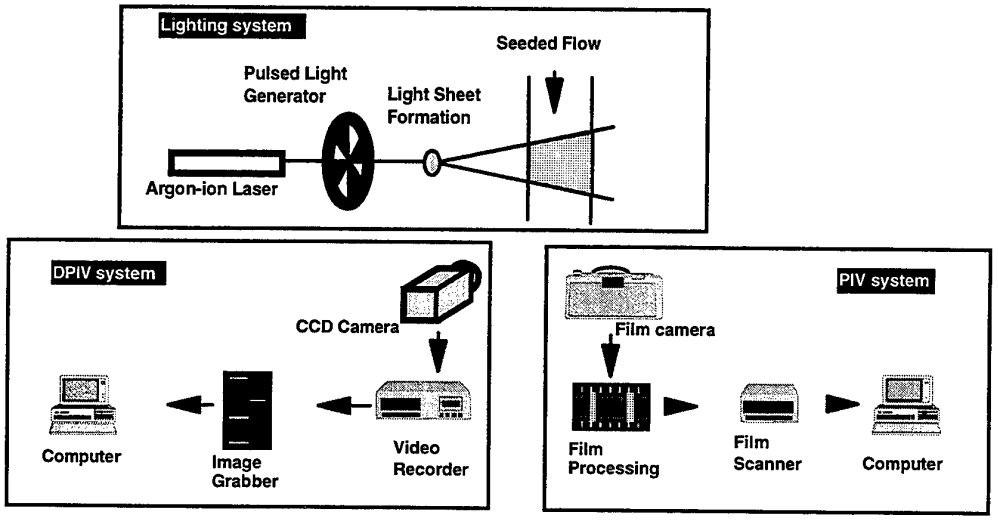

(b) Particle Image Velocimetry Systems

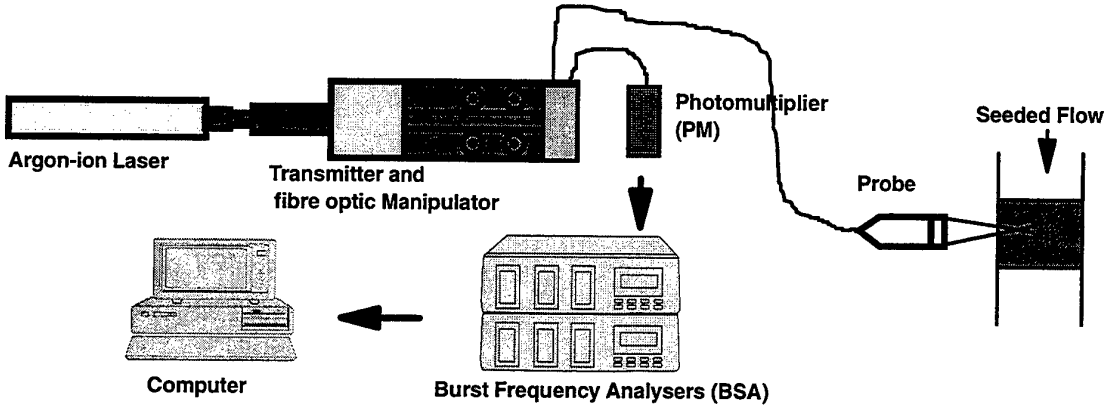

(c) Laser Doppler Anemometry System

Figure 3 Instrumentation

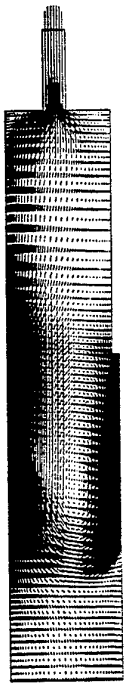

Velocity vectors

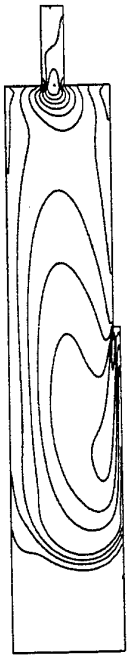

Contour: square-root of turbulence energy

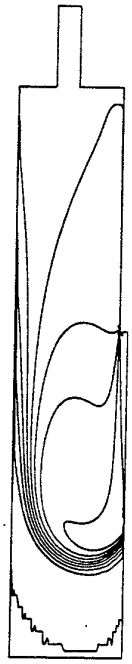

Contour: temperature

(a) Non-buoyant wall jet

Velocity vectors

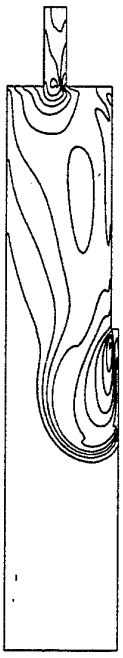

Contour: square-root of turbulence energy

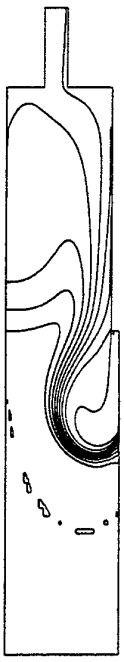

Contour: temperature

(b) Buoyant wall jet (Fr=50)

Figure 4 Computational simulations of distributions of velocity, turbulence and temperature in non-buoyant and buoyant wall jet (Re=3000)

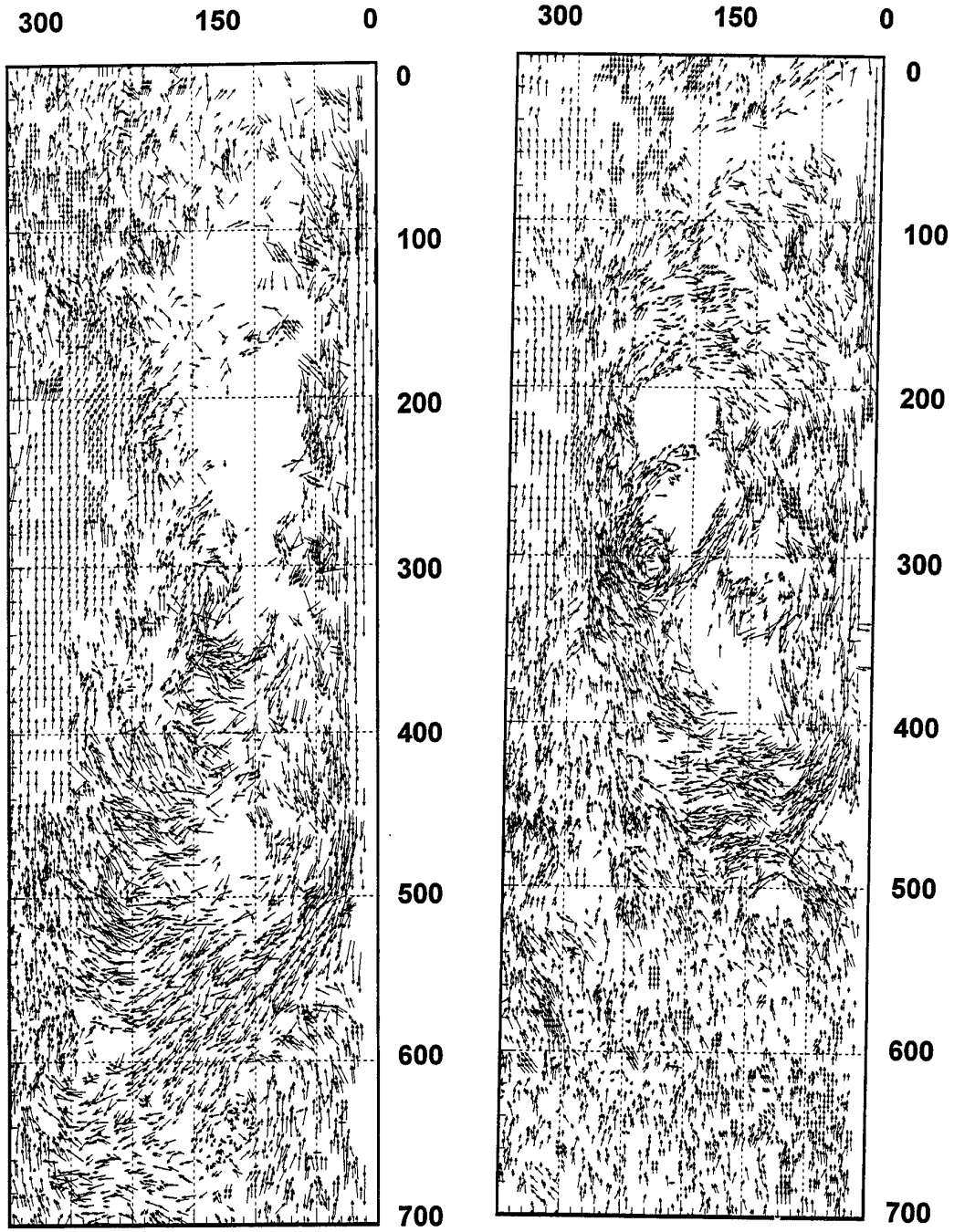

(a) Frame A

(b) Frame B

Figure 5 Velocity vectors in an isothermal vertical wall jet flow

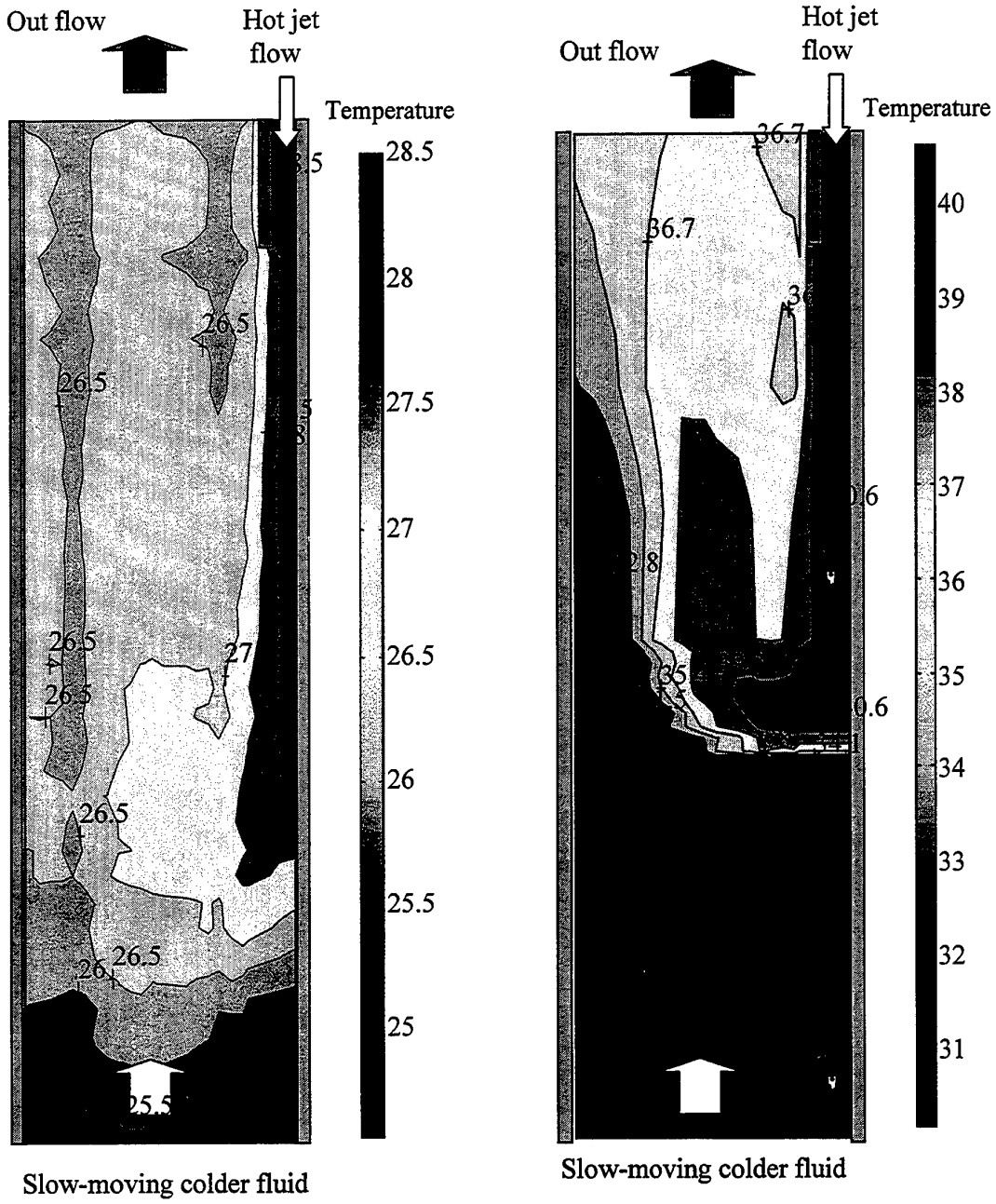

Figure 6 Mean temperature contours

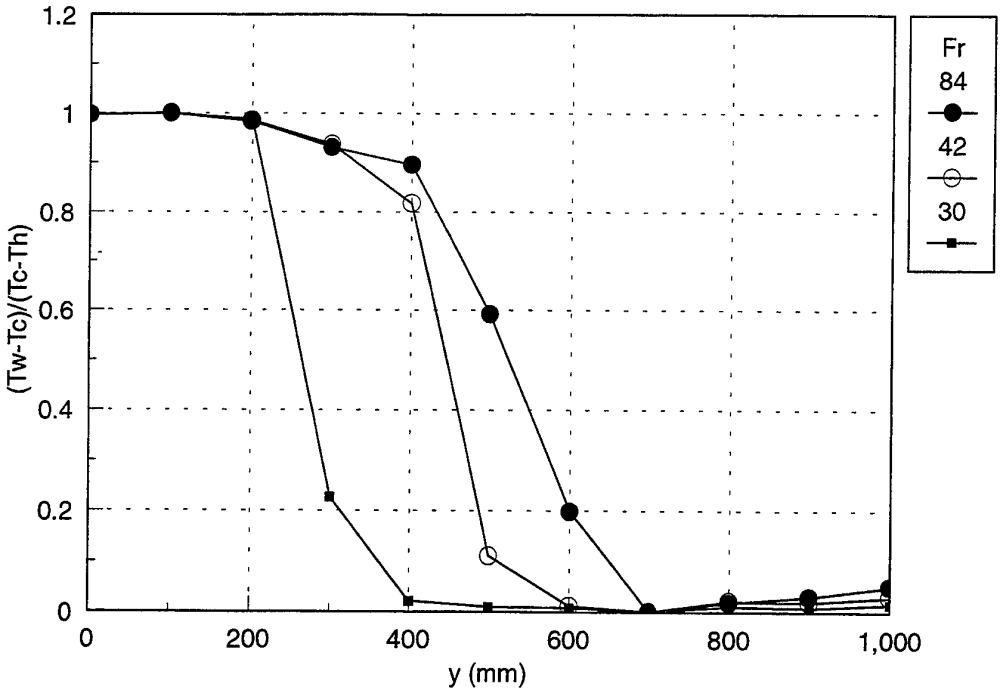

Figure 7 Normalised wall temperature distribution

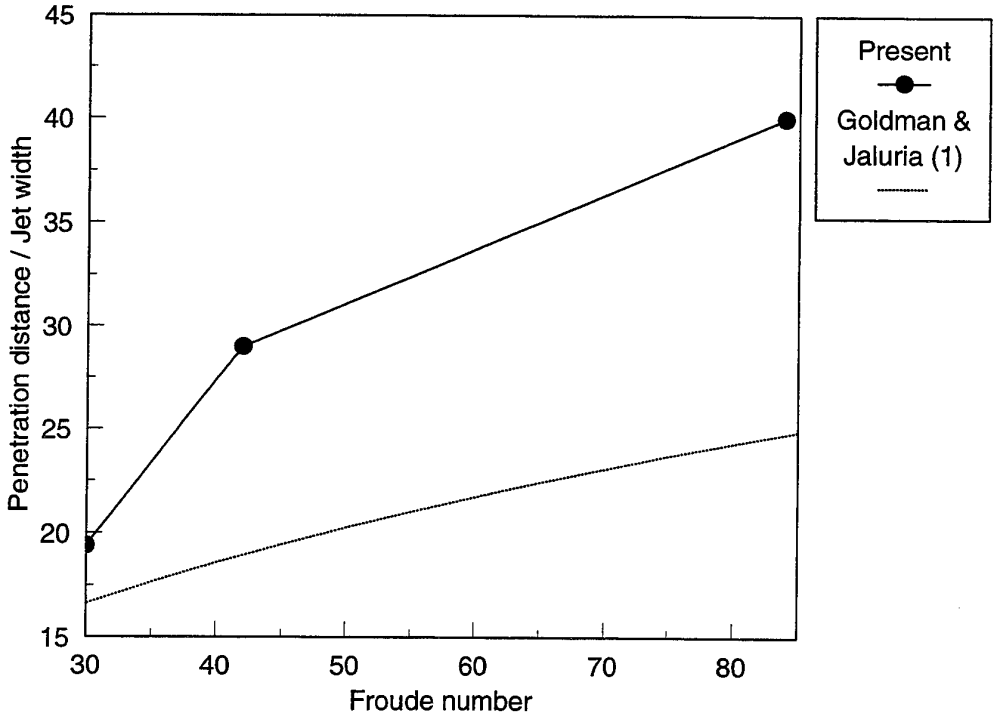

Figure 8 Jet penetration distance

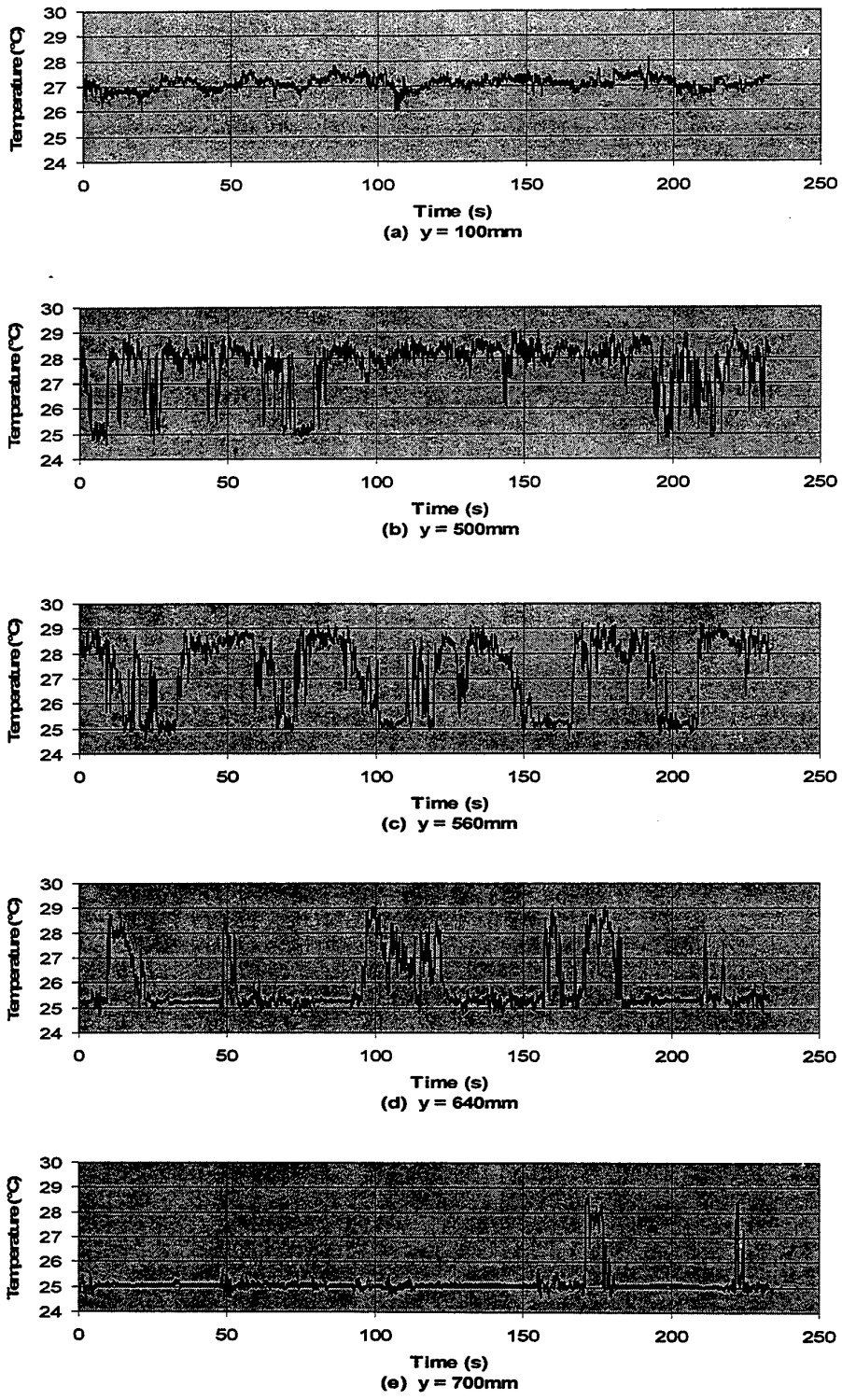

Figure 9 Instantaneous temperature variations (Fr=84, x=241mm)

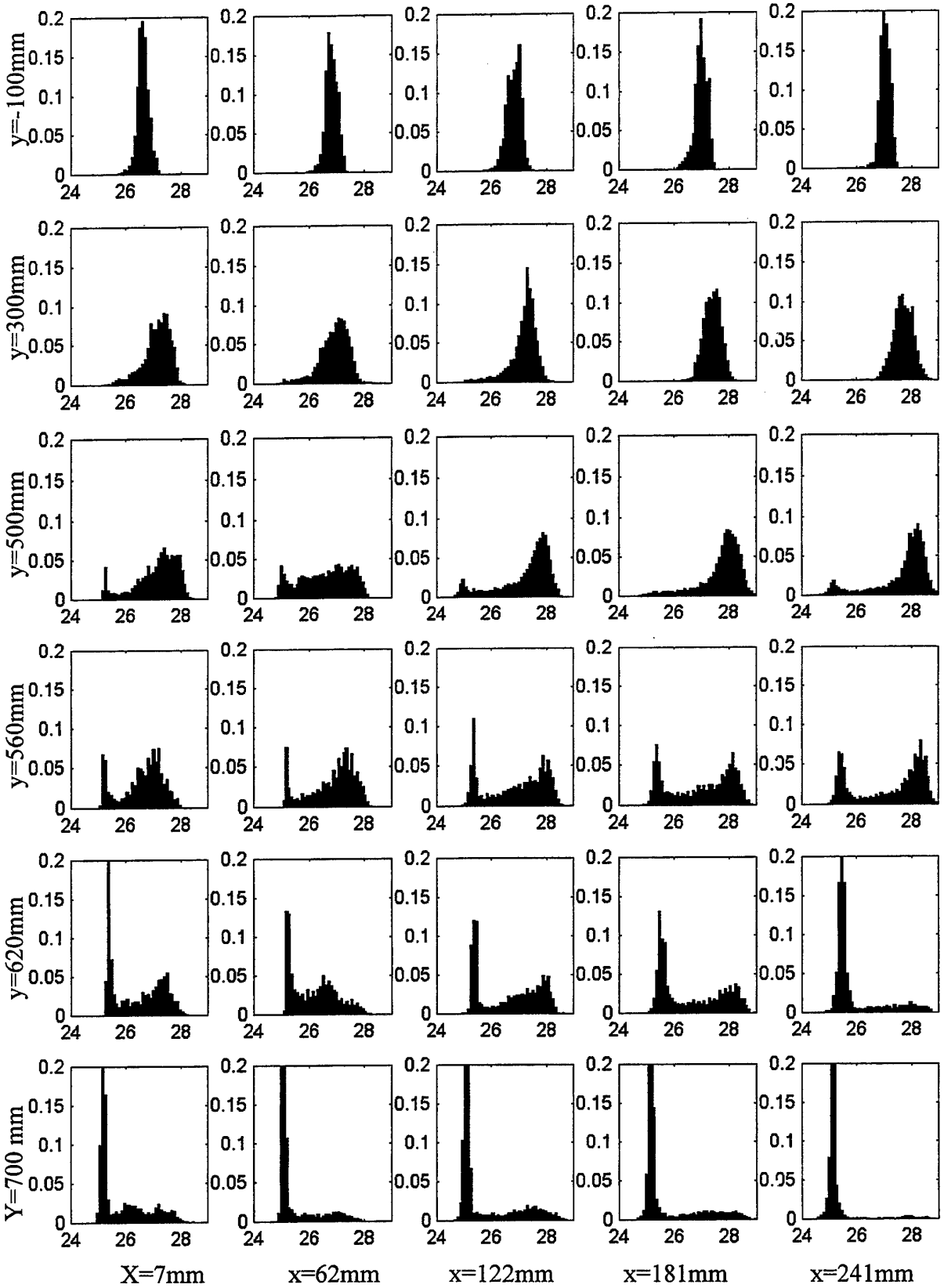

Figure 10 Histogram of fluid temperature at various locations (Fr=84)

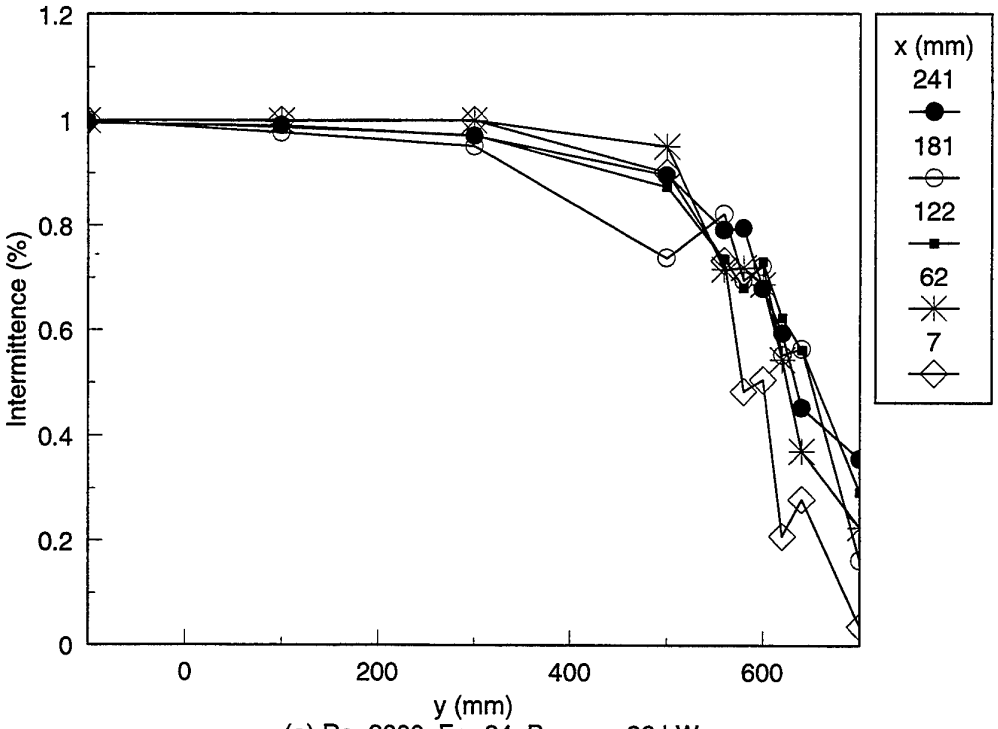

(a) Re=3000, Fr= 84, Power = 36 kW,

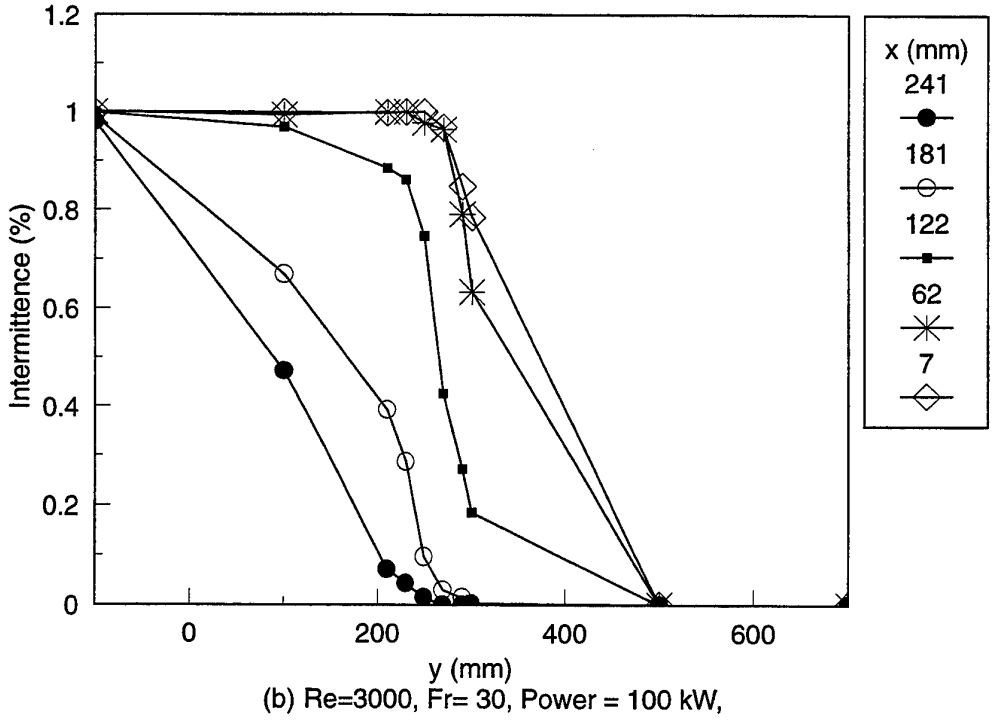

(b) Re=3000, Fr= 30, Power = 100 kW,

Figure 11 Intermittence of jet arrivals

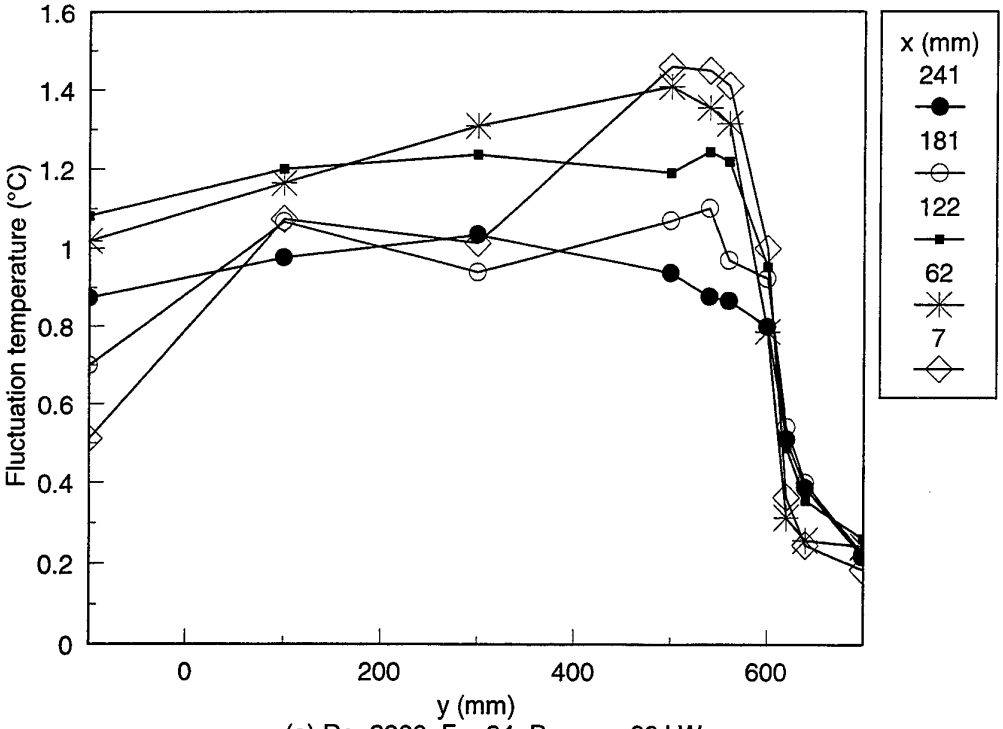

(a) Re=3000, Fr= 84, Power = 36 kW,

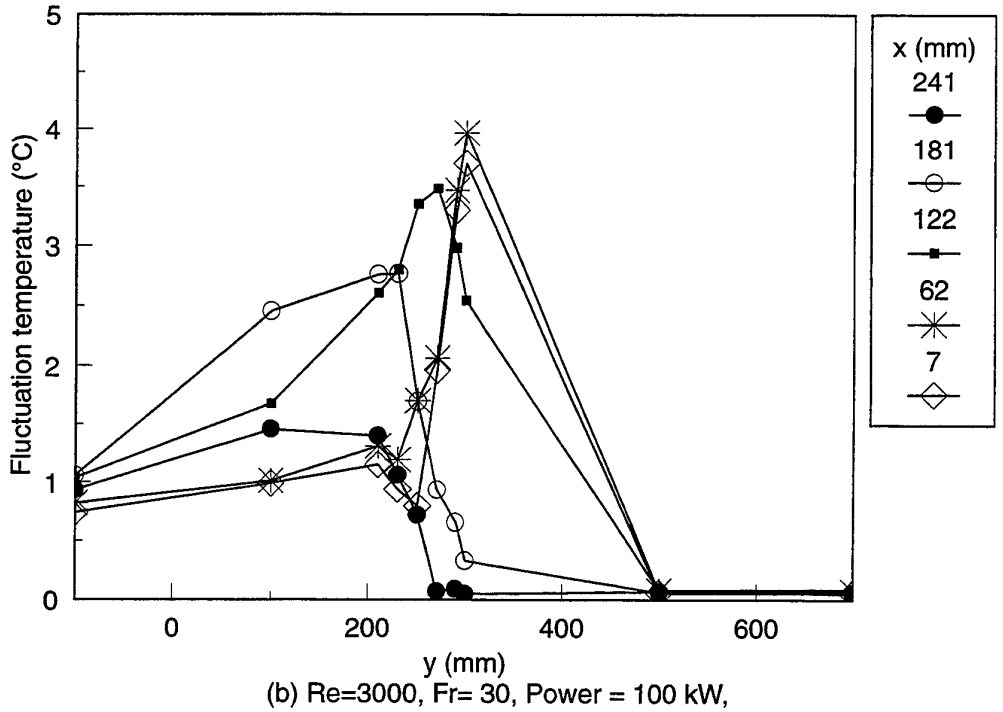

(b) Re=3000, Fr= 30, Power = 100 kW,

Figure 12 RMS fluctuation temperature

Session 5

Horizontal, Stratified Flows

A CRYOGENIC EXPERIMENT FOR THE RAYLEIGH-BENARD CONVECTION STUDY

X. Chavanne, F. Chillà*, B. Castaing, B. Chabaud,
B. Hébral and P. Roche

Centre de Recherches sur les Très Basses Températures,
Laboratoire associé à l'Université Joseph Fourier,
CNRS, BP 166, 38042 Grenoble-Cedex 9, France
email: hydrodyn@labs.polycnrs-gre.fr

* Present address: Ecole Normale Supérieure de Lyon,
46 Allée d'Italie, 69364 Lyon-Cedex 7, France

ABSTRACT

A Rayleigh-Bénard convection experiment has been carried out by using He at low temperature. He properties in the region around its critical point (T_c{EIT90} = 5.1953 K, P_c = 2.275 bars), together with accurate calorimetric techniques, especially a thermocouple designed to measure temperature difference as low as 20 μK, and local probes allow a study of convection ; the heat transfer as well as the characteristic flow behaviour over the cell, are analysed through the turbulent convection range (from Ra = 2 10^7 up to Ra = 2 10^{14}). Above Ra ~10^{11} a new regime is observed where the heat transfer is enhanced by a turbulent rather than a molecular diffusion near the walls. This regime corresponds closely to the ultimate regime predicted by R. Kraichnan (1).

1 INTRODUCTION

Rayleigh-Bénard convection consists of a fluid (^{4}He in the present work) in a closed cell of height h, submitted to a vertical density gradient destabilizing the fluid in the gravity field g. By heating the isothermal bottom surface with a power per unit area q and by cooling the top one at the same rate, a temperature difference along the cell, ΔT, sets up and induces the vertical density gradient. The experimental set up is described in the following paragraph. As mentionned above the Rayleigh number is the main dimensionless control parameter ($Ra = gh^3\alpha\Delta T/\nu\kappa$, α is the He thermal expansivity, ν the kinematic viscosity and κ the thermal diffusivity). An other dimensionless control parameter which may play a role is the Prandtl number ($Pr = \nu/\kappa$), only fluid dependent.

In relation with these numbers, the heat transfer or the Nusselt number ($Nu = qh/(\lambda\Delta T)$, λ is the He thermal conductivity), a characteristic Reynolds number of the convective flow in the central region ($Re = vh/\nu$ where v is a characteristic velocity of He flow) and the friction coefficient on the cell walls have been studied. The results are presented in the third paragraph.

2 EXPERIMENTAL SET UP (2)

2.1 Calorimetric measurements

He in the gaseous phase at low temperature (from 2 K to 8 K) and near its critical point (T_c{EIT90} = 5.1953 K, P_c = 2.275 bars) is mostly used as the working one phase fluid. Thanks to its particular properties it allows to obtain a large Ra range (more than 11 decades) and the highest Ra in a laboratory experiment (up to 2 10^{14} under Boussinesq conditions). Indeed as the critical point is approached He exibits increasingly low values of molecular transport coefficients especially the thermal diffusivity (down to 0 theorically); as a result Ra grows up. Pr may also increases from its value of 0.7 far from the critical point. It must be emphasised that He is a well documented fluid in these pressure and temperature ranges (3).

He is closed in a cylindrical cell of 20 cm height and 10 cm diameter (see fig. 1). Vertical walls are made of a 0.8 mm thin stainless tube allowing a reduced heat leak through (the corresponding thermal conductance is 250 μW/K at 4 K which is worth half the He gas one at rest). Copper plates ensure isothermal conditions at each end of the cylinder. The overall heating power applied by Joule effect on the bottom plate of about 80 cm^2 surface area, ranges from 100 nW up to 1 W measured with a 0.2% precision. The cooling at the top plate is allowed by the liquid He bath surrounding the whole apparatus, through the copper rod. Heat leak through the space between the bottom plate and the calorimeter is prevented by high vacuum (about 10^{-6} torr); the corresponding thermal conductance is about 0.8 μW/K. The induced ΔT along the cell is measured by a 20 μK resolution thermocouple from 1 mK up to 2.5 K with a 1% uncertainty.

By comparison with previous works using He (3) the main originalities of our work are :

— the use of the neighbourhood of the critical point to obtain the highest Ra values.

— the ΔT measurement by a thermocouple instead of two thermometers. Thanks to this accurate device, the thermal adiabatic gradient due to the hydrostatic pressure gradient along the cell height, has been observed and measured (0.4 mK for dilute He gas, 0.75 mK in the critical region).

The experimental procedure is as follows :

— The temperature of the whole appliance is lowered from the room temperature down to around 4 K where the appliance remains for a few months session. During the temperature decrease a high vacuum is obtained in the calorimeter firstly by pumping and then, after closing the

jacket at the nitrogen temperature by cryopumping. The calorimeter remains sealed for the entire session.

— The cell is filled up with different densities during the session. The He average density d runs from a few g/m^3 up to 135 kg/m^3 as well as close to the critical value : 69.6 kg/m^3. d is measured with a 0.7% precision.

— The mean absolute temperature T in the cell is fixed within a 0.1 mK stability and measured with a 2 mK absolute accuracy against the International Temperature Scale of 1990.

— For each fixed d and T, ΔT may vary from 1 mK up to 5 K by changing the heating power.

From the measurement of all the thermodynamical variables and the He properties fitting equations the dimensionless numbers are deduced, in particular Ra, Nu and Pr.

These accurate calorimetric measurements allow us to determine Nu with a 2 % uncertainty and Ra with a 5 % uncertainty far from the critical point. The uncertainties mainly come from the precision on the He properties calculated via T and d. They increase to ~ 5 % for Nu and ~ 10 % for Ra as He approaches the critical point. Pr uncertainty matches roughtly the Ra one.

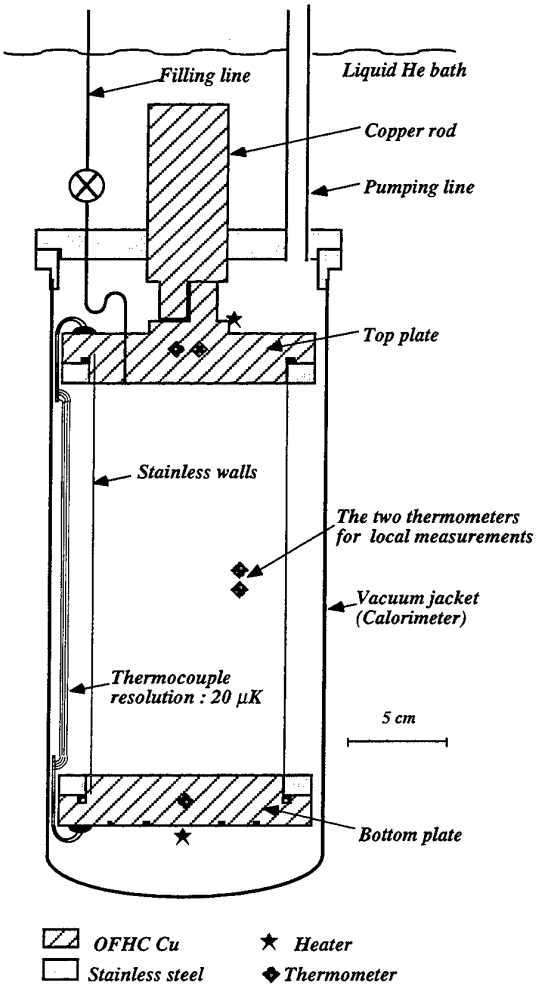

Figure 1 sketch of experimental set up

A few hundreds of points were performed; they are presented in the diagram of fig. 2.

2.2 Local measurements

Besides the calorimetric measurements some local temperature measurements were performed thanks to two semiconductor thermometers (4) of 200 μm size and 2 mm vertically apart, located in the cell at half height and half way between the centre and the wall. At each fixed experimental condition (and so Ra and Pr), temperature time series of 3 million points are recorded from each thermometer with a 14 bits accuracy. The acquisition and the data storage may take until a day in duration. About 35 records were carried out covering the Ra range from Ra = 10^7 up to Ra = 2 10^{14}.

3 RESULTS

Our study focuses on the convection at high Rayleigh numbers (from Ra = 2 10^7 up to Ra = 2 10^{14}.). Two kinds of studies were performed (5) :

- from the calorimetric measurements and the physical quantities relevant for convection, the characteristic dimensionless numbers of the convection are calculated : Ra, Nu, Pr. Experimental points are plotted on the NuRa diagram (fig. 2 at the paper end).

- from the two local detectors the cross spectrum of the two time series is calculated. The phase evidences a characteristic time related to the time lag of thermal coherent structures between the thermometers. Hence a velocity v of the flow in the cell is deduced and accordingly a characteristic Reynolds number, Re.

3.1 Results about Nu

With the same cell and by changing only the He density the Nu Ra curve (fig. 2) runs from the conductive regime (Nu equals 1 by definition) up to Nu ≈ 5000 at Ra ≈ 2 10^{14} (under Boussinesq conditions). Below Ra ≈ 2 10^7 and above the convective threshold the fluid motions undergo different convective stages from laminar and regular roll to fully turbulent flows far from the walls. Transition between these stages are reflected on the Nu Ra curve (6). Above Ra ≈ 2 10^7 a new behaviour settles.

On the Nu Ra diagram is superimposed a theoretical 2/7 power law which fits well the experimental points from Ra ≈ 2 10^7 up to about Ra ≈ 10^{11}. This behaviour has been already noticed in previous works (for instance (6)) but does not match the theorical predictions (1) which support a one third law in this Ra range.

The most striking feature is the departure above Ra ~10^{11} from this 2/7 regime. This departure had never been observed before. The new trend is characterized by a more efficient heat transfer. Indeed a power law may fit the new regime of the NuRa points with a 0.38 exponent from Ra ≈ 3 10^{11} up to Ra ≈ 9 10^{13}.

On the fig. 2, the experimental uncertainties are roughly half the symbol size. So the points scattering corresponds to a real effect of convection : the Nu dependence on Pr. Indeed Pr does not remain constant above Ra ≈ 10^{10}. Pr values as high as 30 have been

reached in our experimental limit. As a consequence special care must be taken into account when studying the Nu Ra curve. Thus the 0.38 exponent of the new regime power law was determined at nearly constant Pr fixed at 2.5. Likewise it must be emphasized that the transition from the 2/7 regime occurs also with liquid He (135 kg/m^3) where Pr remains fixed at 0.7 up to Ra $\approx$ 6 10^{12}. As a counterpart this experimental phenomenon allows us to study the Pr influence for the high Pr values. In the ultimate regime a weak increase of Nu with Pr is noticed (about 20% as Pr rises by a factor 5).

3.2 Results about local measurements

3.2.1 Determination of a characteristic Re

On fig. 3 (corresponding to Re = 10^{12} and Pr = 0.6) is shown the characteristic feature of the cross correlation spectrum phase between temperature signals, obtained from the two close detectors inside the cell ; the phase turns by 180° from 0° as the frequency is increased. The frequency for which phase passes 90° determines a characteristic time ; it corresponds to the characteristic time lag for a coherent thermal structure to go from one detector to another. Using the distance between the two detectors (2.3 mm) we get a characteristic velocity of He flow in the cell. With the height h and the viscosiy ν a characteristic Reynolds number is built up.

3.2.2 Results about Re

With Re, deduced from local measurements, the flow behaviour can be studied in relation with Ra like for the heat transfer. On fig. 4, the Reynolds number is plotted versus Ra from Ra = 10^7 up to Ra = 2 10^{14}. Pr is taken into account by assuming a power law. Its exponent is empirically determined by reducing the points scattering. On the diagram, the points are well fitted by a power law over the entire range : no change is noticed around Ra = 10^{11}. That means the flow in the central region of the cell, since detectors are located in this area, does not experiment noticeable modification and can not explain the Nu Ra curve behaviour.

3.2.3 Results on the wall friction coefficient

The behaviour of the flow near the wall can be studied with help of the quantity Cf = NuRa/Re^{3}Pr^2. NuRa corresponds rigourously to the adimensionned viscous dissipation over the cell volume ; assuming that the dissipation in the central region, due to the friction between the thermal coherent stuctures, is negligible, Cf is equal to the friction coefficient of the large scale flow over the cell walls. Cf is plotted versus Ra on the fig. 2. Its behaviour looks like closely the friction coefficient of a extern flow over a smooth plate. The change in the curve for Re $\approx$ 10^4 can be interpretated as a laminar turbulent transition of the velocity boundary layer near the wall. This transition coincides with that observed in the Nu versus Ra curve at Ra $\approx$ 10^{11}. The laminar boudary layer would correspond to the 2/7 regime while the turbulent boundary layer matches the new regime. Pr influence here is not noticeable.

3.2.4 Prandtl dependence

Following Kraichnan (1), assuming a passive convective heat transport across the turbulent boundary layer, the Nusselt and Reynolds numbers are related to the friction velocity Reynolds number Re* through (7):

$$Re \propto Re^* \ln Re^*$$

and $$PrRe^*/Nu \propto (\ln Re^* + f(Pr)).$$

Figure 6 shows the observed dependence of PrRe*/Nu versus Pr, suggesting that the right hand side of the above relation is dominated by the second term. A power law fit gives an exponent 0.41 close to but lower than the 0.5 proposed by Kraichnan. Anyway it should indicate that the thermal boundary layer is inside the velocity one.

4 CONCLUSION

The new regime we observe above Ra $\approx$ 10^{11} is then characterized by a more efficient heat transfer and by a viscous turbulent dissipation near the wall. These two features are characteristic of the ultimate regime of convection predicted by R. Kraichnan in1962 (1) ; in this theoretical regime the heat transfer near the wall, and so the whole transfer along the cell, is no longer controlled by diffusive transport but by large turbulent eddies coming from the buoyant convection.

Even if the transition happens for much lower values than thoses predicted by R. Kraichnan (Ra $\approx$ 10^{24}) we are confident for our observation of the ultimate regime. Thus one is able to predict situations corresponding at higer Ra values by extrapolation of the newly observed regime.

5 REFERENCES

(1) Kraichnan, R. H. "Turbulent thermal convection at arbitrary Prandtl number", Phys. Fluids, 5, 1374, (1962)

(2) Chavanne, X. Chillà, F. Chabaud, B. Castaing, B. Chaussy, J. and Hébral, B. "High Rayleigh number convection with gaseous helium at low temperature", J. Low Temp. Phys., 104, 109, (1996).
See also Chavanne, X. "Etude du régime turbulent en convection de Rayleigh-Bénard dans l'hélium liquide ou gazeux autour de 5 K", Ph.D. Thesis, Grenoble, (1997) (unpublished).

(3) Arp, V.P. and McCarty, R.D. "Thermophysical Properties of ^{4}He from 0.8 K to 1500 K with pressures up to 2000 MPa", Tech. Note 1334, NIST (1989)
See also Kierstead, H.A. "PVT surface of He^4 near its Critical Point" Phys. Rev., A7, 242, (1973).

(4) Heslot, F. Castaing, B. and Libchaber, A. Phys. Rev., A 36, 5810 (1987)

(5) Chavanne, X., Chillà, F., Castaing, B., Chabaud, B. and Chaussy J. "Observation of the ultimate regime in Rayleigh-Bénard convection", Phys. Rev. Letters, 79, 3648 (1997)

(6) Threlfall, D.C. "Free convection in low temperature gaseous helium", J. Fluid Mech., 67, 17, (1975)

(7) Landau, L, Lifchitz, E. "Mecanique des Fluides", t6, Physique Théorique, ed. Mir, 2ème édition (1989)

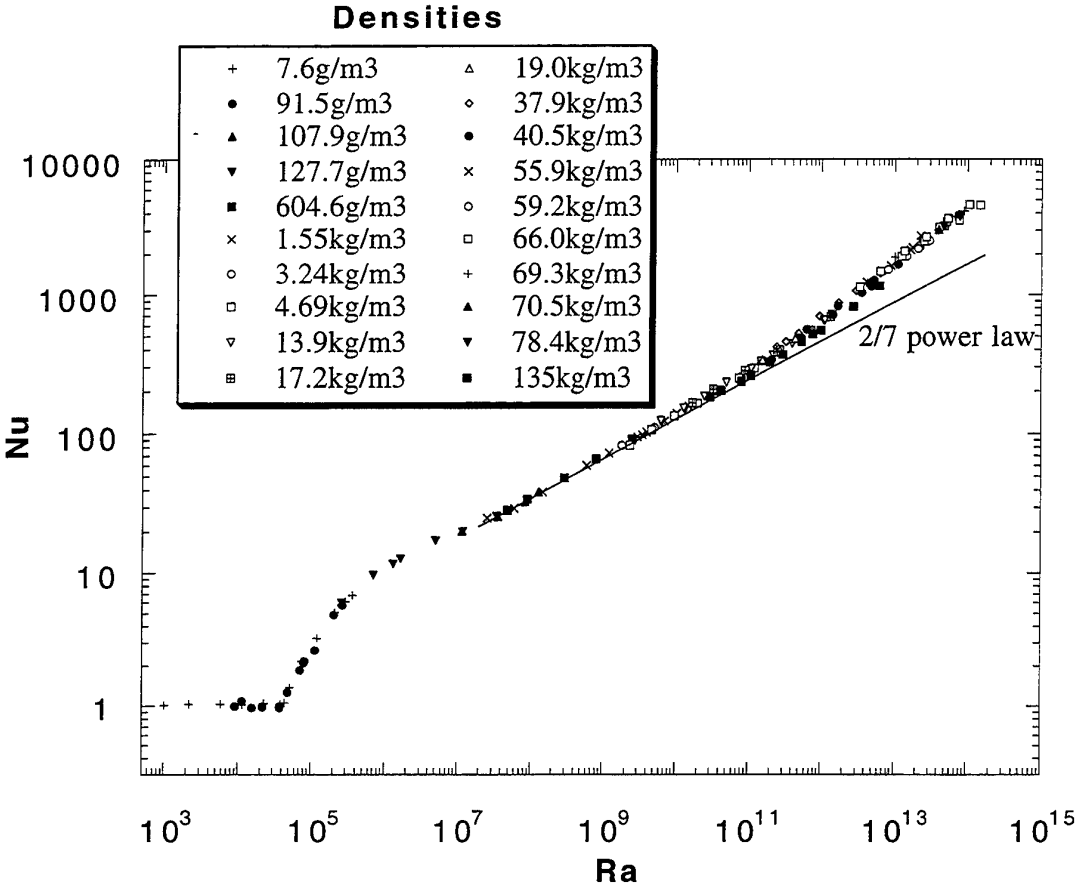

Figure 2 Nu Ra diagram with our experimental points

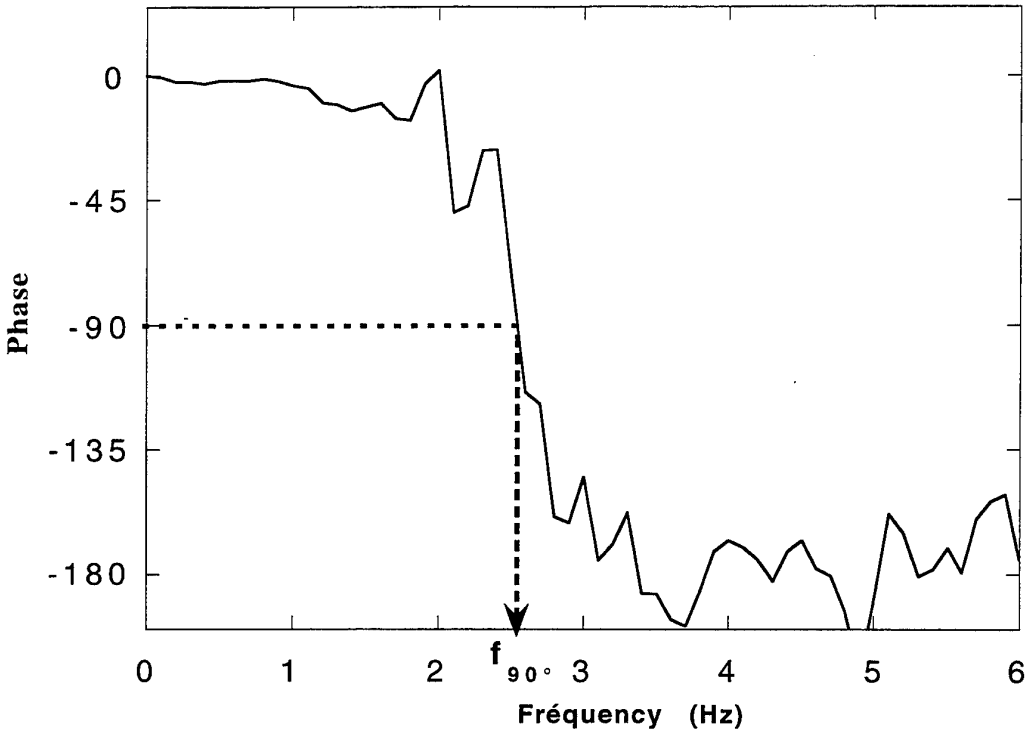

Figure 3 Phase of the cross correlation spectrum between the two thermometers signals.

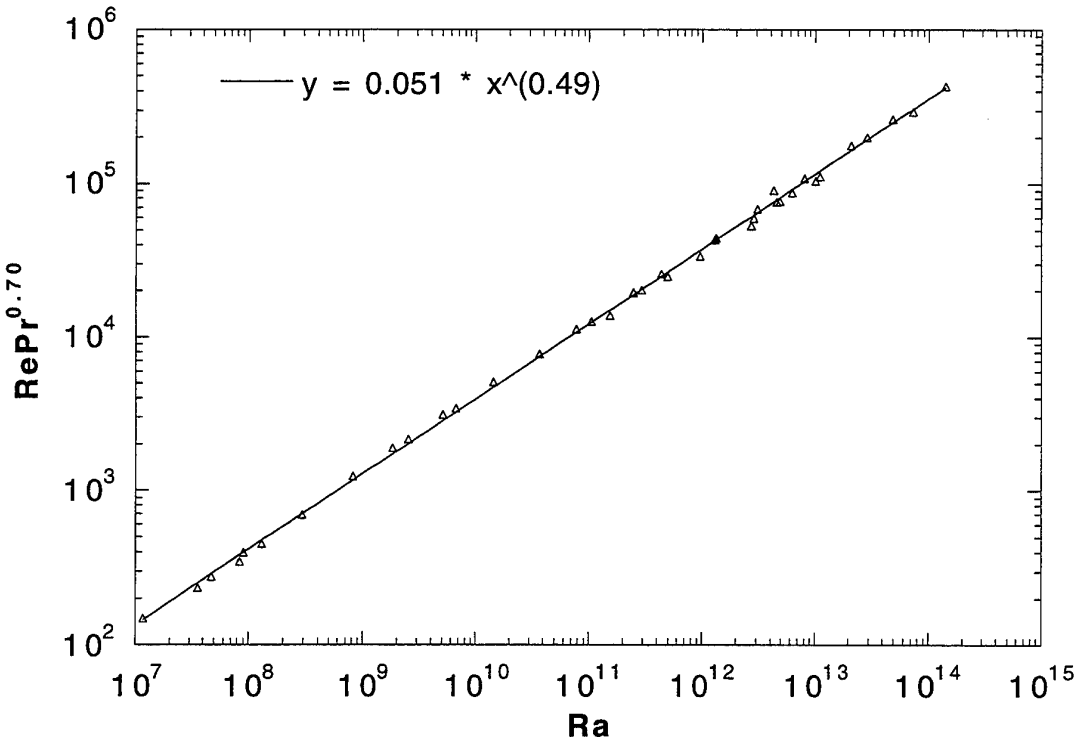

Figure 4 $RePr^{0.70}$ versus Ra. The Pr exponent is obtained by reducing the points scattering.

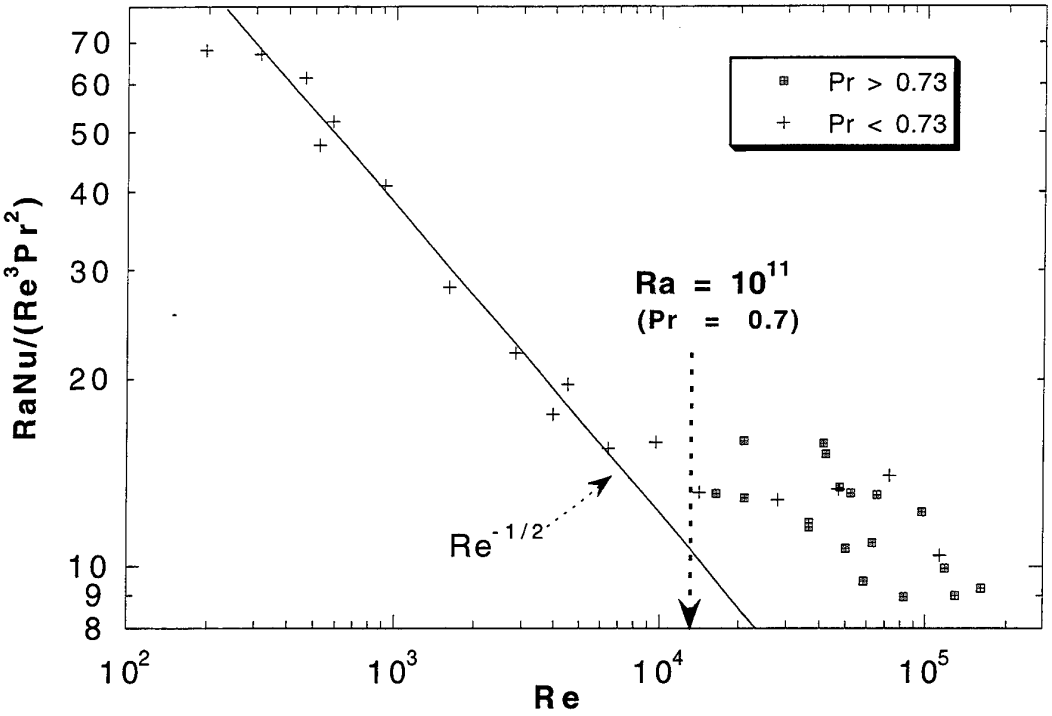

Figure 5 NuRa/(Re^3Pr^2) versus Re for experimental points under the Boussinesq conditions.

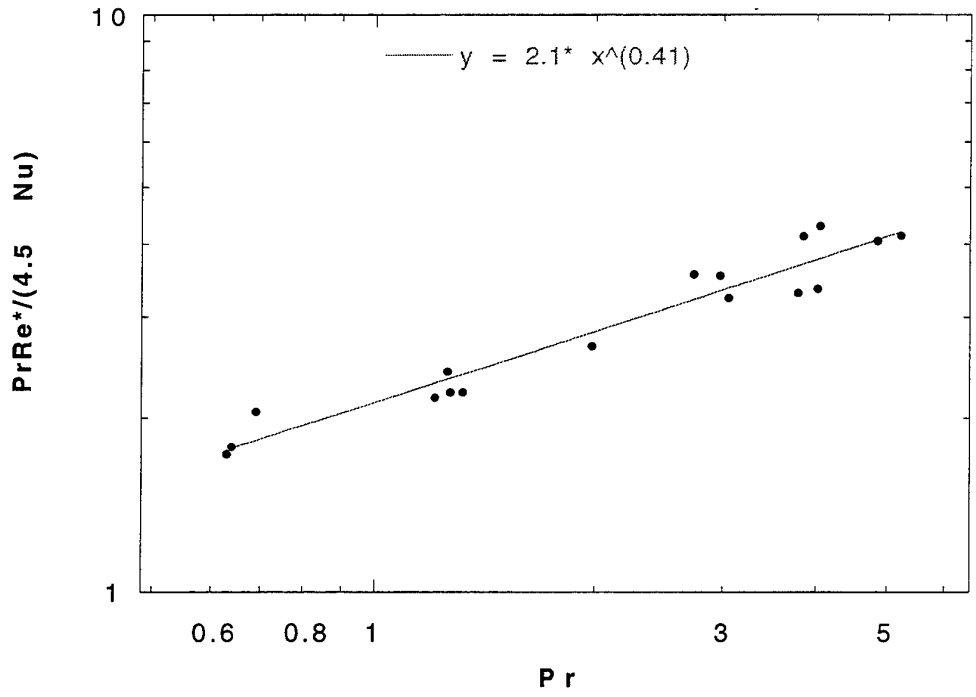

Figure 6 PrRe*/(4.5Na) versus Pr for Re > 30000.

TRANSIENT ANALYSIS OF RAYLEIGH-BÉNARD CONVECTION OVER FLAT AND WAVY WALLS WITH A RANS MODEL

S. Kenjereš and K. Hanjalić

Faculty of Applied Physics, Delft University of Technology
Lorentzweg 1., P.O. Box 5046, 2600 GA, Delft, The Netherlands

Abstract

Rayleigh-Bénard (RB) convection at high Rayleigh numbers with a plane and wavy bottom wall was studied by Transient Reynolds-Averaged-Navier-Stokes (TRANS) approach. The aim of the study was to assess the RANS in reproducing coherent structure and large-scale unsteadiness in buoyancy-driven turbulent flows, which are commonly regarded as intractable to single-point closures. The method can be regarded as a hybrid of the Large Eddy Simulation (LES) and the standard RANS, ('Very Large Eddy Simulation', VLES). Based on experimental and DNS evidence that RB convection consists of large amplitude cellular motion and turbulent fluctuations of much smaller scales, the instantaneous flow properties are decomposed into time-mean, periodic and random (triple decomposition). A conventional single-point closure (here an algebraic low-Re-number $k-\varepsilon-\overline{\theta^2}$ stress/flux model), used for the unresolved motion, reproduces well the near-wall turbulent heat flux and wall heat transfer. The large scale motion, believed to be the major mode of heat and momentum transfer in the bulk central region, is fully resolved by time solutions. In contrast to LES, the contribution of both modes to the turbulent fluctuations are of the same order of magnitude. In the horizontal wall boundary layers the model accounts almost fully for the turbulence statistics, with a marginal contribution of resolved scales. The approach was assessed by comparison with the Direct Numerical Simulations (DNS) and experimental data using several criteria: visual observation of the large structure morphology, different structure identification techniques, and long-term averaged mean flow and turbulence properties. A visible similarity with large structures in DNS was observed. The mean flow variables, second-moments and wall heat transfer show good agreement with most DNS and experimental results for different flow cases considered.

1. Introduction

Experiments and Direct Numerical Simulations (DNS) show that Rayleigh-Bénard convection is characterised by large-scale coherent vortical structure. Its origin is in plumes and thermals that rise from the outer edge of the boundary layer at heated surface (updrafts) and sink downward from the upper cold boundary (downdrafts). This large cellular structure (convection cells), found also in other convective layers heated from below, is regarded as the major heat and momentum carrier both in laminar and turbulent flows in the bulk of the central region. The rise and detachment of plumes (as well as their impingement on the opposing surface) cause horizontal motion in the wall boundary layer, e.g. experiments of Chu and Goldstein (6), DNS of Cortese and Balachandar (8). This motion is ultimately responsible for the wall heat transfer, as well as for the buoyancy, Siggia(28). The latter, in turn, sustains the small-scale buoyant updraft at the edge of the boundary layer, which coalesce into large scale plumes. The morphology of this large structure differs in laminar and turbulent regimes and, particularly in the latter case, depends on the Rayleigh number (Ra). In laminar regime the cells have a regular pattern with fixed locations of thermal release. This regularity disappears with an increase in Ra number when the large structure becomes unsteady and more disorderly, with more persistent horizontal movement. An interesting question (particularly for statistical modelling) is whether this structure in turbulent regime can still be regarded as a form of mean motion (with inherent unsteadiness), or it evolves at certain Ra number fully into turbulence (smooth spectrum and PDF) while retaining some coherence related to the flow geometry, (vertical dimension) and boundary conditions. Both, the experiments and DNS indicate that despite disorder, large coherent structure can be identified even at very high Ra numbers. Recent DNS by Kerr (18) in the range of Ra numbers close to hard turbulence regime ($Ra \leq 2\times10^7$) show that the large structure governs the apparent chaotic behaviour of turbulent RB convection. Beyond this value of Ra number DNS are not available and very little is known about the structure. Regularity and periodicity (except for fundamental mode with wave length associated with the flow height) have not yet been detected with any certainty. However, several sets of DNS results for low and moderate Ra numbers throw more light on the morphology of RB convection. For example, Cortese and Balachandar (8) detected finger-like regions with intense spiralling updrafts extending in vertical direction. The origin of vorticity is regarded to be in horizontal flow induced by large scale motion towards irregularly spaced updrafts (or away from irregularly spaced stagnation points), which is tilted and stretched by buoyancy in vertical direction, producing spiral structures. Chu and Goldstein (6) found that the thermals are released at relatively fixed sites, but this was

probably due to a small aspect ratio, combined with a relatively low Ra number considered. Theertan and Arakeri (30) detected experimentally planform structure with line plumes in between which for Ra=10^6 to 10^7 travel almost the complete distance between the plates (in fact between the outer edges of boundary layers). Cortese and Balachadar (8) distinguish between the extensive plumes for lower Ra numbers and abruptly detached at higher Ra. Another evidence of distinct scales was found by Chu and Goldstein (6) when analysing the temperature fluctuation. They argued that the temperature fluctuation at moderate Ra numbers reaches its maximum at the edge of the boundary layer where the thermals are released. They also found that this fluctuation is characterised by the alternating periods of large-amplitudes thermal release and small amplitude fluctuation (attributed to turbulence). Both findings were later confirmed by DNS.

This brief qualitative overview provides a sufficient evidence of two distinct scales of motion: large amplitudes associated with plumes, thermals and convective cells, and the turbulence generated mainly in the wall boundary layer and carried away by the large scale structure. Whatever the nature of the large structure may be, it seems clear that its scale is well separated from the rest of turbulence, (which, depending on Ra number, may posses a complete spectrum of turbulence scales). This feature renders RB convection (and other turbulent flows with dominant large structure), suitable to single-point turbulence closures in unsteady (transient) computation. By fully resolving the large scale convective structure and associated momentum and heat transport (regarded as particularly difficult to model with single-point closures), a simple eddy-diffusivity- or algebraic closure can be used to model the unresolved motion. The only requirement is that the model is capable of reproducing well the near wall statistical properties, the wall shear and heat transfer. This is the main difference as compared with LES. The other difference is that the model accounts almost fully for the turbulence statistics in the near-wall region. This imposes a stricter requirement on the model of the unresolved motion as compared with a subgrid-scale model (SSG) in LES. However, a number of such models have been shown to satisfy these requirements, at least in simple wall parallel buoyancy driven flows. TRANS brings also a substantial computational advantage. The time step can be larger, allowing implicit time marching, the numerical mesh away from a solid boundary does not need to be very fine, and a good statistics can be obtained with a relatively small number of realisations. The problem of defining inflow conditions at open boundaries is less restrictive. The method can be applied for much higher Ra numbers than it is possible with LES and can, therefore, be used for computation of complex flows of practical relevance.

This paper presents some results of application of the TRANS approach with an algebraic turbulence closure model to the computation of RB convection with a plane and a wavy bottom wall at high Ra numbers. The turbulence model includes the low-Re-number and wall proximity effects allowing integration up to the wall. The computed wall heat transfer, mean flow properties and second-moments are compared with available experimental data, DNS, as well as with results of two-dimensional steady RANS calculations. The transient realisations are analysed using the criteria from the critical point theory for the identification of the coherent structure, its spatial organisation and its role in RB convection at high Rayleigh numbers.

2. Governing equations, model and numerical method

The momentum and energy equation for the instantaneous motion can be written as

$$\frac{\partial \hat{U}_i}{\partial t} = \frac{\partial}{\partial x_j}\left(\nu\frac{\partial \hat{U}_i}{\partial x_j} - \hat{U}_i\hat{U}_j\right) + \beta g_i(\hat{T} - T_{ref}) \quad (1)$$

$$\frac{\partial \hat{T}}{\partial t} = \frac{\partial}{\partial x_j}\left(\alpha\frac{\partial \hat{T}}{\partial x_j} - \hat{T}\hat{U}_j\right) \quad (2)$$

By decomposing any instantaneous fluid property at a point $\hat{\Phi}(x_i,t)$ into time-mean $\overline{\Phi}(x_i)$, periodic $\tilde{\Phi}(x_i,t)$ and random $\phi(x_i,t)$, i.e.

$$\hat{\Phi}(x_i,t) = \overline{\Phi}(x_i) + \tilde{\Phi}(x_i,t) + \phi(x_i,t)$$

and performing a long-term time averaging at a point in space, with the assumption that due to a large spectral gap in between, the periodic and random motion are not directly interacting, the long-term averaged energy equation reduces to

$$\frac{\partial}{\partial x_j}\left(\alpha\frac{\partial \overline{T}}{\partial x_j} - \overline{TU_j} - \overline{\tilde{T}\tilde{U}_j} - \overline{\theta u_j}\right) = 0 \quad (3)$$

The first three terms are supplied from TRANS and the last term from the single-point model. Further averaging over homogeneous (horizontal) planes yields the expression for the total heat flux in vertical direction (z)

$$\alpha\frac{\partial \overline{T}}{\partial z} - \overline{\tilde{T}\tilde{W}} - \overline{\theta w} = \frac{q_w}{\rho c_p} = const \quad (4)$$

The contribution of the unresolved motion to the heat flux $-\overline{\theta u_j}$ is modelled by a 'reduced' algebraic flux/stress model, Dol *et al.*(9), derived from the modelled differential transport equation for $\overline{\theta u_i}$ by assuming weak equilibrium but retaining all major flux production terms:

$$\overline{\theta u_i} = -C\frac{k}{\varepsilon}\left(\overline{u_i u_j}\frac{\partial T}{\partial x_j} + \xi\overline{\theta u_j}\frac{\partial U_i}{\partial x_j} + \eta\beta g_i\overline{\theta^2}\right) \quad (5)$$

The stresses are also supplied from similar algebraic truncation of the full transport equations. The algebraic expressions are closed by solving the transport equations (modified for low-Re-number and near-wall effects) for the turbulence kinetic energy k, its dissipation rate ε and for temperature variance $\overline{\theta^2}$, resulting in a three-equation model k–ε–$\overline{\theta^2}$. This model was earlier applied to steady

RANS computation of a variety of buoyancy driven flows and was found to reproduce well the major mean flow properties, turbulent and wall heat flux in most of the cases considered, Hanjalić (14), Kenjereš and Hanjalić (20), Dol *et al.*(9). It is noted, that the second moment statistics is obtained as a sum of resolved and unresolved (modelled) contributions, as follows from the long-term averaging i.e. for variables Φ and Ψ

$$\overline{\hat{\Phi}\hat{\Psi}} - \overline{\Phi}\,\overline{\Psi} = \overline{\tilde{\Phi}\tilde{\Psi}} + \overline{\phi\psi} \qquad (6)$$

Unlike in LES, both contributions are usually of the same order of magnitude and close to a wall the unresolved part is often larger, as is the case of the turbulent heat flux and temperature variance (see later).

Numerical simulation were performed by a fully vectorised version of finite volume Navier-Stokes solver for three-dimensional flows in structured non-orthogonal geometries, with Cartesian vector and tensor components and collocated variable arrangement. The SIMPLE algorithm was used for the treatment of the pressure-velocity coupling. The second order accurate central difference scheme (CDS) was applied for discretisation of diffusive terms and second order linear-upwind scheme (LUDS) for convective terms. The time marching is performed by fully implicit second order three-time-level method which allows larger time steps to be used, in view of the fact that only large scales are being resolved. Typical computations covered 150−300 nondimensionall time units $\tau^*=\tau\sqrt{\beta g \Delta T H}/H$ which correspond roughly to 10−20 convective time scales based on convective velocity and characteristic cell circumference, Kerr (18).

3. Long-term averaged properties

In order to compare the adopted approach with DNS and LES data and with results of the earlier steady 2D RANS computations, a series of time-dependent simulations of Rayleigh-Bénard convection were performed. Considered were two different configurations and two values of Ra number: (a) the case with a horizontal flat wall at Ra=10^7, for which two different aspect ratios were considered (4:4:1 and 8:8:1) with the grid of 62^3 and $122^2\times62$ CV respectively, and Ra=10^9 with (4:4:1 aspect ratio and grid size of 82^3 CV), and (b) the case with a wavy horizontal wall, with the wavelength λ=H and the wave amplitude δ=$0.1H$ with aspect ratio (4:4:1), (grid size 102×82^3 CV), Fig. 1.

For the lower Rayleigh number considered the configurations were chosen to correspond closely to those for which DNS were previously performed by Grötzbach (12), Cortese and Balachandar (8), Wörner (31), Kerr (18). The LES reported by Eidson (10) and Wong and Lilly (32) were also performed for similar situations and Ra numbers. The larger value of Ra number (10^9) was chosen in order to demonstrate applicability of TRANS in range of high Ra numbers where the application of DNS techniques will require an enormous amount of computational resources, as shown by Grötzbach (13) and Kerr (18). On the other hand, the configuration with a wavy horizontal wall was performed to investigate effects of waviness on the spatial organisation of the large flow structure and heat transfer, as well as to demonstrate applicability of the method for flows in nonorthogonal geometries.

Integral heat transfer characteristics

The first steep in validation of the proposed turbulent closure model for thermal field is to make comparison of integral Nusselt number. We compare our results with several experimental, DNS and LES studies for different values of Ra number. First, the performance of 3D TRANS was compared with previously calculated 2D RANS results, which were performed for a wide range of Ra numbers from 10^6 up to 10^{12}, and for different aspect ratios, as well as different levels in modelling of the turbulent heat flux (20). As seen in Fig. 2a., the obtained values of Nusselt numbers are almost identical at Ra=10^7 and Ra=10^9.

Next we compared the 3D TRANS results in the range of low and moderate Ra numbers with the DNS results of Kerr (18) and with two different sets of LES, reported by Eidson (10) and Wong and Lilly (32). In addition, the experimental correlations proposed by Chu and Goldstein (1973) (6), Fitzjarrald (11), Threlfall (29) and Wu and Libchaber (33) are also plotted, Fig. 2a. The LES of Eidson (10) yielded the values of Nu=8, 9.5, 12.5, 13.8, 18 and 19 for Ra = 3.75×10^5, 6×10^5, 1.5×10^6, 2.5×10^6, 10^7 and 10^8 respectively, which are much different from DNS and experimental correlations. For lower Ra numbers up to 2.5×10^6, LES seriously over-predicts Nu number (by more than 40%). According to Eidson (10), this Ra value was the highest successfully simulated and for higher values of Ra number LES the results show a complete failure. It is interesting to note that Eidson (10) LES predictions at Ra=10^8 gave an almost identical value of Nu number as simulation performed by 2D RANS with a standard isotropic eddy diffusivity hypothesis, denoted in Fig. 2 as SGDH ('simple gradient diffusion hypothesis'). This model was found inadequate for modelling buoyancy driven flows because it presumes a full alignment between the components of the turbulent heat flux and mean temperature gradient, Ince and Launder (16), but also because it does not account for the direct buoyancy effects on the heat flux (the third term in eqn.(5), Hanjalić (14). This leads to a delayed effects of Ra number and produces laminarised solutions at relatively high Ra numbers. Not accounting for buoyancy can be the reason for the failure of LES too (which also seem to laminarise at the highest Ra considered ,10^7), because Eidson (10) used the simple Smagorinsky subgrid model, which is basically akin to the isotropic eddy diffusivity model in RANS. More recently Wong and Lilly (32) discussed the inclusion of the buoyancy effects into SGS model. They proposed a modification and performed LES with two slightly different dynamic SGS models, which resulted in a small difference. Un-

fortunately, they reported simulations for only one value of Ra=3.8×10^5. The computed Nu number for this Ra number was even higher than that of Eidson (10). Similar finding was also reported recently by Peng and Davidson (23) despite the modifications for buoyancy effects in their SGS. This consistent overprediction of Nu number by LES in comparison with Kerr (18) DNS data and experimental correlations show that despite the introduction of buoyancy effect into SGS, LES has difficulties in reproducing the near-wall and wall properties.

Mean temperature, its gradient and temperature variance

Computed long-term and spatially averaged mean temperature and temperature variance for various values of Ra are shown in Fig. 3 and Fig. 4 respectively. The 2D RANS profiles were obtained by cell averaging in order to omit effects of the side boundaries, while 3D TRANS and DNS profiles were obtained by spatial averaging over the entire horizontal planes. As seen in Fig. 3a., the agreement between calculated 3D TRANS and 2D RANS mean temperature profiles with DNS results is good over entire cavity height. Even in the near wall region, both simulations show a very good agreement with DNS results with somewhat better results obtained by 3D TRANS as the distance from the wall increases, Fig. 3b.

The mean temperature profile exhibits a characteristic behaviour with a very steep gradient in the near-wall region and almost isothermal core region. This behaviour of the mean temperature explains why a very fine grid resolution is needed for DNS at high Ra numbers, as argued by Grötzbach (13). On the other hand, the existence of almost isothermal core region clearly shows that simple gradient models for the turbulent heat flux are inappropriate for configurations with heating from below.

The temperature variance is much more difficult to reproduce than the mean temperature. With increasing Rayleigh number the peak moves from the centre closer to the wall indicating a thinning of the thermal boundary layer, Fig. 4. Note two contributions to the total variance (eqn. 6): $\overline{\tilde{T}^2} = \overline{\hat{T}^2} - \overline{T}^2$ from the large scales (full resolution) and from the model $\overline{\theta^2}$ of the unresolved motion (obtained from the transport equation for $\overline{\theta^2}$). The total variance is denoted in Fig. 4 by 'T' and the model contribution by 'M'. As seen, a good agreement is obtained in comparison with a DNS profile at Ra=10^7. The profiles of temperature variance obtained by 3D TRANS show an improvement in the prediction of the peak values in the near-wall region as well as in the central part of the cavity as compared with 2D RANS computations (for which only the modelled part is shown). Fig. 5 shows the two contributions to the turbulent heat flux and temperature variance (squared). As indicated in the introduction, both contributions are of the same order with the modelled one prevailing in the near-wall region. The sum of all three contributions to the total heat flux (eqn. 4), normalised with the wall heat flux, shows that the long-term averaged total heat flux is indeed constant over the entire channel cross-section as it should be, whereas most DNS and, in particular, LES show a substantial variation due to incomplete resolutions. A good modelling of the near wall heat flux and temperature variance is a prerequisite for accurate reproduction of the wall Nu number, which agrees well with the available DNS and experimental correlations (Fig. 2a), as discussed earlier.

Mean temperature gradient in RB convection has been the subject of several studies, aimed at establishing power scaling laws in different regions. Despite substantial experimental and DNS evidence, the power law at high Ra numbers is still very controversial. Two different laws were proposed based on theoretical and similarity considerations. Based on the assumption that only relevant length scale is the actual distance from the wall, Priestley (25) stated that the vertical gradient of the mean temperature obeys a $-4/3$ law. In contrast, Malkus (21) argued that the thermal boundary layer thickness is the characteristic length scale. Together with the assumption that the non-dimensional heat flux is a linear function of this length scale, Malkus arrived to a -2 law. It is interesting to note that most experimental studies confirmed the existence of -2 power law and only a few suggest a possibility of $-4/3$ slope. Adrian *et al.* (1) proposed and experimentally verified a unified multi-layer theory which actually includes both previously mentioned power laws. They also argued that two main reason were responsible for failure in observing of a $-4/3$ law in previously performed experimental studies: the measurements have been made in a range which was not far enough from the wall, or the Ra was not large enough. Of course, numerical simulations can provide a detailed insights in the behaviour of the mean temperature gradient. Unfortunately, the high Ra number range is far beyond the DNS limits (up to 2×10^7 in 1998) so that DNS at present can not provide possible clarification. Contrary to current DNS limitations, TRANS technique can be easily extended to much higher Ra, (Ra=10^{12} was easily computed), with only a moderate computational costs. To demonstrate that, the calculations at $Ra = 10^9$ as a representative of high Ra number range were performed, Fig. 2b. It is interesting to note that both 2D RANS and 3D TRANS equipped with AFM model correctly reproduce the mean temperature gradients which are in excellent agreement with the physical model of Adrian (1) and Chung *et al.* (7). Three distinctive power regions are very well reproduced: a conductive region with a constant mean temperature gradient for $0 \leq z^* \leq 1$, a transitional region with a -2 law up to $z^* \approx 5$ and, finally, a convective region which obeys a $-4/3$ power law for $z^* > 5$.

4. Identification of large structures

The process of visualisation and interpretation of the physical characteristics of three-dimensional unsteady velocity and vorticity fields and their dynamical evolution are still a challenge mainly because of their vectorial character. The most common approach in the representa-

tion of the salient features of three-dimensional unsteady fields is to "freeze" time instantaneous fields and to apply the classical methods for steady-state regimes and plotting velocity vectors, streamlines and contours of specific scalar quantities like temperature, turbulent kinetic energy, temperature variance etc. The RB convection at higher values of Rayleigh numbers is particularly challenging problem because we do not know exactly what general pattern of the flow can we expect. Besides there are still many controversial explanations about the structure of the flow.

The most common definition of coherent structures is associated with vortical motion. However, different possibilities for identification of vortex cores as representatives of a vortical motion have been proposed as well as the definitions of a vortex. The most frequently cited definition in literature is one proposed by Robinson (26): "A vortex exists when instantaneous streamlines mapped onto a plane normal to the vortex core exhibit a roughly circular or spiral pattern, when viewed from a reference frame moving with the centre of the vortex core". But the streamlines representation of velocity fields requires a significant amount of CPU time for their calculations and very often the final output can not bring a clear picture of the flow, especially in complex situations. The clarity can be improved by plotting two-dimensional streamlines projections onto a characteristic planes but problem of high computational costs still remains. In order to avoid extensive calculations, the introduction of some representative scalar quantities is needed. Robinson (26) proposed low-pressure regions as regions which are expected to correspond well to the vortex cores. By analysing the late stage of transition in a channel flow, Sandham and Kleiser (27) confirmed that the same method represents well coherent structures. Kasagi *et al.* (19), adopted the same approach in analysing their DNS database of the channel flow by plotting the instantaneous vectors in various sections and found that many of low-pressure regions correspond to the rotational fluid motions. But low-pressure regions can misrepresent the vortex core due to non-local character of the pressure which may have a larger scale than the vortex core, as shown by Joeng and Hussain (17). The next scalar parameter which has been often used for the identification of the flow topology is the modulus of vorticity: $|\omega_i| = |\varepsilon_{ijk}\partial U_j/\partial x_k|$. This approach was successful in free-shear flows, Joeng and Hussain (17), but problems persists in the near-wall regions where the vorticity magnitude shows a maximum value (regions where maximal velocity gradients naturally occur). However, the high vorticity in the near wall region originates from shear and not from a swirling or rotational motion. This leads to a conclusion that $|\omega_i|$ is not a suitable parameter for vortex identification in RB convection.

A method of critical points (defined as positions where the streamlines slope is indeterminate and the velocity is zero) was introduced in Pery and Chong (24) in order to assess the flow pattern at each point of the flow. According to this theory, the eigenvectors and eigenvalues of the mean velocity gradient tensor (A_{ij}=$\partial U_i/\partial x_j$) evaluated at a critical point define the flow pattern. The eigenvalues and eigenvectors of the velocity gradient tensor (A_{ij}) are obtained by solving the characteristic equation, $\lambda^3 - I_1\lambda^2 + I_2\lambda - I_3 = 0$, where:

$$I_1 = \frac{\partial U_i}{\partial x_i},\ I_2 = -\frac{1}{2}\frac{\partial U_i}{\partial x_j}\frac{\partial U_j}{\partial x_i}, I_3 = Det(A_{ij}) \quad (7)$$

are three invariants of (A_{ij}) and for incompressible flows I_1=0.

A definition of vortex core as a region with complex eigenvalues of (A_{ij}) was proposed in Chong *et al.* (4), implying that the local streamline pattern is closed or spiral in a reference frame moving with the point of interest. The discriminant of the characteristic equation can be written as:

$$\Delta = \left(\frac{1}{3}I_2\right)^3 + \left(\frac{1}{2}I_3\right)^2 \quad (8)$$

This determines the nature of the eigenvalues of A_{ij} as follows: Δ>0 gives one real and two conjugate-complex eigenvalues, Δ<0 gives three real distinct values and finally, Δ=0 gives three real values of which two are equal. A map of all possible solutions of characteristic equations can be created by plotting trajectories of constant discriminant Δ in I_2-I_3 plane. From the definition of the discriminant of the characteristic equation it follows that complex eigenvalues occurs when Δ>0. Recently, Chong *et al.* (5) applied their "Δ" approach to analyse structures of wall-bounded shear flows including the zero-pressure-gradient flow and the boundary layer with separation and reattachment. They found that a positive small value of the discriminant identifies very well vortical regions.

The definition of the eddy structure as the region with positive second invariant I_2 of the velocity gradient tensor A_{ij} was introduced in Hunt *et al.*(15) and Blackburm *et al.* (2). The second invariant I_2, (denoted in figures as Q in accord with notation of Hunt *et al.*, 15) can be interpreted as a measure of the relative importance of the shear strain S_{ij}=$0.5(\partial U_i/\partial x_j + \partial U_j/\partial x_i)$ and the rotation rate Ω_{ij}=$0.5(\partial U_i/\partial x_j - \partial U_j/\partial x_i)$. Where I_2 is positive, the rotational rate prevails over shear strain rate and where I_2 is negative, the reverse is true.

A kinematic vorticity number $\mathcal{N}_k$ was used in Melander and Hussain (22) as a measure of the quality of rotation, defined as:

$$\mathcal{N}_k = \left(\frac{|\omega_i|^2}{2S_{ij}S_{ij}}\right)^{1/2} \quad (9)$$

When $\mathcal{N}_k$=0, the irotational motion is present and in the case $\mathcal{N}_k$=∞, the motion has a character of a solid-body rotation. In the present identification of the large coherent structures in RB convection, we analyse in parallel one realisation of DNS and several realisations of TRANS, using three different criteria: Δ , I_2 and $\mathcal{N}_k$.

Low Ra number

The analysis of the flow structure for TRANS simulations at Ra=10^7 and a direct comparison with DNS re-

sults of Wörner (31) for $Ra=6.3\times10^5$ will be performed first. In order to portray a dynamical behaviour of the flow, the characteristic time evolution of the maximum velocity components as well as the overall Nusselt number at the hot wall for two different aspect ratios are monitored, Fig. 6. Three characteristic time periods can be distinguish: conduction dominant period which takes place in the initial stage of heating, transitional period and fully turbulent convective period. The two different aspect ratios show very similar behaviour of the Nusselt numbers. The main difference is in the position where intensive heat transfer occurs, $\tau^*=110$ for [4:4:1] and $\tau^*=180$ for [8:8:1], where $\tau^*=\tau\sqrt{\beta g\Delta T H}/H$. As seen, the lower aspect ratio promotes turbulent regime earlier. In order to obtain a better insight in the flow structure and to compare how TRANS instantaneous fields correspond to Wörner's DNS data, the streamlines distribution in the central horizontal plane, $z^*=0.5$ and in three vertical planes, $y^*=0.15, 0.5, 0.85$ were plotted for one DNS realisation and for three instantaneous TRANS fields, Fig. 7. The streamlines are plotted by releasing 1500 massless particles from uniformly distributed origins over the sampling planes of the instantaneous fields, and their distributions were calculated by applying second order Runge-Kutta time advection method. Although the streamline pictures portray very complex flow, three main distinctive regimes can be easily observed: the regions with strong and well defined plane circulation (roll structure), the regions with one-dimensional movements (dark lines) and divergent stagnation regions (unstable focus points). As seen, DNS and TRANS results show qualitatively very similar patterns. The only difference is in the size of the rolls - DNS shows smaller roll patterns but this is to expect due to smaller value of Ra number. Another reason is that the TRANS can *per se* capture only the very large structure while the smaller ones are filtered out. In order to demonstrate further the similarity between the hydrodynamic fields and to illustrate that this pattern similarity extends also to the thermal field, the isosurfaces of the temperature, coloured with the vertical velocity component, are show in Fig. 8. The visualised fields show a network of polygonal cell type structures with line plumes in between. These plumes are actually main carriers of the realised heat, and plume locations correspond to those where the local Nusselt numbers reach their maximum values. The plumes move randomly and interacts with each other causing a strong vertical motion. Again, very similar pictures were obtained for DNS and TRANS results, except for a difference in scales. The identical scenario of planform structures have been observed in experimental studies of Theertan and Arakeri (30).

In order to provide a further analysis of the spatial organisation of the flow, various vortex identification techniques were applied in parallel for DNS and TRANS results. The second invariants of the velocity gradient tensor (I_2=Q) were calculated and presented in Fig. 10. By taking different positive values of I_2, regions with different vortical intensities can be easily filtered out. With decreasing values of I_2, the vortical eddy population becomes more dense. In parallel to I_2, the Δ approach was applied to the same dataset. Very similar structures were captured with both methods. The same identification techniques were applied for instantaneous TRANS results. As seen, many of the characteristic vortical-eddy shapes observed in DNS field are recognised in TRANS results too.

High Ra number

As in the previous low Ra case, the characteristic time evolution of the maximum velocity components as well as the overall Nusselt number at hot and cold wall are monitored, Fig. 11. After initial period of time ($0<\tau^*<40$) the flow starts to exhibit a convection dominated regime, characterised by a dramatic increase of all velocity components and, consequently, by very intensive heat transfer ($40<\tau^*<70$). At the end of this period, two different values of the temperature isosurfaces are plotted ($T_1^*=0.565$ and $T_2^*=0.435$, $T^*=T/\Delta T$) in order to present structure of the thermal boundary layers with characteristic peaks, Fig. 9. The existence of a similar structure has been confirmed in DNS by Grötzbach (12) and Kerr (18). The streamlines distribution show very intensive motion over entire flow domain. The spatial distributions of the second invariant of the velocity gradient tensor (I_2) are evaluated and presented in order to portray organised structures in the flow. By means of the visual inspection of the streamlines and the corresponding distribution of I_2, it seems that I_2 approach captures well the regions where rotation is present. Very similar pictures are obtained by applying Δ and $\mathcal{N}_k$ criteria. After $\tau^*=80$, strong irregularly periodic oscillations of all maximum velocity components are still present, but the overall Nu numbers reaches almost a steady value (very low amplitude of oscillations). At $\tau^*=110$ the same properties are plotted again in order to compare with those at the lower time value. The number of peaks in the thermal structures is smaller than for the previous time instant, but the amplitude is higher (the peaks almost reach the opposite wall). The motion is very intensive but still shows well organised spatial regions of I_2. It is important to note that the number of the large coherent structures is lower than in previous case when very intensive process of the heat transfer occurs. This confirms the view that the major role of coherent structures is to promote and intensify mass and heat transfer.

A similar analysis is applied for the configuration with the horizontal wavy wall. The regular wall wave pattern imposes a dominant orientation in U and W velocity components. The V velocity component develops significantly slower in comparison with the other two, Fig. 12. The pronounced increase in heat transfer occurs much earlier than in the case with horizontal flat wall ($\tau^*=10-20$ instead of $\tau^*=40-60$). After this initial period of time, the distribution of the overall Nusselt number shows almost a steady value ($30<\tau^*<110$), then starts to increase again, but less dramatic than in the ini-

tial time period. The second increase in the heat transfer occurs at the time instant $\tau^* \approx 110$ when V velocity component reaches the same value as other two velocity components. This increase in V destroys the dominant two-dimensional orientation of the large structures and, consequently, produces a batter mixing and intensification of the heat transfer. This conclusion is confirmed by distributions of streamlines as well as the kinematic vorticity number at two different time steps, $\tau^*=70$ and $\tau^*=110$, Fig. 12. The two-dimensional orientation of both streamlines and $\mathcal{N}_k$ is clearly visible at the $\tau^*=70$. For $\tau^*=110$, the complete reorganisation of the flow takes place and, as a consequence, a much higher heat transfer occurs than in the case with the flat wall. Again, very similar distributions of the large coherent structures were obtained by applying other criteria, I_2 and Δ.

5. Conclusions

Numerical simulations of a stationary Rayleigh-Beńard convection with a conventional single-point turbulence closure demonstrate that the Reynolds-Averaged-Navier-Stokes method (RANS), applied in transient mode can well reproduce mean flow properties, wall heat transfer and second-moment turbulence statistics. Moreover, the computations capture the large scale structure in accord with DNS and experimental findings. The approach can be regarded as Very Large Eddy Simulations, with a single-point closure playing the role of a 'subgrid scale model'. In comparison with the conventional LES, the model of the unresolved motion (here an algebraic k–ε–$\overline{\theta^2}$ model) covers a much larger part of turbulence spectrum (in fact almost the complete turbulence, apart from the large coherent structure). This contribution becomes predominant in the near wall region. Because the adopted model of the unresolved motion was already tuned to reproduce near-wall flow properties for a variety of situations (though for near-equilibrium conditions), this model ensures good results also in the present transient RANS (TRANS) approach. The weaknesses of the conventional single-point model, particularly in regard to the convective transport by large structures (modelled usually as turbulent gradient diffusion) are removed by time and space resolution of the large structures. The computed mean temperature, its variance, turbulent heat flux and wall heat transfer for Rayleigh Bénard convection over a flat and wavy wall in a range of Rayleigh numbers ($10^6 - 10^9$) agree well with available DNS and experimental results. Application of several structure identification methods (second invariant of the velocity gradient tensor, discriminant of the characteristic equation, and kinematic vorticity number) to a parallel analysis of selected TRANS and DNS realisations show a close similarity of the spatial organisation and features of the large coherent structure. This is also confirmed by instantaneous trajectory visualisation.

Acknowledgements

Authors acknowledge fruitful discussions with Dr. Dominique Laurence from DER-LNH of the Electricite de France, during his stay at the Delft University of Technology as visiting scholar of the J.M. Burgerscentrum for Fluid Mechanics. Thanks are also due to Dr. G. Grötzbach and Dr. M. Wörner, Kernforschungszentrum Karlsruhe, Germany, for providing the DNS realisations. Supercomputing was provided by Stichting Academisch Rekencentrum Amsterdam (SARA), The Netherlands.

References

[1] ADRIAN, R. J., FERREIRA, R. T. D. S. AND BOBERG, T. ,1986. Turbulent thermal convection in wide horizontal fluid layers. *Experiments in Fluids*, Vol. 4, pp. 121–141

[2] BLACKBURN, H. M., MANSOUR, N. N. AND CANTWELL, B. J. ,1996. Topology of fine-scale motions in turbulent channel flow. *J. Fluid Mech.*, Vol. 310, pp. 269–292

[3] CASTAING, B. AND GUNARATNE, G. AND HESLOT, F. AND KADANOFF, L. AND LIBCHABER, A. AND THOMAE, S. AND WU, X. Z. AND ZALESKI, S. AND ZANETTI, G. ,1989. Scaling of hard thermal turbulence in Rayleigh-Bénard convection *J. Fluid Mech.*, Vol. 204, pp. 1–30

[4] CHONG, M. S., PERRY, A. E. AND CANTWELL, B. J. ,1990. A general classification of three-dimensional flow field. *Phys. Fluids, A*, Vol. 2, pp. 765.

[5] CHONG, M. S., SORIA, J., PERRY, A. E., CHACIN, J., CANTWELL, B. J. AND NA, Y. ,1998. Turbulence structures of wall-bounded shear flows using DNS data. *J. Fluid Mech.*, Vol. 357, pp. 225–247

[6] CHU, T. AND GOLDSTEIN, R. J.,1973. Turbulent natural convection in a horizontal layer of water. *J. Fluid Mech.*, Vol. 60, pp. 141–159

[7] CHUNG, M. K. AND YUN, H. C. AND ADRIAN, R. J. ,1992. Scale analysis and wall-layer model for the temperature profile in a turbulent thermal convection *Int. J. Heat Mass Transfer*, Vol. 35, No. 1, pp. 43–51

[8] CORTESE, T. AND BALACHANDAR, S., 1993. Vortical nature of thermal plumes in turbulent convection. *Phys. Fluids, A*, Vol. 5, No. 12, pp. 3226–3232

[9] DOL, H. S., HANJALIĆ, K. AND KENJEREŠ, S., 1997. A comparative assessment of the second-moment differential and algebraic models in turbulent natural convection. *Int. J. Heat and Fluid Flow*, Vol. 18, pp. 4–14

[10] EIDSON, T. M., 1985. Numerical simulation of the turbulent Rayleigh-Bénard problem using subgrid model. *J. Fluid Mech.*, Vol. 158, pp. 245–268

[11] FITZJARRALD, D. E. ,1976. An experimental study of turbulent convection in air. *J. Fluid Mech.*, Vol. 73, pp. 693–719

[12] GRÖTZBACH, G. ,1982. Direct numerical simulation of laminar and turbulent Bénard convection. *J. Fluid Mech.*, Vol. 119, pp. 27–53

[13] GRÖTZBACH, G. ,1983. Spatial resolution requirement for direct numerical simulation of Rayleigh-Bénard convection. *J. Comput. Phys.*, Vol. 49, pp. 241–264

[14] HANJALIĆ, K. ,1994. Achievements and limitations in modelling and computation of buoyant turbulent flows and heat transfer. *Proceedings of the 10th International Heat Transfer Conference*, Vol. 1, pp. 1–10

[15] HUNT, J. C. R., WRAY, A. A. AND MOIN, P. ,1988. Eddies, stream and convergence zones in turbulent flows. *Centre for Turbulence Research Report*, CTR-588, pp. 193

[16] INCE, N.Z. AND LAUNDER, B.E.,1989. On the computation of buoyancy-driven turbulent flows in rectangular enclosures *Int. J. Heat Fluid Flow*, Vol. 10, pp. 110–117

[17] JEONG, J. AND HUSSAIN F., 1995. On the identification of a vortex. *J. Fluid Mech.*, Vol. 285, pp. 69–94

[18] KERR, M. R. ,1996. Rayleigh number scaling in numerical convection. *J. Fluid Mech.*, Vol. 310, pp. 139-179

[19] KASAGI, N., SUMITANI, Y., SUZUKI, Y. AND ILIDA, O. ,1995. Kinematics of the quasi-coherent vortical structure in near-wall turbulence *Int. J. Heat and Fluid Flow*, Vol. 16, No. 1, pp. 1–10

[20] KENJEREŠ, S. AND HANJALIĆ, K. ,1995. On the prediction of thermal convection in horizontal slender enclosures *Proc. 10th Symp. Turbulent Shear Flows*, Pennsylvania State Univ., U.S.A.

[21] MALKUS, W. V. R. ,1954. The heat transport and spectrum of thermal turbulence. *Proc. Roy. Soc., London* , Vol. A, No. 225, pp. 195–212

[22] MELANDER, M. V. AND HUSSAIN, F. ,1992. Polarised vorticity dynamics on a vortex column. *Phys. Fluids, A*, Vol. 5

[23] PENG, S. H. AND DAVIDSON, L. ,1998. Comparison of Subgrid-Scale Models in LES for Turbulent Convection Flow with Heat Transfer *2nd EF Conference in Turbulent Heat Transfer*, Manchester, U.K.

[24] PERRY, A. E. AND CHONG, M. S. ,1987. A description of eddying motions and flow patterns using critical point concepts. *Ann. Rev. Fluid Mech.*, Vol. 19, pp. 125-155

[25] PRIESTLEY, C. H. ,1955. Convection from a large horizontal surface. *Aust. J. Phys.*, Vol. 7, pp. 176-198

[26] ROBINSON, S. K. ,1991. Coherent motions in the turbulent boundary layer. *Annu. Rev. Fluid Mech.*, Vol. 23, pp. 601–639

[27] SANDHAM, N. D. AND KLEISER, L. ,1992. The late stages of transition to turbulence in channel flow *J. Fluid Mech.*, Vol. 245, pp. 319–348

[28] SIGGIA E. D. ,1994. High Rayleigh number convection *Annu. Rev. Fluid Mech.*, Vol. 26, pp. 137–168

[29] THRELFALL, D. C. ,1975. Free convection in low-temperature gaseous helium *J. Fluid Mech.*, Vol. 67, pp. 17–28

[30] THEERTHAN, S. A. AND ARAKERI, J. H.,1997. Planform Structure of Turbulent Free Convection on Horizontal Surfaces *2nd Int. Symposium on Turbulence, Heat and Mass Transfer*, pp. 573–580

[31] WÖRNER, M. ,1994. Direkte Simulation turbulenter Rayleigh-Bénard Konvektion in flüssigem Natrium *Dissertation, Uni. of Karlsruhe*, KfK 5228, Kernforschungszentrum Karlsruhe

[32] WONG, V. C. AND LILLY, D. K. ,1994. A comparison of two dynamical subgrid closure methods for turbulent thermal convection *Phys. Fluids*, Vol. 6, No. 2, pp. 1016–1023

[33] WU, X. Z. AND LIBCHABER, A.,1992. Scaling relations in thermal turbulence: The aspect ratio dependence *Phys. Rev. A*, Vol. 45, No. 2, pp. 842–845

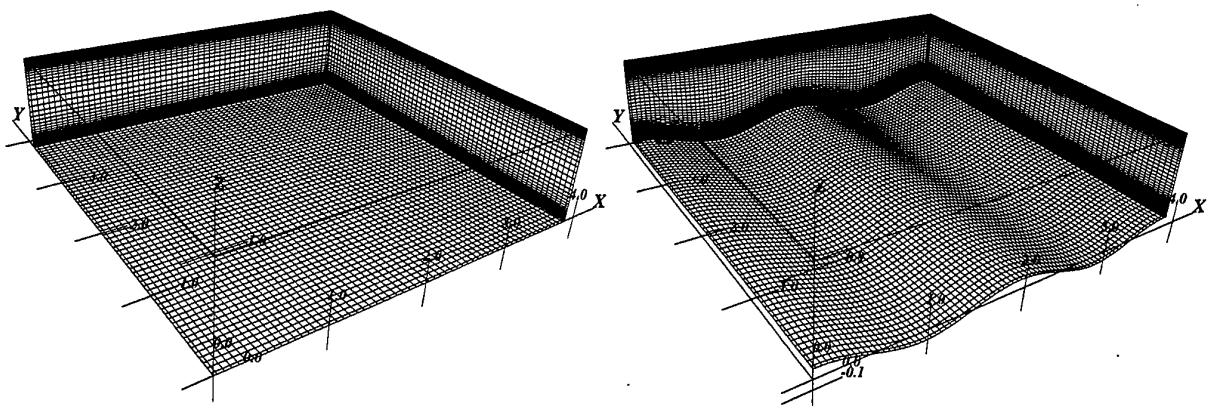

Figure 1: Grid distribution for considered test cases at Ra=10^9: (a.) horizontal flat wall, 80^3 CV; (b.) wavy horizontal wall, 100×80^2 CV, the wavelength λ=H, the wave amplitude δ=$0.1H$

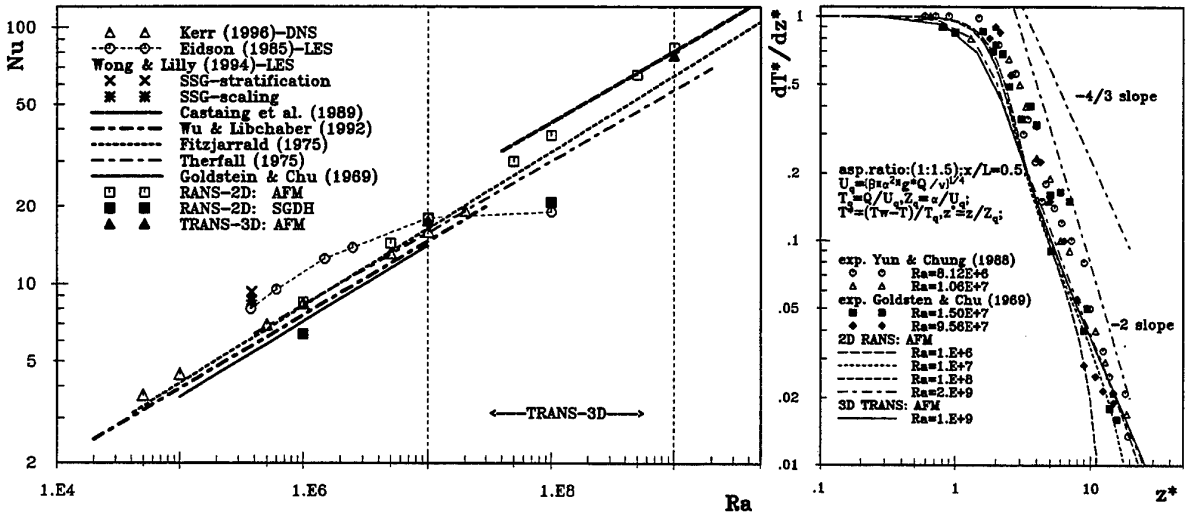

Figure 2: a.) Comparison of the calculated integral Nusselt numbers with experimental correlations, DNS and LES results; b.) Dimensionless mean temperature gradient;

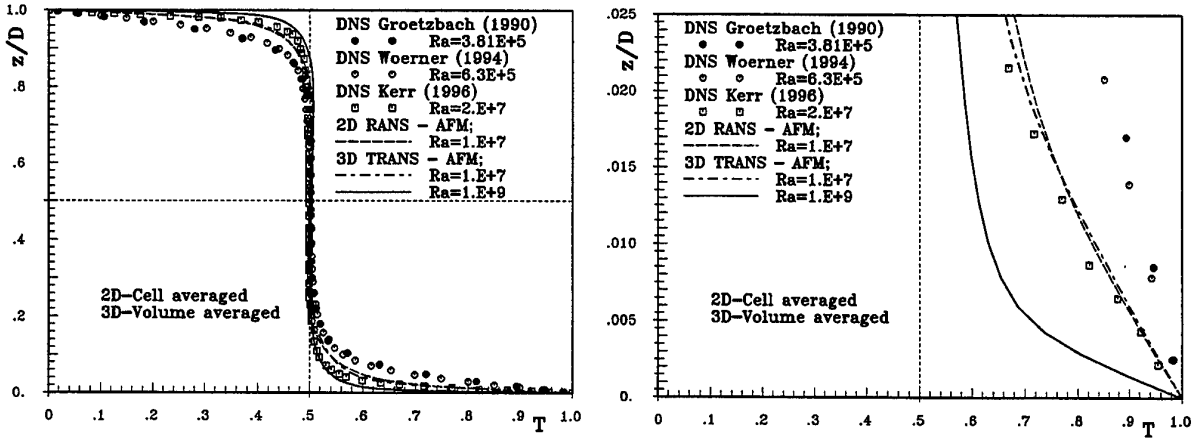

Figure 3: a.) Long-term averaged temperature distribution in RB convection for different Ra numbers; b.) Blow up close to the bottom wall;

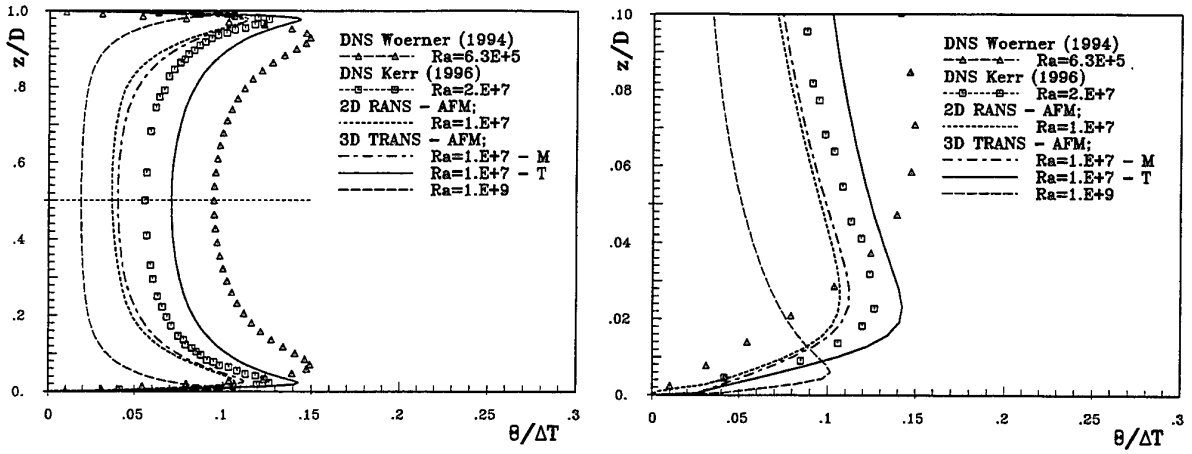

Figure 4: a.) Temperature variance profiles in RB convection for different values of Ra number: M-modelled, T-total; b.) Blow up close to the bottom wall

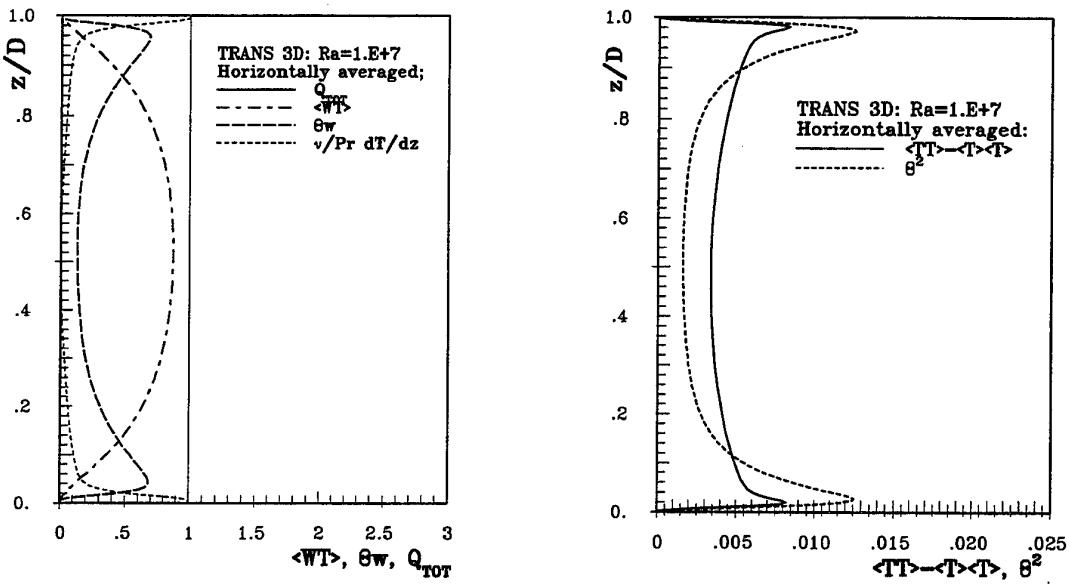

Figure 5: The modelled and resolved parts of: a.) vertical turbulent heat flux; b.) temperature variance

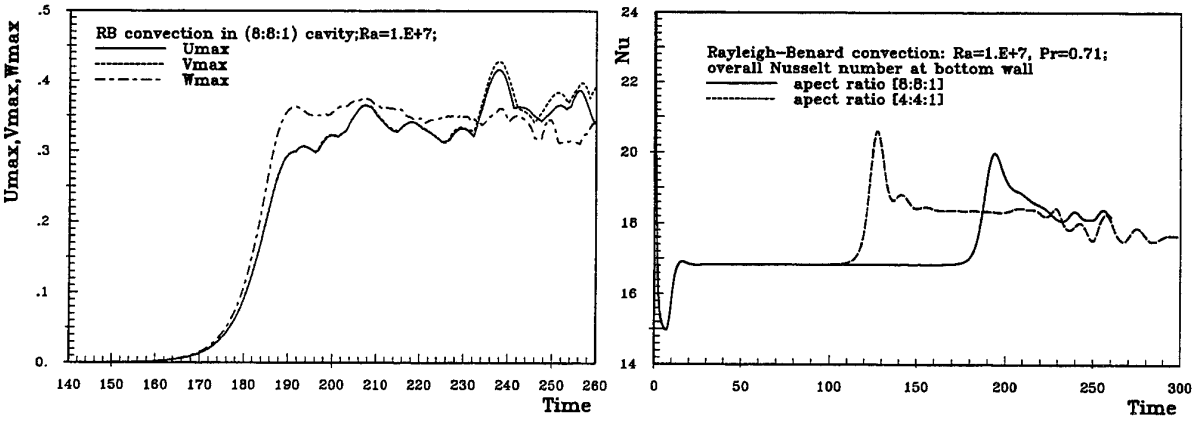

Figure 6: Time evolution of maximum velocity components and overall Nusselt numbers at bottom hot wall for two different aspect ratios, Ra=10^7

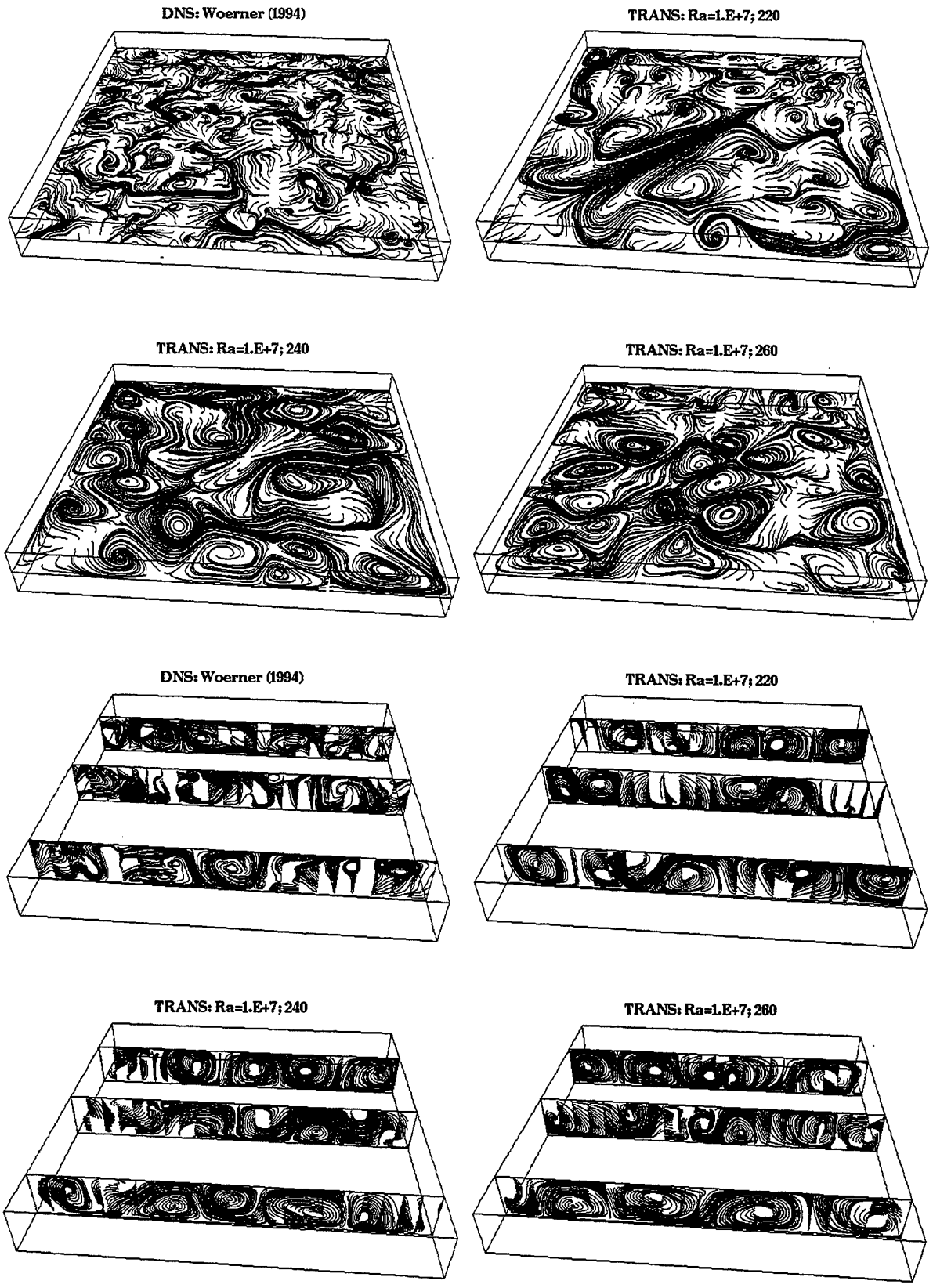

Figure 7: Instantaneous trajectories of massless particles in the central horizontal plane and on three vertical planes for one DNS realisation (Ra=6.5×10^5), and for three TRANS realisations (Ra=10^7)

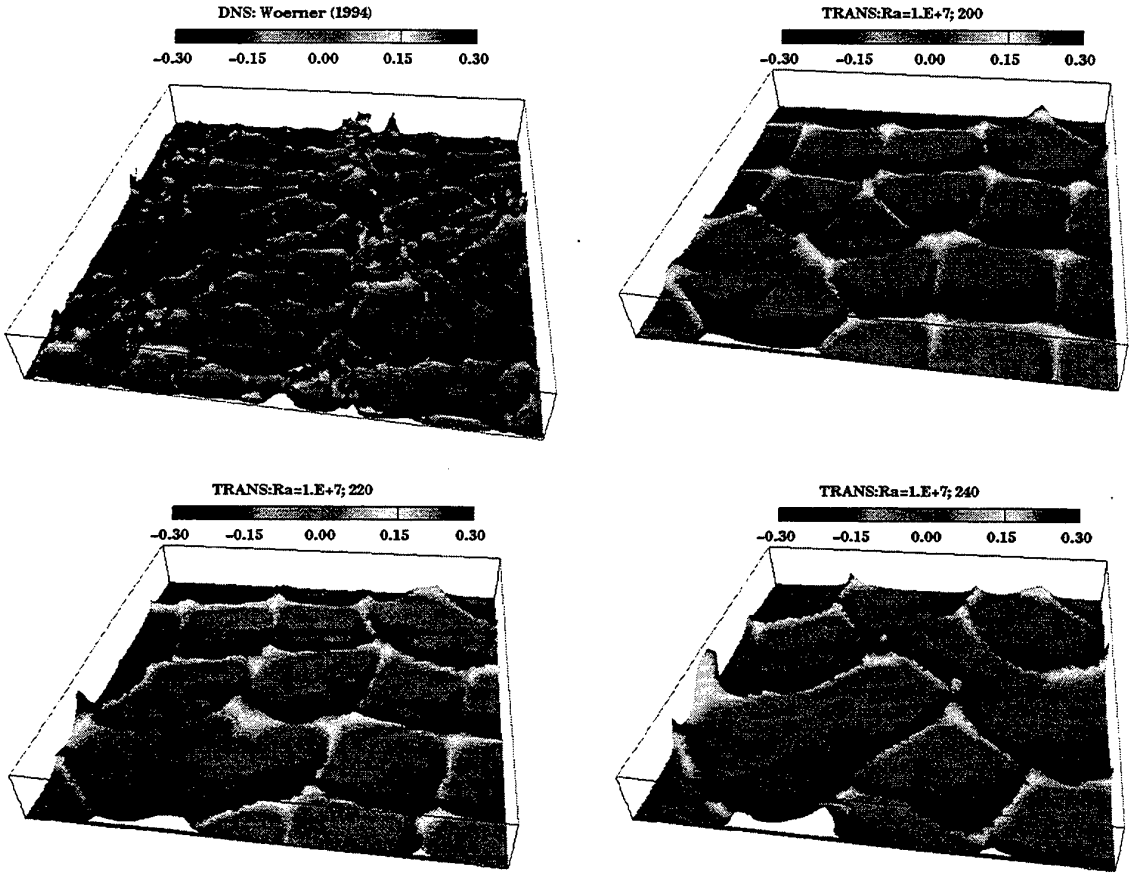

Figure 8: Planform structures with fingerlike plumes in between for one DNS realisation,(Wöerner,31, Ra=6.5×10^5) and for three TRANS realisations (Ra=10^7); Temperature isosurfaces coloured with intensity of vertical velocity

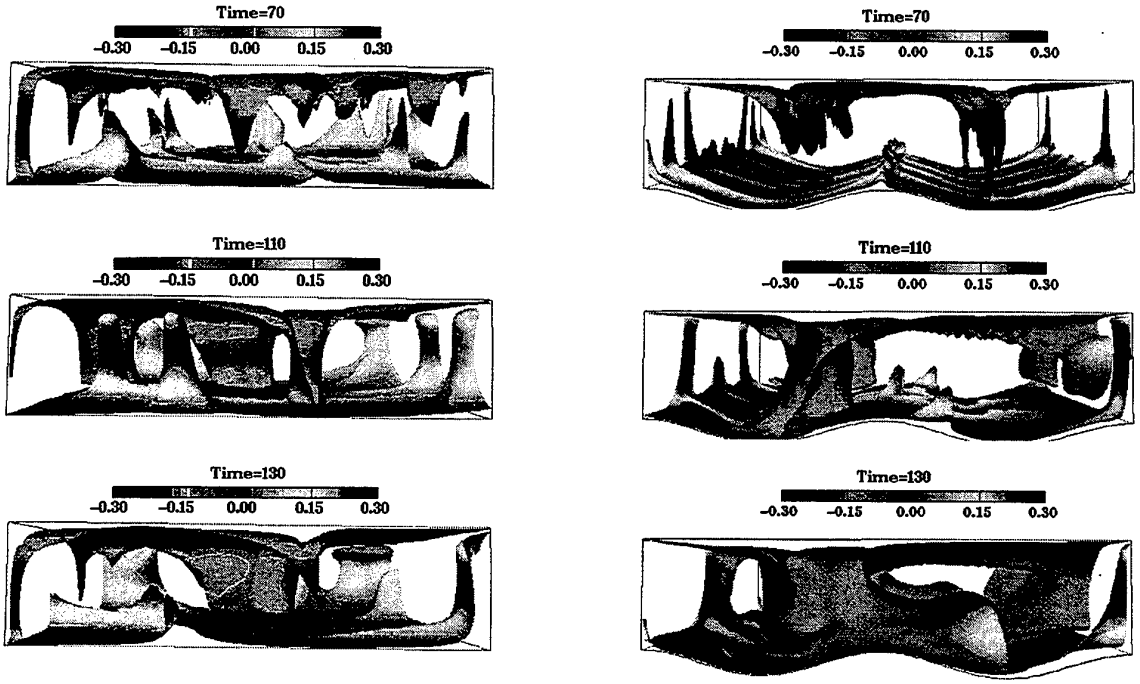

Figure 9: Side view of fingerlike plumes for flat and wavy wall, Ra=10^9; Temperature isosurface coloured with intensity of the vertical velocity

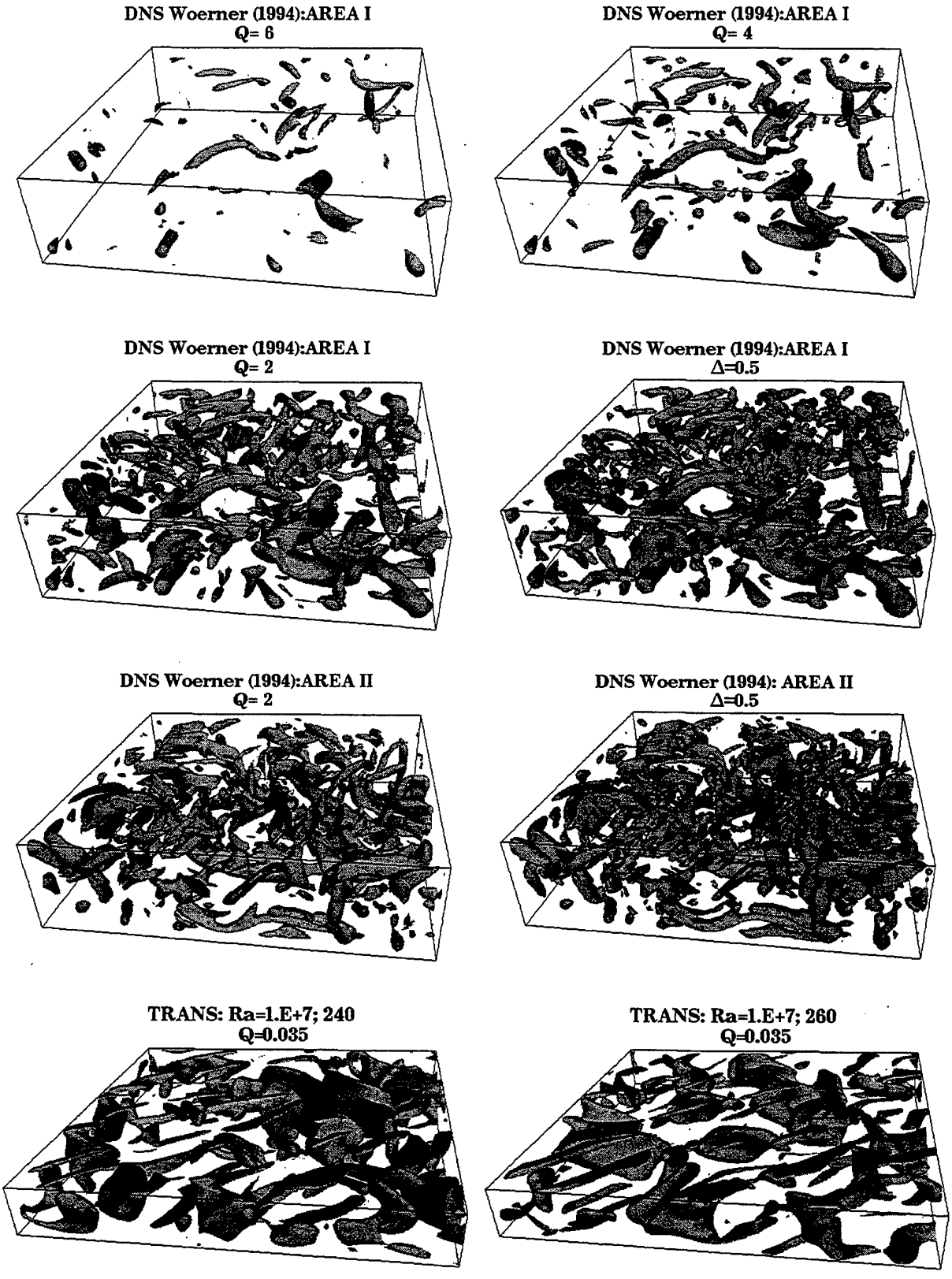

Figure 10: Comparison of vortical structures in DNS and TRANS for different values of the second invariant of the velocity gradient tensor (I_2=Q) and of discriminant of the characteristic equation (Δ)

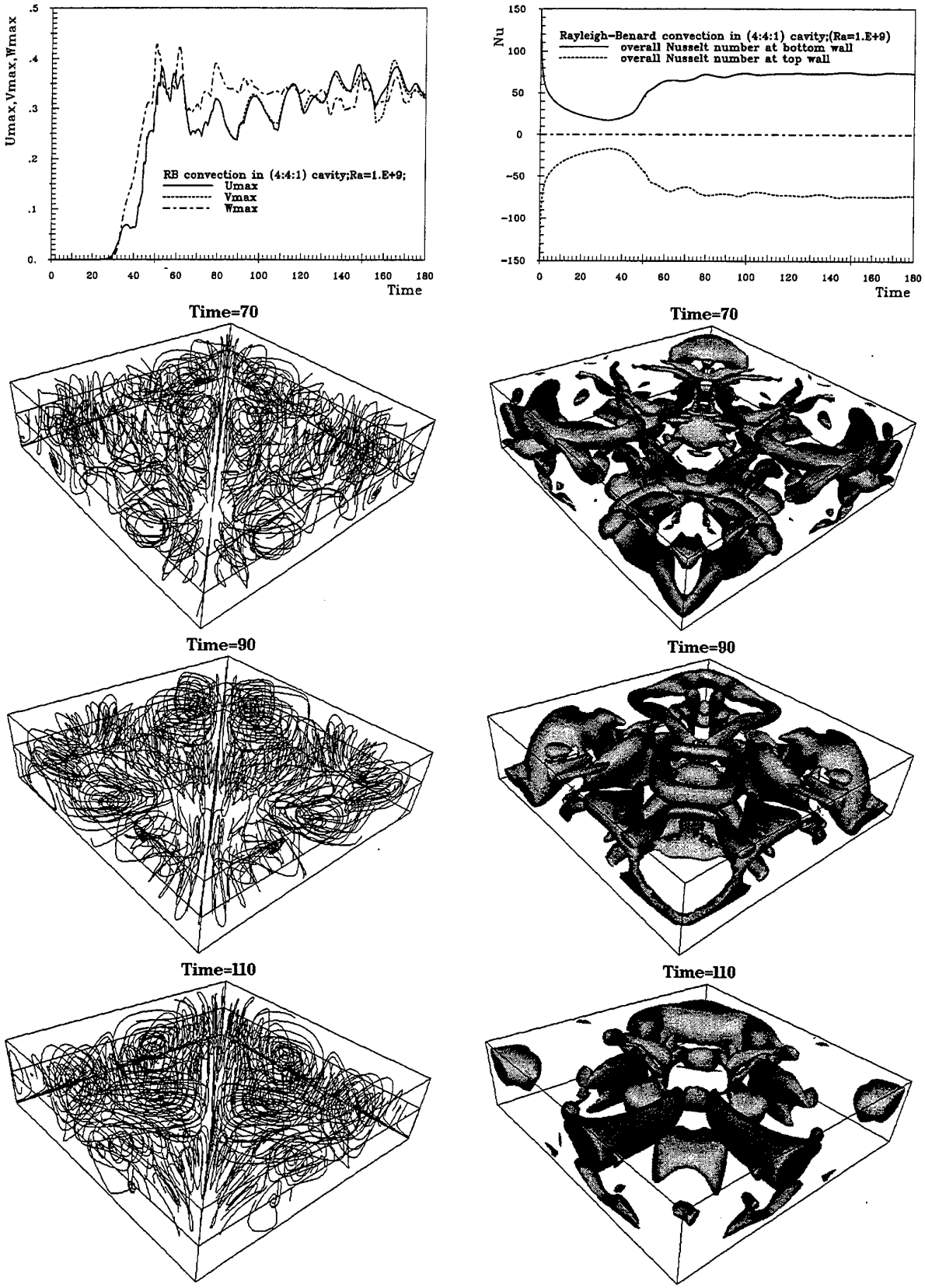

Figure 11: a.) Time evolution of the maximum velocity components; b.)Time evolution of integral surface Nu number; c.) Instantaneous streamlines and the second invariants of the velocity gradient tensor, I_2 for three TRANS realisations at Ra=10^9 for the flat wall

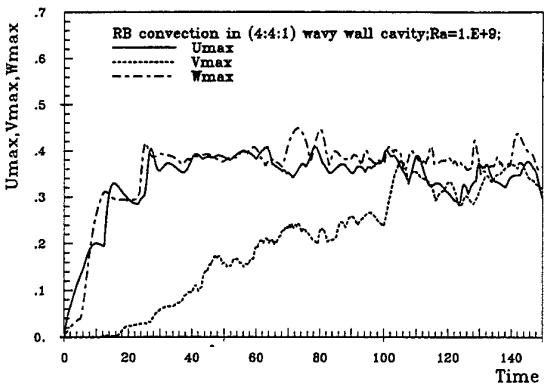

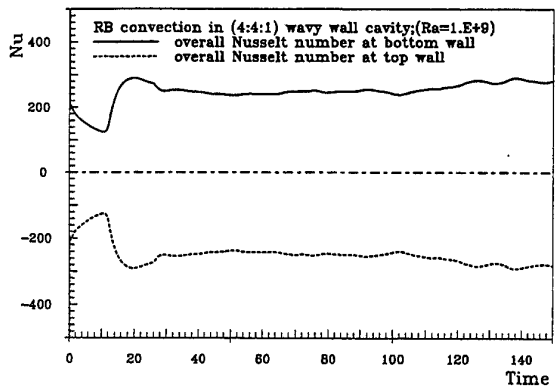

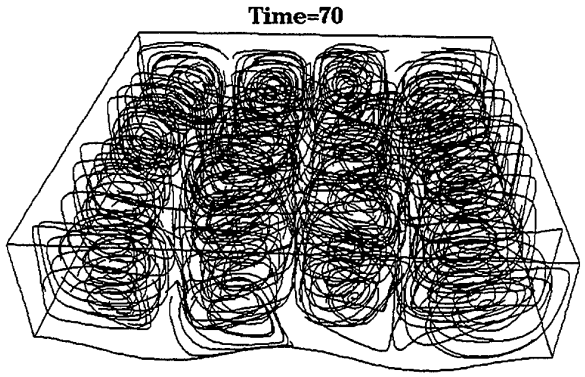

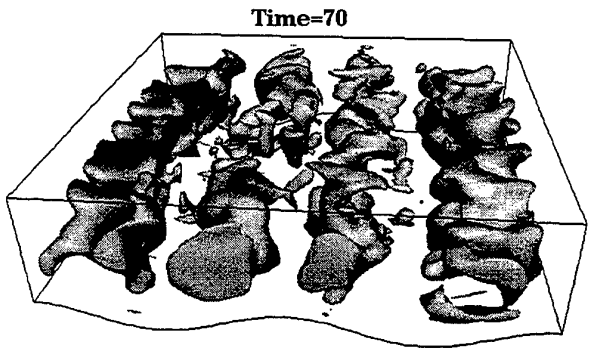

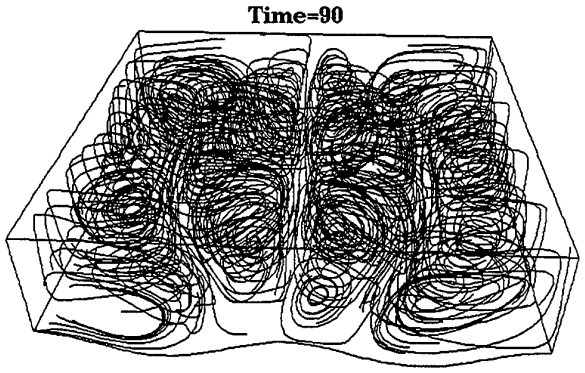

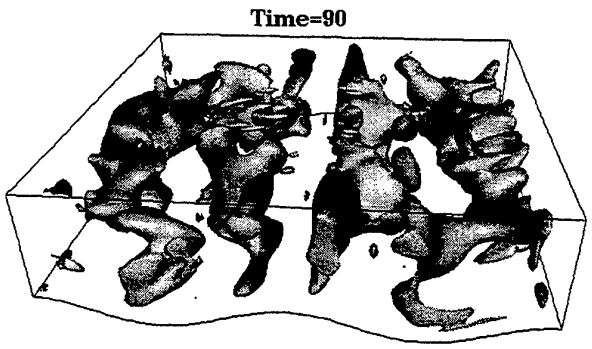

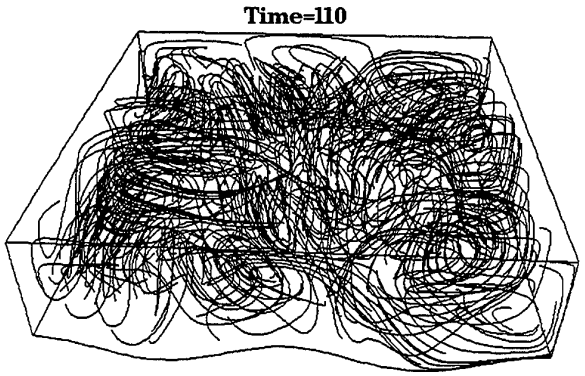

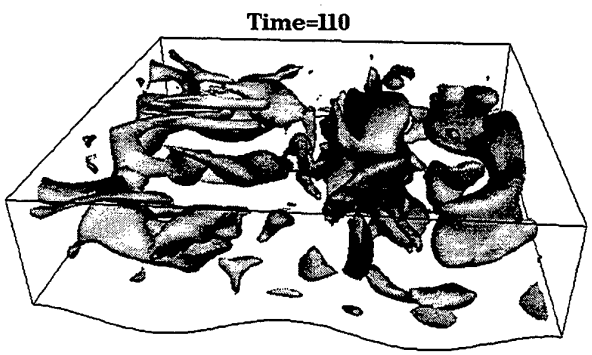

Figure 12: a.) Time evolution of the maximum velocity components; b.) Time evolution of integral surface Nu number; c.) Instantaneous streamlines and the second invariants of the velocity gradient tensor, I_2 for three TRANS realisations at Ra=10^9 for the wavy wall

COMPARISON OF SUBGRID-SCALE MODELS IN LES FOR TURBULENT CONVECTION FLOW WITH HEAT TRANSFER

Shia-Hui Peng* and Lars Davidson

Department of Thermo and Fluid Dynamics
Chalmers University of Technology
S-412 96 Gothenburg, Sweden

ABSTRACT

Dynamic subgrid-scale (SGS) modelling in LES for engineering flows usually uses Smagorinsky's eddy viscosity model as a basis, where the subgrid scaling is constructed by assuming a local equilibrium between the subgrid-scale turbulent shear production and dissipation rate. For turbulent thermal convection flows, an additional buoyant production term can also be included in this argument. The buoyant effect on the SGS eddy viscosity is then explicitly accommodated in the base model. This in turn forms the so-called *buoyancy SGS model*. With this model, a problem usually encountered when solving thermal convection flows is that non-real solutions may arise. To remedy this problem, a new SGS time scaling is proposed to re-construct the buoyancy eddy viscosity base model. In the modified model, the magnitude of the strain rate tensor is employed to weight the SGS time scaling in the base model including buoyancy effects. For thermally stratified flows, this approach also makes the base model be capable of accounting for some energy backscatter from subgrid scales to resolved large scales. The modified model was applied to a Rayleigh-Bénard convection flow, and compared with the scalar model and the buoyancy model. The results are found to be in good agreement with both DNS and experimental data.

1 INTRODUCTION

Computation of turbulent flows is complicated owing to the large range of scales that exists in these flows. Traditional Reynolds-averaging approaches (RANS), e.g., the two-equation models and the second-moment models, are not always satisfactory because the physics of the various scales that contribute to the correlation terms is different. On the other hand, direct numerical simulations (DNS) can as yet not handle high Reynolds-number turbulent flows owing to the limitation in computer capacity. In the past two decades, large eddy simulation (LES) has gained extensive attention for its higher physical ability to describe turbulence than RANS and lower computational cost than DNS.

The basic philosophy of LES is to explicitly resolve the large-scale motion and to model the small scales. To distinguish the small-scale eddies from resolved large scales, a spatial filtering process is usually applied to the Navier-Stokes equations. The resultant subgrid-scale stress tensor, which contains the information about the effect of smaller scales on the evolution of the larger scales, is presumed to be more universal in nature than the Reynolds-averaging stress tensor and thus more amenable to successful modelling. The SGS stresses can be modelled at different levels of complexity. The most widely used SGS model is the Smagorinsky model (1), where the SGS stress tensor is modelled in alignment with the local large-scale strain rate tensor through the eddy viscosity concept. After Smagorinsky's initial development, a number of SGS models has been proposed, examples of which are the vorticity model by Ferziger (2), the scale-similarity and mixed models by Bardina *et al.* (3) and the SGS model based on renormalization group theory by Yakhot *et al.* (4).

The existing conventional SGS model has been successfully applied to the LES of transitional and turbulent flows. Problems have also arisen in these applications, however. The most serious one is the *ad hoc* model constant, which varies within a large range for different flow problems. Other limitations of the Smagorinsky model and of its variants were pointed out in some recent articles, e.g., by Moin *et al.* (5). The dynamic SGS eddy viscosity model developed by Germano *et al.* (6, 7) overcomes most of the deficiencies in the Smagorinsky model. The dynamic approach allows the model coefficient to be a function of both space and time by extrapolating information from the smallest, resolved large-scale structure. In contrast to the absolutely dissipative behavior with the Smagorinsky model, dynamic models are able to render negative SGS eddy coefficient to account for energy backscatter from subgrid scales to resolved large scales, which has been shown to be an effective function in LES, particularly for transitional flows (8).

Effort has also been made in recent years to apply the dynamic SGS model to turbulent thermal convection flows. Using four different SGS eddy viscosity/diffusivity base models, Cabot (9) performed

*Also Department of Work Organization and Technology, National Institute for Working Life, S-171 84 Solna, Sweden.

LES for Rayleigh-Bénard convection flows and flows in an internally heated channel. It was found that, as compared with the buoyancy model for which the SGS Prandtl number, Pr_t, is iteratively determined, the Eidson model (10) promises better predictions and less computational effort by simply setting Pr_t as a constant. Wong and Lilly (11) compared two dynamic SGS models, i.e. the stratification formulation and the scaling formulation for the Rayleigh-Bénard convection at $Ra = 3.8 \times 10^5$. The stratification formulation includes a buoyancy term as in the Eidson model (10), but the SGS turbulent Prandtl number is dynamically computed. This model is thus the same as the buoyancy model in Ref. (9). Wong and Lilly also reported that the stratification formulation (i.e. the buoyancy model) is computationally inefficient due to iterative determination for Pr_t and that this formulation occasionally gives non-real solutions, as shown by Cabot (9). Recently, Bergstrom and Huang (12) applied a dynamic SGS model based on the scalar model (with no buoyancy-related term in the eddy viscosity/diffusivity formulation) to a buoyant cavity flow. A rather limited success in the prediction was reported. Other applications and developments of LES for handling turbulent buoyant flows have been made, e.g., by Wang and Pletcher (13) and Canuto *et al.* (14).

In our work on LES for buoyancy-driven convection flows, it has also been found that the buoyancy model, as used in Refs (9) and (11), sometimes induces non-real solutions. This problem may break down the computation unless some measures are taken, for example, by setting a zero SGS eddy viscosity as the SGS buoyancy production is negatively dominant over the SGS shear production. However, this approach may be inappropriate since a negative SGS eddy viscosity is thought to be physically reasonable in terms of accounting for energy backscatter that often occurs in non-laminar flow regions. In addition, the dynamic procedure might be preserved better without directly and artificially tuning the SGS eddy viscosity, which, instead, should be quantified by both the model coefficient and the SGS turbulent scaling. Peng and Davidson (15) recently proposed a new time scaling to re-construct the SGS buoyancy model in combination with the Smagorinsky model. This approach is able to overcome the problem of entailing non-real solutions in cases of existing stable and significant thermal stratification. In this work, the Smagorinsky model, the Eidson buoyancy model and the modified buoyancy model are applied to a turbulent Rayleigh-Bénard convection flow and compared with each other as well as with DNS and laboratory data.

2 THE SGS CLOSURE FORMULATION

In Large eddy simulation, a filter function is used to split the span of turbulence scales somewhere in the Kolmogorov equilibrium region. The filtered large scales are resolved. The subgrid-scale turbulence is assumed to be more isotropic in nature and is modelled by using the information from the smallest resolved large-scale eddies, requiring less adjustments than RANS approach. Applying the filtering process to the Navier-Stokes equations gives rise of an SGS stress tensor, which represents the energy occurrence between filtered large scales and subgrid scales. The modelling of these unknown SGS stresses has mostly been based on the eddy viscosity concept as in RANS approach. Similar to the Reynolds stresses resulted from the time-averaging process in RANS, the anisotropic part of the SGS stress tensor is modelled in alignment with the local strain rate tensor, i.e.,

$$\tau_{ij} - \frac{\delta_{ij}}{3}\tau_{kk} = -2\nu_t \bar{S}_{ij}, \tag{1}$$

where ν_t is the SGS eddy viscosity and $\bar{S}_{ij}$ is the large-scale strain rate tensor, reading

$$\bar{S}_{ij} = \frac{1}{2}\left(\frac{\partial \bar{u}_i}{\partial x_j} + \frac{\partial \bar{u}_j}{\partial x_i}\right). \tag{2}$$

In analogy to τ_{ij}, the resultant SGS heat fluxes in the filtered energy equation are modelled as

$$h_j = -\alpha_t \frac{\partial \bar{\theta}}{\partial x_j}, \tag{3}$$

where α_t is the SGS eddy diffusivity.

By assuming that the subgrid scales are in local equilibrium, for which a balance holds between the SGS turbulent production and turbulent dissipation rate, the SGS eddy viscosity, ν_t, can be derived as $\nu_t = C\Delta^2/\mathcal{T}$. Similarly, the SGS eddy diffusivity, α_t, is expressed as $\alpha_t = C_t\Delta^2/\mathcal{T}$. In the so-called dynamic *scalar model*, the time scaling, $\mathcal{T}_S$, is equal to the reciprocal of the magnitude of the local strain rate tensor, i.e. $\mathcal{T}_S = 1/|\bar{S}|$, and $|\bar{S}| = \sqrt{2\bar{S}_{ij}\bar{S}_{ij}}$, see e.g. Refs (16, 17). The SGS Prandtl number is given by $Pr_t = \nu_t/\alpha_t = C/C_t$.

Eidson (10) derived the SGS eddy viscosity with a buoyancy term included in the SGS turbulent production. This brings about the *buoyancy model* in which the SGS eddy viscosity takes the form of

$$\nu_t = C\Delta^2\left(|\bar{S}|^2 + \frac{\beta}{Pr_t}\frac{\partial \bar{\theta}}{\partial x_j}g_k\delta_{kj}\right)^{\frac{1}{2}}. \tag{4}$$

Similarly, the SGS eddy diffusivity in Eidson's buoyancy model is expressed as

$$\alpha_t = C_t\Delta^2\left(|\bar{S}|^2 + \frac{\beta}{Pr_t}\frac{\partial \bar{\theta}}{\partial x_j}g_k\delta_{kj}\right)^{\frac{1}{2}}. \tag{5}$$

In equations (4) and (5), g_k denotes the gravitational vector, $g_k = (0, -g, 0)$. The $1/\mathcal{T}_B$ scaling that appears in the buoyancy model is then

$$\frac{1}{\mathcal{T}_B} = \left(|\bar{S}|^2 - \frac{g\beta}{Pr_t}\frac{\partial \theta}{\partial x_j}\delta_{2j}\right)^{\frac{1}{2}}. \tag{6}$$

With this $1/\mathcal{T}_B$ scaling, the eddy viscosity has to be constrained to be equal to zero as $|\bar{S}|^2 < \frac{g\beta}{Pr_t}\frac{\partial\theta}{\partial x_j}\delta_{2j}$ to avoid entailing non-real solutions. Winckelmans *et al.* (18) evaluated several base models with different choices for the $1/\mathcal{T}$ scaling in an *a priori* test of SGS models using available DNS data. It was found that the choice of $1/\mathcal{T}$ scaling in the eddy viscosity is unimportant as it does not significantly affect the correlations between modelled and exact SGS quantities. This suggests that the $1/\mathcal{T}$ scaling does not necessarily need to be derived from the production-dissipation equilibrium argument. Moreover, the problem of inducing non-real solutions with the buoyancy base model, i.e. equation (6), needs to be eliminated. Therefore, the new $1/\mathcal{T}_N$ scaling is proposed as

$$\frac{1}{\mathcal{T}_N} \equiv \bar{N} = \frac{1}{|\bar{S}|}\left(|\bar{S}|^2 - \frac{g\beta}{Pr_t}\frac{\partial\theta}{\partial x_j}\delta_{2j}\right). \qquad (7)$$

The eddy viscosity and the eddy diffusivity in the modified buoyancy base model are then expressed, respectively, as

$$\begin{aligned}\nu_t &= C\Delta^2\bar{N} \\ &= C\Delta^2\frac{1}{|\bar{S}|}\left(|\bar{S}|^2 - \frac{g\beta}{Pr_t}\frac{\partial\bar{\theta}}{\partial x_j}\delta_{2j}\right) \qquad (8)\end{aligned}$$

and

$$\begin{aligned}\alpha_t &= C_t\Delta^2\bar{N} \\ &= C_t\Delta^2\frac{1}{|\bar{S}|}\left(|\bar{S}|^2 - \frac{g\beta}{Pr_t}\frac{\partial\bar{\theta}}{\partial x_j}\delta_{2j}\right). \qquad (9)\end{aligned}$$

Note that for isothermal flows, $\frac{\partial\bar{\theta}}{\partial x_j}\delta_{2j} \equiv 0$, this model then turns out to be the conventional Smagorinsky model, i.e. the scalar model. It is interesting to note a relation for the SGS time scales with the above three base models, i.e. $\mathcal{T}_N/\mathcal{T}_B = \mathcal{T}_B/\mathcal{T}_S$. The modified model is thus a combination of the Smagorinsky model and Eidson's buoyancy model. This combination suggests that the SGS time scale given by the buoyancy model nestles between those given by the scalar model and by the modified model. For flows with stable thermal stratification, the modified model is expected to produce the largest time scale, and the smallest for flows with unstable thermal stratification.

Introducing equations (8) and (9) into the dynamic procedure developed by Germano *et al.* (6) and modified later by Lilly (19), the model coefficients C, C_t and Pr_t can be dynamically determined. The dynamic SGS modelling is based on the use of two filters. A test filter (denoted by a curved overbar) is employed in addition to the grid filter (denoted by an overbar). The grid filter is used to define the subgrid scales, while the test filter, whose width is larger than the grid filter width, produces information from the smallest resolved large-scale structure to formulate the SGS stresses and heat fluxes. Furthermore, a mathematical identity is exploited to determine the model coefficients. This identity relates the SGS stresses on the grid-filtering level, τ_{ij}, and on the test-filtering level, T_{ij}, (and thus similarly the heat fluxes, h_j and H_j, on these two filtering levels) to the resolvable residual stresses, $\mathcal{L}_{ij}$ (and thus similarly the resolvable residual heat fluxes, $\mathcal{E}_j$).

As proposed by Germano *et al.* (6), the test filter width, $\widehat{\Delta}$, is chosen to be twice the grid filter width, Δ, i.e. $\widehat{\Delta} = 2\Delta$. In analogy to the SGS stress tensor in equation (1), the stress tensor on the test filtering level is expressed as

$$T_{ij} - \frac{\delta_{ij}}{3}T_{kk} = -2\widehat{\nu_t}\,\widehat{\bar{S}}_{ij}. \qquad (10)$$

Similarly, the heat fluxes, H_j, are

$$H_j = -\widehat{\alpha_t}\frac{\partial\,\widehat{\bar{\theta}}}{\partial x_j}. \qquad (11)$$

The eddy viscosity and diffusivity for the modified model (and similarly for the scalar model and the buoyancy model), on the test level are expressed, respectively, as

$$\begin{aligned}\widehat{\nu_t} &= C\widehat{\Delta}^2\widehat{\bar{N}} \\ &= C\widehat{\Delta}^2\overline{\frac{1}{|\bar{S}|}\left(|\bar{S}|^2 - \frac{g\beta}{Pr_t}\frac{\partial\bar{\theta}}{\partial x_j}\delta_{2j}\right)} \qquad (12)\end{aligned}$$

and

$$\begin{aligned}\widehat{\alpha_t} &= C_t\widehat{\Delta}^2\widehat{\bar{N}} \\ &= C_t\widehat{\Delta}^2\overline{\frac{1}{|\bar{S}|}\left(|\bar{S}|^2 - \frac{g\beta}{Pr_t}\frac{\partial\bar{\theta}}{\partial x_j}\delta_{2j}\right)}. \qquad (13)\end{aligned}$$

In deriving equations (12) and (13), a scale-invariance assumption has been made. It is assumed that C and C_t are very slowly varying functions of space. This assumption thus allows to use the same model coefficients at both the grid and test filtering levels. The Germano identity (6) indicates that

$$\mathcal{L}_{ij} = T_{ij} - \widehat{\tau}_{ij} = \widehat{\bar{u}_i\bar{u}_j} - \widehat{\bar{u}}_i\widehat{\bar{u}}_j. \qquad (14)$$

For the heat fluxes, this identity takes the following form

$$\mathcal{E}_j = H_j - \widehat{h}_j = \widehat{\bar{u}_j\bar{\theta}} - \widehat{\bar{u}}_j\widehat{\bar{\theta}}. \qquad (15)$$

The right-hand-side residual stresses and fluxes in equations (14) and (15) are resolvable quantities. This feature is then employed to compute the model coefficients. Introducing the SGS eddy viscosity/diffusivity models into the above identities yields

$$\begin{aligned}\mathcal{L}_{ij} - \frac{\delta_{ij}}{3}\mathcal{L}_{kk} &= -2C\widehat{\Delta}^2\widehat{\bar{N}}\,\widehat{\bar{S}}_{ij} \\ &\quad +2C\Delta^2\overline{\bar{N}\bar{S}_{ij}} \qquad (16)\end{aligned}$$

and

$$\mathcal{E}_j = -C_t \widehat{\Delta}^2 \widehat{\bar{N}} \frac{\partial \widehat{\bar{\theta}}}{\partial x_j} + C_t \Delta^2 \widehat{\bar{N} \frac{\partial \bar{\theta}}{\partial x_j}}. \quad (17)$$

By means of the least square approach proposed in Ref. (19), the model coefficients, C and C_t, are formulated, respectively, as

$$\begin{aligned} C &= -\frac{\mathcal{L}_{ij} M_{ij}}{2 M_{ij} M_{ij}}; \\ M_{ij} &= \widehat{\Delta}^2 \widehat{\bar{N}} \widehat{\bar{S}}_{ij} - \Delta^2 \widehat{\bar{N} \bar{S}_{ij}} \end{aligned} \quad (18)$$

and

$$\begin{aligned} C_t &= -\frac{\mathcal{E}_j Q_j}{Q_j Q_j}; \\ Q_j &= \widehat{\Delta}^2 \widehat{\bar{N}} \frac{\partial \widehat{\bar{\theta}}}{\partial x_j} - \Delta^2 \widehat{\bar{N} \frac{\partial \bar{\theta}}{\partial x_j}}. \end{aligned} \quad (19)$$

When using equations (18) and (19) to compute the model coefficients, two principal deficiencies exist: the scale-invariance assumption for the model coefficient is not mathematically self-consistent since it wipes out the time- and spatially-dependent feature from a filtering operation; second, the model is ill-conditioned because the denominators in equations (18) and (19) can be very small, which in turn causes numerical instability. The first can be partly overcome by using approximately localized model coefficients as in, e.g Ref. (20). To remedy the second problem, as in Germano *et al.* (6), the model coefficients are assumed to be only functions of time and inhomogeneous directions. For the Rayleigh-Bénard flow considered in this work, for example, a spatial-averaging for the numerators and denominators in (18) and (19) is then made over two directions of flow homogeneity (the $x-$ and $z-$directions), denoted by $< \cdot >_{xz}$. The model coefficients are thus functions of time and of only the direction normal to the walls, i.e.

$$C(t,y) = -\frac{< \mathcal{L}_{ij} M_{ij} >_{xz}}{2 < M_{ij} M_{ij} >_{xz}}, \quad (20)$$

and

$$C_t(t,y) = -\frac{< \mathcal{E}_j Q_j >_{xz}}{< Q_j Q_j >_{xz}}. \quad (21)$$

Furthermore, to remove the numerical instability attributed to negative total viscosity arising at some points in the flow domain, the total viscosity at those points is artificially set to zero. Nonetheless, this clipping approach allows a small amount of energy backscatter.

There is another model coefficient, Pr_t, in the modified model and the buoyancy model that must be determined. This can be accounted for by using an iterative scheme as in Refs (11, 12) with respect to equations (20) and (21) to get $Pr_t = C/C_t$. Applying such a scheme to the buoyancy model, i.e. equations (4) and (5), Cabot (9) pointed out that an iterative determination of Pr_t doubled the cost on computing the SGS model and sometimes gave either non-real or multiple solutions. It was found in Ref. (9) that, in comparison with the scalar model, the buoyancy model entailed little difference in the results, as Pr_t was locally computed. Instead, improved simulations were obtained by simply using a constant Pr_t in the buoyancy base model with $Pr_t = 0.4$ as used in Ref. (10). This approach, moreover, requires less computational effort, see Ref. (9).

In this work, the scalar model has also been used for comparison. Comparing to the buoyancy model or the modified model, the scalar model is equivalent to setting $Pr_t = \infty$, see equations (4) and (5) or equations (8) and (9). Because of the too costly computation, instead of using an iterative scheme (e.g. Newton's method), we have used the value of C/C_t at the previous time step, say, $(n-1)$, to approximate Pr_t at time step n, giving

$${Pr_t}^n \simeq \left(\frac{C}{C_t}\right)^{n-1}. \quad (22)$$

Equation (22) is an approximation similar to Piomelli and Liu's proposal (20), where they computed the model coefficient, C, in their localized dynamic model by employing the "zeroth-order approximation" and the "first-order approximation". It was argued that the model coefficient is fairly slowly-varying function of time because of the temporal filtering introduced implicitly by the spatial filtering. In addition to using equation (22), $Pr_t = 0.4$ has also been employed for comparison when using both the modified model and the buoyancy model.

3 NUMERICAL METHOD

The central differencing finite-volume method was used to discretize the differential governing equations on a collocated grid, and the second-order Crank-Nicholson scheme was employed for temporal discretization (22, 23).

The filtered Navier-Stokes equation for $\bar{u}_i$ can be written as

$$\begin{aligned} &\frac{\partial \bar{u}_i}{\partial t} + \frac{\partial}{\partial x_j}(\bar{u}_i \bar{u}_j) \\ &= -\frac{1}{\rho}\frac{\partial \bar{p}}{\partial x_i} + \nu \frac{\partial^2 \bar{u}_i}{\partial x_j \partial x_j} - \frac{\partial \tau_{ij}}{\partial x_j}. \end{aligned} \quad (23)$$

By means of an implicit, two-step time advancement method, this equation is discretized as the following

$$\begin{aligned} &\bar{u}_i^{n+1} = \bar{u}_i^n + \Delta t H\left(\bar{u}_i^n, \bar{u}_i^{n+1}\right) \\ &-\frac{1}{\rho}\alpha \Delta t \frac{\partial \bar{p}^{n+1}}{\partial x_i} - \frac{1}{\rho}(1-\alpha)\Delta t \frac{\partial \bar{p}^n}{\partial x_i}, \end{aligned} \quad (24)$$

where $H\left(\bar{u}_i^n, \bar{u}^{n+1}\right)$ denotes the discrete terms on the right-hand side of equation (23) except the pressure-gradient term. Equation (24) is first solved for $\bar{u}_i^{n+1}$.

To reinforce the coupling between the velocity and pressure fields, an intermediate velocity field is then computed as

$$\bar{u}_i^* = \bar{u}_i^{n+1} + \frac{1}{\rho}\alpha\Delta t\frac{\partial \bar{p}^{n+1}}{\partial x_i}. \quad (25)$$

Taking the divergence of equation (25) leads to a Poisson equation for the pressure, i.e.

$$\frac{\partial^2 \bar{p}^{n+1}}{\partial x_i \partial x_i} = \frac{\rho}{\alpha\Delta t}\frac{\partial \bar{u}_i^*}{\partial x_i}. \quad (26)$$

Note that the continuity condition has been implicitly applied at time step $(n+1)$ in the diverging procedure from equation (25) to equation (26). The Poisson equation is solved with an efficient multigrid method (24). The resultant pressure, together with the intermediate velocity obtained through equation (25), is then used to correct the velocity at the volume faces, which consequently gives a continuity-satisfied velocity field.

The box filter was used in the filtering procedure. In a finite volume calculation, the test-filtered flow quantities can be computed by volume-averaging the grid-scale filtered variables over test cells by assuming linear variation of these variables, see Ref. (25). A detailed description of the solution procedure can be found in Refs (22, 26).

4 RESULTS AND DISCUSSION

In this section, the above three SGS models, i.e. the scalar model, the buoyancy model and the modified model, are applied to the Rayleigh-Bénard convection at a Rayleigh number of $Ra = 3.8 \times 10^5$ and a molecular Prandtl number of $Pr = 1.0$. Available DNS and experimental data are used for comparison.

The Rayleigh-Bénard convection is induced in a horizontal channel by a heated bottom boundary and a cooled top boundary. The computational domain used is $6 \times 1 \times 6$, with a grid resolution of $48 \times 48 \times 48$. The boundary condition for the pressure is the Neumann condition at the top and bottom wall surfaces. Periodical boundary conditions have been employed for all variables in the longitudinal and spanwise directions ($x-$ and $z-$directions). The no-slip condition is used at the walls for the velocity components, $\bar{u}_i$. Constant temperatures are specified at the horizontal wall surfaces, with a temperature difference of $\Delta\theta = 10°C$. The computation started with a result computed using the Smagorinsky model. The time unit in the Rayleigh-Bénard convection is $t_0 = D/u_0$, where D is the height of the fluid layer, $u_0 = \sqrt{g\beta\Delta\theta D}$, and β is the volumetric expansion coefficient. The time interval is about $0.05t_0$. The number of time steps used in each calculation is generally 60000. This corresponds to approximately $3000t_0$. The data are analyzed over a period of about $800t_0$. The time-averaged quantity is thus obtained through $< \phi >_t = \int_{T_0}^{T_1} \phi(t')dt'/(T_1 - T_0)$, with $T_0 \simeq 2200t_0$ and $T_1 \simeq 3000t_0$. The time-averaging process is denoted here by $< \cdot >_t$. For convenience, however, this notation will be dropped for time-averaged model coefficients in the following discussion.

Figure 1 shows the history of time-averaging the model coefficients at the mid-point of the domain, where the modified SGS model was used with Pr_t computed by equation (22). It is shown that all the model coefficients at this point remain nearly unchanged with increasing averaging time after $t \simeq 200t_0$. This demonstrates that the time period used for time-averaging in this work is sufficient for data analyses.

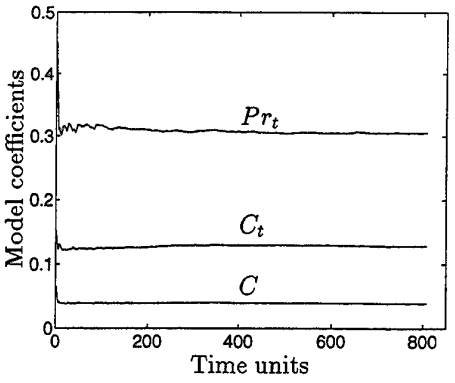

Figure 1: History of time-averaging model coefficients at the mid-point of the domain using the modified model with Pr_t computed by Eq. (22).

In Fig. 2, the vertical distributions of the time-averaged model coefficients are compared when using various SGS models. A large variation can be observed between different models. With the modified model, the coefficients appear to be rather sensitive to the specification of Pr_t: they are generally larger in the core region and smaller in the near-wall outer region when $Pr_t = 0.4$ is used than when Pr_t is locally computed with equation (22). Using the buoyancy model and computing Pr_t with equation (22), non-real solutions were detected occasionally in computations for C and C_t in the near-wall region, which have been smoothed in the figure by means of cut-off. Near the wall, the viscous effect is dominant, where C and C_t are rather small and even become slightly negative indicating a small amount of energy backscatter. In the core region of the flow domain, the scalar model gives a rather flat distribution for C with a value of about 0.048, and the modified model produces a nearly constant distribution for C_t. The buoyancy model calculates a C-profile between those determined with the scalar model and the modified model. Moreover, this model produces very similar distributions for C and C_t when using either of the above two specifications for Pr_t except in the core region, where the coefficients are slightly smaller as

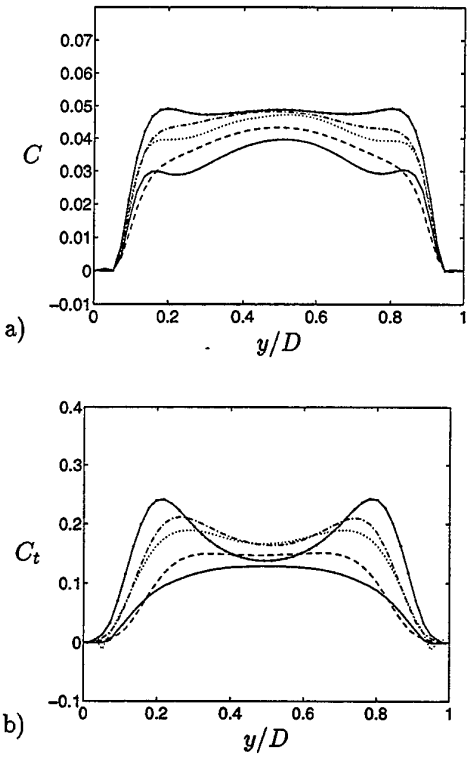

Figure 2: Vertical distributions of computed model coefficients: a) Model coefficient C; b) Model coefficient C_t. Solid-dotted line: Scalar model; Dash-dotted line: Buoyancy model ($Pr_t = 0.4$); Dotted line: Buoyancy model (Pr_t computed with Eq. (22)); Dashed line: Modified model ($Pr_t = 0.4$); Solid line: Modified model (Pr_t computed with Eq. (22)).

Pr_t is locally computed with equation (22).

In Fig. 3, the SGS Pr_t computed with different models is compared. Since Pr_t is not dynamically calculated in the scalar model, it is obtained by taking $Pr_t = C/C_t$ in this figure, and the same is done for both the buoyancy and the modified models as $Pr_t = 0.4$ is used. None of the three models reproduces the standard constant SGS Prandtl number ($Pr_t = 0.4$) as proposed by Eidson (10). The scalar model gives a value of about 0.39 for Pr_t in a narrow core region between $y/D \simeq 0.47 \sim 0.53$, while a value of about 0.3 is given in a wider region by the modified model. Near the walls, the SGS Prandtl number computed by the modified model becomes much larger, reaching 0.68 as equation (22) is used and 0.84 with $Pr_t = 0.4$. Using the buoyancy model, Cabot (9) showed a similar distribution tendency for Pr_t in an LES for Rayleigh-Bénard convection at $Ra = 1 \times 10^7$ and $Pr = 0.71$. A large variation occurs mainly in the near-wall region. Due to slightly negative values for C or C_t close to the wall, Pr_t also becomes negative there. However, the negative Pr_t hardly influences the simulation of the convective flow variables, because both C and C_t are so small in this near-wall viscous boundary layer that the computed SGS eddy coefficients, ν_t and α_t, are much smaller than their molecular counterparts.

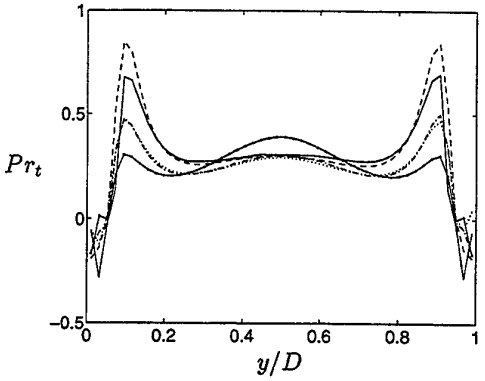

Figure 3: Vertical distributions of computed SGS Pr_t (same legend as in Fig. 2).

The computed vertical distributions for the root mean squares of velocity components and temperature, $\sqrt{<(\bar{u}_i - <\bar{u}_i>_t)^2>_{txz}}$ and $\sqrt{<(\bar{\theta} - <\bar{\theta}>_t)^2>_{txz}}$, i.e. $\bar{u}_{rms}$ or $\bar{w}_{rms}$, $\bar{v}_{rms}$ and $\bar{\theta}_{rms}$ are shown in Fig. 4. Also shown in this figure is the vertical profile of the dimensionless temperature, $(<\bar{\theta}>_{txz} - \bar{\theta}_{cw})/\Delta\theta$, where $\bar{\theta}_{cw}$ is the temperature of the cooled top wall surface. The buoyancy model produces very similar simulations regardless of whether Pr_t is set as a constant ($Pr_t = 0.4$) or locally determined with equation (22) except in the near-wall region where using $Pr_t = 0.4$ gives slightly better distributions. In the following comparisons, the distributions computed by the buoyancy model together with equation (22) are not included, unless otherwise stated. All the models give similar and reasonable results in comparison with both the DNS data from Refs (27, 28) and the laboratory data from Ref. (29). The $\bar{w}_{rms}$ profile (not shown here) is nearly identical to the $\bar{u}_{rms}$ profile. In Fig. 4, the experimental data are adopted from Deardorff and Willis' laboratory investigation (29) for $Ra = 6.3 \times 10^5$. All the models under-predict $\bar{v}_{rms}$ in the core region of the flow domain as compared with the measured and DNS data, but gives better predictions than those in Ref. (11) for the same flow problem, where the buoyancy model (termed *stratification formulation* in Ref. (11)) was applied. The comparison with the experimental data shows that the $\bar{\theta}_{rms}$ profile is generally over-predicted by all the models. Eidson (10) showed a similar prediction in a previous LES. The results, however, agree better with the DNS data for $Pr = 0.71$ given by Wörner and Grötzbach (28). In the DNS by Moeng and Rotunno (27), with $Pr_t = 1.0$, it was stated that the root-mean-square of the temperature has a maxima of 0.15 located about 0.07 away from both walls and a value of about 0.08 at mid-level. This has been approximately reflected in the present prediction as

shown in Fig. 4 c).

In spite of the fact that the model coefficients vary with different models, only can very small difference be observed in the predictions given in Fig. 4. This seems to indicate that the large-scale statistics are fairly insensitive to the base model used for the flow considered. In the LES of Rayleigh-Bénard convection at $Ra = 1 \times 10^7$, Cabot (9) also showed that the scalar model and the buoyancy model gave very similar results. He attributed this to several possible factors: the buoyancy term is generally less than, or comparable to the strain term, or, even with a different scaling, the dynamic eddy viscosities/diffusivities tend to self-adjust to a similar level. To gain a quantitative understanding, the strain term, $\mid \bar{S} \mid^2$, is compared with the buoyancy-related term, $\frac{g\beta}{Pr_t}\frac{\partial \bar{\theta}}{\partial y}$, in the expression for SGS eddy coefficients. This is shown in Fig. 5, where the modified model is employed using $Pr_t = 0.4$. It can be seen that the buoyancy

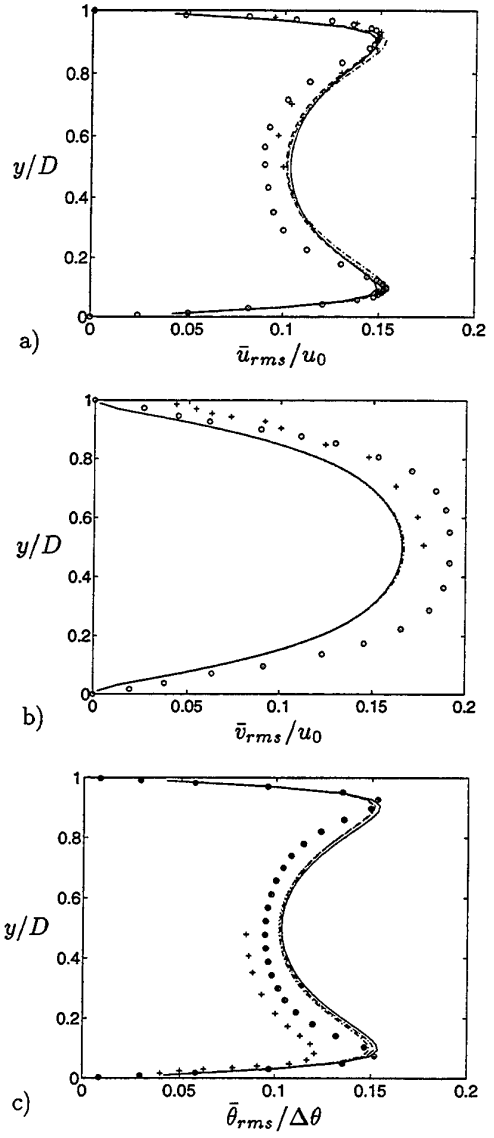

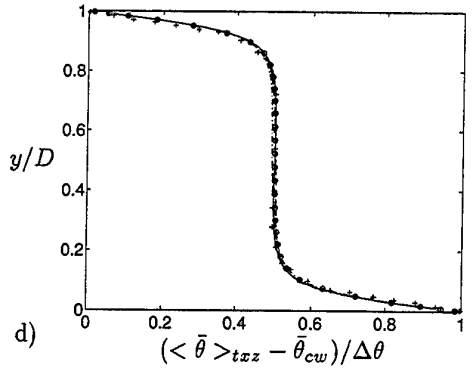

Figure 4: Vertical distributions of the root-mean-squares of the velocity components and temperature and the vertical profile for the dimensionless temperature: a) $\bar{u}_{rms}/u_0$; b) $\bar{v}_{rms}/u_0$; c) $\bar{\theta}_{rms}/\Delta\theta$; d) Dimensionless temperature, $(< \bar{\theta} >_{txz} - \bar{\theta}_{cw})/\Delta\theta$. Dotted line: Scalar model; Dashed line: Modified model ($Pr_t = 0.4$); Solid line: Modified model (Pr_t computed with Eq. (22)); Dash-dotted line: Buoyancy model ($Pr_t = 0.4$); + Experimental data from Ref. (29); ∘ DNS data ($Pr = 1.0$) from Ref. (27); ⊙ DNS data ($Pr = 0.71$) from Ref. (28).

term hardly have any effects in the core region of the flow domain, where this term becomes nearly zero. The SGS eddy coefficients, ν_t and α_t, thus depend mainly on the strain term without being affected by Pr_t. In this region, both the modified model and the buoyancy model show behaviors similar to the scalar model. Within a range of $y/D \simeq 0.2$ near the wall, however, the buoyancy term plays an increasing role towards the wall surface in the determination of SGS eddy coefficients. Approaching the wall, both the strain and buoyancy terms increase, but their effects are actually suppressed to become insignificant owing to very small near-wall coefficients C and C_t (see Fig. 2).

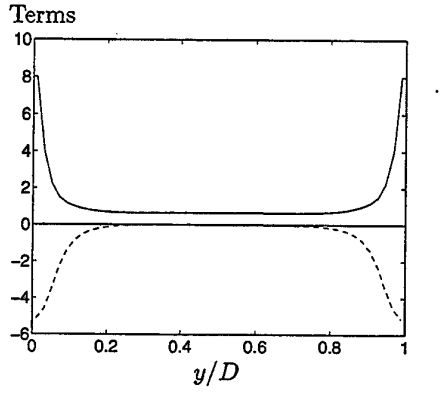

Figure 5: Comparison of the strain term, $\mid \bar{S} \mid^2$, and the buoyancy term, $\frac{g\beta}{Pr_t}\frac{\partial \bar{\theta}}{\partial y}$, using the modified base model with $Pr_t = 0.4$. Solid line: Strain term; Dashed line: Buoyancy term.

The SGS eddy coefficients computed with different models are further compared in Fig. 6. The

distributions in this figure correspond well to the profiles for the model coefficients in Fig. 2. The modified model gives the smallest model coefficients and thus the lowest SGS turbulence level. Very close to the wall ($y/D \simeq 0.06$), the models give negative Pr_t as shown in Fig. 3, owing to negative model coefficients C or C_t whereby backscatter is active. The near-wall buoyancy effect is then fed back into the SGS model with a positive value, as Pr_t is locally determined with either the buoyancy model or the modified model. This in turn should have decreased the SGS time scale and thus increased the SGS eddy viscosity/diffusivity. Nevertheless, it should be noted that, in the viscous boundary layer, coefficients C and C_t have been dynamically set to be very small, as shown in Fig. 2. Consequently, the eddy coefficients in this layer become negligibly small and rather insensitive to a certain range of variation in Pr_t (positive or negative). Although there exist certain differences in the eddy coefficients determined by different models, only slight variations are found in the results. One of the reasons is that the SGS turbulence level is relatively low in the flow considered with a maximum ν_t/ν of about 0.2. This suggests that the simulation for the SGS scales relies to a certain extent on the viscous effects.

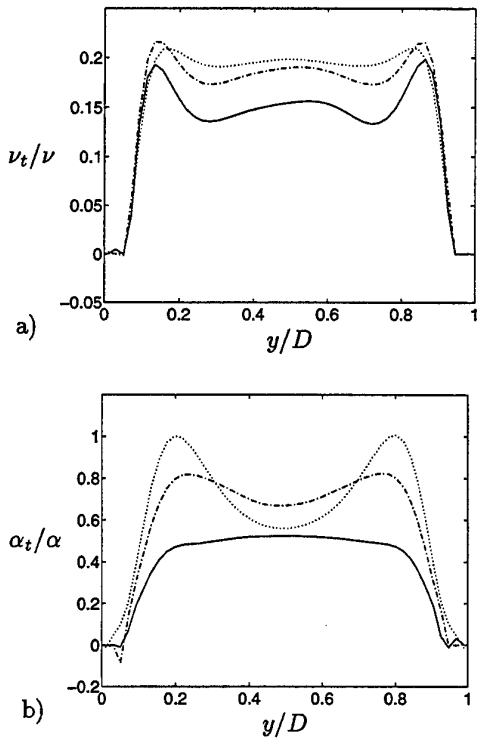

Figure 6: Comparison of SGS eddy coefficients, ν_t/ν and α_t/α: a) SGS eddy viscosity; b)SGS eddy diffusivity. Dotted line: Scalar model; Dash-dotted line: Buoyancy model (Pr_t computed with Eq. (22)); Solid line: Modified model (Pr_t computed with Eq. (22)).

Figure 7 presents the vertical profiles of the Nusselt number, Nu, computed with various models. The Nusselt number in this study is defined as

$$Nu = -\frac{< \bar{v}\bar{\theta} - \kappa \partial\bar{\theta}/\partial y >_{txz}}{\kappa \Delta\theta/D}. \qquad (27)$$

All the models give nearly identical simulations. The distribution of Nu is nearly uniform, with a value of about 6.4 within a wide core region. Near the walls, the Nusselt number varies owning to the large temperature gradient. For comparison, if the Nusselt number is redefined as $Nu = D|\ \partial\bar{\theta}/\partial y\ |_w/\Delta\theta$, the prediction given by the scalar model is 6.43, while it is 6.33 and 6.20, respectively, by the modified model and the buoyancy model with $Pr_t = 0.4$, and 6.29 and 6.08 when Pr_t is computed with equation (22). The measured value is 6.14 in air and 6.50 in gaseous helium (see Ref. (9) for experimental references).

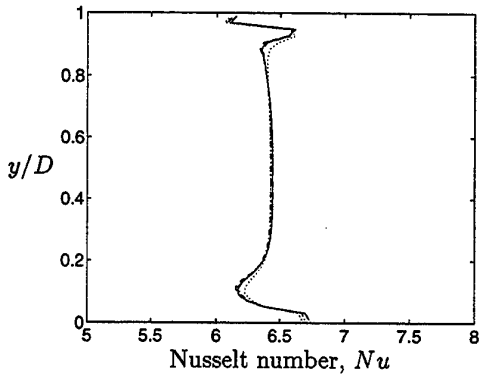

Figure 7: Vertical distribution of Nusselt number, Nu (same legend as in Fig. 4).

Figure 8 shows the vertical profiles for the vertical-velocity variance and skewness: $< v'^3 >_{txz}$ and $< v'^3 >_{txz} / < v'^2 >^{3/2}_{txz}$, where $v' = (\bar{v} - < \bar{v} >_t)$. Note that these quantities have been normalized with the velocity scale, u_0. The results show good agreement with the DNS data, even in the near-wall viscous layers where molecular diffusion and dissipation become dominant. The skewness is negative in the lower layer and positive in the upper layer. This result is consistent with the DNS data, and was well explained by Moeng and Rotunno (27) on deriving a relationship between the skewness and the ratio of updraft area and downdraft area. There is no apparent difference between the results computed with various models.

For a straightforward view of the flow structure, Figure 9 illustrates the vertical cross sections of the vertical velocity and temperature fluctuations. A few upward eddies are able to penetrate to the top. Some updrafts mix out their heat excess and are penetrated by downdrafts. As found in DNS (27), Fig. 9 indicates that the area occupied by an individual

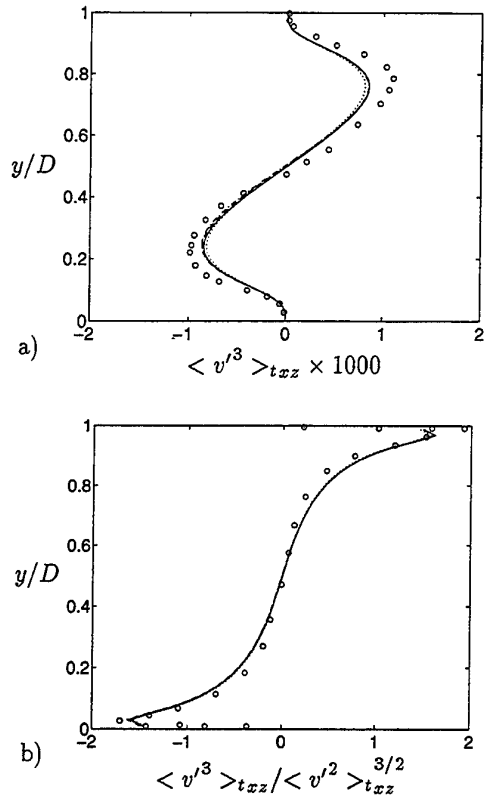

Figure 8: Vertical distributions of a) Variance of $\bar{v}$ and b) Skewness of $\bar{v}$ (same legend as in Fig. 4).

updraft remains nearly constant with height in the lower layers, although the vertical velocity increases over this lower portion. This phenomenon implies that the mass flux in the updraft is increased due to lateral entrainment in the lower layer. The temperature fluctuations correspond well to the vertical velocity contour. In general, the regions occupied by the thermals (with positive fluctuations) are those in which updrafts exist and *vice versa*.

Fig. 10 shows the horizontal cross sections of the vertical velocity and temperature fluctuations at three levels. Near the heated bottom wall, $y = 0.09$, small spots of downdrafts are surrounded by broad updrafts and *vice versa* near the cooled top wall ($y = 0.91$). This structure corresponds to the profile of the skewness of the vertical velocity $\bar{v}$ shown in Fig. 8. At the mid-level, $y = 0.51$, both the downdraft and the updraft penetrate with similar areas. The contour for the temperature fluctuations shows that the thermals near the heated bottom wall are narrow and elongated, while they are isolated near the cooled top wall. The eddy structure shown in this figure was also observed in DNS (27).

5 CONCLUDING REMARKS

Comparison have been made for three dynamic SGS models for handling turbulent convection flow with

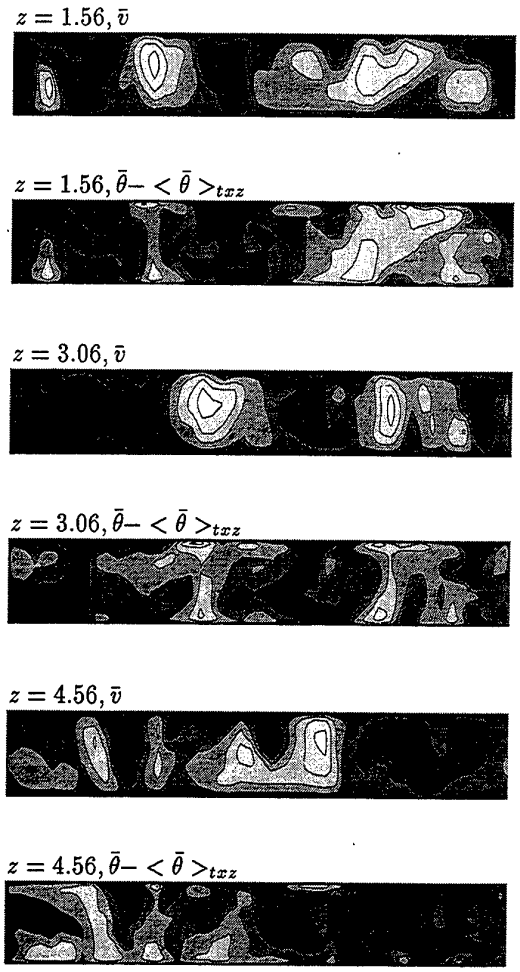

Figure 9: Instantaneous contours of $\bar{v}$ (contour interval is $0.1u_0$) and $\bar{\theta} - < \bar{\theta} >_{txz}$ (contour interval is $0.1\Delta\theta$) at vertical cross sections, simulated by the modified model using $Pr_t = 0.4$; the dark-colored areas indicate downdrafts and the light-colored areas indicate updrafts.

heat transfer. These include the scalar model, the buoyancy model and a modified buoyancy model. For thermally stratified flows, the buoyancy model may entail no-real solutions. To remedy this problem, the modified model re-constructs the time scaling in the SGS eddy viscosity/diffusivity formulation, and keeps the buoyancy effect being directly accommodated as in the buoyancy model. This model returns to the scalar model for isothermal flows. It thus works with fully developed turbulence generated by shear or by buoyancy, or by both. LES has been performed for the turbulent Rayleigh-Bénard flow at $Ra = 3.8 \times 10^5$ with these models. The results agree well with both the experimental and DNS data.

In comparison with the other models, the modified model gives very similar results for the flow considered. The model coefficients in various models, however, show rather different dynamic features. Corresponding with the computed smaller values of

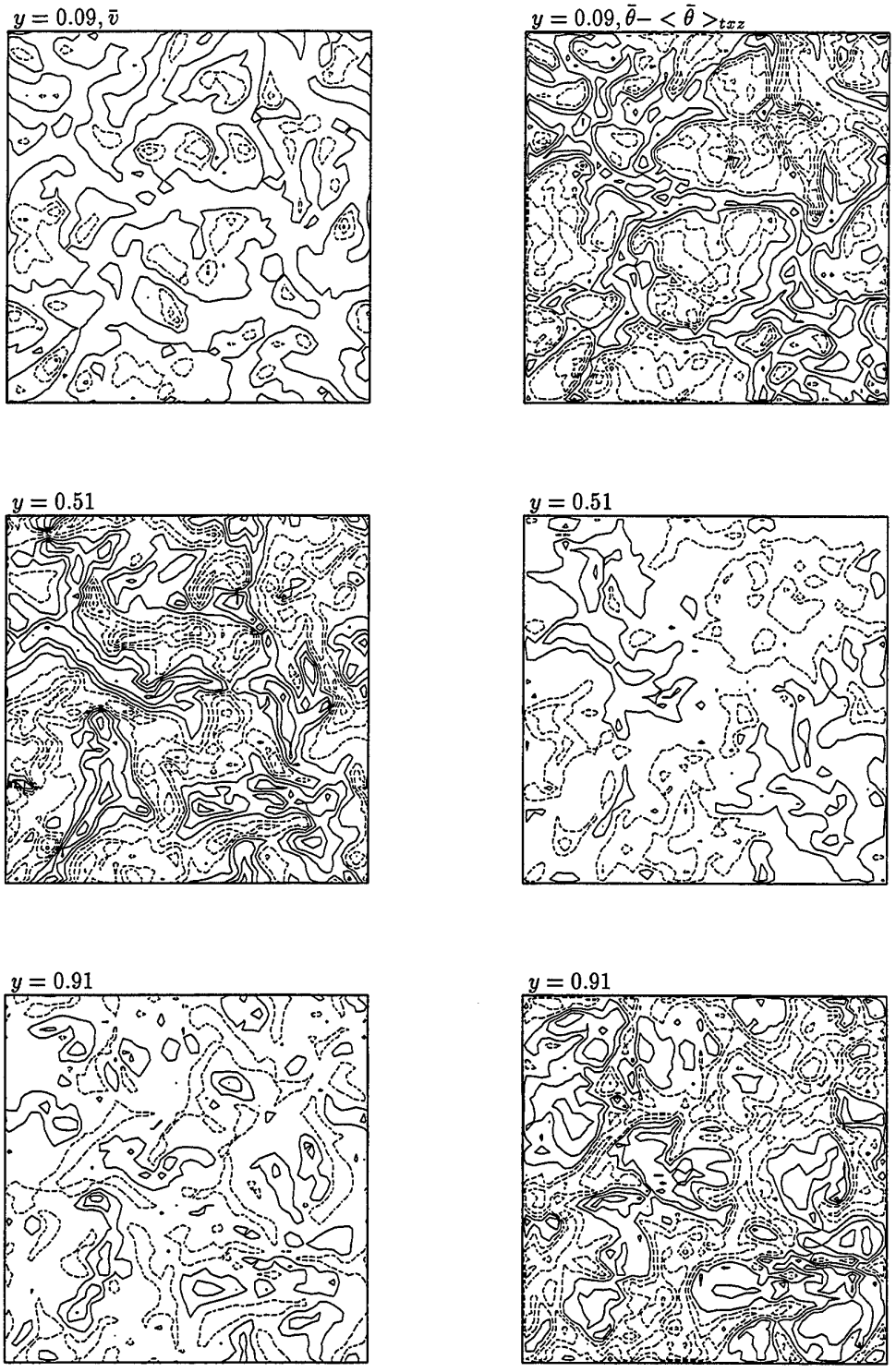

Figure 10: Instantaneous contours of $\bar{v}$ (contour interval is $0.1u_0$) and $\bar{\theta} - < \bar{\theta} >_{txz}$ (contour interval is $0.1\Delta\theta$) at horizontal cross sections, simulated by the modified model using $Pr_t = 0.4$; the solid and dotted contour lines indicate positive and negative values, respectively.

coefficients C and C_t, the modified model returns lower SGS eddy viscosities and diffusivities out of the near-wall boundary layer. However, only a small variation is found in the resultant simulations. This might be attributed to the relatively low turbulence level in the Rayleigh-Bénard convection flow considered. In future work, these SGS models need to be further investigated in applications to highly turbulent thermal convection flows.

REFERENCES

(1) Smagorinsky, J. General circulation experiments with the primitive equations, *Monthly Weather Review*, 1963, Vol. 91, pp. 99-165.

(2) Ferziger, J.H. Large eddy numerical simulations of turbulent flows, *AIAA J.*, 1977, Vol. 15, pp. 1261-1267.

(3) Bardina, J., Ferziger, J.H. and Reynolds, W.C. Improved subgrid scale models for large eddy simulation, AIAA Paper 80-1357, Snomass, Colorado, 1980.

(4) Yakhot, A., Orszag, S.A. and Yakhot, V. Renormalization group formulation of large eddy simulations, *J. Sci. Comp.*, 1989, Vol. 4, pp. 139-158.

(5) Moin, P., Squires, K., Cabot, W. and Lee, S. A dynamic subgrid-scale model for compressible turbulence and scalar transport, *Phys. Fluids A*, 1991, Vol. 11, pp. 2746-2757.

(6) Germano, M., Piomelli, U., Moin, P. and Cabot, W.H. A dynamic subgrid-scale eddy viscosity model, *Phys. Fluids A*, 1991, Vol. 3, pp. 1760-1765.

(7) Germano, M., Piomelli, U., Moin, P. and Cabot, W.H. Erratum, *Phys. Fluids A*, 1991, Vol. 3, pp. 3128.

(8) Piomelli, U., Cabot, W.H., Moin, P. and Lee, S. Subgrid-scale backscatter in turbulent and transitional flows, *Phys. Fluids A*, 1991, Vol. 3, pp. 1766-1771.

(9) Cabot, W. Large-eddy simulations of time-dependent and buoyancy-driven channel flows, in *Annual research Brief*, 1992, pp. 45-60, Center for Turbulence Research, Stanford Univ./NASA Ames Research Center.

(10) Eidson, T.M. Numerical simulation of the turbulent Rayleigh-Bénard problem using subgrid modelling, *J. Fluid Mech.*, 1985, Vol. 158, pp. 245-268.

(11) Wong, V.C. and Lilly, D.K. A comparison of two dynamic subgrid closure methods for turbulent thermal convection, *Phys. Fluids A*, 1994, Vol. 6, pp. 1016-1023.

(12) Bergstrom, D.J. and Huang, X. LES of buoyant cavity flow: Challenges for subgrid scale models, in *Proc. 2nd Int. Symp. on Turbulence, Heat and Mass Transfer*, 1997, pp. 421-430, Delft University Press.

(13) Wang, V.M. and Pletcher, R.H. On the large eddy simulation of a turbulent channel flow with significant heat transfer, *Phys. Fluids A*, 1996, Vol. 8, pp. 3354-3366.

(14) Canuto, V.M., Dubovikov, M.S. and Dienstfrey, A. A dynamic model for turbulence: IV. Buoyancy-driven flows, *Phys. Fluids A*, 1997, Vol. 9, pp. 2118-2131.

(15) Peng, S.-H. and Davidson, L. A proposed subgrid-scale model in large eddy simulation for turbulent thermal convection flow, Report 97/21, 1997, Department of Thermo and Fluid Dynamics, Chalmers University of Technology, Gothenburg.

(16) Cabot, W. and Moin, P. Large-eddy simulations of scalar transport with the dynamic subgrid-scale model, in *Large Eddy Simulation of Complex Engineering and Geophysical Flows*, 1993, pp. 141-158, Cambridge University Press, New York.

(17) Moin, P. A new approach for large eddy simulation of turbulence and scalar transport, in *Proc. Monte Veritá Coll. on Turbulence*, 1993, Birkhäuser, Bale.

(18) Winckelmans, G.S., Lund, T.S., Carati, D. and Wray, A.A. A priori testing of subgrid-scale models for the velocity-pressure and vorticity-velocity formulations, in *Proc. Summer Program*, 1996, pp. 309-328, Center for Turbulence Research, Stanford Univ./NASA Ames Research Center.

(19) Lilly, D.K. A proposed modification of the Germano subgrid-scale closure method, *Phys. Fluids A*, 1992, Vol. 4, pp. 633-635.

(20) Piomelli, U. and Liu, J. Large-eddy simulation of rotating channel flow using a localized dynamic model, *Phys. Fluids A*, 1995, Vol. 7, pp. 839-848.

(21) Sullivan, P.P. and Moeng, C.-H. An evaluation of the dynamic subgrid scale model in buoyancy-driven flows, in *Proc. 10th Symp. on Turbulence and Diffusion*, 1993, pp. 82-91, Portland, Oregon.

(22) Davidson, L. LES of recirculating flow without any homogeneous direction: A dynamic one-equation subgrid model, in *Proc. 2nd Int. Symp. on Turbulence, Heat and Mass Transfer*, 1997, pp. 481-490, Delft University Press.

(23) Davidson, L. and Farhanieh, B. CALC-BFC: A finite-volume code employing collocated variable arrangement and Cartesian velocity components for computation of fluid flow and heat transfer in complex three-dimensional geometries. Report 92/4, 1992, Department of Thermo and Fluid Dynamics,

Chalmers University of Technology, Gothenburg.

(24) Emvin, P. and Davidson, L. Development and implementation of a fast large eddy simulations method. Report, 1997, Department of Thermo and Fluid Dynamics, Chalmers University of Technology, Gothenburg.

(25) Zang, Y., Street, R.L. and Koseff, J.R. A dynamic mixed subgrid-scale model and its application to turbulent recirculating flows, *Phys. Fluids A*, 1993, Vol. 5, pp. 3186-3196.

(26) Davidson, L. Implementation of a large eddy simulation method applied to recirculating flow in a ventilated room. Report ISSN 1385-7956 R9611, 1996, Department of Building Technology and Structural Engineering, Aalborg University.

(27) Moeng, C.-H. and Rotunno, R. Vertical-velocity skewness in the buoyancy-driven boundary layer, *J. Atomos. Sci.*, 1990, Vol. 47, pp. 1149-1162.

(28) Wörner, M. and Grötzbach, G. DNS database of turbulent convection in horizontal fluid layers, in http://hbksun17.fzk.de:8080/IRS/eng/IRS3turbit_DNS_database.html.

(29) Deardorff, J.W. and Willis, G.E. Investigation of turbulent thermal convection between horizontal plates, *J. Fluid Mech.*, 1967, Vol. 28, pp. 675-704.

SECOND–MOMENT MODELLING OF COMBINED TURBULENT HEAT AND SPECIES TRANSFER IN MULTIPLY STRATIFIED FLUID BODIES.

C.A. Armitage, B.E. Launder and M.A. Leschziner.
Department of Mechanical Engineering,
UMIST, Manchester, M60 1QD, UK.

ABSTRACT

The paper presents a preliminary application of second–moment closures to transient 1D double–diffusive flow. A two–layer modelling approach has been adopted, where the high–Re second–moment closures are interfaced with a low–Re k–ε model in the sublayer. The latter model has been adapted to include, in a simplified way, the effects of buoyancy on the second moments. The selection of the modelling framework is supported by the application of the models to 1D penetrative, single–diffusive flow, and to flow in an infinitely tall cavity at $Ra = 5.4 \times 10^5$ for which results are presented. The models are then applied to double–diffusion in a salt–stratified layer heated from below.

1 INTRODUCTION

The simultaneous mixing of heat and one or more species in a stratified system is generally referred to as *double diffusion* or *double–diffusive convection.* This process occurs in a number of environmental conditions and engineering applications, including solar ponds, discharges of heated contaminant–containing effluents, silicon–crystal melts and storage tanks for liquid hydrocarbons.

The particular context of the present study is Liquefied Natural Gas (LNG) storage in large tanks which can be $50m$ in diameter and $30m$ high. Density stratifications tend to arise in these tanks as a result of the combination of preferential evaporation of lighter constituents from the surface and the replenishment of fresh LNG, usually from above. With LNG having a temperature of about $-160°C$, at the relatively low super–atmospheric storage pressure feasible in practice, there arises significant heat transfer through the base and sides, causing penetrative convection, buoyancy–driven side–wall boundary layers and circulation cells, and thus resulting in a progressive erosion of the stratification. In adverse circumstances, the lower, initially heavier LNG layer accumulates heat at a relatively high saturation pressure, eventually becoming lighter than the upper layer and provoking a *rollover.* As a result, substantial amounts of superheated lower–layer LNG reach the surface quickly and a hazardous flash evaporation of methane occurs. A key aspect of the above processes is that the geometric scales involved are large, with Grashof numbers being of order 10^{14}, so that turbulence is likely to be the primary mixing mechanism. This is in contrast to small–scale double–diffusive systems in which Grashof numbers are typically of order 10^6 and where mixing occurs by the formation of distinct circulation cells and *fingers* (long, narrow convection cells) which do not contain the wide range of scales characteristic of statistical turbulence.

Previous studies of double–diffusive systems, both experimental and computational, have focused mainly on non–turbulent systems in which the primary objective has been to gain insight into the formation and propagation of circulation cells or fingering and the processes leading to the erosion of stratification and eventually full mixing. Several computational studies (eg Takao et al [1], Rastogi and Poulikakos [2], Phanikumar [3], Lee and Hyun [4], Béghein et al [5], Kamakura and Ozoe [6]) have considered the influence of lateral and/or vertical heating (or cooling) on enclosed fluid bodies with solutal stratification. Typically, these studies set out to examine, by solving 2D forms of the Navier Stokes, energy and species–concentration equations for laminar flow, the dependence of the evolution of the cells and the fluid body as a whole on the ratio of thermal and solutal Rayleigh number and pertinent geometric parameters.

While several simple theoretical models exist to describe the global parameters of turbulent double–diffusive 1D systems, numerical studies investigating the detailed structure of such layers or multi–dimensional turbulent configurations are rare. Michioku and Plate [7] have applied a one–equation k–l model, in conjunction with highly simplified algebraic relations for stresses and fluxes, to a 1D salinity–stratified layer heated from below, for which they also obtained experimental data. Their calculations revealed an intricate, continuously changing multi–layer system, each layer being quite thin and well mixed — a structure qualitatively in line with that described by Turner [8]. Bergman et al [9] applied a low–Re k–ε model, in conjunction with a correlation for the turbulent Prandtl number

derived by Gibson and Launder [10] from second-moment closure studies of buoyant flows, to several 1D salinity-stratified layers measured by the same authors [11]. Hullender and Laster [12] used the same model to investigate wind-induced erosion in a 2D system. Both studies demonstrate fair-to-good agreement, the former with experimental temperature distributions and the latter with salinity profiles and mixed-layer thickness. However, the effectiveness of the model appears to have been quite sensitive to the level of background turbulence and a specially devised boundary condition for ε at the lower heated wall. The only application of second-moment-closure to double-diffusive layers appears to be that of Hanjalić and Musemić [13] who used an algebraic truncation of such a closure to model the same 1D saline-thermal systems examined by Bergman et al [9]. The most complex system, including an LNG-like rollover phenomenon at realistic thermal and solutal Grashof numbers of order 10^{14}, was investigated by Pham and Petit [14] using a k-ε model. The study was performed for idealised 2D conditions to examine the possible scenarios leading to a rollover, and no comparisons with experimental data were made.

Although most real double-diffusive systems are multi-dimensional, the focus of several of the studies noted above on 1D turbulent diffusion reflects the recognition that this generic model, shown schematically in Figure 1, features many of the challenging turbulence-transport processes which need to be resolved if realistic systems are to be predicted correctly. Indeed, this 1D system is, arguably, more challenging than multi-dimensional ones as the former normally excludes any strain (unless driven by wind, say), while virtually all turbulence models have been calibrated primarily by reference to shear flows.

A second generic 1D configuration which may be viewed as a principal ingredient of realistic double-diffusive systems is buoyancy-driven flow in an infinitely tall cavity with opposite walls maintained at different temperatures as shown in Figure 2. In fact, many double diffusive systems may be considered as formed by an interaction of the processes occurring in the basic geometries of Figures 1 and 2.

In both generic systems, the use of eddy-viscosity models can give rise to serious predictive errors. In the case of Figure 1, the erosion of stratification is associated with buoyancy-driven fluxes which are not linked to the temperature or species gradients. In the flow of Figure 2, an eddy-viscosity model may give a fair representation of the wall-normal flux, which is driven, principally, by the temperature gradient, but will fail (unless generalised in an *ad-hoc* fashion to include buoyancy generation) to give a realistic description of the flux in the flow direction, which may be larger than the wall normal flux, despite the zero streamwise temperature gradient. While this weakness may be of little consequence to the representation of the mean-flow properties in purely 1D conditions (say, that very close to a vertical wall), it may cause significant predictive errors in more general flows involving 2D/3D features, with or without double-diffusion, in regions which are somewhat removed from the wall. These considerations justify the assumption that the minimum level of closure likely to provide a realistic description of either case and certainly their interactive combination would need to be based on evolution equations for the active Reynolds stresses and turbulent fluxes. This is the assumption which underlies the approach in the study documented herein.

The present paper thus reports our initial steps towards developing a turbulence model capable of reproducing the phenomena described above, which are associated with the occurrence of rollover in LNG storage vessels. It limits attention to a study of the generic elements associated with natural convection from vertical or horizontal surfaces, the latter including double diffusion. Apart from the near wall sublayer, variants of full second-moment closure are considered. The performance of these variants is examined first by reference to data assembled by Willis and Deardorff [15] for a study of penetrative convection into a thermally-stratified body. There follows a study of infinitely tall cavity flow by reference to DNS data of Boudjemadi et al [16]. Finally computations are presented for which experimental data have been obtained by Bergman et al [9].

2 MODELLING FRAMEWORK

2.1 Introductory Remarks

A realistic statistical description of turbulent double-diffusion in stratified fluids hinges on an accurate quantification of the fluxes of heat and species-concentration. The simplest possible approach to determining these fluxes is to use an eddy-diffusivity-type model which relates the fluxes quasi-linearly to associated mean-property gradients :

$$\overline{u_i\theta} = -\frac{\nu_t}{\sigma_\theta}\frac{\partial \Theta}{\partial x_i}. \qquad (1)$$

However, regardless of the manner in which the eddy-diffusivities are modelled, this is known to be an unacceptably simplified route, which can yield rates of diffusion for these types of flows which are seriously in error. This misrepresentation arises from the fact that a substantial proportion of the vertical fluxes are generated by buoyancy, rather than by the mean property gradients, hence substantial vertical fluxes can co-exist with very weak mean-property gradients.

The reality is that any one of the fluxes is sensitively linked to all other fluxes. all active components of the Reynolds-stress tensor, the gradient of all properties, the gravitational body force and the

variance of the temperature and species concentration. The nature of this complex interlinkage and the mutual interaction is represented exactly by the transport equations governing the evolution of the turbulent stresses, which can be derived from the Navier–Stokes equations:

$$\frac{DU_i}{Dt} = -\frac{1}{\rho}\frac{\partial P}{\partial x_i} + \nu\frac{\partial^2 U_i}{\partial x_j^2} - \frac{\partial \overline{u_i u_j}}{\partial x_j} + g_i, \qquad (2)$$

$$\begin{aligned}\frac{D\overline{u_i u_j}}{Dt} = &-\left(\overline{u_i u_k}\frac{\partial U_j}{\partial x_k} + \overline{u_j u_k}\frac{\partial U_i}{\partial x_k}\right) \qquad (3)\\ &- \left[g_i\left(\beta_\Theta \overline{u_j\theta} + \beta_S \overline{u_j s}\right) + g_j\left(\beta_\Theta \overline{u_i\theta} + \beta_S \overline{u_i s}\right)\right]\\ &+ \overline{\frac{p}{\rho}\left(\frac{\partial u_i}{\partial x_j} + \frac{\partial u_j}{\partial x_i}\right)} - 2\nu\overline{\frac{\partial u_i}{\partial x_k}\frac{\partial u_j}{\partial x_k}}\\ &- \frac{\partial}{\partial x_k}\left(\overline{u_k u_i u_j} + \frac{\overline{pu_j}}{\rho}\delta_{ik} + \frac{\overline{pu_i}}{\rho}\delta_{jk} - \nu\frac{\partial \overline{u_i u_j}}{\partial x_k}\right),\end{aligned}$$

and the equivalent energy and species-concentration equations. Thus, with Θ denoting temperature,

$$\frac{D\Theta}{Dt} = \gamma_\Theta\frac{\partial^2\Theta}{\partial x_j^2} - \frac{\partial \overline{u_j\theta}}{\partial x_j}, \qquad (4)$$

$$\begin{aligned}\frac{D\overline{u_i\theta}}{Dt} = &-\left(\overline{u_i u_j}\frac{\partial\Theta}{\partial x} + \overline{u_j\theta}\frac{\partial U_i}{\partial x_j}\right) \qquad (5)\\ &- g_i\left(\beta_\Theta\overline{\theta^2} + \beta_S\overline{\theta s}\right)\\ &+ \overline{\frac{p}{\rho}\frac{\partial\theta}{\partial x_i}} - (\gamma_\Theta + \nu)\overline{\frac{\partial\theta}{\partial x_k}\frac{\partial u_i}{\partial x_k}}\\ &- \frac{\partial}{\partial x_k}\left(\overline{u_k u_i\theta} + \frac{\overline{p\theta}}{\rho}\delta_{ik} - \gamma_\Theta\overline{u_i\frac{\partial\theta}{\partial x_k}} - \nu\theta\frac{\partial u_i}{\partial x_k}\right),\end{aligned}$$

$$\begin{aligned}\frac{D\overline{\theta^2}}{Dt} = &-2\overline{u_i\theta}\frac{\partial\Theta}{\partial x_i} - 2\gamma_\Theta\overline{\frac{\partial\theta}{\partial x_i}^2} \qquad (6)\\ &- \frac{\partial}{\partial x_i}\left(\overline{u_i\theta^2} - \gamma_\Theta\frac{\partial\overline{\theta^2}}{\partial x_i}\right).\end{aligned}$$

The corresponding equations for mean species-concentration are obtained by replacing Θ and θ by S and s (and vice versa). The correlation between the temperature fluctuations and the species-concentration fluctuations, $\overline{\theta s}$, is given by :

$$\begin{aligned}\frac{D\overline{\theta s}}{Dt} = &-\left(\overline{u_i\theta}\frac{\partial S}{\partial x_i} + \overline{u_i s}\frac{\partial\Theta}{\partial x_i}\right) \qquad (7)\\ &- (\gamma_\Theta + \gamma_S)\overline{\frac{\partial\theta}{\partial x_i}\frac{\partial s}{\partial x_i}}\\ &- \frac{\partial}{\partial x_i}\left(\overline{u_i\theta s} - (\gamma_\Theta + \gamma_S)\frac{\partial\overline{\theta s}}{\partial x_i}\right).\end{aligned}$$

While these equations are exact, they contain various unknown terms which require closure. However, the generative agencies require no approximation, this modelling strategy ensures that the linkages between the various correlations, which are crucially important for double–diffusive flows, are retained.

In addition to the modelling challenges posed by double–diffusion, an important requirement is to quantify wall–heat transfer accurately. This is especially important in the 2D and 3D conditions in which heat diffuses into the fluid through a vertical side wall, which sets up the influential near–wall convective motions. These motions are highly sensitive to the turbulent structure near the wall. As the near–wall region is semi–viscous, the modelling in this region must be based on low–Re closures which account for the complications that arise from the interaction between viscosity and turbulence.

Although the wall–normal heat transfer is well correlated with the wall–normal temperature gradient close to the wall, a simple eddy–diffusivity model does not approximate the heat–flux vector realistically, as the flux components are interlinked and also coupled to the Reynolds stresses. Here again, the use of second–moment closure would appear to be the most rational route to follow. However, there are no well–developed closures for the turbulent scalar fluxes across this thin sublayer. Accordingly, across the sublayer an extended version of the usual k–ε model is adopted.

A two–layer modelling framework has thus been adopted which aims to provide the flexibility required to represent both the side–wall heat transfer and the complexities of double–diffusive flow. Some details of the scheme are given in sections 2.2 and 2.3.

2.2 Near–Wall Sublayer

An elaboration of the low Re k–ε model of Launder and Sharma [17] has been applied across the semi–viscous sublayer. The turbulence energy and its dissipation rate are obtained from their respective transport equations:

$$\begin{aligned}\frac{Dk}{Dt} = &\frac{\partial}{\partial x_j}\left(\left(\nu + \nu_t\right)\frac{\partial k}{\partial x_j}\right) - \overline{u_i u_j}\frac{\partial U_j}{\partial x_j} \qquad (8)\\ &- g_i\left(\beta_\Theta\overline{u_i\theta} + \beta_S\overline{u_i s}\right) - \varepsilon,\end{aligned}$$

$$\begin{aligned}\frac{D\tilde{\varepsilon}}{Dt} = &\frac{\partial}{\partial x_j}\left(\left(\nu + \frac{\nu_t}{\sigma_\varepsilon}\right)\frac{\partial\tilde{\varepsilon}}{\partial x_j}\right) - c_{\varepsilon 1}\frac{\tilde{\varepsilon}}{k}\overline{u_i u_j}\frac{\partial U_j}{\partial x_j} \qquad (9)\\ &- c_{\varepsilon 3}\frac{\tilde{\varepsilon}}{k}g_i\left(\beta_\Theta\overline{u_i\theta} + \beta_S\overline{u_i s}\right)\\ &- c_{\varepsilon 2}\frac{\tilde{\varepsilon}^2}{k} + 2\nu\nu_t\left(\frac{\partial^2 U_i}{\partial x_k}\right)^2. \qquad (10)\end{aligned}$$

where $\tilde{\varepsilon} = \varepsilon - 2\nu(\partial k^{1/2}/\partial x_k)^2$. In a conventional eddy–viscosity model the turbulent stresses are eval-

uated from :

$$\overline{u_i u_j} = \frac{2}{3}\delta_{ij}k - \nu_t\left(\frac{\partial U_i}{\partial x_j} + \frac{\partial U_j}{\partial x_i}\right), \qquad (11)$$

where $\nu_t = c_\mu \rho k^2/\tilde{\varepsilon}$.

The empirical coefficients are taken as :

$$c_\mu = 0.09 exp\left(-\frac{3.4}{(1.+R_t/50)^2}\right), \quad c_{\varepsilon 1} = 1.44,$$
$$c_{\varepsilon 2} = 1.92\left(1. - 0.3 exp\left(-R_t^2\right)\right), \quad R_t = k^2/\nu\tilde{\varepsilon},$$
$$\sigma_\varepsilon = 1.3.$$

However, such an approximation excludes the buoyancy generation terms from the transport equations, and therefore, for the shear stress we make a local-equilibrium truncation of a simple second-moment closure. This leads to :

$$\overline{uv} = -\frac{k}{\varepsilon}\frac{1}{c_1}\left[(1-c_2)P_{12} + (1-c_3)G_{12}\right] \qquad (12)$$

which, to a first approximation, may be written (for single-diffusive flow):

$$\overline{uv} = -\frac{k}{\varepsilon}\frac{1}{c_1}\left[c_1 c_\mu k\left(\frac{\partial U}{\partial y} + \frac{\partial V}{\partial x}\right) + \beta g \overline{v\theta}\,(1-c_3)\right] \qquad (13)$$

where $c_1 = 1.8$, c_μ takes its value from the conventional eddy-viscosity model, and $c_3 = 0.5$.[1]

The scalar fluxes are approximated using a similar extension, applied to Daly and Harlow's [18] generalised gradient diffusion hypothesis, GGDH. Assuming the scalar fluxes to be in local equilibrium and adopting the usual linear redistribution of fluxes by pressure fluctuations leads to,

$$\overline{u_i\theta} = -\frac{1}{c_{1\theta}}\frac{k}{\varepsilon}\left[\overline{u_i u_j}\frac{\partial \Theta}{\partial x_j} + (1-c_{2\theta})\overline{u_j\theta}\frac{\partial U_i}{\partial x_j} + (1-c_{3\theta})g_i(\beta_\Theta\overline{\theta^2} + \beta_S\overline{\theta s})\right] \qquad (14)$$

where, $c_{1\theta} = 3.0$, $c_{2\theta} = 1/3$ and $c_{3\theta} = 1/3$.

Thus, effectively, the standard GGDH formulation (the first term) has been modified to include the exact production terms from the mean-velocity gradients and buoyancy (diminished by pressure fluctuations). At the very least, this practice ensures that a finite value for the flux is obtained for those flows in which the mean-temperature gradients are very small — or buoyancy effects are dominant. An entirely analogous equation is employed for $\overline{u_i s}$.

[1] Or, in tensor notation :

$$\overline{u_i u_j} = -\frac{1}{c_1}\frac{k}{\varepsilon}\left\{c_1\frac{\varepsilon}{k}\left[\frac{2}{3}\delta_{ij}k - \nu_t\left(\frac{\partial U_i}{\partial x_j} + \frac{\partial U_j}{\partial x_i}\right)\right] + (1-c_3)\,g_i\left(\beta_\Theta\overline{u_j\theta} + \beta_S\overline{u_j s}\right)\right\}$$

2.3 High-Re Region

The extended k-ε model has been interfaced with full second-moment-closure models in the high-Re region. Some details of the closure approximations are now given.

In the transport equation for the turbulent stresses (3), the production,

$$P_{ij} \equiv -\left(\overline{u_i u_k}\frac{\partial U_j}{\partial x_k} + \overline{u_j u_k}\frac{\partial U_i}{\partial x_k}\right) \qquad (15)$$

and buoyancy generation

$$G_{ij} \equiv -\left[g_i\left(\beta_\Theta\overline{u_j\theta} + \beta_S\overline{u_j s}\right) + g_j\left(\beta_\Theta\overline{u_i\theta} + \beta_S\overline{u_i s}\right)\right] \qquad (16)$$

terms are exact and need no approximation. For the pressure-strain interaction, both the linear (basic) Gibson and Launder [10], and cubic, realizable (Craft et al [19]) closure approximations have been implemented; these are given in Table 1. For the dissipative terms the assumption of local isotropy gives:

$$\varepsilon_{ij} = 2\nu\overline{\frac{\partial u_i}{\partial x_k}\frac{\partial u_j}{\partial x_k}} = \frac{2}{3}\delta_{ij}\varepsilon \qquad (17)$$

where the following transport equation is solved for ε :

$$\frac{D\varepsilon}{Dt} = \frac{\partial}{\partial x_k}\left[\left(\frac{k}{\varepsilon}\overline{u_k u_l} + \nu\delta_{kl}\right)\frac{\partial \varepsilon}{\partial x_l}\right] + \frac{c_{\varepsilon 1}}{2}\left(P_{kk} + G_{kk}\right) - c_{\varepsilon 2}\frac{\varepsilon^2}{k}. \qquad (18)$$

The form of the ε equation is identical for the basic and cubic models. However, the coefficient $c_{\varepsilon 2}$ is taken as a function of the stress invariants for the cubic model.

	basic	cubic
$c_{\varepsilon 1}$	1.44	1.
$c_{\varepsilon 2}$	1.92	$1.92/(1. + 0.7A_2^{1/2}A)$

For both models the diffusion term is represented by Daly and Harlow's GGDH.

Similarly, for each of the scalar fluxes, the transport equation (5) requires closure. The production and buoyancy-related generation terms,

$$P_{i\theta} \equiv -\left(\overline{u_i u_j}\frac{\partial \Theta}{\partial x_j} + \overline{u_j\theta}\frac{\partial U_i}{\partial x_j}\right) \qquad (19)$$

$$G_{i\theta} \equiv -g_i\left(\beta_\Theta\overline{\theta^2} + \beta_S\overline{\theta s}\right) \qquad (20)$$

are determinable; the pressure-scalar gradient interaction is approximated using either the basic or cubic, realizable model (both presented in Table 2); the assumption of local isotropy renders the dissipation term zero, i.e.

$$\epsilon_{i\theta} = (\gamma_\Theta + \nu)\overline{\frac{\partial \theta}{\partial x_k}\frac{\partial u_i}{\partial x_k}} = 0. \qquad (21)$$

and the Daly–Harlow proposal is used for the diffusion term.

For the scalar variances, $\overline{\theta^2}$ and $\overline{s^2}$ (which appear in the buoyant generation term in the scalar–flux transport equations), their respective transport equations (6) require approximations for the diffusion term and the dissipation term; the production terms again require no approximation. The diffusion term is closed using the GGDH, while for the dissipative contribution the following common approximation is adopted :

$$\varepsilon_\theta \equiv 2\gamma_\Theta \overline{\frac{\partial\theta}{\partial x_i}}^2 = \frac{R}{2}\frac{\overline{\theta^2}\varepsilon}{k}, \qquad (22)$$

where the time–scale ratio, R, is taken as a constant. In this study, R has been taken as 2.

The cross–correlation term, $\overline{\theta s}$, which couples the turbulent transport of heat and species concentration, is also determined from the solution of its transport equation (7). An analogous approach to that used for the scalar variances has been employed, namely the diffusion terms have been approximated via the GGDH, and a constant time–scale ratio has been used for the dissipation term, ie :

$$\varepsilon_{\theta s} \equiv (\gamma_\Theta + \gamma_S)\overline{\frac{\partial\theta}{\partial x_i}\frac{\partial s}{\partial x_i}} = \frac{R}{2}\frac{\overline{\theta s}\varepsilon}{k} \qquad (23)$$

3 NUMERICAL FRAMEWORK

The system of strongly coupled transport equations are solved in a semi–implicit manner. The solution algorithm is based on the TEAM code, which is described by Huang and Leschziner [21]. Briefly, this is a structured finite–volume solver with a staggered, orthogonal grid, which may be Cartesian or cylindrical polar. The code uses central–differencing for the diffusion terms and the QUICK (Leonard [22]) scheme to evaluate the convective fluxes. The pressure–velocity coupling is maintained though the SIMPLE algorithm of Patankar [23]. The equations are discretised in time using the Euler implicit method.

4 MODEL PERFORMANCE

4.1 Single Penetrative Diffusion

Initially, attention is directed towards the physically simpler cases of buoyantly–driven convection and diffusion arising purely from temperature gradients. The first case is that of an initially stably stratified flow, heated from below. A key feature of interest is the progress of the interface between the well–mixed lower layer and the stably stratified upper layer, Figure 3. Such flow situations commonly arise in the atmosphere where the diurnal heating of the ground creates a near–ground mixed layer.

As heat is supplied from below to this idealised two–layer system, the interface moves progressively upwards. If heat is supplied at a constant rate, a self–similar solution eventually develops (although the flow continues to develop in time), which allows the behaviour of any property at any time to be displayed by way of a single distribution. Willis and Deardorff [15] assembled data from a range of sources (some measurements from the atmosphere, some laboratory data), and presented them in this self–similar form.

To bypass the need to generate turbulence from an initially quiescent field, and to bridge the viscous sub–layer, an initial turbulence profile is prescribed, and the lower–boundary values are calculated from empirical algebraic relations, given by Zeman and Lumley [24]. Thus, in these calculations, the low–Re k–ε model is not employed: the flow is calculated using only the high–Re second–moment–closure models.

Figure 2 shows self–similar profiles of some of the turbulence correlations. The turbulent temperature fluctuations, vertical heat flux and vertical velocity fluctuations show good agreement within the experimental scatter, even though, as indicated in Figure 3, there is negligible mean–temperature variation across the region $z < z_i$. The predictions for the horizontal turbulent stress appear to indicate a higher level of anisotropy than observed in the experiments and environmental observations. However, overall, both of the pressure–strain/pressure–scalar–gradient models give good agreement with the observed profiles.

Whilst the two pressure–strain/pressure–scalar gradient models do not give decisively different results for these flow conditions, it is interesting to note that, for the cubic model, there are no empirical coefficients relating to either the buoyant terms or the heat fluxes, nor are there any wall–reflection corrections.

4.2 Vertical Flow in an Infinite Cavity

The buoyancy–driven flow in an infinitely tall cavity, which is shown schematically in Figure 2, is an interesting one to investigate, since any model applied to such a flow must be able to represent the wall heat transfer and the resulting buoyancy–induced circulation. The two–layer approach which was described in Section 2 was examined and refined by application to this flow.

Figure 5 compares DNS data from Boudjemadi et al [16] with the present closure predictions for a Rayleigh number, $\beta g D^3 \Delta\Theta/\gamma\nu$ of 5.4×10^5. The buoyancy–modified GGDH, which was used to evaluate the scalar fluxes in the near–wall region, links the temperature gradient and the buoyancy terms with the heat fluxes. With the basic model, the heat–flux profile clearly shows the interface between the

regions where the GGDH is applied and where the transport equations are solved. Since the absence of diffusive transport of $\overline{u\theta}$ is the only difference from the basic version of the transport equation for $\overline{u\theta}$ it would appear that it is this process which is responsible for the discontinuity in Figure 5b. In contrast — though perhaps fortuitously — the cubic model leads to a smoothly continuous profile of $\overline{u\theta}$.

However, the cubic model returns appreciably too low levels of mean velocity which is partly a consequence of predicting too low levels of shear stress in the core, Figure 5d, and partly of too low mean-temperature (and thus density) gradients there, Figure 5a. It should perhaps be noted that the DNS data, while unquestionably of good accuracy, gives rise to such low turbulent Reynolds numbers that it is hardly surprising that these high-Reynolds-number models should exhibit anomalies. Finally, before leaving this case, the good agreement with the shear stress close to the wall is noted. Interestingly, despite the mean-velocity gradient changing sign, the DNS data indicate a turbulent shear stress that is everywhere positive. This behaviour is due partly to a diffusion of shear stress towards the wall (from the core region where the shear stress is large and positive) and partly to the fact that the shear stress is affected in a stratified flow by the horizontal heat flux. The former effect cannot be accounted for in a local-equilibrium formulation but, in the extended formula for the shear stress adopted here, Equation (13) the latter effect *is*. This practice enables a reasonably satisfactory accord with the DNS data to be achieved.

4.3 1D Double Diffusion

The double-diffusive system initially comprises a uniform temperature distribution and a linear, stabilising salinity gradient, as shown schematically in Figure 1. This initially quiescent system is heated from below. The heating initiates Bénard convection, turbulence is generated and a lower, mixed layer develops; thus, the salinity gradient is gradually eroded.

One of the additional complications that arises in calculating a flow such as this, is that the stable salinity gradient inhibits the generation of turbulence energy. Although, in reality, the onset of heating of the system generates sufficient turbulence to erode the salinity gradient, here it is necessary to provide an initial level of background turbulence to overcome the salinity-related damping.

The experimental data from Bergman et al [9], show the development of the lower mixed layer at different times. Figures 6a and 6b compare the experimental temperature profiles with predictions at two different times. Both closures predict the evolution of the lower mixed layer. The computed salinity profiles, Figures 6c and 6d, show (qualitatively) the erosion of the stablising salinity gradient, as the turbulent lower mixed layer evolves.

Bergman's calculations, based on a k—ε model with an eddy-diffusivity-type model for the scalar fluxes, show turbulence energy levels two orders of magnitude higher than those found in the present study. However, calculations by Hanjalić and Musemić [13], who used a k-ε model in conjunction with an algebraic flux model for the turbulent scalar quantities, give turbulence-energy levels in line with those predicted in the present research.

5 CONCLUSIONS

The paper has reported results obtained within a two-layer-modelling framework selected with the aim of accounting for some of the complexities of transient double-diffusive flow within an acceptable computing budget. These preliminary results indicate that the model is capable of capturing some of the features characteristic of the double-diffusive system observed in LNG storage tanks.

In particular, the penetrative single-diffusive study indicated that the model can reproduce correctly the progressive erosion of a stable stratification. The buoyancy-driven cavity study demonstrated that the model represents heat-transfer through a vertical wall reasonably well, although further development of the ε equation in the sublayer model may be desirable to improve the overall turbulence predictions.

The 1D double-diffusion study showed promising results and indicated that the model should extend well to consideration of the 2D geometry. It is worth noting that in the 2D and axi-symmetric flows to be examined in the future, there will also be turbulence production through shear, and it is for shear flows that the second-moment closures have predominantly been tested.

Acknowledgements This work was supported by the EPSRC and British Gas plc. under grant GR/K00165. Carol Armitage would like to thank Dr Tim Craft for his assistance, invaluable advice and encouragement throughout the course of this research. Thanks are also due to Dr Nadir Ince for making his computational code available.

NOMENCLATURE

a_{ij}	dimensionless anisotropic stress
A	flatness parameter $\equiv 1 - 9/8(A_2 - A_3)$
A_2, A_3	invariants of Reynolds stresses: $A_2 \equiv a_{ij}a_{ji}$, $A_3 \equiv a_{ij}a_{jk}a_{ki}$.
D_{ij}	tensor appearing in ϕ_{ij} : $-(\overline{u_iu_k}\partial U_k/\partial x_j + \overline{u_ju_k}\partial U_k/\partial x_i)$
g_i	gravitational acceleration vector
G_{ij}	buoyant generation rate of $\overline{u_iu_j}$

$G_{i\theta}$	buoyant generation rate of $\overline{u_i\theta}$
k	turbulent kinetic energy
n_i	component of unit vector normal to wall
p	fluctuating pressure
P	mean pressure
P_{ij}	shear generation of $\overline{u_iu_j}$
$P_{i\theta}$	generation rate of $\overline{u_i\theta}$
$P_{\theta\theta}$	generation rate of $\overline{\theta^2}$
R	time-scale ratio
Ra	Rayleigh number, $g\beta D^3\Delta\Theta/\gamma\nu$
Re	Reynolds number, UD/ν
s	species-concentration fluctuation
S	mean-species concentration
t	time coordinate
u_i	velocity-fluctuation vector
$\overline{u_iu_j}$	kinematic Reynolds stress
$\overline{u_i\theta}$, $\overline{u_is}$	kinematic scalar flux
U_i	mean-velocity vector
w	vertical-velocity fluctuations
x_i	position coordinate
z	vertical coordinate
β_Θ, β_S	expansion coefficient for temperature and species concentration
β_i	buoyancy parameter in direction x_i
γ	molecular diffusivity
ε	rate of turbulence energy dissipation
θ	temperature fluctuation
Θ	mean temperature
μ	dynamic viscosity
ν	kinematic viscosity
ν_t	turbulent viscosity
ϕ_{ij}	pressure-strain term of $\overline{u_iu_j}$
$\phi_{i\theta}$	pressure-scalar-gradient term of $\overline{u_i\theta}$
ρ	density
σ_t	turbulent Prandtl number
i,j,k	tensor indices
0	reference value
s	solutal
t	turbulent
Θ	thermal

REFERENCES

1. Takao, S., Tsuchiya, M., Narusawa, U., "Numerical study of the onset of double-diffusive cellular convection due to a uniform lateral heat flux", J. Heat Transfer, 1982, Vol 104, pp. 649-655.

2. Rastogi, S.K., Poulikakos, D., "Double-diffusion in a liquid layer underlying a permeable solid region", Num. Heat Transfer, 1993, Vol 24, pp. 427-449.

3. Phanikumar, M.S., "Thermo-solutal convection in a rectangular enclosure with strong side-walls and bottom heating", Int. J. Heat Fluid Flow, 1994, Vol 15, pp. 325-336.

4. Lee, J.W., Hyun, J.M., "Time-dependent double-diffusion in a stably stratified fluid under lateral heating", Int. J. Heat Mass Transfer, 1991, Vol 34, pp. 2409-2421.

5. Béghein, C., Haghighat, F., Allard, F., "Numerical study of double-diffusive natural convection in a square cavity", Int. J. Heat Mass Transfer, 1992, Vol 35, pp. 833-846.

6. Kamakura, K., Ozoe, H., "Experimental and numerical analyses of double-diffusive natural convection heated and cooled from opposing vertical walls with an initial condition of a vertically linear concentration gradient", Int. J. Heat Mass Transfer, 1993, Vol 36, pp. 2125-2134.

7. Michioku, K., Plate, E., " Turbulence modelling of double-diffusive convection", 5^{th} Int. Symp. on Refined Flow Modelling and Turbulence Measurement, Paris, 1993, pp. 753-761.

8. Turner, J.S., "The coupled turbulent transport of salt and heat across a sharp density interface", Int. J. Heat Mass Transfer, 1965, Vol 8, pp. 759-767.

9. Bergman, T.L., Incropera, F.P., Viskanta, R., "A differential model for salt-stratified, double-diffusive systems heated from below", Int. J. Heat Mass Transfer, 1985, Vol 28, 1985, pp. 779-788.

10. Gibson, M.M., Launder, B.E., "Ground effects on pressure fluctuations in the atmospheric boundary layer", J. Fluid Mech., 1978, Vol 86, pp. 491-511.

11. Bergman, T.L., Incropera, F.P., Stevenson, W.H., "Miniature fibre-optic refractometer for measurement of salinity in double-diffusive thermohaline systems", Rev. Sci. Instrum., 1985, Vol 56, pp. 291-296.

12. Hullender, T.A., Laster, W.R., "Numerical model of wind-induced entrainment in a double-diffusive thermohaline system", 1994, Vol 25, pp. 43-55.

13. Hanjalić, K., Musemić, R., "Modelling the dynamics of double-diffusive scalar fields at various stability conditions", Int. J. Heat Fluid Flow, 1996, Vol 18, pp. 360-367.

14. Pham, C.T., Petit, J.P., "Simultaneous heat and mass transfers with or without evaporation in unsteady turbulent natural convection and application to liquefied natural gas storage",

15. Willis, G.E., Deardorff, J.W., "A laboratory model of the unstable planetary boundary layer", J. Atmos. Sci., 1974, July, pp. 1297–1307.

16. Boudjemadi, R., Maupu, V., Laurence, D., "Budgets of turbulent stresses and fluxes in vertical slot natural convection at Rayleigh numbers, $Ra = 10^5$ and $Ra = 5.4 \times 10^5$", Turbulent Heat Transfer Conf., San Diego, 1996, (Engineering Foundation).

17. Launder, B.E., Sharma, B.I., "Application of the energy dissipation model of turbulence to the calculation of flows near a spinning disk", Int. J. Heat Mass Transfer, 1974, Vol 1, p. 131.

18. Daly, B.J., Harlow, F.H., "Transport equations in turbulence", Phys. Fluids, 1970, Vol 13, p. 2634.

19. Craft, T.J., Ince, N.Z., Launder, B.E., "Recent developments in second–moment closure for buoyancy–affected flow", Dynamics of Atmos. Oceans, 1996, Vol 23, pp. 99–114.

20. Lumley, J.L., "Computational modelling of turbulent flows", Adv. Appl. Mech., 1978, Vol 18, p. 123.

21. Huang, P.G., Leschziner, M.A., "An introduction and guide to the computer code TEAM", 1983, TFD/83/9(R).

22. Leonard, B.P., "A stable and accurate convective modelling procedure based ion quadratic upstream interpolation", 1979, Comp. Meth. Appl. Mech. Eng., Vol 19, pp. 59–98.

23. Patankar, S.V., "Numerical heat transfer and fluid flow", 1980, (Hemisphere Publishing Corporation, McGraw Hill).

24. Zeman, O., Lumley, J.L., "Modelling buoyancy–driven mixed layers", 1976, J. Atmos. Sci., Vol 33, pp. 1974–1988.

$$\phi_{ij} = \phi_{ij1} + \phi_{ij2} + \phi_{ij3} + \phi^w_{ij}$$

Linear model :

$$\phi_{ij1} = -c_1 \epsilon a_{ij} \qquad \phi_{ij2} = -c_2 \left(P_{ij} - 1/3 \delta_{ij} P_{kk}\right) \qquad \phi_{ij3} = -c_3 \left(G_{ij} - 1/3 \delta_{ij} G_{kk}\right)$$

$$\begin{aligned} \phi^w_{ij} &= c_{w1} \frac{\varepsilon}{k} \left[\overline{u_l u_m} n_l n_m \delta_{ij} - \frac{3}{2} \overline{u_i u_l} n_j n_l - \frac{3}{2} \overline{u_j u_l} n_i n_l \right] \frac{k \overline{v^2}^{1/2}}{1.5 \varepsilon y} \\ &\quad + c_{w2} \left[\phi_{lm2} n_l n_m \delta_{ij} - \frac{3}{2} \phi_{il2} n_j n_l - \frac{3}{2} \phi_{jl2} n_i n_l \right] \frac{k \overline{v^2}^{1/2}}{1.5 \varepsilon y} \end{aligned}$$

where $\overline{v^2}$ is the stress normal to the wall, $c_1 = 1.8, c_2 = 0.6, c_3 = 0.5, c_{w1} = 0.5$ and $c_{w2} = 0.3$.

Cubic model :

$$\begin{aligned} \phi_{ij1} &= -c_1 \epsilon \left(a_{ij} + c_1' \left(a_{ik} a_{jk} - 1/3 A_2 \delta_{ij}\right)\right) - \epsilon a_{ij} \\ \phi_{ij2} &= -0.6 \left(P_{ij} - 1/3 \delta_{ij} P_{kk}\right) + 0.3 \epsilon a_{ij} \left(P_{kk}/\epsilon\right) \\ &\quad - 0.2 \left[\frac{\overline{u_k u_j}\, \overline{u_l u_i}}{k} \left(\frac{\partial U_k}{\partial x_l} + \frac{\partial U_l}{\partial x_k} \right) - \frac{\overline{u_l u_k}}{k} \left(\overline{u_i u_k} \frac{\partial U_j}{\partial x_l} + \overline{u_j u_k} \frac{\partial U_i}{\partial x_l} \right) \right] \\ &\quad - c_2 \left[A_2 \left(P_{ij} - D_{ij}\right) + 3 a_{mi} a_{nj} \left(P_{mn} - D_{mn}\right) \right] \\ &\quad + c_2' \left\{ \left(\frac{7}{15} - \frac{A_2}{4} \right) \left(P_{ij} - 1/3 \delta_{ij} P_{kk}\right) + 0.1 \epsilon \left[a_{ij} - 1/2 \left(a_{ik} a_{kj} - 1/3 \delta_{ij} A_2\right) \right] \left(P_{kk}/\epsilon\right) - 0.05 a_{ij} a_{lk} P_{kl} \right. \\ &\quad + 0.1 \left[\left(\frac{\overline{u_i u_m}}{k} P_{mj} + \frac{\overline{u_j u_m}}{k} P_{mi} \right) - 2/3 \delta_{ij} \frac{\overline{u_l u_m}}{k} P_{ml} \right] \\ &\quad \left. + 0.1 \left[\frac{\overline{u_l u_i}\, \overline{u_k u_j}}{k^2} - 1/3 \delta_{ij} \frac{\overline{u_l u_m}\, \overline{u_k u_m}}{k^2} \right] \left[6 D_{lk} + 13 k \left(\frac{\partial U_l}{\partial x_k} + \frac{\partial U_k}{\partial x_l} \right) \right] + 0.2 \frac{\overline{u_l u_i}\, \overline{u_k u_j}}{k^2} \left(D_{lk} - P_{lk}\right) \right\} \\ \phi_{ij3} &= -\left(\frac{4}{10} + \frac{3 A_2}{80} \right) \left(G_{ij} - 1/3 \delta_{ij} G_{kk}\right) + \frac{1}{4} a_{ij} G_{kk} \\ &\quad + \frac{3}{20} \left(g_i \frac{\overline{u_m u_j}}{k} + g_j \frac{\overline{u_m u_i}}{k} \right) \left(\beta_\Theta \overline{u_m \theta} + \beta_S \overline{u_m s} \right) - \frac{1}{10} \delta_{ij} g_k \frac{\overline{u_m u_k}}{k} \left(\beta_\Theta \overline{u_m \theta} + \beta_S \overline{u_m s} \right) \\ &\quad - \frac{1}{4} g_k \left(\frac{\overline{u_k u_i}}{k} \left(\beta_\Theta \overline{u_j \theta} + \beta_S \overline{u_j s} \right) + \frac{\overline{u_k u_j}}{k} \left(\beta_\Theta \overline{u_i \theta} + \beta_S \overline{u_i s} \right) \right) + \frac{1}{20} \delta_{ij} g_k \frac{\overline{u_m u_n}\, \overline{u_m u_k}}{k^2} \left(\beta_\Theta \overline{u_n \theta} + \beta_S \overline{u_n s} \right) \\ &\quad - \frac{1}{8} \left[\frac{\overline{u_m u_j}}{k} \left(\beta_\Theta \overline{u_i \theta} + \beta_S \overline{u_i s} \right) + \frac{\overline{u_m u_i}}{k} \left(\beta_\Theta \overline{u_j \theta} + \beta_S \overline{u_j s} \right) \right] \frac{\overline{u_m u_k}}{k} g_k \\ &\quad + \frac{1}{8} \left[\frac{\overline{u_k u_i}\, \overline{u_m u_j}}{k^2} + \frac{\overline{u_k u_j}\, \overline{u_m u_i}}{k^2} \right] g_k \left(\beta_\Theta \overline{u_m \theta} + \beta_S \overline{u_m s} \right) \\ &\quad - \frac{3}{40} \left(g_i \frac{\overline{u_m u_j}}{k} + g_j \frac{\overline{u_m u_i}}{k} \right) \frac{\overline{u_m u_n}}{k} \left(\beta_\Theta \overline{u_n \theta} + \beta_S \overline{u_n s} \right) + \frac{1}{4} g_k \frac{\overline{u_m u_k}\, \overline{u_i u_j}}{k^2} \left(\beta_\Theta \overline{u_n \theta} + \beta_S \overline{u_n s} \right) \\ \phi^w_{ij} &= 0. \end{aligned}$$

where $c_1 = 3.1 (A_2 A)^{1/2}, c_1' = 1.2, c_2 = 0.55$ and $c_2' = 0.6$.

Table 1: Pressure–strain models for $\overline{u_i u_j}$ equations

$$\phi_{i\theta} = \phi_{i\theta 1} + \phi_{i\theta 2} + \phi_{i\theta 3}$$

Linear model :

$$\phi_{i\theta 1} = -c_{1\theta}\frac{\epsilon}{k}\overline{u_i\theta} \qquad \phi_{i\theta 2} = c_{2\theta}\overline{u_k\theta}\frac{\partial U_i}{\partial x_k} \qquad \phi_{i\theta 3} = -c_{3\theta}G_{i\theta}$$

where $c_{1\theta} = 3.0, c_{2\theta} = 1/3$ and $c_{3\theta} = 1/3$.

Cubic model:

$$\begin{aligned}
\phi_{i\theta 1} &= -1.7\left[1 + 1.2\left(A_2 A\right)^{1/2}\right] R^{1/2}\frac{\epsilon}{k}\left[\overline{u_i\theta}\left(1 + 0.6A_2\right) - 0.8a_{ik}\overline{u_k\theta}\right. \\
&\quad \left. + 1.1a_{ik}a_{kj}\overline{u_j\theta}\right] - 0.2A^{1/2}Rka_{ij}\frac{\partial\Theta}{\partial x_j} \\
\phi_{i\theta 2} &= 0.8\overline{u_k\theta}\frac{\partial U_i}{\partial x_k} - 0.2\overline{u_k\theta}\frac{\partial U_k}{\partial x_i} + 1/6\frac{\epsilon}{k}\overline{u_i\theta}(P_{kk}/\epsilon) \\
&\quad - 0.4\overline{u_k\theta}a_{il}\left(\frac{\partial U_k}{\partial x_l} + \frac{\partial U_l}{\partial x_k}\right) \\
&\quad + 0.1\overline{u_k\theta}a_{ik}a_{ml}\left(\frac{\partial U_m}{\partial x_l} + \frac{\partial U_l}{\partial x_m}\right) \\
&\quad - 0.1\overline{u_k\theta}\left(a_{im}P_{mk} + 2a_{mk}P_{im}\right)/k \\
&\quad + 0.15a_{ml}\left(\frac{\partial U_k}{\partial x_l} + \frac{\partial U_l}{\partial x_k}\right)\left(a_{mk}\overline{u_i\theta} - a_{mi}\overline{u_k\theta}\right) \\
&\quad - 0.05a_{ml}\left[7a_{mk}\left(\overline{u_i\theta}\frac{\partial U_k}{\partial x_l} + \overline{u_k\theta}\frac{\partial U_i}{\partial x_l}\right) - \overline{u_k\theta}\left(a_{ml}\frac{\partial U_i}{\partial x_k} + a_{mk}\frac{\partial U_i}{\partial x_l}\right)\right] \\
\phi_{i\theta 3} &= 1/3g_i\left(\beta_\Theta\overline{\theta^2} + \beta_S\overline{\theta s}\right) - g_k\left(\beta_\Theta\overline{\theta^2} + \beta_S\overline{\theta s}\right)a_{ik}
\end{aligned}$$

Table 2: Pressure–scalar flux models in $\overline{u_i\theta}$ equations

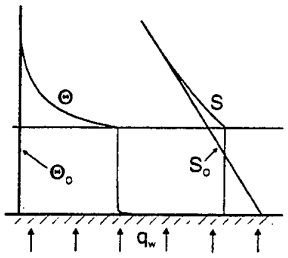

Figure 1. Schematic of double-diffusive flow.

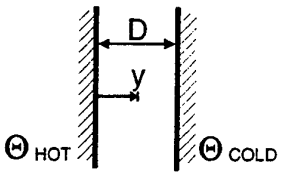

Figure 2. Schematic of flow in infinitely tall cavity.

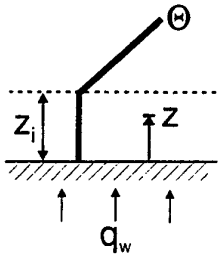

Figure 3. Schematic of 1D single-diffusive layer.

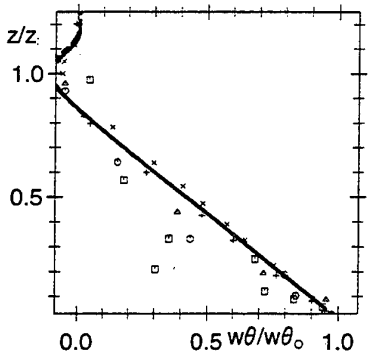

Figures 4. Normalised, self-similar profiles of turbulent correlations for 1D penetrative diffusion. — cubic,- - basic, symbols experiments.
Figure 4a. Fluctuating vertical heat flux.

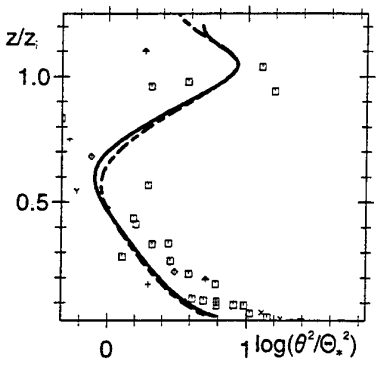

Figure 4b. Fluctuating temperature.

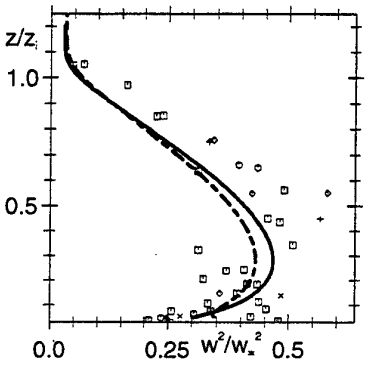

Figure 4c. Fluctuating vertical velocity.

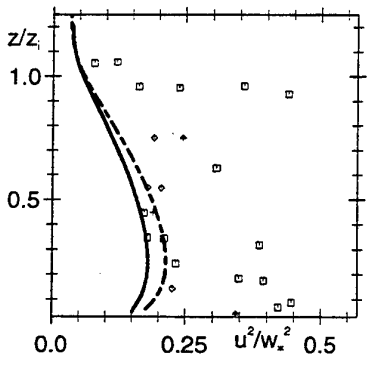

Figure 4d. Fluctuating horizontal velocity.

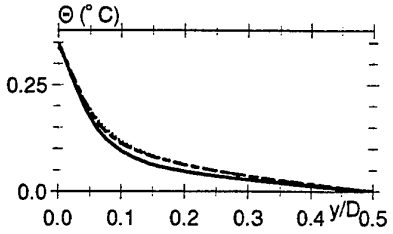

Figure 5. Property profiles for infinitely tall cavity, $Ra = 5.4 \times 10^5$. — cubic, - - linear, o DNS data from Boudjemadi et al.
Figure 5a. Mean temperature.

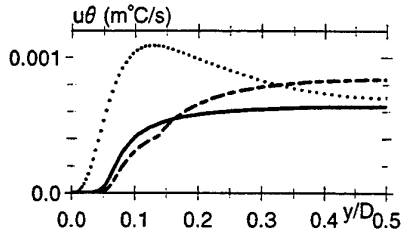

Figure 5b. Streamwise heat flux.

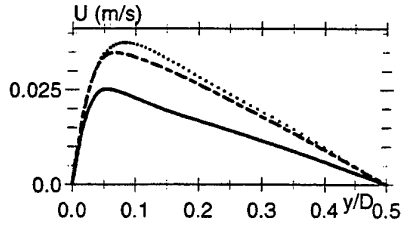

Figure 5c. Mean velocity.

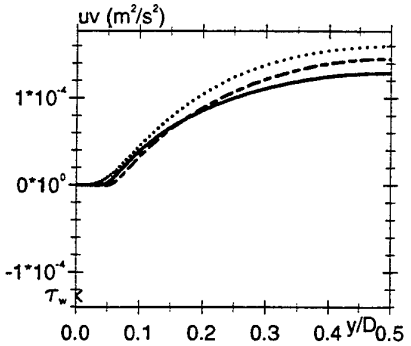

Figure 5d. Shear stress.

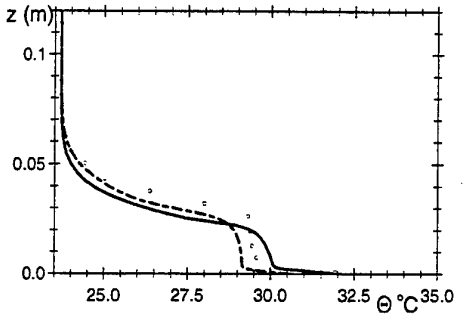

Figure 6. 1D double–diffusion case: — cubic, - - basic, o experiments from Bergman et al.
Figure 6a. Temperature Profiles at 30 mins.

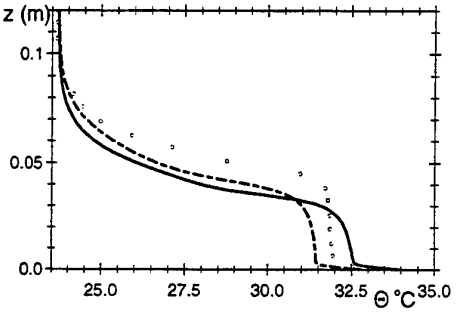

Figure 6b. Temperature Profiles at 60 mins.

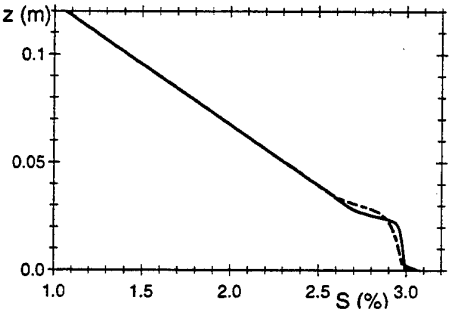

Figure 6c. Salinity Profiles at 30 mins.

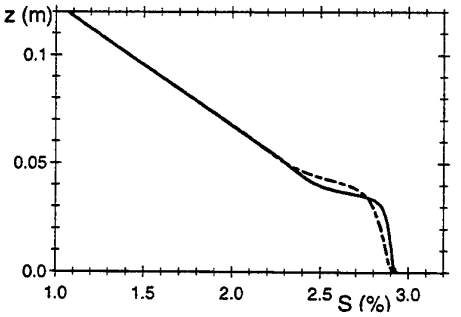

Figure 6d. Salinity Profiles at 60 mins.

Modelling the non-local turbulent transport of momentum, heat and substance in the convective PBL

B.B.Ilyushin

Institute of Theoretical & Applied Mechanics
Russia

ABSTRACT
Anisotropic properties of buoyancy effect an influence of PBL stratification mainly in the long-wave region of the turbulent fluctuation spectrum. This region corresponds to large-scale eddy formation (LSEF) containing the main part of the turbulence energy. The pdf's of turbulent fluctuations become essentially non-gaussian under the effects of intermittency and asymmetry of the vertical turbulent transport which are conditioned by LSEF. As a results, such (non-local) transport cannot be described within "standard" turbulent diffusion models of gradient type. To describe correctly the non-local turbulent transport, it is proposed to take into account the LSEF effects characterised by asymmetry and excess coefficients. The results of modelling the turbulent transport of momentum and heat in the convective PBL with using the elaborated fourth-order cumulant and triple-correlation models are presented. For describing the process of substance dispersion, the model accounting directly the effect of substance transfer by LSEF (in advection terms of the equation for the concentration) is used.

1 Modelling the turbulent transfer of momentum and heat in the convective PBL

Recent directions in turbulent flows research based on creating closed turbulent transport equations and their numerical solution on computers have been intensively developed. Such methods based on a two-parameter turbulence model and also simplified second-order closure models has led to sufficiently reliable results for many applications. However, using these models for prediction of the turbulent transfer in the convective PBL gives results that are qualitatively incorrect in some cases (see, for example (1-4)). Anisotropic properties of buoyancy effect an influence of flow stratification mainly in the long-wave region of the turbulent fluctuation spectrum (5). This region corresponds to large-scale eddy formations (LSEF) containing the main part of the turbulence energy. Experimental investigations confirm the formation of such LSEF in stratified flows: turbulent spots in stable stratification and coherent structures in unstable stratification. The turbulent transfer is achieved mainly by the action of these structures. The long lifetimes of LSEF results in a fluid (pollutant) particle, being absorbed in the field of such an eddy and, being transferred a significant distance by LSEF without any appreciable direction change. This feature is not in agreement with postulates of Euler's theory of turbulence diffusion in which the turbulent transfer is considered analogous to Brownian motion; that is, a random wandering process. As a result, such (non-local) transport cannot be described within "standard" turbulent diffusion models of gradient type. The pdf's of turbulent fluctuations become essentially non-gaussian under the effects of intermittency and asymmetry of the vertical turbulent transport which are conditioned by LSEF.

1.1 On application of the Millionshikov's quasinormality hypothesis

To describe correctly the momentum, heat and substance transport in stratified turbulent flows, it is proposed to take into account effects (on turbulent transport) of intermittency and asymmetry within the statistical moments model. For this purpose the closure model is proposed wherein the third-order correlations (asymmetry of PDF of thermohydrodynamic fields fluctuations) are calculated from differential transport equations. The quasi-normality Millionshikov hypothesis, which assumes zero fourth-order cumulants (excess coefficients) is normally used to determine processes of turbulent diffusion connected with the fourth moments thus creating semi-empirical second- and third-order turbulence models. Using this hypothesis in the transport equations for triple correlations allows one to join the terms of turbulent diffusion and production of non-linear interaction of fluctuations. The third-moment differential equations are of first order and do not take into account the essential mechanisms of the triple correlations that result. This mechanism is connected closely with the irreversibility of the energy-transformation process from large-scale eddies to dissipative ones. It was taken into account in (6-7) using the procedure of "clipping" the triple correlation values in accordance with the generalised Schwartz inequalities (the 'clipping' approximation). It is obvious that such a procedure is physically incorrect. It has been shown in modelling (8) the propagation of a passive scalar from line sources and in modelling (9) turbulence structure in the stable-stratification mixing layer that the necessary mechanism of triple correlations decreasing can be taken into account by additional diffusion terms in the third-moment equations. As it is known, using of the quasi-normality hypothesis in some cases gives the results which are contrary to physical laws (5) (for example, in (10,11) negative values appear in the turbulence kinetic energy (TKE) spectrum). The latter is a consequence of the fact that for fixed second and third moments the probability distribution with zero fourth cumulants cannot exist; it is connected closely with the inadmissibility of arbitrarily cutting the Taylor series for the characteristic functional logarithm. Velocity fluctuations of large-scale convective eddies correspond to small values of wave vector k of the TKE

spectrum. The inadequacy of the Millionshikov hypothesis for three-dimensional turbulence (it is displayed as a region of negative values in the TKE spectrum at small wave number) shows that using the hypothesis can be the reason for turbulence models incorrectly describing transport due to LSEF. It has been shown in (11) that for prediction of the early stages of turbulence the use of the quasi-normal hypothesis (i.e. the assumption of zero fourth-order cumulants) is limited to small fluctuation magnitudes in which third moments are small. On the other hand, using the hypothesis assuming zero fifth-order cumulants (for non-zero fourth-order cumulants) allows the width of applicability of the model to be markedly widened. The same strategy has been also employed in the present research.

1.1 Fourth-order cumulants model

The fourth-order cumulants for a Boussinesq fluid are written as:

$$\mathbf{C}_{ijkl} = <u_i u_j u_k u_l> - <u_i u_j><u_k u_l> - <u_i u_k><u_j u_l> - <u_i u_l><u_k u_j>,$$

$$\mathbf{C}_{ijk\theta} = <u_i u_j u_k \theta> - <u_i u_j><u_k \theta> - <u_i u_k><u_j \theta> - <u_i \theta><u_k u_j>, \qquad /1/$$

$$\mathbf{C}_{ij\theta\theta} = <u_i u_j \theta^2> - <u_i u_j><\theta^2> - 2<u_i \theta><u_j \theta>,$$

$$\mathbf{C}_{i\theta\theta\theta} = <u_i \theta^3> - 3<u_i \theta><\theta^2>,$$

$$\mathbf{C}_{\theta\theta\theta\theta} = <\theta^4> - 3<\theta^2><\theta^2>,$$

The transport equation for fourth-order cumulant $\boldsymbol{C}_{ijkl}$ assuming zero fifth-order cumulants in the high Reynolds number can be written as

$$\frac{\partial \mathbf{C}_{ijkl}}{\partial t} = \sum_{ijkl}\left[-\mathbf{C}_{ijkm}\frac{\partial U_l}{\partial x_m} - \mathbf{C}_{ijk\theta}\beta g_m \delta_{ml} - \frac{1}{\rho}\left\{\left\langle u_i u_j u_k \frac{\partial p}{\partial x_l}\right\rangle - <u_i u_j>\left\langle u_k \frac{\partial p}{\partial x_m}\right\rangle - <u_i u_k>\left\langle u_j \frac{\partial p}{\partial x_m}\right\rangle\right\}\right.$$
$$- <u_j u_k>\left\langle u_i \frac{\partial p}{\partial x_m}\right\rangle\Big\} - <u_i u_j u_m>\frac{\partial <u_k u_l>}{\partial x_m} \qquad /2/$$
$$- <u_i u_k u_m>\frac{\partial <u_j u_l>}{\partial x_m} - <u_j u_k u_m>\frac{\partial <u_i u_l>}{\partial x_m}$$
$$\left. - <u_i u_m>\frac{\partial <u_j u_k u_l>}{\partial x_m}\right],$$

where symbol Σ means the sum of functions with the cyclical rearrangement of indexes (for example: $\Sigma_{ijkl}F(u_i,u_j\ u_k,u_l,u_m) = F(u_i,u_j,u_k\ u_l,u_m) + F(u_l,u_i,u_j,u_k,u_m) + F(u_k,u_l,u_i,u_j,u_m) + F(u_j,u_k,u_l,u_i,u_m)$). With the relaxation model applied to the cumulant of the pressure containing correlation (the terms in the braces), it is possible to derive from /2/ the algebraic model for the cumulant $\boldsymbol{C}_{ijkl}$ in the stationary case:

$$\mathbf{C}_{ijkl} = -\frac{\tau}{C_4}\left\{\sum_{ijkl}\left[\mathbf{C}_{ijkm}\frac{\partial U_l}{\partial x_m} + \mathbf{C}_{ijk\theta}\beta g_m \delta_{lm} + <u_i u_j u_m>\frac{\partial <u_k u_l>}{\partial x_m} + <u_i u_m>\frac{\partial <u_j u_k u_l>}{\partial x_m}\right]\right.$$
$$\left. + <u_i u_k u_m>\frac{\partial <u_j u_l>}{\partial x_m} + <u_j u_l u_m>\frac{\partial <u_i u_k>}{\partial x_m}\right\} \qquad /3/$$

By the same way, the models for the mixed cumulants are derived:

$$\mathbf{C}_{ijk\theta} = -\frac{\tau}{C_{4\theta}}\left\{\sum_{ijk}\left[\mathbf{C}_{ijm\theta}\frac{\partial U_k}{\partial x_m} + \mathbf{C}_{ijkm}\frac{\partial \Theta}{\partial x_m} + \mathbf{C}_{ij\theta\theta}\beta g_m \delta_{km}\right.\right.$$
$$+ <u_i u_j u_m>\frac{\partial <u_k \theta>}{\partial x_m} + <u_i \theta u_m>\frac{\partial <u_j u_k>}{\partial x_m} +$$
$$\left.\left. <u_i u_m>\frac{\partial <u_j u_k \theta>}{\partial x_m}\right] + <\theta u_m>\frac{\partial <u_i u_j u_k>}{\partial x_m}\right\}$$

$$\mathbf{C}_{ij\theta\theta} = -\frac{\tau}{C_{4\theta}}\left\{\sum_{ij}\left[\mathbf{C}_{im\theta\theta}\frac{\partial U_j}{\partial x_m} + 2\mathbf{C}_{ijm\theta}\frac{\partial \Theta}{\partial x_m} + \mathbf{C}_{i\theta\theta\theta}\beta g_m \delta_{jm}\right.\right.$$
$$+ <\theta u_m>\frac{\partial <u_i u_j \theta>}{\partial x_m} + 2<u_i \theta u_m>\frac{\partial <u_j \theta>}{\partial x_m} + <u_i u_m>\frac{\partial <u_j \theta^2>}{\partial x_m}\Big]$$
$$\left. + <\theta^2 u_m>\frac{\partial <u_i u_j>}{\partial x_m} + <u_i u_j u_m>\frac{\partial <\theta^2>}{\partial x_m}\right\} \qquad /4/$$

$$\mathbf{C}_{i\theta\theta\theta} = -\frac{\tau}{C_{4\theta}}\left\{\mathbf{C}_{m\theta\theta\theta}\frac{\partial U_i}{\partial x_m} + 3\mathbf{C}_{im\theta\theta}\frac{\partial \Theta}{\partial x_m} + \mathbf{C}_{\theta\theta\theta\theta}\beta g_m \delta_{im}\right.$$
$$+ 3<\theta^2 u_m>\frac{\partial <u_i \theta>}{\partial x_m} + 3<u_i u_m \theta>\frac{\partial <\theta^2>}{\partial x_m}$$
$$\left. + 3<\theta u_m>\frac{\partial <u_i \theta^2>}{\partial x_m} + <u_i u_m>\frac{\partial <\theta^3>}{\partial x_m}\right\}$$

$$\mathbf{C}_{\theta\theta\theta\theta} = -\frac{\tau}{C_{4\theta}}\left\{4\,\mathbf{C}_{m\theta\theta\theta}\frac{\partial \Theta}{\partial x_m} + 6<u_m \theta^2>\frac{\partial <\theta^2>}{\partial x_m}\right.$$
$$\left. + 4<u_m \theta>\frac{\partial <\theta^3>}{\partial x_m}\right\}$$

Since the relaxation mechanism in transport equations for the cumulants is conditioned by different physical processes, the coefficients C_4, $C_{4\theta}$ and $C_{4\theta\theta}$ are distinguished.

The Schwarz' inequalities for the triple correlations is following:

$$<u_i^2><u_i^4> - <u_i^3>^2 \geq 0,$$

$$<u_i^2><u_i^2\theta^2> - <u_i^2\theta>^2 \geq 0, \qquad /5/$$

$$<\theta^2><\theta^4> - <\theta^3>^2 \geq 0.$$

Necessary relaxation of the triple correlations by Andre et al. (3) has been achieved by clipping their values (clipping approximation) with use of the generalised

Schwarz' inequality (using the quasinormality hypothesis). Taking into account /5/, the more strong inequality for the cumulants can be written:

$$\mathbf{C}_{ijkl} \geq \frac{< u_i^3 >^2}{< u_i^2 >},$$

$$\mathbf{C}_{ij\theta\theta} \geq \frac{< u_i^2\theta >^2}{< u_i^2 >}, \qquad /6/$$

$$\mathbf{C}_{\theta\theta\theta\theta} \geq \frac{< \theta^3 >^2}{< \theta^2 >}.$$

Conditions /6/ are used to estimate values of the coefficients C_4, $C_{4\theta}$ and $C_{4\theta\theta}$. For this, decay of homogeneous turbulence and heat dispersal process in the case of non-zero third- and fourth-order cumulants at initial conditions (marking by subsymbol zero) is considered satisfying the following relations:

$$< w^2 >=< w^2 >_o \exp\left[-\frac{t}{\tau}\right],$$

$$< u_i\theta >=< u_i\theta >_o \exp\left[-C_{1\theta}\frac{t}{\tau}\right],$$

$$< \theta^2 >=< \theta^2 >_o \exp\left[-r\frac{t}{\tau}\right],$$

$$< w^3 >=< w^3 >_o \exp\left[-C_3\frac{t}{\tau}\right],$$

$$< u_i^2\theta >=< u_i^2\theta >_o \exp\left[-C_{3\theta}\frac{t}{\tau}\right], \qquad /7/$$

$$< \theta^3 >=< \theta^3 >_o \exp\left[-C_{3\theta\theta}\frac{t}{\tau}\right],$$

$$\mathbf{C}_{ijkl} = \mathbf{C}_{ijkl_o} \exp\left[-C_{4\theta}\frac{t}{\tau}\right],$$

$$\mathbf{C}_{ij\theta\theta} = \mathbf{C}_{ij\theta\theta_o} \exp\left[-C_{4\theta\theta}\frac{t}{\tau}\right],$$

$$\mathbf{C}_{\theta\theta\theta\theta} = \mathbf{C}_{\theta\theta\theta\theta_o} \exp\left[-C_{\theta}\frac{t}{\tau}\right],$$

Then, it follows from /6/ taking into account /7/ that: $C_4 \leq 2C_3 - 1$, $C_{4\theta} \leq 2C_{3\theta} - r$ and $C_{4\theta\theta} \leq 2C_{3\theta\theta} - C_{1\theta}$. Using the model /3/,/4/ for the cumulants in the stationary case assumes that the fourth-order cumulant's relaxation speed is quicker than the triple-correlation one. Therefore in calculations the upper values $C_4 = 2C_3 - 1$, $C_{4\theta} = 2C_{3\theta} - r$ and $C_{4\theta\theta} = 2C_{3\theta\theta} - C_{1\theta}$ of this estimation are used.

1.2. Cumulants model testing.

The absence of detailed experimental data base on fourth-order cumulants in the convective PBL does not allow us directly to check the physical correctness of elaborate cumulants model applied to the noted types of flows. Cumulants models are tested on the basis of comparison of measured and calculated excess coefficient distributions in the neutrally stratified boundary layer on a plate (12). The experimental profiles of $<w^2>$ and $<w^3>$ are interpolated by analytic functions and are used for calculation of the kurtosis coefficient $K_w = <w^4>/<w^2>^2$ (w is the vertical velocity fluctuation). Since the distribution of turbulence time-scale τ or dissipation ε are absent in (12), in this case the assumption of correctness of algebraic triple-correlation model is used:

$$< w^3 >= -\frac{3\tau}{C_3} < w^2 > \frac{\partial < w^2 >}{\partial z}, \qquad /8/$$

where C_3 is the coefficient of the model (the values of coefficients see below in a table). The model of the cumulant C_{3333} in a neutrally stratified case is obtained from /3/:

$$\mathbf{C}_{3333} = -\frac{\tau}{C_4}\left[6 < w^3 > \frac{\partial < w^2 >}{\partial z} + 4 < w^2 > \frac{\partial < w^3 >}{\partial z}\right], \qquad /9/$$

Then, from /9/ taking into account /8/ expression for calculation of C_{3333} can be written:

$$\mathbf{C}_{3333} = \frac{C_3/3}{2C_3 - 1}\left[6\frac{< w^3 >^2}{< w^2 >} + 4 < w^3 > \frac{\partial < w^3 > / \partial z}{\partial < w^2 > / \partial z}\right], \qquad /10/$$

The result of calculation of kurtosis coefficient by /10/ is show in fig.1. It can be seen that the calculated profile of kurtosis is in a good agreement with the experimental data.

1.3 Modelling the convective PBL evolution

The gradient type third-order moment models (3,4) used at the present paper can not describe in agreement with experimental data a behaviour of both the skewness factor S_w and the vertical flux of the turbulent kinetic energy $<wE'>$ ($E' = 1/2 u_i u_i$) across the whole height of the PBL, from the ground up to the upper boundary. Moreover, in the surface layer the calculated skewness factor is negative in contrast with the observed data (13). Andre et al. (6) retained the full third-order moment prognostic equations without eddy damping terms. The profiles of $<wE'>$ calculated by Andre's model are positive across the whole height of the convective PBL, but they were forced to clip the third-order moments. It can be noted that such procedure is not physically correct. Furthermore, the model (6) is unnecessarily complex. The results of the convective PBL modelling by the new triple correlations models with using the algebraic fourth-order cumulants model /3,4/ are presented in (14). Analysing of separate tems contributions to the common balance of transport equations, it is supposed to construct an algebraic version of the triple-correlations

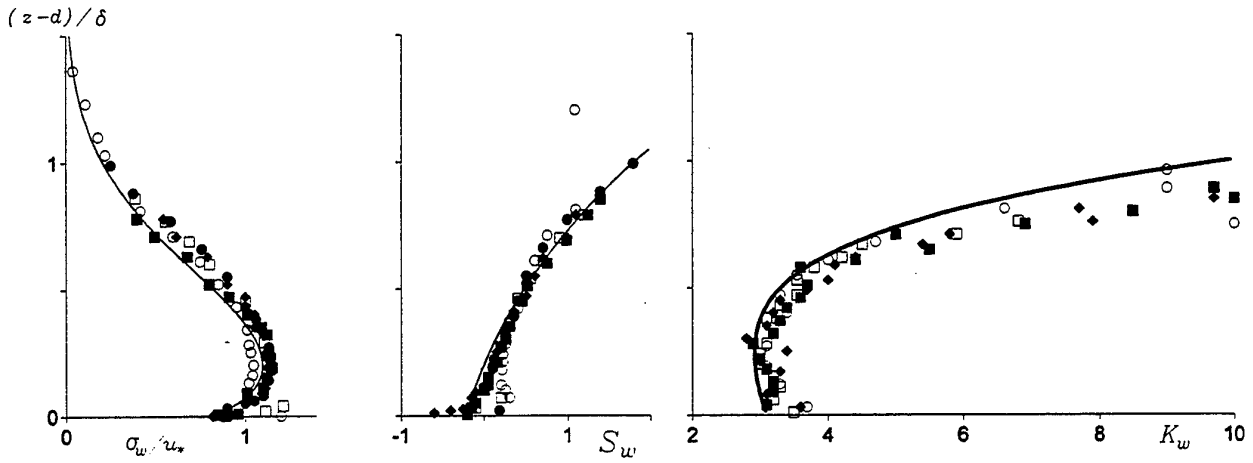

Fig. 1. The distribution of dispersal $\sigma_w=<w^2>^{1/2}$, asymmetry $S_w=<w^3>/\sigma_w^3$ and kurtosis $K_w=<w^4>/\sigma_w^4$ coefficients of vertical variance: lines correspond to interpolated functions for σ_w and S_w; line on the the right diagram is the calculated profile of kurtosis K_w with using /10/; symbols are experimental data (12).

model (15) containing computational effectivity with reliability of obtained results. This algebraic triple-correlation model is used in the present work.

The model of turbulent transport in the PBL homogeneous in horizontal plates (15) includes equations for the mean wind components U_x and U_y, mean potential temperature Θ, its dispersion $<\theta^2>$, vertical $<w^2>$ and horizontal e_h components of the turbulent kinetic energy, and its dissipation ε. The shear components of the Reynolds stress tensor $<u_iu_j>$, horizontal components of the turbulent kinetic energy e_h as well as heat flux $<u_i\theta>$ are calculated by the gradient transport models taking into account both anisotropy of turbulent transport and dependence of the turbulence time scale on the Brunt-Vaisala frequency N ($N^2=\beta g\partial\Theta/\partial z$). The triple correlations $<w^3>$, $<w^2\theta>$ and $<w\theta^2>$ are calculated from the algebraic model (15):

$$<w^3>=-\frac{3\tau_3}{C_3}\left[<w^2>\frac{\partial<w^2>}{\partial z}+\frac{2(\tau_3\beta g)^2}{C_3C_{3\theta}\left(1+\frac{4}{C_3C_{3\theta}}\tau_3^2N^2\right)}<w^2>\frac{\partial<\theta>}{\partial z}\right],$$

$$<w^2\theta>=-\frac{2\tau_3^2\beta g<w^2>}{C_3C_{3\theta}\left(1+\frac{4}{C_3C_{3\theta}}\tau_3^2N^2\right)}\frac{\partial<\theta^2>}{\partial z}, \qquad /11/$$

$$<w\theta^2>=-\frac{\tau_3<w^2>}{C_3\left(1+\frac{4}{C_3C_{3\theta}}\tau_3^2N^2\right)}\frac{\partial<\theta^2>}{\partial z},$$

where τ_3 is the time-scale of relaxation of the triple correlations calculated in (16) taking into account the Kolmogoroff spectrum of turbulence fluctuations:

$$\tau_3=\frac{\tau}{1+H(N^2)\frac{\pi}{18}\tau^2N^2}, \qquad H(N^2)=\begin{cases}0 \text{ when } N^2<0\\ 1 \text{ when } N^2\geq 0\end{cases}$$

The details of elaboration of the triple correlations model (algebraic and differential) and definition of values of model coefficients can be seen in the paper (17). These values are used in the present work: C_3=4.0, $C_{3\theta}$=5.0.

Fig.2 shows the calculated profiles of the second- and third-order correlations (different lines correspond to time from 10 a.m. to 5 p.m.). For comparison the observed data are also shown in Fig. 2 (from (1) for second-order moments and from (5) for third-order moments). Here it can be seen that the results of calculation are in agreement with the experimental data, in particular, the calculated profiles of $<w^3>$ and $<E'w>$ are positive in the whole height of the PBL including the surface layer. The calculated profiles are used for modelling the pollutant spreading in the convective PBL.

2. Modelling the turbulent transfer of substance in the convective PBL

Experimental and theoretical investigations confirm the formation of LSEF in the convective PBL characterised by the long lifetimes and periodicity (1,18). A fluid is transported by such LSEF (coherent structures) from Earth's surface, where the turbulent energy is generated by wind shear, to the top of PBL and from the top of PBL, where the turbulent energy is suppressed by stability stratification, to the surface. Such asymmetrical mechanism of the vertical transport and the effects of intermittency of small-turbulence fluid from the top of PBL to the mixing layer are conditioned by the positive value of the correlations $<wE>$ and $<w^3>$ in the convective PBL. For describing the process of passive pollutant dispersion the model can be account an influence of coherent structures who play a key role in the

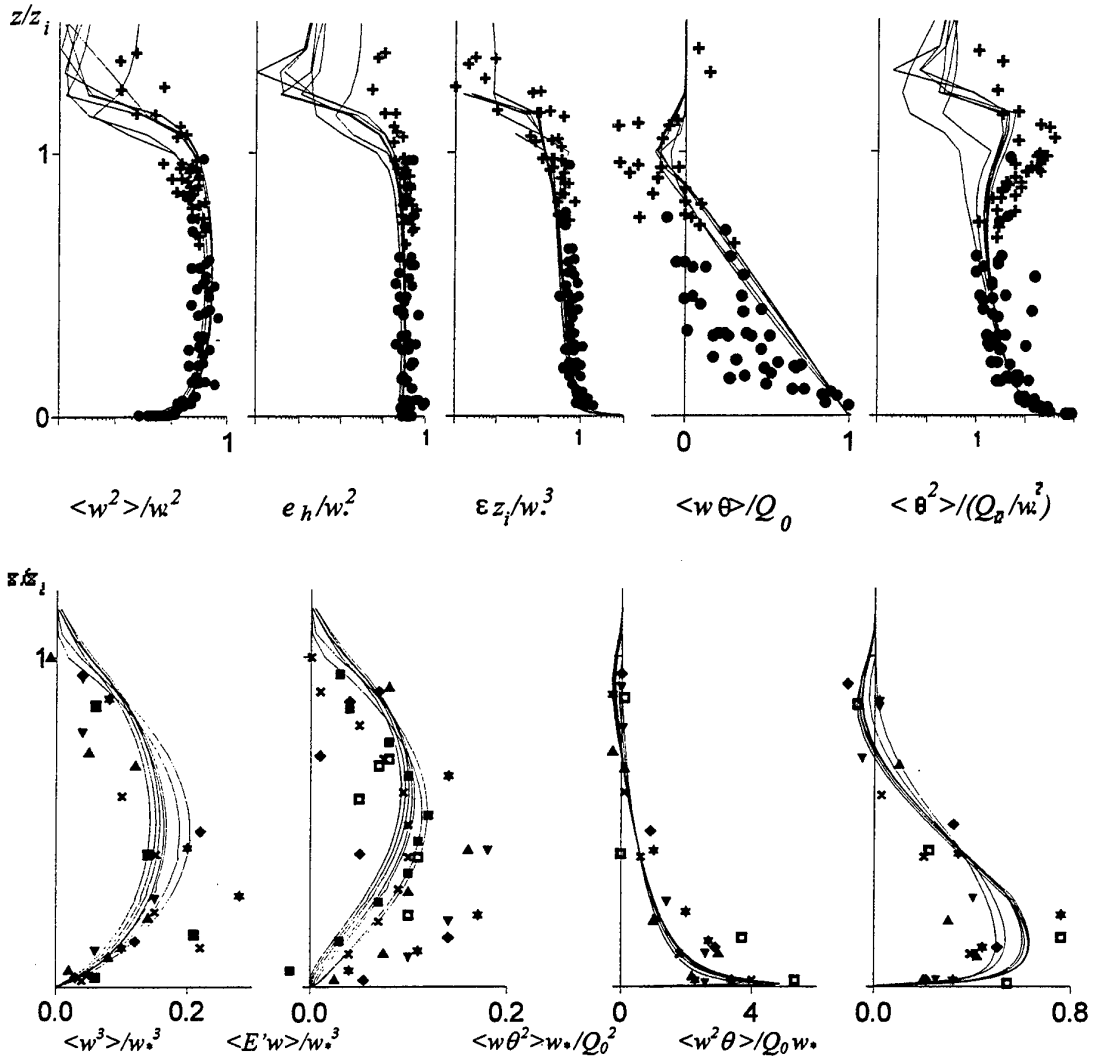

Fig. 2. Results of simulation of the convective PBL evolution: solid lines are calculated profiles of second- and third-order correlations (different lines according to time from 10 a.m. to 5 p.m.); symbols are the experimental data.

turbulent transfer of substance in the convective PBL. In the present work to model the spreading a passive pollutant in the convective PBL, it is proposed to develop a method, which is intermediate between the statistical moments method and the large-eddy-simulation approach. The velocity field of large-scale eddies (coherent structures) corresponding to a long-wave region of the turbulent fluctuations spectrum is reconstructed from calculated distributions of moments of vertical velocity fluctuations. The transfer of scalar by coherent structures account in the model directly, namely in the advection terms of the scalar concentration transport equation. To account for the pollutant turbulent diffusion due to "background" turbulence corresponding to the inertial interval of the turbulent fluctuations spectrum, the "standard" models of statistical moments are applied. Calculations of substance dispersion correspond to 3 p.m. of the PBL evolution (developed PBL).

2.1 Method of reconstruction of the velocity field of the coherent structures in the convective PBL

The pdf of turbulent fluctuations of the vertical velocity is represented as a superposition of two independent distributions: inertial interval of turbulent spectrum (background turbulence) $P_b(u)$ and large-wave region of spectrum (coherent structures) pdf $P_c(v)$ (u and v are the vertical velocity fluctuations of background turbulence and the vertical velocity field of coherent structures, correspondingly)

$$P(u,v)=\frac{1}{2\pi\sigma_b}exp\left\{-\frac{u^2}{2\sigma_b^2}\right\}\left[\frac{a^+}{\sigma_c^+}exp\left\{-\frac{(m^+-v)^2}{2(\sigma_c^+)^2}\right\}+\frac{a^-}{\sigma_c^-}exp\left\{-\frac{(m^--v)^2}{2(\sigma_c^-)^2}\right\}\right], \qquad /12/$$

where σ_b is the dispersion of background turbulence; a^+ and a^- are the weight coefficients, σ_c^+ and σ_c^- are the dispersions, m^+ and m^- are the centers of distributions of upflow and downflow of coherent structures, correspondingly. Considering the total turbulent velocity fluctuation w as the sum of u and v, one can receive the total PDF:

$$P(w) = \int_R P(u,v)\delta(w-u-v)dudv$$
$$= \frac{a^+}{2\pi\sigma_+} exp\left\{-\frac{(m^+-w)^2}{2\sigma_+^2}\right\} + \frac{a^-}{2\pi\sigma_-} exp\left\{-\frac{(m^--w)^2}{2\sigma_-^2}\right\}, \quad /13/$$

where $\sigma_+^2=(\sigma_c^+)^2+\sigma_b^2$, $\sigma_-^2=(\sigma_c^-)^2+\sigma_b^2$. From the conditions

$$\int_R P(w)dw = 1, \qquad \int_R wP(w)dw = 0, \qquad /14/$$
$$\int_R w^2 P(w)dw = < w^2 >, \quad \int_R w^3 P(w)dw = S_w\sigma^3,$$

($\sigma = <w^2>^{1/2}$ is the dispersion and $S_w=<w^3>/<w^2>^{3/2}$ is the skewness factor) the connections for a^+, a^-, σ_+^2, σ_-^2, m^+ and m^- are following:

$$a^+ + a^- = 1,$$
$$a^+m^+ + a^-m^- = 0,$$
$$a^+\left[(m^+)^2+\sigma_+^2\right] + a^+\left[(m^+)^2+\sigma_-^2\right] = \sigma^2, \qquad /15/$$
$$a^+\left[(m^+)^3+3m^+\sigma_+^2\right] + a^-\left[(m^-)^3+3m^-\sigma_-^2\right] = S_w\sigma^3,$$

The conditions for σ_+^2 and σ_-^2 are found from the assumption (19) that the square of dispersions σ_+^2 and σ_-^2 can be equal to the square of centers of distribution $(m^+)^2$ and $(m^-)^2$ correspondingly. Necessary condition for closure of the equations set (for σ_b) is found from the wavelet model (20). The simplified eddy with the typical wave number k_v is considered in a form of the localized perturbation of energy in the wave number space (wavelet) with the energy $E_v=E(k_v)k_v$. This consideration ensured the cascade transfer of turbulent energy from large-scale eddies to dissipative eddies. In the present work the coherent structure in the convective PBL is assumed to be the wavelet containing the energy $E_c=a\varepsilon^{2/3}k_{max}^{-2/3}$ ($a=1.6 \pm 0.02$ is Kolmogoroff constant (21)), k_{max} is the maximum of the spectrum of the turbulent energy. The total turbulent energy is equal to

$$E = \sum_{k_{min}}^{k_{max}} E_v(k_v) \approx E_v(k_{max}) \sum_{i=0}^{\infty} \left[3^{-2/3}\right]^i \approx 2E_c. \qquad /16/$$

This result can be obtained by another way:

$$E \approx \int_{k_{max}}^{\infty} a\varepsilon^{2/3}k^{-5/3}dk + \frac{1}{2}E_c = 2E_c. \qquad /17/$$

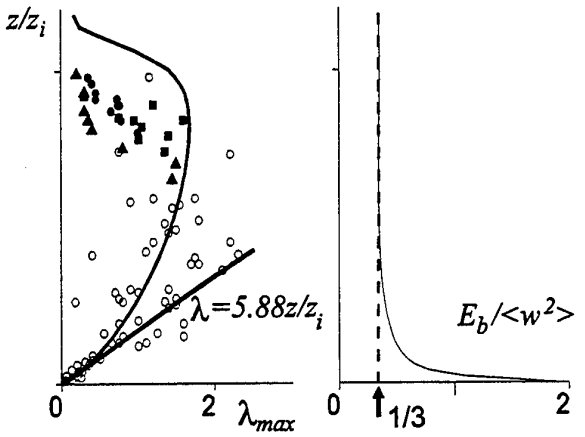

Fig.3. The calculated profile of λ_{max} and the ratio $E_b/<w^2>$, symbols are the experimental data (1).

Regarding this result, k_{max} is expressed as $k_{max}=(2a/E)^{3/2}\varepsilon$ and then $\lambda_{max}=2\pi/k_{max}$. The calculated profile of λ_{max} and the ratio $E_b/<w^2>$ are shown in fig.3. Here it can be seen that the calculated distribution of λ_{max} is in agreement with the observed data (1) in the whole. The differences between the calculated and measured (1) profile of λ_{max} near the inversion layer and in the upper part of the PBL can be connected with an insufficiency of using the simplified pressure-strain correlations model in the stable stratification region. The calculated ratio $E_b/<w^2>$ is equal to *1/3* in the mixing layer of PBL.

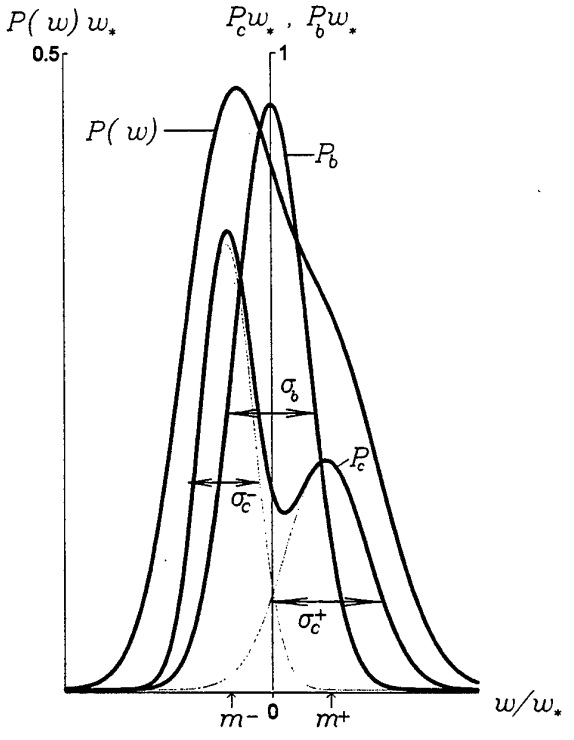

Fig.4. The reconstructed profile of pdf of the vertical velocity fluctuations.

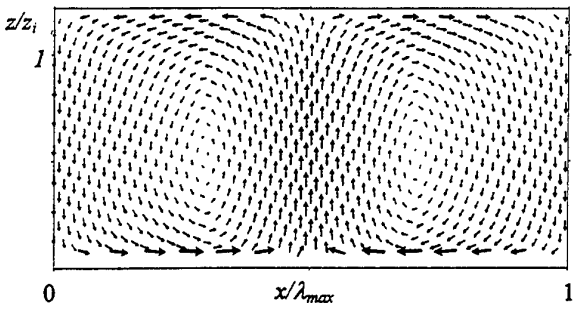

Fig.5. The reconstructed velocity field of the coherent structure in convective PBL.

Analysis of the experimental spectrum of $<w^2>$ in the atmosphere (5) gives the same result $E_b/<w^2> \approx 1/3$. The necessary condition for the dispersion of the background turbulence σ_b is: $\sigma_b^2 = 1/3<w^2>$.

The results of reconstruction of pdf with using the calculated distributions of the second- and third-order moments are shown in fig.4. It can be seen that the results of reconstruction of pdf correspond to the observed data: an upflow within a coherent structure with larger turbulent energy (σ^+_c) and larger velocity (m^+) occupy smaller region (of size $\approx P_c(m^+) < P_c(m^-)$) than a downflow with smaller energy ($\sigma_c^- < \sigma_c^+$) and smaller velocity ($m^- < m^+$).

The horizontal size of two coherent structures is equal to λ_{max}. This fact follows from the continuity of velocity on the border between the coherent structures. The size of a horizontal region of the coherent structures (where the vertical velocity is equal to w) is taken to be proportional to the probability $P_c(w)$:

$$\frac{dx}{\lambda_{max}/2} = P_c(w)dw \qquad /18/$$

The vertical velocity field of the coherent structures $w(x,z)$ can be found from the differential equation /18/. The horizontal velocity field $u(x,z)$ is determined from the equation of mass conservation:

$$\frac{\partial u}{\partial x} + \frac{\partial w}{\partial z} = 0 \quad \text{or} \quad u(x,z) = -\int \frac{\partial w(x,z)}{\partial z} dx. \qquad /19/$$

The result of reconstruction of the coherent structures velocity field (u,w) in the convective PBL is shown in fig 5.

2.2 Modeling the turbulent transport of substance

For describing the process of substance dispersion in the convective PBL, the model accounting directly an effect of the substance transfer by coherent structures (in advection terms of the equation for the crosswind integrated concentration (4)) is used. For accounting the substance turbulent diffusion under the effect of background turbulence, the "standard" gradient diffusion model is applied:

$$\frac{\partial C_y}{\partial t} + (U+u)\frac{\partial C_y}{\partial x} + w\frac{\partial C_y}{\partial z} = \frac{\partial}{\partial z}\left[C_s \tau < w^2 > \frac{\partial C_y}{\partial z}\right], \qquad /20/$$

where C_s is coefficient of the model. The value of C_s is determined from the condition that the coefficient of turbulent diffusion near the surface approximated by $\kappa u_* z$ (5):

$$C_s \tau < w^2 > \xrightarrow[z \to 0]{} \frac{2}{3} C_s \frac{E_0^2}{\varepsilon_0} \approx 4.5^2 \frac{2}{3} C_s \kappa u_* z \Rightarrow C_s \approx 0.07$$

The results of simulation of the pollutant jet spreading from sources placed both on the PBL ground surface and in the middle of the mixed layer are presented. The averaging (over one period λ_{max}/U_x) crosswind integrated concentration fields are shown in figs.6,7. A near-ground source was realized at $z_s/z_i = 0.068$. The maximum concentration centerline (e.g., the locus of maximum concentrations) firstly moves parallel to the surface and then starts to rise rapidly at the downwind distance $x^* = 0.5$ ($x^* = x w_*/(z_i U_x)$),

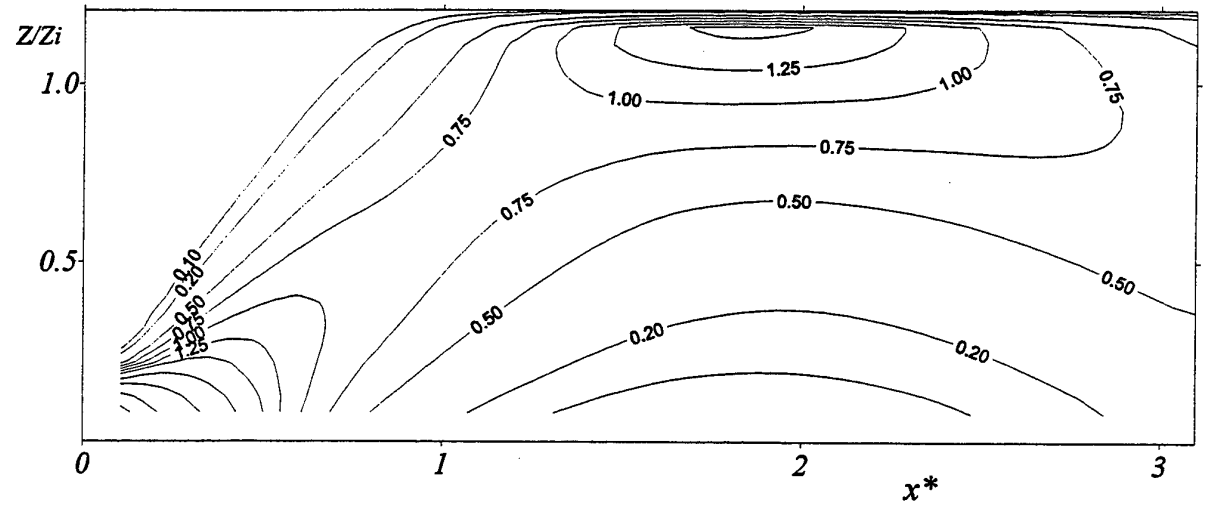

Fig.6. Calculated non-dimensional crosswind integrated concentration $C_y z_i U_x/q_0$ for point sources of height $z/z_i = 0.067$.

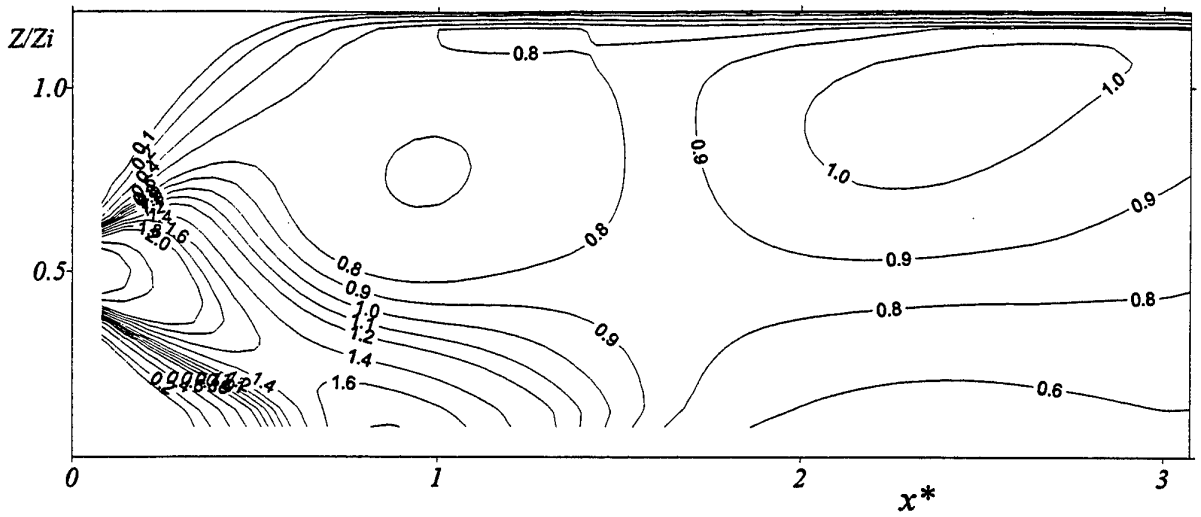

Fig.7. Calculated non-dimensional crosswind integrated concentration for point sources of height $z/z_i=0.5$.

creating the local maximum of concentration near the inversion layer. This maximum is placed at the height of $z=1.1z_i$ at about $x^*=2.0$. This is the same distance downwind as observed in the laboratory experiments of Deardorff and Willis (21) ($x^*=1.75$), but the height is higher ($z=0.75\ z_i$ in (22)). This difference between the calculation and the experiment data (22) can be connect to larger size of coherent structures at calculation (see fig. 3, $\lambda_{max}(z)$) near inversion layer then in observed data in PBL. At about $x^*=2.5$, the centerline begins to descend back into the middle of the PBL in a manner similar to the laboratory results.

The plum centerline for the midlevel elevated source descends rapidly, impinging on the ground at $x^*=0.9$, with a maximum concentration there of $C_y=1.8\ q_0/(z_iU_x)$ (see fig.9). Both these features are in good agreement with the experiments (23). The plume then rebounds from the surface, producing a second line of high concentrations which rises near inversion layer. The calculated (lines) and observed in (22,23) (symbols) ground-level concentrations are shown in fig.8,9.

The calculated behavior of the plum centerline for both cases with a source situated near the ground and with source situated in the middle of the mixing layer correspond to Willis and Deardorff's tank experiments (22,23). It should be noted that these laboratory experiments had not wind-shear and Koriolis effects in contrast with the natural PBL observation and simulation.

Fig. 10 shows the calculated instantaneous (quasi-instantaneous, because the LSEF are reconstructed in these calculations only) crosswind-integrated concentration field for the ground-source situation. The pollutant

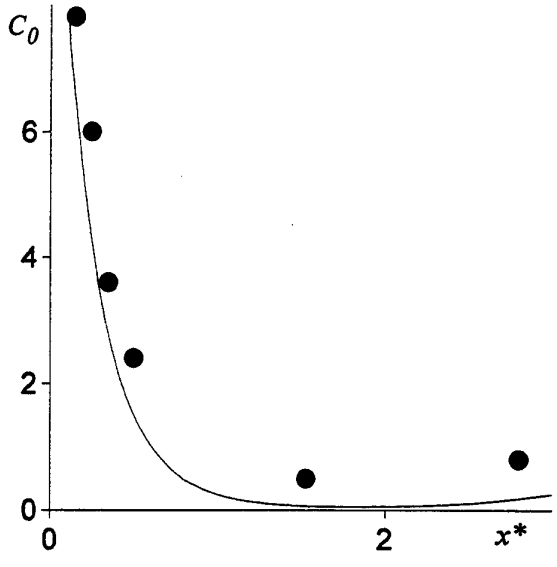

Fig.8. The calculated ground-level concentration (solid line) compared with the corresponding value from the laboratory experiment (solid circles) for source height at $0.067\ z_i$

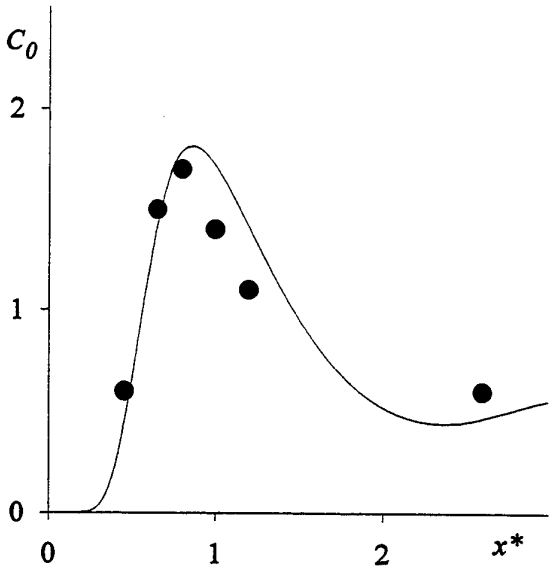

Fig.9. The calculated ground-level concentration for source height at $0.5\ z_i$. Line and symbols are as in fig.8.

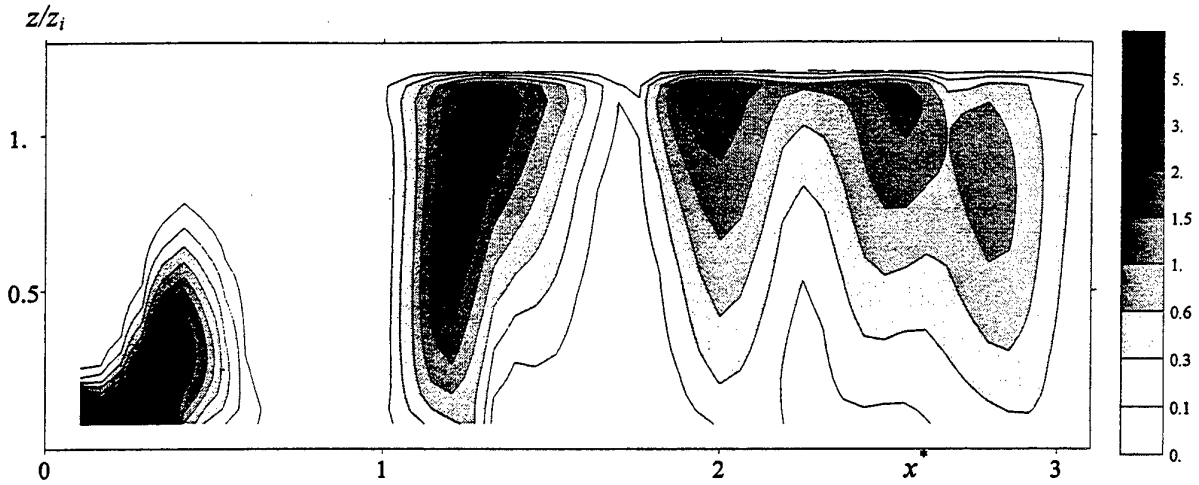

Fig. 10. The calculated instantantaneous crosswind-integrated concentration field for the ground-source situation.

particles can be used for visualization of fluid entrainment from the upper part of the PBL to the mixing layer by the coherent structures. This effect results in the intermittent structure of concentration field. Fig. 10 shows the collapse effect of the pollutant plum near the inversion layer also. These effects cannot be described within simplified second-order closure models.

3. Conclusion

The presented results of modelling the turbulent transfer of momentum and heat in the convective PBL show that the elaborated fourth-order cumulants model can be used for parameterization of the fourth-order moments in the triple correlation model. The algebraic version of the triple correlation model gives the results corresponding to the experimental data for the second- and third-order moments and can be used for simulation of evolution of the convective PBL. The present method of reconstruction of pdf and velocity field of the coherent structures in the connective PBL is allowed to account directly the coherent structures effects (in advection terms of the equation for the concentration) for calculation of the pollutant jet spreading from a point source in the convective PBL.

This wor was financially supported by the Russian Foundation for Basic Research (Grant N98-01-00719)

The author is thankful to Organising Committee of THT-2 and Professor B.E.Launder for financial support of participation in the conference.

4. Nomenclature

a^+, a^- are weight coefficients of upflow and downflow in pdf;
C_1, $C_{1\theta}$, ... are models coefficients;
C_y is crosswind-integrated concentration of substance;
C_{ijkl}, $C_{ijk\theta}$, ... is fourth-order cumulant;
$E=1/2u_iu_i$ is turbulent kinetic energy;
g is gravitational acceleration;
$K_w=\langle w^4\rangle/\langle w^2\rangle^2$ is kurtosis of vertical velocity;
k_{max} is maximum of the turbulence energy spectrum;
m^+,m^- are centers of distributions of upflow and downflow in pdf;
N is Brunt-Vaisala frequency $(N^2=\beta g\partial\Theta/\partial z)$;
p is pressure variance;
Q_0 is surface temperature flux;
q_0 is surface temperature flux;
$r=\tau/\tau_\theta$ is ratio of time scales;
$S_w=\langle w^3\rangle/\langle w^2\rangle^{3/2}$ is skewness of the vertical velocity;
u is horizontal velocity variance;
U_i is mean velocity vector;
u_* is friction velocity;
u_i is velocity variance vector;
w is vertical velocity variance;
$w_*=(\beta g z_i Q_0)^{1/3}$ is convective velocity scale;
z_i is height of inversion;
$\beta=1/\Theta$ is volumetric expansion coefficient;
ε is dissipation rate of turbulent kinetic energy;
$\kappa=0.41$ is Karman constant;
$\lambda_{max}=2\pi/k_{max}$ is wave length corresponding to k_{max};
Θ is mean potential temperature;
θ is potential temperature variance;
σ_b is dispersion of background turbulence in pdf;
σ_+, σ^- are dispersions of upflow and downflow in pdf;
$\tau=E/\varepsilon$ is time scale of turbulent velocity variance;
τ_θ is time scale of turbulent temperature variance.

5. References

(1) Atmospheric Turbulence and Air Pollution Modeling / Edited by Nieuwstadt F.T.M. and van Dop H. 1982, D.Reidel, Dodrecht.
(2) Zeman O., Lumley J.L. Modeling buoyancy driven mixing layer //J.Atmos.Sci. 1976. V.33. P.1974-1988.
(3) Canuto V.M., Minotti F., Ronchi C., Ypma R.M., Zeman O. Second-order closure PBL model with new third-order moments: comparison with LES data // J.Atmos.Sci. 1994. V.51. N 12.P.1605-1618
(4) Ilyushin B.B., Kurbatskii A.F. Modeling the pollutant spreading in the convective ABL // Izvestiya RAN. Physics of Atmosphere and Ocean. 1996 Vol.32, No.3. P.307-322.

(5) Monin A.S., Yaglom A.M. Statistical Hydromechanics (Part 1,2). Moscow: Science, 1967.
(6) J.C. Andre, G De Moor, P.Lacarrere, G. Therry and R du Vachat. Modeling the 24-Hour Evolution of the Mean and Turbulent Structures of the Planetary Boundary Layer // J. Atmos. Sci. 1978, vol.35, P.1861-1883
(7) Andre J.C., De Moor G., Lacarrere P. and Du Vachat R. Turbulence approximation for inhomogeneous flow: Part 1. The clipping approximation // J.Atmos. Sci. 1976. V.33. P.476-481.; Part 2. The numerical simulation of penetrative convection experiment // J.Atmos.Sci. 1976. V.33. P.482-491.
(8) T.J.Craft, J.W. Kidger and B.E.Launder. Importance of third-moment modelling in horizontal, stably-stratified flows // Proc. Eleventh Symposium on Turbulent Shear Flows. Sep.8-11, 1997, Grenoble, France. vol. 2, pp. 2013-2018.
(9) Deardorff J.W. Closure of second- and third-moment rate equations for diffusion in homogeneous turbulence // Phys.Fluids 1978, vol.21, pp. 525-530
(10)Ogura Y. Energy transfer in a normally distributed and isotropic turbulent velocity field in two dimensions // Phys. Fluids. 1962, N.4, p.395-401.
(11)Hazen A.M. To non-linear theory of appearance of turbulence // DAN USSR. 1963. Vol.163, No.6. P.1282-1287.
(12)M.R.Raupach. Conditional statistics of Reynolds stress in rough-wall and smooth turbulent boundary layers // J.Fluid Mech. vol.108, pp.363-382.
(13) Lenschow D.H.,Wyngaard J.C.,Pennel W.T. Mean-field and second-moment budgets in a baroclinic, convective boundary layer/J.Atmos.Sci. 1980, vol. 37, pp.1313-1326.
(14) Ilyushin B.B. Kurbatskii A.F. turbulence E-ε-$\langle w^2\rangle$-$\langle w^3\rangle$ model of the convective planetary boundary layer //Proc. Saint-Venant Symposium: Multiple scale analysis and coupled physical systems. Aug. 28-29, 1997, Paris, France. P.127-132.
(15) Boris B. Ilyushin and Albert F. Kurbatskii. Modeling of turbulent transport in PBL with third-order moments // Proc. Eleventh Symposium on Turbulent Shear Flows. Sep.8-11, 1997, Grenoble, France. Vol.2, pp. 2019-2024.
(16) Weinstock J. A theory of turbulent transport/J.Fluid Mech. 1989, vol.202, pp.319-338.
(17) Ilyushin B.B., Kurbatskii A.F. New triple correlations models in PBL// Izvestiya RAN. Physics of Atmosphere and Ocean. 1998 (in press).
(18) Schmidt H., Schumann U. Coherent structure of the convective boundary layer derived from large-eddy simulations// J.Fluid Mech. 1989, v.200, pp.511-562.
(19)Anne F. De Baas, Han van Dop and Frans T.M. Nieuwstadt. An application of Langevin equation for inhomogeneous conditions to dispersion in a convective boundary layer//Quart. J. R. Met. Soc. 1986, v.112, pp. 165-180.
(20) Tennekes H.,Lumley J.L., A First Course in Turbulence, 1972, MIT Press, Cambridge, Massachusetts.
(21)Andreas, E.L. Spectral measurements in a disturbed boundary layer over snow//J.Atmos.Sci. 1983, v.44, pp.1912-1939
(22) Willis, G.E.,and J.W.Deardorff. A laboratory model of diffusion into the convective boundary layer//Quart. J. Roy. Meteor. Soc. 1976, v.102, pp.427-445.
(23) Willis, G.E.,and J.W.Deardorff. A laboratory study of dispersion from a source in the middle of the convective boundary layer//Atmos. Environ. 1981, v.15, pp.109-117.

EFFECTS OF ROTATION ON UNSTABLY STRATIFIED TURBULENCE

S. Tsujimura, O. Iida and Y. Nagano

Department of Mechanical Engineering
Nagoya Institute of Technology, JAPAN

ABSTRACT

The mechanism of heat transport in geostrophic flows under various density stratifications has been studied by using both direct numerical simulation and rapid distortion theory. It is found that under both unstable and stable stratification with rotation, baroclinic vortices are formed. The effects of the non-linear term on the generation mechanisms of baroclinic vortices are investigated in detail.

1 INTROQUCTION

In geophysically and astrophysically important flows, two kinds of body forces, i.e., the buoyancy and Coriolis forces, are simultaneously imposed. Recently, increasing attention has been paid to their mixed effects on turbulence to resolve planetary circulation issues.

The density stratification associated with the buoyancy force can be classified into two categories, i.e., stable stratification and unstable stratification. The mixed effects of the Coriolis force and the unstable stratification on turbulence are studied mainly on the convection problem observed in wall-bounded flows.[1-8] The flow pattern of Rayleigh-Bénard convection under rotation can be classified approximately by both Rayleigh number and Taylor number. The experiments of Boubnov & Golitsyn[4,5], Fernando et al.[6,7], and Sakai[8] have been performed at sufficiently high values of Rayleigh and Taylor numbers to generate turbulent convection. When the Rayleigh number is below the critical value, the fluid is at rest and heat transport is accomplished by thermal conductivity. This critical Rayleigh number is the minimum Rayleigh number required for onset of convection, and was first found as a function of Taylor number by Nakagawa & Frenzen.[1] However, even beyond this critical Rayleigh number typical Rayleigh-Bénard convection does not appear when imposed rotation is sufficiently large, while thin elongated vortex columns with vertical axis are generated between the two walls. It is also found that the horizontal scale of these vortex columns becomes small as Rossby number decreases, while their vertical scale increases and more intense isolated vortex columns can be observed. Almost all these vortex columns are cyclonic, which can not be explained sufficiently in these experiments.

Direct numerical simulations and large eddy simulations of the rotating Rayleigh-Bénard convection have been carried out by Raash & Etling[9], Cabot et al.[10] and Julien et al.[11,12] Their results were qualitatively in good agreement with the previous experiments, although exact comparisons were not possible due to different values for Rayleigh, Taylor and Prandtl numbers. In both the numerical studies of Cabot et al.[10] and Julien et al.[11,12], two kinds of surface boundary conditions, i.e., non-slip and free-slip walls, were imposed on the channel, and the effects of wall boundary condition on vortex columns and heat transfer associated with them were discussed in detail. Julien et al.[12] found that the vortex columns became cyclonic in the process in which stationary fluid was ejected toward the central region of a channel by buoyancy, and the vorticity in the generated plume was intensified by the vortex stretching associated with the horizontal convergence of the flow. However, it is still unknown how the buoyancy force, Coriolis force and especially the non-linear term affect their generation, respectively.

The generation mechanism of vortex columns was also studied by the experiments and numerical simulation of injecting dense saltwater into rotating water tank.[13-16] The saltwater sank into the underlying less-dense homogeneous water forming a growing three-dimensional (3D) turbulent layer. When the turbulent front reached a transition depth, Coriolis force affected turbulence and quasi-2D vortex structures were generated beneath the 3D turbulent mixed layer. These vortices then penetrated downward to produce vortex columns and eventually occupied the rest of the tank beneath the upper mixed layer. In these previous experiments, the parameters governing the characteristic length and velocity scale of the vortex columns were determined.

The vortex columns are closely associated with the dust-devil observed in the lower atmosphere near the ground[7] and the oceanic vortices associated with hydrothermal plumes.[17] Hence, the rotating turbulence under unstable stratification is im-

portant, especially in the geophysical flows. Unfortunately, all of these studies were conducted on wall-bounded flows, whereas there are none for the homogeneous turbulence which is equally important in the geophysical flow. In homogeneous turbulence, it is possible to investigate the generation mechanism of vortex columns by expansion of velocity fluctuations into Fourier spectra in all directions.

Homogeneous turbulence has been used as an objective flow field, although to the authors' knowledge there is no previous DNS study on rotational homogeneous turbulence under unstable stratification. The effect of rotation has been successfully demonstrated in the studies on homogeneous turbulence without buoyancy.[18-22] All these numerical simulations and experiments showed a quasi-two dimensionalization, where integral-length scale increased in the direction parallel to the rotational axis. However, no study has ever noted the marked tendency for the velocity vector to align itself perpendicular to the rotational axis, as predicted by the Taylor-Proudmann theorem. Another remarkable feature is that the rotation reduces the non-linear triad interaction and the energy cascade of turbulence. Thus, turbulent kinetic energy is piled up at low-wave numbers, while high-wave-number energy decreases markedly. The experiment of Komori et al.[23] showed that under unstable stratification, turbulence activity was enhanced over all wave numbers and the energy cascade. Hence, the effects of rotation and stratification are in conflict with each other.

The effects of rotation on stably stratified turbulence are also investigated in detail in the present study. One of the most interesting phenomena associated with the combined effects of the Coriolis and buoyancy forces is the generation of baroclinic vortices of which axises are aligned in the vertical direction. Previously, the effects of rotation on stably stratified turbulence has been mainly studied with the geostrophically approximated equation for the potential vorticity, where the effects of the non-linear term are totally neglected.[24,25,26] In the quasi-geostrophical equations, there should be no difference between the cyclonic and anticyclonic baroclinic vortices. Metais et al.[27] carried out three-dimensional numerical simulations of strongly stratified and rotating turbulence. Their study shows the inverse energy cascade which represents the two-dimensionalization of the flow due to stable stratification. However, their study is limited especially to the effects of stable stratification on turbulence. We have still few knowledge on the effects of the non-linear term on the baroclinic vortices.

The main objective of the present study is to numerically investigate the combined effects of rotation and stratification on turbulence. The three-dimensional Navier-Stokes equation with the Boussinesq approximation is solved, and the coherent structures and heat transfer in geostrophic flows are studied in detail.

2 NUMERICAL PROCEDURE

All computations are carried out in the domain of a cubic box of which sides are set to be 2π, and periodic boundary conditions are assumed on each side. The cubic box is also assumed to rotate around the x_3 axis. Both the mean temperature gradient ($S_\theta \equiv d\Theta/dx_3$) and the gravitational acceleration g are imposed in the x_3 direction.

The parameters included in the governing equations are kinematic viscosity ν, thermal diffusivity α, angular velocity Ω, and buoyancy parameter $g\beta$, where β represents the volume expansion rate. The typical values studied are listed in Table 1 . In the table, neutrally stratified cases are designated by an N, and stably and unstably stratified cases are represented by S and U, respectively, while rotation is designated by a following R. Because the gravitational acceleration g is imposed in the downward direction, the negative mean temperature gradient indicates the unstable stratification, while the positive gradient makes the flow field stable in the dynamical sense. In all stratified cases with rotation, i.e., Case NR1 and UR1, the rapid distortion theory (RDT) is applied as well as the direct numerical simulations. From Case N to UR6 listed in Table 1, the same energy spectrum (ES1) is used as the initial condition, while from Case UR7 to UR12 the other initial energy spectrum (ES2) is used. The energy spectra ES1 and ES2 are defined in the following:

$$\mathrm{ES1}(\kappa_1,\kappa_2,\kappa_3) = 0.018\,\kappa^2 \exp\left(-\frac{\kappa^2}{25}\right), \qquad (1)$$

$$\mathrm{ES2}(\kappa_1,\kappa_2,\kappa_3) = 0.18\,\kappa \exp\left(-\frac{\kappa}{3}\right), \qquad (2)$$

where $\mathrm{ES2}(\kappa_1,\kappa_2,0)$ is set to be zero. In the above equation, κ_i represents the wave number in the i-th direction, while κ is the three-dimensional wave number. In the energy spectrum ES2, the velocity fluctuations at $\kappa_3 = 0$, are set to be zero, indicating that there is no integral scale in the x_3 direction. It should be noted that without the initial integral scale, RDT can not predict any evolution of velocity fluctuations of $\kappa_3 = 0$.

The numerical procedure is based on the pseudo-spectral method where the governing equations are discretized by the Fourier-collocation method. The maximum number of grid points used in the study is 64^3. The second-order Runge-Kutta method is used for the time integration. The initial condition of the velocity field is artificially generated isotropic turbulence without any temperature fluctuation. Temperature fluctuations are generated spontaneously by turbulence activity under the imposed mean temperature gradient.

Table 1: Computational conditions for neutrally and unstably stratified flows

Case	N	NR1	NR2	U	UR1	UR2	UR3	UR4	UR5	UR6	UR7	UR8	UR9	UR10	UR11	UR12
N_g	32^3										64^3					
ν	0.0243										0.012					
Pr	0.71		10	0.71												
S_θ	1			-1												
$g\beta$	0	0	0	4	4	1	4	1	4	16	4	1	4	1	4	16
Ω	0	10		0	10	5	20	10	5	10	10	5	20	10	5	10
S					0.1		0.05		0.2		0.1		0.05		0.2	

$(S = \sqrt{|g\beta S_\theta|}/2\Omega)$

The Boussinesq-approximated Navier-Stokes equation, the continuity equation and the equation of temperature fluctuation θ take the following forms when non-dimensionalized by the appropriate length scale L, the velocity scale U, and the temperature scale $\Delta T(\equiv |S_\theta|L)$:

$$\frac{Du_i}{Dt} = -\frac{\partial p}{\partial x_i} + \frac{1}{Re}\frac{\partial^2 u_i}{\partial x_j \partial x_j} - \frac{1}{Ro}(-u_2\delta_{i1} + u_1\delta_{i2}) + \frac{\theta}{Bo}\delta_{i3}, \quad (3)$$

$$\frac{\partial u_i}{\partial x_i} = 0, \quad (4)$$

$$\frac{D\theta}{Dt} = -u_3 + \frac{1}{RePr}\frac{\partial^2 \theta}{\partial x_j \partial x_j}, \quad (5)$$

where $D/Dt = \partial/\partial t + u_j \partial/\partial x_j$, and $Re = UL/\nu$, $Ro = U/(2\Omega L)$ and $Bo = U^2/(Lg\beta\Delta T)$ are the Reynolds number, the Rossby number, and the buoyancy parameter, respectively. Also, u_i and p are the i-th component of velocity vector and pressure, respectively. The ratio of the viscosity to the Coriolis force results in the Ekman number $Ek = \nu/(2\Omega L^2)$. When the square root of the turbulent kinetic energy $\sqrt{k}$ and the characteristic length scale of turbulence $k^{3/2}/\epsilon$ are used as the reference scales, these parameters become $Re = k^2/\epsilon\nu$, $Ro = \epsilon/(2\Omega k)$, $Bo = \epsilon/(\sqrt{k}g\beta\Delta T)$, $Ek = \nu\epsilon^2/(2\Omega k^3)$, respectively. In all cases except the unstable stratification, the Reynolds number is below 20. In the most complex case of unstable stratification with rotation, the Reynolds number begins to increase markedly just after vortex columns are generated as discussed later. However, our dominant objective is to investigate the generation mechanism of vortex columns, which begins at relatively low-Reynolds numbers. Both the Rossby and the Ekman numbers are around 0.1 in all cases. Thus, all the flow fields become geostrophic flow, where the balance between the pressure and the Coriolis force is retained.

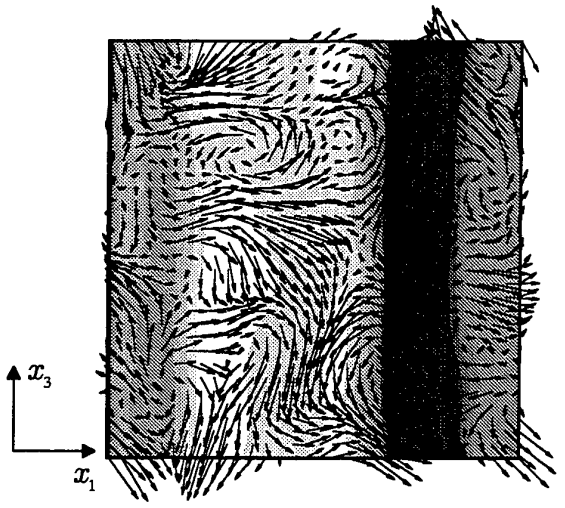

Figure 1: Distributions of temperature fluctuation and velocity vectors in the x_1–x_3 plane (Case NR1): Black to white; -0.5 to 0.5, $t = 2.0$.

3 RESULTS AND DISCUSSION

3.1 Effects of rotation on unstably stratified turbulence

Figure 1 shows the distribution of the temperature fluctuations and the velocity vectors in the x_1-x_3 plane in the neutrally stratified case with rotation. It becomes evident that the iso-surfaces of the temperature fluctuations are aligned in the direction parallel to the axis of the rotation, indicating that the temperature field becomes two-dimensional when solid body rotation is imposed.

The effects of rotation on temperature fluctuations are studied through RDT. By neglecting both the non-linear and viscous terms, the following solutions are obtained analytically for the Fourier spectrum of the velocity and temperature, i.e., $\hat{u}_i$, $\hat{\theta}$:

$$\vec{\kappa} = (\kappa_1, \kappa_2, \kappa_3), \kappa = \sqrt{\kappa_1^2 + \kappa_2^2 + \kappa_3^2}. \quad (6)$$

When $\kappa_3 \neq 0$,

$$\left.\begin{aligned}
\hat{u}_1(\vec{\kappa},t) &= \hat{u}_1(\vec{\kappa},0)\cos ft \\
&\quad + \{\gamma\hat{u}_1(\vec{\kappa},0) + \zeta\hat{u}_2(\vec{\kappa},0)\}\sin ft \\
\hat{u}_2(\vec{\kappa},t) &= \hat{u}_2(\vec{\kappa},0)\cos ft \\
&\quad - \{\eta\hat{u}_1(\vec{\kappa},0) + \gamma\hat{u}_2(\vec{\kappa},0)\}\sin ft \\
\hat{u}_3(\vec{\kappa},t) &= \hat{u}_3(\vec{\kappa},0)\cos ft \\
&\quad + (\tfrac{1}{\kappa})\{\kappa_2\hat{u}_1(\vec{\kappa},0) - \kappa_1\hat{u}_2(\vec{\kappa},0)\}\sin ft \\
\hat{\theta}(\vec{\kappa},t) &= (S_\theta/2\Omega\kappa_3)[\kappa_2\{\hat{u}_1(\vec{\kappa},t) - \hat{u}_1(\vec{\kappa},0)\} \\
&\quad - \kappa_1\{\hat{u}_2(\vec{\kappa},t) - \hat{u}_2(\vec{\kappa},0)\}]
\end{aligned}\right\} \quad (7)$$

with

$$f = 2\Omega\frac{\kappa_3}{\kappa},\ \gamma = \frac{\kappa_1\kappa_2}{\kappa_3\kappa},\ \zeta = \frac{\kappa^2-\kappa_1^2}{\kappa_3\kappa},\ \eta = \frac{\kappa^2-\kappa_2^2}{\kappa_3\kappa}.$$

When $\kappa_3 = 0$,

$$\left.\begin{aligned}
\hat{u}_j(\vec{\kappa},t) &= \hat{u}_j(\vec{\kappa},0) \\
\hat{\theta}(\vec{\kappa},t) &= \hat{\theta}(\vec{\kappa},0) - S_\theta\hat{u}_3(\vec{\kappa},0)\,t,
\end{aligned}\right\} \quad (8)$$

where κ_i is the wave number of the i-th direction. RDT solution for velocity field is also obtained by Bartello et al. (1994).[22] From the above equations, it is found that the temperature fluctuations associated with the $\kappa_3 = 0$ mode should increase linearly, while the fluctuations at other wave numbers oscillate and fail to develop. Thus, the temperature fluctuations should become independent in the x_3 direction, and hence become two-dimensional when the flow develops sufficiently.

Figure 2 shows distributions of the temperature fluctuation and velocity vectors in the x_1-x_3 plane in the unstably stratified case with rotation. The temperature fluctuations in this case also become approximately two-dimensional. Note that the fluids move upward in the regions of positive temperature fluctuations, while they move downward when the temperature fluctuations take negative values. Interestingly, both the upward and downward motions are twisted in the spanwise direction.

Figures 3(a) and (b) show the iso-surfaces of the vertical component of the vorticity ω_3 in the case of the unstable stratification with and without rotation, respectively. Under the unstable stratification with rotation, the vortex columns of ω_3 are clearly observed to be elongated in the direction parallel to the axis of rotation. However, in cases without rotation or stable stratification (not shown here), no elongated vortex columns are generated. In addition, in the calculation using the RDT, though the figure is not shown here, the vortex columns are not formed regardless of the initial condition, thus indicating that the non-linear effects are absolutely required to generate the vortex columns.

Figures 4(a) and (b) show the joint probability density function (p.d.f.) between the vertical

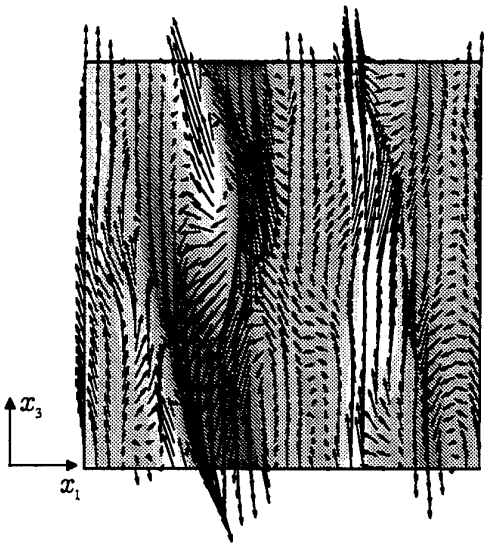

Figure 2: Distributions of temperature fluctuation and velocity vectors in the x_1-x_3 plane (Case UR1): Black to white; -1.8 to 1.8, $t = 2.0$.

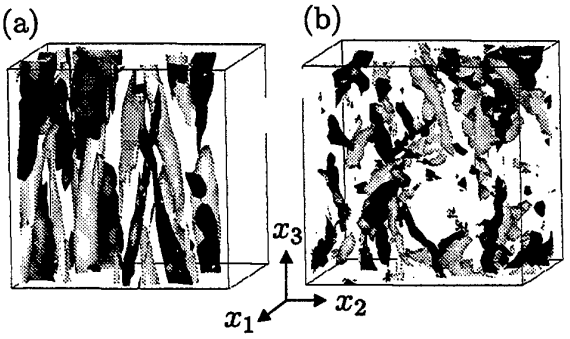

Figure 3: Iso-surfaces of ω_3 at $t = 2.0$. White iso-surfaces represent $\omega_3/\omega_{3\mathrm{rms}} = 2.0$ while black iso-surfaces are $\omega_3/\omega_{3\mathrm{rms}} = -2.0$; (a) Case UR1, (b) Case U.

vorticity ω_3 and the pressure fluctuation p in Cases UR1 and U, respectively. In Case UR1, the large positive vertical vorticity is indeed most likely associated with the large negative pressure fluctuation, whereas the large negative vertical vorticity is associated with the large positive pressure fluctuation. Thus, the observed vortex columns are generated under the geostrophic balance between the pressure gradient and the Coriolis force. In the case without rotation, both large positive and negative vertical vorticities tend to be associated with negative pressure fluctuations.

Next, we investigate the generation of the vertical vorticity in more detail. The equation of the

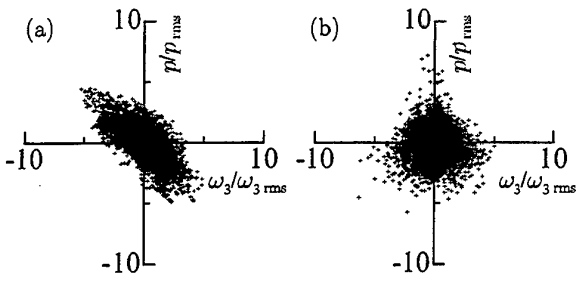

Figure 4: Joint p.d.f. between pressure p and vertical vorticity ω_3; (a) Case UR1, $t = 2.0$, (b) Case U, $t = 2.0$.

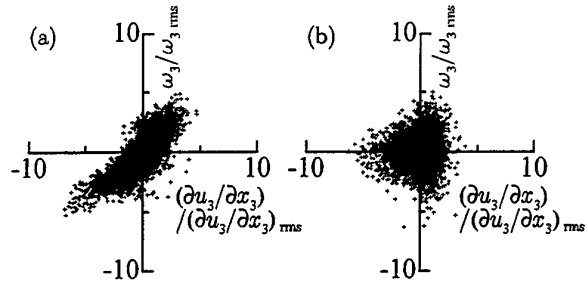

Figure 5: Joint p.d.f. between vertical vorticity ω_3 and $\partial u_3/\partial x_3$; (a) Case UR1, $t = 2.0$, (b) Case U, $t = 2.0$.

vertical vorticity ω_3 is given as follows:

$$\frac{D\omega_3}{Dt} = \omega_3\frac{\partial u_3}{\partial x_3} + 2\Omega\frac{\partial u_3}{\partial x_3} + \left(\frac{\partial u_3}{\partial x_2}\frac{\partial u_1}{\partial x_3} - \frac{\partial u_3}{\partial x_1}\frac{\partial u_2}{\partial x_3}\right) + \nu\frac{\partial^2\omega_3}{\partial x_j\partial x_j}. \quad (9)$$

In Eq. (9), the first and second terms on the right-hand side represent the non-linear and linear vortex-stretching terms, respectively. Figures 5(a) and (b) show the joint p.d.f. between the vertical vorticity ω_3 and the strain rate $\partial u_3/\partial x_3$ in Cases UR1 and U, respectively. In Case U, large plus and minus vertical vorticities are mainly associated with the intensive $\partial u_3/\partial x_3$ with a positive sign. This indicates that the vertical vorticity is generated mostly by the non-linear term $\omega_3(\partial u_3/\partial x_3)$ in Eq. (9). On the other hand, in Case UR1 where vortex columns of ω_3 are clearly observed, the large ω_3 is indeed most likely associated with the large $\partial u_3/\partial x_3$ with the same signs as ω_3. Thus, the observed vortex columns of ω_3 must be generated by the vortex stretching associated with the linear term $2\Omega(\partial u_3/\partial x_3)$.

The generation mechanism of vortex columns can be explained by using the equation on a potential vorticity defined as

$$\pi = (\vec{\omega} + 2\vec{\Omega})\cdot\nabla\tilde{\rho} = \beta(\vec{\omega} + 2\vec{\Omega})\cdot\nabla(\Theta + \theta)$$

$$= \beta\left(\omega_3 S_\theta + \vec{\omega}\cdot\nabla\theta + 2\Omega S_\theta + 2\Omega\frac{\partial\theta}{\partial x_3}\right), \quad (10)$$

where $\tilde{\rho}$ is non-dimensionalized density and the symbol $\vec{}$ represents a vector. In the above equation, $\vec{\omega}\cdot\nabla\theta$ can be neglected because Ω and Θ are sufficiently large in comparison to $\vec{\omega}$ and θ, respectively. Then, from the conservation law of a potential vorticity[26], the following equation is obtained:

$$\frac{D\pi}{Dt} = \beta S_\theta\left[\frac{D\omega_3}{Dt} + \frac{D}{Dt}\left(\frac{2\Omega}{S_\theta}\frac{\partial\theta}{\partial x_3}\right)\right] = 0. \quad (11)$$

It should also be noted that ω_3 and $(2\Omega/S_\theta)\partial\theta/\partial x_3$ represent barotropic and baroclinic vorticities, respectively.

Because the non-linear terms included in an equation of the temperature fluctuation θ were not required to generate vortex columns (not shown here), the time derivative of $\partial\theta/\partial x_3$ can be approximated as

$$\frac{D}{Dt}\frac{\partial\theta}{\partial x_3} = -S_\theta\frac{\partial u_3}{\partial x_3}. \quad (12)$$

Then, the time derivative of a potential vorticity should satisfy

$$\beta S_\theta\left(\frac{D\omega_3}{Dt} - 2\Omega\frac{\partial u_3}{\partial x_3}\right) = 0. \quad (13)$$

This result indicates that the vortex columns are generated in the process by which the baroclinic vorticity is transformed into the barotropic vorticity, which mechanism can be represented by the linear vortex-stretching term [see Eq. (9)].

Figure 6 shows the time evolution of r.m.s. value of the vertical vorticity ω_3 in Cases UR1-6, where both ω_3 and t are non-dimensionalized by the imposed rotation rate Ω. The parameter S given in Fig. 6 is the ratio of the Brunt-Väisälä frequency $N = \sqrt{g\beta S_\theta}$ to the angular frequency of rotation. In the case of unstable stratification ($S_\theta < 0$), S is defined as

$$S \equiv \frac{\sqrt{|g\beta S_\theta|}}{2\Omega}. \quad (14)$$

As shown in Table 1, the value of S increases from 0.05 to 2.0 in Cases UR1 to UR6 and UR7 to UR12. In the cases with the same value of S, it can be seen from Fig. 6 that the vertical vorticity begins to increase at the same normalized time $\Omega t/2\pi$, and its time evolutions almost coincide with each other. This indicates that the vortical structure of unstably stratified rotating turbulence is almost entirely determined by the parameters S and Ω associated with the body force terms. Our results are interestingly similar to the experiments of injecting dense salty water into the rotating tank, where the evolution of the vortex columns is determined by the parameter S.[15] It is also found that the small S, i.e., smaller effects of buoyancy than the Coriolis force, does delay the increase in ω_3.

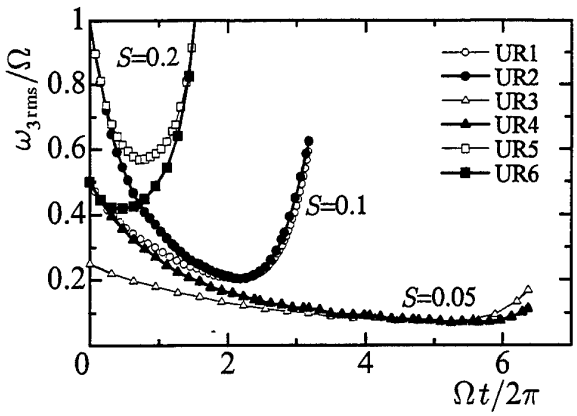

Figure 6: Time evolution of ω_3 in Cases UR1–6.

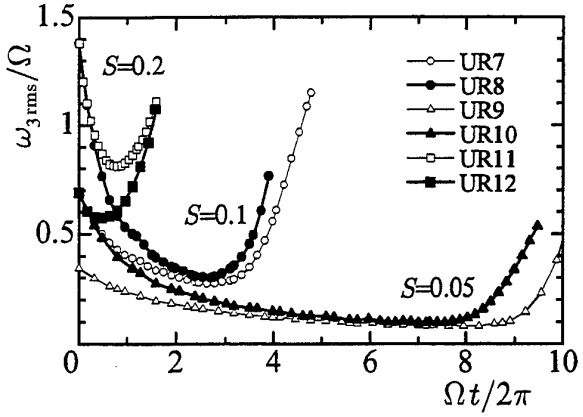

Figure 8: Time evolution of ω_3 in Cases UR7–12.

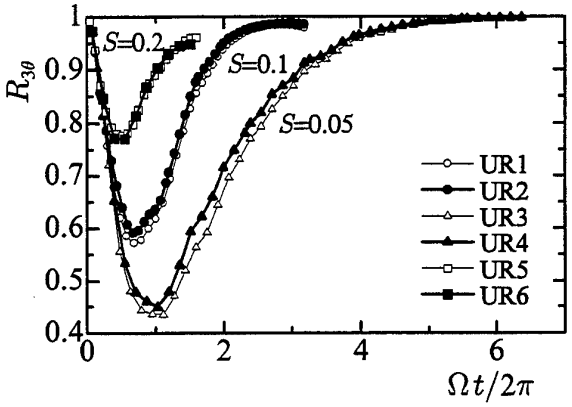

Figure 7: Time evolution of $R_{3\theta}$ in Cases UR1–6.

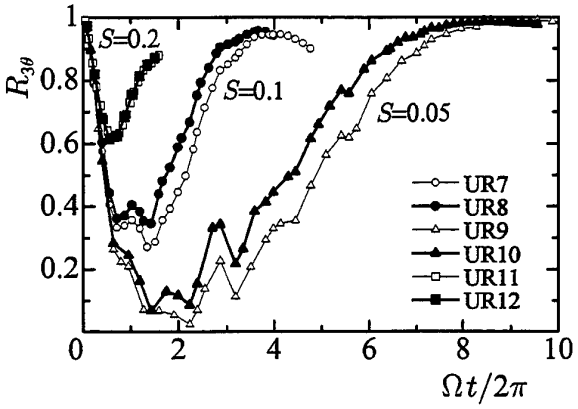

Figure 9: Time evolution of $R_{3\theta}$ in Cases UR7–12.

The corresponding time evolution of the cross-correlation of u_3 and θ is presented in Fig. 7. Initially, the cross-correlation $R_{3\theta}$ decreases due to the effects of rotation, then begins to increase almost up to unity under the effects of rotation.

Figures 8 and 9 show the time evolution of ω_3 and $R_{3\theta}$ in Cases UR7 to UR12, respectively. Their time evolutions are qualitatively similar to those observed in the cases with the initial integral scale (UR1-6). This should be because even if the initial integral scales are set to be zero as in UR7-12, the imposed rotation enhances the backscatter of the energy cascade and increases the integral scale in the x_3 direction.[20,21,22] This mechanism is thought to be a prelude to a Taylor-Proudmann reorganization into two-dimensional turbulence[20], although the present generation mechanism of vortex columns itself is not due to the Taylor-Proudmann theory, but directly related to the above-mentioned vortex stretching in the vertical direction. In the cases without the integral scale, more time is needed to generate vortex columns.

Comparison of Figs. 7 and 9 with Figs. 6 and 8 reveals that ω_3 begins to increase when $R_{3\theta}$ has reached almost unity, indicating that the vortical structures begin to emerge after both temperature and velocity fluctuations become two-dimensional.

Figure 10 shows the vertical structure of temperature and velocity vectors, while Figure 11 shows the iso-surfaces of ω_3. Symbols (a) and (b) appended to figures represent the cases of $S = 0.1$ and 0.05, respectively. These figures are the snapshots at the instance when spatially averaged vertical vorticity begins to increase as shown in Figs. 6 and 8. It is noted from Fig. 10 that both temperature and velocity fluctuations tend to be aligned in the vertical direction, and become almost two-dimensional. It is also found that the vortex columns as observed in Fig. 3(a) begin to emerge in both cases of $S = 0.05$ and 0.1.

The effects of the non-linear term on the generation mechanisms of vortex columns should be

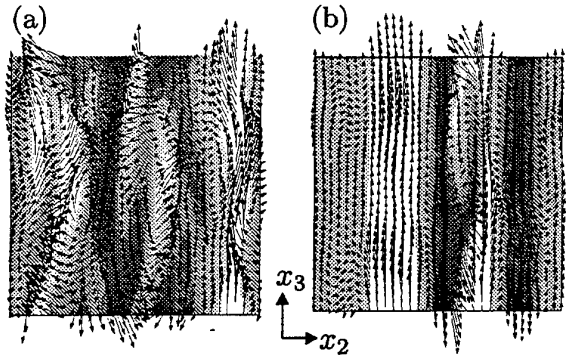

Figure 10: Vertical structures of temperature fluctuations and velocity vectors in the (x_1, x_3) plane at the instance when the vertical vorticity ω_3 begins to increase; (a) Case UR7, $\Omega t/2\pi = 3.98$, black to white: $\theta = -2.5$ to 2, (b) Case UR10, $\Omega t/2\pi = 8.75$, black to white: $\theta = -5$ to 4.

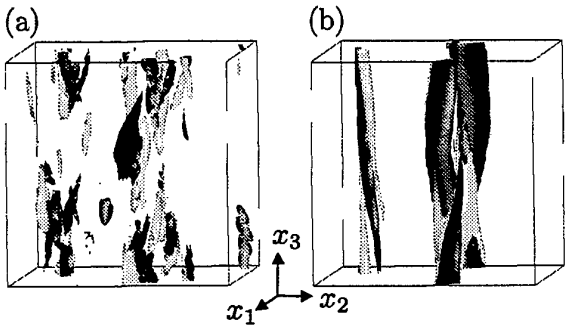

Figure 11: Iso-surfaces of vorticity ω_3 at the instance when the vertical vorticity ω_3 begins to increase. Black iso-surfaces represent $\omega_3/\omega_{3\mathrm{rms}} = -2.5$ while white iso-surfaces are $\omega_3/\omega_{3\mathrm{rms}} = 2.5$; (a) Case UR7, $\Omega t/2\pi = 3.98$, (b) Case UR10, $\Omega t/2\pi = 8.75$.

discussed. Figure 12 shows the time evolution of Reynolds normal stresses in Cases U and UR1. After the initial period of decaying, both $\overline{u_1^2}$ and $\overline{u_2^2}$ in Case UR1 begin to increase remarkably at $t \simeq 1.7$, while in Case U an increase in $\overline{u_1^2}$ and $\overline{u_2^2}$ occurs gradually from a much earlier time of $t = 0.8$. In Case UR1, the increase of $\overline{u_3^2}$ is also delayed in comparison to Case U. Thus, the increase of velocity fluctuations due to the effect of unstable stratification is delayed by imposing rotation. Interestingly, in the RDT for Case UR1, neither $\overline{u_1^2}$ nor $\overline{u_2^2}$ increases during all the period of the calculation, although the time evolution of $\overline{u_3^2}$ almost agrees with the result of DNS. Therefore, the increase of both $\overline{u_1^2}$ and $\overline{u_2^2}$, which should be associated with the occurrence of horizontal eddies, results from the effects of the non-linear term, whereas the increase of $\overline{u_3^2}$ relates mainly to the linear term. Figure 13 shows the time evolution of the r.m.s. value of the strain rate $\partial u_3/\partial x_3$. The difference is clearly observed between RDT and DNS for Case UR1 after the time t becomes 1.7. We also find that the time evolution of both $\overline{u_1^2}$ and $\overline{u_2^2}$ is closely associated with that of $\overline{(\partial u_3/\partial x_3)^2}$, i.e., the increase of these quantities begins almost at the same time. These results shown in Figs. 12 and 13 support our supposition that the elongated vortex columns are generated by the vortex stretching term associated with the externally imposed rotation and the strain rate $\partial u_3/\partial x_3$.

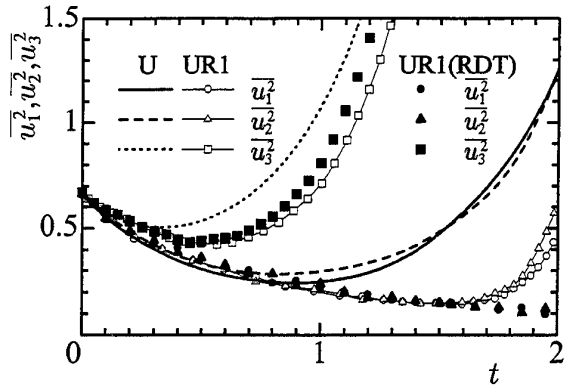

Figure 12: Time evolution of Reynolds stresses in Cases U and UR1.

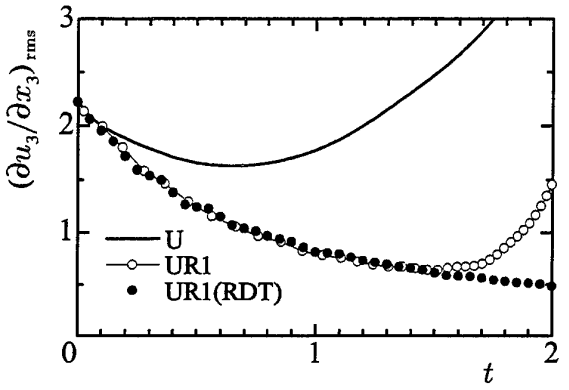

Figure 13: Time evolution of the r.m.s. value of strain rate $\partial u_3/\partial x_3$ in Cases U and UR1.

Figures 14(a) and (b) show the energy spectra of the vertical velocity and vorticity, respectively. It is useful to divide the energy spectrum into two parts; one in the region where the wave numbers satisfy the following formula,

$$f^2 = \frac{N^2(\kappa_1^2 + \kappa_2^2) + 4\Omega^2\kappa_3^2}{\kappa_1^2 + \kappa_2^2 + \kappa_3^2} < 0,$$

the other in the region where the wave numbers satisfy $f^2 > 0$. The domain which satisfies $f^2 > 0$ is

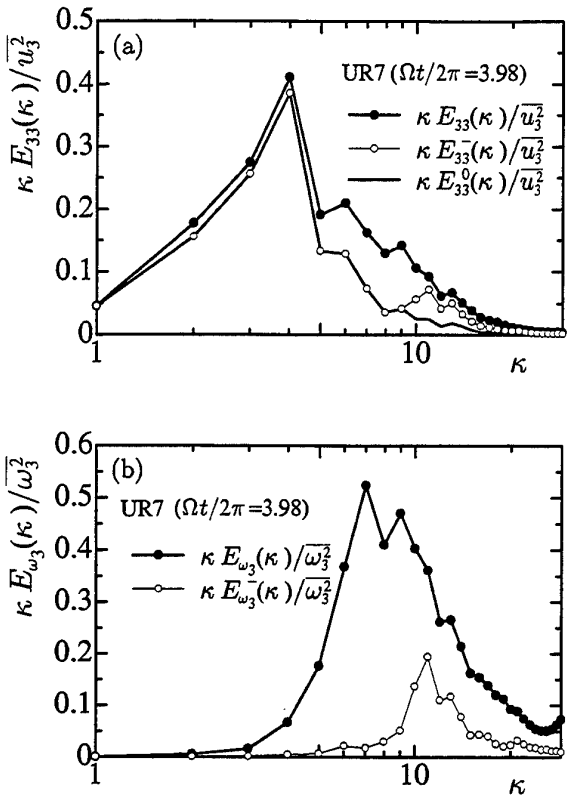

Figure 14: The energy spectra in Case UR7 at the instance $\Omega t/2\pi = 3.98$. The superscripts 0 and $-$ represent energy in the region $\kappa_3 = 0$ and $f^2 < 0$, respectively; (a) Energy spectra of vertical velocity, (b) Energy spectra of vertical vorticity.

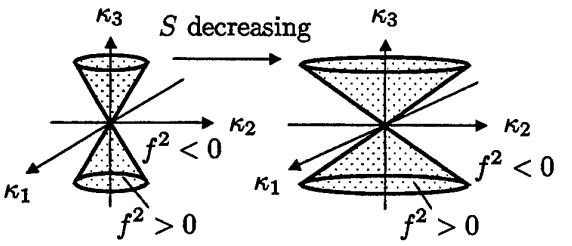

Figure 15: Region of the wave numbers which satisfy $f^2 > 0$.

in a cone, as illustrated in Fig. 15. When a value of the parameter S decreases, the ratio of the height to the base of the cone becomes large, indicating that the domain satisfying $f^2 > 0$ increases and the RDT gives the oscillating solutions over more wave numbers.

The importance of this criterion for the sign of f^2 can be found by analytically solving the equations of RDT as shown in the following.

• $f^2 > 0$

$$\left.\begin{aligned}
&\hat{u}_3(\vec{\kappa},t) = \hat{u}_3(\vec{\kappa},0)\cos ft \\
&\quad + (2\Omega\kappa_3/f\kappa^2)\{\kappa_2\hat{u}_1(\vec{\kappa},0) - \kappa_1\hat{u}_2(\vec{\kappa},0)\}\sin ft \\
&\hat{\theta}(\vec{\kappa},t) = -S_\theta\{\hat{u}_3(\vec{\kappa},0)/f\}\sin ft \\
&\qquad + S_\theta(2\Omega\kappa_3/f^2\kappa^2) \\
&\qquad \{\kappa_2\hat{u}_1(\vec{\kappa},0) - \kappa_1\hat{u}_2(\vec{\kappa},0)\}(\cos ft - 1)
\end{aligned}\right\} \quad (15)$$

• $f^2 < 0$

$$\left.\begin{aligned}
&\hat{u}_3(\vec{\kappa},t) = \hat{u}_3(\vec{\kappa},0)\cosh ft \\
&\quad + (2\Omega\kappa_3/f\kappa^2)\{\kappa_2\hat{u}_1(\vec{\kappa},0) - \kappa_1\hat{u}_2(\vec{\kappa},0)\}\sinh ft \\
&\hat{\theta}(\vec{\kappa},t) = -S_\theta\{\hat{u}_3(\vec{\kappa},0)/f\}\sinh ft \\
&\qquad + S_\theta(2\Omega\kappa_3/f^2\kappa^2) \\
&\qquad \{\kappa_2\hat{u}_1(\vec{\kappa},0) - \kappa_1\hat{u}_2(\vec{\kappa},0)\}(\cosh ft - 1)
\end{aligned}\right\} \quad (16)$$

• $\kappa_3 = 0$

$$\left.\begin{aligned}
\hat{u}_3(\vec{\kappa},t) &= \hat{u}_3(\vec{\kappa},0)\cosh Nt \\
\hat{\theta}(\vec{\kappa},t) &= -(S_\theta/N)\,\hat{u}_3(\vec{\kappa},0)\sinh Nt
\end{aligned}\right\} \quad (17)$$

As is evident in the above formulas, without non-linear terms, both the temperature and vertical velocity spectra increase in the region where f^2 takes a negative value, while they fail to develop in the positive f^2 region. One should also note that in the region of $\kappa_3 = 0$, time evolution of both vertical velocity and temperature field is only dependent on the Brunt-Väisälä frequency N, and thus determined only by buoyancy. In Fig. 14(a), almost all vertical energy is contained in the region $f^2 < 0$, suggesting that it is possible to predict the increase of $\overline{u_3^2}$ without the non-linear term [see Eq. (16)]. It is also found that the energy satisfying $f^2 < 0$ is, at the same time, located in the region $\kappa_3 = 0$. However, around $\kappa = 8$, E_{33} increases in the positive f^2 region where κ_3 takes a non-zero value, and thus contributes to the increase of $\partial u_3/\partial x_3$.

On the other hand, the energy spectrum of ω_3 shown in Fig. 14(b) is almost in the region $f^2 > 0$, and concentrated around $\kappa = 8$ where the energy of $\overline{u_3^2}$ in the region $f^2 > 0$ increases, indicating that the vertical velocity fluctuations satisfying $f^2 > 0$ contribute to the generation of the vortex columns through the linear vortex stretching. Thus, the role of the non-linear term is to increase u_3 at the non-zero value of κ_3 due to the cascade-type energy transfer from the lower to higher wave numbers, which should interrupt oscillation of vertical velocity fluctuations in the region $f^2 > 0$ and enhance their magnitude. This energy cascade should be enhanced by buoyancy force as suggested recently by Komori & Nagata.[23]

When f^2 takes positive value, the following relation is obtained between horizontal and vertical

Table 2: Computational conditions for stably stratified flows

Case	SA	SRA1	SRA2	SB	SRB1	SB2	SRB2	SRB3	SRB4	SRB5	SRB6	SRBF2
N_g	64^3											128^3
r	$\overline{u_1^2}=\overline{u_2^2}>\overline{u_3^2}$			$\overline{u_1^2}=\overline{u_2^2}<\overline{u_3^2}$								
ν	0.012											0.0045
Pr	0.71											
S_θ	1											
$g\beta$	4		16	4		16			25	36	16	
Ω	0	10	2	0	10	0	2	2.5	2		1	2
S	-	0.1	1		0.1		1	0.8	1.2	1.5	2.0	1

wave numbers associated with vortex columns,

$$\frac{2\pi}{\sqrt{\kappa_1^2+\kappa_2^2}} > \frac{2\pi}{\kappa_3}S.$$

The right-hand side of the equation, i.e., $2\pi S/\kappa_3$ represents the internal Rossby radius of deformation. Thus, in the generated vortex columns their horizontal length scale must be larger than the Rossby radius of deformation. This indicated that the Coriolis force directly affects the horizontal structures of vortex and geostrophic balance is pertained, although their vertical structure is determined only by buoyancy force.

3.2 Effects of rotation on stably stratified turbulence

In a stably stratified flow without any injection from the outside, the velocity should be damped in the vertical direction and the flow will become two-dimensional. However, when the flow is disturbed by the thermal plumes and/or internal gravity waves, the velocity component in the vertical direction would become larger than others. In this study, two kinds of the anisotropic flow fields are used as initial conditions, which in the event affect generation of the baroclinic vortices. The computational conditions for stably stratified rotating turbulence are listed on table 2. The anisotropic initial velocity fields are generated by the method similar to Shumann & Patterson[29]. The initial energy spectrum is defined as Eq. (2) in all cases but Case SRBF2 of which energy spectrum has the same form as in Eq. (2) with somewhat different coefficients. In the cases including a classification letter A, e.g., Case SA, an initial flow field is at the two-dimensional state where the vertical component of velocity is exactly zero, while in the cases including a letter B, the vertical velocity surpasses the horizontal ones. Especially, in Case SRB2, the calculation of higher Reynolds number is also carried out with finer resolution which is labeled as Case SRBF2. The parameter S, which should affect the baroclinic instability,

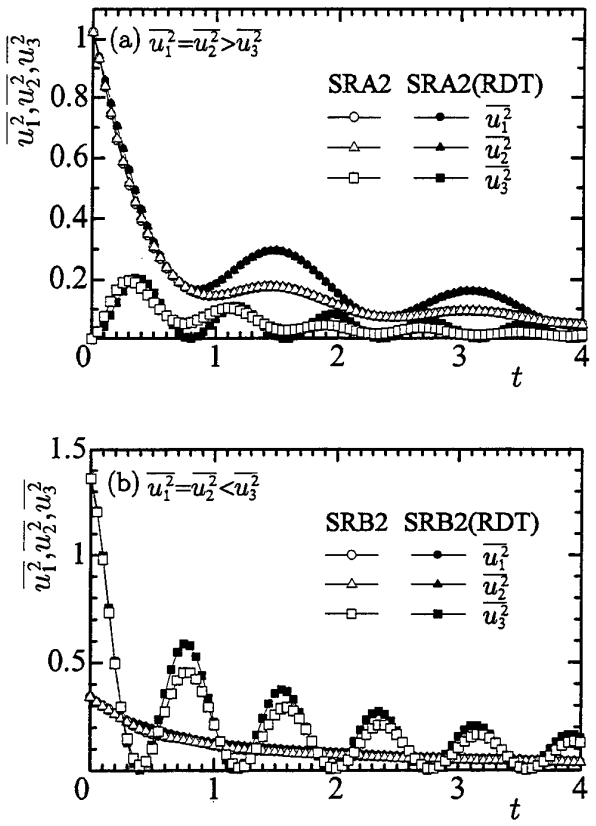

Figure 16: Time evolution of Reynolds normal stresses,(a) Cases SRA2, (b) Case SRB2.

is varied from 0.1 to 2.0 systematically. In the case $S = 0.1$, the rotation surpasses the buoyancy effects, while in the case $S = 2.0$, the rotational effect becomes negligible as discussed later. Thus, the results for case $S = 1$, where the buoyancy and rotational effects are in proportion to each other, are to be discussed in detail to study their combined effects.

Figures 16(a) and (b) show the time evolution of Reynolds normal stresses in Cases SRA2 and SRB2, respectively. For reference, the results of RDT

is also included. In the DNS of Case SRA2, two-dimensionalization of the flow almost persists. In this case, the RDT follows the DNS results qualitatively, although the former gives more oscillatory solutions. This is also true in Case SRB2, in which oscillation of $\overline{u_3^2}$ is clearly observed in both DNS and RDT results. Interestingly, in Case SRB2 the horizontal velocities $\overline{u_1^2}$ and $\overline{u_2^2}$, decay monotonously without oscillation. At $t = 0.4$, 1.2, 2.0, 2.8 and 3.6, the value of $\overline{u_3^2}$ becomes almost zero and the flow becomes two-dimensional instantaneously.

The time evolutions of vorticities are shown in Figs. 17(a), (b) and (c). The symbols (a), (b) and (c) represent Case SRA2, SRB2 and SB2, respectively. It is also found from Figs. 16 and 17(a) that in Case SRA2, the non-linear term suppresses the oscillation of vorticites as well as Reynolds normal stresses. In the DNS results of Case SRA2, all components of vorticities decrease monotonously without much oscillation. On the other hand, in Case SRB2 oscillations of vorticities are clearly observed in both the DNS and RDT. By comparing the results of Fig. 16(b) and Fig. 17(b), one can find that the variance of the vertical vorticity $\overline{\omega_3^2}$ takes a maximum value at the instance when the vertical velocity takes a minimum value and the flow becomes almost two-dimensional. It is interesting that the vertical vorticity oscillates in accordance with the vertical velocity. The oscillation of the vertical vorticity is not observed in the case without rotation as shown in Fig. 17(c). Thus, oscillations of $\overline{\omega_3^2}$ should stem from the baroclinic instability associated with both the rotation and stratification. The non-linear term is not so vitally important for the oscillation of $\overline{\omega_3^2}$. Although not shown here, the time evolutions of the baroclinic and barotropic vorticities, i.e., $(2\Omega/S_\theta)\partial\theta/\partial x_3$ and ω_3, coincide well with each other and the joint p.d.f. between them is negatively well correlated, indicating that the summation of both vorticites always becomes zero. Thus, $\overline{\omega_3^2}$ oscillates in the process that the baroclinic and barotropic vorticities interchange with each other in conformity to the conservation law of the potential vorticity. By comparing the DNS and RDT results in Case SRB2, it is also found that the differences between the RDT and DNS are substantial especially when $\overline{\omega_3^2}$ is decreasing, thus indicating that under the effect of the non-linear term, once generated, vorticites become difficult to disappear.

Figure 18 shows the p.d.f.s of ω_3. In the figure, the dashed curves represent the Gaussian distribution. Initially, all components of the velocity are given as the Gaussian. Hence, without the non-linear term the p.d.f. becomes the Gaussian during the decaying process, and there is no difference between the cyclonic and anticyclonic vortices. In Case SRA2, where two-dimensionalization of the flow is almost retained, the p.d.f.s incline toward the negative

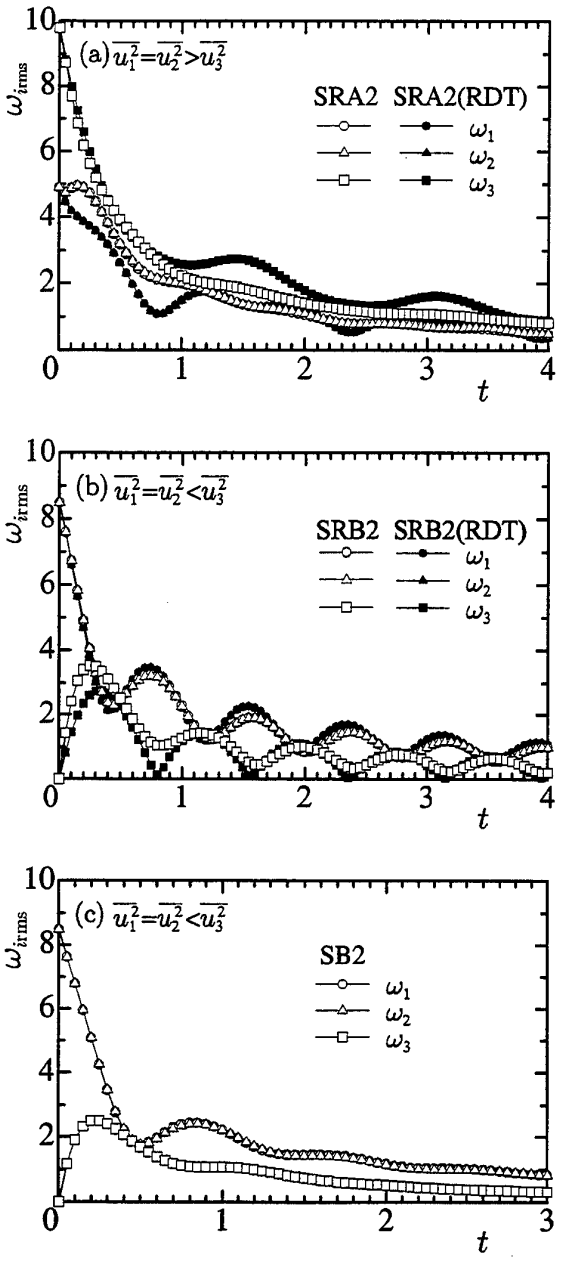

Figure 17: Time evolution of variance of vorticity, (a) Cases SRA2, (b) Case SRB2, (c) SB2.

side of ω_3, indicating that intensive vortices tend to appear as the anticyclonic. On the other hand, in Case SRB2, intensive vortices tend to be cyclonic, especially when the flow becomes two-dimensional. Thus, the anisotropy of Reynolds stresses determines the direction toward which the p.d.f of ω_3 inclines. It is also found that at the time 2.4 when ω_3 becomes almost zero, the p.d.f. deviates markedly from the Gaussian and becomes rather close to an exponential distribution observed in the vorticity p.d.f.

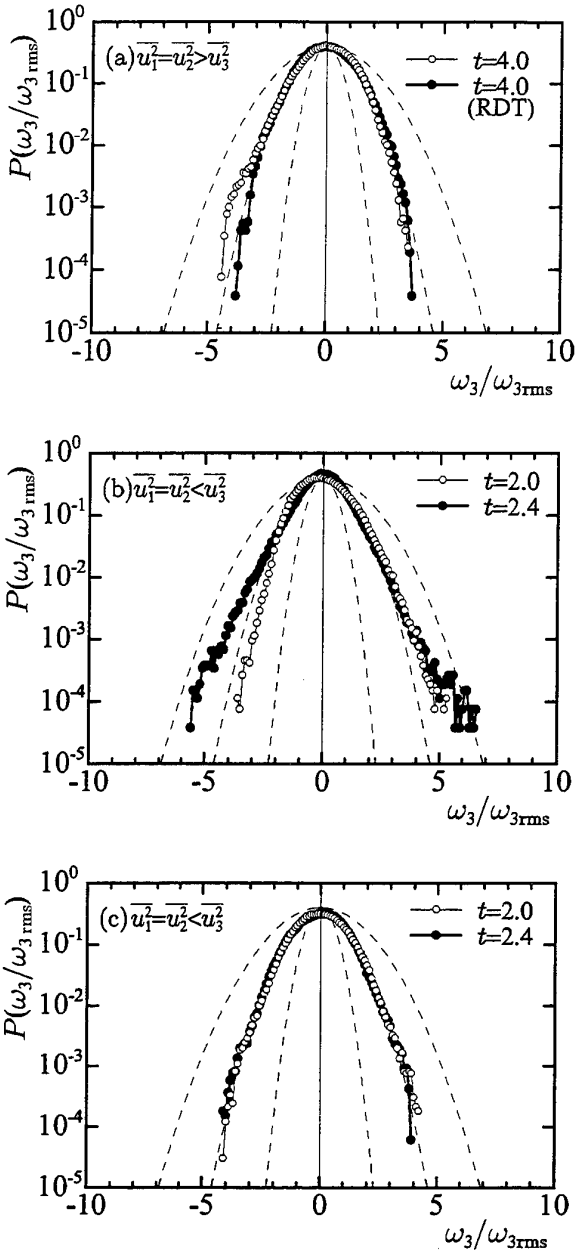

Figure 18: P.d.f.s of vertical vorticity ω_3; (a) Case SRA2, (b) Case SRB2, (c) RDT of Case SRB2.

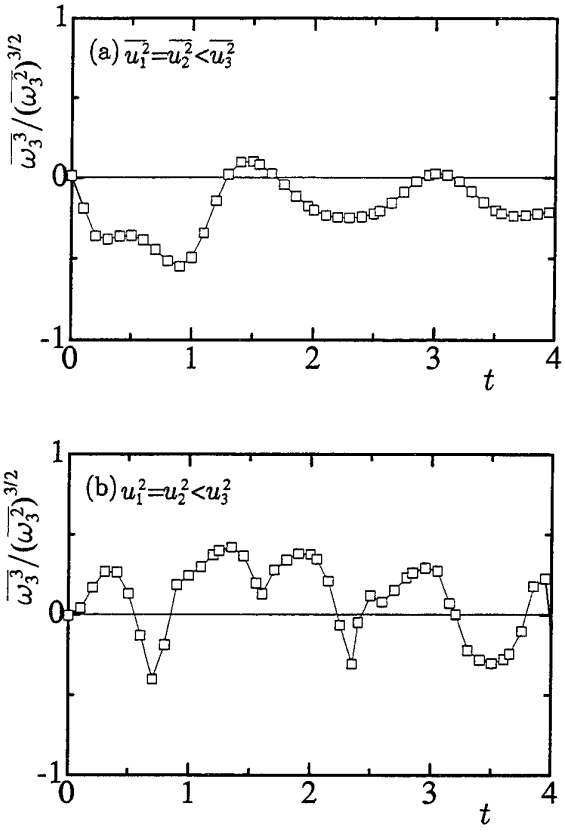

Figure 19: Time evolution of the skewness factor of ω_3, (a) Cases SRA2, (b) Case SRB2.

of uniformly sheared turbulence[30]. In Case SRA2, however, significant deviation from the Gaussian distribution is not observed at any time of decaying.

The time evolutions of the skewness factor of ω_3 are shown in Figs. 19. In Case SRA2 the skewness factor takes a negative value almost over the entire period of calculation. On the other hand, in Case SRB2, it always takes a positive value excluding the period where the $\overline{\omega_3^2}$ becomes almost zero.

Figure 20 shows the instantaneous distribution of the vortices in Case SRBF2 at the time when $\overline{\omega_3^2}$ takes a maximum value. The results of Case SRBF2 are qualitatively similar to those observed in Case SRB2. However, the differences between the DNS and RDT are more clearly seen in Case SRBF2.

In the RDT, there is no difference between the cyclonic and anticyclonic vortices. The DNS result shows that the cyclonic vortices are stretched in the vertical direction and become the tube-like structures. This is because the non-linear vortex-stretching term intensifies and elongates those vortices in the vertical direction. Thus, the p.d.f. of ω_3 is skewed and inclined toward the positive side. Such elongation of cyclonic vortices is also observed in Case SRA2. However, the stretched cyclonic vortices become more dissipasive when flow is almost steady and the generation of $\overline{\omega_3^2}$ is week. Thus, in Case SRA2 the non-linear term reinforces dispersion of cyclonic vortices and makes them more difficult to sustain the initial structures, which results in the emergence of the intensive anticyclonic vortices. The dominance of the anticyclonic vortices was also assured in the experiment[31,32] on stably stratified rotating turbulence, although there has been no related DNS study on homogeneous decaying turbulence.

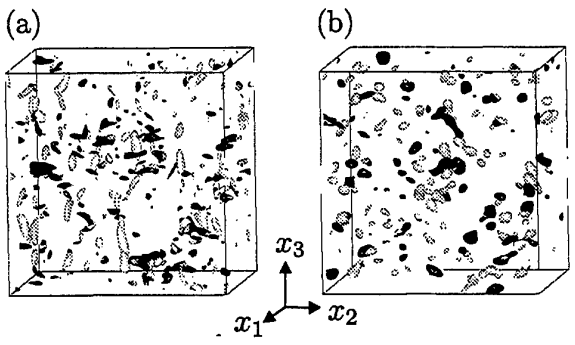

Figure 20: Iso-surfaces of the second invariant of deformation tensor, White iso-surfaces represent the cyclonic vortices, while black iso-surfaces are the anticyclonic vortices at $t = 2.0$ in Case SRBF2; (a) DNS, (b) RDT.

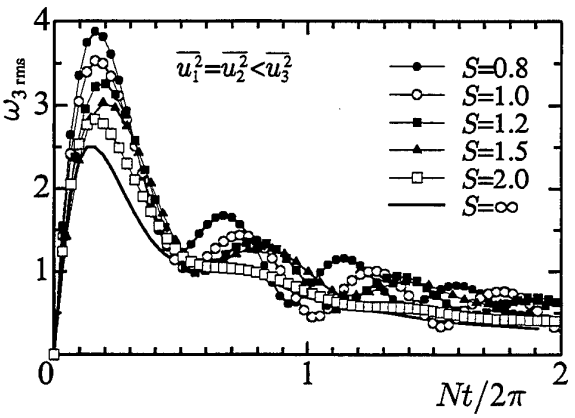

Figure 21: Time evolution of $\overline{\omega_3^2}$.

Finally, we investigate the effects of parameter S on the generation of the baroclinic vortices. Figure 21 shows the time evolution of $\overline{\omega_3^2}$ at the different values of S. When the value of S increases, the oscillation period becomes longer and its amplitude smaller, indicating that the exchange of vorticity between the baroclinic and barotropic vorticities is attenuated. It should be noted that the results of $S = 2.0$ is almost similar to those in the case without rotation. Thus, at this value of S, any vital effects of the rotation and stratification are not observed.

4 CONCLUSIONS

By using both direct numerical simulation and rapid distortion theory, the combined effects of the buoyancy, Coriolis and non-linear term are studied in detail, and the following conclusions are established pertaining to the geostrophic flow under density stratification.

In the neutrally stratified case with rotation, the heat transfer occurs in the direction of rotational axis. Thus, the iso-surfaces of the temperature fluctuations are aligned in the direction parallel to the axis of rotation, and become very close to two-dimensional.

In the unstably stratified case with rotation, the elongated vortex columns are generated in the direction parallel to the axis of rotation. These vortex columns are generated by the effect of linear vortex stretching associated with the externally imposed rotation Ω and strain rate $\partial u_3/\partial x_3$. The linear vortex stretching is closely associated with the process of energy conversion from baroclinic vorticity to barotropic vorticity. RDT cannot generate the vortex columns, because the non-linear term is required to suppress the oscillation and enhance the magnitude of the strain rate $\partial u_3/\partial x_3$.

It is also found that the time evolution of vortex columns is determined by the parameter representing the ratio of the Brunt-Väisälä frequency to the angular frequency of rotation. The vortex columns begin to emerge when both velocity and temperature fluctuations become two-dimensional, and their cross-correlation coefficient becomes almost unity. The horizontal length scale of the vertical vortex becomes larger than the Rossby radius of deformation. Thus, the Coriolis force directly affects the horizontal structures of the vortex, although their vertical structure should be determined by the buoyancy force.

In the stably stratified case with rotation, two kinds of anisotropic initial conditions are used. The effects of parameter S on the generation of baroclinic vortices are also discussed in detail. When the vertical component of velocity is larger than the horizontal counterparts, the exchange of vorticity between the baroclinic and barotropic vortices are activated, and the intensive vortices tend to become cyclonic due to the effect of the non-linear vortex stretching term, while the anticyclonic vortices are attenuated accordingly. On the other hand, when a flow remains to be two-dimensional and the generation of the barotropic vortices is not activated, the non-linear term reinforces dispersion of cyclonic vortices, and makes them more difficult to endure. The combined effects of the Coriolis and buoyancy terms become remarkable, especially in the case where the value of the parameter S is around unity.

NOMENCLATURE

Bo : Buoyancy parameter $= \epsilon/(\sqrt{k}g\beta\Delta T)$

ES1(κ), ES2(κ) : initial three-dimensional energy spectra

$E_{33}(\kappa)$: three-dimensional energy spectrum of vertical velocity

$E_{\omega_3}(\kappa)$: three-dimensional energy spectrum of vertical vorticity

Ek : Ekman number $= \nu\epsilon^2/(2\Omega k^3)$

f : angular frequency

k : turbulent energy $= \overline{u_i u_i}/2$

N : Brunt-Väisälä frequency $= \sqrt{g\beta S_\theta}$

N_g : number of grid points

Pr : Prandtl number $= \nu/\alpha$

p : pressure

Re : Reynolds number $= k^2/(\epsilon\nu)$

Ro : Rossby number $= \epsilon/(2\Omega k)$

$R_{3\theta}$: cross-correlation of vertical velocity fluctuation and temperature fluctuation $= \overline{u_3\theta}/\sqrt{\overline{u_3^2}}\sqrt{\overline{\theta^2}}$

S : ratio of Brunt-Väisälä frequency to angular freuency of rotation $= N/2\Omega$

S_θ : mean temperature gradient $= d\Theta/dx_3$

t : time

u_i : velocity components in the x_i direction

x_i : coordinates of i-th direction

α : thermal diffusivity

β : volume expansion rate

ϵ : dissipation rate of turbulent energy

$\overline{\Theta}$,θ : mean and fluctuating temperature

κ : wave number $= |\vec{\kappa}| = \sqrt{\kappa_i\kappa_i}$

κ_i : wave number in the i-th direction

$\vec{\kappa}$: vector of wave number $= (\kappa_1, \kappa_2, \kappa_3)$

ν : kinematic viscosity

ρ : density

Ω : angular frequency of rotation

ω_i : vorticity fluctuations in the x_i direction

$\overline{(\ )}$: ensemble average

$(\ \hat{}\ )$: Fourier spectrum

REFERENCES

(1) Nakagawa, Y. & Frenzen, P., 1955, A theoretical and experimental study of cellular convection in rotating fluids, *Tellus*, **7**, 1.

(2) Rossby, H. T., 1969, A study of Bènard convection with and without rotation, *J. Fluids Mech.*, **36**, 309.

(3) Busse, F. H. & Hikes, K. E., 1980, Convection in a rotating layer: A simple case of turbulence, *Science*, **208**, 173.

(4) Boubnov, B. M. & Golitsyn, G. S., 1986, Experimental study of convective structures in rotating fluids, *J. Fluid Mech.*, **167**, 503.

(5) Boubnov, B. M. & Golitsyn, G. S., 1990, Temperature and velocity field regimes of convective motions in a rotating plane fluid layer, *J. Fluid Mech.*, **219**, 215.

(6) Fernando, H. J. S., Boyer, D. L. & Chen, R., 1989, Turbulent thermal convection in rotating stratified fluids, *Dyn. Atmos. Oceans*, **13**, 95.

(7) Fernando, H. J. S., Chen, R-R. & Boyer, D. L., 1991, Effects of rotation on convective turbulence, *J. Fluids. Mech.*, **228**, 513.

(8) Sakai, S., 1997, The horizontal scale of rotating convection in the geostrophic regime, *J. Fluid Mech.*, **333**, 85.

(9) Raasch, S. & Etling, D., 1991, Numerical simulation of rotating thermal convection, *Beitr. Phys. Atmosph.*, **64**, 185.

(10) Cabot, W., Hubickyj, O., Pollack, J. B., & Cassen, P., 1990, Direct numerical simulations of turbulent convection:I. Variable gravity and uniform rotation, *Geophys. Astrophys. Fluid Dynmics*, **53**, 1.

(11) Julien, K., Legg, S., McWilliams, J., & Werne, J., 1996, Hard turbulence in rotating Rayleigh-Bénard convection, *Physical Review E*, **53**, 5557.

(12) Julien, K., Legg, S., McWilliams, J., & Werne, J., 1996, Rapidly rotating turbulent Rayleigh-Bénard convection, *J. Fluid Mech.*, **322**, 243.

(13) Jones, H. & Marshall, J. M., 1993, Convection in a neutral ocean; a study of open-ocean deep convection, *J. Phys. Oceanogr.*, **23**, 1009.

(14) Maxworthy, T. & Narimousa, S., 1994, Unsteady, turbulent convection into a homogeneous, rotating fluid with oceanographic applications, *Journal of Physical Ocranography*, **24**, 865.

(15) Helfrich, K. R., 1994, Thermals with background rotation and stratification, *J. Fluid Mech.*, **259**. 265.

(16) Helen, J., & Marshall, J., 1993, Convection with rotation in a neutral ocean: A study of open-ocean deep convection, *Journal of Physical Oceanography*, **23**, 1009.

(17) Speer, K. G., 1989, A forced baroclinic vortex around a hydrothermal plume, *Geophys. Res. Lett.*, **16**, 461.

(18) Bardina, J., Ferziger, J. H., & Rogallo, R. S., 1985, Effect of rotation on isotropic turbulence, *J. Fluid Mech.*, **154**, 321.

(19) Jacquin, L., Leuchter, O., Cambon, C. & Mathieu, J., 1990, Homogeneous turbulence in the presence of rotation, *J. Fluid Mech.*, **220**, 1.

(20) Mansour, N. N., Cambon, C., & Speziale, C. G., 1992, Theoretical and computational study of rotating isotropic turbulence, *Studies in Turbulence*, edited by Gatski, T. B., Sarker, S., & Speziale, C. G., Springer.

(21) Mansour, N. N., Cambon, C., & Speziale, C. G.,

1991, Single point modelling of initially isotropic turbulence under uniform rotation. *In Annual Research Briefs. Center for Turbulence Research, NASA-Ames Research Center-Stanford University.*
(22) Bartello, P., Metais, O., & Lesieur, M., 1994, Coherent structures in rotating three-dimensional turbulence, *J. Fluid Mech*, **273**, 1.
(23) Komori, S. & Nagata, K., 1997, Effects of unstable stratification and mean shear on the chemical reaction in grid-generated turbulence, *Proc. of 11th symposium of Turbulent Shear Flows*, **2**, 21-25, Grenoble, France.
(24) McWilliams, J. C., 1989, Statistical properties of decaying geostrophic turbulence, *J. Fluid. Mech.*, **198**, 199.
(25) McWilliams, J. C., Weiss, J. B., & Yavneh, I., 1994, Anisotropy and coherent vortex structures in planetary turbulence, *Science*, **264**, 410.
(26) Lesieur, M., 1990, *Turbulence in Fluids*, 2nd ed., Kluwer Academic Publishers, The Netherlands.
(27) Metais, O., Bartello, P., Garnier, E., Riley, J. J., & Lesieur, M., 1996, Inverse cascade in stably stratified rotating turbulence, *Dynamics of Atmospheres and Oceans*, **23**, 193.
(28) Gill, A. E., 1982, *Atmosphere-Ocean Dynamics*, Academic Press.
(29) Shumann, U. & Patterson, G. S., 1978, Numerical study of pressure and velocity fluctuations in nearly isotropic turbulence, *J. Fluid Mech.*, **88**, 711.
(30) Kida, S. & Tanaka, M., 1992, Reynolds stress and vortical structure in a uniformly sheared turbulence, *J. Phys. Soc. Japan*, **61**, 4400.
(31) Hopfinger, E. J., 1992, Baroclinic turbulence, *Rotating fluids in geophysical and industrial applications*, Ed., Hopfinger, E. J., Springer-Verlag, Wien-New York, 359.
(32) Dalziel, S. B. & Linden, P. F., 1995, Experiments on turbulence in stratified rotating flows, *Mixing in Geophysical Flows*, Eds., Redondo, J. M. & Metais, O., CIMNE, Barcelona, Spain, 195.

Session 6

Engineering Turbulence Models

NUMERICAL SIMULATION OF TRANSVERSE HYDROGEN INJECTION INTO MACH 6.3 AIRFLOW AND ITS EFFECT ON SURFACE COOLING

D.E. Musielak

Mechanical and Aerospace Engineering Department
University of Texas at Arlington
Arlington, Texas 76019, USA

ABSTRACT

A study was made to determine the effect of transverse fuel injection on the convective heat transfer of an inlet surface, for application to a hypersonic engine. In this model, the flow is predominantly supersonic, but there are regions of flow reversal and boundary layer separation due to shock interaction caused by the fuel jet injected transversally to the freestream air at Mach 6.3. Injection and combustion processes are modeled with a full Navier-Stokes computer code, which incorporates a κ-ω turbulence model, and a seven species/seven equations chemical kinetics model. The flowfield for various hydrogen injection conditions, including the shock-induced reaction zone and the boundary layer separation, is simulated. Results from this study suggest that premixing fuel and air, if properly controlled, can reduce the heat transfer to the inlet walls of high-speed vehicles.

1 INTRODUCTION

In the past several years, there has been renewed interest in the development of pre-mixed, shock-induced combustion for application to hypersonic propulsion. In this concept, hydrogen fuel is injected from both lower and bottom surfaces of the engine's inlet, at several locations upstream from the burner, with the objective of reducing combustor length[1,2]. Other advantages of premixing include reduction of skin friction drag, and the potential for cooling the engine's inlet surfaces. Many challenges exist prior to establishing shock-controlled combustion as a practical concept. These challenges include fuel injection schemes that can provide proper air-fuel mixing without creating large losses, and control of the combustion process so that early ignition or combustion propagation through the inlet boundary layer does not occur. Another challenge lies on the computation and modeling of the supersonic turbulent reacting flows in shock-induced combustion, especially when flow separation is present. Injecting a gas into a supersonic airstream creates an interaction shock, which may separate the incoming boundary layer. Due to the reduced fluid velocity near the solid walls, the flow is very sensitive to streamwise pressure variations and, as a consequence, flow reversal can be induced by the injection of the fuel jet. At some injection conditions, an unstable recirculation zone can form near the wall, upstream and downstream of the injection point. In addition, the condition of the wall also influences the extent of the boundary layer interaction. Cooling of the wall, for example, leads to a decrease in displacement thickness of the viscous sublayer, and the contribution due to the main part of the boundary layer is proportional to the induced pressure rise, according to some relationship that depends on the Mach number of the flow.

Work to develop methods for modeling turbulent supersonic combustion, concentrates on the coupling between the fluid mechanics and the chemistry of the reactant flows. Turbulent fluctuations in the flow variables have a direct effect on the species production rates. Furthermore, correct prediction of boundary layer separation relies to a great extent on the ability of the turbulence model to properly account for adverse pressure gradient flow conditions. Between 1987 and 1995, Menter[3] set up a data base of well documented research flows, and tested a large number of turbulence models against these data. He developed a two-equation model designed to give results similar to those of the original ω-κ model of Wilcox, but without its strong dependency on arbitrary freestream values. As reported by Menter[4], its Shear Stress Transport model has the ability to account for the transport of the principal shear stress in adverse pressure gradient boundary layers.

This paper addresses the cooling effect resulting from injecting hydrogen fuel into high-speed air streams. Because experimental facilities for high hypersonic flows are scarce, a computational modeling approach provides a relatively accurate solution of complex flows, and helps to design needed experiments. This work is part of an ongoing investigation to simulate boundary layer-shock phenomena caused by fuel injection[5,6]. The NASA Langley Algorithm for Research in Chemical Kinetics (LARCK), a multi-dimensional computer program is used to solve laminar and boundary layer flows. The code incorporates various kinetics and turbulence models which can be tailored to fit different applications. This paper reports results using Menter's turbulence model applied to a two-dimensional flow domain.

2 TURBULENCE MODEL AND BOUNDARY CONDITIONS

The equations governing turbulent flow of a high-speed multi-species gas mixture are the Reynolds-averaged Navier-Stokes equations augmented with species

continuity equations. Using Menter's two-equation turbulence model, these equations are solved by LARCK assuming that the gas mixture is described by the perfect gas law. The model assumes that the temperature and species are independent of one another and the following gradient diffusion approximation is used:

$$\overline{\rho u_j'' e''} = -\frac{\mu_T}{\mathrm{Pr}_T}\frac{\partial \tilde{e}}{\partial x_j}$$

where Pr_T is the turbulent Prandtl number, assumed to be 0.90 for this computation.

The turbulent viscosity, μ_T, is defined as

$$\mu_T = \bar{\rho}\frac{a_1 \tilde{\kappa}}{\max(a_1\tilde{\omega},\ \Omega F_2)}$$

where the ω is the specific dissipation rate of turbulent kinetic energy, Ω is the magnitude of the vorticity, a_1 is a constant, and F_2 is a near-wall blending function. The blending function was introduced to recover the original formulation of the eddy-viscosity for free-shear layers where Bradshaw's assumption does not necessarily hold[3,4]. LARCK uses finite-volumes to discretize the flux terms, and an explicit Runge-Kutta time integration to solve the governing equations.

The heat flux vector is modeled with Fourier's law,

$$q_j = -\kappa\, \partial T/\partial x_j + \rho \sum f_n v_{nj} h_n$$

where κ is the coefficient of thermal conductivity, f_n is the mass fraction, v_{nj} is the diffusion velocity of species n in the x_j direction, and h_n is the enthalpy of species n. The coefficient of viscosity for each species in the mixture is calculated using Sutherland's law, and the coefficient of thermal conductivity is computed using the Prandtl number relationship, $\kappa = \mu\, Cp/Pr$.

The code was applied to compute mainly transverse gas injection into a supersonic Mach 6.3 turbulent air stream, at 1000 K and 0.068 MPa static conditions. To simulate transverse fuel injection in a two-dimensional inlet, a flat plate with a flush-wall slot injector was chosen as the model. The plate is 30.48 cm long and the slot is located 10 cm from the leading edge. The transverse dimension of the computational domain is 7.62 cm. The flow and boundary conditions chosen for this investigation are shown in Table 1. The isothermal wall temperature was set at 290 K to be consistent with expected experimental conditions.

3 RESULTS AND DISCUSSION

The character of the undisturbed boundary layer is illustrated by the velocity and temperature profiles in Figures 1 and 2. At the slot position x = 0.10 m, the boundary layer has a thickness δ = 1.49 mm.

Table 1
Flow Conditions
Unit Re = 2.02×10^6

Parameter	Air	Hydrogen
Mach Number	6.3	2.0
Temperature (K)	1000.0	161 - 444
Pressure (kPa)	6.9	353
Boundary Conditions		
Isothermal Wall	T_w = 290 K	
Adiabatic Wall	One comparison case	
Fuel Injection Angle	0, 4, 20, 30	
Slot Size (mm)	0.457 -1.488	

The temperature of the gas has a well-defined transverse distribution in the boundary layer, with temperatures up to 1846 K. As illustrated in Figure 2, starting at the outer edge of the boundary layer and going toward the wall, the gas temperature first increases, reaches a peak at $(y/x)Re^{1/2} = 1.032$, and then decreases to its prescribed cold-wall value T_w = 290 K.

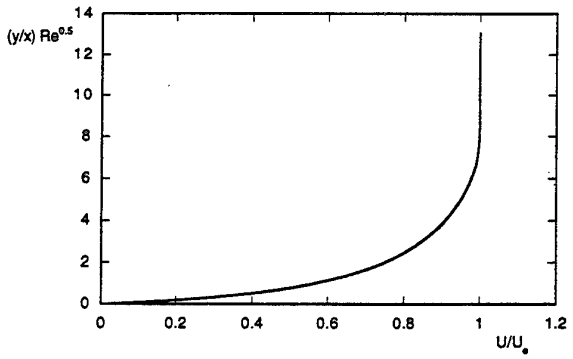

Figure 1 Velocity in Undisturbed Boundary Layer

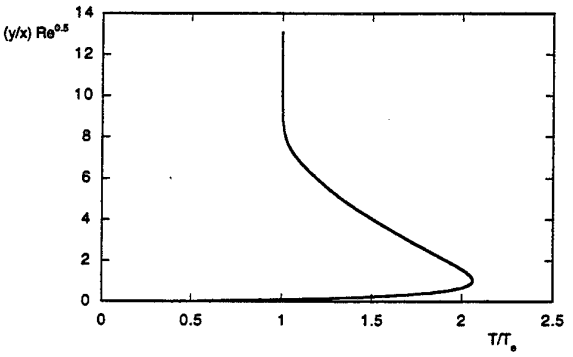

Figure 2 Temperature in Undisturbed Boundary Layer

3.1 Flow Structure of Transverse Injection

Injecting hydrogen into the supersonic airstream creates an interaction shock which separates the incoming air boundary layer. Due to the reduced fluid velocity near the solid wall, the flow is very sensitive to streamwise pressure variations and, as a consequence, flow reversal is induced by the injection of the fuel jet. The flow structure of this interaction is illustrated in Figures 3-4. The supersonic air flow is displaced by the hydrogen jet as if a bluff body was inserted into the airstream boundary layer. As a result, a bow-shock upstream of the injection point is formed causing the upstream boundary layer to separate. The degree of boundary layer separation is a function of the injection angle.

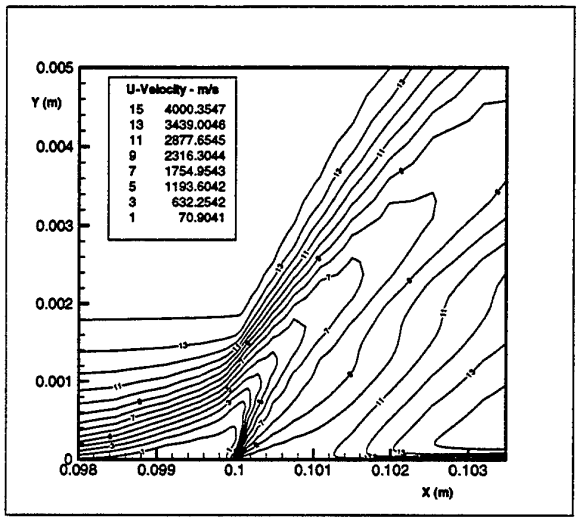

Figure 3 Streamwise Velocity for 30° H_2 Injection

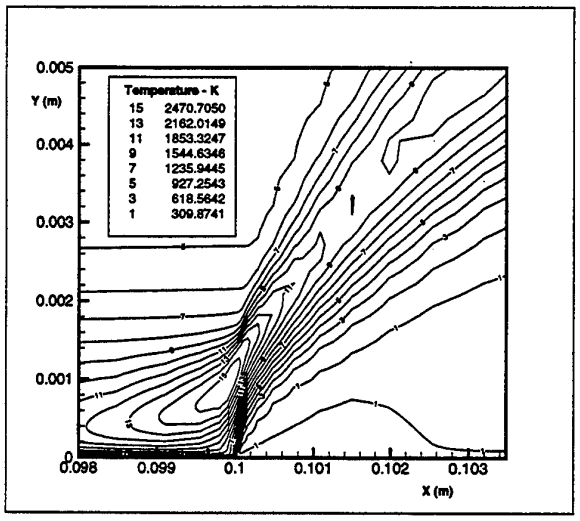

Figure 4 Temperature Field for 30° H_2 Injection

Furthermore, the shock produced by the fuel jet creates a sudden static temperature rise in the airstream which exceeds the ignition temperature of hydrogen. As shown in Figure 4, the peak gas temperature is about 2490 K. The shock is represented by the hot gas region immediately over the hydrogen jet exit. The reaction front follows downstream of the shock, along the high temperature zone depicted in the figure.

3.2 Effect of Fuel Injection on Heat Transfer

The undisturbed boundary layer (no injection) with turbulent flow, using the adiabatic wall condition, is characterized by its large thickness. For example, at the axial location that corresponds to the injection point, the boundary layer thickness is approximately 4.4 mm, and at the exit plane it has increased by a factor of 2.4.

Preliminary estimates of convective heat transfer for thermal boundary layers with variable properties are based on an equation that represents the heat flux at the surface, q_w, as the product of a conductance and an enthalpy difference. A heat transfer coefficient, C_h, can be defined as the ratio $q_w/[\rho u C_p(T_{aw}-T_w)]$. Two computations are needed to determine C_h, i.e., an isothermal wall case and an adiabatic wall case. For the isothermal case the wall temperature is set to 290 K, and the local heat transfer $q_w(x)$ is computed. For the adiabatic case, the zero wall temperature gradient $\partial T/\partial x = 0$ is used as the boundary condition, and the local adiabatic wall temperature $T_{aw}(x)$ is computed. For the undisturbed boundary layer case of this study, the adiabatic wall temperature ranges from 5560 K to 7094 K, with the largest values at the plate's leading edge. Naturally, an adiabatic wall condition would not be practical for any propulsion system. This is because the large stagnation enthalpy of the flow in the boundary layer will heat the wall material beyond its allowable working temperature. The adiabatic wall case is included here only to help establish the effect of the injected fuel on the heat loads for this model.

On the other hand, the isothermal wall condition is of practical interest. As it is well known, a cold wall mitigates the magnitude of the viscous interaction[7]. This is due to the higher density in the boundary layer which results in a thinner boundary layer. In a propulsion system, regenerative cooling with the onboard fuel is usually required, and the cold wall condition of this study is representative of such situation. Also, T_w = 290 K is consistent with the small test times that will be available for experimental validation of these results.

3.2.1 Isothermal Wall

The nature of the undisturbed turbulent boundary layer in the presence of the cold wall, is characterized by a hot sublayer with temperatures up to 1850 K immediately above the cooled viscous layer. With hydrogen injection, the boundary layer gas temperature downstream from the

injector is lowered a few hundred Kelvin, due to mixing of air with hydrogen. As shown, the gas temperature near the wall, downstream from the injector, has been cooled considerably. This results in a reduction of the heat flux, as illustrated in Figure 5, where the effect of injection angle is included. The peaks of the distributions indicate the regions of the shock wave-boundary layer interaction caused by the fuel jet.

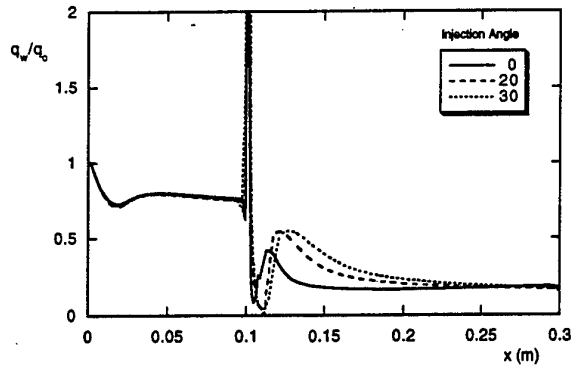

Figure 5 Heat Flux as a Function of Injection Angle

For all injection conditions, the first peak of the normalized heat flux occurs immediately upstream from the injection point. This is to be expected since the boundary layer is lifted in that region. The heat flux begins to increase when the boundary begins to separate, and rapidly increases to its maximum value at the flow impingement point of the incident shock. Downstream from the injector, the normalized heat flux first decreases to a minimum value, increases again to attain the second peak that is dependent on the injection angle, and then decreases smoothly for all cases. The second peak of the heat flux occurs farther downstream for the 30° jet due to stronger recompression shock for this case. At approximately 15 cm downstream from the injector, the effect of injection angle on heat flux is diminished. For all injection cases, however, a considerable cooling effect is evident.

The heat flux distribution follows a profile similar to that of the wall pressure, as shown in Figures 6 and 7 for streamwise and transverse injection respectively. Flow separation begins where the first increase in wall pressure is observed. The flow separates upstream of the injector due to the interaction of the shock with the boundary layer, and it re-attaches at a point downstream, dependent on the jet angle. Correspondingly, at the point of separation, the heat transfer begins to decrease. The minimum value of the heat flux, q_{sv}, represents the lifting of the boundary layer upstream from the injector. As described by Anderson[8], heat transfer and pressure tend to follow the same qualitative variations. These results are consistent with the relationship

$$q_{sv} \propto p_w^n$$

where n depends on the shock-boundary layer interaction.

Streamwise injection is desirable because of its low total pressure losses. As shown in Figures 6 and 7, for 0° injection the normalized wall pressure peaks to a value less than 3 times the freestream value, but it increases over 6 times for 30° injection. However, streamwise injection produces low fuel penetration and low mixing efficiency. Thus, transverse injection should be used if acceptable penetration and mixing are required Furthermore, the increased mixing will ultimately result in a colder boundary layer downstream from the injection point. This is evident in Figure 7, where the normalized heat flux with 30° injection is reduced to 0.147 at the exit plane.

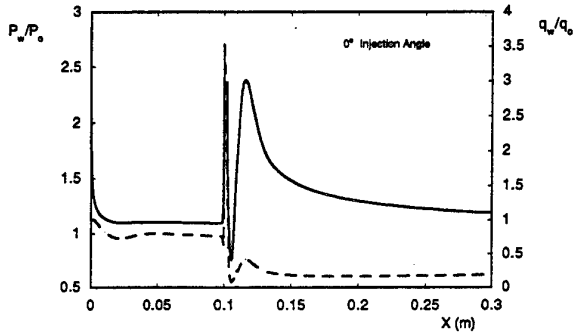

Figure 6 Heat Flux and Wall Pressure - Streamwise Injection

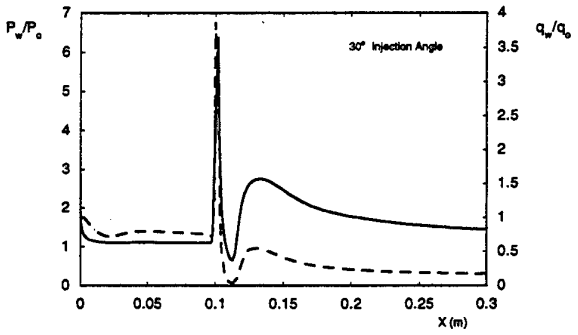

Figure 7 Heat Flux and Wall Pressure - Transverse Injection

The distribution of heat flux upstream and downstream from the slot for 30° injection is given in Figures 8 and 9. The heat flux immediately downstream from the fuel injection point is almost four times that of the undisturbed flow condition. This localized increase is due to the shock wave front immediately above and to the right of the zone where the fuel jet impinges upon the freestream air.

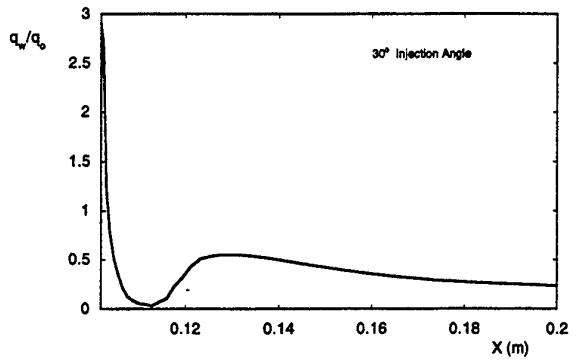

Figure 8 Heat Flux Reduction due to Cooled Boundary

Figure 9 shows the specific heat fluxes in the region of interaction of the boundary layer and the oblique shock. As shown, the value of the heat flux is almost four times higher in the zone of the shock, and one and a half times higher in the zone of boundary layer separation for the 30° jet. However, upon reattachment of the boundary layer, the level of the heat flux decreases dramatically downstream. This is because the heat load is lowered by the effect of the cold hydrogen jet mixing with the hotter air.

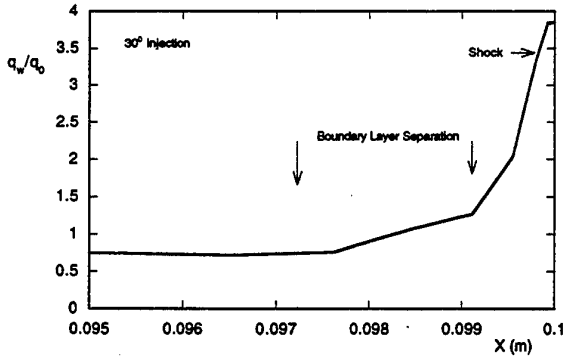

Figure 9 Heat Flux and Boundary Layer-Shock Interaction

3.2.2 Cooling Effect

The wall heat transfer is reduced dramatically by the effect of the hydrogen jet injected tangentially into the airstream. This effect was observed using either isothermal or adiabatic wall conditions. As shown in Table 2, the heat transfer is reduced almost 57 percent with hydrogen injected parallel to the streamwise direction. Also note that, at the injection angle of 20°, for cases 1a and 3c, the total heat transfer rate is approximately the same, but the heat transfer rate downstream from the injector is fifty percent lower with the smallest slot diameter.

The three dimensional nature of the fuel injection process may produce thermal loads that are unevenly distributed. Thus, one can only conclude with these results that, if properly designed, transverse fuel injection into supersonic flows of the type studied herein may result in considerable reduction of the heat transfer.

Table 2
Effect of Fuel Injection on Heat Transfer

Case	m	d mm	Jet Angle	q MW/m^2	Percent Reduction
0	Without H_2 Injection			0.3663	
1a	2.73	0.457	20	0.1735	52.63
3a	6.60	0.457	4	0.1649	54.98
3d	6.60	1.487	0	0.1585	56.73
3c	6.60	1.487	20	0.1713	53.24
3f	6.60	1.487	30	0.1796	50.93

$m = (\rho u)_{fuel}/(\rho u)_{air}$

4 CONCLUSIONS

A detailed calculation of the heat transfer and gas dynamic processes for hydrogen injection in supersonic air flow has been carried out. Analysis of the computed results indicates that injecting cold hydrogen fuel into a supersonic airflow at Mach 6.3 results in significant reduction of the heat load. Injection angle seems to have some effect on the magnitude of heat transferred, however, this effect is concentrated in the region of fuel-air impingement where the level of shock-boundary layer interaction is dependent on the jet angle.

Shock created a sudden static temperature rise in the airstream and the magnitude of the temperature exceeds the ignition temperature of hydrogen. Thermal choking and boundary layer separation were observed.

Additional simulations of the three-dimensional cases are currently in progress. To validate the CFD code, a comparison with limited data reported in the literature will be made and reported in a separate paper.

5 LIST OF SYMBOLS

C_h	wall heat transfer coefficient
d	slot diameter
H_2	hydrogen fuel
L	length of computational domain (flat surface)
m	mass flow parameter
P	gas pressure
Pr	Prandtl Number
q_w	heat flux
T	gas temperature
U	streamwise velocity

u,v	Cartesian velocity components
x,y	Cartesian coordinates
δ	boundary layer thickness
κ	coefficient of thermal conductivity
ρ	gas density

6 REFERENCES

(1) Rubins, P.M. and Bauer, R.C., Review of Shock-Induced Supersonic Combustion Research and Hypersonic Applications, J. of Propulsion and Power, Vol. 10, No. 5, Sept.-Oct. 1994.

(2) Rubins, P.M. and Bauer, R.C., A Hypersonic Ramjet Analysis with Premixed Fuel Combustion, AIAA Paper 66-648.

(3) Menter, F.R., Assessment of Higher Order Turbulence Models for Complex Two- and Three-Dimensional Flowfields, NASA TM 103944, 1992.

(4) Menter, F.R., Improved Two-Equation k-w Turbulence Model for Aerodynamic Flows, NASA TM-103975, 1992.

(5) Musielak, D.E., Simulation of the Fluid Dynamic Behaviour of Transverse Hydrogen Injection in a Hypersonic Airstream . Paper AIAA 97-2224 presented at the 15th Applied Aerodynamics Conference, Atlanta, GA, June 23-25, 1997.

(6) Musielak, D.E., Computational Study of Inlet Injection for Pre-Mixed, Shock-Induced Combustion. Paper AIAA 96-4560, 7th International Spaceplanes and Hypersonic Systems and Technologies Conference, Norfolk, VA, Nov. 18-22, 1996.

(7) J.D. Anderson, Hypersonic and High Temperature Gas Dynamics. McGraw-Hill, Inc. 1989.

(8) Heiser, W.H. and Pratt, D.T., Hypersonic Airbreathing Propulsion, AIAA Education Series, 1994.

Low-Reynolds Number Modelling of Transpired Flows

C. B. Hwang and C. A. Lin*
Department of Power Mechanical Engineering
National Tsing Hua University
Hsinchu, TAIWAN 30043

Abstract

An improved low Reynolds-Number $k - \tilde{\varepsilon}$ model was adopted to predict the dynamic and thermal fields in flows with transpiration. The performance of the adopted model was first contrasted with the DNS data of channel flow with uniform wall injection and suction. The validity of the present model in applying to flows with high level of transpiration was further examined. To explore the model's performance in complex environments, the model was further applied to simulate a transpired developing channel flow. By contrasting the predictions with DNS data and measurements, the results indicated that the present model reproduced correctly the deceleration and acceleration of the flow caused by the injection and suction from the permeable part of the wall. Turbulence structure of transpired flows was also well captured and the superior performance of the adopted model was reflected by the predicted correct level of ε with the maximum locating at both of the injection and suction walls. Predicted thermal field by the present model also compared favourably with the DNS data and measurements.

*corresponding author

1 Introduction

The adoption of wall transpiration as a flow control technique is frequently encountered in a variety of engineering applications. Injection from the permeable wall, for example, has been found to be an effective tool to produce film coolingfor turbine-blades exposed to a hot freestream. As the result of fluid injection into the mainstream, a thicken boundary layer is created and consequently the surface skin friction and hence drag decreases. An elevated level of turbulent kinetic energy is also observed. In aeronautical applications, suction, on the other hand, is frequently used to delay the boundary-layer separation and to inhibit the transition to turbulence. Even though the magnitude of the transpiration rate is often low compared to the mainstream, it significantly changes the surface skin friction as well as turbulence quantities near the wall.

With an aim to investigate the effects of wall transpiration on boundary layers development and heat transfer characteristics, many experiments[1][2][3] had been performed. Despite these efforts, the higher statistical quantities and the detailed near wall flow structure of transpired flows are still lacking. This, however, is partly alleviated by the arrival of the direct numerical simulation (DNS) of transpirational flows[4][5]. The simulated results not only reproduce the previous observed experimental findings of lower moments of the flowfield, but also provide the detailed budgets of the turbulent kinetic energy and its dissipation rate in the vicinity of the wall. The DNS data indicate that the magnitude of the maximum turbulence generation rate is larger on the injection wall and smaller on the suction wall compared to that on the wall without transpiration. Furthermore, the maximum dissipation rate is observed to locate on the transpired wall, as in the case of the non-transpired flows.

Although the DNS data can provide useful transpired flow information, the application of the direct numerical simulation is still restricted to low Reynolds number flows, which are rarely encountered in practical engineering applications. Therefore, it is a common practice to adopt turbulence models to predict transpired flows at elevated Reynolds number[6][7][8]. It is expected that the success in predicting transpired flow should rely on the sufficiently resolved turbulence transport processes and consequently the heat transfer characteristics in the vicinity of the wall. However, due to the lack of detailed and reliable measurements of the near-wall turbulence structure, the forms of the low Reynolds number model were based on ad hoc adjustments of the model constants and damping functions to reproduce the flow fields.

Although DNS data can provide a route towards the modelling of wall turbulence, few of the many proposed models completely satisfy the asymptotic limit and the DNS data[9][10][11]. Based on recent direct numerical simulation data, a simplified form of low-Reynolds-number two-equation turbulence model was proposed[11]. Key features of the model are the adoption of the Taylor microscale in the damping function and the inclusions of the pressure diffusion terms in the k and ε equations. However, the focus of the turbulence modelling was concentrated on non-permeable flows and only a limited number of numerical predictions were directed to transpired flows. In the present study, the proposed model is further applied to predict dynamic and thermal field in flows with transpiration. The predictive performance of the model is assessed by comparisons with DNS data and measurements of transpired flows.

2 Governing Equations

The Reynolds-averaged continuity, Navier-Stokes and temperature equations can be written as,

$$\frac{\partial U_j}{\partial x_j} = 0 \qquad (1)$$

$$\frac{\partial U_j U_i}{\partial x_j} = -\frac{1}{\rho}\frac{\partial P}{\partial x_i} + \frac{\partial}{\partial x_j}[\nu(\frac{\partial U_i}{\partial x_j} + \frac{\partial U_j}{\partial x_i}) - \overline{u_i u_j}]$$

$$\frac{\partial U_j \Theta}{\partial x_j} = \frac{\partial}{\partial x_j}[\frac{\nu}{\sigma}\frac{\partial \Theta}{\partial x_j} - \overline{u_j\theta}] \quad (3)$$

where ν and σ are kinematic viscosity and Prandtl numbers, respectively.

Within the framework of eddy-viscosity and adopting Boussinesq approximation, the Reynolds stress and heat flux are approximated as,

$$-\overline{u_i u_j} = \nu_t(\frac{\partial U_i}{\partial x_j} + \frac{\partial U_j}{\partial x_i}) - \frac{2}{3}\delta_{ij}k \quad (4)$$

$$-\overline{u_j\theta} = \frac{\nu_t}{Pr_t}\frac{\partial \Theta}{\partial x_j} \quad (5)$$

where ν_t and Pr_t are turbulent kinematic viscosity and turbulent Prandtl number, respectively.

In the present applications, the turbulence model adopted is the $k-\varepsilon$ model[12]. When applying the model towards the wall, the contribution of molecular viscosity on the shear stress increases, and the standard high-Reynolds-number turbulence must be modified to account for the diminishing effect of the near-wall turbulence levels. The construction of the low-Reynolds-number model is the focus of the next section.

3 Turbulence Modelling

In the present approach the turbulence is described by the eddy viscosity model which solves the transport equations for turbulent kinetic energy and turbulent dissipation rate. There are currently two directions in solving the dissipation rate equation. The first one is the solution of the ε equation. The second approach is the decomposition of the dissipation rate into two parts, i.e., $\varepsilon = \tilde{\varepsilon} + \hat{\varepsilon}$, and the definitions of ε and $\hat{\varepsilon}$ are,

$$\varepsilon = \nu\overline{\frac{\partial u_i}{\partial x_j}\frac{\partial u_i}{\partial x_j}} \quad (6)$$

$$\hat{\varepsilon} = 2\nu(\frac{\partial\sqrt{k}}{\partial y})^2 \quad (7)$$

Here the form $\tilde{\varepsilon}$ is adopted and the advantage of the approach is that $\tilde{\varepsilon}$ reaches zero at the wall, $\varepsilon_w = \hat{\varepsilon}_w$, and $\tilde{\varepsilon}$ equals to ε at about $y^+ > 15$.

From order of magnitude analysis and the asymptotic study[9][11], it was found that extra terms were needed to compensate the unbalanced terms in the k and $\tilde{\varepsilon}$ equations in the near wall region. These, as argued by Kawamura[9], necessitate the inclusion of the pressure diffusion term in the k and $\tilde{\varepsilon}$ equations.

Based on the above approach, an improved low Reynolds number $k-\tilde{\varepsilon}$ model[11] was proposed and takes the from as,

$$\nu_t = 0.09 f_\mu(y_\lambda)\frac{k^2}{\tilde{\varepsilon}} \quad (8)$$

$$\frac{\partial U_j k}{\partial x_j} = \frac{\partial}{\partial x_j}[\nu\frac{\partial k}{\partial x_j}] + \frac{\partial}{\partial x_j}[\frac{\nu_t}{\sigma_k}\frac{\partial k}{\partial x_j}] \underbrace{-\frac{1}{2}\nu\frac{\partial}{\partial y}[\frac{k}{\varepsilon}\frac{\partial \hat{\varepsilon}}{\partial y}]}_{\Pi_k} - \overline{u_i u_j}\frac{\partial U_i}{\partial x_j} - (\tilde{\varepsilon} + \hat{\varepsilon}) \quad (9)$$

$$\frac{\partial U_j \tilde{\varepsilon}}{\partial x_j} = \frac{\partial}{\partial x_j}[\nu\frac{\partial \tilde{\varepsilon}}{\partial x_j}] + \frac{\partial}{\partial x_j}[\frac{\nu_t}{\sigma_{\tilde{\varepsilon}}}\frac{\partial \tilde{\varepsilon}}{\partial x_j}] \underbrace{-\nu\frac{\partial}{\partial y}[\frac{\tilde{\varepsilon}}{k}\frac{\partial k}{\partial y}]}_{\Pi_{\tilde{\varepsilon}}} - 1.44\overline{u_i u_j}\frac{\partial U_i}{\partial x_j}\frac{\tilde{\varepsilon}}{k} - 1.92\frac{\tilde{\varepsilon}^2}{k} \quad (10)$$

where $y_\lambda = y/\sqrt{\nu k/\tilde{\varepsilon}}$, $\sqrt{\nu k/\tilde{\varepsilon}}$ is the Taylor microscale, and Π_k and $\Pi_{\tilde{\varepsilon}}$ are pressure diffusion terms in the k and $\tilde{\varepsilon}$ equations. The damping functions of the model are set to be,

$$f_\mu = 1 - exp(-0.01y_\lambda - 0.008y_\lambda^3)$$

$$\sigma_k = 1.4 - 1.1exp(-\frac{y_\lambda}{10})$$
$$\sigma_{\tilde{\varepsilon}} = 1.3 - 1.0exp(-\frac{y_\lambda}{10})$$

The adoption of y_λ avoids the obvious defect, i.e. the singularity occurring at the reattaching point by adopting $y^+ = U_\tau y/\nu$. The damping functions are chosen to retain the high-Reynolds-number form away from solid boundaries. The asymptotic values of turbulent Prandtl number σ_k and $\sigma_{\tilde{\varepsilon}}$ are adopted as 0.3 to obtain sufficient dissipation rate in the vicinity of the wall. In the core region of the flow, $\sigma_k > \sigma_{\tilde{\varepsilon}}$ is chosen to eliminate the common drawback that turbulent diffusion of k overwhelms that of ε[13].

The adopted form of the damping function f_μ reproduces correctly the asymptotic limit, i.e. $f_\mu \propto y$ and hence $-\overline{uv} \propto y^3$ towards the wall. The satisfaction of the asymptotic limit also guarantees the correct levels of ε with the maximum locating at the wall itself. This modification is important to properly mimic the turbulence levels and transfer rates as a wall is approached. Besides, the modelled pressure diffusion term $\Pi_{\tilde{\varepsilon}}$ also generates the extra source for $\tilde{\varepsilon}$ in the buffer zone, completely replacing the commonly adopted form of extra term, $2\nu\nu_t(U_{i,jk})^2$[14].

Here, the performance of the $k - \tilde{\varepsilon}$ models proposed by Launder & Sharma (LS)[14] and Chien (CH)[15], which were rated best in the review of Patel et al.[16] and Savill[17], are to be contrasted with the present model's predictions. It should be pointed out that the CH model also includes a different form of pressure diffusion term for $\tilde{\varepsilon}$ equation. The constants and functions adopted by the models are compiled in table 1.

4 Numerical Procedure

The present numerical procedure[18] solves discretised versions of all equations over a staggered finite-volume arrangement. The principle of mass-flux continuity is imposed indirectly via the solution of pressure-correction equations according to the SIMPLE algorithm[19]. The flow-property values at volume faces contained in the convective fluxes which arise from the finite-volume integration process are approximated by the quadratic upstream-weighted interpolation scheme(QUICK)[20].

It was found that the employment of the third order approximation of the surface derivatives arising from the viscous and pressure diffusion processes is essential in reproducing the correct flow near-wall asymptotic behavior, by ensuring that the derivative is evaluated right at the surface.

The computed solution is assumed to have converged to its steady-state when the magnitude of the absolute residual sources of mass and momentum, normalized by the respective inlet fluxes, falls below 0.01%.

5 Results and Discussions

5.1 Channel flow with uniform transpiration-dynamic field

The performance of the proposed model is first contrasted with the DNS data of a channel flow with uniform wall injection and suction[5]. The schematic picture of the flow

is shown in Figure 1. The Reynolds number Re_τ, based on the wall friction velocity U_τ and the channel half-width δ, was set to be 150, where U_τ is the averaged wall shear stress on the two walls. The mass flux ratios on both walls were $F = \frac{v_o}{U_m} = 0.00344$, in which v_o is the wall-normal velocity and U_m is the axial bulk mean velocity.

Grid densities of sizes 60 and 100 in the direction normal to the wall were used to check the grid independence. Preliminary results indicated that the two meshes produced nearly identical results, therefore, the 60 grid was used for all subsequent calculations. To ensure the resolution of the viscous sub-layer, the first grid node near the wall was placed at $y^+ \approx 0.1$.

The influence of the wall transpiration on the flow can be seen by the asymmetric axial velocity distribution across the channel, shown in Figure 2. For comparisons, the $Re_\tau = 150$ DNS data[21] in a fully developed channel flow without wall transpiration are also shown in the figure. It can be clearly seen that the location of the maximum axial velocity is observed to shift towards the suction side, in which the near-wall velocity is accelerated due to the suction flux. The log-law plots on both of the walls are shown in Figures 3 and 4, and a marked different distribution to that without wall transpiration is observed. Referring to Figure 3, an improved prediction by the adopted model is observed in the injection region, and the predicted profile agrees well with the DNS distribution.

Regarding the Reynolds stress, all the models can deliver reasonable predictions, as shown in Figure 5. Further examination of the performances of the models can be directed to the k^+ distributions shown in Figure 6, in the near-wall region. In strong contrast to the shear stress distributions, not all the model can accurately predict the distributions of the turbulent kinetic energy. While the Launder and Sharma model underpredicted the peak value, the best result is predicted by the proposed model. By contrasting the results without wall transpiration, the effects of the presence of injection and suction on the wall are observed to promote and inhibit turbulence generation, respectively.

The effect of the inclusion of pressure diffusion terms as indicated earlier, is best exemplified by observing the ε^+ distributions in the near-wall region, shown in Figures 7. Despite the presence of wall transpiration, the DNS indicate the location of the maximum dissipation rate is right on the wall, as in the case without wall transpiration. The present model shows the correct level of ε with the maximum located at the wall and, in strong contrast, the CH and LS models indicate a misplaced local maxima.

The overall performance of the model is evaluated by examining the predicted turbulence kinetic energy budgets in the near wall region, shown in Figures 8, 9 and 10, where Figure 8 shows the results without wall transpiration. By contrasting with the DNS data, the quality of the present model predictions can be further ascertained. The $k-$budget is in general dominated by production and dissipation processes away from the wall. In the vicinity of the wall, the dissipation rate balances the viscous diffusion process. The effects of the presence of injection and suction at the wall can be

observed to promote and inhibit turbulence generation, respectively. The maximum generation rate on the injection and suction wall is about three times and a quarter to the maximum one without wall transpiration.

To explore the model's performance in the high-Reynolds-number flows, the predicted skin friction coefficients with different level of wall transpiration are contrasted with the LES data[22] and measurements[23][24]. Three transpiration rates were used in this study, and the flow conditions adopted are listed in table 2.

The present fully developed channel flows are compared with the constant pressure case measurements[23][24], i.e. the accelerating parameter, $K = \frac{\nu}{U_\infty^2}\frac{dU_\infty}{dx}$ is zero. This is motivated by the work of Piomelli et al.[22], which indicated that the physical phenomena encountered in a fully developed transpired channel are sufficiently similar to those in a constant pressure boundary layer to allow comparison with the constant pressure boundary-layer results. Therefore, the adopted measurements are with constant free stream velocity. The Reynolds number (Re_δ) based on the momentum thickness ranges from 667 to 3151, and the mass flux ratio (F) is in the range of 0.008 to -0.002.

The predicted friction coefficient normalized with the friction coefficient without wall transpiration is shown in Figure 11, where the solid line is based on the equation proposed by Simpson et al.[25]. The dashed line is the direct extension of the Simpson et al.'s equation to the suction side. It can be clearly seen that the predicted skin-friction coefficient of the present model agrees well with the LES and experimental data, and this indicates the validity of the present model in applying to flows with high level of transpiration.

5.2 Channel flow with uniform transpiration-thermal field

In this section, the focus here is on the predictive capability of the model to thermal field with constant wall temperature within the aforementioned channel flow with wall transpiration[5]. Traditionally, the thermal diffusivity is assumed to be $\alpha_t = \nu_t/\mathrm{Pr}_t$ and the commonly adopted value of Pr_t is 0.9[12]. However, the recent DNS data[26, 27] indicate that the wall value of the turbulent Prandtl number is about 1.1 for normal and large viscous Prandtl number fluids. Preliminary predictions with two different Pr_t indicate marginal difference, though prediction with $\mathrm{Pr}_t = 1.1$ shows more accurate turbulent heat fluxes.

The predicted normalized temperature and turbulent heat flux are shown in Figures 12 to 13, together with DNS data[5]. It can be observed that the assumption of constant turbulent Prandtl number could capture the essential characteristics of the thermal field. Referring to Figures 13 and 14, it can be clearly seen that the present model shows a much better results than the rest of the two models do. This might be attributed to the correct dynamic field predicted.

5.3 Developing Channel Flow with Uniform Injection

To further explore the model's performance in complex environments, the model is applied to

simulate flow in a two-dimensional duct with fluid injection from a permeable part of the wall. Measurements[7] of the flow quantities as well as wall heat transfer characteristics are available to evaluate the model's performance. The geometry of the duct is shown in Figure 14. Flows with three Reynolds number, $Re_m(2hU_{mo}/\nu)$=6700, 9030, and 18500, were investigated, where h is the channel height, U_{mo} is the average inlet streamwise velocity and ν is the kinematic viscosity. Different levels of injection from the permeable wall were also investigated and the injection rate is defined as $F_o = v_w/U_{mo}$, where v_w is the injection velocity. Based on previous investigation of non-permeable flow[11] and the results from previous section, grid, size 100 $\times$ 60, which was nonuniform in both the x and y, was adopted. The first near-wall grid node was placed at $y^+ \leq 0.5$.

Attention here is drawn to the predictions by the present model, and the predictions by CH model is also shown for comparisons. The influences of the injection on the flows at different Reynolds numbers and injection rates can be seen from the streamwise velocity, shown in Figures 15 to 17. Due to the presence of the injection from the bottom wall, the location of the maximum velocity has been shifted upward. An excessive deceleration of the streamwise velocity near the permeable wall was predicted by the CH model compared to the measurements, and the simulation by the present model shows the correct level of flow development.

Finally, attention is directed to the heat transfer predictions at different levels of wall transpiration. Figure 18 shows the local Nusselt number along the permeable wall at Re_m =6000. It can be clearly seen that the elevated level of wall transpiration causes the reduction of Nusselt number. Although both the present and CH models can reproduce this phenomenon, the reduction of Nu predicted by the CH model is excessive compared to the measurements.

6 Conclusion

Dynamic and thermal field within flows with wall transpiration were predicted by an improved low-Reynolds-Number $k-\tilde{\varepsilon}$ model. The performance of the proposed model was first contrasted with the DNS data of channel flow with uniform wall injection and suction. Despite the presence of wall transpiration, the DNS data indicated the location of the maximum dissipation rate is right on the wall, as in the case without wall transpiration. The superior performance of the adopted model was reflected by the predicted correct level of ε with the maximum locating at the wall and, in strong contrast, the CH and LS models indicated a misplaced local maxima. By comparing the predicted skin-friction coefficient with the DNS and LES data, the validity of the present model in applying to flows with high level of transpiration was ascertained. Predicted thermal field by the present model also compared favourably with the DNS data. The model was further applied to simulate a transpired developing channel flow. By contrasting the predicted results with measurements, the results indicated that the present model reproduced correctly the deceleration of the flow caused by the wall

injection and the near-wall heat transfer behavior.

7 Acknowledgements

This research work was supported by the National Science Council of Taiwan under grant NSC-85-2212-E-007-057 and the computational facilities were provided by the National Centre for High-Performance Computing of Taiwan which the authors gratefully acknowledge.

References

[1] Schildknecht, M., Miller, J.A. and Meier, G.E.A., The influence of suction on the structure of turbulence in fully developed pipe flow. *Journal of Fluid Mechanics*, 1979, **90**, PP. 67-107.

[2] Sano, M., Turbulent structure in channel flow with injection. *Trans. JSME, B*, 1994, **60**, PP. 2377-2382.

[3] Antonia, R.A., Zhu, Y., and Sokolov, M., Effect of concentrated wall suction on a turbulent boundary layer. *Physics of Fluids*, **7**, PP. 2465-2474.

[4] Mariani, P., Spalart, P., and Kollmann, W., Direct simulation of a turbulent boundary layer with suction. In *Near-Wall Turbulent Flows*, ed R.M.C. So, C.G. Speziale, and B.E. Launder. Elsevier, Amsterdam, 1993, pp. 347-356.

[5] Sumitani, Y. and Kasagi, N., Direct numerical simulation of turbulent transport with uniform wall injection and suction. *AIAA Journal*, 1995, **33**, pp.1220-1228.

[6] So, R.M.C. and Yoo, G.J., Low reynolds number modeling of turbulent flows with and without wall transpiration. *AIAA Journal*, 1987, **25**, PP. 1556-1564.

[7] Abdel-Rahman, A.K., Hagiwara, Y. and Suzuki, K., Turbulent flow and heat transport in a duct with fluid injection from wall. *Proceeding of the 9th Symposium on Turbulent Shear Flow*, Kyoto, Japan, 1993, pp. 18.4.1-18.4.6.

[8] Sofialidis, D. and Prinos, P.. A., Wall suction effects on the structure of fully developed turbulent pipe flow. *ASME Journal of Fluids Engineering*, 1996, **118**, PP. 33-38.

[9] Kawamura, H, A $k - \varepsilon - \overline{v^2}$ model with special relevance to the near wall turbulence. *Proceeding of the 8th Symposium on Turbulent Shear Flow*, Munich, Germany, 1991, pp. 26.4.1-26.4.6.

[10] Nagano, Y. and Shimada, M., Development of a two-equation heat transfer model based on direct simulations of turbulent flows with different prandtl numbers. *Physics of Fluids*, 1996, *8*, PP. 3379-3402.

[11] Hwang, C. B. and Lin, C. A., An improved low-reynolds-number $k - \tilde{\varepsilon}$ model based on direct numerical simulation data. *AIAA Journal*, 1998, Vol. 36, No. 1, pp. 38-43.

[12] Jones, W. P., and Launder, B. E., The calculation of low-reynolds-number phenomena with a two-equation model of turbulence. *International Journal of Heat and Mass Transfer*, 1973, **16**, pp. 1119-1130.

[13] Nagano, T. and Tagawa, M., An improved $k - \varepsilon$ model for boundary layer flows. *ASME Journal of Fluids Engineering*, 1990, **112**, pp. 33-39.

[14] Launder, B. E., and Sharma, B. I., Application of the energy dissipation model of turbulence to the calculation of flow near a spinning disc. *Letters in Heat and Mass Transfer*, 1974, **1**, pp. 131-138.

[15] Chien, K. Y., Predictions of channel and boundary layer flows with a low-reynolds-number
turbulence model. *AIAA Journal*, 1982, **20**, pp. 33-38.

[16] Patel, V. C., Rodi, W., and Scheuerer, G., Turbulence models for near-wall and low-reynolds number flows: a review. *AIAA Journal*, 1985, **23**, pp. 1308-1319.

[17] Savil, A. M., Some recent progress in the turbulence modelling of by-pass transition. In *Near-Wall Turbulent Flows*, ed R.M.C. So, C.G. Speziale, and B.E. Launder. Elsevier, Amsterdam, 1993, pp. 829-848.

[18] Lin, C. A. and Leschziner, M. A., Three-dimensional computation of transient interaction between radially injected jet and swirling cross-flow using second-moment closure. *Computational Fluid Dynamics Journal*, 1993, **1**, pp. 423-432.

[19] Patankar, S. V., Numerical heat transfer and fluid flow. Hemisphere Publishing Corporation, 1980.

[20] Leonard, B. P., A stable and acurate cnvective mdelling procedure based on quadratic upstream interpolation. *Computer Methods in Applied Mechanics and Engineering*, 1979, **19**, pp. 59-98.

[21] Kuroda, A., Kasagi, N., and Hirata, M., Direct numerical simulation of turbulent plane couette-poiseuille flows: effect of mean shear on the near wall turbulence structure. *Proceeding of the 9th Symposium on Turbulent Shear Flow*, Kyoto, Japan, 1993, pp. 8.4.1-8.4.6.

[22] Piomelli, U., Moin, P. and Ferziger, J., Large eddy simulation of the flow in a transpired channel. *Journal of Thermophysics*, 1991, **5**, pp. 124-128.

[23] Julien, H.L, Kays, W.M. and Moffat, R.J., Experimental hydrodynamics of the accelerated turbulent boundary layer with and without mass injection. *ASME Journal of Heat Transfer* 1971, **93**, pp. 373-379.

[24] Anderson, P.S., Kays, W.M. and Moffat, R.J., Experimental results for the transpired turbulent boundary layer in an adverse pressure gradient. *Journal of Fluid Mechanics*, 1975, **69**, pp. 353-375.

[25] Simpson, R.L., Moffat, R.J. and Kays, W.M., The turbulent boundary layer on a porous plate: experimental skin friction with variable injection and suction.

International Journal of Heat and Mass Transfer, 1969, **12**, pp. 771-789.

[26] Antonia, R.A. and Kim, J., Turbulent prandtl number in the near-wall region of a turbulent channel flow. *International Journal of Heat and Mass Transfer*, 1991, **34**, pp. 1905-1908.

[27] Kim, J. and Moin, P., Transport of Passive Scalars in a Turbulent Channel Flow. In *Turbulent Shear Flow 6*, 1989, pp. 85-96, Springer, Berlin.

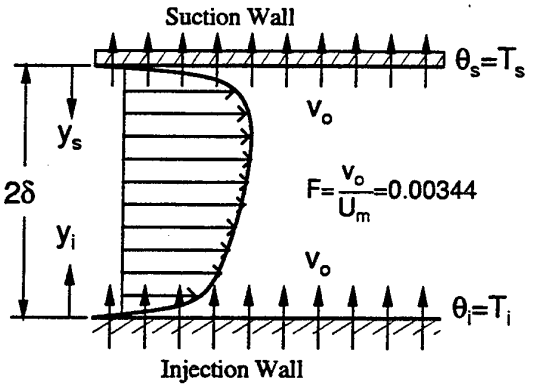

Figure 1: Geometry of turbulent plane flow with uniform wall transpiration

Code	LS(1974)[14]	CH(1982)[15]	present
Type	$k-\tilde{\varepsilon}$	$k-\tilde{\varepsilon}$	$k-\tilde{\varepsilon}$
f_μ	$\exp[-\frac{3.4}{(1+\frac{R_t}{50})^2}]$	$1-\exp[-\frac{1.15y^+}{100}]$	$1-\exp[-\frac{y_\lambda}{100}-\frac{8y_\lambda^3}{1000}]$
Π_k	0	0	$-\frac{1}{2}\nu\frac{\partial}{\partial x_j}[\frac{k}{\varepsilon}\frac{\partial \varepsilon}{\partial x_j}]$
C_μ	0.09	0.09	0.09
σ_k	1.0	1.0	$1.4-1.1\exp[-\frac{y_\lambda}{10}]$
$\widehat{\varepsilon}$	$2\nu(\frac{\partial\sqrt{k}}{\partial y})^2$	$2\nu\frac{k}{y^2}$	$2\nu(\frac{\partial\sqrt{k}}{\partial y})^2$
ε_w	0	0	0
f_1	1	1	1
f_2	$1-0.3\exp[-R_t^2]$	$1-0.22\exp[-(\frac{R_t}{6})^2]$	1
Π_ε	0	$-2\nu(\frac{\varepsilon_w}{y^2})\exp(-0.5y^+)$	$-\nu\frac{\partial}{\partial x_j}[\frac{\varepsilon}{k}\frac{\partial k}{\partial x_j}]$
E	$2\nu\nu_t(\frac{\partial^2 U_i}{\partial x_j \partial x_k})^2$	0	0
$C_{\varepsilon 1}$	1.44	1.35	1.44
$C_{\varepsilon 2}$	1.92	1.8	1.92
σ_ε	1.3	1.3	$1.3-1.0\exp[-\frac{y_\lambda}{10}]$
	$R_t=\frac{k^2}{\nu\varepsilon}$	$R_t=\frac{k^2}{\nu\varepsilon}$ $y^+=\frac{y u_\tau}{\nu}$	$R_t=\frac{k^2}{\nu\varepsilon}$ $y_\lambda=\frac{y}{\sqrt{\frac{\nu k}{\varepsilon}}}$

Table 1: The constants and functions of various forms of $k-\tilde{\varepsilon}$ models

LES data (Exit Re_m = 56840)				
	Blowing		Suction	
	present	LES[22]	present	LES[22]
$F=v_o/U_{max}$	0.00375	0.004	-0.00375	-0.004
$b_f=2F/c_{f,NT}$	2.071	2.030	-2.071	-2.030
LES data (Exit Re_m = 23853)				
	Blowing		Suction	
	present	LES[22]	present	LES[22]
$F=v_o/U_{max}$	0.002	0.00188	-0.002	-0.00188
$b_f=2F/c_{f,NT}$	0.9	0.85	-0.9	-0.85
DNS data (Exit Re_m = 4446)				
	Blowing		Suction	
	present	DNS[5]	present	DNS[5]
$F=v_o/U_{max}$	0.003	0.003	-0.003	-0.003
$b_f=2F/c_{f,NT}$	0.899	0.9	-0.92	-0.9

Table 2: The operating conditions for transpired flows

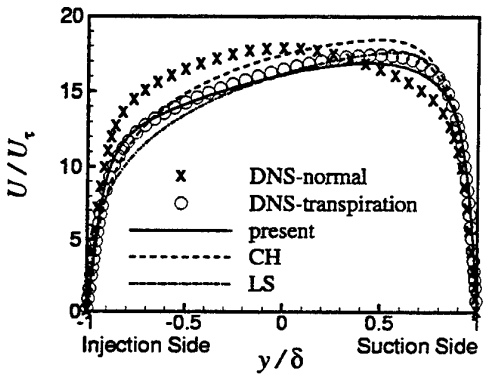

Figure 2: Mean velocity profile

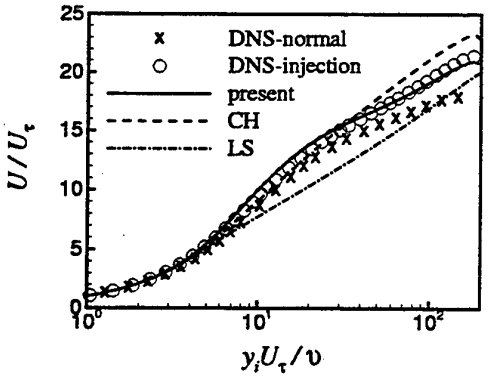

Figure 3: Mean velocity plotted from the injection wall

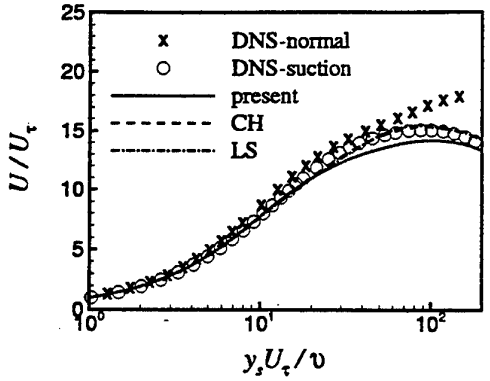

Figure 4: Mean velocity plotted from the suction wall

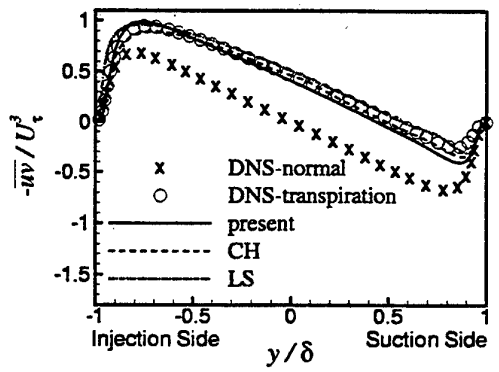

Figure 5: Reynolds shear stress distribution

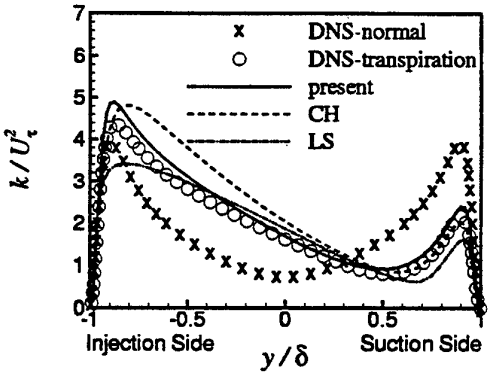

Figure 6: Turbulent kinetic energy distribution

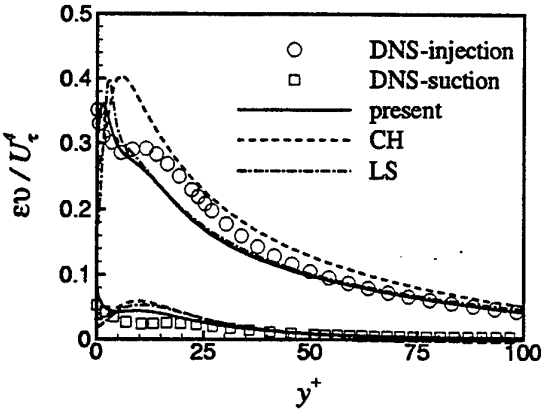

Figure 7: Turbulent dissipation rate distributions

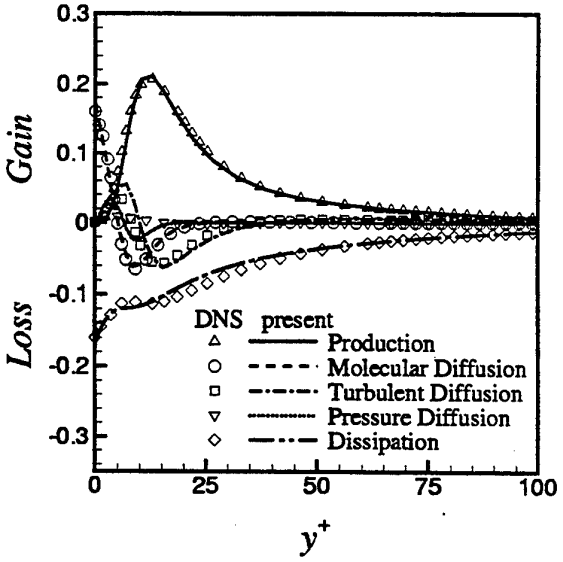

Figure 8: Budget of turbulent kinetic energy without transpiration

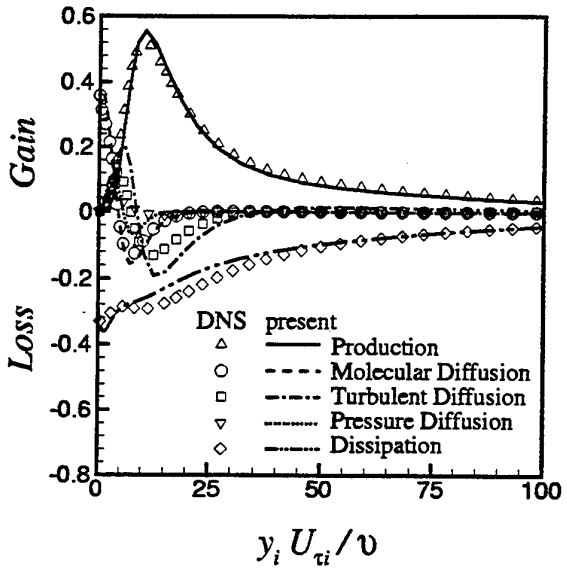

Figure 9: Budget of turbulent kinetic energy in the injection region

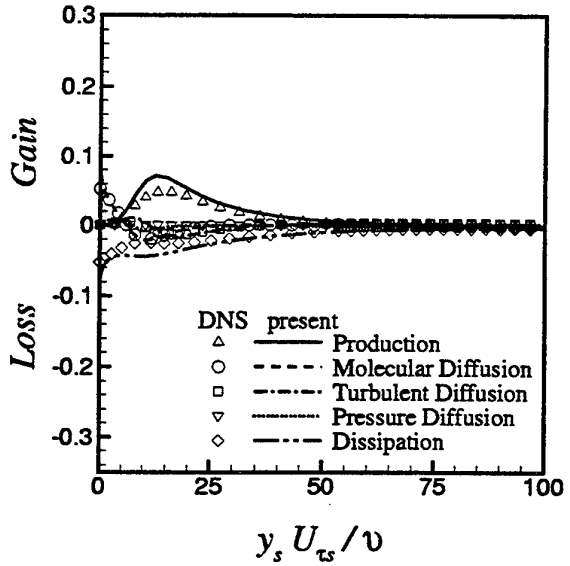

Figure 10: Budget of turbulent kinetic energy in the suction region

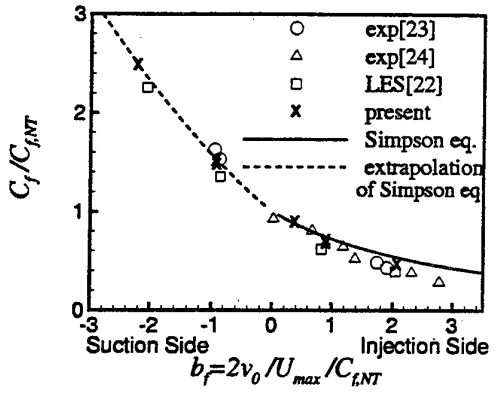

Figure 11: Ratio of friction coefficient to friction coefficient without transpiration

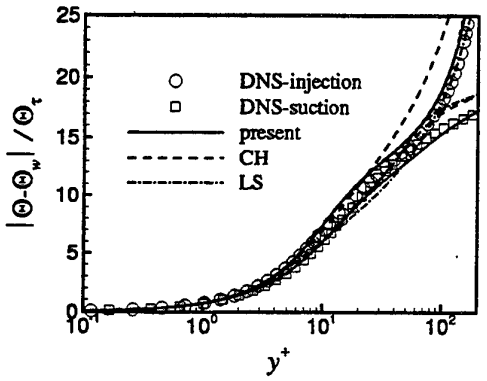

Figure 12: Mean temperature profile for Pr = 1.1

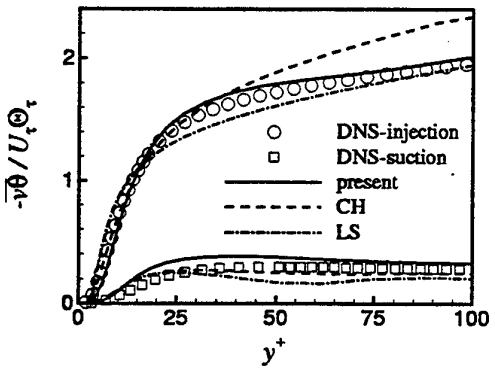

Figure 13: Turbulent heat flux for Pr = 1.1

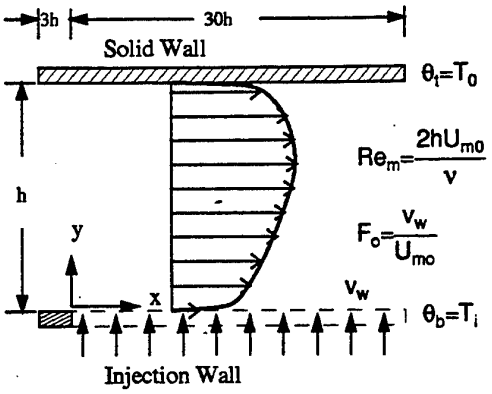

Figure 14: Geometry of duct flow with fluid injection from wall

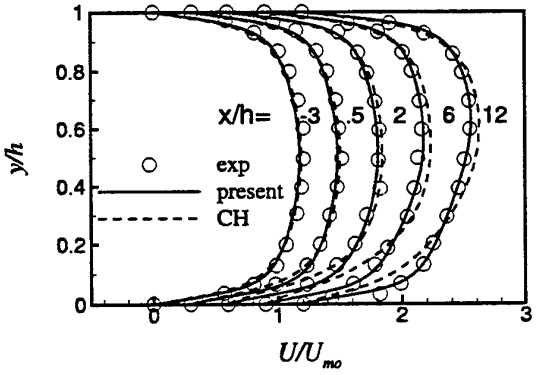

Figure 15: Axial velocity distribution-Re_m = 6700, $F_0 = 0.0087$

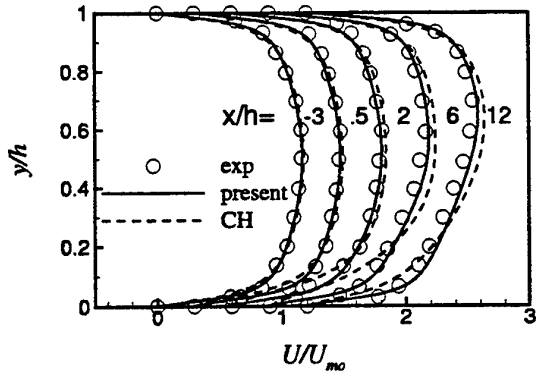

Figure 16: Axial velocity distribution-Re_m = 9030, $F_0 = 0.01$

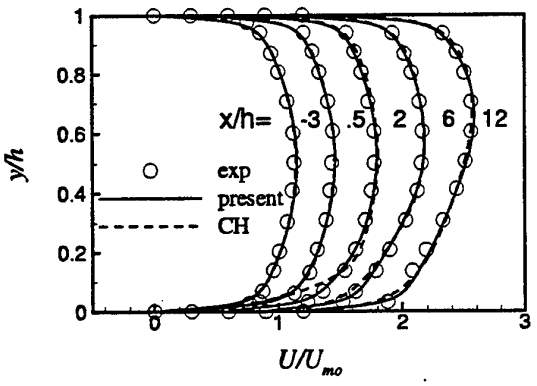

Figure 17: Axial velocity distribution-Re_m = 18500, $F_0 = 0.015$

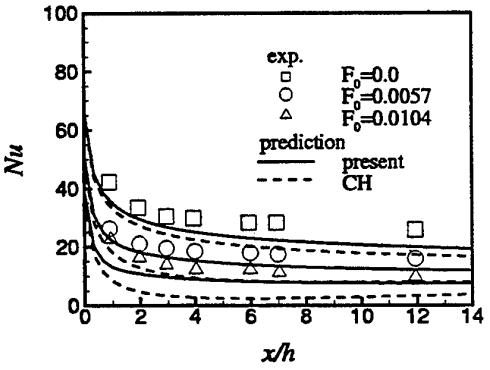

Figure 18: Nusselt number distribution-$Re_m = 6000$

THEORY FOR THE USE OF FOREIGN GAS IN SIMULATING FILM COOLING

T.V. Jones
Department of Engineering Science
University of Oxford
Oxford OX1 3PU
U.K

1. SUMMARY

In the film cooling of turbines the coolant is significantly cooler than the freestream. Consequently the coolant is at a higher density and this plays an important role in determining the flowfield. In laboratory experiments with small temperature differences this density difference is simulated by using dense foreign gas. This paper analyses the effect of molecular properties on the thermal measurements so that they may be related to the cold air situation.

2. NOMENCLATURE

A,B,C - functions of position, eqn (15)
Cp -specific heat at constant pressure
f_1, f_2 - functions
$G_{x,y}$ - mass flux, $\rho u_{x,y}$
i - specific enthalpy
k - thermal conductivity
M - mole fraction
m - mass fraction
Nu_x - Nusselt number = $\dfrac{qx}{k_g(T_{aw}-T_w)}$
Pr - Prandtl number
q - heat flux
Re_x - Reynolds number based on freestream and x
T - Temperature
x - coordinate in freestream direction
y - coordinate perpendicular to surface
β $= \left(\dfrac{\partial B}{\partial y}\right)_b$
δ - viscous sublayer thickness
ε - diffusivity
ζ - thermal diffusion coefficient
η - film cooling effectiveness
λ - mass diffusion coefficient
ξ $= \varepsilon\rho$
ρ - density
μ - viscosity
ϕ $= -\left(\dfrac{\partial C}{\partial y}\right)_b$

Suffices

A - cold air coolant
aw - adiabatic wall
b - evaluated at the bottom of the turbulent region
c - coolant
FG - foreign gas coolant
g - freestream
w - evaluated at the wall

3. INTRODUCTION

The use of foreign gas in film cooling experiments has been prevalent throughout the history of the subject. The foreign gas has been employed in the coolant flows for the following reasons.

1. To act as a tracer gas to determine the distribution of coolant (Goldstein, 1971).
2. To enable coolants of different density to be injected while at the same time acting as a tracer gas. The experiment is essentially isothermal (Goldstein, 1971 and Pedersen et al, 1977).
3. To simulate coolants of different densities in heat transfer experiments (Teekaram et al., 1989).
4. To simulate coolants of different densities in aerodynamic experiments (Day et al., 1996).
5. Although not directly germaine to the present subject there is a class of experiments in which the mass transfer to heat transfer analogy is employed (Eckert, 1986).

Combinations of these techniques are employed whereby the mass transfer analogy is used with a foreign gas injection (e.g. Ammari, Hay and Lampard, 1989) or a tracer gas is used within a different foreign gas (e.g. Salcudean et al., 1994).

The objective of the present paper is to explore the interpretation of the third class of experiments, referred to as *case (3)* in the following.

Although there are situations where gases dissimilar to the freestream are injected for film cooling purposes this paper is concerned with the simulation of the gas turbine situation. In this case a significant ratio of coolant to freestream density occurs, resulting from their temperatures. The coolant temperature may be 1000K and the freestream 2000K giving density ratios of approximately two. In order to reproduce such large density ratios in a laboratory situation recourse to the use of heavy foreign gas as the coolant has been common. At present there is no general scaling parameter or procedure for the film cooling process and hence the need simulate the coolant density. The first tests of the use of foreign gas to simulate the injection of relatively cold air coolant were those of Teekaram,

Forth and Jones (1989). In these experiments equivalent densities and mass flow rates were achieved by injecting CO_2 and air at different temperatures. The different thermal boundary conditions were taken into account by the normalisation of temperatures, inherent in the definition of film cooling effectiveness. Thus the mass flux and the momentum flux of coolant were reproduced and the assumption was that this generated the same flow field. At the same time little thought was given to the fact that the molecular properties of air and CO_2 were different, other than to note this difference and argue that the effects on the similarity of the parameters measured would be small. The experiments were performed to test this assumption and indeed showed good agreement between the air and CO_2 injection at the same coolant to freestream density ratio and injection to freestream velocity ratio. Since this time other workers have employed foreign gas to simulate density differences in heat transfer experiments (e.g. Han and co-workers 1993, 1995 and 1997).

In this paper analysis of the simulation of the thermal field is undertaken. This results in a justification for the close correspondence in the CO_2/air experiments and also gives formulae to correct experimental data for different gases.

4. SIMULATION OF COOLANT FLOWS

The boundary layer flow field in gas turbine film cooling is highly turbulent. The transport of species, momentum and enthalpy is thus dependent on the turbulent flow field generated by the coolant injection. The role of viscosity is secondary other than in the surface sublayer and perhaps within the injection geometry. Thus, if coolant of the same density although a different gas, is injected with the same velocity then the turbulent flowfield should be similar. Discharge coefficients of blade cooling holes are only Reynolds number dependent at low flow rates (Rowbury et al 1998). Also the thickness of a viscous sublayer under a flat plate turbulent boundary layer is dependent on Reynolds number to the tenth power. Hence the effects of Reynolds number changes due to foreign gas can be considered small in the first instance. Of course, freestream conditions and hence Reynolds number are assumed to be the same. It should be pointed out that the correspondence between flow fields referred to above obtains when both coolant density and mass flow (i.e. velocity) are simulated. Merely matching momentum flux is not a sufficient condition. Many workers do make the latter assumption and compare results for film cooling effectiveness and heat transfer coefficient in this case. It is obvious that such comparisons are approximate at best.

5. BASIC EQUATIONS

The basic boundary layer differential equations for flows of gas mixtures are given in Kays and Crawford (1993). For a binary mixture of an inert, foreign gas coolant in a freestream gas the mass concentration equation is,

$$G_x \frac{\partial m}{\partial x} + G_y \frac{\partial m}{\partial y} - \frac{\partial}{\partial y}\left(\lambda \frac{\partial m}{\partial y}\right) = 0 \qquad (1)$$

The energy equation is

$$G_x \frac{\partial i}{\partial x} + G_y \frac{\partial i}{\partial y} - \frac{\partial}{\partial y}\left(\varsigma \frac{\partial i}{\partial y}\right) = 0 \qquad (2)$$

m is the mass concentration of the coolant and i is the specific enthalpy of the mixture

i.e. $i = i_g\,(1\text{-}m) + i_c m.$ (3)

The local mass flux is G and λ and ς are the mass and thermal diffusion coefficients respectively. It has already been assumed that the diffusion coefficients are equal in arriving at these approximate governing equations. In the context of the present turbulent flow they refer to the turbulent quantities and their equality means that the turbulent Lewis number is unity. For gases this assumption is reasonable (Kays and Crawford 1993).

The thermal problem must generally be specified in terms of enthalpy, i, boundary conditions rather than in terms of temperature, T, which is the conventional method. The use of temperature arrives at the usual description of film cooling in terms of the film cooling effectiveness, η, where,

$$\eta = \frac{T_g - T_{aw}}{T_g - T_c}$$

suffices aw, g and c refer to the adiabatic wall, freestream and coolant respectively. The effectiveness is independent of the temperature boundary conditions as may be shown by superposition (Jones, 1991).

In the *case (1)* of experiments where a low concentration of tracer gas is employed the flow is essentially composed of a single gas and the energy equation may be written in terms of temperature.

$$G_x \frac{\partial T}{\partial x} + G_y \frac{\partial T}{\partial y} - \frac{\partial}{\partial y}\left(\varsigma \frac{\partial T}{\partial y}\right) = 0 \qquad (4)$$

The adiabatic wall case corresponds to that of an impermeable wall for the concentration equation. Thus at the wall (suffix w);

$$\left(\frac{\partial m}{\partial y}\right)_w = \left(\frac{\partial T}{\partial y}\right)_w = 0 \qquad (5)$$

The concentration field thus corresponds to the temperature field and,

$$\frac{m}{m_c} \equiv \frac{T - T_g}{T_c - T_g} \qquad (6)$$

giving the film cooling effectiveness as

$$\frac{m_w}{m_c} = \frac{T_{aw} - T_g}{T_c - T_g} = \eta \qquad (7)$$

In *case (2)* dense foreign gas is injected such that coolant density is significantly different to that of the freestream. This corresponds to the higher density of cold air injection. Again the majority of the flowfield and boundary conditions correspond for the adiabatic wall case and the film cooling effectiveness is given by eqn. (7). There is possibly an influence of different properties in the sublayer on the flowfield due to the molecular viscosity being different.

6. THERMAL FIELD FOR AN ADIABATIC WALL

The *case (3)* considered in this section obtains when the foreign gas is at a different temperature to the freestream. The adiabatic wall temperature is determined in an experiment and the effectiveness for the equivalent air case is sought. In this case the enthalpy boundary conditions relate to the mass fraction as Cp is not constant. From eqn. (3)

$$Cp = Cp_g(1-m) + Cp_c m \qquad (8)$$

In the following it is assumed that Cp's of air and foreign gas are independent of temperature. Hence Cp is only a function of concentration. This assumption is valid for the foreign gas experiments as these are conducted at modest temperature differences, the large density differences being simulated by the concentration of foreign gas as already described. For the air or engine cases, large temperature differences are present, however, the value of C_p can be taken as being essentially constant. Thermal conductivity is dependent on temperature and the local value is used for the engine situation. Again, the thermal conductivity is a function of concentration for the foreign gas experiment.

At the wall

$$\left(\frac{\partial i}{\partial y}\right)_w = \left(\frac{\partial Cp}{\partial y}\right)_w T_w + \left(\frac{\partial T}{\partial y}\right)_w Cp_w = Cp_w \left(\frac{\partial T}{\partial y}\right)_w = 0$$

as the wall is impermeable and adiabatic.

Thus the boundary conditions for i and m are identical if the isothermal case at T_g is subtracted from the case considered as this is also a zero heat transfer situation. Thus:-

Freestream	$\frac{i}{0}$	$\frac{m}{0}$
Coolant	$Cp_c(T_c - T_g)$	1
Wall	$C_{p_w}(T_{aw} - T_g)$	m_w

Thus $$\frac{Cp_w(T_g - T_{aw})}{Cp_c(T_g - T_c)} = \frac{m_w}{1}$$

but in this case $\left(\frac{T_g - T_{aw}}{T_g - T_c}\right) = \eta_{FG}$ i.e. the film cooling effectiveness measured with foreign gas. The film cooling effectiveness for cold air η_A with the same coolant density is given by setting $Cp_c = Cp_g$. Thus

$$m_w = \eta_A = \frac{Cp_w}{Cp_c}\eta_{FG} \qquad (9)$$

Cp_w is found from eqn (8), giving,

$$\eta_{FG} = \frac{Cp_c \eta_A}{Cp_g(1-\eta_A) + Cp_c \eta_A} \qquad (10a)$$

also,

$$\eta_A = \frac{C_{p_g}\eta_{FG}}{Cp_c(1-\eta_{FG}) + Cp_g \eta_{FG}} \qquad (10b)$$

The suffices FG and A refer to the cases for foreign gas and air respectively.

7. HEAT TRANSFER

The equivalence between the air and foreign gas enthalpy fields is not exact in *case (3)* when heat transfer is present as the sublayer molecular properties will be influential and different. However, as in the previous section it may be assumed that the turbulent flow field does correspond. If correspondence is thus sought for the turbulent region, the sublayer may be added subsequently. The temperature at the bottom of the turbulent layer is given by T_b as shown in Fig.1.

The heat transfer at b in Fig.1 is given by,

$$q_b = \xi_b \left(\frac{di}{dy}\right)_b \qquad (11)$$

where $\xi_b = \varepsilon_b \rho_b$

ε and ρ being the turbulent diffusivity and density respectively. As $\left(\frac{\partial m}{\partial y}\right)$ at the wall is zero it can be assumed that

$$\left(\frac{\partial C_p}{\partial y}\right)_b = \left(\frac{\partial C_p}{\partial y}\right)_w = 0 \qquad (12)$$

Thus $q_b = \varepsilon_b \rho_b C\dot{p}_w \left(\frac{dT}{dy}\right)_b$ (13)

Assuming that heat transfer takes place by conduction through the sublayer of thickness δ.

$$q_b = k_b\left(\frac{T_b - T_w}{\delta}\right) \qquad (14)$$

where k is the conductivity.

The enthalpy field in the turbulent region will be of the form

$$i = A + BCp_c\left(T_c - T_g\right) + CCp_w\left(T_b - T_g\right) \qquad (15)$$

where A,B and C are functions of position.

This expression arises due to the linearity of the energy equation, eqn. (2), in enthalpy allowing superposition of the enthalpy fields for different boundary conditions given in Fig.2. A is the enthalpy field for isothermal conditions; B that for a coolant of unit enthalpy and zero enthalpy in the freestream and at the wall; C corresponds to unit enthalpy at the wall and zero freestream and coolant enthalpy.

Differentiating eqn. (15) with respect to y and using eqn. (11) gives the heat transfer rate as,

$$\frac{q}{\xi_b} = \beta Cp_c\left(T_c - T_g\right) - \phi Cp_w\left(T_b - T_g\right) \qquad (16)$$

where $\beta = \left(\frac{\partial B}{\partial y}\right)_b$ and $\phi = -\left(\frac{\partial C}{\partial y}\right)_b$

When the wall is adiabatic then $T_b = T_{bad} = T_{aw}$.

Thus $\left(\frac{T_g - T_{aw}}{T_g - T_c}\right) = \frac{Cp_c\beta}{Cp_w\phi} = \eta_{FG}$

When $Cp_c = Cp_w = Cp_g$ this equals η_A and therefore,

$$\eta_A = \frac{Cp_w}{Cp_c}\eta_{FG}$$

This equation is the same as found previously, eqn. (9). Substituting back in eqn. (16) for T_g -T_c gives,

$$\frac{q}{\varepsilon_b \rho_b} = \phi Cp_w\left(T_{aw} - T_b\right) \qquad (17)$$

Eliminating T_b using eqn (14) gives

$$\frac{q}{\left(T_{aw} - T_w\right)} = \frac{\phi \varepsilon_b \rho_b Cp_w}{1 + \frac{\phi \varepsilon_b \rho_b Cp_w \delta}{k_w}} \qquad (18)$$

Thus the Nusselt number, Nu, becomes

$$Nu = \frac{qx}{k_g\left(T_{aw} - T_w\right)} = \frac{\phi \varepsilon_b \rho_b x}{k_g} \frac{Cp_w}{1 + \frac{\phi \varepsilon_b \rho_b \delta Cp_w}{k_w}} \qquad (19)$$

Dimensional reasoning shows that the term in eqn. (19) $\phi\varepsilon_b\rho_b x$ may be expressed as a function of freestream Reynolds number and coolant injection properties,

$$\frac{\phi \varepsilon_b \rho_b x}{\mu_g} = f_1\left(\mathrm{Re}_{xg}, \frac{\rho_c}{\rho_g}, \frac{u_c}{u_g}\right)$$

The term containing δ may be similarly expressed in terms of function f_2. Hence eqn. (19) becomes,

$$Nu = \frac{\mathrm{Pr}_g \frac{Cp_w}{Cp_g} f_1}{1 + \mathrm{Pr}_g \frac{Cp_w}{Cp_g} \cdot \frac{k_g}{k_w} f_2} \qquad (20)$$

Thus the ratio of Nusselt number for the cold air or engine case to that for the foreign gas simulation which is at the same Reynolds number and coolant to freestream density and velocity ratios becomes,

$$\frac{Nu_A}{Nu_{FG}} = \left(\frac{Cp_w}{Cp_g}\right)_{FG} \cdot \frac{1 + \left[\mathrm{Pr}_g \frac{Cp_w}{Cp_g}\frac{k_g}{k_w}\right]_{FG} f_2}{1 + \left[\mathrm{Pr}_g \frac{k_g}{k_w}\right]_A f_2} \qquad (21)$$

Again it is assumed that Cp for air is independent of temperature.

Analytical solutions for constant property flows matching the viscous sublayer to the turbulent region above are available and use may be made of these to obtain an approximate value of f_2.

Thus an estimate of the flowfield term f_2 in eqn (21) may be made from the heat transfer to a flat plate in a uniform flow. From standard texts (e.g. Kays and

Crawford, 1993) the constant property equation, for gases, is,

$$Nu_x = \frac{0.0287\,\mathrm{Re}_x^{\,0.8}\,\mathrm{Pr}}{0.169\,\mathrm{Re}_x^{\,-0.1}(13.2\,\mathrm{Pr}-8.66)+0.85} \qquad (22)$$

Pr is the Prandtl number and Re_x is the Reynolds number based on distance, x, from the leading edge. Eqn (22) may be rearranged to give,

$$Nu_x = \frac{\mathrm{Pr}\,f_1(\mathrm{Re}_x)}{1+\dfrac{2.62\,\mathrm{Pr}}{\mathrm{Re}_x^{\,0.1}-2.00}} \qquad (23)$$

The last term in the denominator corresponding to the thermal resistance of the sublayer represented by the term f_2Pr in eqns. (20) and (21). As can be seen the term is relatively insensitive to Reynolds number and as stated refers to the constant property case.

$$f_2 = \frac{2.62}{\mathrm{Re}_x^{\,0.1}-2.00} \qquad (24)$$

For $Re_x=10^5, f_2=2.25$ and for $Re_x=10^6, f_2=1.32$

Cp_{wFG} and k_{wFG} are determined from $\eta_A=m$ found from eqn.(10b). Cp_{wFG} is given by eqn.(8). k_{wFG} is approximately given by an equation of the same form, i.e.,

$$k = k_g(1-M)+k_cM \qquad (25)$$

but in this case M is the mole concentration determined from m. The value of k for the air case is determined by the relevant temperature.

It should finally be mentioned that the foregoing analysis has assumed that the local wall temperature represents, the isothermal wall situation. This is not exact, however, as Eckert (1992) points out "the upstream temperature or heat flux distribution has little effect on the local Stanton number in a turbulent boundary layer".

8. EXPERIMENTAL RESULTS

Heat transfer results are available for carbon dioxide injection and for injection using a gas mixture of sulphur hexafluoride and Argon. The mixture has the property that its ratio of specific heats is 1.4 i.e. the same as that of air. In this manner compressibility effects should also be reproduced although the analysis in this paper does not include compressibility. The properties are given in the Table 1 below

Gas	Density ratio	C_p ($KJ.k_g^{-1}$)	k ($W.m.^{-1}k^{-1}$)	P_r	μ $K_g.m^{-1}.s^{-1}$
AIR (300K)	1.0	1.005	2.614×10^{-2}	0.711	1.85×10^{-5}
CO_2 (300K)	1.52	0.852	1.662×10^{-2}	0.768	1.499×10^{-5}
SF_6+A (300K)	1.77	0.564	1.67×10^{-2}	0.733	2.17×10^{-5}
AIR (1000K)	-	1.141	6.72×10^{-2}	0.709	4.177×10^{-5}
AIR (1800K)	-	1.286	0.111	0.701	6.07×10^{-5}

Table 1- Properties of Air, CO_2 and SF_6+A mixtures. (Air and SF_6 + A from Oldfield and Guo (1998)).

Eqn. (10b) gives the air film cooling effectiveness as a function of the measured foreign gas effectiveness and this is plotted in Fig.3 for CO_2 and SF_6+A mixtures. There is little correction for the CO_2 injection whereas the correction is significant for SF_6+A. The experimental results of Teekaram, Forth and Jones (1986) for CO_2 injection are given in Fig.4. These are compared with experimental results for the same injection density and velocity ratios but with air as the coolant. As can be seen the results are extremely close. In general the results for the CO_2 are slightly below that for air as would be predicted by eqn. (10b). However the experimental error obscures close analysis of the difference.

Examples of the correction necessary to give engine film cooling effectiveness and heat transfer coefficient are given in Figs. (5) and (6). In these cases SF_6+A was the foreign gas employed. The correction can be seen to be significant.

9. CONCLUSIONS

An approximate procedure has been set out for the correction of film cooling experimental results which employ foreign gas to achieve large coolant densities compared to the freestream. This takes into account the difference in specific heat and thermal conductivity. The correction has been shown to agree with the experimental observation that there is little correction necessary in the case of CO_2 injection. In general both film cooling effectiveness and Nusselt number require correction according to the formulae presented.

10. REFERENCES

Ammari, H.D., Hay, N. and Lampard, D., Effect of Density Ratio on the Heat Transfer Coefficient from a Film Cooled Flat Plate, ASME Paper 89-GT-176, 1989.

Day, C.R.B., Oldfield, M.L.G. and Lock G.D., The Influence of Film Cooling on the Efficiency of an Annular Nozzle Guide Vane Cascade, ASME Paper 97-GT-521, 1997.

Eckert, E.R.G., Similarity Analysis of Model Experiments for Film Cooling in Gas Turbines, Wärme-und Stoffubertragung 27, 217-223, 1992

Eckert, E.R.G., Analogies to Heat Transfer Processes, in Eckert, E.R.G., Measurements in Heat Transfer, 2nd Ed., Washington, Hemisphere, 1986.

Goldstein, R.J., Film Cooling, in Irvine, T.F., Hartnett, J.P., Advances in Heat Transfer, New York, Academic Press, 1971 pp 327-329.

Guo, S.M., Lai, C.C., Jones, T.V., Oldfield, M.L.G., Lock, G.D. and Rawlingson, A.J., The Application of Thin-Film Technology to Measure Turbine Vane Heat Transfer and Effectiveness in a Film-Cooled, Engine-Simulated Environment, to be published in Int J. of Heat and Fluid Flow.

Han, J.C., and co-workers in ASME Papers: 93-GT-134, 1993, 95-GT-11, 1995, and 97-GT-181, 1997.

Jones, T.V., Definitions of Heat Transfer Coefficients in the Turbine Situation, Turbomachinery: Latest Developments in a Changing Scene, I. Mech. E., pp201-206, 1991

Kays, W.M and Crawford, M.E., Convective Heat and Mass Transfer, 3rd Edition, McGraw-Hill Series in Mechanical Engineering, 1993.

Oldfield, M.L.G. and Guo, S., Aerothermal Properties of Foreign Gas (SF_6/Av) and Air: Recommended Formulae from 160-1000 K, Oxford University Report, OUEL 2141/97, 1997.

Pedersen, D.R., Eckhert, E.R.G., Goldstein, R.J. Film Cooling with Large Density Differences between Mainstream and the Secondary Fluid Measured by the Mass Transfer Analogy, J. Heat Transfer 99 pp 620-627, 1977.

Rowbury, D.A., Oldfield, M.L.G., Lock, G.D. and Dancer, S.N., Scaling of Film Cooling Discharge Coefficient Measurements to Engine Conditions, ASME Gas Turbine Conference to be held in Stockholm, 1998.

Salcudean, M., Gartshore, I., Zhang, K. and Barnea, Y., Leading Edge Film Cooling of a Turbine Blade Model through Single and Double Row Injection, ASME Paper 94-GT-2, 1994.

Teekaram, A.J., Forth, C.J.P. and Jones, T.V., The use of Foreign Gas to Simulate the Effect of Density Ratio in Film Cooling, ASME, J. of Turbomachinery Vol. III, pp 57-62, 1989

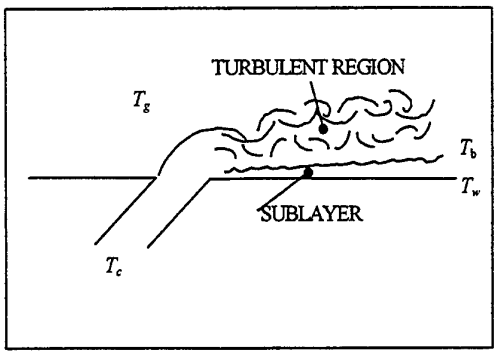

Fig.1. Schematic diagram showing turbulent region and sublayer

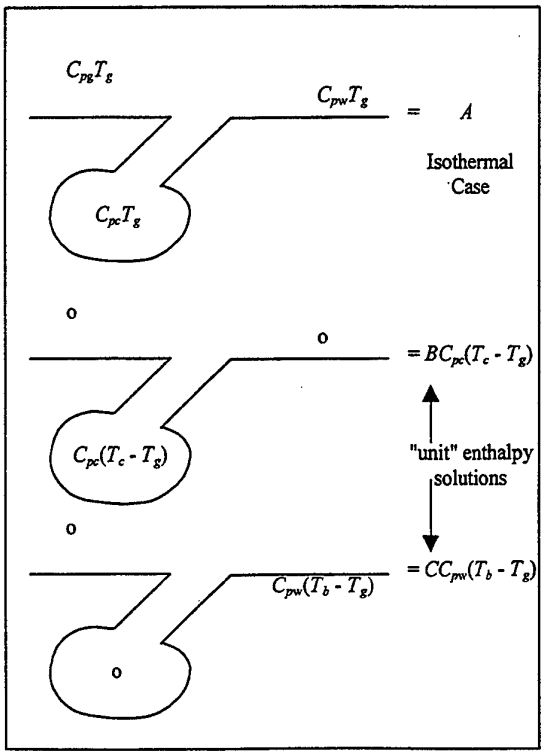

Fig.2. Boundary conditions which when superposed give the desired enthalpy boundary conditions of Fig.1.

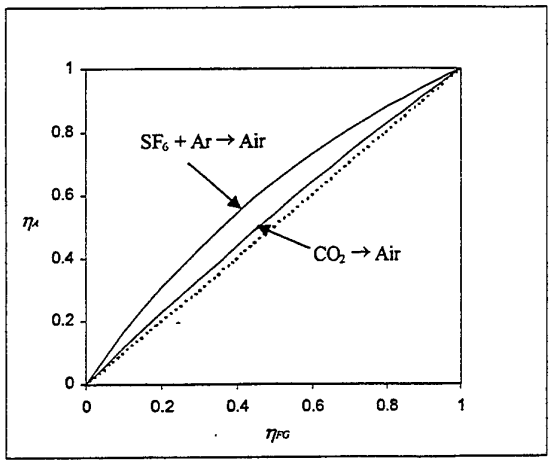

Fig.3. Film cooling effectiveness for cold air, η_A, versus the equivalent value for foreign gas, η_{FG}. Eqn (10b).

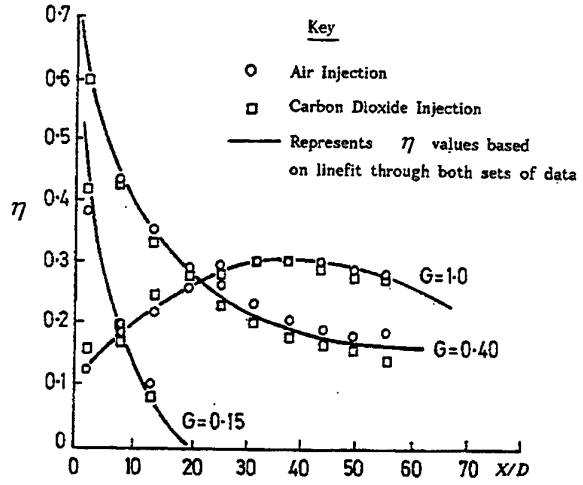

(a) Density ratio $\frac{\rho_c}{\rho_g} = 1.25$

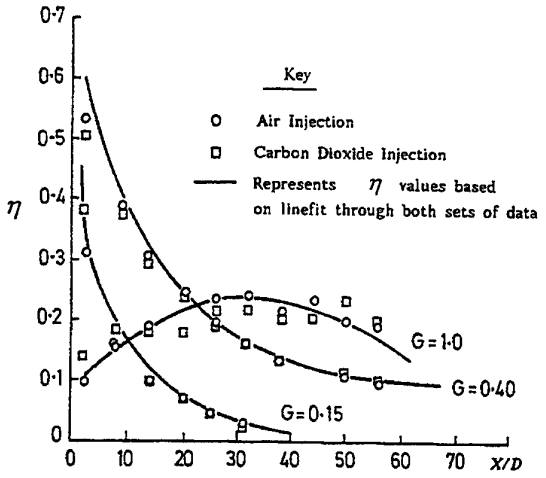

(b) Density ratio $\frac{\rho_c}{\rho_g} = 1.67$

Fig.4. Results for effectiveness η versus distance X/D downsream from a single row of 30° holes of diameter D. Carbon Dioxide and air injection results for the same density ratios. From Fig.3. it can be seen that the results for air are expected to be slightly above those for CO_2.

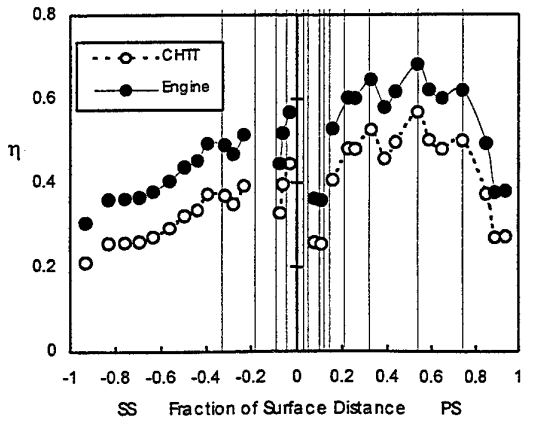

Fig.5. Film cooling effectiveness, η, on an NGV determined from experiments using SF_6 + A as the coolant and the value determined for the engine using eqn (10b). The lines show the positions of rows of film cooling holes.

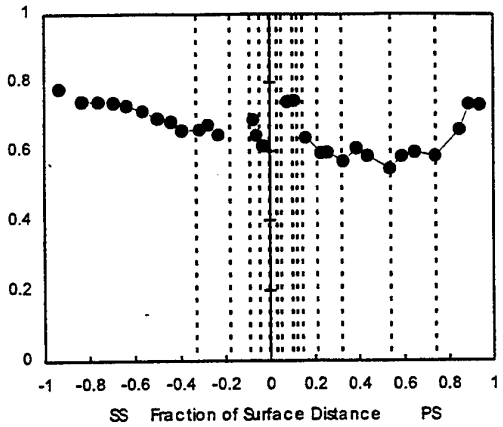

Fig.6 The ratio of Nusselt No. for the engine to that determined for SF_6 + A coolant in an experiment on an NGV from eqn (21). Dotted lines are rows of coolant injection holes.

EVALUATION OF ADVANCED LOW-REYNOLDS NUMBER k-ϵ TURBULENCE MODELS FOR PREDICTING CONVECTIVE HEAT TRANSFER

D. Giebert, R. Koch, A. Schulz and S. Wittig

Institut für Thermische Strömungsmaschinen
University of Karlsruhe (TH), Germany

ABSTRACT

An assessment of three recently published low Reynolds number k-ϵ models (Abe, Kondoh and Nagano [1], Cho and Goldstein [8], Chang, Hsieh and Chen [6]) especially tuned for separating and reattaching flows is presented. For comparison, the popular low Reynolds number model by Lam and Bremhorst [17] is included. All models are investigated for the prediction of convective heat transfer phenomena in complex engineering flows. For the calculation of the thermal field a zero-equation heat transfer model has been pursued for all models by assuming a constant value of the turbulent Prandtl number. Additionally, a first order closure of the thermal field proposed by Abe, Kondoh and Nagano [2] is applied to take into account the variability of the turbulent Prandtl number. A variety of numerical results with heat transfer by using these models are compared partly for flow situations for which these models have not been tested yet. Results are shown for a fully developed channel flow with thermal field, two backstep flows with dissimilar wall thermal condition, and a flow around a convectively cooled turbine blade. The models are assessed by comparying heat transfer coefficients and selected fluid dynamic data with available DNS or experimental references. On the basis of that comparison the strengths and weaknesses of the models are revealed for both reproduction of the real physics and computational efficiency.

1. INTRODUCTION

A widely used method for calculating turbulent flows with heat transfer is the linear k-ϵ turbulence model. Due to its simplicity and effectiveness, this model is often preferred over more sophisticated nonlinear k-ϵ models (Speziale [33], Park and Sung [23]) and higher order turbulence models (Sommer, So and Zhang [32]) or LES and DNS, particularly for engineering applications. However, the accuracy of heat transfer rates predicted by the k-ϵ model is strongly affected by the treatment of the near wall region. In gerneral, to avoid modeling of the immediate vicinity of the wall, the so-called wall function approach (Launder and Spalding [19]) is employed to bridge across this region (Ciofalo and Collins [9], Djilali, Gartshore and Salcudean [10]). This method may fail when complex flows are encountered due to its inappropriate model assumptions.

A more general and also more detailed description of the flow characteristics and heat transfer near the wall is provided by low-Reynolds-number (LRN) k-ϵ turbulence models. By integrating the transport equations of the turbulent kinetic energy and its dissipation to the wall, this approach attempts to model the direct influence of molecular viscosity and wall proximity. LRN k-ϵ models yield quite satisfactory results for attached boundary-layers (Patel, Rodi and Scheuerer [25], Sieger, Schulz, Crawford and Wittig [31], Sieger, Schiele, Schulz and Wittig [30]), but their suitability for complex separating and reattaching flows is rather limited because of both, the use of inappropriate parameters in the model damping functions (e.g. the friction velocity u_τ) and the prediction of an excessive level of turbulent length-scales near reattachment zones. The latter leads to an overestimation of heat transfer rates by several orders of magnitude (Launder [18], Chieng and Launder [7]). In recent years, research towards the development of a linear LRN k-ϵ turbulence model which is capable to predict separated flows with and without heat transfer has been actively pursued. The results reported so far (Abe, Kondoh and Nagano [1], Abe, Kondoh and Nagano [2], Cho and Goldstein [8], Chang, Hsieh and Chen [6]) are for quite different test cases making an evaluation of the models difficult. Therefore, there is a need for a comparative study to reveal an accurate classification of these models.

In the present study a variety of numerical results for flows with practical engineering application including heat transfer by using the models by Abe, Kondoh and Nagano [1], Cho and Goldstein [8],

Chang, Hsieh and Chen [6] will be compared. The results of the popular model by Lam and Bremhorst [17] are included as reference representing a well-established LRN model tuned for attached boundary-layers.

2. GOVERNING EQUATIONS

The time-averaged turbulent transport of mass, momentum and energy for a steady flow of an ideal gas can be written in Cartesian co-ordinates as:

$$\frac{\partial}{\partial x_i}(\rho u_i) = 0, \tag{1}$$

$$\frac{\partial}{\partial x_j}(\rho u_j u_i) = -\frac{\partial p}{\partial x_i} + \frac{\partial}{\partial x_j}\left[\mu\left(\frac{\partial u_i}{\partial x_j} + \frac{\partial u_j}{\partial x_i} - \frac{2}{3}\frac{\partial u_k}{\partial x_k}\delta_{ij}\right) - \rho\overline{u_i' u_j'}\right], \tag{2}$$

$$\frac{\partial}{\partial x_i}(\rho u_i h) = \frac{\partial}{\partial x_i}\left(\frac{\mu}{Pr}\frac{\partial h}{\partial x_i} - \rho\overline{u_i' h'}\right) + S. \tag{3}$$

In this formulation, it is assumed that the turbulent density fluctuations are negligible. The additional source S in the energy equation contains terms which correspond to the work done by pressure as well as viscous and Reynolds-stresses. The evaluation of the Reynolds stress terms $\rho\overline{u_i' u_j'}$ and the turbulent heat fluxes $\rho\overline{u_i' h'}$ in Eqs. (2) and (3) requires a turbulence model.

2.1 Turbulence modeling of the velocity field

Within a linear LRN-k-ϵ turbulence model, formulation of the Reynolds-stresses $-\rho\overline{u_i' u_j'}$ are described by the Bousinesq eddy viscosity concept which relates the turbulent transport of momentum to the eddy viscosity and the mean velocity gradients:

$$-\rho\overline{u_i' u_j'} = \mu_t\left(\frac{\partial u_j}{\partial x_i} + \frac{\partial u_i}{\partial x_j} - \frac{2}{3}\frac{\partial u_k}{\partial x_k}\delta_{ij}\right) - \frac{2}{3}\rho k\delta_{ij}. \tag{4}$$

The eddy viscosity is calculated from the relation

$$\mu_t = \rho f_\mu C_\mu \frac{k^2}{\epsilon}, \tag{5}$$

where the two turbulent parameters k and ϵ obey the following transport equations:

$$\frac{\partial}{\partial x_i}(\rho u_i k) = \frac{\partial}{\partial x_i}\left[\left(\mu + \frac{\mu_t}{\sigma_k}\right)\frac{\partial k}{\partial x_i}\right] + P_k - \rho\epsilon, \tag{6}$$

$$\frac{\partial}{\partial x_i}(\rho u_i \epsilon) = \frac{\partial}{\partial x_i}\left[\left(\mu + \frac{\mu_t}{\sigma_\epsilon}\right)\frac{\partial \epsilon}{\partial x_i}\right] + (C_1 f_1 P_k - \rho C_2 f_2 \epsilon)\frac{\epsilon}{k} + E, \tag{7}$$

with the production term P_k of the turbulent kinetic energy

$$P_k = \left[\mu_t\left(\frac{\partial u_j}{\partial x_i} + \frac{\partial u_i}{\partial x_j} - \frac{2}{3}\frac{\partial u_k}{\partial x_k}\delta_{ij}\right) - \frac{2}{3}\rho k\delta_{ij}\right]\frac{\partial u_j}{\partial x_i}. \tag{8}$$

In Eqs. (5) - (7), C_μ, C_1, C_2, σ_k and σ_ϵ are model constants, whereas the model damping functions f_μ, f_1, f_2 and the additional term E reflect the effect of wall-proximity.

In this study the LRN treatment is based on models by Abe, Kondoh and Nagano [1], Cho and Goldstein [8], Chang, Hsieh and Chen [6] (abbreviated subsequently as AKN, CG, CHC) and their capabilities in calculating complex flows typical for engineering applications including heat transfer phenomena are investigated. The selection of the models stems from the requirement that the inherent model damping functions must not reveal any singularities at separation and reattachment due to inappropriate model parameters. For comparison with a well established LRN turbulence model, the k-ϵ model by Lam and Bremhorst [17] (subsequently referred to as LB model) originally tuned for attached boundary layers, is included as reference.

For the models examined, the LRN functions, the model constants, and the additional term E as well as the boundary condition (BC) assigned to ϵ at solid walls are summarized in Table 1. For completeness Table 1 also contains the constants of the standard k-ϵ model.

Subsequently, the main characteristics of the models and their differences are briefly described. For details regarding the model development and formulations the reader is referred to Abe, Kondoh and Nagano [1], Cho and Goldstein [8], Chang, Hsieh and Chen [6] or Lam and Bremhorst [17].

It should be noted that the AKN model is an extension of the model of Nagano and Tagawa [20]. Unlike the Nagano and Tagawa model, it is tuned for the prediction of separating and reattaching flows. This capability is achieved by introducing the Kolmogorov velocity scale $u_\epsilon = (\nu\epsilon)^{0.25}$ in the model functions f_μ and f_2 instead of the friction velocity u_τ. Moreover, the model constants C_1, C_2, σ_k and σ_ϵ differ in part significantly from the standard values (cf. Table 1). They have been reevaluated by computational optimization in order to give better agreement with experimental data of recirculating flows (Abe, Kondoh and Nagano [1]) and to satisfy the relation $C_1 = C_2 - \kappa^2/(\sigma_\epsilon\sqrt{C_\mu})$ to which the equation of the dissipation rate is reduced in zero pressure gradient local-equilibrium flows with a logarithmic velocity distribution (Patel, Rodi and

Table 1: Summary of the model constants, damping functions and additional terms

Model	$\epsilon_w - BC$	C_μ	C_1	C_2	σ_k	σ_ϵ	f_μ	f_1	f_2	E
St. k-ϵ	Wall-Fkt.	0.09	1.44	1.92	1.0	1.3	1.0	1.0	1.0	0
LB	$\frac{\partial \epsilon}{\partial y_n} = 0$	0.09	1.44	1.92	1.0	1.3	$\left[1 - e^{(-0.0163 Re_y)}\right]^2 \cdot (1 + \frac{20.0}{Re_t})$	$1 + \left(\frac{0.055}{f_\mu}\right)^3$	$1 - e^{(-Re_t^2)}$	0
AKN	$\epsilon_w = 2\nu \frac{k_P}{{x_P}^2}$	0.09	1.5	1.9	1.4	1.4	$\{1 + \frac{5}{Re_t^{0.75}} \cdot e^{[-(\frac{Re_t}{200})^2]}\} \cdot [1 - e^{(-\frac{y^*}{14})}]^2$	1.0	$\{1 - 0.3 \cdot e^{[-(\frac{Re_t}{6.5})^2]}\} \cdot [1 - e^{(-\frac{y^*}{3.1})}]^2$	0
CG	$\frac{\partial \epsilon}{\partial y_n} = 0$	0.09	1.44	1.92	1.0	1.3	$1 - 0.95 \cdot e^{(-5 \cdot 10^{-5} {Re_t}^2)}$	1.0	$1 - 0.222 \cdot e^{(-\frac{{Re_t}^2}{36})}$	S_ϵ
CHC	$\epsilon_w = \nu \frac{\partial^2 k}{\partial y_n^2}$	0.09	1.44	1.92	1.0	1.3	$\left[1 - e^{(-0.0215 Re_y)}\right]^2 \cdot \left(1 + \frac{31.66}{Re_t^{1.25}}\right)$	1.0	$[1 - 0.01 \cdot e^{(-Re_t^2)}] \cdot (1 - e^{(-0.0631 Re_y)})$	0

With: k_P, x_P: values of k, y_n at the grid point closest to the wall, y_n: normal distance from the wall,

$$S_\epsilon = 1.44(1 - f_\mu)\left[\frac{2\mu\mu_t}{\rho}\left(\frac{\partial^2 u_i}{\partial x_j \partial x_k}\right)^2 + 2\mu\left(\frac{\partial \sqrt{k}}{\partial x_j}\right)^2 \frac{\epsilon}{k}\right] + \rho \cdot max\left[0.83\frac{\epsilon^2}{k}\left(\frac{l}{C_l y_n} - 1\right)\left(\frac{l}{C_l y_n}\right)^2, 0.0\right]$$

$l = \frac{k^{1.5}}{\epsilon}$, $C_l = 2.44$, $Re_t = \frac{k^2}{\nu\epsilon}$, $Re_y = \frac{\sqrt{k} y}{\nu}$, $y^* = \frac{u_\epsilon y}{\nu}$ with $u_\epsilon = (\nu\epsilon)^{0.25}$

Scheuerer [25]). On the other hand, the CG, CHC, and LB model use the same model constants as the standard k-ϵ model.

As far as the wall limiting conditions are concerned ($-\overline{u'v'} \propto y_n^3, k \propto y_n^2, \mu_t \propto y_n^3, f_\mu \propto y_n^{-1}, f_2 \propto y_n^2$ (in absence of an extra source term E in the ϵ-equation) and $\epsilon \rightarrow \epsilon_w$) both the AKN and CHC model comply with these requirements. In contrast, the CG as well as the LB model do not satisfy the conditions for both the model damping function $f_\mu \propto y_n^{-1}$ and the shear stress $-\overline{u'v'} \propto y_n^3$ at the wall. A series expansion of f_μ leads to $f_\mu \propto y_n^0$ for both models. In the LB model, the requirement $f_2 \propto y_n^2$ which is demanded by the ϵ-equation at the wall is not satisfied (Patel, Rodi and Scheuerer [25]). In contrast to the AKN and the CHC model, the CG as well as the LB model increase the magnitude of ϵ in the proximity of the wall by an additional extra source term E and a model function f_1 in the ϵ-equation, respectively. As can be seen from Table 1, the term E in the CG model is composed of three terms. A detailed analysis of E near the wall with $k \propto y_n^2, f_\mu \propto y_n^0$, and $\mu_t \propto y_n^4$ [1], indicates that the first terms in E ($=1.44 \cdot (1 - f_\mu) \cdot \frac{2\mu\mu_t}{\rho}\left(\frac{\partial^2 u_i}{\partial x_j \partial x_k}\right)^2$) increases with y_n^4 with wall distance, whereas the second term ($=1.44 \cdot (1 - f_\mu) \cdot 2\mu\left(\frac{\partial \sqrt{k}}{\partial x_j}\right)^2 \frac{\epsilon}{k}$) shows a quadratic groth of ϵ when approaching the wall. Both terms are related only to regions near the wall and within the buffer layer and vanish in the fully turbulent region. The last term in E is adopted from Yap [36] to improve the prediction of the heat transfer rate in regions near reattachment due to damping of the turbulent length scales ($l = k^{3/2}/\epsilon$). However, if the length scale is less or equal to $C_l y_n$ (the value found for a flow in local equilibrium) last term in E is not effective.

[1] relations revealed by the CG model near the wall

2.2 Turbulence modeling of the temperature field

When heat transfer phenomena are considered, the most common way of calculating the turbulent heat fluxes $\rho\overline{u_i' h'}$ is to apply a simple gradient-transport-type model, where the fluxes are related to mean values of the thermal field:

$$\rho\overline{u_i' h'} = \frac{\mu_t}{Pr_t}\left(\frac{\partial h}{\partial x_i}\right). \qquad (9)$$

Table 2: Summary of the model constants and damping functions for the heat transfer model

$\epsilon_{\theta,w}-BC$	σ_h	C_{P1}	C_{P2}	C_{D1}	C_{D2}	C_λ	f_{P1}	f_{P2}	f_{D1}	f_{D2}
$\alpha\left(\frac{\partial\sqrt{k_\theta}}{\partial y_n}\right)^2$	1.6	1.9	0.6	2.0	0.9	0.1	$\left(1-e^{(-y^*)}\right)^2$	1.0	$\left(1-e^{(-y^*)}\right)^2$	$\frac{1}{C_{D2}}\left(C_2 f_2-1\right)\left[1-e^{(-y^*/5.7)}\right]^2$

Conventionally, turbulent heat transfer is modeled with the assumption of a constant turbulent Prandtl number (in general $Pr_t = 0.9$) and the eddy diffusivity of heat ($\alpha_t = \lambda/(\rho c_p) = \mu_t/(\rho Pr)$) is assumed to be proportional to the eddy viscosity μ_t. This assumption which is essentially a zero-equation heat transfer model works well in many flow situations where the similarity between the velocity and the temperature field holds, despite the fact that even in simple attached boundary layers the turbulent Prandtl number is far away from a constant universal value (Bagheri, Strataridakis and White [4], Reynolds [26]). However, for a flow situation with a complete dissimilarity between velocity and thermal field, e. g. due to sudden change of the thermal condition at the wall, a strong variation of Pr_t is found (Antonia, Danh and Prabhu [3]), which generally cannot be neglected.

In the present study, two approaches will be examined to calculate heat transfer phenomena. They differ in the treatment of the turbulent Prandtl number and therefore in the order of the heat transfer model. On the one hand, a constant turbulent Prandtl number of $Pr_t = 0.9$ is assumed for calculating the turbulent heat fluxes (Eqn. (9)) by all LRN models considered here (AKN, CG, CHC, and LB). A first order closure of the problem is attained by solving two additional transport equations for the temperature variance k_θ and its dissipation ϵ_θ, respectively, to determine the eddy diffusivity of heat α_t. This approach allows the variation of the turbulent Prandtl number and seems to be a more general strategy for solving heat transfer problems when the turbulent Prandtl number is unknown. In the present study, the variability of Pr_t is only taken into account within the AKN model. It is subsequently referred to as AKN_{ext} to distinguish it from the AKN model where a constant turbulent Prandtl number is assumed. The AKN_{ext} model therefore contains higher order modeling terms and can be regarded as a tuned extension for the AKN model as far as the model constants and model damping functions are concerned.

Following the strategy of Abe, Kondoh and Nagano [2], the governing equations for the two equation heat transfer model are:

$$\frac{\partial}{\partial x_i}(\rho u_i k_\theta) = \frac{\partial}{\partial x_i}\left[\rho\left(\alpha+\frac{\alpha_t}{\sigma_h}\right)\frac{\partial k_\theta}{\partial x_i}\right] + 2P_\theta - 2\rho\epsilon_\theta, \tag{10}$$

$$\frac{\partial}{\partial x_i}(\rho u_i \epsilon_\theta) = \frac{\partial}{\partial x_i}\left[\rho\left(\alpha+\frac{\alpha_t}{\sigma_h}\right)\frac{\partial \epsilon_\theta}{\partial x_i}\right] + C_{P1} f_{P1}\frac{\epsilon_\theta}{k_\theta}P_\theta + C_{P2} f_{P2}\frac{\epsilon_\theta}{k}P_k - C_{D1} f_{D1}\rho\frac{{\epsilon_\theta}^2}{k_\theta} - C_{D2} f_{D2}\rho\frac{\epsilon\epsilon_\theta}{k}. \tag{11}$$

P_θ represents the rate of production of the temperature fluctuation

$$P_\theta = \rho\alpha_t\left(\frac{\partial T}{\partial x_i}\right)^2. \tag{12}$$

The eddy diffusivity for heat may be written as follows:

$$\alpha_t = C_\lambda\left[\frac{k^2}{\epsilon}\left(\frac{2R}{0.5+R}\right) + 3\sqrt{k}\left(\frac{\nu^3}{\epsilon}\right)^{0.25}\frac{\sqrt{2R}}{Pr}e^{-(R_t/200)^2}\right] \cdot\left[1-e^{-y^*/14}\right]\cdot\left[1-e^{-\sqrt{Pr}y^*/14}\right], \tag{13}$$

where R is the time-scale ratio which represents the ratio of the characteristic decay times of the turbulent temperature and velocity

$$R = \frac{\tau_t}{\tau_u} = \frac{k_\theta/2\epsilon_\theta}{k/\epsilon}. \tag{14}$$

The turbulent Prandtl number is calculated from the relation

$$Pr_t = \frac{\mu_t}{\rho\alpha_t}. \tag{15}$$

In Eqs. (10)-(13) σ_h, C_{P1}, C_{P2}, C_{D1}, C_{D2}, C_λ, f_{P1}, f_{P2}, f_{D1}, and f_{D2} are constants and model damping functions, respectively. They are listed in Table 2. In addition, Table 2 also contains the wall-boundary condition for ϵ_θ.

It should be noted that this two equation heat transfer model is based on the LRN heat transfer

model by Nagano, Tagawa and Tsuji [21] which has been developed for the calculation of heat transfer phenomena of air ($Pr = 0.71$) in attached boundary layer situations. It is applicable to predict the thermal field of separating and reattaching flows without singularities arising from inappropriate parameters in the model damping functions.

3. NUMERICAL PROCEDURE

3.1 Numerical method

The current numerical study has been performed using a three-dimensional Navier-Stokes code developed at the "Institut für Thermische Strömungsmaschinen" at the University of Karlsruhe. The capabilities and performance of this code have been demonstrated for a wide range of technical flow configurations (Giebert, Gritsch, Schulz and Wittig [12], Kurreck and Wittig [16], Benz and Wittig [5]).

In this CFD code, the governing equations are formulated in a body-fitted non-orthogonal curvilinear co-ordinate system. It is based on a fully conservative, structured finite volume discretization method. The transport equations for the Cartesian velocity components and other scalars are solved using a non-staggered grid. All flow variables are stored at the same nodes ('cell-centered'). The solution procedure is iterative and the pressure-based SIMPLE algorithm (Patankar and Spalding [24]) is used to derive a pressure-correction equation.

To avoid checkerboard pressure-velocity oscillations an interpolation scheme similar to that of Rhie and Chow [27] is applied. For the discretization of the diffusive terms, a second order central difference scheme is used, whereas the convective terms of all transport equations are discretisized by the second order accurate Monotonized-Linear-Upwind scheme (MLU) (Noll [22]). This high resolution scheme is bounded and, therefore, physically unrealistic over- and undershoots are avoided. The stability of this scheme allows to use it also for the convective terms of all turbulence equations (Eqs. (6), (7), (10), (11)).

The system of the algebraic equations is solved by the strongly implicit procedure (SIP) of Stone [34].

3.2 Boundary conditions

Unless otherwise stated, the following boundary conditions have been specified: Along the wall the velocities satisfy the no-slip condition and the turbulent kinetic energy k, the temperature variance as well as the pressure gradient $\partial p/\partial y_n$ are set to zero. The boundary conditions for the dissipation rate of the turbulent kinetic energy and the temperature variance at the wall are listed in Table 1 and 2, respectively. Additionally, either the wall temperature or the wall heat flux are specified. At the inlet, the velocities, the turbulent kinetic energy and the temperature are derived from experimental data, whereas the dissipation rate ϵ is specified by the relation given by Hassid and Poreh [13]. Following the strategy of Abe, Kondoh and Nagano [2], the temperature fluctuation and its dissipation are set to a sufficiently small value in the order of 10^{-7} at the inflow boundary.

If DNS-data are available, all inlet profiles were taken from DNS solution in order to reduce the run times.

At the outlet, the gradient of the flow variables in flow direction is set to zero.

3.3 Computational details

The computations were run on a SUN ULTRA workstation with $166MHz$ processor. Unless otherwise noted, the numerical solution was considered as fully converged when the normalized sum of absolute residuals (L_1 norm) of each transport equation was below a pre-selected value of 10^{-4}. Additionally, the non-dimensional norm of two successive iterations of all governing equations has been checked. The inner iterations were stopped once the residual fell below 0.3 of its initial value for all transport quantities except for the pressure correction, where a value of 0.05 was specified. Underrelaxation was used to account for the nonlinearity of the equations. Since optimum values of the underrelaxation parameters depend on both the turbulence model used and the flow situation, the following data represent only standard values. The underrelaxation parameters are in the order of 0.7 and 0.4 for the velocities and turbulence quantities, respectively, and 0.2 for the pressure correction.

4. RESULTS AND DISCUSSION

The main goal of this study is the analysis of the performance of the LRN models AKN, CG, CHC, and LB when calculating complex flow situations including both recirculation and heat transfer phenomena. In a first step, the principal capabilities and limitations of the models will be examined on the basis of a fully developed channel flow situation. This simple test case is discussed because DNS results are available and thus a detailed insight into the behaviour of the different models is possible.

After that, two well documented backward facing

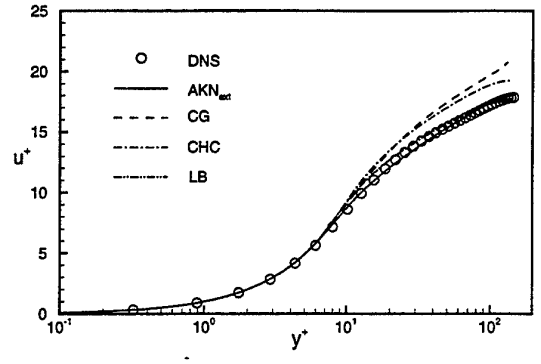

Figure 1: Mean velocity profile (DNS from [14])

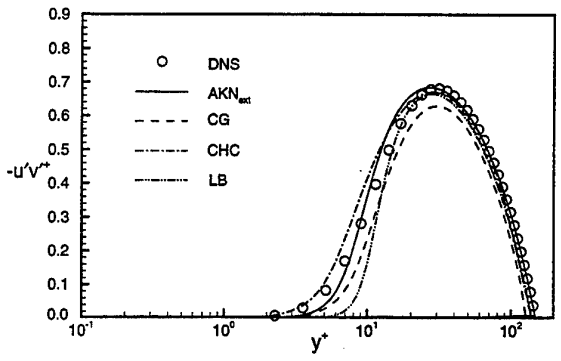

Figure 3: Profile of turbulent shear stress (DNS from [14])

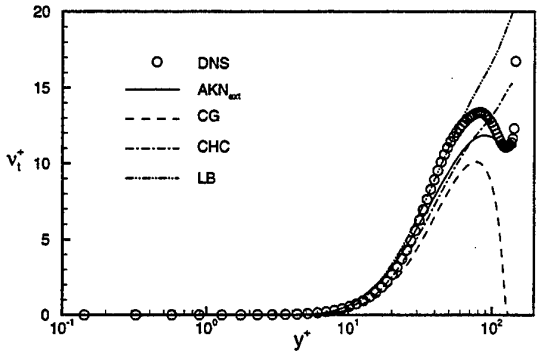

Figure 2: Profile of turbulent viscosity (DNS from [14])

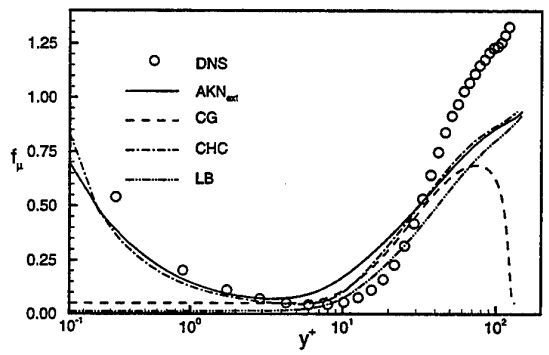

Figure 4: f_μ distribution (DNS from [14])

step flows are considered, namely those of Vogel and Eaton [35] and Scherer and Wittig [28]. Additionally, the flow around a convectively cooled turbine blade has been selected to demonstrate the model capabilities in engineering flow situations.

4.1 Fully developed channel flow

Subsequently, the model predictions will be compared to DNS profiles (Kasagi, Tomita and Kuroda [14]) of a fully developed thermal field of a two-dimensional turbulent channel flow of air (Pr = 0.71). As boundary condition for the thermal field at the wall, a constant heat flux is imposed so that the mean temperature linearly increases in the streamwise direction. The Reynolds number Re_τ based on the channel half-height and the friction velocity is 150. For the predictions, a non-equidistant computational grid has been used with 130 grid points accross the channel half-height. A grid sensivity study revealed that this number is sufficient for a grid-independent solution with a minimum wall distance of $y^+ = 0.15$. All quantities are normalized by the wall variables friction velocity u_τ, kinematic viscosity ν, and the friction temperature T_τ, respectively. The results are plotted with a semi-logarithmic scaling in order to better illustrate the behaviour in the proximity of the wall. In the figures, the maximum value of y^+ corresponds to the channel half-height or the channel center. As far as the AKN model is concerned, results shown here are obtained by taking into account the two equation heat transfer model. This is due to the fact, that no mentionable differences are found between this result and the AKN model prediction when a constant turbulent Prandtl number is applied.

Fig. 1 shows the mean velocity profile obtained by the various models. As can be seen, both the AKN and LB model give the best agreement with DNS data, whereas the CG and the CHC model overpredict the velocity distribution towards the channel centre. The good agreement with DNS data shown by the AKN model for the fully developed channel flow is not surprising since it was calibrated by such data. The overprediction of the mean velocity by the CHC model starting at $y^+ \approx 20 - 30$ can be explained by focusing the distribution of the turbulent kinematic viscosity ν_t, the turbulent

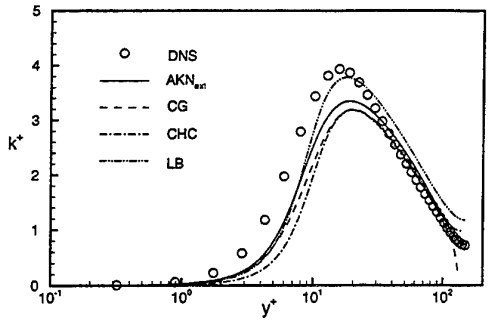

Figure 5: Profile of turbulent kinetic energy (DNS from [14])

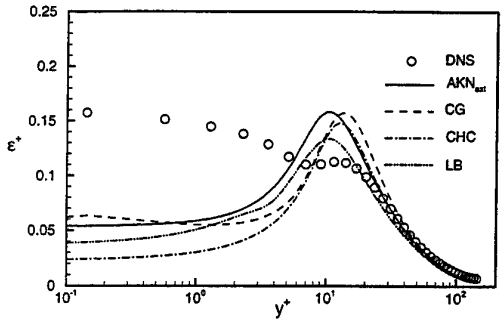

Figure 6: Profile of dissipation rate (DNS from [14])

shear stress $\overline{u'v'}^+$ (Figs. 2 and 3), and the relation $\overline{u'v'} = \nu_t \partial u/\partial y$ [2]. The lower calculated turbulent viscosity in this region, compared to the AKN and LB model predictions, requires an increase in the slope of the velocity profile in order to capture the maximum in the turbulent shear stress. Similar to that phenomenon, the CG model shows a severe underestimation of the turbulent viscosity with a following break-down in the ν_t prediction in the channel half-width, which can be only compensated by increasing intensively the gradient in the velocity profile. This abnormality in the CG's ν_t distribution is caused by the severe reduction of the damping function f_μ (Fig. 4). In contrast to the behaviour of the CG model, both the LB and CHC model reveal an overestimation of ν_t at the channel centre (Fig. 2). Good agreement in ν_t with the DNS for $y^+ \geq 60$ gives the AKN model which even captures the local maximum in ν_t in that region.

The comparison of the model damping function f_μ with DNS data in Fig. 4 indicates that in close wall proximity the AKN as well as the CHC model predict the correct growth rate. As already mentioned in section 2.1, both the LB and CG model give a constant value for f_μ as wall limiting condition. The misbehaviour of the model damping function of the CG model in the fully turbulent region is caused by using solely Re_t as argument in f_μ (cf. Table 1). In the low Re channel flow considered, Re_t shows a maximum value at $y^+ \approx 20$ and a subsequent decrease for larger y^+.

Fig. 5 shows the profiles of the turbulent kinetic energy. All models except the LB model clearly underpredict the peak level of k. Only the LB model gives a fairly good agreement with the DNS data. The differences in the turbulent kinetic energy are related to discrepancies in the maximum value of the dissipation rate ϵ. As displayed in Fig. 6, the LB model gives the lowest peak value which results in higher turbulence levels in that region. None of the LRN models is capable to capture the growth in ϵ very close to the wall as indicated by the DNS.

The comparison between the model predictions and DNS data for the mean temperature field is presented in Fig. 7. Here again, the AKN model is superior in reproducing the DNS data with only a minor underestimation at the channel centre. Underprediction of the temperature near the channel centre by the LB model is caused by the strong overprediction of the turbulent viscosity in that region (cf. Fig. 2). The CG and CHC model slightly overpredict in this region.

Fig. 8 shows the RMS values of the temperature fluctuations of both the DNS data and the AKN_{ext} model. Qualitative agreement is quite good, but in the buffer layer an underestimation is revealed for the AKN_{ext} model.

The profile of the dissipation of the temperature variance is plotted in Fig. 9. The peak of ϵ_θ^+ is overpredicted by the AKN_{ext} model which is the reason for the too low values of the temperature fluctuations in that region. Underestimation by the AKN_{ext} model is found for the dissipation close to the wall but the slight increase depicted by DNS is also indicated by the calculation.

The variation of the turbulent Prandtl number is shown in Fig. 10. In contrast to the DNS data, the AKN_{ext} model prediction shows a dip in the Pr_t-profile, whereas towards the channel centre this model predicts a fairly constant value. However, the low variation of Pr_t is of minor importance in that flow situation.

Beside the correct prediction of the physics, an important factor affecting the choise of a model for engineering applications is its behaviour in terms of robustness and computational efficiency. In order to illustrate the performance of the different models, the sum of the residuals averaged over all

[2] $\overline{u'v'}$ represents the only Reynolds stress of importance in the momentum equations in an attached near-wall flow

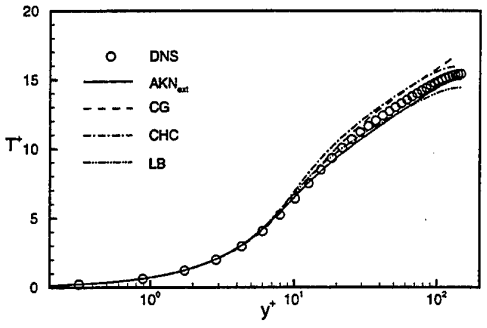

Figure 7: Profile of mean temperature (DNS from [14])

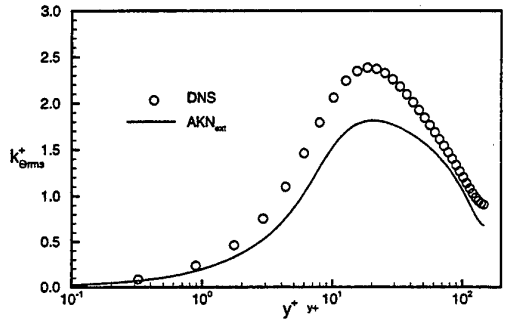

Figure 8: Profile of rms temperature fluctuations (DNS from [14])

transport equations is plotted versus the number of outer iterations (Fig. 11). It should be mentioned that a tight convergence criterion of 10^{-5} has been chosen, in order to reduce the initial residual by approximately 4 orders of magnitude. The AKN, AKN_{ext} and CG model show the best convergence rate with a very similar progression. The total number of outer iterations required by the LB and CHC model are higher by a factor of ≈ 2 and ≈ 3, respectively. This effect is due to lower relaxation factors used for the LB and CHC model in order to prevent divergence. Table 3 shows the CPU times of the different models relative to the CPU time of the AKN model. Although two additional transport equations have to be solved within the AKN_{ext} model for taking into account the variation of the turbulent Prandtl number, only an increase of about 30% in computing time is found compared to the conventional AKN model.

4.2 Backward facing step flow with constant wall heat flux

The test case considered is the backward facing step studied experimentally by Vogel and Eaton [35]. In this configuration, the bottom wall downstream

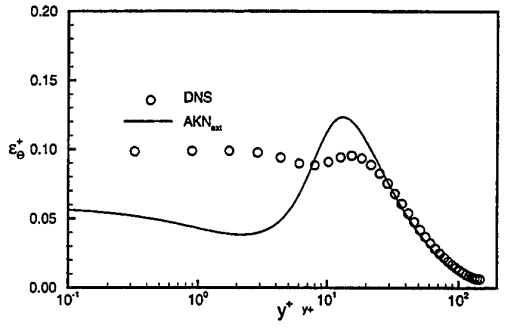

Figure 9: Profile of dissipation of temperature fluctuation (DNS from [14])

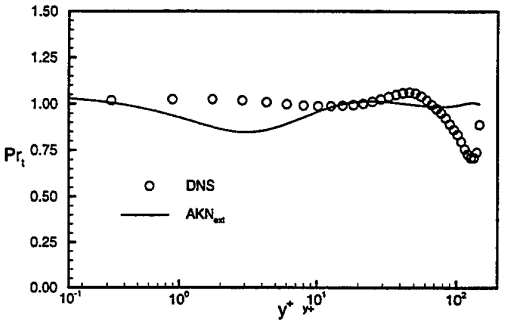

Figure 10: Profile of turbulent Prandtl number (DNS from [14])

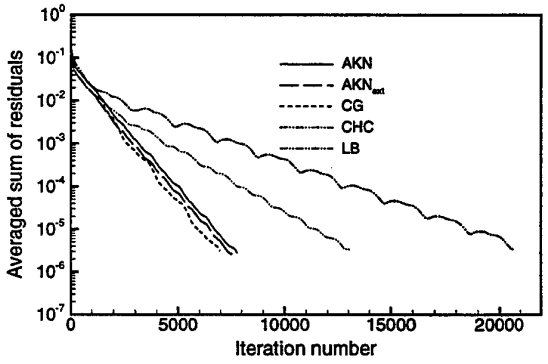

Figure 11: Convergence history for the different models, channel flow [14]

Table 3: Relative CPU time needed to reach convergence, channel flow [14]

	AKN	AKN_{ext}	CG	CHC	LB
CPU	1.0	1.31	1.14	2.74	1.93

of the step is heated. The test section has an expansion ratio of 1.25 and an aspect ratio (spanwise width/step height) of about 12, making three-dimensional effects near the centerline negligible. Two-dimensional calculations were conducted for a Reynolds number of $Re_H = 28000$ based on the step height. The boundary layer thickness at separation is $\delta/H = 1.1$. The computations were performed using a 273×145 grid, which is fine enough to ensure grid independent solutions. The axial length of the computational domain is $-3.8H \leq x \leq 25H$. For the calculations, the dimensionless distance y^+ of the grid points adjacent to the bottom wall is below 0.1. Boundary conditions for the thermal field are specified by a constant heat flux at the heated wall equal to the experimental value, while the temperature gradient normal to the wall is set to zero at the other walls.

A comparison of the predicted flow reattachment length x_R/H (determined by zero velocity in main-flow direction at the closest grid point to the wall) with the experimental data is presented in Table 4. All models underpredict the experimental value but noticible differences are revealed in the amount of underestimation. Good results are obtained by the CG and the AKN model, whereas the LB and CHC model underpredict the experimental value of approximately 20%. The general underprediction of the reattachment point when applying the linear k-ϵ turbulence model is mainly caused by its inherent assumption of isotropy which is important mainly in the free shear layer. Therefore, the differences shown in the LRN model predictions are thought to be attributable to discrepancies in the prediction of the turbulent length scale or turbulent viscosity near the wall which influences the reattachment length to a certain amount. For substantiation, Table 4 also contains the reattachment length predicted by the CG model (subsequently denoted as CG_{mod} model), where the correction term of Yap [36] ($\rho \cdot max[0.83\frac{\epsilon^2}{k}\left(\frac{l}{C_l y_n} - 1\right)\left(\frac{l}{C_l y_n}\right)^2, 0.0]$) in the extra source term E (cf. Table 1), which extenuates the turbulent length scales in regions near reattachment, was set to zero. It is found by the CG and CG_{mod} model prediction that the level of the turbulent length scales near reattachment has a major influence on the reattachment point.

In Fig. 12, the velocity profiles as reproduced by the LRN models are compared to the experimental data. All models predict almost identical results which are in good agreement with the measurement even in the recirculation zone. Far downstream of the reattachment point ($x/H \geq 9.53$) the streamwise velocity is slightly underestimated by all models.

Table 4: Comparison of flow reattachment length x_R/H, backstep flow [35]

Experiment	AKN	CG	CHC	LB	CG_{mod}
6.67	6.0	6.3	5.2	5.3	5.7

The turbulent kinetic energy profiles at different axial locations are shown in Fig. 13. Good results are obtained for all models in the recirculation zone but underprediction of k is found downstream of reattachment. Almost identical results are predicted by the LB and CHC model. The CG and AKN model predictions deviate from those of the LB and CHC at the wall and in the free shear layer, respectively. Near the wall, the CG model gives a smooth variation of the turbulent kinetic energy. That effect is attributable to the damping of the turbulent length scales inherent in the CG model (by increased ϵ and thus reduced k) caused by Yap's correction term (see CG_{mod} prediction for comparison). In the free shear layer ($y/H \approx 1$), the AKN model shows a reduced increase of k. This phenomenon is due to the high value of the model constant σ_k leading to a reduction of the turbulent diffusion of k in that region. The same effect has been found previously for different test cases by Giebert, Bauer and Wittig [11] for that model and by Chang, Hsieh and Chen [6] for the model by Nagano and Tagawa [20] in which the same value for σ_k is used.

The comparison is continued by the analysis of the skin friction coefficient at the bottom wall along the normalized streamwise co-ordinate $(x-x_R)/x_R$, as shown in Fig. 14. Fairly good agreement with the experiment is obtained with the AKN and LB model whereas the CHC model overpredicts the skin friction by several orders of magnitude. The lowest values are revealed by the CG model which underpredicts the experimental data downstream of reattachment. However, if Yap's correction is omitted, an increase of c_f of approximately 30% is found which results in better agreement with the experiment downstream of reattachment.

The predicted turbulent viscosity μ_t close to the wall is shown in Fig. 15 for two axial locations x/H. The plots clearly demonstrate that skin friction is directly linked to the level of μ_t. Low values of μ_t cause an underprediction in c_f and vice versa. If the damping of the turbulent length scale is omit-

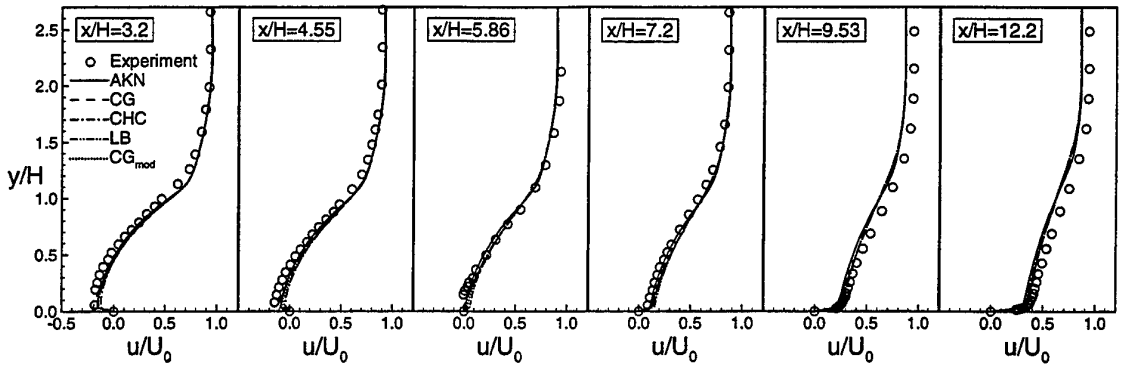

Figure 12: Streamwise mean velocity profiles, experiment: [35]

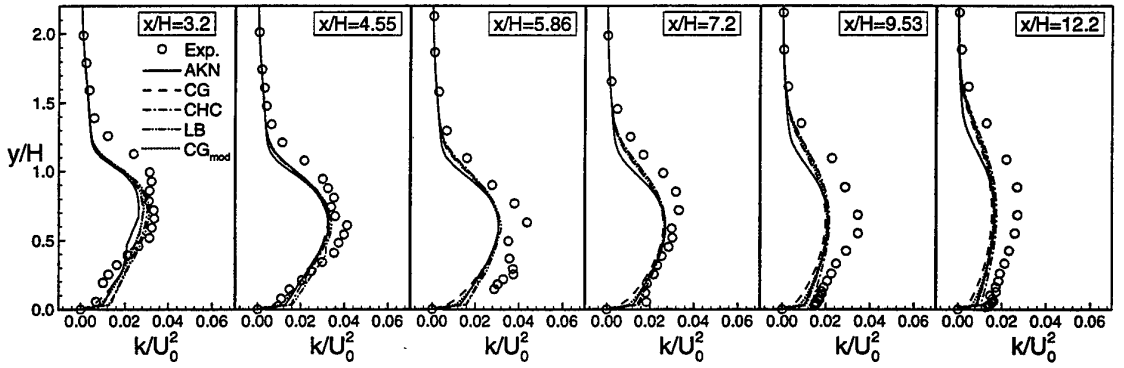

Figure 13: Turbulent kinetic energy profiles, experiment: [35]

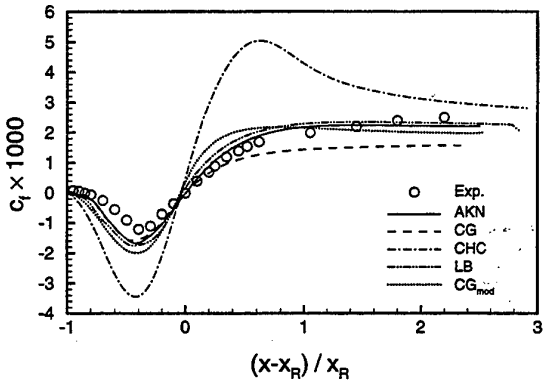

Figure 14: Measured and predicted skin friction coefficient, experiment: [35]

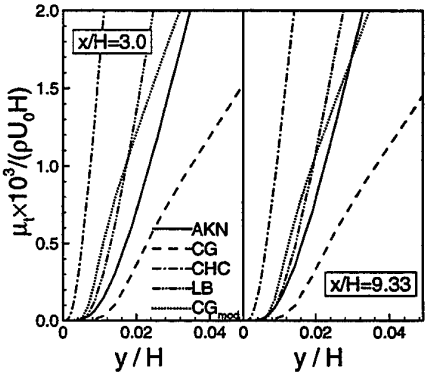

Figure 15: Normalized turbulent viscosity near the wall, backstep flow [35]

ted in the CG model (see CG_{mod} prediction), the same level of μ_t as for the AKN and LB model is predicted.

In Fig. 16, the calculated mean temperature field is compared with the experimental data for different axial locations. Additionally, the results of the extended AKN_{ext} model which includes the two equation heat transfer model are also shown. All the models give nearly identical results which almost coincide with the experiment except at the corner region of the step ($x/H = 0.33$). At this location, an overestimation in temperature is found for the AKN_{ext} and the CG model, whereas the CHC shows the lowest values. These effects are thought to be caused by an over- or underprediction of the vertical velocities at the corner region.

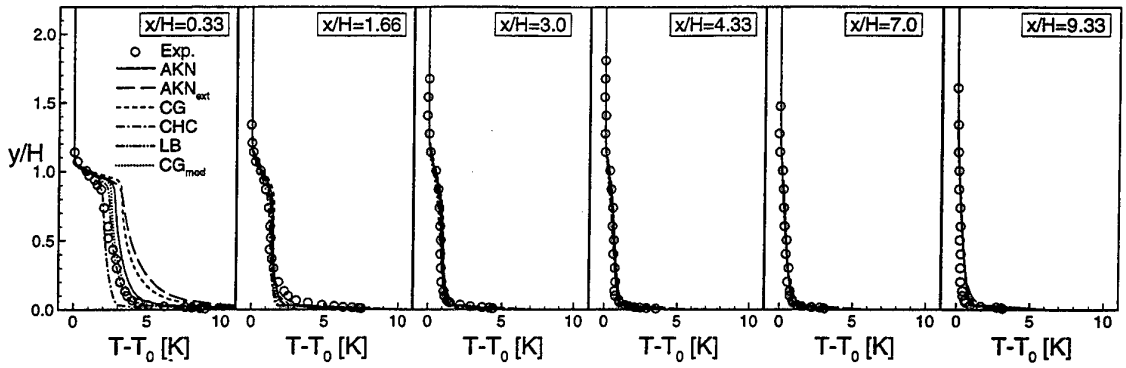

Figure 16: Mean temperature profiles, experiment: [35]

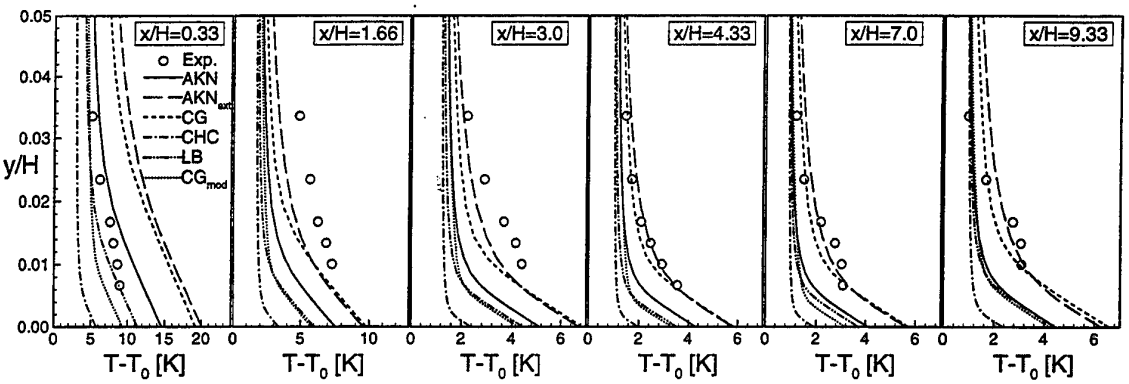

Figure 17: Near-wall temperature profiles, experiment: [35]

The overall mean temperature gradients near the wall resulting from the model predictions are plotted together with the experimental data in Fig. 17. There are significant differences of the predicted temperature gradients in the conduction-dominated region where heat transfer is effective. Except of the AKN_{ext} and CG model, all models underpredict the temperature gradient in the region adjacent to the viscous sublayer for $x/H \geq 1.66$. The reason for this is in the level of the calculated turbulent length scales or turbulent viscosity, which determine directly the temperature variation when a constant turbulent Prandtl number is assumed (cf. Eqs. (3) and (9)): The higher the turbulent viscosity near the wall the lower the predicted temperature gradients. The fairly good agreement of the CG model in terms of the temperature variation is due to the damping of the turbulent length scales which causes an increase of the temperature gradient (cf. CG_{mod} prediction). Almost identical results to those of the CG model are obtained by the AKN_{ext} model. However, the increase of the temperature gradient near the wall is not attained by damping of the turbulent length scales but by taking into account the variability of the turbulent Prandtl number. It was found that Pr_t-values in the order of 2.5 are reached in the conduction-dominated layer near reattachment which leads to a significant reduction of the turbulent dynamic thermal diffusivity (μ_t/Pr_t). Accordingly, the similarity in the temperature distribution predicted by the AKN_{ext} and CG model do correspond to a similar variation of μ_t/Pr_t, which is illustrated in Fig. 18.

Fig. 19 shows the calculated Stanton number profiles along the bottom wall. Very good agreement with the experiment is found for both the AKN_{ext} and CG model. An excessive overprediction is shown by the CHC model caused by very high values of the turbulent viscosity μ_t. Lower values for μ_t predicted by the AKN, CG_{mod} and LB model result in lower heat transfer coefficients, but still an overestimation of about $2-3$ orders of magnitude is found for these models.

The convergence history for the backstep flow studied is shown in Fig. 20. In terms of the total number of outer iterations, the AKN model gives the best result, whereas the CG model needs

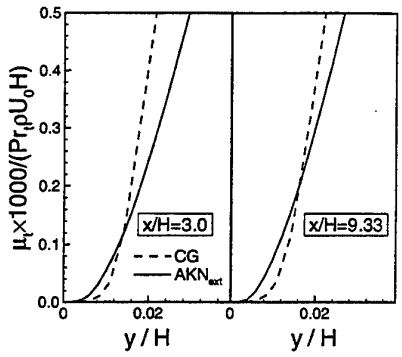

Figure 18: Variation of normalized turbulent dynamic thermal diffusivity, backstep flow [35]

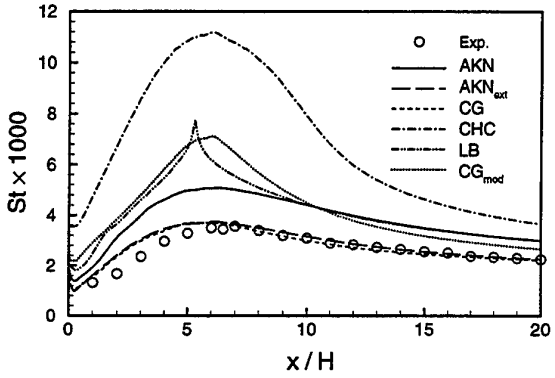

Figure 19: Stanton number profiles, experiment: [35]

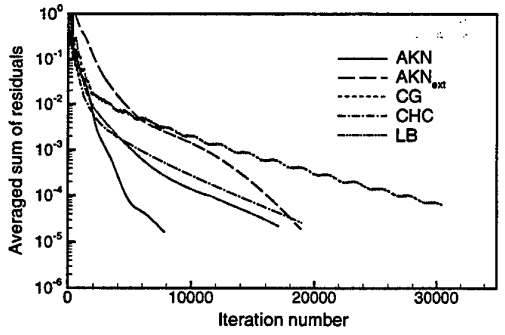

Figure 20: Convergence history for the different models, backstep flow [35]

Table 5: Relative CPU time needed to reach convergence, backstep flow [35]

	AKN	AKN_{ext}	CG	CHC	LB
CPU	1.0	2.9	4.7	2.4	2.1

the highest number of iterations. It should be noted that with the AKN model higher relaxation factors for the turbulence quantities k and ϵ in the order of 0.6 can be used, whereas the CG, CHC, and LB model require underrelaxation of those quantities by approximately 0.3 to prevent divergence. The stiffness and strong coupling of the transport equations of the two equation heat transport model likewise requires strong underrelaxation of k_θ and ϵ_θ slowing down the convergence rate of the AKN_{ext} model.

In Table 5, the relative CPU times for reaching convergence of the different models are listed. Again the AKN model is the fasted one. The lower convergence rate of the AKN_{ext} model is reflected by an increase of the run time by a factor of approximately 3. Similar values are obtained by the LB and CHC model, whereas the highest CPU time is required by the CG model.

4.3 Backward facing step flow with constant wall temperature

The results presented subsequently refer to the backward facing step flow as discussed by Scherer and Wittig [28]. The expansion ratio of the test section is 1.36. Three-dimensional effects are negligible, therefore, the flow at the centreline is to be assumed two-dimensional. The Reynolds number Re_H based on the step height is 66400. The fully turbulent boundary layer thickness at separation is $\delta/H = 0.4$. For the calculations, a computational grid with a total number of 305×153 grid points has been used which ensures grid-independent solutions. The grid points adjacent to the bottom wall were located with $y^+ \leq 0.15$. The axial length of the computational domain covers $-0.8H \leq x \leq 32H$. For the thermal field, the temperature at the bottom wall downstream of the step has been specified. A zero wall heat flux has been prescribed at the remaining wall boundaries. The temperature ratio (T_{inl}/T_w) is 1.5. Thus, the equations of the velocity- and thermal field are fully coupled.

Table 6 shows a comparison of the predicted reattachment lengths with the experimental data. Again it is found that the CG model is in best agreement with the measurement, whereas underprediction is revealed for the remaining models. The excellent agreement with the measurement of the CG model is achieved mainly by Yap's damping of the turbulent length scales (cf. CG_{mod} model prediction). In this flow situation, the variability of Pr_t has only a minor effect on the reattachment length, as it is demonstrated by the AKN model prediction.

The Nusselt number distribution along the bot-

Table 6: Comparison of flow reattachment length x_R/H, backstep flow [28]

Exp.	AKN	AKN_{ext}	CG	CHC	LB	CG_{mod}
6.54	5.7	5.83	6.4	5.3	5.6	5.6

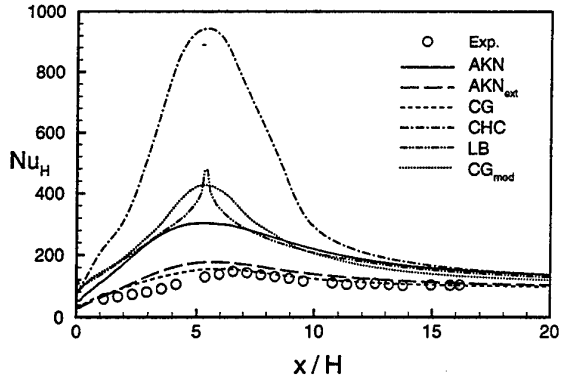

Figure 21: Nusselt number profiles, experiment [28]

Table 7: Relative CPU time needed to reach convergence, backstep flow [28]

	AKN	AKN_{ext}	CG	CHC	LB
CPU	1.0	1.24	1.68	4.15	2.95

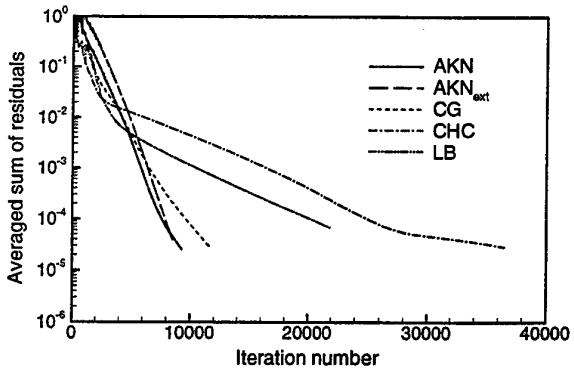

Figure 22: Convergence history for the different models, backstep flow [28]

tom wall is depicted in Fig. 21. The results are quite similar to those of the Stanton number variation (Fig. 19). Again, good agreement with the experiment is revealed for CG model as well as the AKN_{ext} model by which the two equation heat transfer model is taken into account. All other models significantly overpredict the experimental values. The reason is again attributable to the level of the predicted turbulent viscosity in the region adjacent to the viscous sublayer which affects significantly the temperature gradient and heat transfer coefficient at the wall.

Fig. 22 shows the convergence history for the different models. Very similar convergence rates are obtained for the AKN, AKN_{ext} and CG model. An increase in the number of outer iterations is given by the LB model whereas the highest number of outer iterations are required by the CHC model for this testcase.

The relative CPU times needed by the models to reach the stopping criterion is shown in Table 7. An increase in computing time of approximately 25% was found for the AKN model when the two equation heat transport model is applied. The higher total number of outer iterations required by the LB and CHC model leads to a CPU time enhancement by a factor of ≈ 3 and ≈ 4, respectively. The CPU time required by the CG model is comparable to that of the AKN_{ext} model.

4.4 Flow around a convectively cooled turbine blade

As a typical application of turbomachinary design, the flow around an highly loaded turbine blade has been chosen. The flow and heat transfer has been investigated experimentally by Schiele, Sieger, Schulz and Wittig [29]. A cross section of the blade is shown in Fig. 23. The calculations were performed at a Reynolds number based on the blade chord of 87.000. The freestream turbulence intensity is $Tu = 1.5\%$. At the inlet of the computational domain, experimental data of the total pressure, total temperature, dissipation length scale, and flow direction have been used as boundary conditions for the numerical calculations. At the outlet, the static pressure was prescribed. Along the blade surface, the measured temperature distribution has been specified as thermal wall condition. The modification of the production term of the turbulent kinetic energy proposed by Kato and Launder [15] has been included into all models in order to reduce the excessive production of k at the leading edge of the blade. The computations have been performed on a 210 × 100 grid. For the grid points closest to the blade surface, the co-ordinate y^+ is below 0.8. Because of the bad performance in predicting the skin friction and heat transfer rates, the CHC model is excluded from the following investigation.

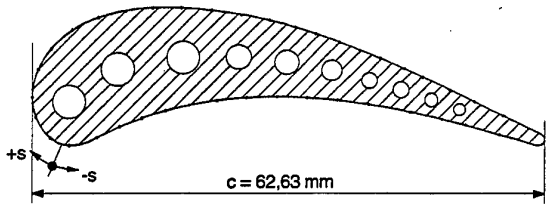

Figure 23: Cross section of the turbine blade

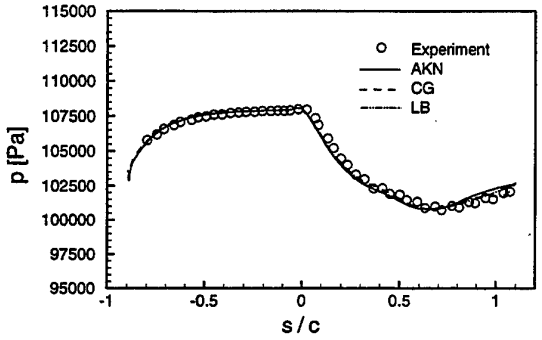

Figure 24: Predicted and measured static pressure distribution

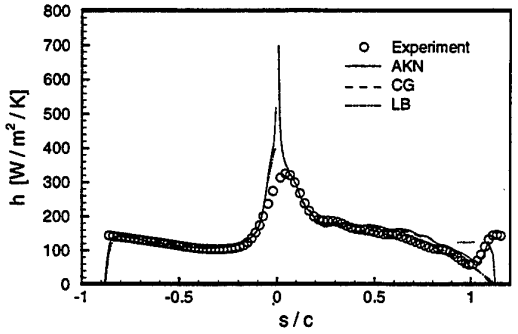

Figure 25: Predicted and measured heat transfer coefficient

Fig. 24 shows the comparison of the measured and predicted distribution of the static pressure along the pressure ($s < 0$) and suction side ($s > 0$) of the blade. All models predict almost identical results on the pressure side. On the suction side, near the trailling edge, minor differences are found. Here, the AKN model gives a slightly more pronounced increase in pressure.

In Fig. 25, experimental and calculated heat transfer coefficients are compared. Similar results which are in very good agreement with the measurements could be obtained for all models in the laminar flow region on the pressure and suction side, respectively. As indicated by the experimental data, the laminar-turbulent transition is located at the very end of the suction side. The transition is only captured by the AKN model whereas the CG and LB models both fail. The reason is thought to be attributable to the fact that the predicted positive pressure gradient of the AKN model is higher at the location where transition starts which seems to be sufficient to initiate transition.

SUMMARY AND CONCLUSIONS

The objective of the present study was to evaluate three recently published linear LRN k-ϵ models (AKN, CG and CHC), especially tuned for separating and reattaching flows, with particular emphasis on their capabilities in predicting complex flows of engineering application. As reference, the LRN model by Lam and Bremhorst (LB) has been included.

For a fully developed channel flow with heat transfer, the assessment of the models reveals that the results by the AKN model are overall in better agreement with DNS data than those of the CG, CHC, and LB model.

When calculating separated and reattaching flows, the velocity and temperature predictions coincide well with the experimental data in the farfield region of the wall for all models. Differences are found near the wall. It could be shown that the errors in predicting the skin friction coefficient are caused by inconsistencies of the predicted turbulent viscosity, which in turn affect significantly the temperature field. The CHC model totally overpredicts the skin friction, whereas the AKN and LB model results coincide well with the experiment. The regular CG model underpredicts skin friction, however, good agreement is found when Yap's damping term is ommitted. Very good agreement with measured heat transfer coefficients gives the CG model due to damping of the turbulent length scales, which causes a reduction of the turbulent dynamic thermal diffusivity in the energy equation. Since this approach is not included in the AKN, CHC, and LB model, a severe overprediction of heat transfer coefficient is found. By using the first order closure of the thermal field for the AKN model, good agreement for the temperatur variation near the wall similar to that predicted by the CG model is achieved.

For the flow around a convectively cooled turbine blade is was shown that the AKN, CG and LB model agree fairly well with the experiment on the pressure side of the turbine blade, whereas only the

AKN model is able to predict the laminar-turbulent transition at the trailling edge on the suction side.

From the computational standpoint, the standard AKN model which is based on a constant turbulent Prandtl number is the most efficient in terms of computing time, mostly because less relaxation is required for the turbulence quantities k and ϵ. Moreover, when including the two equation heat transfer model into the AKN model, it is still competitive with the much less accurate CG model.

In conclusion, the AKN_{ext} model which takes the variation of the turbulent Prandtl number into account shows an advantage over the conventional zero-equation heat transfer models studied in this paper in the prediction of heat transfer rates near the wall of separating and recirculation flows. Its main advantage over the standard strategy, where a constant value of Pr_t is assumed, is the ability to reduce the turbulent dynamic thermal diffusivity near reattachment by high values of Pr_t. The reduction of the turbulent dynamic thermal diffusivity can also be achieved by damping of the turbulent length scales. However, this approach does not seem to be appropriate for this type of flow since it significantly changes the capability of LRN k-ϵ turbulence models in predicting correct values of both the skin friction coefficient and the reattachment length. For the attached boundary layer situations examined in this study, the AKN model partly performs even better than the reliable LB model as far as heat transfer coefficients and fluid dynamic data are concerned. However, it is difficult to give a global preference to the AKN model because of its significant deviation from the well established standard values of the k-ϵ model constants. This may have a significant effect on the prediction of the fluid dynamic data in the fully turbulent region.

ACKNOWLEDGEMENTS

This work was supported by a grant of the *Deutsche Forschungsgemeinschaft* in the context of the *Graduiertenkolleg Energie- und Umwelttechnik* and the *Sonderforschungsbereich 167 Hochbelastete Brennräume-stationäre Gleichdruckverbrennung* which are gratefully acknowledged.

Nomenclature

C_1, C_2, C_μ	constants of k-ϵ model
C_λ	constant in equation for eddy diffusivity for heat
C_l	slope of length scale l in near wall equilibrium layer, here $C_l = 2.44$
$C_{P1}, C_{P2}, C_{D1}, C_{D2}$	constants in transport equation for ϵ_θ
c	blade cord
c_f	skin friction coefficient
c_p	specific heat at constant pressure
E	extra source term in ϵ equation
f_μ, f_1, f_2	damping functions in velocity field turbulence model
$f_{P1}, f_{P2}, f_{D1}, f_{D2}$	damping functions in temperature field turbulence model
h	enthalpie
h	heat transfer coefficient, $q_w/(T_0 - T_w)$
H	height of backward facing step
k	turbulent kinetic energy
k_θ	temperature variance
l	turbulent length scale, $k^{1.5}/\epsilon$
Nu_H	Nusselt number, $q_w H/\lambda(T_0 - T_w)$
Pr	Prandtl number, α/ν
Pr_t	turbulent Prandtl number, α_t/ν_t
p	static pressure
P_k	produktion of turbulent energy
P_θ	produktion of temperature variance
q_w	wall heat flux
R	time scale ratio, τ_t/τ_u
Re_t	turbulent Reynolds number, $k^2/\nu\epsilon$
Re_y	turbulent Reynolds number, $\sqrt{k}y/\nu$
Re_H	Reynolds number based on step height $U_0 H/\nu$
Re_τ	Reynolds number based on friction velocity, $U_\tau H/\nu$
St	Stanton number, $q_w/[\rho c_p U_0(T_w - T_0)]$
S_ϵ	extra source term in ϵ equation, $S_\epsilon = E$
s	surface length
T	mean temperature
T_0	reference temperature
T^+	nondimensional mean temperature, $(T_w - T)/T_\tau$
Tu	turbulence intensity
T_τ	friction temperature, $q_w/(\rho c_p u_\tau)$
u	mean velocity in x-direction
u_i	Cartesian velocity in i-direction
u_ϵ	Kolmogorov velocity scale, $(\nu/\epsilon)^{0.25}$
u_τ	friction velocity, $\sqrt{\lvert\tau_w\rvert/\rho}$
U_0	reference velocity
x	Cartesian co-ordinate
x_R	flow reattachment length
y	Cartesian co-ordinate, distance from the wall
y_n	distance from the wall
y^+	normalized distance from the wall, $u_\tau y/\nu$
y^*	normalized distance from the wall, $u_\epsilon y/\nu$

Greek Symbols

α	diffusivity for heat
δ	boundary layer thickness
δ_{ij}	Kronecker delta
ϵ	dissipation rate of k
ϵ_θ	dissipation rate of k_θ
λ	thermal condictivity
μ	dynamic viscosity
ν	kinematic viscosity
ρ	density
$\sigma_k, \sigma_\epsilon$	model constants of turbulent diffusion for k, ϵ
σ_h	model constants of turbulent diffusion for $k_\theta, \epsilon_\theta$
τ_u	time scale of velocity field, k/ϵ
τ_t	time scale of temperature field, $k_\theta/2\epsilon_\theta$

Subscripts

ext	extended (cf. AKN model)
i, j, k	Cartesian directions
inl	inlet
mod	modified (cf. CG model)
n	normal direction from the wall
R	flow reattachment point
t	turbulent
w	wall surface
0	reference value

Superscripts

$+$	normalized quantity
$*$	normalized quantity
$'$	fluctuation
$-$	time averaged

References

[1] Abe, K., Kondoh, T. and Nagano, Y.: A New Turbulence Model for Predicting fluid flow and Heat Transfer in Separating and Reattaching Flows-I. Flow Field Calculations. International Journal of Heat and Mass Transfer, 37, No. 1, pp. 139–151, 1994.

[2] Abe, K., Kondoh, T. and Nagano, Y.: A New Turbulence Model for Predicting fluid flow and Heat Transfer in Separating and Reattaching Flows-II. Thermal Field Calculations. International Journal of Heat and Mass Transfer, 38, No. 8, pp. 1467–1481, 1995.

[3] Antonia, R., Danh, H. and Prabhu, A.: Response of a turbulent boundary layer to a step change in surface heat flux. Journal of Fluid Mechanics, 80, pp. 153–177, 1977.

[4] Bagheri, N., Strâtaridakis, C. and White, B.: Measurements of Turbulent Boundary Layer Prandtl Numbers and Space-time Temperature Correlations. AIAA Journal, 30, No. 1, pp. 35–42, 1992.

[5] Benz, E. and Wittig, S.: Prediction of the Interaction of Coolant Ejection with the Main Stream at the Leading Edge od a Turbine Blade: Attached Grid Application. Int. Symp. on Heat Transfer in Tubomachinery, 1992. Athen, Greece.

[6] Chang, K., Hsieh, W. and Chen, C.: A Modified Low-Reynolds-Number Turbulence Model Applicable to Recirculating Flow in Pipe Expansion. Transactions of the ASME - I - Journal of Fluids Engineering, 117, No. 3, pp. 417–423, 1995.

[7] Chieng, C. and Launder, B.: On the Calculation of Turbulent Heat Transport Downstream from an Aprupt Pipe Expansion. Num. Heat Transfer, 3, pp. 189–207, 1980.

[8] Cho, H. and Goldstein, R.: An Improved Low-Reynolds-Number k, ϵ Turbulence Model for Recirculating Flows. International Journal of Heat and Mass Transfer, 37, No. 10, pp. 1495–1508, 1994.

[9] Ciofalo, M. and Collins, M.: k, ϵ Predictions of Heat Transfer in Turbulent Recirculating Flows Using an Improved Wall Treatment. Numerical Heat Transfer, 15, pp. 21–47, 1989.

[10] Djilali, N., Gartshore, I. and Salcudean, M.: Calculation of Convective Heat Transfer in Recirculating Turbulent Flow using various Near-Wall Turbulence Models. Num. Heat Transfer, 16, pp. 189–212, 1989.

[11] Giebert, D., Bauer, H. and Wittig, S.: A Comparative Study of Two Low-Reynolds Number k-ϵ Turbulence Models for Recirculating Flows with and without Heat Transfer. Proceedings of the 3rd International Symposium on Engineering Turbulence Modelling and Measurements, 1996. May 27-29, Crete, Greece.

[12] Giebert, D., Gritsch, M., Schulz, A. and Wittig, S.: Film-Cooling from Holes with Expanded Exits: A Comparison of Computational Results with Experiments. ASME Paper No. 97-GT-163, 1997.

[13] Hassid, S. and Poreh, M.: A Turbulent Energy Dissipation Model for Flows With Drag Reduction. ASME–Journal of Fluids Engineering, 100, pp. 107–112, 1978.

[14] Kasagi, N., Tomita, Y. and Kuroda, A.: Direct Numerical Simulation of Passive Scalar Fiel in a Turbulent Channel Flow. ASME–Journal of Heat Transfer, 114, No. 8, pp. 598–606, 1992.

[15] Kato, M. and Launder, B.: The Modelling of Turbulent Flow Around Stationary and Vibrating Square Cylinders. Proceedings of the 9th Symposium on Turbulent Shear Flows, 1993. August 16-18, Kyoto, Japan.

[16] Kurreck, M. and Wittig, S.: Prediction of Turbulent Three-dimensional Combustor Flows on Parallel Computing Systems. Technical Report Paderborn Center for Parallel Computing/TR-009-94, pp. 74–76, 1994.

[17] Lam, C. and Bremhorst, K.: A Modified Form of the k, ϵ Model for Predicting Wall Turbulence. Journal of Fluids Engineering, 103, pp. 456–460, 1981.

[18] Launder, B.: On the Computation of Convective Heat Transfer in Complex Turbulent Flows. ASME–Journal of Heat Transfer, 110, pp. 1112–1128, 1988.

[19] Launder, B. and Spalding, D.: The Numerical Computation of Turbulent Flows. Computer Methods in Applied Mechanics and Engineering, 3, pp. 269–289, 1974.

[20] Nagano, Y. and Tagawa, M.: An Improved k, ϵ Model for Boundary Layer Flows. J. of Fluids Engineering, 112, pp. 33–39, 1990.

[21] Nagano, Y., Tagawa, T. and Tsuji, T.: An Improved Two-Equation Heat Transfer Model for Wall Turbulent Shear Flows. ASME/JSME Thermal Engineering Proceedings, 3, pp. 233–240, 1991.

[22] Noll, B.: Evaluation of a Bounded High-Resolution Scheme for Combustor Flow Computations. AIAA Journal, 30, No. 1, pp. 64–69, 1992.

[23] Park, T. and Sung, H.: A Nonlinear Low-Reynolds-Number k-ϵ model for turbulent separated and reattaching flows – I. Flow field computations. International Journal of Heat and Mass Transfer, 38, No. 14, pp. 2657–2666, 1995.

[24] Patankar, S. and Spalding, D.: A Calculation Procedure for Heat, Mass and Momentum Transfer in Three-Dimensional Parabolic Flows. International Journal of Heat and Mass Transfer, 15, pp. 1787–1806, 1972.

[25] Patel, V., Rodi, W. and Scheuerer, G.: Turbulence Models for Near-Wall and Low Reynolds Number Flows: A Review. AIAA Journal, 23, No. 9, pp. 1308–1319, 1985.

[26] Reynolds, A.: The prediction of turbulent Prandtl and Schmidt numbers. International Journal of Heat and Mass Transfer, 18, pp. 1055–1069, 1975.

[27] Rhie, C. and Chow, W.: Numerical Study of the Turbulent Flow Past an Airfoil with Trailing Edge Separation. AIAA Journal, 21, No. 11, pp. 1525–1532, 1983.

[28] Scherer, V. and Wittig, S.: The Influence of the Recirculation Region: A Comparison of the Convective Heat Transfer Downstream of a Backward-Facing Step and Behind a Jet in a Cross Flow. ASME Paper 89-GT-59, 1989.

[29] Schiele, R., Sieger, K., Schulz, A. and Wittig, S.: Heat Transfer Investigations on a Highly Loaded, Aerothermally Designed Turbine Cascade. F.S. Billig (Edt.), 12th Int. Symposium on Air Breathing Engines, Melbourne, Australia, 1995.

[30] Sieger, K., Schiele, R., Schulz, A. and Wittig, S.: Gas Turbine Blade Heat Transfer Calculations: An Assessment of Different Low-Reynolds Number k-ϵ-Turbulence Models. Fifth International Symposium on Transport Phenomena and Dynamics of Rotating Machinery, Kaanapali, Maui, Hawaii, USA, May 8-11, 1994.

[31] Sieger, K., Schulz, A., Crawford, M. and Wittig, S.: An Evaluation of Low-Reynolds Number $k - \epsilon$ Turbulence Models for Predicting Transition under the Influence of Free-Stream Turbulence and Pressure Gradient. 2nd Int. Symp. on Engineering Turbulence and Measurements, May 31-June 2, Florence, Italy, 1993.

[32] Sommer, T., So, R. and Zhang, H.: Supersonic Flow Calculations Using a Reynolds-Stress and a Thermal Eddy Diffusivity Turbulence Model. ASME–Journal of Fluids Engineering, 116, pp. 469–476, 1994.

[33] Speziale, C.: On Nonlinear k-l and k-ϵ Models of Turbulence. Journal of Fluid Mechanics, 178, pp. 459–475, 1987.

[34] Stone, H.: Iterative Solution of Implicit Approximations of Multidimensional Partial Differential Equations. SIAM Journal of Numerical Analysis, 5, No. 3, pp. 530–558, 1968.

[35] Vogel, J., C. and Eaton, J.: Heat Transfer and Fluid Mechanics Measurements in the Turbulent Reattaching Flow Behind a Backward-Facing Step. Report MD-44, Thermo. Div., Dept. of Mechanical Engineering, Stanford Univ., California, 1984.

[36] Yap, C.: Turbulent Heat Transfer in Recirculating and Impinging Flows. Ph. D. Thesis, University of Manchester, 1987.

DNS AND SCALAR-FLUX TRANSPORT MODELLING IN A TURBULENT CHANNEL FLOW

P. M. Wikström and A. V. Johansson

Department of Mechanics
KTH, Stockholm, Sweden

ABSTRACT

A direct numerical simulation (DNS) of a turbulent channel flow with a passive scalar has been made at a Prandtl number of 0.71 and a Reynolds number, based on the centerline mean velocity, of 4800. Second order statistics including Reynolds fluxes, $\overline{u_i\theta}$, are determined along with all the terms appearing in the Reynolds-flux transport equations. Models for the pressure scalar-gradient correlation, appearing in the transport equation of the Reynolds fluxes, are compared to the DNS data. A significant improvement of the simplest model, $-c_{\theta 1}\frac{1}{\tau}\overline{u_i\theta}$, is achieved by including a model for the rapid term that is linear in the mean velocity gradients.

1 INTRODUCTION

Turbulent transport of passive scalars play an important part in many engineering applications and atmospheric flows. The passive scalar may for example be temperature, humidity, pollutant or any other chemical species. The transport equation of the mean scalar is given by

$$\frac{\partial \Theta}{\partial t} + U_l\frac{\partial \Theta}{\partial x_l} = \frac{\partial}{\partial x_l}\left(\alpha\frac{\partial \Theta}{\partial x_l} - \overline{u_l\theta}\right). \quad (1)$$

Here an unknown flux term, $\overline{u_i\theta}$, appears. In analogy with the eddy-viscosity concept this may be approximated by a simple gradient diffusion model,

$$\overline{u_i\theta} = -\frac{\nu_t}{Pr_t}\frac{\partial \Theta}{\partial x_i}. \quad (2)$$

In a zero equation model an assumption of a constant turbulent Prandtl or Schmidt number is made. For many engineering applications this is not accurate enough. If the turbulent Prandtl or Schmidt number is not assumed to be constant, the transport equations of the scalar variance, $\overline{\theta^2}$, and the scalar dissipation rate, ε_θ, are needed, in analogy with $k-\varepsilon$ modelling. The simple eddy-diffusivity approach is unable to give a correct prediction of all components of $\overline{u_i\theta}$ in many flows. In the two dimensional heated cylinder wake, for example, a zero prediction of the streamwise heat flux is obtained, whereas inclusion of a nonlinear term improves the situation considerably, Wikström et al. (8). To involve more of the physics of heat flux transport, in the two-equation model approach, algebraic scalar-flux models which are obtained from the transport equations of the scalar fluxes may be used. The formulation of these involves the use of some equilibrium assumption equivalent to that used in algebraic Reynolds stress models. The basic platform here consists of transport equations of $\overline{\theta^2}$ and ε_θ. Explicit forms of these algebraic models are attractive since they lead to decreased numerical problems and computational efforts as compared to full second-order modelling. A second-order Reynolds flux model gives, in conjunction with a second-order Reynolds stress model, a turbulence closure consisting of twelve transport equations for turbulence quantities if the flow is three-dimensional.

The transport equation for the scalar fluxes, $\overline{u_i\theta}$, is given by

$$\frac{\partial \overline{u_i\theta}}{\partial t} + U_l\frac{\partial \overline{u_i\theta}}{\partial x_l} = -\overline{u_iu_l}\frac{\partial \Theta}{\partial x_l} - \overline{u_l\theta}\frac{\partial U_i}{\partial x_l}$$
$$-\frac{\partial}{\partial x_l}(\overline{u_iu_l\theta} + \overline{\frac{p}{\rho}\theta\delta_{il}} - \alpha\overline{\frac{\partial\theta}{\partial x_l}u_i} - \nu\theta\overline{\frac{\partial u_i}{\partial x_l}}) + \Psi_i \quad (3)$$

$$\Psi_i = \overline{\frac{p}{\rho}\frac{\partial\theta}{\partial x_i}} - (\alpha+\nu)\overline{\frac{\partial\theta}{\partial x_l}\frac{\partial u_i}{\partial x_l}} \quad (4)$$

The right hand side of the transport equation contains two production terms, a transport term consisting of two turbulent and two molecular diffusion terms, a pressure scalar-gradient correlation term, $\Pi_{\theta i}$, and diffusive and viscous destruction, $\varepsilon_{\theta i}$. The sum of these two last terms is here denoted by Ψ_i. At high Reynolds numbers the molecular diffusion terms are small compared to the turbulent ones and may be neglected. Also the viscous and diffusive destruction terms should then be negligible, since the small scales are nearly isotropic at high Reynolds numbers. By modelling the turbulent diffusion, $-\frac{\partial}{\partial x_l}\left(\overline{u_iu_l\theta} + \overline{\frac{p}{\rho}\theta\delta_{il}}\right)$, and Ψ_i a modelled differential Reynolds-flux equation is obtained. Through approximation of the modelled transport equation we may obtain an algebraic scalar-flux model, in which the model for Ψ_i would be one of the ingredients.

When modelling the transport equation for the turbulent scalar fluxes, a model for the pressure scalar-gradient correlation term is needed. This term may be divided into a slow part and a rapid part, where the slow part modelled by, $-c_{\theta 1}\frac{1}{\tau}\overline{u_i\theta}$, may also include effects of destruction, Shih (7). Two major questions now arise. What is the appropriate timescale, τ, and when are the rapid terms important? Launder (4) suggested that both the thermal and the dynamical timescales are important. Since they are generally not proportional, i.e Pr_t is not constant, a mixture of these should then be used to blend both thermal and mechanical contributions. An objection to this approach could be that inclusion of the thermal timescale results in a violation of the superposition principle for passive scalars. On the other hand an analogous violation is made in non-linear models of the pressure-strain rate. In a DNS of homogeneous shear flow by Rogers et al. (5), it was found that the sum of

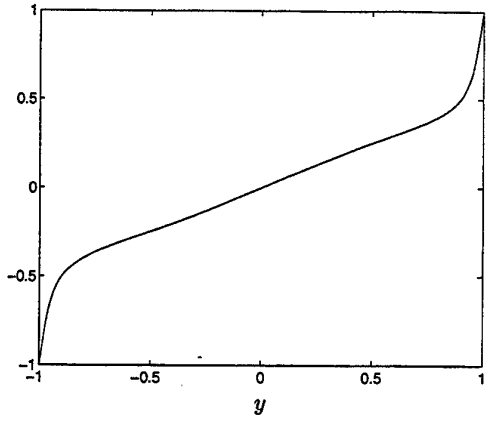

Figure 1: The mean temperature profile in the channel.

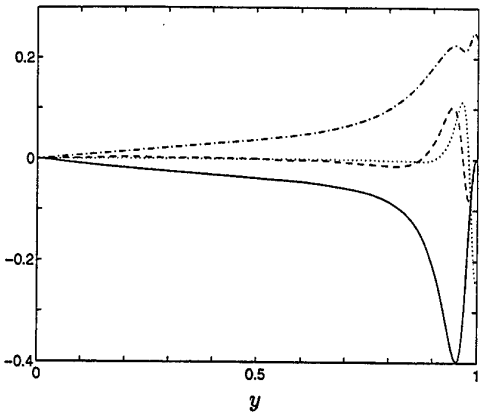

Figure 2: Terms in the budget of the streamwise flux, $\overline{u\theta}$, in plus units. —, $-\overline{uv}\frac{\partial\Theta}{\partial y} - \overline{v\theta}\frac{\partial U}{\partial y}$; - - -, $-\frac{\partial}{\partial y}\overline{uv\theta}$; ⋯, $\frac{\partial}{\partial y}\left(\alpha\overline{\frac{\partial\theta}{\partial y}u} + \nu\overline{\theta\frac{\partial u}{\partial y}}\right)$; - · -,$\Psi_1$

the pressure scalar-gradient and the destruction terms, in the turbulent scalar flux transport equation, are approximately aligned with the flux vector itself. This has also been found in a heated cylinder wake, Wikström et al. (9). However, such an approximate alignment does not exclude the possibility to substantially improve the predictions by including rapid terms in the modelling of these terms. Effects of rapid terms in the modelling of Ψ_i, in a turbulent channel flow with a passive scalar, are investigated in the present paper.

2 NUMERICAL PROCEDURES

A direct numerical simulation (DNS) of a turbulent channel flow with a passive scalar has been performed for a Prandtl number of 0.71. The Reynolds number based on the centerline mean velocity is 4800 and the Reynolds number based on the wall friction velocity, u_τ, and the channel half width, δ, is 265. The simulation code uses spectral methods, with Fourier representation in the streamwise(x) and spanwise(z) directions, and Chebyshev polynomials in the wall-normal(y) direction. The computational domain is 12.56δ, 2δ, 5.5δ in the streamwise, wall-normal and spanwise directions respectively and the number of grid points are 256×193×192. This gives a resolution in the x-, y-and z-directions of 13.0, 2.7(in average) and 7.6 wall units respectively. Time integration is made using the Crank-Nicolson scheme for viscous terms and a four stage Runge-Kutta scheme for the nonlinear terms. As the velocity field is advanced for each time step, the corresponding scalar field is obtained by integrating the conservation equation for the passive scalar,

$$\frac{\partial\Theta'}{\partial t} + \frac{\partial}{\partial x_l}\Theta' U'_l = \frac{1}{RePr}\frac{\partial^2\Theta'}{\partial x_l \partial x_l}, \qquad (5)$$

where Θ' and U'_i are the dimensionless total scalar field, $\Theta+\theta$, and velocity field, U_i+u_i, respectively. The initial and boundary conditions used for the scalar field are

$$\Theta'(x,y,z,0) = \frac{\log_{10}\left\{\frac{(y_0+y)}{(y_0-y)}\right\}}{\log_{10}\left\{\frac{(y_0+1)}{(y_0-1)}\right\}}, \quad y_0 = 1.005 \qquad (6)$$

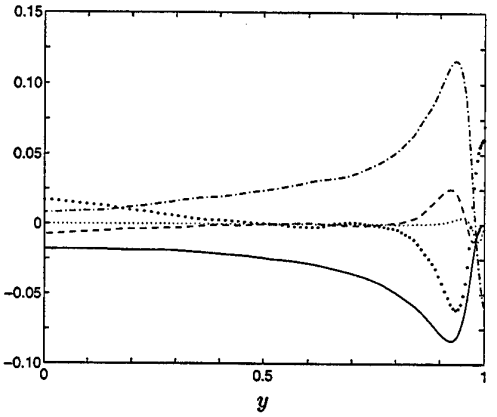

Figure 3: Terms in the budget of the wall normal flux, $\overline{v\theta}$, in plus units. —, $-\overline{v^2}\frac{\partial\Theta}{\partial y}$; - - -, $-\frac{\partial}{\partial y}\overline{v^2\theta}$; ⋯, $\frac{\partial}{\partial y}\left(\alpha\overline{\frac{\partial\theta}{\partial y}v} + \nu\overline{\theta\frac{\partial v}{\partial y}}\right)$; - · -,$\Psi_2$; ⋯, $\frac{\partial}{\partial y}\left(\overline{\frac{p}{\rho}\theta}\right)$.

$$\Theta'(x,-1,z,t) = -1, \quad \Theta'(x,1,z,t) = 1 \qquad (7)$$

The temperature at each wall is thus kept constant with a higher temperature of the upper wall. This boundary condition, which represents a case where the passive scalar is introduced at the upper wall ($y=1$) and removed from the lower wall ($y=-1$), results in an antisymmetric mean temperature profile in the channel. This profile is shown in Fig. 1. The DNS data presented in the following consist of averages of 24 statistically independent fields.

3 RESULTS

In Figs. 2–3 the terms in the transport equations for $\overline{u\theta}$ and $\overline{v\theta}$ are shown. All terms are normalized by $\alpha\left\{\frac{\partial U}{\partial y}\frac{\partial\Theta}{\partial y}\right\}_{wall}$. The Ψ_1 and Ψ_2 terms are of significant importance and may not be neglected. In the $\overline{u\theta}$-equation there is essentially a balance between production and Ψ_1 except in the near-wall region. This is approximately also the case for the $\overline{v\theta}$-equation except in the central

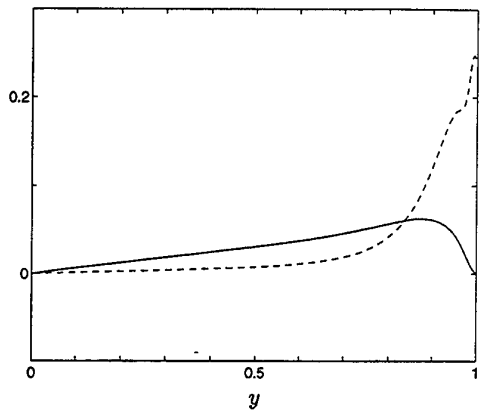

Figure 4: The two parts of Ψ_1. —, $\Pi_{\theta 1}$; - - -, $\varepsilon_{\theta 1}$.

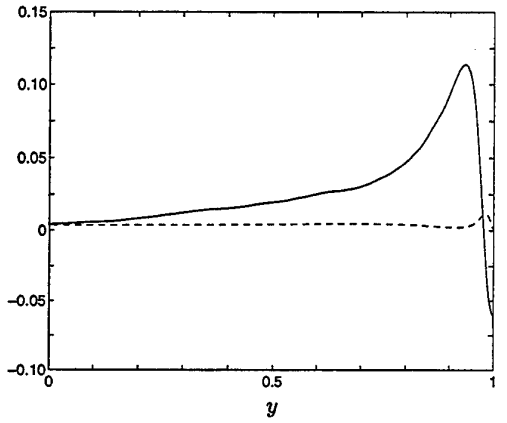

Figure 5: The two parts of Ψ_2. —, $\Pi_{\theta 2}$; - - -, $\varepsilon_{\theta 2}$.

parts of the channel. For $|y| < 0.3$ the turbulent and especially the pressure diffusion terms are as important as the production and Ψ_2.

In Fig.4 and Fig.5 the two parts of Ψ_1 and Ψ_2 are shown respectively. For Ψ_1 the destruction term, $\varepsilon_{\theta 1}$, is negligible compared to $\Pi_{\theta 1}$ except in the near-wall region, where $\varepsilon_{\theta 1}$ is strongly dominating. For Ψ_2 the destruction term, $\varepsilon_{\theta 2}$, is small compared to Ψ_2 except in a narrow region in the center of the channel and in a narrow region near the wall.

3.1 Model comparison for Ψ_i

In the following model comparison the primary objective is to investigate the importance of rapid terms when modelling Ψ_i. Since damping functions, needed in the near-wall region, are not included here only the interval $|y| \leq 0.6$ is considered. The distance to the wall is there larger than about 100 wall units.

In Fig. 6 the inclination angles of the turbulent scalar flux, $\overline{u_i\theta}$, and Ψ_i are compared. In this figure we see that Ψ_i is approximately parallel to the scalar-flux vector with a maximum deviation of less than 10 degrees. An approximate alignment between these has been found earlier by Rogers et al. (5) in a homogeneous shear flow and by Wikström et al. (9) in a heated cylinder wake. A linear relaxation relation, $\Psi_i = -c_{\theta 1}\frac{1}{\tau}\overline{u_i\theta}$, seems

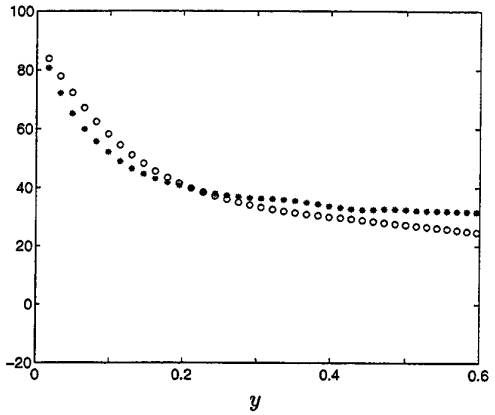

Figure 6: The inclination angles of $\overline{u_i\theta}$ and Ψ_i. ∘, $\tan^{-1}\left(\overline{v\theta}/\overline{u\theta}\right)$; ∗, $\tan^{-1}\left(\Psi_2/\Psi_1\right)$

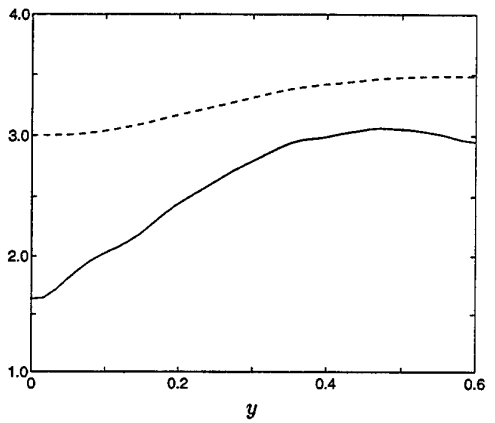

Figure 7: The ratio of the amplitudes of $\frac{\varepsilon}{k}\overline{u_i\theta}$ and Ψ_i. —, $\frac{k}{\varepsilon}\frac{|\Psi_i|}{|\overline{u_i\theta}|}$; - - -, $3.8 - 2.8\exp\left(-\frac{Re_t}{100}\right)$

from this figure to be a good candidate for modelling Ψ_i, where τ often is taken as the dynamical timescale, k/ε. In Fig. 7 the ratio of the amplitudes of Ψ_i and $\frac{\varepsilon}{k}\overline{u_i\theta}$, i.e. the effective $c_{\theta 1}$, from the DNS data is shown together with the curve $3.8-2.8\exp\left(-\frac{Re_t}{100}\right)$, where $Re_t = k^2/\nu\varepsilon$ is the turbulence Reynolds number. The latter expression was found to by Kawamura et al. (2) to describe the Reynolds number variation of $c_{\theta 1}$ in a set of DNS data of isotropic turbulence with an imposed constant mean temperature gradient.

In studies, where a constant value of $c_{\theta 1}$ has been calibrated against experimental data, a value of about 3.0 has been found, see Gibson et al. (1), and Launder (3). From Fig. 7 it is seen that the amplitude ratio is far from constant and deviates severely from the $c_{\theta 1}$ values obtained by Kawamura et al. The model, $\Psi_i = -c_{\theta 1}\frac{1}{\tau}\overline{u_i\theta}$, will thus not be able to give good predictions using either of these parameter choices. Rapid terms has been found to be important when modelling Ψ_i in a heated cylinder wake, Wikström et al. (9). This should also be expected to be the case in the present turbulent channel flow.

The following, more general, model for Ψ_i including rapid terms will be compared to the present DNS data:

$$\Psi_i = -c_{\theta 1}\frac{\varepsilon}{k}\overline{u_i\theta} + c_{\theta 2}\overline{u_l\theta}U_{i,l} + c_{\theta 3}\overline{u_l\theta}U_{l,i} + c_{\theta 4}\overline{u_iu_l}\Theta_{,l} \quad (8)$$

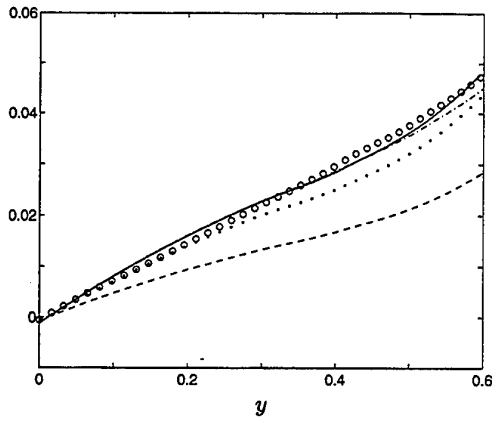

Figure 8: Model predictions of Ψ_1 using the parameter combinations given in Table 1. - - -, (a); - · -, (b); · · ·, (c); —, (d); ∘, Ψ_1 from DNS.

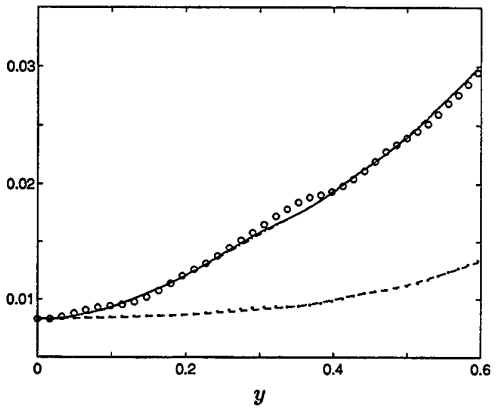

Figure 9: Model predictions of Ψ_2 using the parameter combinations given in Table 1. - - -, (a); - · -, (b); · · ·, (c); —, (d); ∘, Ψ_2 from DNS.

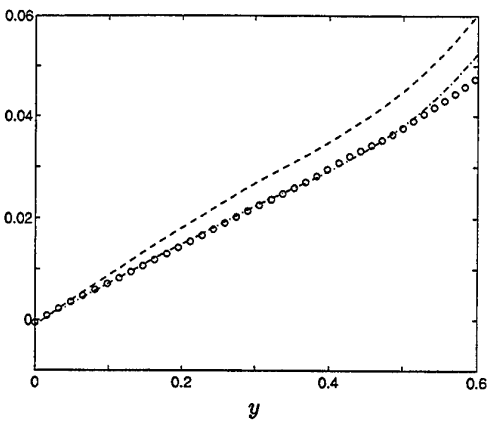

Figure 10: Model predictions of Ψ_1 using the parameter combinations given in Table 2. - - -, (e); - · -, (f); ∘, Ψ_1 from DNS.

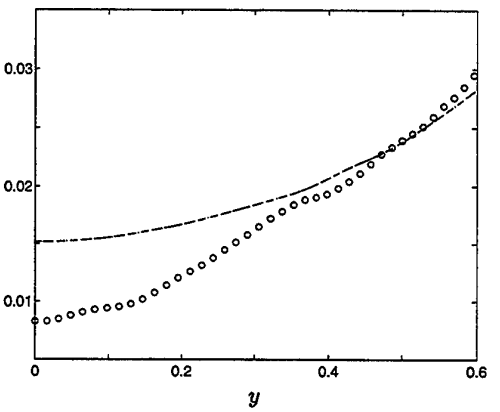

Figure 11: Model predictions of Ψ_2 using the parameter combinations given in Table 2. - - -, (e); - · -, (f); ∘, Ψ_2 from DNS.

This is the most general form, conserving the superposition principle for passive scalars, see Shabany et al. (6). By formal solution of the Poisson equation for the rapid pressure, a linear model for the pressure scalar-gradient correlation may be derived, see e.g. Shih (7). In that model only rapid terms involving mean velocity gradients are present. In the present plane shear flow the $c_{\theta 2}$ term contributes only to the Ψ_1 component and the $c_{\theta 3}$ term contributes only to the Ψ_2 component. Neither of these give any contribution at $y = 0$ since the mean velocity gradients are zero here. This is not the case though for the $c_{\theta 4}$ term. At $y = 0$ the mean temperature gradient has a non-zero value in the present channel flow.

In Figs. 8–9 the model predictions of Eq. 8, using the parameter combinations given in Table 1, are compared to the DNS data. For the aligned model, model (a), the value of $c_{\theta 1}$ is taken to 1.65 to be able to give the correct prediction of Ψ_2 at $y = 0$. This model underpredicts both components of Ψ_i, especially Ψ_2, and the deviation from the DNS data increases with y. When including rapid terms involving mean velocity gradients, and using the parameter choice of model (b), a very good prediction of both components of Ψ_i is obtained. In model (c) the rapid term involving mean scalar gradients is included instead. The $c_{\theta 1}$ parameter has here been taken to 3.0, which is much more consistent with previously suggested values of $c_{\theta 1}$. A correct prediction of Ψ_2 at the centerline is then obtained with $c_{\theta 4} = -0.39$. This model gives perhaps an acceptable prediction of Ψ_1 but the prediction of Ψ_2 is the same as that of model (a). When including all the rapid terms , model (d), an excellent agreement may be obtained for both components of Ψ_i.

In Fig. 10–11 the model predictions of Eq. 8, using the parameter combinations given in Table 2, are compared to the DNS data. The $c_{\theta 1}$ parameter is here taken to be $3.8 - 2.8 \exp\left(-\frac{Re_t}{100}\right)$ in each case. For the aligned model, (e), the prediction of Ψ_1 is better than that of model (a), while an overprediction of Ψ_2 is obtained in the center of the channel with a maximum deviation at $y = 0$. This deviation is due to the fact that $c_{\theta 1} = 3.0$ at $y = 0$. An inclusion of the $c_{\theta 4}$ term is then needed to be able to give a correct prediction of Ψ_2 at $y = 0$. Since the $c_{\theta 4}$ term was not taken into account in the calibration of Kawamura et al. their $c_{\theta 1}$ parameter values are to be used in a model of Ψ_i excluding the $c_{\theta 4}$ term. Model (f) therefore only includes rapid terms due to mean velocity gradients. The best agreement for Ψ_1 is then obtained with a negative value of $c_{\theta 2}$. The predictions of the Ψ_2

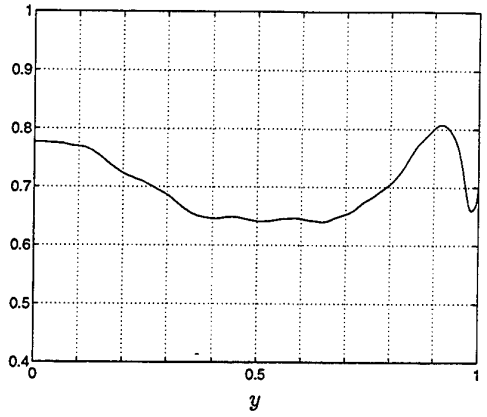

Figure 12: The time-scale ratio $r = \frac{1}{2}\overline{\theta^2}\varepsilon/k\varepsilon_\theta$.

component increases as the $c_{\theta 3}$ term increases, and decreases as $c_{\theta 3}$ is decreased. The influence of this term may be seen from the comparison of models (a) and (b) in Fig. 9. With $c_{\theta 3}$=0 a quite good agreement is obtained for $|y| > 0.3$ in the present region.

The DNS of homogeneous shear flow by Rogers et al. gives a constant timescale ratio, $\frac{1}{2}\overline{\theta^2}\varepsilon/k\varepsilon_\theta$, of about 0.6, where ε_θ is the dissipation rate of $\frac{1}{2}\overline{\theta^2}$. In Fig. 12 the timescale ratio in the present channel flow is shown. In the region $|y| \leq 0.6$ it ranges from 0.63 to 0.78. Using the thermal timescale instead of the dynamical timescale, k/ε, in the model given by Eq. 8, qualitatively the same behaviour of the model predictions is obtained. Different parameter values are of course needed to obtain the best possible predictions. This is also the case when using the mixed timescale, $\sqrt{k\overline{\theta^2}/\varepsilon\varepsilon_\theta}$, which blends both thermal and mechanical contributions.

In Figs. 13-14 models (a), (b), (d) and (f) are compared to the DNS data throughout the channel. In each case there is a need for damping functions as well as wall reflection terms to achieve better prediction near the wall. The aligned model (a) gives a better qualitative and quantitative prediction of Ψ_1 near the wall than model (b), and it is therefore a need to damp out the $c_{\theta 2}$ parameter in this region. If the $c_{\theta 3}$ term is included a severe overprediction of Ψ_2 near the wall is obtained, models (b) and (d). At the wall all the rapid terms vanish and Ψ_i is here obtained by $-\left\{c_{\theta 1}\frac{\varepsilon}{k}\overline{u_i\theta}\right\}_{wall}$. At the wall this expression is able to capture Ψ_1 but not Ψ_2. This is due to the fact that $\overline{v\theta}$ approaches zero more rapidly than $\frac{\varepsilon}{k}$ near the wall. This is also the case for the thermal or mixed timescales. A modification of timescale for normalization near the wall is hence needed. This is analogous to the situation for near-wall modelling of the Reynolds stresses.

4 CONCLUSIONS

A direct numerical simulation (DNS) of a turbulent channel flow with a passive scalar has been made at a Prandtl number of 0.71 and a Reynolds number, based on the centerline mean velocity, of 4800. The sum of the pressure scalar-gradient correlation and the destruction terms, Ψ_i, appearing in the Reynolds-flux transport equations are of

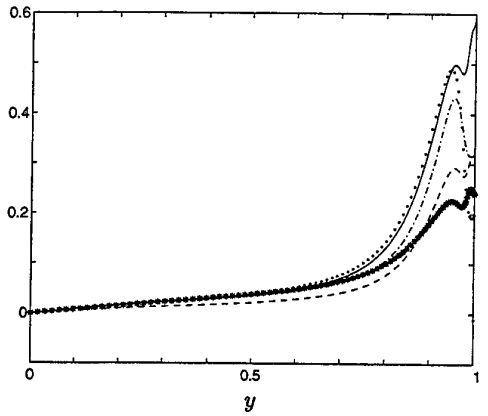

Figure 13: Model predictions of Ψ_1 using some of the parameter combinations given in Table1 and Table2. - - -, (a); - · -, (b); —, (d); · · ·, (f); ∗, Ψ_1 from DNS.

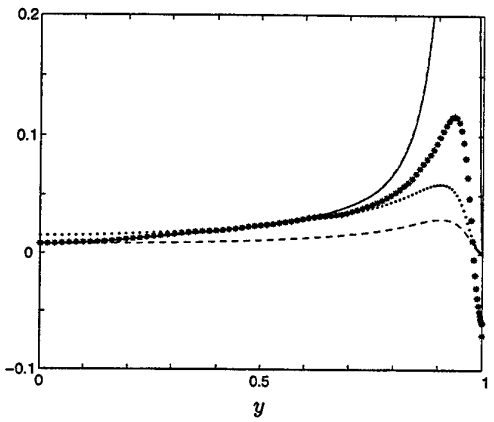

Figure 14: Model predictions of Ψ_2 using some of the parameter combinations given in Table1 and Table2. - - -, (a); - · -, (b); —, (d); · · ·, (f); ∗, Ψ_2 from DNS.

significant importance and needs to be modelled. A significant improvement of the simplest model, $-c_{\theta 1}\frac{1}{\tau}\overline{u_i\theta}$, is obtained by including rapid terms that are linear in the mean velocity gradients.

Table 1: Different combinations of the model parameters used in Eq. 8.

model	$c_{\theta 1}$	$c_{\theta 2}$	$c_{\theta 3}$	$c_{\theta 4}$
(a)	1.65	0	0	0
(b)	1.65	0.7	0.33	0
(c)	3.0	0	0	−0.39
(d)	3.0	0.20	0.33	−0.39

Table 2: Different combinations of the model parameters used in Eq. 8.

model	$c_{\theta 1}$	$c_{\theta 2}$	$c_{\theta 3}$	$c_{\theta 4}$
(e)	$c_{\theta 1}(\mathrm{Re}_t)$	0	0	0
(f)	$c_{\theta 1}(\mathrm{Re}_t)$	−0.33	0	0

LIST OF SYMBOLS

δ_{ij}	Kronecker delta
α	molecular diffusivity
ν	kinematic viscosity
ν_t	eddy viscosity
Re	numerical Reynolds number, $1/\nu$
Re_t	turbulence Reynolds number, $k^2/\nu\varepsilon$
Pr	Prandtl number, ν/α
Pr_t	turbulent Prandtl number
U_i'	total velocity
U_i	mean velocity
u_i	fluctuating velocity
Θ'	total scalar field
Θ	mean scalar field
θ	fluctuating scalar field
p	fluctuating pressure
k	turbulent kinetic energy
ε	dissipation rate of k
$\overline{\theta^2}$	scalar variance
ε_θ	dissipation rate of $\frac{1}{2}\overline{\theta^2}$
τ	turbulent timescale

REFERENCES

(1) Gibson, M. M., and Launder, B. E., 1978, "Ground effects on pressure fluctuations in the atmospheric boundary layer", *J. Fluid Mech.*, Vol. 86, pp. 491–511.

(2) Kawamura, H., and Ihira, H., 1996, "DNS and modeling of scalar transport in homogeneous turbulence", *In Engineering Turbulence Modelling and Experiments 3.*, pp. 239–249. Rodi and Bergeles, eds., *Elsevier.*

(3) Launder, B. E., 1975, "On the effects of a gravitational field on the turbulent transport of heat and momentum", *J. Fluid Mech.*, Vol. 67, pp. 569–581.

(4) Launder, B. E., 1978, "Heat and mass transport", *In Topics in Physics*, Vol. 12, pp. 231–287. Bradshaw, editor, *Springer, New York*

(5) Rogers, M. M., Mansour, N. N., and Reynolds, W. C., 1989, "An algebraic model for the turbulent flux of a passive scalar", *J. Fluid Mech.*, Vol. 203, pp. 77–101.

(6) Shabany, Y., and Durbin, P. A., 1997, "Explicit algebraic Scalar Flux Approximation", *AIAA Journal*, Vol. 35, pp. 985–989.

(7) Shih, T. H., 1996, *Chapter 4 of Turbulence and transition modeling* Hallbäck et al., eds., *Kluwer ERCOFTAC Series.*

(8) Wikström, P. M., Hallbäck, M., and Johansson, A. V., 1996, "Measurements and modeling of temperature fluctuations in a heated cylinder wake", *In Flow Modeling and Turbulence Measurements VI.*, pp. 143–150. Chen et al., eds., *Balkema.*

(9) Wikström, P. M., Hallbäck, M., and Johansson, A. V., 1998, "Measurements and heat-flux transport modelling in a heated cylinder wake", Special issue of the *International Journal of Heat and Fluid Flow*, August 1998.

A PROPOSAL FOR ANISOTROPIC EDDY-DIFFUSIVITY MODEL FOR SCALAR FLUXES

S.Fu and C.Wang

Department of Engineering Mechanics
Tsinghua University, Beijing 100084, PRC

ABSTRACT

An anisotropic eddy-diffusivity model, derived from algebraic scalar-flux model, for the scalar fluxes is proposed in the present study. The model is applied to the computation of the natural convection between two parallel plates with different temperatures. The comparisons of this model results with experiments and the computational results obtained with some other more elaborate approaches indicate similar performance quality.

1 INTRODUCTION

Modelling of the scalar fluxes, $-\overline{u_i\theta}$, in the framework of eddy-diffusivity approach has been mostly following the gradient-transport hypothesis in which the scalar flux is believed to give rise to enhanced diffusion transport through an added eddy-diffusivity coefficient Γ_t. Mathematically, the model is typically written as

$$-\overline{u_i\theta} = \Gamma_t \frac{\partial T}{\partial x_i} \qquad (1)$$

where Θ denotes to the mean scalar and Γ_t is normally related to eddy-viscosity coefficient ν_t through $\Gamma_t = \nu_t/\sigma_c$. The turbulent flux Prandtl number usually takes a value close to unity especially in the case of a passive scalar transport. The advantage of the eddy-diffusivity model (EDM) is that it offers significant simplicity in mathematical formulation and, hence, in numerical implementation. In terms of turbulence physics this scalar-flux model can provide adequate representation of the cross-stream component $-\overline{v\theta}$ when the cross-stream derivative $\partial T/\partial y$ becomes the dominant mean scalar gradient. This is the case, for instance, when the mean scalar transport is parabolic in nature with the streamwise scalar flux $-\overline{u\theta}$ being inactive to the mean scalar. In fact, $-\overline{u\theta}$ diminishes as returned from eq.(1) for $\partial T/\partial x = 0$.

However, this model behavior constitutes a major weakness in representing the streamwise scalar flux. In reality $-\overline{u\theta}$ is finite and its magnitude can be as twice larger as that of $-\overline{v\theta}$ [1]. This model deficiency will become significant when it is applied to complex scalar field. A much better approach to resolve the scalar fluxes is to solve their transport equations, but this leads to considerably increased numerical efforts. There is, however, another approach to remedy this weakness in the EDM framework. The inadequate representation of the streamwise scalar flux can be attributed to the isotropic from of the eddy-diffusivity coefficient Γ_t. Thus, adaptation of an anisotropic eddy-diffusivity coefficient in EDM may be a preferable alternative. This will retain the numerical efficiency of the EDM while capturing more scalar-flux physics and, hence, offering wider applicability.

Modelling of the anisotropic EDM has been a research focal point in recent years [1,11]. This is, at least, partly inspired by the progress achieved recently in the search of anisotropic eddy-viscosity model (EVM) or nonlinear EVM. In the formulation of the anisotropic EVM the Boussinesq viscosity model is effectively generalized by adding nonlinear strain rate and vorticity tensors to the model expression, the coefficients attached to these nonlinear terms can then be determined through a variety of routes. This approach, however, can not be adapted directly to obtain the anisotropic EDM, for the scalar-flux model must obey the consistent constraint in which the scalar fluxes have to be related to the mean scalar gradients linearly. Nevertheless, the nonlinear EVM as the explicit form of algebraic stress model (ASM) serves an appropriate guide for the derivation of the anisotropic EDM as the explicit form of algebraic flux model (AFM). Similar to the ASM which provides a set of algebraic expressions for the Reynolds stresses while keeping those important stress generation, redistribu-tion and dissipation mechanisms [10], the AFM is also a simplified form of the scalar-flux transport closure which also retains flux generation and redistribution effects. The present work represents an approach of deriving an anisotropic EDM through AFM.

The performance of the present proposal of the anisotropic eddy-diffusivity model for the scalar fluxes is examined in the computation of the natural convection between two differently heated vertical walls at a variety of Rayleigh numbers. After some extensive experimental and numerical studies [2,9,12] this case is shown to be a challenging flow to turbulence model validations. In the present computation, the present proposal is applied in conjunction with the realizable

anisotropic eddy-viscosity model, RQEVM [4], which is employed to resolve the Reynolds stresses. Thus, the present approach, in effect, requires the solution of $k-\varepsilon$ and $\overline{\theta^2}-\varepsilon_\theta$ models equations for the closures of Reynolds stresses and scalar fluxes, respectively, forming 2-equation + 2-equation, (or simply '2+2') approach. The comparison of this '2+2' approach with some of the existing closures, related to differential stress models, indicate similar quality in the present computation.

2 MATHEMATICAL FORMULATION OF THE FLOW

2.1 Mean -flow equations

The natural convection induced by two parallel vertical plates with different wall temperatures represents a one dimensional flow characterized by Prandtl and Rayleigh numbers. The mean-flow governing equations can be written as

$$\frac{\partial}{\partial y}\left(\mathrm{Pr}\frac{\partial U}{\partial y}-\overline{uv}\right)+\mathrm{Pr}\,\mathrm{Ra}\,T=0 \qquad (2)$$

$$\frac{\partial}{\partial y}\left(\frac{\partial T}{\partial y}-\overline{v\theta}\right)=0 \qquad (3)$$

which U and T are non-dimensional with κ/D and ΔT. respectively, D is the half width between the slot and ΔT is the magnitude of the difference between the wall and the centre-line temperatures. The non-dimensional parameters are:

$$Ra=\frac{g\beta\Delta TD^3}{\nu\kappa}, \qquad \mathrm{Pr}=\frac{\nu}{\kappa} \qquad (4)$$

It should be noted from eq.(2) that the flow is purely driven by the buoyancy term. It will soon be seen that eq.(3), governing the temperature distribution, is indirectly influenced by the velocity and dynamic turbulence fields through the heat fluxes. The dynamic and heat fields are therefore coupled.

2.2 The Reynolds-stress models

The present study employs two types of Reynolds-stress closures to resolve the Reynolds stresses: the basic differential Reynolds-stress model (RSM) and the RQEVM of Fu et al [4]. The RSM will be applied in conjunction with the basic eddy-diffusivity model (EDM), Sommer & So (SS) model and transport flux model (TFM) to resolve as model packages for the present flow computations. The mathematical description of the RSM can be given as follows.

2.2.1 Reynolds stress transport equations

The basic RSM equations with the buoyancy effects takes the form

$$\frac{D\overline{u_iu_j}}{Dt}=-\overline{u_iu_k}\frac{\partial U_j}{\partial x_k}-\overline{u_ju_k}\frac{\partial U_i}{\partial x_k}-g_i\beta\overline{u_j\theta}-g_j\beta\overline{u_i\theta}+d_{ij}+\Phi_{ij}-\varepsilon_{ij} \qquad (5)$$

with the diffusion, redistribution and dissipation terms adopting the following closures

$$d_{ij}=\frac{\partial}{\partial x_k}\left[\left(\nu+c_s\frac{k}{\varepsilon}\overline{u_ku_l}\right)\frac{\partial\overline{u_iu_j}}{\partial x_l}\right],$$

$$\Phi_{ij}=\Phi_{ij1}+\Phi_{ij2}+\Phi_{ij3},$$

$$\Phi_{ij1}=-c_1\frac{\varepsilon}{k}\overline{u_iu_j}+\frac{2}{3}c_1\delta_{ij}\varepsilon,$$

$$\Phi_{ij2}=-c_2\left(P_{ij}-\frac{1}{3}\delta_{ij}P_{kk}\right),$$

$$\Phi_{ij3}=-c_3\left(G_{ij}-\frac{1}{3}\delta_{ij}G_{kk}\right),$$

$$\varepsilon_{ij}=\overline{u_iu_j}\,\varepsilon/k.$$

Though eq.(5) is written in complete form, the stress convection term is actually not needed in computation as the flow can be regarded as fully-developed. The coefficients in the basic RSM take the values: $c_s=0.22$, $c_1=1.8$, $c_2=0.6$ and $c_3=0.3$.

2.2.2 The RQEVM

This model is the anisotropic eddy-viscosity two-equation model developed by Fu et al [4] based on the explicit formulation of Rodi-type algebraic stress model [10]. The actual form of the model reads

$$\overline{u_iu_j}=\frac{2}{3}\delta_{ij}k-2\nu_t\left\{S_{ij}+\frac{k}{\varepsilon}\left[\beta_2\left(S_{ik}W_{kj}+S_{jk}W_{ki}\right)-\beta_3\left(S_{ij}^2-\tfrac{2}{3}\delta_{ij}S_{kk}^2\right)\right]\right\} \qquad (6)$$

with

$$\nu_t=c_\mu^*\frac{k^2}{\varepsilon}, \qquad c_\mu^*=\frac{3\beta_1}{3-2\eta^2+6\xi^2}$$

$$\eta^2=\frac{1}{8}\left(S\beta_3\right)^2, \qquad \xi^2=\frac{1}{2}\left(\Omega\beta_2\right)^2,$$

$$S=\frac{k}{\varepsilon}\sqrt{2S_{kk}^2}, \quad \Omega=\frac{k}{\varepsilon}\sqrt{-2W_{kk}^2}.$$

Here, S_{ij} and W_{ij} represent strain rate and vorticity tensors respectively. A set of different values of the coefficients to the original proposal in the above formulations are taken: $\beta_1 = 0.178$, $\beta_2 = 0.294$, $\beta_3 = 0.294$.

In the above equations the turbulence energy and the dissipation rate are obtained through modelled transport equations. Considering one dimensional nature of the flow, the turbulence energy equation is written as

$$\frac{\partial}{\partial y}\left[\left(\mathrm{Pr}+\frac{\nu_t}{\sigma_k}\right)\frac{\partial k}{\partial y}\right]+P_k+G_k-\varepsilon=0. \qquad (7)$$

The dissipation rate equation takes the form

$$\frac{\partial}{\partial y}\left[\left(\mathrm{Pr}+\frac{\nu_t}{\sigma_\varepsilon}\right)\frac{\partial \varepsilon}{\partial y}\right]+c_{\varepsilon 1}\frac{\varepsilon}{k}\left(P_k+G_k\right)-c_{\varepsilon 2}\frac{\varepsilon}{k}\varepsilon=0 \qquad (8)$$

in the case of '2+2' approach, and

$$\frac{\partial}{\partial y}\left[\left(\mathrm{Pr}+c_\varepsilon\frac{k}{\varepsilon}\overline{vv}\right)\frac{\partial \varepsilon}{\partial y}\right]+c_{\varepsilon 1}\frac{\varepsilon}{k}\left(P_k+G_k\right)-c_{\varepsilon 2}\frac{\varepsilon}{k}\varepsilon=0 \qquad (9)$$

in the RSM solutions. The turbulence generation terms consist of two parts

$$P_k=\frac{1}{2}P_{kk}=-\overline{uv}\frac{\partial U}{\partial y} \text{ and } G_k=\mathrm{Pr}\,Ra\overline{u\theta}.$$

The first term is the conventional energy generation due to shear and the second term the energy generation through buoyancy effects.

2.3 The heat-flux models

Four different heat-flux models are to be discussed in the present work: (1) transport flux model (TFM), (2) eddy-diffusivity model (EDM), (3) Sommer & So Model (SS) and (4) the present model (FW).

2.3.1 Heat flux transport model

The closure of the heat-flux transport equations follows the analogy of the Reynolds-stress transport model. Written mathematically the closure equation has the form of [8]

$$c_{i\theta}=d_{i\theta}+P_{i\theta 1}+P_{i\theta 2}+\Phi_{i\theta}-\varepsilon_{i\theta} \qquad (10)$$

where c_{ic} and d_{ic} represent the flux convection and diffusion respectively, P_{ic1} and P_{ic2} are the flux generation terms defined as

$$P_{i\theta 1}=-\overline{u_j\theta}\frac{\partial U_i}{\partial x_j},\quad P_{i\theta 2}=-\overline{u_iu_j}\frac{\partial T}{\partial x_j}.$$

The redistribution and dissipation terms, Φ_{ic} and ε_{ic}, can be modelled to take the form [7,8]

$$\Phi_{i\theta}-\varepsilon_{i\theta}=-C_{1\theta}\frac{\overline{u_i\theta}}{T}+C_{2\theta}\overline{u_j\theta}\frac{\partial U_i}{\partial x_j}$$

$$\varepsilon_{i\theta}=0.$$

Thus, the modelled transport flux equations can be written as

$$\frac{D\overline{u_i\theta}}{Dt}=\frac{\partial}{\partial x_k}\left[c_{s\theta}\frac{k}{\varepsilon}\left(\overline{u_iu_l}\frac{\partial\overline{u_k\theta}}{\partial x_l}+\overline{u_ku_l}\frac{\partial\overline{u_i\theta}}{\partial x_l}\right)\right]$$
$$-\overline{u_iu_j}\frac{\partial T}{\partial x_j}-\overline{u_j\theta}\frac{\partial U_i}{\partial x_j}-c_{1\theta}\sqrt{\frac{\varepsilon}{k}\frac{\varepsilon_\theta}{\overline{\theta^2}}}\overline{u_i\theta} \qquad (11)$$
$$+c_{2\theta}\overline{u_j\theta}\frac{\partial U_i}{\partial x_j}+c_{3\theta}g_i\beta\overline{\theta^2}-g_i\beta\overline{\theta^2}$$

with $c_{1\theta}=3.28$, $c_{2\theta}=0.4$ and $c_{3\theta}=0.4$.

2.3.2 The EDM

The EDM is one of the most simple scalar-flux closures adapting the gradient transport hypothesis. It is usually written as

$$\overline{u_j\theta}=-\alpha_t\frac{\partial T}{\partial x_j} \qquad (12)$$

where $\alpha_t=c_\lambda k\sqrt{k\overline{\theta^2}/\varepsilon\varepsilon_\theta}$ representing the eddy-diffusivity coefficient, T the mean temperature and the coefficient $c_\lambda=0.095$.

2.3.3 Sommer & So's anisotropic model

The SS flux model was derived from the explicit formulation of the algebraic scalar-flux model (AFM) with simplification in assuming Boussinesq Reynolds stress variation in the fluxes to achieve a more compact form. A great advantage of this approach is that the buoyancy effect on the flux can be accounted for directly as it naturally appears in AFM. The model reads

$$-\overline{u_i\theta}=\alpha_t\frac{\partial T}{\partial x_i}-\frac{1}{c_{1\theta}}\sqrt{\frac{k\overline{\theta^2}}{\varepsilon\varepsilon_\theta}}\left\{\left[\left(2\nu_t+\left(1-c_{2\theta}\right)\alpha_t\right)S_{ik}\right.\right. \qquad (13)$$
$$\left.\left.+\left(1-c_{2\theta}\right)\alpha_tW_{ik}\right]\partial T/\partial x_k-\left(1-c_{2\theta}\right)g_i\beta\overline{\theta^2}\right\}$$

The model coefficients are given in [11].

2.4 The equations for $\overline{\theta^2}$ and ε_θ

In all the above flux closures the determination of the turbulent time scale for the fluxes requires the solution of the transport equations of the scalar variance $\overline{\theta^2}$ and its dissipation ε_θ. The present work adopts the following modelled forms [7,8,11]

$$\frac{D\overline{\theta^2}}{Dt} = \frac{\partial}{\partial x_i}\left[\left(k + c_{\theta^2}\frac{k}{\varepsilon}\overline{u_i u_j}\right)\frac{\partial \overline{\theta^2}}{\partial x_j}\right] - 2\overline{u_j\theta}\frac{\partial T}{\partial x_j} - 2\varepsilon_\theta \tag{14}$$

$$\frac{D\varepsilon_\theta}{Dt} = \frac{\partial}{\partial x_k}\left[\left(\kappa + c_{\varepsilon_\theta}\frac{k}{\varepsilon}\overline{u_k u_j}\right)\frac{\partial \varepsilon_\theta}{\partial x_j}\right] + c_{d1}\frac{\varepsilon_\theta}{\overline{\theta^2}}P_\theta + c_{d2}\frac{\varepsilon}{k}P_\theta + c_{d3}\frac{\varepsilon_\theta}{k}P_k - c_{d4}\frac{\varepsilon_\theta}{\overline{\theta^2}}\varepsilon_\theta - c_{d5}\frac{\varepsilon}{k}\varepsilon_\theta \tag{15}$$

The coefficients in eq.(14,15) are

$c_{\theta^2} = 0.11$, $c_{\varepsilon_\theta} = 0.11$, $c_{d1} = 1.8$, $c_{d2} = 0$, $c_{d3} = 0.72$, $c_{d4} = 2.2$, $c_{d5} = 0.8$.

3 PRESENT PROPOSAL FOR ANISOTROPIC EDDY-DIFFUSIVITY MODEL

In the algebraic simplification of the flux transport model, eq.(11), the flux convection and diffusion terms are assumed to be proportional to the transport terms of $\sqrt{k\overline{\theta^2}}$ which, in modeled form, can be written as [7]

$$c_{i\theta} - d_{i\theta} = \overline{u_i\theta}\frac{\varepsilon}{2k}(\lambda - 1) + \overline{u_i\theta}\frac{\varepsilon_\theta}{2\overline{\theta^2}}(\lambda_\theta - 1) \tag{16}$$

where $\lambda = P_k/\varepsilon$ and $\lambda_c = P_c/\varepsilon_c$ with P_k, P_c and ε_c representing the turbulence energy generation, scalar-variance generation and dissipation, respectively. Substituting relation (16) in (11) one can obtain an algebraic equation for the scalar fluxes which reads

$$\left[\frac{C_{1\theta}}{T_f} + \frac{\varepsilon}{2k}(\lambda - 1) + \frac{\varepsilon_\theta}{2\overline{\theta^2}}(\lambda_\theta - 1)\right]\overline{u_i\theta} = -(1 - C_{2\theta})\overline{u_j\theta}\frac{\partial U_i}{\partial x_j} - \overline{u_i u_j}\frac{\partial T}{\partial x_j} + (1 - C_{2\theta})G_{i\theta} \tag{17}$$

or

$$g_c\overline{u_i\theta} = -\alpha\overline{u_j\theta}\frac{\partial U_i}{\partial x_j} - \overline{u_i u_j}\frac{\partial T}{\partial x_j} + \alpha G_{i\theta} \tag{18}$$

with $\alpha = 1 - C_{2c}$ and

$$g_c = \frac{C_{1\theta}}{T_f} + \frac{\varepsilon}{2k}(\lambda - 1) + \frac{\varepsilon_\theta}{2\overline{\theta^2}}(\lambda_\theta - 1).$$

It is clear that this algebraic equation of the scalar fluxes forms a linear system whose solution can be written as

$$\overline{u_i\theta} = -\frac{(1 - A_{ll}^2/2)D_i + A_{ij}D_j + A_{ij}^2 D_j}{1 - A_{ll}^2/2 - A_{ll}^3/3} \tag{19}$$

where

$$A_{ij} = \frac{\alpha}{g_c}(S_{ij} + W_{ij}), \quad D_j = \frac{\overline{u_i u_j}}{g_c}\frac{\partial T}{\partial x_j} - \frac{\alpha}{g_c}G_{j\theta} \tag{20}$$

and $A_{ij}^2 = A_{ip}A_{pj}$. Eq.(19) formally represents the explicit expression of AFM. It can be easily manipulated to show that the explicit AFM is equivalent to an anisotropic EDM for expression (19) can be further written as

$$-\overline{u_i\theta} = \Gamma_{ij}\frac{\partial T}{\partial x_j} \tag{21}$$

with

$$\Gamma_{ij} = \frac{(1 - A_{ll}^2/2)\delta_{ip} + A_{ip} + A_{ip}^2}{1 - A_{ll}^2/2 - A_{ll}^3/3}\frac{\overline{u_p u_j}}{g_c} \tag{22}$$

being a second-rank tensor function of strain rate, vorticity and Reynolds stresses. Γ_{ij} can be referred to as the anisotropic eddy-diffusivity coefficients.

In formulating the anisotropic eddy-diffusivity coefficient Γ_{ij} *explicitly* in terms of S_{ij} and W_{ij}, decision has to be made here on what type of Reynolds-stress closures is to be implemented. In the SS-approach the Boussinesq model is opted for the Reynolds stresses [11]. Since the present modelling strategy is to follow the nonlinear EVM based on the explicit ASM, it is thus consistent to implement an explicit ASM for the Reynolds stresses here. In particular, the RQEVM, a variant of the explicit ASM, is chosen for the present purpose. This model is quadratically nonlinear and represents the analytical solution of the ASM for two-dimensional flow [6]. It has been shown that this model is able to resolve, adequately, the turbulence anisotropy when applied even to three-dimensional flow [5]. Therefore, keeping the explicit AFM formulation in 2-D form is consistent with the Reynolds-stress model and may also be a good approximation for applications for 3-D scalar transport problems.

In fact, the anisotropic EDM expressed in eq.(19) has a much simpler form in 2-D case. It can be proved that the two-dimensionality of the velocity and scalar fields leads the anisotropic eddy-diffusivity coefficient effectively to

$$\Gamma_{ij} = \frac{\delta_{ip} + A_{ip_{ip}}^{\ 2}}{1 - A_{II}^2/2} \frac{\overline{u_p u_j}}{g_c}. \qquad (23)$$

Thus, the anisotropic EDM, given in eq.(19), in 2-D case can be written as

$$\overline{u_i\theta} = -\left(\Psi_1\delta_{ij} + \Psi_2 S_{ij} + \Psi_3 W_{ij} + \Psi_4 S_{ik}W_{kj}\right)\frac{\partial\theta/\partial x_j}{g_c\left(1-\frac{1}{2}A_{qq}^2\right)} \qquad (24)$$
$$+\left(\delta_{ij} + A_{ij}\right)\frac{\alpha G_{j\theta}}{g_c\left(1-\frac{1}{2}A_{qq}^2\right)}$$

with $\Psi_1 = \frac{2}{3}k + \nu_t S_{II}^2\left(\frac{\beta_3 k}{3\varepsilon} - \frac{\alpha}{g_c}\right)$,

$$\Psi_2 = \frac{2\alpha k}{3g_c} - 2\nu_t\left[1 - \left(\beta_2 W_{II}^2 + \beta_3\frac{S_{II}^2}{6}\right)\frac{\alpha k}{g_c\varepsilon}\right]$$

$$\Psi_3 = \frac{2\alpha k}{3g_c} - 2\nu_t S_{II}^2\left[\left(\beta_2 + \frac{\beta_3}{6}\right)\frac{\alpha k}{g_c\varepsilon}\right],$$

$$\Psi_4 = 2\nu_t\left(2\beta_2\frac{k}{\varepsilon} - \frac{\alpha}{g_c}\right),$$

$$g_c = \frac{c_{1\theta}}{T_f} + \frac{\left(P_k - \varepsilon\right)}{2k} + \frac{\left(P_\theta - \varepsilon_\theta\right)}{2\overline{\theta^2}},$$

and $G_{j\theta} = -g_j\beta\overline{\theta^2}$ representing the buoyancy effect on the heat fluxes.

4 RESULT AND DISCUSSION

The anisotropic EDM proposed in relation (24) contains a free parameter α. While this parameter should take the value from the flux transport equation or be re-calibrated against experiments, application of this model to 3-D flows suggests that it may be determined from analysis. It is observed in 2-D flows that

$$S_{ik}W_{kj} = \gamma_1 S_{ik}W_{kj} + \gamma_2 S_{jk}W_{ki} \qquad (25)$$

provided $\gamma_1 + \gamma_2 = 1$. In 3-D flows this relation does not hold indicating the term related to it in eq.(24) not unique. Hence, the 2-D model (24) applied to 3-D flows may give multiple solutions for the scalar fluxes depending on the choice of γ_1 and γ_2 values. To avoid this nonuniqueness in relation (24) it is therefore appropriate to infer that $\Psi_4 = 0$, i. e., the constraint on α is

$$\alpha/g_c = 2\beta_2\, k/\varepsilon \qquad (26)$$

The implication of this constraint means that the relation (24) contains only one parameter from the scalar-flux transport equations and it affects only the overall rate of scalar diffusion.

With the assumption (26), the present anisotropic EDM has similar form to Sommer & So's model but with difference in the coefficient expressions Ψ_1, Ψ_2 and Ψ_3. The present approach still retains the non-linearity in Reynolds stress-strain relation. Also, it can be shown that the ratio of the streamwise to the cross-stream component of the scalar fluxes, in the simple shear flow with $\partial T/\partial y$ being the dominant scalar gradient, is determined sorely by the dynamic field properties. This is also a consequence of assumption (26). This model behaviour may not be desirable and should be reckoned to be a penalty caused by the 2-D assumption in the derivation of the explicit AFM, eq.(24).

Concerning the computational results Figure 1-3 show the comparisons between the present computation and experimental and DNS data. In these figures RSM indicates the basic differential Reynolds-stress model being applied for the Reynolds stresses; RQEVM refers to the nonlinear EVM of Fu et al [4]; EDM the basic eddy-diffusivity model employed for the heat fluxes; SS, FW and TFM denote to the heat-flux models being Sommer & So, the present and the basic transport types, respectively. It can be seen that RSM+EDM approach consistently over predicts the mean-flow velocity while the present approach provides somewhat under predicted values for all Rayleigh numbers. The reason for this under prediction may be attributed to the omission of the buoyancy effect in the Reynolds-stress closures, RQEVM, as can be seen from eq.(6). However, the present approach provides, generally speaking, similar results compared with the transport closures. In fact, none of the model packages can be said to have provided satisfactory results. But the present model package offers much more mathematical and computational simplicity.

5 CONCLUSION

This work presents a anisotropic EDM based on the explicit AFM. In the derivation procedure the flow is assumed to be two-dimensional which leads to a much simplified model expression while retaining the anisotropy property in the scalar fluxes. Numerical computation of the present model proposal indicates that its predictive quality is similar to those obtained with the transport closures as compared with the DNS and experimental results.

Acknowledgment This work is support by Nature Science Foundation of China, Ministry of Education, TU Berlin and Tsinghua University.

Nomenclature

D	width between the wall slot
G	generation of k due to buoyancy

G_{ij}	generation of $\overline{u_i u_j}$ due to buoyancy
g	acceleration due to gravity
g_i	i th component of gravity vector
k	turbulent kinetic energy
Pr	Prandtl number = ν/κ
P_{ij}	production of Reynolds stresses due to mean shear
P_k	production of k due to mean shear
P_θ	production of temperature variance
Ra	Rayleigh number = $g\beta\Delta TD^3/\nu\kappa$
S_{ij}	mean strain rate tensor
T	mean temperature
T_c	mean temperature at the center line
T_w	mean temperature at the wall
T^*	friction temperature
U_i	ith component of the Reynolds averaged velocity
U	Reynolds averaged velocities along x-directions
U^*	friction velocity
$\overline{u_i u_j}$	Reynolds stress
$\overline{u_i\theta}$	heat fluxes
W_{ij}	mean vorticity tensor
x, y, z	coordinates in streamwise, wall normal and transverse directions

Greek

α_t	thermal eddy diffusivity
ε	dissipation rate of turbulent energy
ε_θ	dissipation rate of temperature variance
β	coefficient of thermal expansion
κ	thermal diffusivity
ν	fluid kinematic viscosity
ν_t	eddy viscosity
$\overline{\theta^2}$	temperature variance

Reference

1. K. Abe, T. Kondoh & Y. Nagano, A new turbulence model for predicting fluid flow and heat transfer in separating and reattaching floes-I: thermal field calculations, *Inter. J. Heat Mass Transfer* 38:139-151, 1995
2. Boudjemadi, R., Maupu, V., Laurence, D., Le Quere, P. Budgets of turbulent stresses and fluxes in a vertical slot natural convection flow at Rayleigh Ra=105 and 5.4x105, *Int. J. Heat Fluid Flow*, 18, 70-79 1997.
3. T. Craft, S. Fu, B. E. Launder & D. P. Tselepidakis, Developments in modelling the turbulent seond-moment pressure correlations, UMIST, Mech. Eng. Dept. Report TFD/89/1, 1989
4. S. Fu, T. Rung & F. Thiele, Realizability of the nonlinear stress-strain relationship for Reynolds-stress closures, *11th Symp. Turbul. Shear Flows*, Sept. 1997, Toulouse, France
5. S. Fu, T. Rung & F. Thiele, C. Wang, Validation of the realizable quadratic eddy-viscosity model in turbulent secondary flow, ISCFD8, Sept., 1997, Beijing, PRC
6. T. B., Gatski and C. G., Speziale. On explicit algebraic stress models for complex turbulent flows. *J. Fluid Mech.* 254:59-78, 1993
7. M. M., Gibson An algebraic stress and heat-flux model for turbulent shear flow with streamline curvature. *International Journal of Heat and Mass Transfer,* 21:1609-1617, 1978b
8. B. E. Launder, Second-moment closure: methodology and practice, in Turbulence models and their applications, Vol. 2, ed. Launder et. al. Eyrolles, 1984
9. Nieuwstadt, F.T.M., Versteegh, T.A.M. DNS of natural convection between two vertical, differentially heated walls, *Proc. 11th Turbulent Shear Flows Symposium*, Grenoble, 1997.
10. W. Rodi A new algebraic relation for calculating the Reynolds stresses. *ZAMM* 56:219-221, 1976
11. R. M. C., So and T. P. Sommer An explicit algebraic heat-flux models for the temperature field. *Int. J. Heat Mass Transfer.* Vol. 39, No. 3, pp455-465, 1995
12. Versteegh, T.A.M., Nieuwstadt, F.T.M. Coherent structures in natural convection between two vertical, differentially heated walls, *Proc. 2nd Int. Symposium on Turbulence, Heat and Mass Transfer*, Delft, 1997.

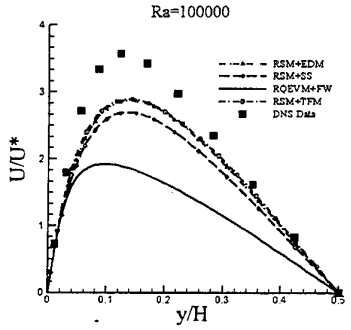

Fig 1-a

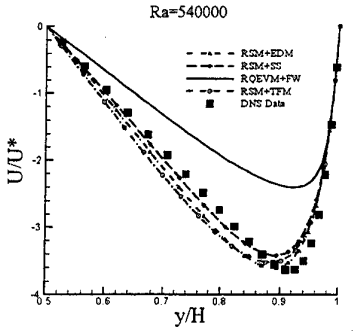

Fig 2-a

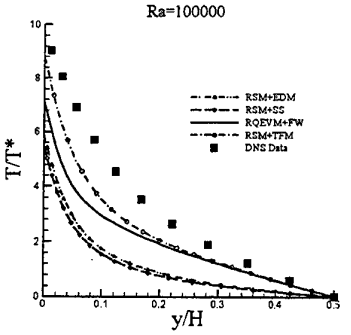

Fig 1-b

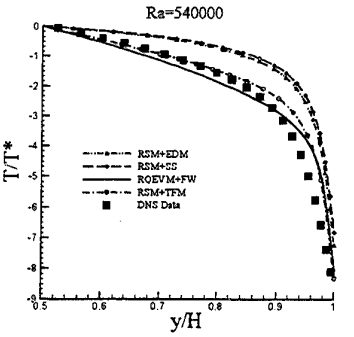

Fig 2-b

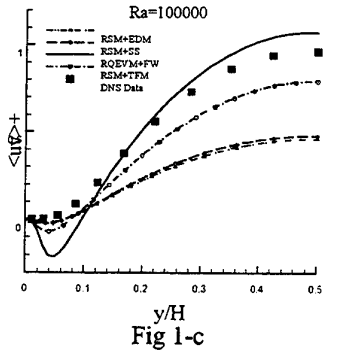

Fig 1-c

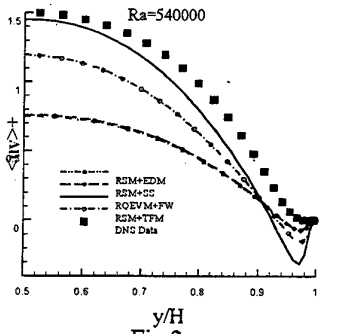

Fig 2-c

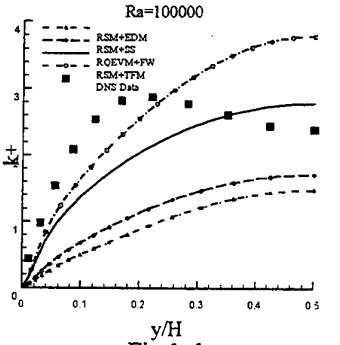

Fig 1-d

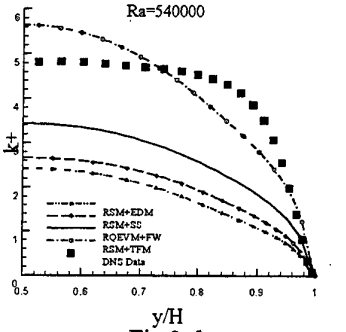

Fig 2-d

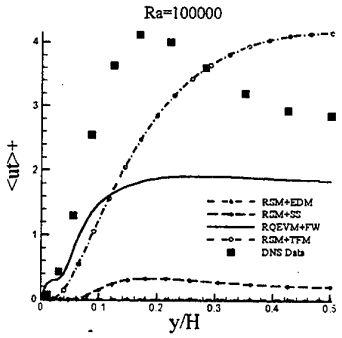

Fig 1-e

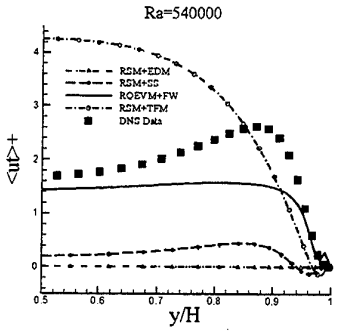

Fig 2-e

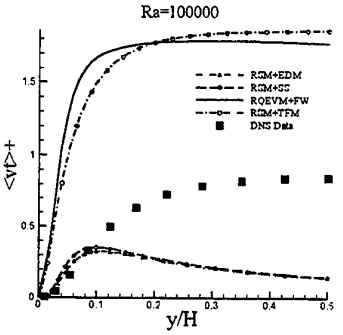

Fig 1-f

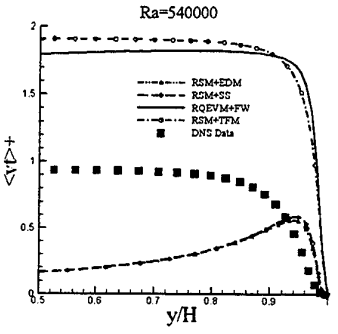

Fig 2-f

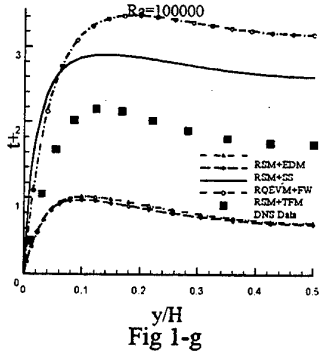

Fig 1-g

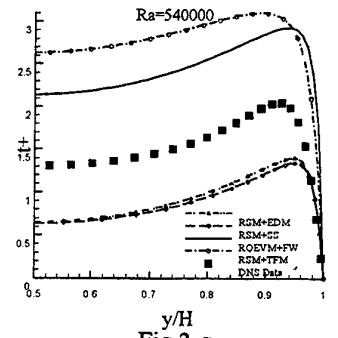

Fig 2-g

Figure 1 Comparisons of cross-sectional profiles for the natural convection between two parallel walls with different temperatures, Ra=100000 [2]

Figure 2 Comparisons of cross-sectional profiles for the natural convection between two parallel walls with different temperatures, Ra=540000 [2]

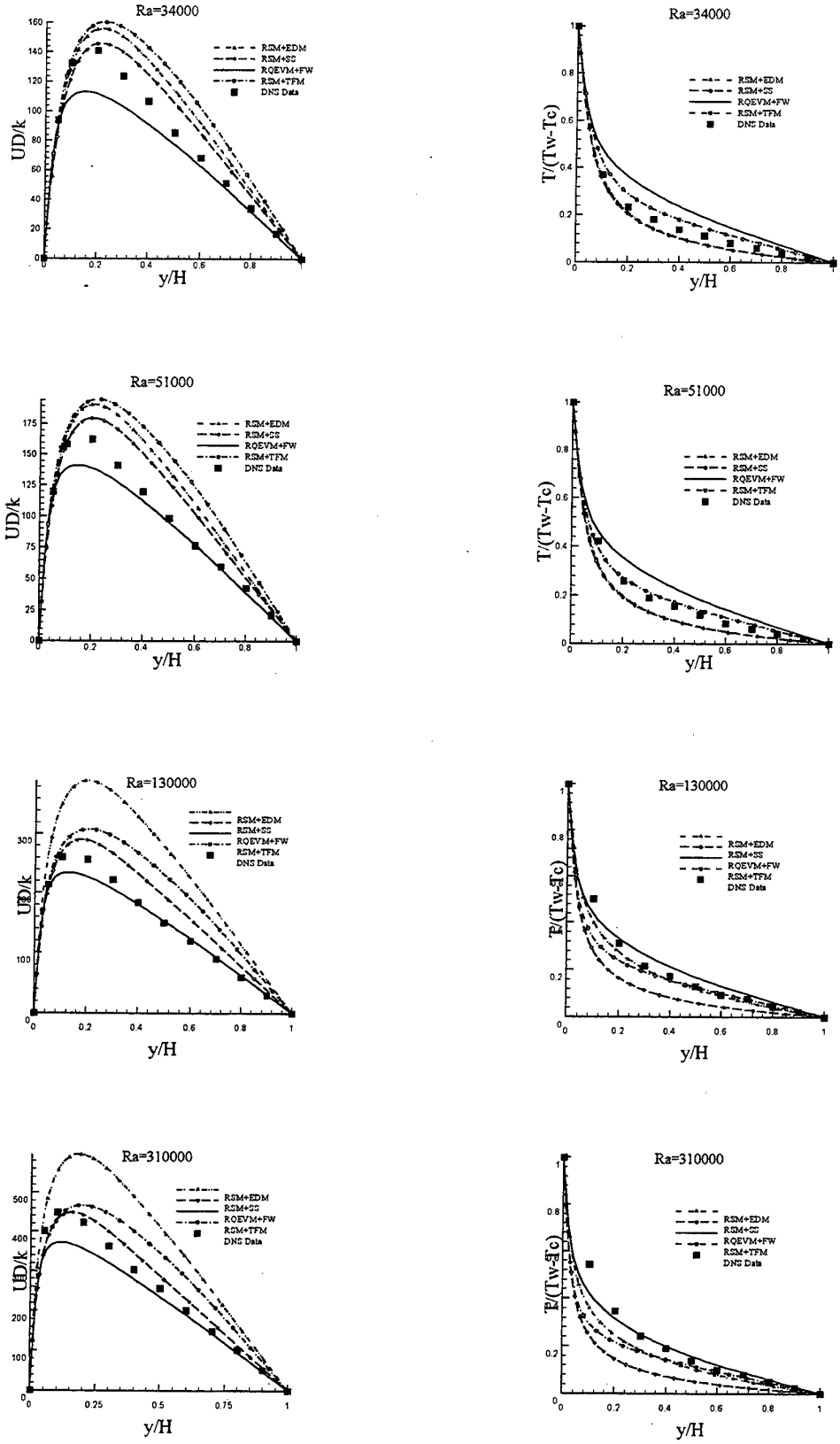

Figure 3 Comparisons of cross-sectional profiles for the natural convection between two parallel walls with different Rayleigh numbers. The DNS data are from [9,12].